

# RECENT ADVANCES IN REFRACTORY ALLOYS FOR SPACE POWER SYSTEMS

[REDACTED]



NATIONAL AERONAUTICS AND SPACE ADMINISTRATION



# RECENT ADVANCES IN REFRACTORY ALLOYS FOR SPACE POWER SYSTEMS

A conference held at  
Lewis Research Center, Cleveland, Ohio  
June 26, 1969

Prepared by Lewis Research Center



*Scientific and Technical Information Division*  
OFFICE OF TECHNOLOGY UTILIZATION  
NATIONAL AERONAUTICS AND SPACE ADMINISTRATION  
1970  
Washington, D.C.

## FOREWORD

Numerous materials technology programs have been conducted over the past years in support of advanced nuclear space power systems. The performance that might be achieved by these systems can be limited by one or more properties of the materials utilized in construction. The systems requirements are characterized by very high temperatures, 2000<sup>0</sup> F and above, and very long service lives. The materials limitations may be strength, corrosion, or fabricability of available materials.

The results of the many programs in materials technology have been or will be reported in various publications. All of these data will be published in the course of time, but at present the data are scattered. Because of the considerable work already completed, a summary of the field is timely.

In a meeting under the chairmanship of Thomas A. Moss, material was presented that had been prepared by contractor personnel from information generated under contracts to the NASA Lewis Research Center. The NASA Project Managers for the contracts were Thomas A. Moss, Robert L. Davies, and Paul E. Moorhead of the Lewis Research Center Space Power Systems Division.

**Page intentionally left blank**

## CONTENTS

|  | Page |
|--|------|
| I. REFRACTORY-ALLOY REQUIREMENTS FOR SPACE POWER SYSTEMS                                 |      |
| T. A. Moss, R. L. Davies, and G. J. Barna . . . . .                                      | 1    |
| II. DEVELOPMENT OF HIGH STRENGTH TANTALUM BASE ALLOYS                                    |      |
| R. W. Buckman, Jr., and R. T. Begley . . . . .   | 19   |
| III. THERMAL STABILITY OF REFRACTORY METAL ALLOYS  |      |
| G. G. Lessmann and R. E. Gold . . . . .  | 39   |
| IV. CREEP BEHAVIOR OF REFRACTORY ALLOYS IN ULTRAHIGH VACUUM                              |      |
| K. D. Sheffler, J. C. Sawyer, and E. A. Steigerwald . . . . .                            | 75   |
| V. EFFECT OF HEAT TREATMENT ON CREEP PROPERTIES OF THE<br>TANTALUM BASE ALLOY ASTAR-811C |      |
| D. L. Harrod and R. W. Buckman, Jr. . . . .  | 127  |
| VI. HIGH FREQUENCY FATIGUE PROPERTIES OF TZC AND T-111 ALLOYS                            |      |
| E. A. Steigerwald, K. D. Sheffler, and J. C. Sawyer . . . . .                            | 143  |
| VII. FABRICATION OF T-111 TEST LOOP SYSTEMS  |      |
| W. R. Young . . . . .  | 165  |
| VIII. T-111 ALLOY CRACKING PROBLEMS DURING PROCESSING AND<br>FABRICATION                 |      |
| R. A. Ekvall, R. G. Frank, and W. R. Young . . . . .                                     | 221  |
| IX. WELDABILITY OF TUNGSTEN BASE ALLOYS  |      |
| G. G. Lessmann and R. E. Gold . . . . .  | 261  |

# I. REFRACTORY-ALLOY REQUIREMENTS FOR SPACE POWER SYSTEMS

T. A. Moss,\* R. L. Davies,\* and G. J. Barna\*

## SUMMARY

Various types of large nuclear space power systems are being investigated in support of missions projected for the post-1980 period. Among the approaches being considered to meet projected needs are the potassium Rankine cycle, Brayton cycle, and thermionic systems operating at relatively high temperatures in order to achieve high performance. All these systems require refractory alloys for structural purposes and employ alkali metals as process fluids. Heat for driving the systems would be supplied by a liquid-metal-cooled fast reactor. In the potassium Rankine engine, liquid potassium is vaporized in a boiler and used to power a vapor turbine similar to a central station steam-electric powerplant. Inert gas is compressed, heated, and expanded through a turbine in the Brayton cycle similar to air in the jet engine. Thermionic systems are dependent upon boiling electrons off a hot nuclearly heated surface and collecting them on a colder adjacent surface. The Rankine engine is characterized by a moderate system efficiency and small radiator; the Brayton cycle usually exhibits a high efficiency with a relatively large radiator but a relatively low system efficiency. The system specific weights for the Rankine and Brayton engines are approximately the same, while that of the thermionic system would be higher. Technology programs have been conducted in support of all three types of systems and, in particular, considerable effort has been placed on characterizing the refractory alloys which would be required for the construction of the systems. Papers presented in this report are the result of these refractory-alloy technology programs.

## INTRODUCTION

Since the beginning of the space age with the launching of the first Sputnik, electric power used on spacecraft of all types has continued to increase from tens

---

\*NASA Lewis Research Center, Cleveland, Ohio.

of watts to the low-kilowatt level. This growth of auxiliary electric power for space applications is compared to the growth of power requirements for aircraft in figure I-1. Power requirements started out at relatively low levels for airplanes like the Ford Trimotor and gradually increased over the years as the size of the aircraft and mission requirements increased. Larger power requirements for cabin air-conditioning, communication, navigation aids, weapon systems, and countermeasures gradually increased the amount of electric power needed to sustain normal operation. Although in recent years the rate of growth of demand by aircraft for electric power has diminished, the required powers have increased to several hundred kilowatts.

Not unlike aircraft, the power requirements for spacecraft started at a relatively low level (fraction of a kilowatt) and, as the sophistication of the missions increased, the demand for power increased over the years. The power requirements for nearly all the unmanned satellites have been met by utilizing a combination of solar cells and batteries, while the manned spacecraft have utilized both fuel cells and batteries. Unmanned spacecraft like Nimbus and OAO typically require between 400 and 800 watts of electrical power, which is easily met by solar cells and batteries. Solar-cell systems as large as 3 kilowatts have been flown in a few unmanned satellites, and it is likely that solar-cell systems in the tens of kilowatts will be flown in the 1970's. However, because of the low efficiency of the solar cell and the low power density of solar flux, the relatively large areas and orientation toward the Sun which solar panels require limit their usefulness for these large powers.

Manned spacecraft have used hydrogen-oxygen fuel cells coupled with batteries to meet their present needs. An inherent characteristic of the fuel cell is that it requires a continual supply of reactants in order to produce power; therefore, for long missions the weight of the power supply is directly proportional to the length of the mission. For missions longer than 1 or 2 months, more advanced systems using nuclear energy as the power source appear more promising because of their lower specific weights. Earth-orbiting space laboratories are presently estimated to require a few hundred kilowatts of electric power during the early 1980's.

Several types of power systems could potentially satisfy these demands for electric power for future Earth-orbit space missions. The general area in which each type of power system has the lowest weight is shown in figure I-2. For missions longer than 10 weeks and requiring powers of 100 kilowatts or more, nuclear reactor systems offer advantages over the solar-cell and fuel-cell systems used on space missions to date. These future reactor systems which will produce high power for long times are discussed in this paper.

In order for these reactor power systems to be both compact and of low weight,

they must have the following general characteristics. The nuclear reactor must be small in size, for reactor size has a marked effect on shield weight, which is substantial for manned missions. The alkali liquid metals permit high heat-transfer rates and thus help reduce reactor size if they are used as the reactor coolant. Attainment of high efficiency in the conversion of heat into electric power also helps decrease weight per electric kilowatt for the reactor and shield, simply because a larger amount of electric power can be produced from a given reactor and shield if the conversion efficiency is high. For thermionic systems, the great sensitivity of this conversion efficiency to operating temperatures makes desirable the use of the highest practical temperatures. Radiator size is another factor affecting both the size and weight of these power systems, and high operating temperatures drastically reduce radiator size. Therefore, for all these reactor power systems, alkali liquid metals and the highest practical operating temperatures (perhaps 2000° F or higher) are both desirable.

Operating at temperatures of 2000° F or above presents a number of materials problems, but especially alloy strength and compatibility with the process fluids. Figure I-3 shows the typical strength of superalloys and tantalum alloys. Because these nuclear power systems are required to operate for several years, the data shown are for 1 percent creep in 3 years. The superalloys have little strength at temperatures above 1600° F; for higher temperatures, refractory alloys must be considered. Shown specifically are data for the relatively fabricable tantalum-base alloys, which have strength over the temperature range 1800° to 2600° F superior to that of most other alloys. It is, in part, for this reason that the tantalum alloy T-111 (Ta-8W-2Hf) has been selected as the reference alloy for most high-temperature space power systems.

The use of refractory alloys and the 2000° F temperature limits the substances that can be employed for process fluids to the inert gases and alkali metals. Inert gases can be used with confidence over the temperature range of interest and present no compatibility problem with refractory alloys if they are maintained free of oxygen and other contaminants. Alkali metals must also be kept free of contaminants if compatibility with the refractory metals is to be maintained. In addition, extreme care must be exercised to prevent contamination of the refractory alloy with oxygen during processing, fabrication, and terrestrial testing.

As shown in figure I-4, the alloy Ta-10W is severely attacked by potassium at 1800° F, the potassium penetrating the whole wall thickness of the refluxing capsule within 128 hours. On the other hand, exposure of the T-111 (Ta-8W-2Hf) alloy in figure I-5 to potassium at 2400° F for 2000 hours resulted in essentially no attack. These alloys are nearly identical in composition except for the addition of the 2 weight percent hafnium to the T-111 alloy. In the case of the Ta-10W, oxygen

picked up during processing and testing is dissolved in the tantalum base matrix and produces a high oxygen concentration at the grain boundaries. The alloy is then susceptible to preferential attack by the alkali metal in these regions of high oxygen content, oxygen and base metal being removed by the alkali metal to form voids along the grain boundaries. This type of intergranular attack is clearly visible in the Ta-10W alloy.

Hafnium in the T-111 alloy getters oxygen picked up during processing or testing, combining with it to form the very stable hafnium oxide ( $\text{HfO}_2$ ). This oxide is relatively unaffected by the alkali metal, as are the pure elements columbium, tantalum, tungsten, molybdenum, and rhenium. If, however, the hafnium in the alloy becomes totally oxidized, the Ta-10W and T-111 alloys behave similarly, both being attacked. The control of the oxygen level and the gettering of any oxygen in the containment alloy are thus the most important items in successfully containing alkali metals. In general, alloys containing hafnium display negligible corrosion in contact with the alkali metal for periods of up to 10 000 hours at temperatures up to at least 2200° F when the proper procedures are followed.

Since alkali metals are desired as process fluids for these high-temperature nuclear systems, most of the alloys being considered for these systems contain a gettering element such as hafnium. In addition, stringent controls are exercised throughout the programs conducted in support of these systems in order to limit the amount of oxygen present in the alloy, in the alkali metal, or added during either welding or testing.

A number of different schemes can be employed to convert the thermal energy from a nuclear reactor into electricity. Three basic types of systems which are presently being actively developed by NASA for large nuclear power requirements are the potassium Rankine cycle, the Brayton cycle, and thermionic systems. In the potassium Rankine system, potassium vapor is used to drive a turbine similar to steam in a central powerplant. For the Brayton-cycle system, inert gas is compressed, heated, and then expanded through a turbine as is done in the jet engine; and the thermionic systems depend upon boiling electrons off the hot surface of an electron emitter and collecting them on a cooler surface, thereby generating a voltage between the hot and cold electrodes. Each of these approaches has its own inherent advantages and disadvantages, which are covered later in this paper, and they must operate at temperatures of the order of 2000° F or above in order to achieve low specific weights. It will be shown that each system utilizes refractory alloys for structural purposes and requires alkali metal loops to transport heat about the system.



## POTASSIUM RANKINE CYCLE

The potassium Rankine system is shown schematically in figure I-6. The engine consists of four separate fluid loops: an all-liquid reactor loop, a two-phase power-conversion loop, an all-liquid waste-heat-rejection loop, and an all-liquid cooling loop. In the reactor primary loop, lithium at  $2100^{\circ}\text{F}$  is pumped through the nuclear reactor, where it is heated to  $2200^{\circ}\text{F}$ . The lithium then flows through a tube-and-shell counterflow heat exchanger, where heat from the lithium is used to boil potassium; from this heat exchanger, the lithium is returned to the primary pump.

In the boiling-and-condensing power conversion loop,  $1000^{\circ}\text{F}$  potassium is discharged from the pump through the boiler, where it is converted from liquid to superheated vapor at  $2100^{\circ}\text{F}$ . The high-pressure potassium vapor is expanded through a turbine which is used to turn an alternator and generate electricity. From the turbine the mixture of vapor and liquid at  $1220^{\circ}\text{F}$  is exhausted into the condenser, where the remaining vapor is condensed. The tube-and-shell condenser is cooled by  $980^{\circ}\text{F}$  sodium-potassium eutectic (NaK), which is circulated to a space radiator by a pump; waste heat from the cycle is rejected by radiation from this radiator to space. The low-temperature-potassium cooling loop is an appendage of the power-conversion loop and is used to provide  $700^{\circ}\text{F}$  potassium lubricant to the turboalternator bearings and cooling to electrical windings.

Lithium is used in the primary loop to cool the reactor because of its relatively low vapor pressure at  $2200^{\circ}\text{F}$  and its high specific heat, which results in low pumping power. Potassium is selected for the two-phase working fluid because of its appropriate vapor pressure for this application. NaK is utilized in the radiator because its relatively low melting temperature prevents freezing of the fluid during initial startup of the engine. Fluid in each of the loops could be circulated by electromagnetic pumps, although centrifugal pumps would improve system efficiency. All of the piping and major components in the lithium primary and two-phase potassium loops are of refractory metal; transition from refractory alloys to superalloys is made between the condenser and the radiator.

An artist's sketch of the system and its major components as configured for an unmanned spacecraft is shown in figure I-7. The nuclear reactor is placed at the cone apex or nose of the payload with a shadow nuclear shield of tungsten and lithium hydride immediately below it. The remaining power conversion components and the rest of the spacecraft are hidden behind the shadow shield, where the radiation dose rate is of an acceptable level, usually  $5 \times 10^{12}$  nvt for unmanned applications. Shaping of the various components and lines is used to obtain efficient compact packaging of the engine within its radiator. Typically, conical or cylindrical radiators are

used for these engines. One of the biggest advantages of the Rankine engine is that its relatively high main radiator temperature results in a relatively low specific radiator area (approx.  $3 \text{ ft}^2/\text{kWe}$ ),<sup>1</sup> which can easily be fitted on available launch vehicles. The net system efficiency for a nominal-300-kilowatt-electric Rankine system is approximately 19 percent at the temperatures shown in figure I-6.

A conceptual 2-megawatt-thermal fast-spectrum nuclear reactor which could be used in conjunction with the Rankine and other power conversion systems is shown in figure I-8. The once-through lithium-cooled reactor consists of approximately 250 fuel elements containing uranium-235 nitride fuel clad in T-111 tantalum alloy. Uranium nitride was selected as the fuel form because of its relative compatibility with the lithium coolant as compared to the oxide or carbide. However, a 5-mil tungsten barrier must be interposed between the nitride fuel and the 60-mil T-111 cladding in order to prevent reaction between the fuel and hafnium in the cladding. The fuel elements are not vented and, therefore, the cladding must withstand fission-gas pressure buildup during the lifetime of the reactor. Each fuel element will be approximately 3/4 inch in diameter and be contained in a honeycomb matrix of T-111 tubes.

Control of the reactor is achieved by rotating six control drums containing fuel in half the drum and tantalum (T-111) neutron absorber on the opposite half with electric stepping motors external to the pressure vessel. As fuel is turned toward the center of the core and tantalum neutron absorber moves away from the core, reactor reactivity can be increased in order to compensate for fuel burnup. Conversely, rotating the fuel out and tantalum in reverses the process. Each control drum assembly is supported on lithium-lubricated bearings.

The pressure vessel would be fabricated from T-111 alloy, as would be the whole primary loop. The approximate overall dimensions of the pressure vessel would be an outside diameter of 23 inches and a length of 32 inches. Estimated fuel burnup of such a reactor would be approximately 3.8 atomic percent in 50 000 hours.

The potassium boiler (fig. I-9) is a counterflow tube-and-shell heat exchanger in which the hot lithium is used to vaporize and superheat the potassium to  $2100^\circ \text{F}$  and 163 psia. For a 2-megawatt-thermal boiler, approximately 31 tubes of 0.5-inch diameter, 0.035-inch wall, and 80-inch length are required to provide the necessary heat-transfer area. Special twisted-tape or wire-coil inserts are used in each tube to enhance heat transfer and avoid possible zero-gravity effects on the boiling process. The T-111 alloy is used throughout, and the boiler is designed in

---

<sup>1</sup>All specific radiator areas are based on total radiator area, i.e., sum of the main radiator, intermediate temperature radiator, and electronic coolant radiator areas necessary for controls and pump power conditioning.

a C-shaped configuration to accommodate differential thermal expansion between the relatively hot shell and cooler tubes.

One potassium turboalternator being considered for the Rankine engine consists of a 10-stage axial-flow turbine straddle mounted on potassium-lubricated bearings and flexibly coupled to the alternator, which also has its own set of potassium-lubricated bearings. Potassium vapor entering the turbine at  $2100^{\circ}\text{F}$  is expanded through the first five stages and is then ducted from the turbine to an external moisture separator or reheater. The dry or nearly dry vapor then passes through the last five stages and exits at approximately  $1220^{\circ}\text{F}$  and 5.4 psia to the condensers. Interstage moisture extraction might be employed prior to the last-stage rotor in order to maintain the potassium quality at a high enough level. Turbine tests presently under way will help determine the vapor quality required in order to keep erosion damage to the blades at an acceptable level.

Scroll and casing for the first five stages would be T-111 alloy for temperature resistance, while the intermediate and exit scrolls and the aft casing would be Cb-1Zr alloy for reduced weight, as shown by figure I-10. TZM (Mo-0.5Ti-0.08Zr) has been selected for the turbine rotor and blades because of its superior strength-to-density ratio at the design conditions. The turboalternator would be approximately 6 feet long and 2 feet in diameter at the alternator and would weigh approximately 1300 pounds.

## BRAYTON CYCLE

Another high-temperature dynamic system of interest for high power levels is the Brayton-cycle engine shown in figure I-11. A reactor similar to that used for the Rankine engine would supply heat to, say, four parallel power conversion systems, one of which is shown. Lithium, exiting the reactor at  $2200^{\circ}\text{F}$ , would heat in a compact heat exchanger a compressed mixture of He-Xe gases, with an average molecular weight of approximately 40. This molecular weight is the same as that of argon; however, the mixture is used because it has relatively high thermal conductivity owing to the helium, while the average molecular weight of argon favors the performance of the compressor in the system.

In the power conversion loop, the inert gas is compressed by the compressor, preheated to  $1443^{\circ}\text{F}$  in the recuperator, heated to  $2100^{\circ}\text{F}$  in the heat-source exchanger, and then expanded through the turbine to produce mechanical energy. The turbine exhaust energy is then used in the recuperator to preheat the compressor discharge and so increase the overall cycle efficiency. One of the main advantages of this cycle is its high overall efficiency of approximately 25 percent.

The turbine exhaust, after leaving the recuperator, is ducted to the waste heat exchanger and then back to the compressor to complete the closed cycle. Waste heat from the cycle is transported from the waste heat exchanger to the radiator by means of a liquid coolant loop of highly refined mineral oil. A separate organic loop is used to cool bearings and electrical equipment. Since the radiators for this engine operate at such relatively low temperatures ( $556^{\circ}$  to  $211^{\circ}$  F), the specific radiator area for the engine is approximately 15 square feet per kilowatt electric, or roughly five times as large as for the Rankine engine. Refractory metals need be used only in the reactor primary loop, heat-source heat exchanger, turbine, and turbine scroll of this engine.

A compact heat-exchanger core similar to that required for the heat-source heat exchanger of the Brayton engine is shown in figure I-12. It consists of a liquid manifold feeding 21 tubes of 1/8-inch diameter, each tube having 30 extended-surface fins per inch along its length. In the design shown, the liquid makes eight passes as it loops up and down across the gas duct. Such a heat exchanger for the high-temperature Brayton engine would be constructed primarily from T-111 but would possibly have Cb-1Zr fins brazed to the tubes.

Figure I-13 is an isometric drawing of a possible configuration for a high-temperature Brayton rotating unit with the turbine, alternator, and compressor all on the same shaft. A single-stage radial-flow turbine is employed instead of a multistage axial turbine as was used for the Rankine engine. A single-stage radial-flow compressor is also used. Hydrodynamic gas bearings are shown supporting the shaft; however, oil-lubricated bearings are also being considered. The high-temperature Brayton rotating unit will probably operate above 24 000 rpm, and windage loss caused by the drag of gases in the alternator rotor cavity is of serious concern in the design of the machine. For this reason, the alternator will have a smooth rotor.

## NUCLEAR THERMIONIC SYSTEMS

Thermionic static conversion systems are also being considered for large space electric power systems. As mentioned earlier, the basic phenomenon of the thermionic system depends upon boiling electrons off a hot emitter surface of a diode and collecting them on the nearby cold collector surface; useful work is done in an external load as the electrons are returned to the emitter. Typically, a very high temperature is required in order to maintain the thermionic process, a factor which limits the materials used in these devices to the refractory metals. Nuclear systems using the thermionic principle may contain the diodes within the reactor

core or may use a liquid-metal-cooled reactor similar to the one previously described and place the diodes external to the core within a liquid-to-liquid heat exchanger.

A schematic of the in-core thermionic system in figure I-14 shows the system to consist of three major components: reactor, radiator, and electromagnetic pump. An alkali metal is used to transport the waste heat of the system from the diode collector within the core to the radiator. Also, figure I-14 shows a cross section of a typical flashlight diode array. Uranium dioxide or carbide fuel is encapsulated by vapor-deposited tungsten, which acts as the diode emitter. Tungsten with preferential crystal orientation is used for the emitter in order to increase the performance of the diode. Compatibility of the fuel with the cladding and fuel swelling during operation at  $3000^{\circ}\text{F}$  are major problem areas of the system.

The hot emitter is separated from the columbium collector by 10 mils. The separation distance between the emitter and collector has a large effect on the performance of the diode and must be maintained within acceptable levels. The gap between the collector and emitter usually contains cesium at a low (perhaps 1 torr) pressure in order to increase diode performance and stability. Each diode emitter is separated from another by alumina insulation. Alumina is also used to insulate the collectors from each other and from the coolant channel. Degradation of the insulators by neutron damage may be one of the major problems of the concept.

The power density of the diode depicted in figure I-14 might be 11 watts per square centimeter at 0.7 volt. Within each flashlight string, the diodes are connected in a series. Individual strings within the reactor would then be connected in a series-parallel array in order to achieve the desired voltage output from the system. Net system efficiency of approximately 12 percent may be achieved with a specific radiator area of about 5 square feet per kilowatt electric, which is somewhat higher than for the Rankine engine. Reactor size would also be increased by the volume occupied by the diodes.

Figure I-15 shows the schematic for the thermionic system in which the diodes are contained in a heat exchanger external to the reactor core. Lithium, circulated by an electromagnetic pump, is heated in the reactor to  $2800^{\circ}\text{F}$  and used to heat the diode emitters in the heat exchanger. The heat exchanger is made up of a large number of diode strings similar to that shown in the cross section (fig. I-14). Hot lithium flows down the center T-111 tube, which is surrounded by the individual diodes. The oriented-tungsten emitter, the lithium-containment tube, and the alumina insulator separating them form a monolithic bonded structure which is referred to as a trilayer. A metallurgical bond must be maintained between the individual layers of the trilayer if adequate thermal conductivity is to be maintained between the emitter surface and the hot lithium.

A second trilayer is required between the collector and the NaK coolant of the radiator loop. As before, diodes in a string are connected in series. The power density of these converters would be approximately 6 to 8 watts per square centimeter at 0.5 volt, and system efficiency would be about 10 percent. Since the radiator temperature is lower than for the in-core system and efficiency is also lower, the specific radiator area is higher by about 8 square feet per kilowatt. The transition between refractory alloys and superalloys would be made between the diode heat exchanger and the radiator.

## PROGRAM APPROACH

The program approach which has been used to develop space electric power systems for future space missions has included the following procedures: conceptual engines were defined to satisfy general mission application, power ranges, and lifetimes, after which the engines were analyzed for potential problem areas where technology programs had to be undertaken to support their development. As an example, extensive technology programs were conducted in the areas of turbine erosion, boiling heat transfer, alkali-metal compatibility, and refractory-alloy strength. Work on gas bearings was done in support of the Brayton cycle engine, while for the thermionic system primary emphasis has been on the diodes. After the supporting technology is well in hand and understood, a more definitized or nominal engine is evolved, and development of major engine components is undertaken. Following component demonstration, proven components will be integrated into a complete nuclear system, which will be tested in the Space Power Facility at Plum Brook.

The refractory-metal technology which is covered in the remaining papers was performed in support of the various systems that have been described. At the present time, most of the technology necessary to support development of major components has been completed, and some components such as the boiler-feed pump for the Rankine engine are built and ready for testing. During the next 2 or 3 years, the emphasis of the program will continue to shift from supporting technology to component development in which new problems associated with building hardware will be encountered.

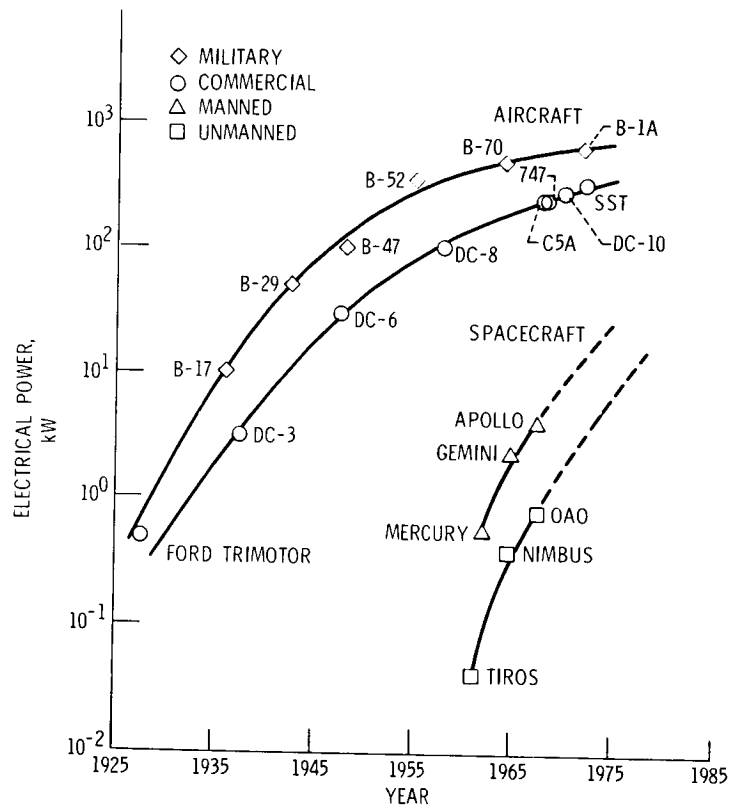


Figure I-1. - Growth of aeronautical and space power systems.

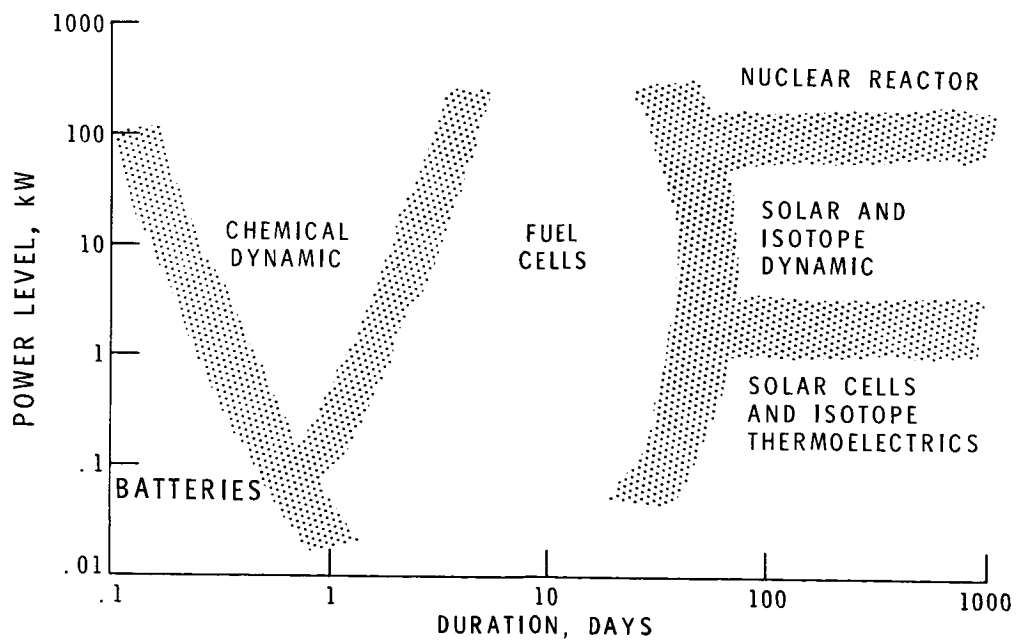


Figure I-2. - Electric power systems for Earth orbit.

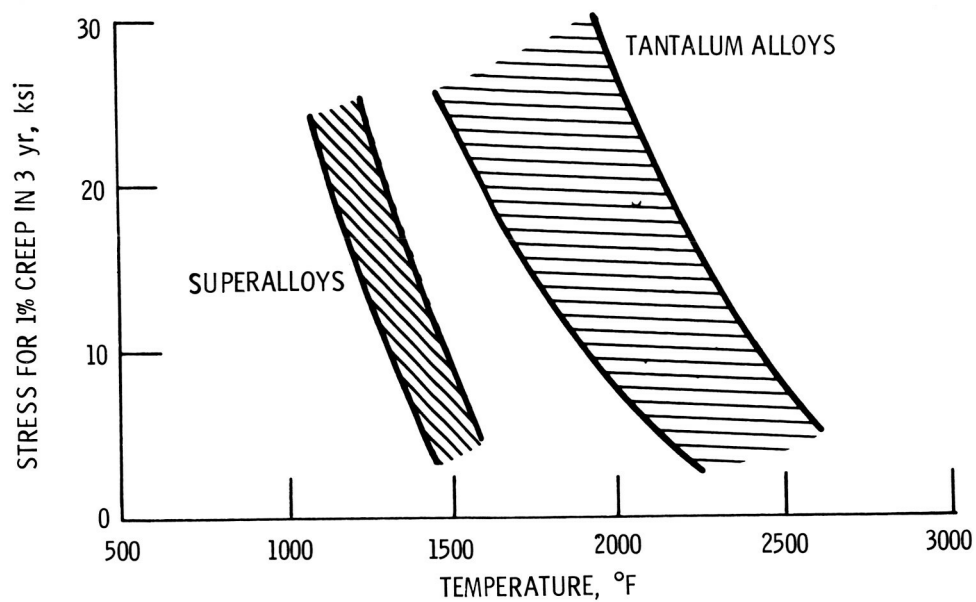


Figure I-3. - Strength capability of tubing alloys.

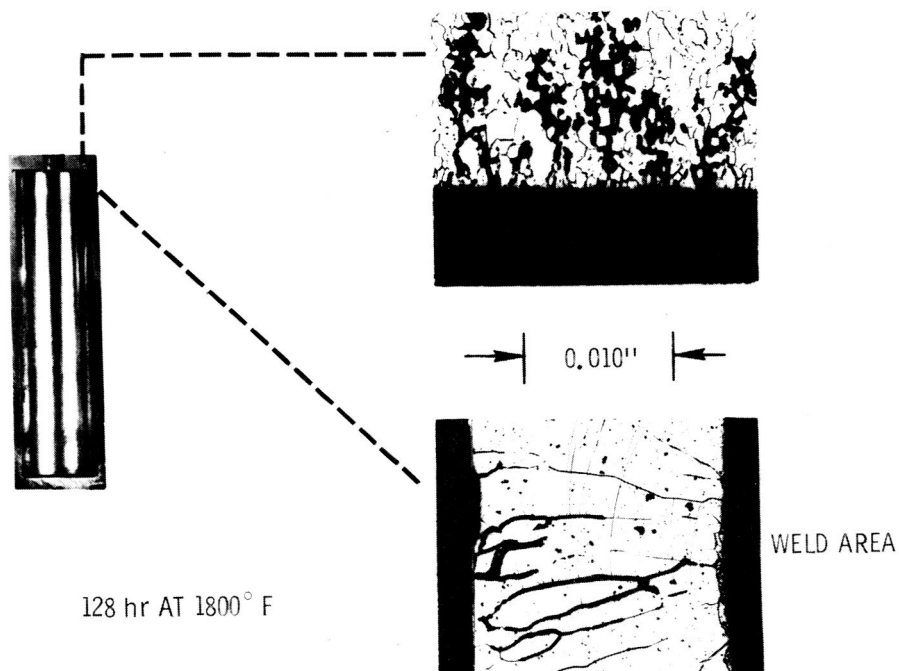


Figure I-4. - Corrosion of tantalum-10 tungsten alloy by potassium. Ungettered alloy.



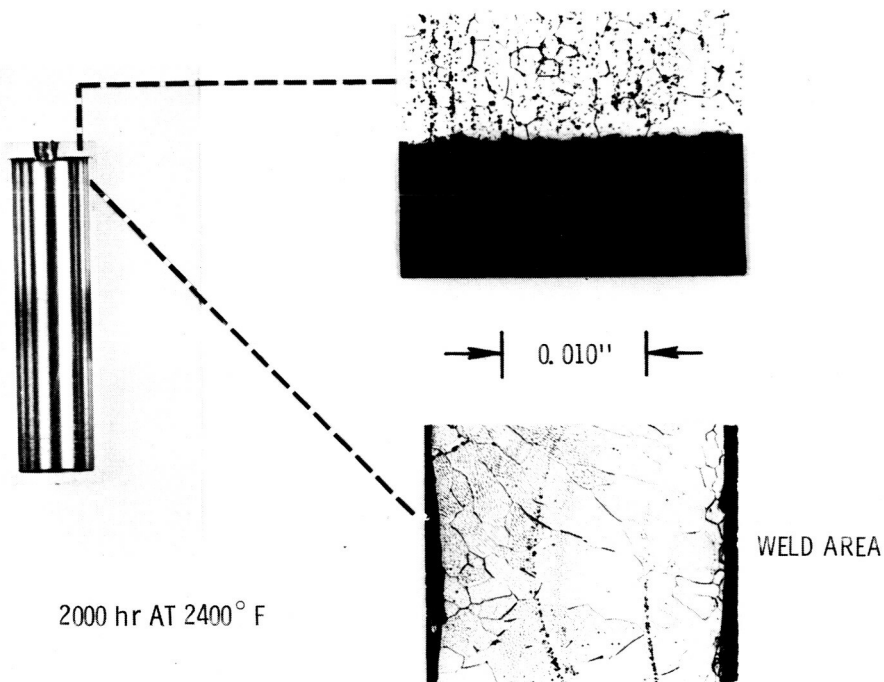


Figure I-5. - Corrosion of T-111 alloy by potassium. Gettered alloy.

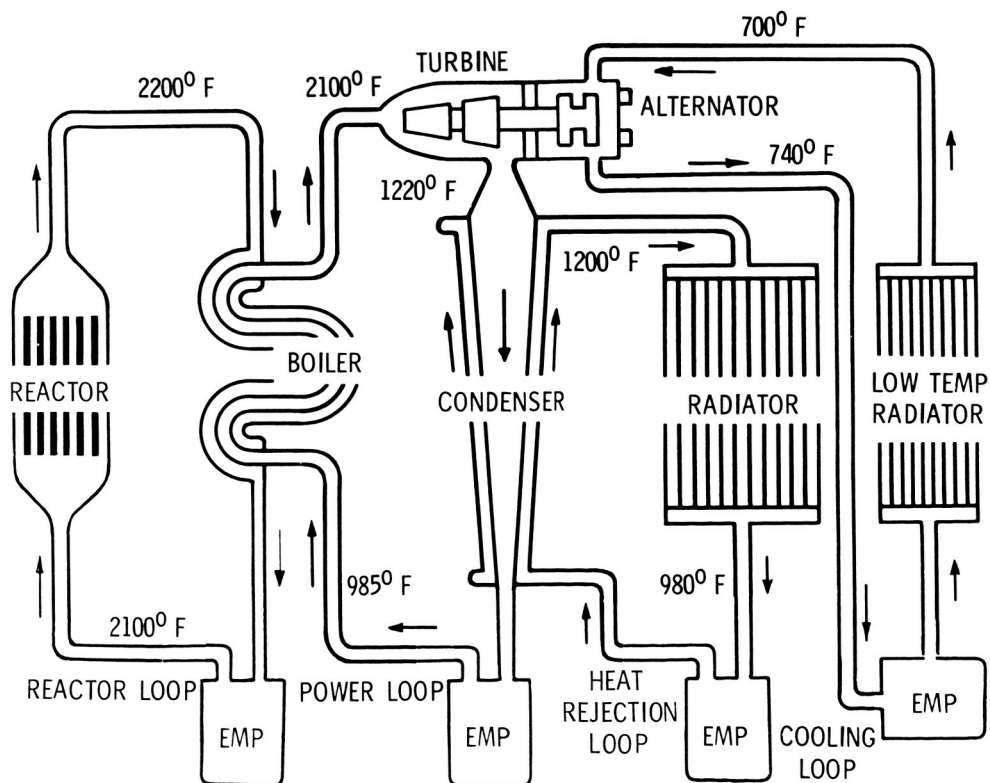


Figure I-6. - Potassium Rankine system.

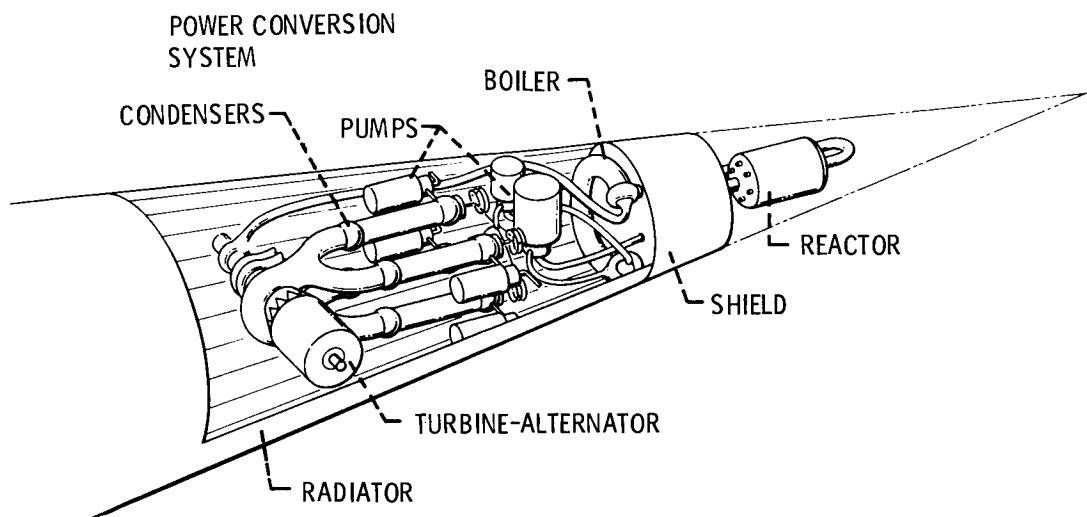


Figure I-7. - Typical flight configuration.

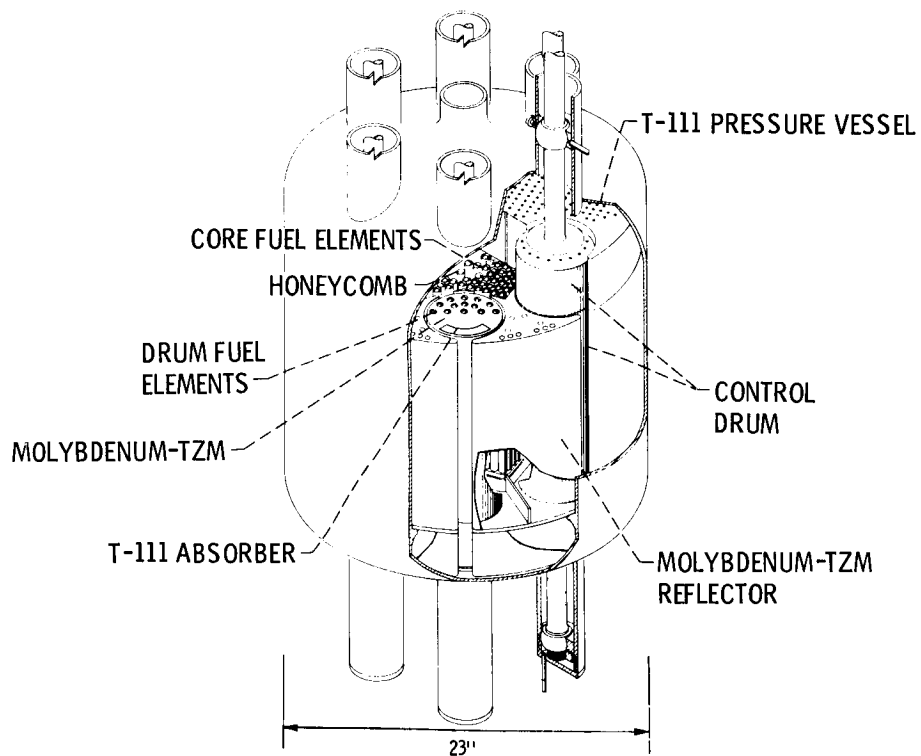


Figure I-8. - Nuclear powerplant reactor.

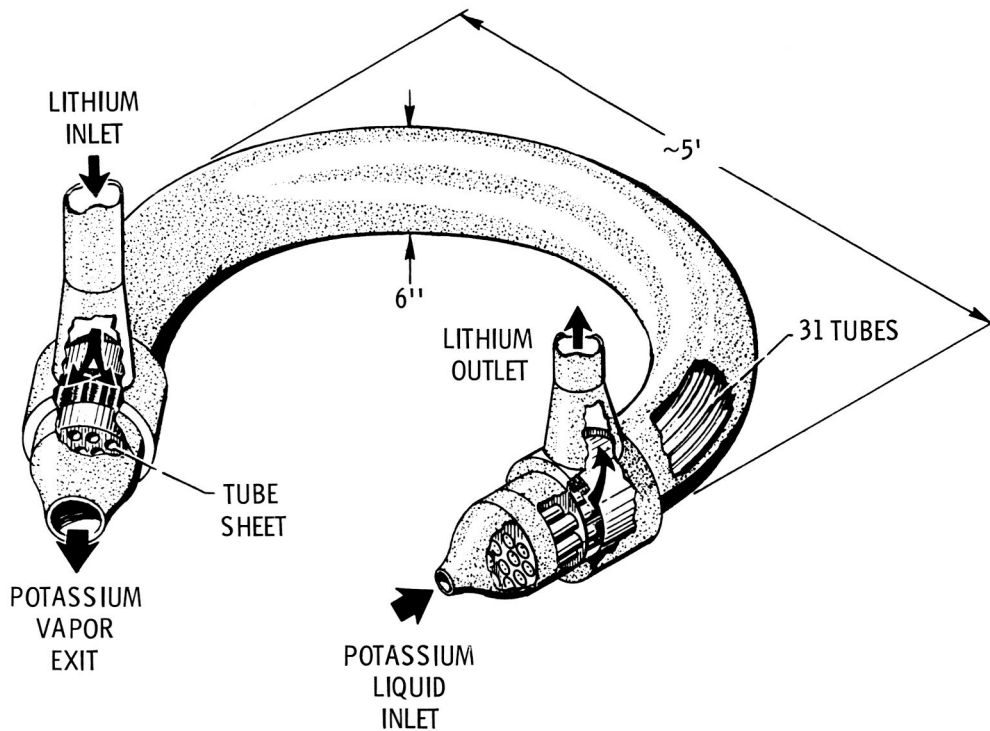


Figure I-9. - T-111 potassium boiler. Nominal power, 2000 kilowatts thermal; heating fluid, lithium; potassium outlet temperature, 2100° F.

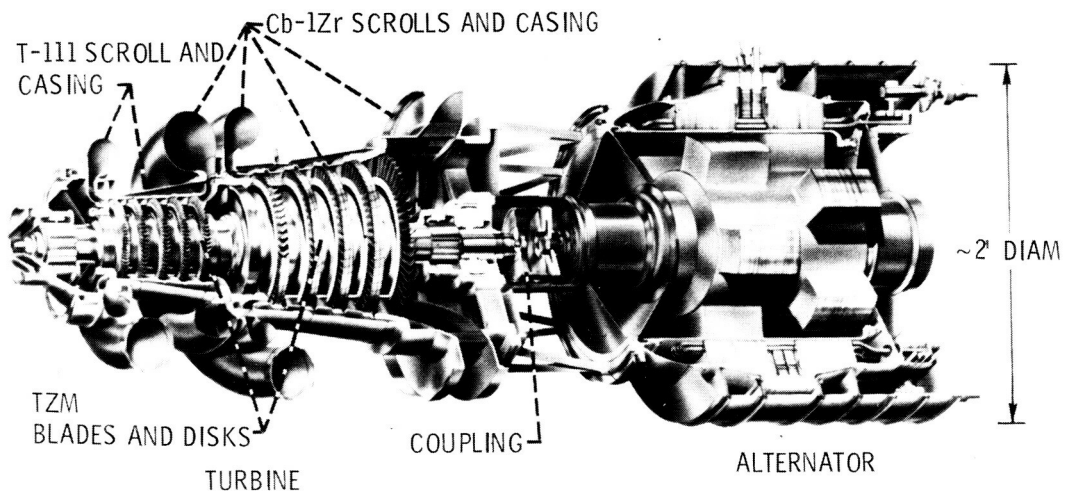


Figure I-10. - Potassium turbine-alternator.

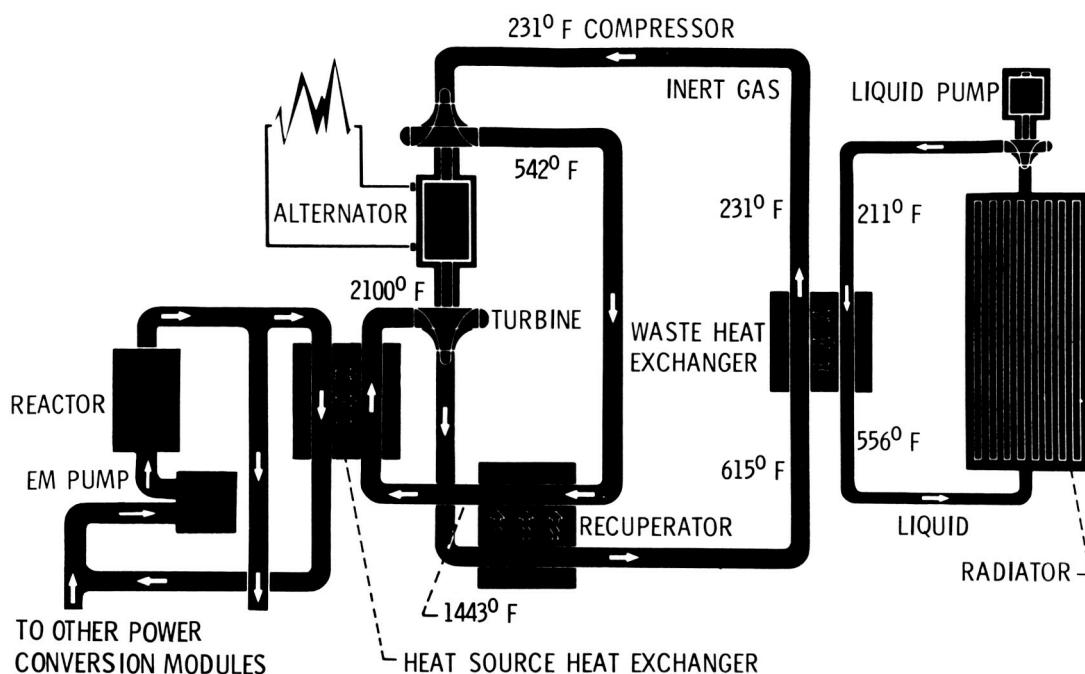


Figure I-11. - High-temperature reactor Brayton cycle.

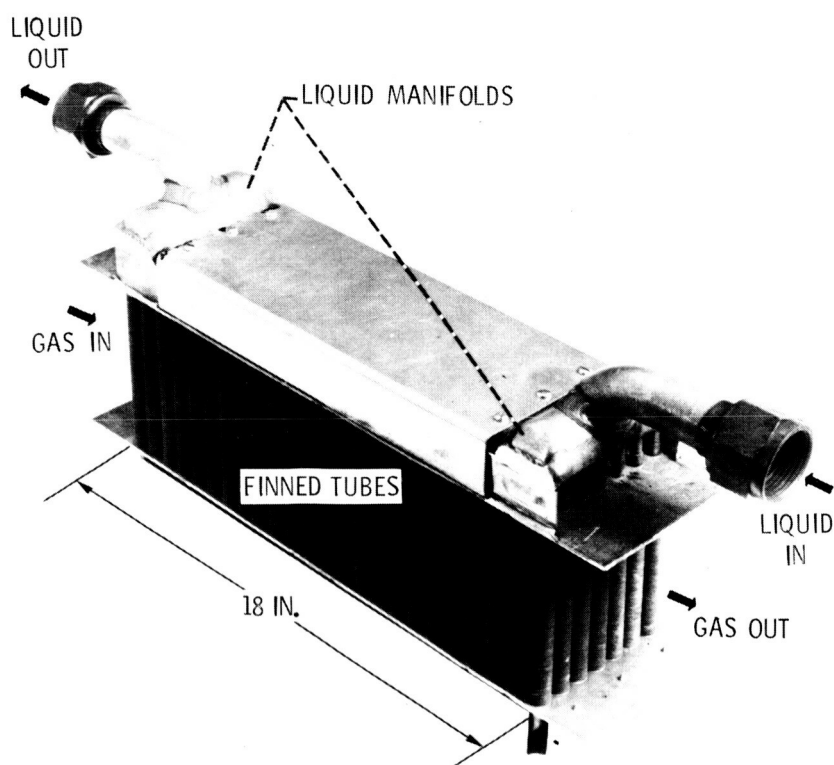


Figure I-12. - Typical compact heat exchanger core.

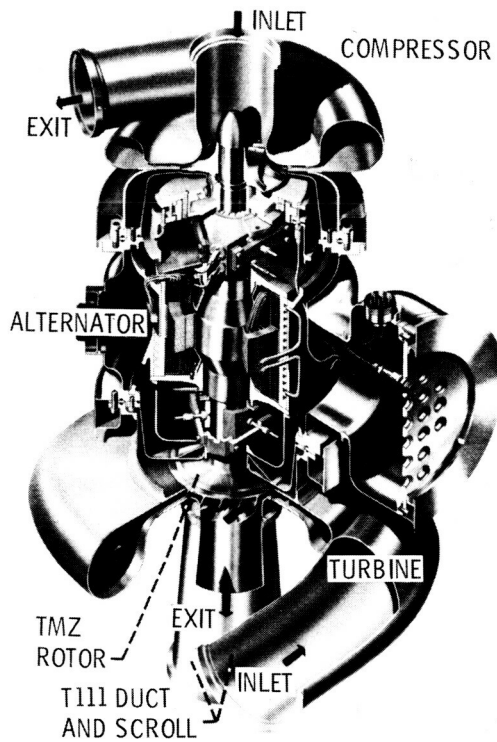


Figure I-13. - Brayton turbine-alternator-compressor.

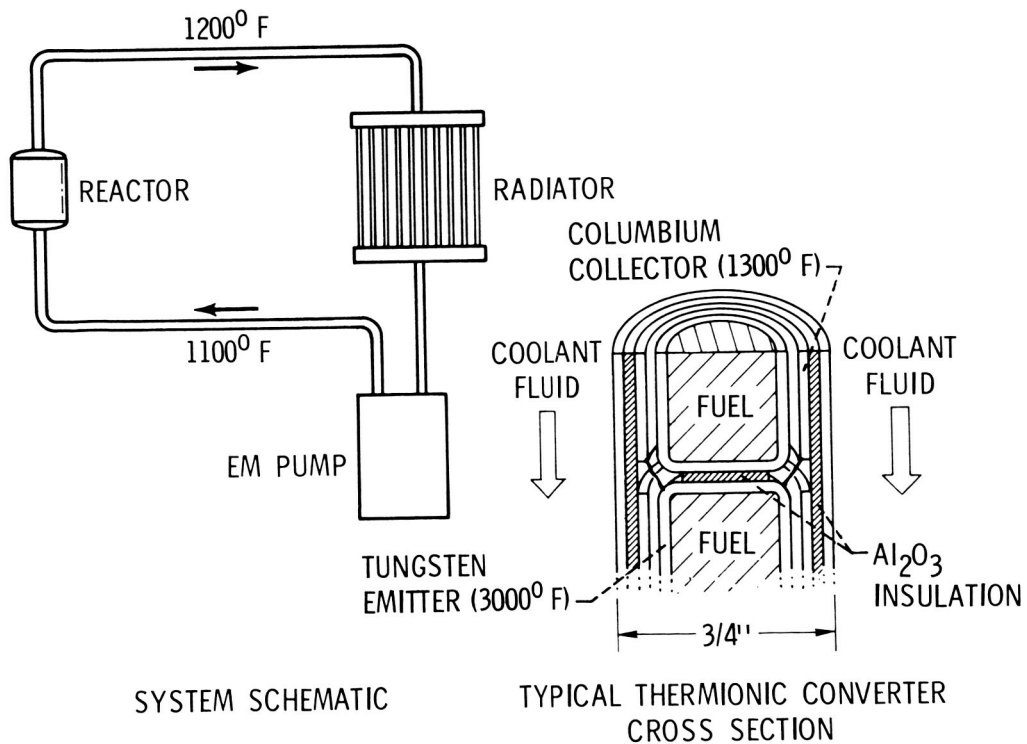


Figure I-14. - In-core thermionic system.

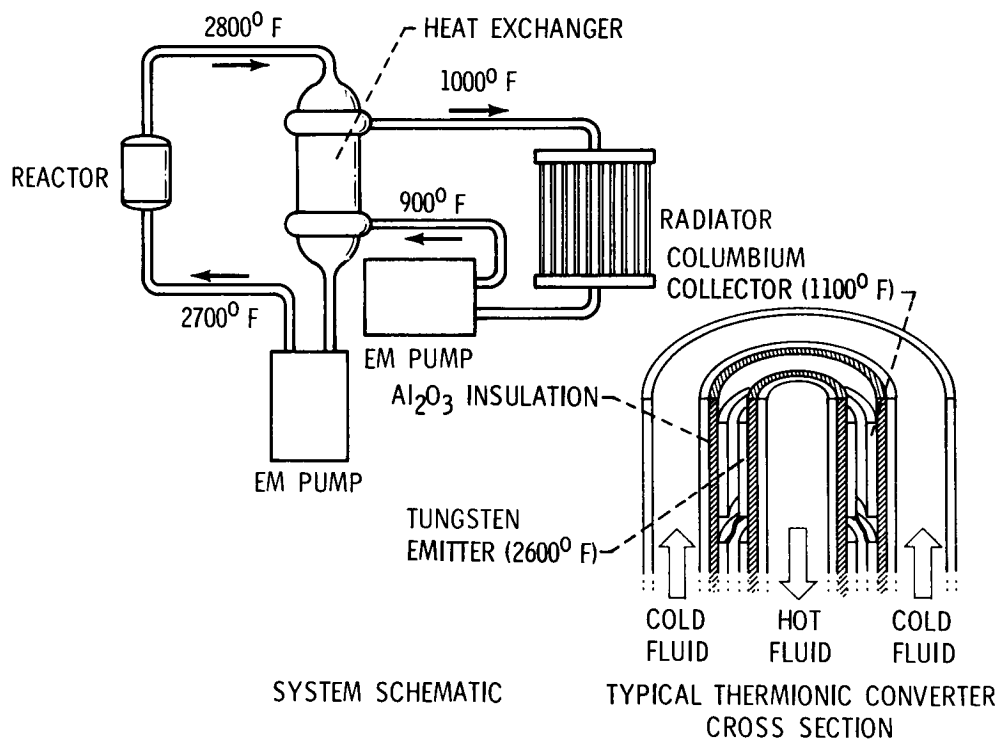


Figure I-15. - Out-of-core thermionic system.

## II. DEVELOPMENT OF HIGH STRENGTH TANTALUM BASE ALLOYS\*

R. W. Buckman, Jr.,<sup>†</sup> and R. R. Begley\*\*

This paper describes the development of tantalum base alloys intended for application in advanced space power systems. For components such as piping in alkali metal Rankine cycle systems, radioisotope capsules, and fuel claddings in nuclear reactors, critical property criteria include excellent fabricability, good welding characteristics, long time thermal stability, and high creep strength. Tantalum base alloys which successfully meet these criteria were achieved by a balanced combination of solid solution and dispersed phase strengthening, as typified by the alloy ASTAR-811C (Ta-8W-1Re-0.7Hf-0.025C). This alloy has creep strength significantly superior to T-111 (Ta-8W-2Hf) at temperatures up to 2600° F, without sacrifice of fabricability or welding characteristics. The DBTT of TIG welds is of the order of -250° F, and that of recrystallized base metal is below -320° F. Data are presented for tensile and long time creep properties of this alloy, and the role of carbide precipitates in improving high temperature strength is discussed.

Greatly improved high temperature tensile and creep properties can be achieved by an increase in tungsten level and by a substitution of nitrogen for carbon. While this strength increase is obtained with some sacrifice in fabricability, the alloys of increased solute level are attractive for high temperature applications where weldability is not a critical design requirement.

### INTRODUCTION

In 1963 the Lewis Research Center of NASA initiated a program at the Westinghouse Astronuclear Laboratory to develop tantalum base alloys for application in advanced space power systems. The intent of the program was to develop alloy(s) which would have improved properties in the 2000° to 3000° F temperature range,

---

\*Based on work done under NASA contracts NAS 3-2542 and NAS 3-10939.

<sup>†</sup>Westinghouse Astronuclear Laboratory, Pittsburgh, Pennsylvania.

\*\*Westinghouse Research Laboratory, Pittsburgh, Pennsylvania.

with the major emphasis on application in Rankine cycle nuclear electric power systems which would operate at 2000<sup>0</sup> to 2600<sup>0</sup> F. The extended operational life of the systems (>10 000 hr) dictated that resistance to creep deformation be the principal strength criterion. An additional requirement was that the alloys developed be compatible with alkali metals, the intended working fluids in these systems. Since the material would be used in complex heat transfer systems, good fabricability and welding characteristics were also essential.

The intent of this paper is to review the development of a series of fabricable, creep resistant tantalum base alloys which resulted from this program and summarize the properties achieved, rather than treat in detail any specific aspect of the investigation.

## EXPERIMENTAL DESIGN

The alloy base selected for evaluation was the tantalum rich corner of the Ta-W-Hf-C system. This system was selected as the most promising based upon earlier work at Westinghouse which led to the development of the alloys T-111 (Ta-8W-2Hf)<sup>1</sup> and T-222 (Ta-10W-2.5Hf-0.01C) (ref. 1). The alloys investigated were of the basic type

$$M + M_{S.S.} + M_{R.E.} + M_1 = \text{Alloy}$$

where

|                   |                            |
|-------------------|----------------------------|
| M                 | Ta                         |
| M <sub>S.S.</sub> | substitutional solute(s)   |
| M <sub>R.E.</sub> | reactive element solute(s) |
| M <sub>1</sub>    | interstitial solute(s)     |

This type of alloy derives its strength from a combination of solution and dispersed phase strengthening, the latter arising from the precipitation of an interstitial compound. The Ta-W-Hf-C alloy base was modified by the addition and/or substitution of rhenium and molybdenum for tungsten, zirconium for hafnium, and nitrogen for carbon. The presence of a reactive element (zirconium and/or hafnium) significantly affects the alkali metal corrosion resistance of tantalum and columbium alloys by reducing the oxygen solubility of the matrix, tying up oxygen

---

<sup>1</sup>Composition given in weight percent.



as a  $\text{HfO}_2$  or  $\text{ZrO}_2$  precipitate (ref. 2). Thus all of the alloys contained a minimum of 1 atomic percent reactive element to assure adequate corrosion resistance.

The reactive elements were also intended to provide precipitation strengthening by reacting with the interstitial elements to form stable carbide and/or nitride phases. However, as will be shown, strengthening by carbides can be achieved in alloys of this type without the reactive element entering into the precipitation reaction. Several alloys were prepared without intentional carbon and nitrogen additions to establish the properties of the solid solution matrix.

The substitutional solutes investigated were selected on the basis of their solubility in tantalum and their effects on matrix elastic modulus and diffusivity as discussed in a recent review of creep of refractory metals by Begley, Harrod, and Gold (ref. 3). The alloying behavior of tantalum with particular reference to those factors which affect high temperature mechanical properties and low temperature ductility has been described by Buckman and Goodspeed (ref. 4); hence a detailed discussion of the considerations involved in defining the experimental program will not be presented here.

## EXPERIMENTAL PROCEDURES

Ta and Ta-10W produced by electron beam melting and containing less than 100 ppm total interstitials was used as the base material. Alloys for initial studies were prepared in the form of  $1\frac{3}{4}$  pound buttons by nonconsumable arc melting in a high purity argon atmosphere. Alloys for more detailed evaluations were prepared as 2-inch-diameter ingots weighing 7 pounds by double vacuum arc melting, using ac power. Finally, the optimized compositions were scaled up to 4-inch-diameter 80-pound ingots which were also prepared by vacuum arc melting.

Ingot breakdown was achieved by high energy rate forging and/or extrusion in the temperature range of  $2200^{\circ}$  to  $3100^{\circ}$  F, depending on alloy composition. The as-cast ingot material was coated with either a Al-12Si alloy or plasma sprayed Mo to reduce contamination during high temperature processing. Following careful conditioning, material was produced in the form of sheet by a combination of warm ( $800^{\circ}$  F) and cold rolling. Bar stock of a number alloys was prepared by hot and cold swaging, with the specific processing schedule varying depending on alloy composition.

All intermediate and final annealing was performed on material which was conditioned and chemically cleaned to remove any contaminated surface layers and then wrapped in tantalum foil to prevent contamination during annealing. Heat treatments were conducted in a tantalum resistance heated furnace at pressures  $\leq 1 \times 10^{-5}$  torr.

Specimens were generally annealed 1 hour at 3000<sup>0</sup> F prior to evaluation. Elevated temperature tensile tests were also carried out in vacuum at pressures  $\leq 1 \times 10^{-5}$  torr with the specimen gage length wrapped in tantalum foil. Creep tests were performed in sputter ion pumped vacuum systems of the type described by Buckman and Hetherington (ref. 5) at pressures below  $1 \times 10^{-8}$  torr. The low pressures achieved in these units are required to prevent test environment interactions which would lead to spurious creep test results (refs. 6 and 7).

Alloy sheet specimens 0.04 inch thick were evaluated by both TIG and electron beam welding. Automatic TIG welding was performed in a vacuum purged weld chamber back-filled with He containing less than 1 ppm total active impurities. The chamber was equipped with instrumentation to continuously monitor oxygen and water vapor concentrations in the welding atmosphere. The welding procedures used have been described by Lessmann (ref. 8). Electron beam welds were made in a 100-kilovolt Hamilton Zeiss unit evacuated to less than  $5 \times 10^{-6}$  torr prior to welding. Welds were evaluated primarily by bend tests to establish the ductile-brittle bend transition temperature. Bend deflection rate was 1 inch per minute and a 1.8 t bend radius was used.

During all phases of alloy preparation, processing, and evaluation, particular care was devoted to achieving homogeneity and freedom from contamination, and extensive chemical analyses were performed to monitor the effectiveness of the techniques used. A more detailed description of the experimental procedures is reported by Buckman and Goodspeed (ref. 9).

## RESULTS

The effects of compositional and structural variations were evaluated on the basis of their effect on fabricability, weldability, ductile to brittle transition temperature, and high temperature creep strength. The initial studies were largely directed at establishing the boundaries for satisfactory fabricating characteristics.

### Fabricability

The combined effect of tungsten, hafnium, and carbon content on as-cast hardness is illustrated in figure II-1. The dashed line approximates the composition beyond which fabricability was impaired, this being defined as the onset of edge cracking with a 50-percent reduction in billet height resulting from a single blow of a Dynapak high energy rate forging unit. Forging temperature was 2200<sup>0</sup> to 2300<sup>0</sup> F

for those alloys having an as-cast hardness of less than 300 DPH and 2700<sup>o</sup> F for those over 300 DPH. The forging results could be correlated with microstructure. At carbon levels where a continuous grain boundary carbide phase formed, edge cracking was encountered. The carbon level at which the continuous carbide phase formed decreased as the W + Hf content was increased. At W + Hf levels in excess of 12 percent and carbon levels greater than 0.1 percent, a subboundary network decorated with a continuous carbide phase was observed. As-cast ingots exhibiting this characteristic microstructure had very poor forgeability.

Substitution of nitrogen for carbon resulted in degradation of forgeability as the nitrogen level was increased above 400 ppm. Substitution of 1.5 percent Re and 0.85 percent Mo in an alloy of 9 percent total solute level and 0.07 C did not result in any decrease in fabricability.

The same general trends observed for primary working applied to the secondary working of the alloys. Alloys containing up to 10 percent W + Hf and 0.1 percent carbon could be cold rolled to good quality strip.

## Weldability

Experimental compositions exhibiting marginal fabricating characteristics were readily identified during the primary and secondary working operations. However, the changes in ductile-brittle bend transition temperature (DBTT) resulting from fusion welding provided a much more sensitive fabricability index. Material annealed 1 hour at 3000<sup>o</sup> F to provide a fully recrystallized microstructure was TIG welded and the ductile-brittle transition temperature determined. The transition temperature is defined as the lowest temperature at which a full 90<sup>o</sup> bend (1.8 t bend radius) was obtained without any indication of cracking. As shown in figure II-2, the addition of carbon to the Ta-W-Hf matrix results in a significant increase in the as-TIG welded transition temperature. At a W + Hf content of 9 to 10 percent, the addition of 400 ppm carbon raises the DBTT to approximately room temperature. Recrystallized base metal of the same composition has a DBTT below -320<sup>o</sup> F. Metallographic examination of welds in alloys containing up to 0.05 C revealed an essentially single phase fusion and heat affected zone, while the adjacent base metal showed characteristic carbide precipitates. During welding, the carbides are dissolved and largely retained in solution on cooling. Hardness measurements taken across the welds showed a significant increase in the hardness of the fusion and heat affected zone areas as compared to the base metal, thus confirming the retention of carbon in solution (or as a very fine precipitate which forms on cooling). The increase in DBTT of the as-welded material is readily explained on this basis.

Postweld annealing at temperatures of 2600<sup>o</sup> to 2700<sup>o</sup> F was found to be effective in reducing the transition temperature by permitting carbide precipitation to occur. The minimum temperature for satisfactory recovery of bend ductility was not established in this study, however.

Nitrogen additions were found to raise the DBTT of weld material, the effect being significantly greater than for equivalent carbon additions.

## Creep Behavior

High temperature creep strength increased with increasing tungsten level, as expected. The substitution of small amounts of rhenium for tungsten had an unexpectedly potent effect in increasing the creep strength of Ta-W-Hf and Ta-W-Hf-C alloys, as shown in figure II-3. Additions of the order of 1 percent conferred significantly improved properties while larger amounts had no additional effect. This behavior cannot be rationalized in terms of simple solution strengthening, nor does it appear to be related to effects on precipitate morphology or stability since it is observed in alloys having no interstitial addition. Buckman and Goodspeed (ref. 4) have suggested that it may be due to an electronic contribution.

The effect of carbon additions on the 2400<sup>o</sup> F creep properties of Ta-W-Hf alloys is summarized in figure II-4. These results show that the strength of the matrix increases appreciably with increasing carbon content, reaching a maximum at about 250 to 300 ppm C, and decreasing thereafter. However, all of these alloys were annealed 1 hour at 3000<sup>o</sup> F prior to testing. It is presumed that the carbide phase is coarser in the alloys of higher carbon content, providing a poorer structure for creep resistance. The carbon solubility in the Ta-W-Hf matrix at 3000<sup>o</sup> F is approximately 100 ppm; thus only a small fraction of the carbon in the alloys of higher carbon content was dissolved during the 3000<sup>o</sup> F anneal. The carbon not in solution at this temperature would tend to agglomerate as coarse carbide precipitates. It would be expected that if the annealing temperature were raised above the carbon solvus, and the cooling rate from the solution anneal sufficiently rapidly to precipitate a fine carbide phase, then strength would continue to increase with increasing carbon content. Studies of Cb alloys and results to be discussed later in this paper show that best creep results for carbide hardened alloys are achieved by annealing above the carbon solvus.

The carbide phases present in the Ta-W-Hf-C alloys were identified as either the dimetal carbide, Ta<sub>2</sub>C, or the monocarbide, (Ta,Hf)C<sub>1-x</sub>. Depending on composition, either or both of these carbides were observed in the matrix. The creep behavior of the experimental alloys could be rationalized on the basis of location in

the Ta-W-Hf-C quasi-ternary phase diagram, as illustrated in figure II-5. It is apparent that compositions exhibiting the best creep properties contained only the dimetal carbide as the precipitating phase (curves labeled A in the lower portion of fig. II-5). The compositions having the poorest properties (curves C) contained only the monometal carbide,  $(\text{Ta, Hf})\text{C}_{1-x}$ , while those containing both carbide phases had intermediate properties. It does not appear to be the identity of the precipitate per se which controls creep resistance, but rather that in order to stabilize the monocarbide phase fairly large additions of hafnium are necessary. In an alloy containing 500 ppm carbon, for example, approximately 3 percent Hf is required to stabilize the monocarbide. This results in a significant hafnium concentration in the matrix which has a deleterious effect on creep resistance (ref. 4). For this reason the best creep properties are achieved in alloys containing the  $\text{Ta}_2\text{C}$  precipitate since these alloys have hafnium concentrations of the order of 1 percent.

The minor compositional variations investigated by substituting different atom species, that is, nitrogen for carbon, molybdenum for tungsten, and zirconium for hafnium, provided a marked improvement in  $2400^\circ\text{F}$  creep properties, as shown by the data of figure II-6. This strength improvement is primarily associated with the increased effectiveness of the nitride precipitate in creep strengthening as compared to the carbide, at temperatures up to  $2400^\circ\text{F}$ . In the nitrogen containing alloys, the nitrogen is present as a reactive metal mononitride. The remarkable strength properties of the nitride hardened alloys are evidenced by the alloy composition Ta-5.3W-0.65Mo-1.56Re-0.52Zr-0.08N. This composition had a tensile strength in excess of 100 000 psi at  $2400^\circ\text{F}$ , as well as excellent  $2400^\circ\text{F}$  creep properties. However, as noted previously, the fabricability and weldability of alloys containing moderate nitrogen additions are marginal for alloys intended for use in the form of sheet and tubing. In applications where excellent fabricability and weldability are not critical requirements, the nitride strengthened compositions possess very attractive potential.

## ALLOY OPTIMIZATION

Based upon the requirement for excellent fabricability and good as-welded ductility, a substitutional solute level of approximately 9 percent, and a carbon content of 0.025 percent was selected. Hafnium was maintained at the minimum level judged adequate for good alkali metal corrosion resistance, approximately 1 percent. Since significantly enhanced creep resistance was shown to result from small additions of rhenium without loss of fabricability, an addition of 1 percent Re

was selected for the optimized composition. The optimized fabricable alloy thus has the composition Ta-8W-1Re-1Hf-0.025C. This alloy, designated ASTAR-811C was scaled up for rather extensive evaluation of fabricating characteristics, weldability, and mechanical properties. The mechanical properties of ASTAR-811C are compared to those of the tantalum alloys T-111 and T-222 in table II-1. As can be seen, the tensile properties of ASTAR-811C are intermediate between those of T-111 and T-222. All three alloys have ductile-brittle transition temperatures below  $-320^{\circ}$  F. In the as-TIG welded condition, the DBTT of ASTAR-811C is slightly higher than that of T-222, ranging from  $-250^{\circ}$  to  $-150^{\circ}$  F depending upon the welding parameters utilized. However, the major difference between ASTAR-811C and the other two alloys is the markedly superior creep strength of ASTAR-811C. Figure II-7 is a Larson-Miller plot which compares the creep properties of ASTAR-811C to T-111 and shows the significant improvement in properties realized in the creep optimized alloy. Also included in figure II-7 are data for a Ta-8W-1Re-1Hf alloy, which is the matrix composition of ASTAR-811C without the carbon addition. As can be seen, the carbide phase provides a substantial strengthening increment at the lower temperatures. However, at temperatures of the order of  $2600^{\circ}$  F the carbide phase makes no appreciable contribution to creep strength.

Further improvement in the creep strength of ASTAR-811C can be achieved by proper heat treatment. Generally, annealing at or above the carbon solvus improves creep resistance, as discussed in the paper by Harrod and Buckman in this volume.

Tensile data for ASTAR-811C are plotted as a function of temperature in figure II-8. Moderate strength and excellent ductility are maintained over the entire temperature range from  $-320^{\circ}$  to  $3000^{\circ}$  F. Similar tensile tests conducted on TIG welded material showed essentially 100 percent joint efficiency and excellent ductility. Initial thermal stability studies of both base and weld metal have not indicated the presence of aging reactions which would result in ductility impairment.

## HIGH STRENGTH ALLOYS

In the selection of the ASTAR-811C composition, maintenance of excellent fabricating and welding characteristics was a major consideration. The results of the investigation clearly demonstrated that greatly improved high temperature properties could be realized if the fabricability and weldability constraints could be relaxed. For components such as turbine blades and disks, bolts, etc. these properties can be compromised somewhat to achieve better high temperature strength. Consequently, studies are currently in progress to establish the properties obtain-

able in alloys which have adequate fabricability for use in the form of forgings and bar stock.

Figure II-9 shows the effect of increasing substitutional solute content (W + Re) on the tensile properties of a tantalum alloy base containing 0.7 percent Hf and 0.025 percent C. Elevated temperature tensile strength increases monotonically with increasing solute level. However, room temperature ductility decreases drastically at substitutional solute level over approximately 15 percent. This effectively establishes the upper composition limit for alloys of this type which will have a desirable combination of engineering properties. Creep properties of several of the high strength alloys are plotted in figure II-10. These experimental alloys have creep strength greatly superior to ASTAR-811C, as well as being significantly better than Cb-TZM. Some of these compositions have been satisfactorily welded by electron beam welding techniques. Detailed evaluation of these high strength alloys is currently in progress.

## SUMMARY OF RESULTS

A series of tantalum base alloys has been developed which have many potential applications in space power systems. The progress which has been made in improving high temperature creep properties is illustrated in figure II-11, where stress for 1 percent creep in 1000 hours is plotted as a function of temperature. These alloys provide the best combination of strength, fabricability, and weldability available for applications in the 2000<sup>o</sup> to 2600<sup>o</sup> F temperature range. The highly fabricable alloy ASTAR-811C appears to have many potential applications in advanced space power systems, including reactor fuel claddings, pressure vessels, and piping; radioisotope fuel capsules, thermionic reactor components, and components in advanced Brayton cycle power systems. Long term creep, thermal stability, weldability, and alkali metal corrosion tests are currently in progress under NASA sponsorship to provide the design data necessary for the successful utilization of this material in a wide variety of space power system applications.

## REFERENCES

1. Ammon, R. L.; and Harrod, D. L.: Strengthening Effects in Ta-W-Hf Alloys. Refractory Metals and Alloys IV, Research and Development. Vol. 1. R. I. Jaffee, G. M. Ault, J. Maltz, and M. Semchyshen, eds., Gordon and Breach Sci. Publ., 1968, pp. 423-442.

2. Hoffman, E. E.; and Harrison, R. W.: The Compatibility of Refractory Metals with Liquid Metals. Refractory Metal Alloys: Metallurgy and Technology. I. Machlin, R. T. Begley, and E. D. Weisert, eds., Plenum Press, 1968, pp. 251-287.
3. Begley, R. T.; Harrod, D. L.; and Gold, R. E.: High Temperature Creep and Rupture Behavior of the Refractory Metals. Refractory Metal Alloys: Metallurgy and Technology. I. Machlin, R. T. Begley, and E. D. Weisert, eds., Plenum Press, 1968, pp. 41-83.
4. Buckman, R. W., Jr.; and Goodspeed, R. C.: Considerations in the Development of Tantalum Base Alloys. Refractory Metal Alloys: Metallurgy and Technology. I. Machlin, R. T. Begley, and E. D. Weisert, eds., Plenum Press, 1968, pp. 373-394.
5. Buckman, R. W., Jr.; and Hetherington, J. S.: Apparatus for Determining Creep Behavior under Conditions of High Vacuum. Rev. Sci. Instr., vol. 37, no. 8, Aug. 1966, pp. 999-1003.
6. Buckman, R. W., Jr.: Operation of Ultra-High Vacuum Creep Testing Laboratory. Transactions Vacuum Metallurgy Conference. American Vacuum Society, 1966, pp. 25-37.
7. Inouye, H.: Interactions of Refractory Metals with Active Gases in Vacua and Inert Gas Environments. Refractory Metal Alloys: Metallurgy and Technology. I. Machlin, R. T. Begley, and E. D. Weisert, eds., Plenum Press, 1968, pp. 165-195.
8. Stoner, D. R.; and Lessmann, G. G.: Measurement and Control of Weld Chamber Atmospheres. Welding J. Res. Suppl., vol. 44, no. 8, Aug. 1965, pp. 337-s - 346-s.
9. Buckman, R. W., Jr.; and Goodspeed, R. C.: Development of Precipitation Strengthened Tantalum Base Alloys. Rep. WANL-PR-Q-017, Westinghouse Electric Corp.
10. Sawyer, J. C.; and Steigerwald, E. A.: Generation of Long Time Creep Data of Refractory Alloys at Elevated Temperatures. NASA CR-1115, 1968.



TABLE II-1. - SUMMARY OF MECHANICAL PROPERTIES OF T-111, T-222, AND ASTAR-811C

| Property  | T-111<br>(Ta-8W-2Hf) | T-222<br>(Ta-10W-2.5Hf-0.01C) | ASTAR-811C<br>(Ta-8W-1Re-1Hf-0.025C) |
|---|----------------------|-------------------------------|--------------------------------------|
| 0.2 Percent offset yield strength, psi                                  |                      |                               |                                      |
| -320° F   | 131 000              | 181 000                       | 147 000                              |
| 75° F   | 68 600               | 109 200                       | 85 000                               |
| 2000° F   | 30 000               | 42 200                        | 35 000                               |
| 2400° F   | 26 400               | 40 200                        | 30 400                               |
| Creep strength - time to strain 1 percent at 2400° F and 15 000 psi, hr | 20                   | 80                            | 260                                  |
| Ductile brittle transition temperature, °F                              |                      |                               |                                      |
| Base metal  | <-320                | <-320                         | <-320                                |
| As-TIG welded   | <-320                | -250                          | -150 to -250                         |

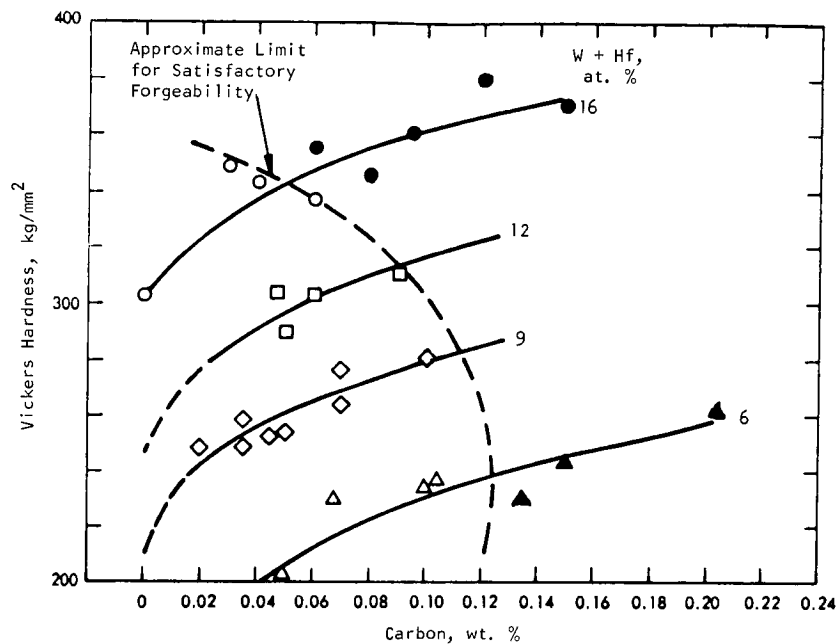


Figure II-1. - Effect of carbon on as-cast hardness of Ta-W-Hf compositions. (Open symbols, good forgeability; closed symbols, poor forgeability.)

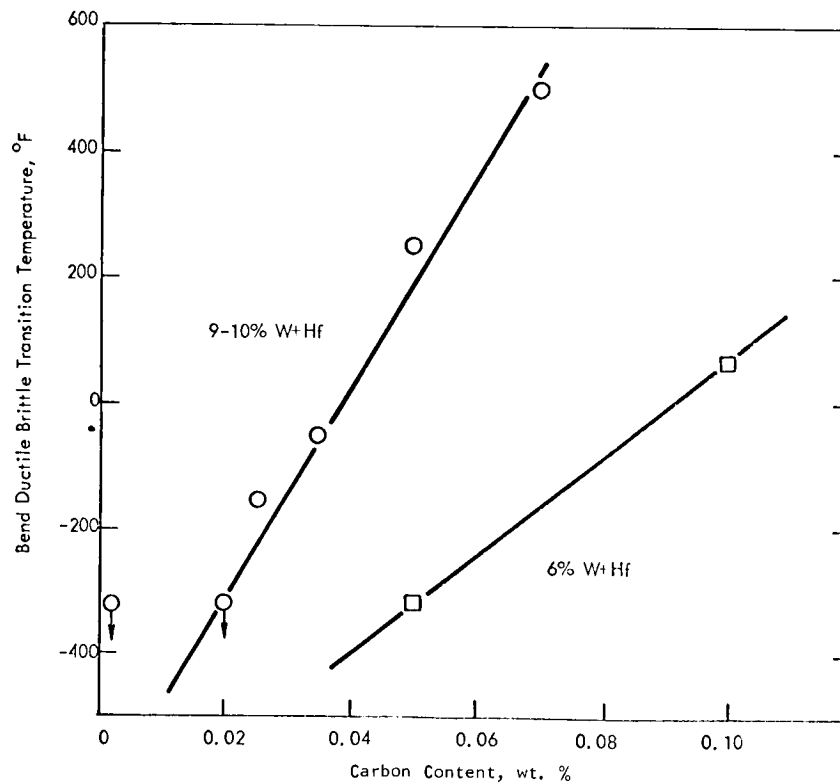


Figure II-2. - Effect of carbon on ductile-brittle transition temperature of As-TIG-welded experimental Ta-W-Hf-C alloy sheet.

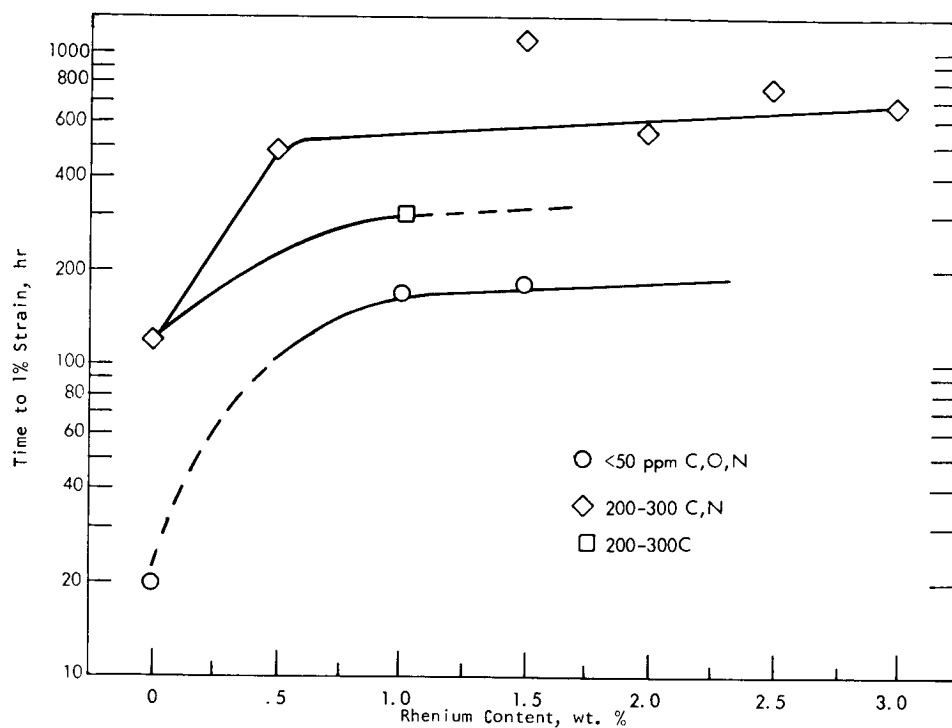


Figure II-3. - Effect of rhenium on creep properties of Ta-W-Hf alloys tested at 2400° F and 15 000 psi. Specimens annealed 1 hour at 3000° F prior to test.

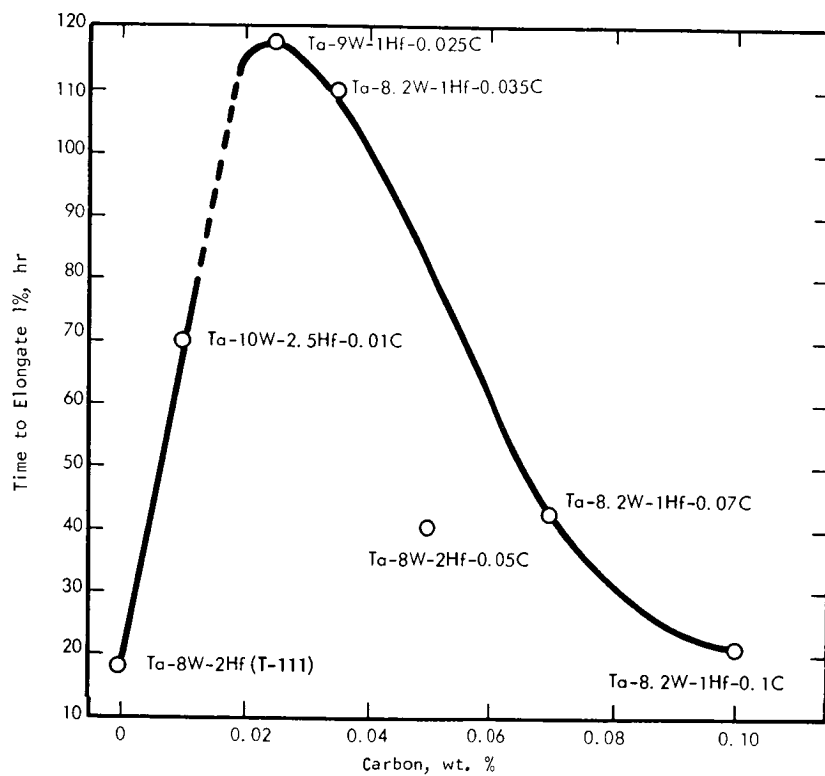


Figure II-4. - Effect of carbon on creep behavior of Ta-W-Hf alloys at 2400° F and 15 000 psi.

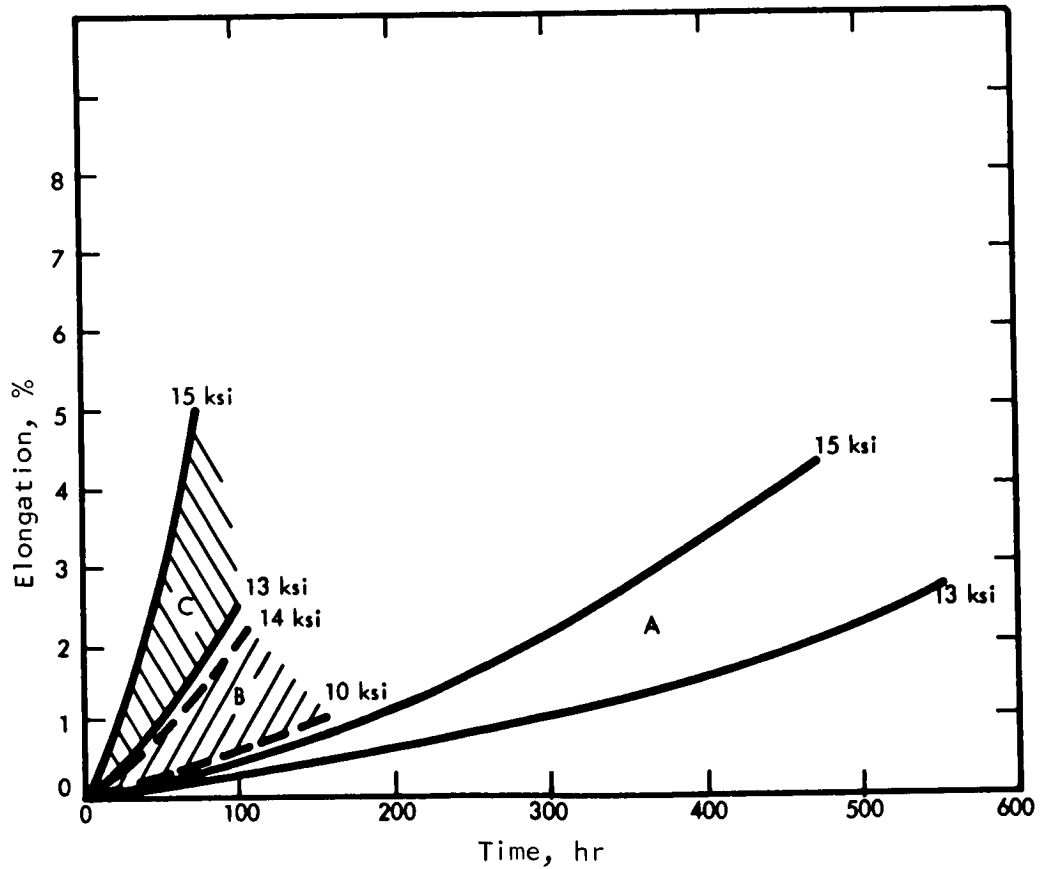
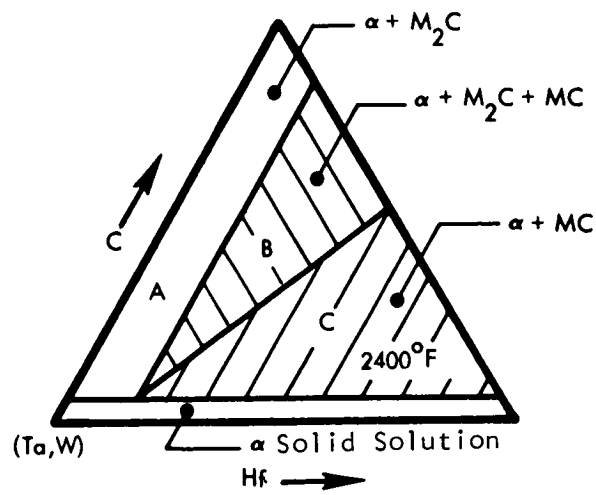


Figure II-5. - 2400°F creep behavior of Ta-W-Hf-C alloys. Tantalum base 9W 0.5Hf 0.02-0.10C alloy annealed 1 hour at 3000°F prior to testing.

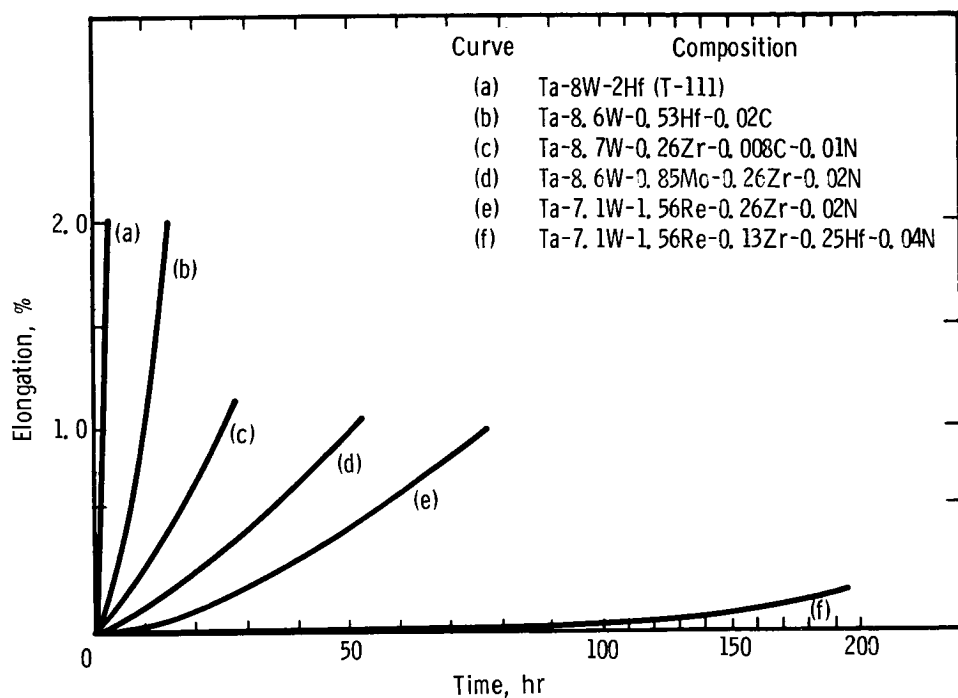


Figure II-6. - Effect of composition on creep behavior of experimental tantalum alloys. Test temperature, 2400° F; stress, 20 000 psi.

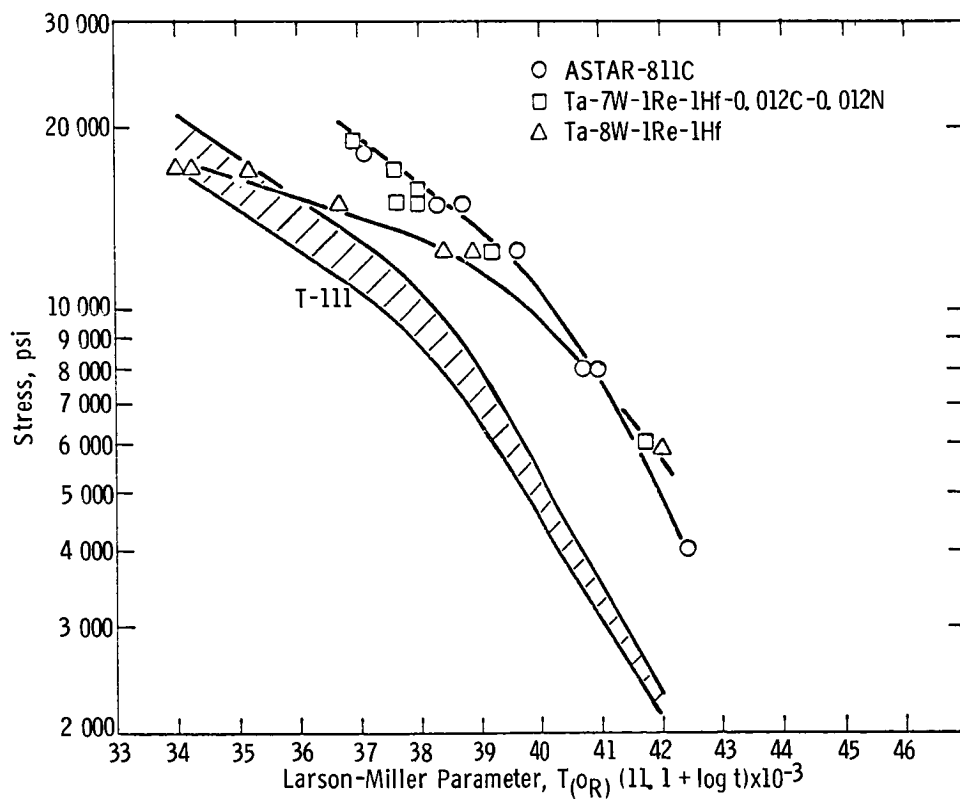


Figure II-7. - Larson-Miller plot comparing time to 1 percent elongation for tantalum alloys.

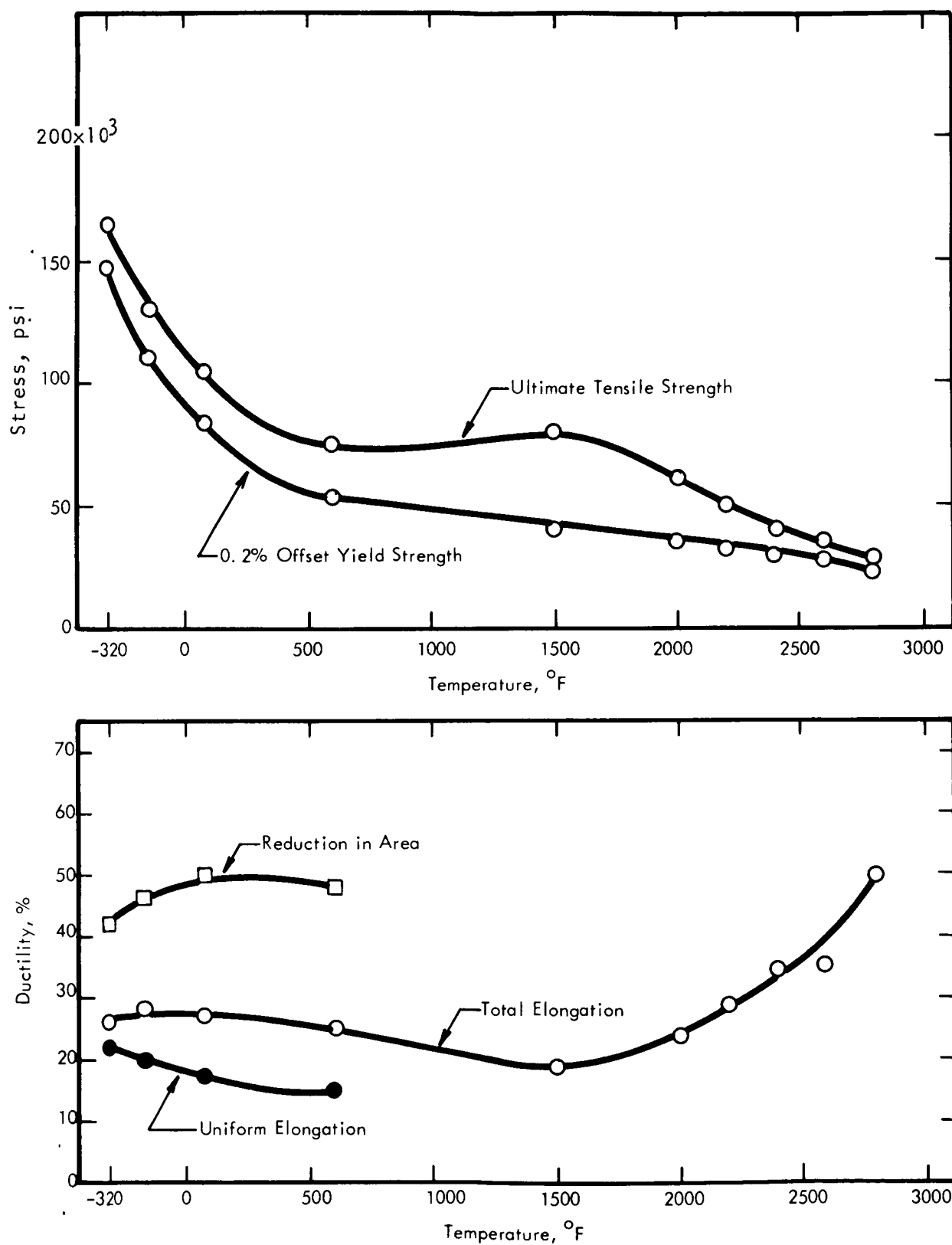


Figure II-8. - Tensile properties of ASTAR-811C.

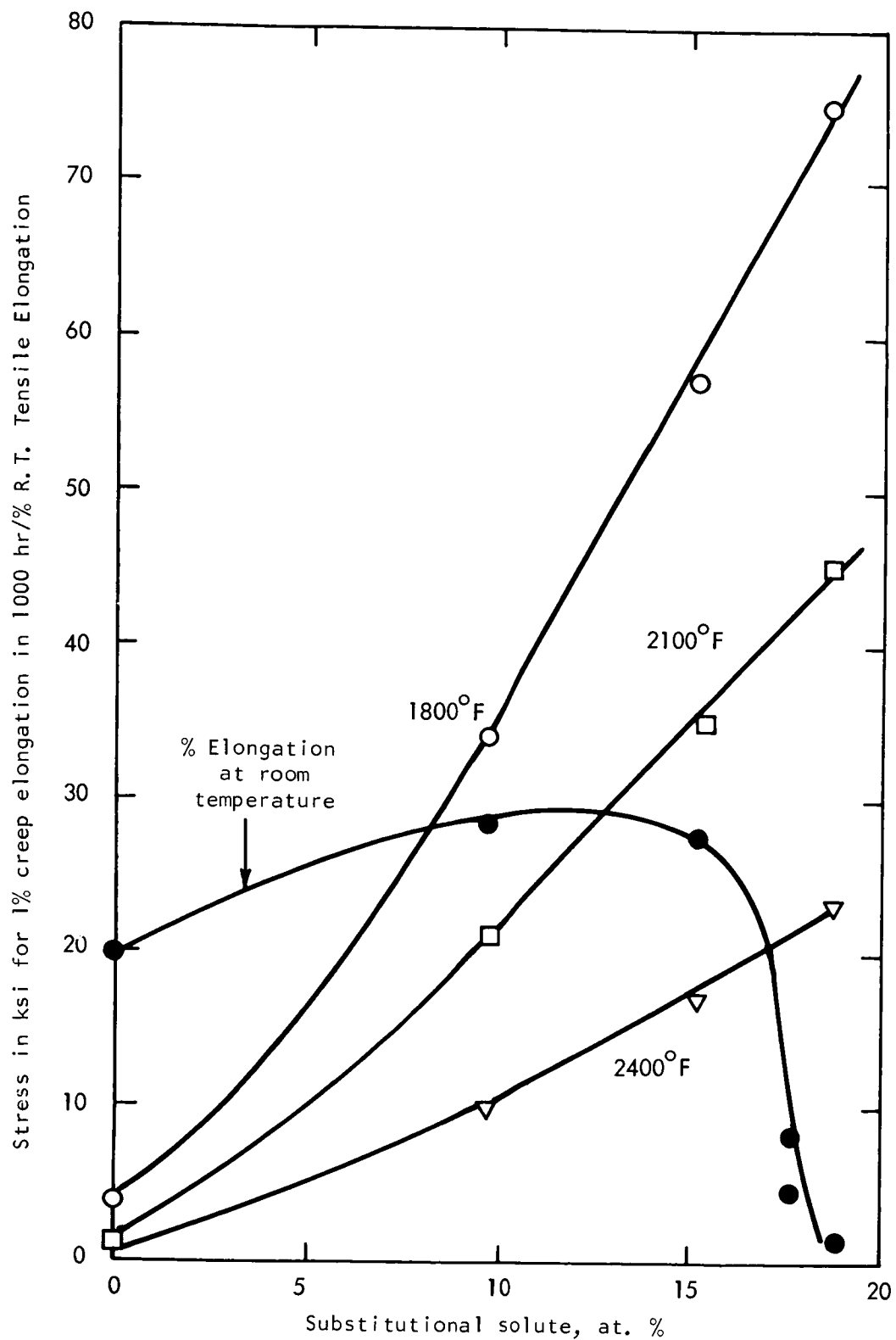


Figure II-9. - Effect of substitutional solute level on creep properties and room temperature elongation of Ta-8-16W-1-2Re-0.7Hf-0.025C alloy rod. Annealed 1 hour at 3300° F prior to test.

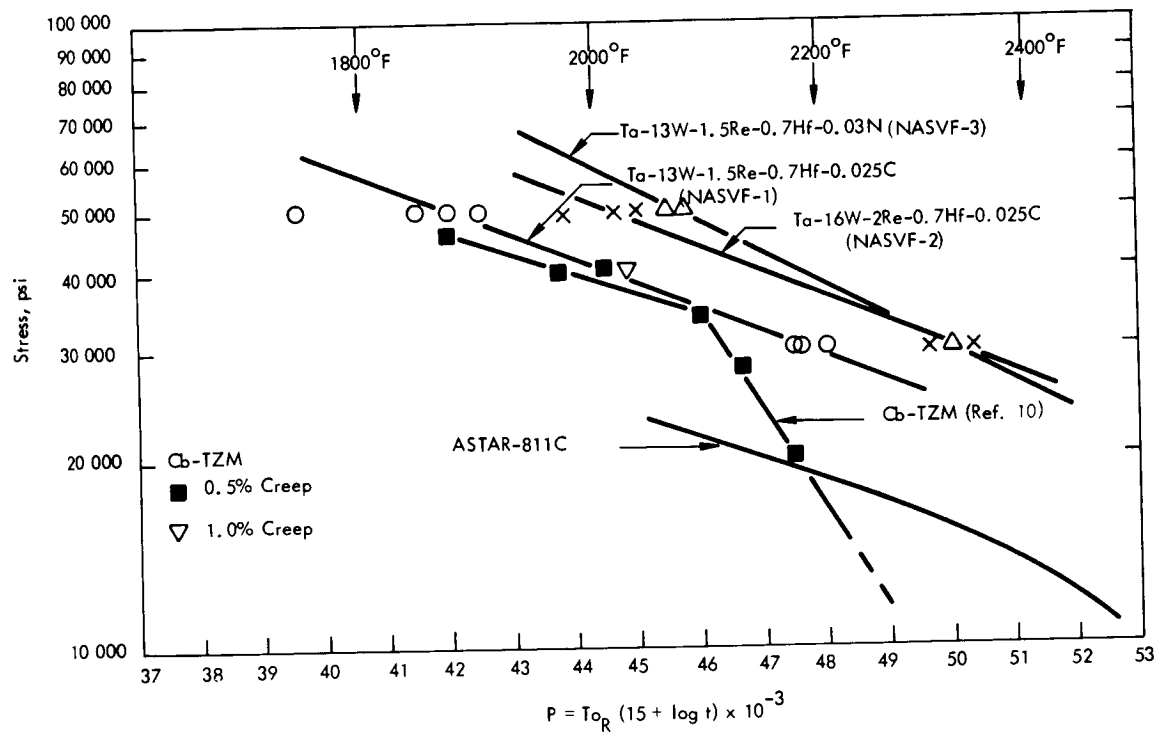


Figure II-10. - Creep properties of experimental tantalum base alloy rod.



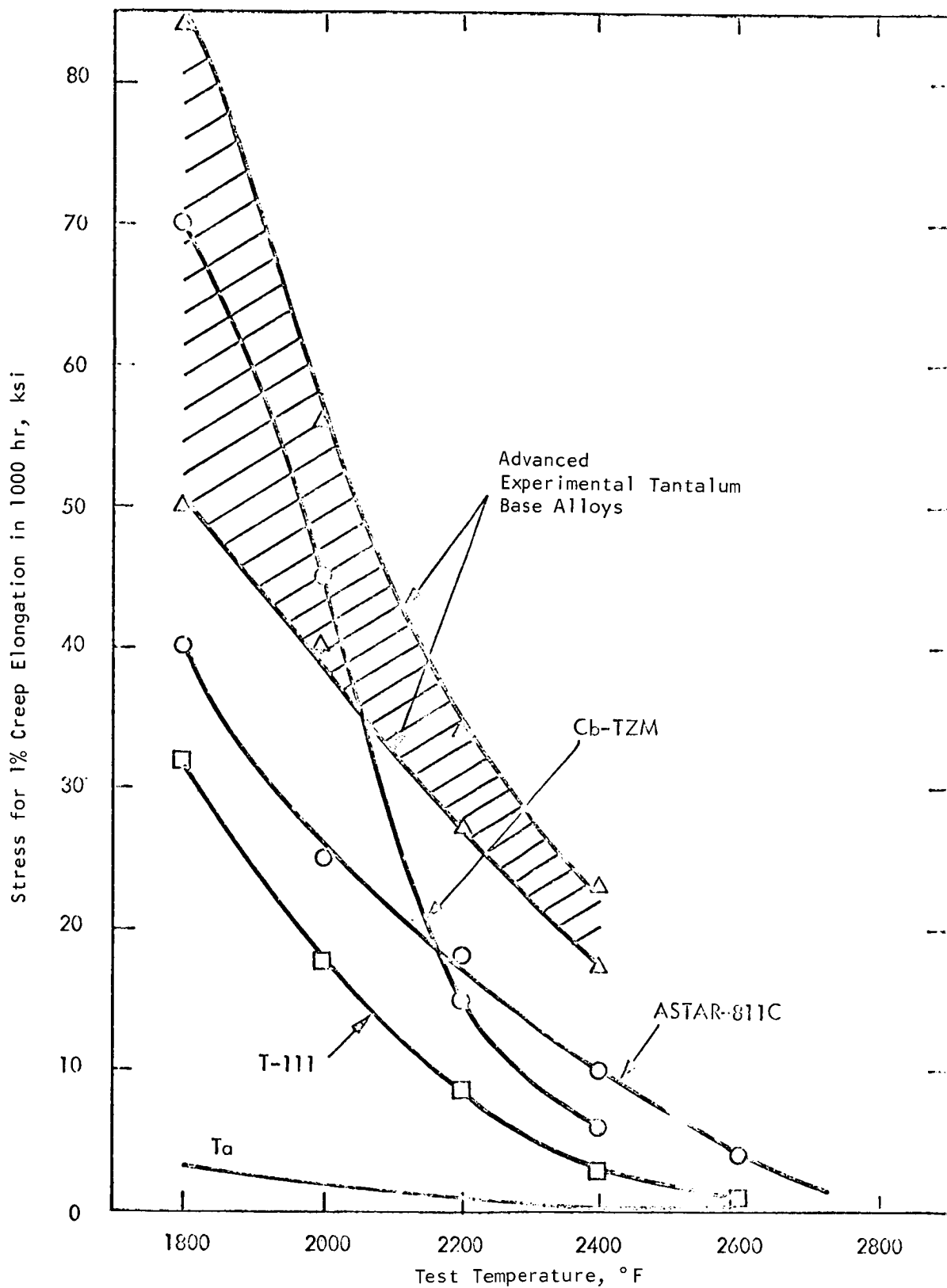


Figure II-11. - Creep properties of refractory metal alloys.

**Page intentionally left blank**

### III. THERMAL STABILITY OF REFRACTORY METAL ALLOYS\*

G. G. Lessmann<sup>†</sup> and R. E. Gold<sup>†</sup>

#### SUMMARY

The thermal stability of refractory metal alloys which showed promise for application in high temperature space power systems was determined. Only the very fabricable columbium and tantalum base alloys were evaluated. These included T-111, T-222, Ta-10W, FS-85, D-43, B-66, C-129Y, Cb-752, and SCb-291. These represent all of the commercial alloys prominent at the inception of the aging studies. T-111, T-222, and FS-85 eventually received the greatest emphasis because they demonstrated a superior balance of creep strength, weldability, and liquid metal corrosion resistance when evaluated in concurrent programs.

The purpose of this study was to screen the fabricable alloys for high temperature stability over long exposure times. This required that the effects on welds in particular be emphasized since welds represent severe metallurgical discontinuities whose behavior cannot be readily predicted. The alloys were thoroughly evaluated before and after aging to ascertain if degradation of mechanical properties occurred or if structural instability was otherwise noted. Bend testing for ductility changes as reflected in the bend transition temperature was emphasized as a screening technique. Considerable success was achieved using this procedure since changes in ultimate ductility and transition behavior reflect a wide spectrum of structural interactions. Tensile testing, hardness determinations, and extensive optical and electron metallography were also employed. Electron beam and gas tungsten arc welds were evaluated as well as base metal.

Instabilities were noted in all the alloys evaluated in this program. None of these were particularly detrimental in the normal application of these materials and, at most, would require only modest adjustment in hardware design. For the solid solution strengthened alloys Ta-10W and SCb-291 instabilities were confined

---

\*Based on work done under NASA contract NAS 3-2540.

<sup>†</sup>Westinghouse Astronuclear Laboratory, Pittsburgh, Pennsylvania.

to grain growth, whereas for the more advanced alloys responses were more complicated. The alloys with the highest creep strengths (T-111, T-222, and FS-85) demonstrated strikingly similar responses associated almost entirely with cored weld structure. These responses did not lend themselves to metallurgical analysis even under close scrutiny. D-43 displayed a classic overaging response ascribed to precipitation and subsequent coarsening of carbides while varying degrees of complexity in responses were displayed by the remaining alloy systems. In these latter systems responses were ascribed insofar as possible to previously identified mechanisms.

Fracture mode differed markedly for the tantalum based alloys as compared with the columbium based alloys. Even though bend test results indicated a weld aging response in T-111 and T-222, bend test fractures occurred through ductile grain boundary tearing and did not represent a design limitation. In contrast, columbium alloys displayed an abrupt change from ductile to brittle behavior at the transition. These results reflect the same general observation of the weldability evaluation of these materials; namely, based on fabricability the columbium alloys appear to have been alloyed to the maximum extent possible, whereas current tantalum alloys are conservatively alloyed.

## INTRODUCTION

This paper summarizes results of thermal stability studies sponsored by NASA. In this program the structural effects of high temperature exposure were determined for promising refractory metal alloys. These alloys are uniquely suited for space power hardware applications because of excellent high temperature strength and compatibility with liquid alkali metal working fluids. However, they have not been extensively utilized because of their relatively high cost. Hence, this program provided the impetus for the detailed definition of the long time and high temperature performance of these materials.

The alloys evaluated were primarily those considered to be fabricable by welding. Hence, weld stability as well as base metal stability was emphasized. The thermal stability study was preceded by a weldability study in which the base line weld parameters were established for use throughout the thermal stability study. This assured a consistent basis for processing and comparing the stability of the various alloys.

The alloys were screened for thermal stability by exposures between 1500<sup>0</sup> and 2400<sup>0</sup> F and hold times up to 10 000 hours. Sputter ion pumped furnaces were used exclusively, providing an optimum furnace environment of less than 10<sup>-8</sup> torr

total pressure. This assured that specimens would remain uncontaminated even after 10 000-hour exposures. Further, the potential load loss in event of furnace failure was nil since ion pumped systems are totally closed and do not lose vacuum with loss of power.

Bend testing (to determine the ductile-brittle transition temperature) was used extensively for screening since it provides an excellent indication of a wide variety of structural interactions. Over 3000 bend tests were required. Bend test screening was complemented by tensile testing to 2400<sup>0</sup> F for each alloy requiring over 600 tensile tests. Final analyses of instabilities were supported with optical and electron microscopy as required.

## TECHNICAL PROGRAM

### Alloys

The alloys evaluated in this program are listed in table III-1, which shows their nominal composition and general metallurgical classification. Specific processing parameters, as-received structure, and chemistry have been documented elsewhere (ref. 1). All these materials were procured in the recrystallized condition and to optimum processing schedules where these were identified by suppliers. Hence, insofar as possible, all alloys were normalized for long life testing.

Of the alloys evaluated, T-111, T-222, and FS-85 eventually received the greatest emphasis in this program. This resulted because they were identified in the earlier welding phase of this program and in companion creep and corrosion test evaluations as those alloys demonstrating optimum combinations of these characteristics. Hence, they demonstrated the greatest potential for advanced space power system applications.

## AGING PARAMETERS

The aging matrix for this program was as follows:

| Aging time,<br>hr | Aging<br>temperature,<br>°F |
|-------------------|-----------------------------|
| 100               | 1500                        |
| 1 000             | 1800                        |
| 5 000             | 2100                        |
| 10 000            | 2400                        |

All alloys were tested at all temperatures through 1000 hours of aging. The most promising alloys were carried through completely to 10 000 hours. T-111, T-222, and FS-85 were aged at all combinations; D-43 and B-66 received modest attention beyond 1000 hours; and all the other alloys were evaluated only through 1000 hours.

For each temperature-time combination each alloy was evaluated by determining bend transition temperatures of base metal, tungsten arc welds, and electron beam welds, all in both the longitudinal and transverse directions. In addition, room and elevated temperature tests were conducted in accordance with the test matrix shown in figure III-1. Optical and electron metallography, hardness traverses, and chemistry determinations were performed as required to analyze results and demonstrate adequacy of experimental techniques.

### Specimen Preparation

Specimens were prepared for aging by pickling, welding, postweld annealing, blanking and machining, and repickling in sequence. Following final pickling specimens were handled only with clean cotton gloves prior to aging. Specimen groups were packaged by alloy and wrapped in tantalum foil for aging. All alloys were then aged together for any particular time-temperature combination. Welding parameters and postweld anneals were selected to provide maximum ductility as previously established (ref. 1). These are listed in table III-2. Since alloys were normalized to optimum starting ductility, we rationalized that they would be most sensitive to structural instability. Selection of a postweld anneal further satisfied a general requirement for corrosion resistance in refractory metal alloys. All specimens were produced from 0.035-inch sheet. Again, general details of specimen preparation, dimensions, and test procedures have been previously documented (refs. 1 and 2). Maintenance of optimum cleanliness was emphasized in every phase of processing.

Aging was accomplished in Varian ultrahigh vacuum sputter-ion pumped furnaces. These provided pressures from  $\sim 10^{-11}$  to  $10^{-8}$  torr for aging. Numerous

checks for contamination of specimens were performed, and all proved negative, as shown typically in table III-3. These furnaces have been fully characterized for this application (ref. 3). The high vacuum facility is shown in figure III-2.

## RESULTS AND DISCUSSION

### High Strength Alloys of Greatest Interest (T-111, T-222, FS-85)

These alloys are grouped for discussion because of both similarities in thermal stability results and excellent balance of creep strength, weldability, and liquid metal corrosion resistance. Behavior of FS-85 differed only in being typical of other columbium alloys in fracture mode. FS-85 displayed a classic transition from ductile-to-brittle behavior in bend testing. In contrast, T-111 and T-222 bend specimens responded to aging by displaying an increased temperature for ductile tearing primarily in the weld metal. This was based on the 1t bend test, which is essentially a "go - no go" test for  $33\frac{1}{3}$  percent outer fiber strain.

The behavior of T-111, T-222, and FS-85 following long time exposures at elevated temperatures was markedly similar. The ultimate tensile strength at room temperature and 1800<sup>o</sup>, 2100<sup>o</sup>, and 2400<sup>o</sup> F as a function of aging time is shown in figures III-3, III-4, and III-5 for T-111, T-222, and FS-85, respectively. The tensile strength of FS-85 shows no change within the range of conditions evaluated, while a modest decrease in the tensile strength of T-111 and T-222 is seen to result from the aging. The decrease is most significant for tests at 1800<sup>o</sup> F. This could be rationalized on the basis of strain aging, which is pronounced at this temperature for both T-111 and T-222. Aging at 1500<sup>o</sup> F had much less effect on the 1800<sup>o</sup> F tensile strength than aging at the higher temperatures.

Unlike the tensile test results, determinations of the bend ductile-brittle transition temperature indicated a significant aging response for T-111, T-222, and FS-85 (figs. III-6, III-7, and III-8). Several similarities are noted for the three alloys:

- (1) The magnitude of the response is greatest for gas tungsten arc welds and least for base metal specimens.
- (2) Ductility is not impaired by aging at 2400<sup>o</sup> F.
- (3) Aging at 1500<sup>o</sup> F caused no discernible effect in T-111 and T-222, but some response was noted for the lower melting, columbium-base FS-85.
- (4) Maximum response for these alloys was after aging at 1800<sup>o</sup> and 2100<sup>o</sup> F.

Subsequent to the aging study reported here, the aging response for T-111 received further scrutiny to more completely define its characteristics. It was deter-

mined that T-111 weld aging was not responsive to postweld annealing to 3000° F. Hence, an averaged structure was not achievable using any practical annealing temperature. This is shown in figure III-9. Further, the aging response as measured by the longitudinal tensile ductility of T-111 gas tungsten arc welds was not as severe as might be inferred from the bend test data. This is shown in figure III-10 for tensile tests run at 32° F. The welds all have good ductility but less than that required to pass the 1t bend test of this study, which produces  $33\frac{1}{3}$  percent outer fiber strain. In this respect the bend test should always be viewed as a "go - no go" test for a given level of strain. Figures III-9 and III-10 show that no thermal solution to aging could be achieved in this alloy and also that based on tensile ductility no solution was required. However, the necessity to understand the observed aging response could not definitely be dismissed. Hence, a considerable effort was expended to identify the mechanism responsible for the observed aging response. It does not appear that the observed aging compromises the uses of T-111. This stems from the fact that all tantalum alloy fractures occurred by intergranular tearing exhibiting considerable ductility.

T-111 (Ta-8W-2Hf). - Responses of T-111 were evaluated in greatest detail both because of its general importance and because the similarity of responses indicated that only one alloy of this group required detailed analysis. Microstructures of the weld zone, heat affected zone (HAZ), and base metal of selected T-111 specimens are shown in figure III-11. Gas tungsten arc welds are shown since these represent the condition of maximum response.

The 1 hour 2400° F postweld anneal (fig. III-11(a)) has resulted in a weld zone relatively precipitate-free. In the HAZ the only evidence of precipitates is along the grain boundaries. The bend DBTT of this structure was below -320° F.

After aging for 10 000 hours at 1800° F the microstructure is altered from that of figure III-11(a) to that shown in figure III-11(b). Weld zone precipitates can be observed in the aged structure, mainly along the interdendritic boundaries of the original cored weld structure. This suggests that gradients in solute concentration associated with the cored structure provide the driving force for this precipitation. There is, in addition, a nearly continuous precipitate phase located at the grain boundaries of the fusion zone. Fine, dispersed precipitates are apparent in the HAZ, while the base metal appears to be quite clean except for the presence of coarse precipitates along the grain boundaries. The bend DBTT of this specimen was 125° F.

The effect of aging T-111 at 2100° F for 5000 hours can be seen in figure III-11(c). The amount of interdendritic precipitate has decreased while the amount of grain boundary precipitate in the fusion zone has remained relatively unchanged. Little change has occurred in the HAZ except that possibly a little more precipita-



tion has occurred. The base metal, shown at a magnification of 500, is similar to that shown in figure III-11(b). The bend DBTT is now  $-25^{\circ}\text{ F}$ .

After 10 000 hours at  $2400^{\circ}\text{ F}$ , for which the bend DBTT was below  $-320^{\circ}\text{ F}$ , complete homogenization had occurred, and, except for isolated coarse precipitates at the grain boundaries, the structures were single phase. This structure could essentially be restored in specimens aged 10 000 hours at  $1800^{\circ}\text{ F}$  by postaging anneals of 1 and 16 hours at  $2400^{\circ}\text{ F}$ . The microstructures of weld, HAZ, and base metal following these anneals are shown in figure III-12. Comparison with figure III-11(b) indicates the postage anneals have effected a reduction in the amount of weld zone precipitates at both interdendritic and grain boundary areas and the nearly complete elimination of precipitates in the HAZ while having virtually no effect on the base metal. The postage annealed structure appears to be quite similar to the 1 hour  $2400^{\circ}\text{ F}$  postweld annealed structure of figure III-11(a).

There appears to be a correlation between the bend transition temperature and the amount of interdendritic and grain boundary precipitates in the weld fusion zone. Since the transition temperature decreases with a decrease in the amount of precipitate, it seems likely that a cause-effect relation exists between them. Further evidence of such a relation, particularly in the case of the grain boundary precipitates, is the fact that weld fractures during bend testing were invariably intergranular. Hence, efforts were directed toward identification of the precipitates in order to obtain an understanding of the ductility impairment mechanism.

Bulk extraction residues were obtained from base metal and weld metal specimens of T-111 both before and after aging. Debye-Scherrer diffraction patterns of these residues indicated the presence of monoclinic  $\text{HfO}_2$ , the FCC monocarbide  $(\text{Hf}, \text{Ta})\text{C}$ , and the dimetal carbide  $\text{Ta}_2\text{C}$ . The relative amounts of these phases did not vary significantly with specimen history. While these results are meaningful and useful, it must be recognized that there are a number of limitations of this technique. Some of these are

- (1) Some phases present may be attacked and dissolved by the bromine-methanol-tartaric acid solution used to dissolve the matrix.
- (2) If a dispersed phase is present in a very small quantity, it may be obscured by the background radiation.
- (3) No information is obtained regarding the size, shape, and distribution of the extracted particles.

To supplement the X-ray selected area electron diffraction was performed on standard fractograph replicas of T-111 specimens aged as follows:

| Time,<br>hr | Temperature,<br>°F |
|-------------|--------------------|
| 5 000       | 1800               |
| 10 000      | 1800               |
| 1 000       | 2100               |
| 5 000       | 2100               |

The fractograph replicas were prepared from the surfaces of freshly fractured specimens which were fractured by bending in a vise at  $-320^{\circ}$  F. Standard replicating procedures were used except that shadowing was not employed since the primary aim was to ascertain the existence of, and to identify if possible, any particles which might be associated with the fracture surface. Examination with the electron microscope revealed second phase particles had been successfully retained on the replicas. Despite the fact that high quality single crystal selected area electron patterns were obtained on a number of particles, efforts to identify them were not successful. A typical electron micrograph and an electron diffraction pattern are shown in figure III-13.

Additional extraction replicas were prepared from the fracture surfaces of GTA welds aged 1000 hours at  $2100^{\circ}$  F and 5000 hours at  $1800^{\circ}$  F. Platelet particles on these replicas were chemically analyzed at Advanced Metals Research Corporation using a focusing X-ray spectrometer attachment to a Philips EM-200 Electron Microscope. With this instrument the exciting electron beam can be focused to a diameter of about 1 micron on the surface of the specimen being analyzed. The chemical analysis of the excited area is afforded by analysis of the characteristic radiation of the specimen by the X-ray spectrometer. Tantalum was the only metallic element found in the platelets analyzed. This suggests the platelets are light element compounds of tantalum such as carbides, oxides, or nitrides.

To further characterize the weld zones and the effect of aging, electron microprobe techniques were employed to study microsegregation in GTA welds of T-111 in the as-welded plus 1 hour  $2400^{\circ}$  F postweld annealed condition and also in a similar weld aged 10 000 hours at  $1800^{\circ}$  F. The results of this work, also performed at Advanced Metals Research Corporation, are given in table III-4.

These measurements indicate the magnitude of the coring which exists in the weld structure after the 1 hour  $2400^{\circ}$  F postweld anneal is being affected very little by 10 000 hour aging at  $1800^{\circ}$  F, an observation not unexpected since the kinetics of W and Hf diffusion would be quite slow at that temperature.

The results presented above indicate a case can be made for the existence of two different phases in the fusion zone. The observed W and Hf segregation indi-

cates the interdendritic precipitates may be a heavy metal phase such as  $W_2Hf$ , whereas the grain boundary phase is more likely a light element compound of tantalum. Observations of a decreasing amount of precipitate at both regions with higher aging temperatures are consistent with enhanced diffusion kinetics. The fact that the fractures appear to be intergranular rather than interdendritic and the fact that some aging response is observed in uncured base metal suggest that, if two different phases are involved, the grain boundary phase may be more important with respect to the aging response.

Briefly reviewing the precipitate behavior, we find

(1) No evidence of the grain boundary precipitate is seen in the fusion zones of T-111 welds in either the as-welded or the as-welded and postweld annealed specimens. Modest interdendritic precipitation was noted (fig. III-11(a)).

(2) Aging at  $1800^{\circ}$  and  $2100^{\circ}$  F results in precipitation on fusion zone grain and dendrite boundaries (figs. III-11(b) and (c)).

(3) Short time annealing at  $2400^{\circ}$  F of welds aged at  $1800^{\circ}$  and  $2100^{\circ}$  F decreases the amount of both grain and dendrite boundary precipitate (fig. III-12).

The fact that the amount of precipitate observed after aging at  $1800^{\circ}$  and  $2100^{\circ}$  F is seen to decrease on subsequent exposure at  $2400^{\circ}$  F suggests a solvus temperature is being exceeded and the precipitate is going into solution.

Hypothesis for the T-111 aging response. - The  $1800^{\circ}$  to  $2100^{\circ}$  F reaction range suggests that the grain boundary precipitate is an interstitial compound behaving in a manner typified by  $Ta_2C$ . The interdendritic precipitate occurs simultaneously but in such large quantity and at a slower rate such that one is inclined to suspect this to be an intermetallic compound typified by  $W_2Hf$ . Neither was identified using the various experimental techniques of this program. However, the expected behavior of these two types of precipitates appears consistent with the observed aging response. The grain boundary precipitate exerts the most pronounced influence since the fractures were intergranular. The interdendritic precipitate probably has an indirect influence on the aging response. Its substructure-like arrangement could lead to strengthening within the weld grains. This would lead progressively to a greater differential between grain boundary and matrix strength forcing the grain boundaries to accommodate an increasingly larger share of the total strain with aging. This enhances the tendency for grain boundary failures, a failure mode already promoted in welds by their large grain size (and, hence, low total grain boundary area). This hypothesis is shown schematically in figure III-14.

The evidence suggesting that the grain boundary precipitate is an interstitial compound such as  $Ta_2C$  (ref. 4) is as follows:

- (1) Located preferentially at grain boundaries
- (2) Stable within the approximate aging temperature range

- (3) Unstable at or about 2400° F (may transform and go into solution at this temperature)
- (4) Primarily Ta-base (no W or Hf) as observed by X-ray spectrometry of the fracture surface compound

The evidence suggesting the presence of an intermetallic phase (such as  $W_2Hf$ ) at the interdendritic boundaries is as follows:

- (1) The observed sluggishness in formation is typical of an intermetallic compound.
- (2) The large volume fraction of interdendritic precipitate seems to preclude the possibility it is an interstitial compound.
- (3) Solute redistribution to dendrite boundaries, as determined by electron beam microprobe analysis, results in W and Hf concentrations nearly stoichiometric with  $W_2Hf$ .

The compromising evidence for this hypothesis includes

- (1) Neither the grain boundary phase nor the interdendritic phase was positively identified.  $Ta_2C$  was detected by X-ray diffraction of bulk extraction residues but could not be definitely associated with the grain boundaries. Extraction of the intermetallic would be particularly difficult.

- (2) Phase relations for  $W_2Hf$  in the ternary system are not known.

Other possibilities which were considered but seem to be precluded by the experimental evidence include

- (1) That the grain boundary precipitate is the MC phase (or some analogous phase), since this phase invariably is Hf-rich, a possibility refuted by the results of the X-ray spectrometry. Also, MC exhibits no preference for grain boundary precipitation.
- (2) That the interdendritic phase is a complex Ta-Hf compound forming due to the  $\beta' - \beta''$  miscibility gap known for this alloy system. For such a reaction to occur an enormous local concentration of Hf (>30 percent) would be required.
- (3) That either the interdendritic or the grain boundary phase is  $HfO_2$  since this compound, both in the monoclinic and cubic forms, is easily and routinely extracted and its concentration determined using bulk diffraction techniques. The  $HfO_2$  concentration did not vary with location or aging conditions.

T-222 (Ta-9.6W-2.4Hf-0.01C). - The aging response of this alloy as revealed by changes in the bend transition temperature was similar to that of T-111. The rationale developed and presented for T-111 extends quite well to T-222, requiring only minor modification.

Typical microstructures of T-222 welds aged at 1800°, 2100°, and 2400° F are shown in figure III-15. Comparison of figure III-15(a) with figure III-11(b) reveals that, after 10 000 hours at 1800° F, the aging reaction has resulted in a substantially

greater amount of both grain boundary and interdendritic precipitation in T-222 than occurred in T-111. This was not an isolated case but was true for most aging conditions. The greater amounts of precipitate formed by the 1800<sup>0</sup> and 2100<sup>0</sup> F aging coupled with the fact that the carbon level was apparently greater than the 2400<sup>0</sup> F solubility limit in the alloy resulted in residual precipitates being apparent in the structures aged 10 000 hours at 2400<sup>0</sup> F. The intragranular precipitates observed in the HAZ regions in figures III-15(a) and (b) appear to be those identified by Ammon and Harrod (ref. 4) as the Hf-rich monocarbide (Hf, Ta)C. After 10 000 hours at 2400<sup>0</sup> F this carbide appears to be undergoing coarsening.

Efforts at phase identification were much more limited for this alloy than for T-111. However, the similarity of aging response, microstructural features, and fracture behavior suggests that only modest revision of the hypothesis presented for T-111 would be required for T-222.

FS-85 (Cb-27Ta-10W-1Zr). - While the aging response of this columbium-base alloy was generally similar to that of T-111 and T-222, several important differences were noted in the bend test results. The fracture mode of this alloy was generally by brittle cleavage and not by ductile grain boundary tearing as was noted for T-111 and T-222. An apparent effect of this failure mode was that fractures in weld specimens were not arrested in the base metal. Further, this fracture mode probably accounts for the increased response of base metal and electron beam welds to aging as compared with T-111 and T-222. This fracture behavior is typical of columbium-base alloys, and does not in itself imply any difference with respect to the aging mechanism of this alloy. Finally, FS-85 responded to aging at a lower temperature than T-111 or T-222, perhaps partly because of its lower melting point.

Microstructures of FS-85 are shown in figure III-16 for several aging conditions. In figures III-16(b) and (c) the interdendritic precipitate is visible in the weld zone. For most aging conditions there appeared to be less grain boundary and interdendritic precipitation than was observed in comparably aged T-111 and T-222.

In FS-85, zirconium is the reactive metal addition which behaves in a manner analogous to that of hafnium in tantalum-base alloys. However, in FS-85 there is only about 1 atomic percent Zr, whereas the tantalum-base T-111 and T-222 alloys contain approximately 2.0 and 2.4 atomic percent Hf, respectively. One might reasonably expect then that the zirconium enrichment at interdendritic boundaries in FS-85 welds does not approach the hafnium enrichment in T-111 and T-222 welds. In addition, the carbon level of the FS-85 sheet used for this program was notably less (in terms of atomic ppm) than that of either tantalum-base alloy. Both of these conditions would tend to decrease, relative to T-111 and T-222, the amount of interdendritic and grain boundary precipitate in the fusion zones.

Note the hypothesis presented for T-111 can be extended quite well to FS-85 since  $W_2Zr$  and  $Cb_2C$  provide direct analogs to  $W_2Hf$  and  $Ta_2C$ . In view of the differences in the amount of precipitate between FS-85 and T-111, it may not be possible to ascribe the exact same rationale to their respective aging responses. Admittedly there are two possible explanations which could account for the similarity in behavior in spite of the microstructural differences:

(1) A very small volume of precipitate is required to control the observed aging response in that FS-85 fractured largely by brittle cleavage.

(2) The similarity may be strictly fortuitous. The response observed in the bend transition temperature may be reflecting the bulk or net change of a number of complex interacting factors.

Following  $2400^{\circ}F$  aging, for which microstructures are not shown, considerable grain growth had occurred, weld zones could no longer be distinguished from HAZ and base metal, and very little evidence of precipitates remained. The fact that the bend DBTT was about  $-150^{\circ}$  to  $-175^{\circ}F$  for all types of test specimens after aging 10 000 hours at  $2400^{\circ}F$  implies a ductility limit due to grain size has been realized.

## Miscellaneous Other Solid Solution and Dispersion Strengthened Alloys

(B-66, D-43, Cb-752, C-129Y)

B-66 (Cb-5Mo-5V-1Zr). - Considerable grain growth and modest changes in mechanical properties marked the response of B-66 to long time, elevated temperature aging. Base metal, GTA welds and EB welds were aged for times to 10 000 hours and temperatures to  $2400^{\circ}F$ .

Almost without exception, the results of tensile tests and bend DBTT tests could be interpreted in terms of grain size of the test specimens. Most of the aging temperatures employed in this study are quite high for this alloy, and the large grain sizes noted in the postage microstructures are not unexpected. Changes in ultimate and yield tensile strengths at room temperature and  $1800^{\circ}$ ,  $2100^{\circ}$ , and  $2400^{\circ}F$  were quite modest because of the thermal exposures.

The only significant exception to the above rationale would appear to be the slight "peak" in the bend DBTT found for GTA welds after  $1500^{\circ}F$  aging (fig. III-17). That this peak diminishes with increased aging time at  $1500^{\circ}F$  suggests the possibility that a classic precipitation reaction is occurring. By 5000 hours the overaged condition has apparently been attained and no ductility loss is apparent from the bend test results. Program emphasis did not allow further definition of

this reaction, but the slight improvement in room temperature yield strength for specimens aged at 1500° F relative to the other aging temperatures lends credence to this suggestion. After 5000 hours of aging, ductility of base metal and EB welds normalized to that of GTA welds, an effect easily explained in terms of grain size.

Like other columbium alloys this alloy displayed a classic abrupt transition in bend testing from ductile-to-brittle behavior.

D-43 (Cb-10W-1Zr-0.1C). - This carbide-dispersion strengthened alloy provided the prime example of classic overaging and subsequent loss of strength of the alloys included in the aging study. This alloy has been the object of considerable metallurgical interest, primarily because of its aging reactions. As a result, extensive investigations of these reactions have led to a unique, for refractory metal alloys, and precise identification of the various reaction stages and products. The work of Ostermann and Bollenrath (ref. 5) is particularly outstanding in this respect.

The ultimate tensile strength as a function of aging time and temperature for base metal and GTA welds is shown in figure III-18 for tensile tests conducted at room temperature and 1800°, 2100°, and 2400° F. That only overaging behavior observed is believed due to an apparent optimum condition achieved in the as-received D-43 sheet using a 2400° F postweld anneal. The microstructure of the base metal, as viewed by light microscopy at a magnification of 1500, changed very little from that of the as-received sheet throughout aging treatments as long as 10 000 hours at 1800° F, being composed of a very fine (Cb, Zr)C precipitate dispersed throughout the grain interiors and a coarser columbium carbide,  $\text{Cb}_2\text{C}$ , present as intragranular platelets and a grain boundary precipitate.

The microstructure of the base metal following 10 000-hour aging at 1800° and 2100° F is shown in figure III-19 along with representative weld heat-affected-zone (HAZ) areas for each of these aging conditions. In the base metal both the fine (Cb, Zr)C precipitates and the  $\text{Cb}_2\text{C}$  precipitates have coarsened somewhat during the long-time aging at 2100° F relative to those resulting from aging at 1800° F or lower. The reaction in the HAZ regions is quite different from that occurring in the base metal. During welding, complete solutioning occurs in the HAZ and, because of the rapid cooling to temperatures below about 1000° F, rejection of carbon from solid solution results in the formation of metastable  $\epsilon$  carbides. These carbides are unstable at higher temperatures and transform to the hexagonal  $\text{Cb}_2\text{C}$  and the cubic (Cb, Zr)C, the relative amounts of which depend on temperature of transformation. Hence, the carbides in the HAZ following 10 000-hour aging at 1800° F appear to be a mixture of  $\epsilon$  carbide and  $\text{Cb}_2\text{C}$ , while after 10 000 hours at 2100° F they are a mixture of  $\text{Cb}_2\text{C}$  and cubic (Cb, Zr)C.

The precipitate-free zones adjacent to grain boundaries which are apparent in

figure III-19, particularly following the 2100<sup>0</sup> F aging treatment, are probably indicative of carbon and/or vacancy depletion of the matrix due to interstitial and/or vacancy diffusion to grain boundaries. While solute depletion of the matrix by diffusion of Zr (or W) could lead to the same type of structure, the relatively low aging temperature renders this much less likely.

The averaged condition implied by the tensile data of figure III-17 for a base metal specimen aged 10 000 hours at 2400<sup>0</sup> F is shown in figure III-20.

The bend DBTT data followed the trend established by the tensile data in that, for nearly every aging condition, the aging process increased the ductility (i.e., lowered the bend DBTT). Hardness traverses of aged specimens were of little value as indicators of the aging process. Bend transitions were generally abrupt changes from ductile to brittle behavior as characteristic of columbium base alloys.

From this screening study it would appear the instabilities in structure and mechanical properties of D-43 which result from aging warrant careful consideration for applications involving long times at temperatures above 1500<sup>0</sup> F.

Cb-752 (Cb-10W-2.5Zr). - The response of this alloy to 1000 hour exposures at temperatures from 1500<sup>0</sup> to 2400<sup>0</sup> F was somewhat random. Bend DBTT tests indicated slight, irregular changes with aging temperature. Fracture behavior was typical of columbium alloys. The general trend, however, was for an improvement in bend ductility for specimens aged at 2400<sup>0</sup> F. Results of tensile tests indicated that, except for room temperature ultimate and yield strength, aging time and temperature had very little effect. In figure III-21, the room temperature strength is shown to improve while the elevated temperature strength is relatively unaffected by the aging.

Cb-752 is reported to achieve optimum tensile strength through the use of a duplex annealing treatment during processing (ref. 6). This treatment consists of a 1-hour, 2800<sup>0</sup> F solution anneal followed by a final cold reduction (40 percent) and a 1-hour, 2400<sup>0</sup> F aging anneal. The final anneal is used to induce (Zr,Cb)C precipitation, which provides dispersed phase strengthening. The Cb-752 sheet evaluated in this aging study was produced by a previous processing schedule which did not incorporate an in-process solution anneal and used a 1-hour, 2200<sup>0</sup> F final anneal. Hence, the program Cb-752 was presumably not in the optimum condition with respect to mechanical strength. Comparing the data of figure III-21 with those of Bewley (ref. 6) indicates the following:

- (1) The unaged room temperature tensile strength found in this study is noticeably lower than that attained using the duplex annealing treatment.

- (2) Following the 100- and 1000-hour aging at elevated temperatures, the tensile strengths determined in this study (fig. III-21) are identical with those expected for similarly aged, duplex annealed sheet.



(3) Elevated temperature tensile strength of the program Cb-752 (base metal and GTA welds) is approximately equal to that indicated for duplex annealed sheet.

Similar observations apply to the respective yield strength data.

These results imply that, at least with respect to the factors affecting mechanical strength, very little difference exists between the Cb-752 evaluated in this program and that produced by duplex annealing. The only notable exception appears to be the inferior unaged room temperature strength of the sheet used for this evaluation. This is probably due to the lack of an in-process solution anneal and the use of a lower final annealing temperature for the program Cb-752. Both of these would detrimentally affect the amount and distribution of the strengthening precipitates and would therefore contribute to the observed deficiency in room temperature tensile strength.

C-129Y (Cb-10W-10Hf-0.1Y). - Thermal exposures to 1000 hours at 2400° F had no discernible effect on the tensile properties of this alloy, while data from bend DBTT tests indicated some minor, nongeneral responses to aging had occurred. In typical fashion, the greatest response was seen in gas tungsten arc welds. Fracture behavior was again typical of columbium alloys.

Metallographic examination of aged specimens indicated the grain refining effect of the yttria was effective in controlling grain size of the base metal. Conversely, loss of yttria during welding is implied by continuous grain growth, which occurs in the weld fusion zones as a function of the severity of thermal exposure.

### Solid Solution Alloys (Ta-10W, SCb-291)

The solid solution alloys included in this study were SCb-291 (Cb-10W-10Ta) and Ta-10W. For moderate temperature applications these alloys can be expected to perform adequately for extended periods of time. For the purposes of this program, however, their inclusion is mainly to provide base-line data to permit discrimination between those effects due to solid solution strengthening and those due to dispersed phase strengthening in more complex alloys. Alternatively, since these alloys should be very stable, they also acted as "referee" alloys to double check the aging and handling procedures. Their stable responses to aging did in fact demonstrate the adequacy of the experimental procedures.

Ta-10W. - No instability in structure or tensile strength resulted from 1000-hour exposures at temperatures to 2400° F. Bend transition temperatures of base metal, GTA welds, and EB welds were -320° F for all aging conditions. Microstructures in every case were single phase. Weld structures, particularly GTA welds, were characterized by extremely large grains which resulted in rather low

tensile elongation during tensile testing. However, this behavior was in no way influenced by the aging but rather was a property of the weld structure.

SCb-291 (Cb-10W-10Ta). - This Cb-base alloy demonstrated excellent thermal stability for all aging-time - temperature conditions evaluated. Aging was not performed beyond 1000 hours. Tensile properties showed no significant changes due to the thermal exposures. Bend transition temperatures were generally unaffected by aging except for a slight lowering of bend ductility following the 1000 hour exposures at the highest aging temperatures. Fracture mode in bend testing was brittle cleavage so that bend transitions always occurred with a classic change from ductile to brittle behavior. Subsequent metallography indicated this to be the result of the considerable grain growth which occurs at the most severe thermal exposures. Microstructures were single phase in all cases. Grain growth appeared to be a continuous process as expected for a single-phase, solid-solution alloy.

In conclusion, SCb-291 offers excellent structural and mechanical property stability following long time elevated temperature exposures. Its usefulness, however, is limited by its relatively low high temperature strength.

## CONCLUSIONS

1. The alloys evaluated displayed a wide range of responses to the thermal exposures employed in this program. In most cases, these responses were most easily understood in terms of the metallurgy of the respective alloy system.

2. The alloys generally displayed satisfactory stability, as would typically be required for engineering applications. However, several alloys are temperature limited with respect to thermal stability. D-43 displayed loss of strength with increasing aging time and temperature. This would have to be accommodated in setting design stresses for long time applications for temperatures above 2000° F. SCb-291 and B-66 were prone to loss of ductility with increasing grain size caused by high temperature aging. Hence, these alloys should be used only at the lower temperatures for long time applications. Likewise, Ta-10W displayed similar grain growth related instabilities. Otherwise the alloys investigated were generally acceptable for high temperature application from the standpoint of structural stability.

3. The magnitude of the aging response tended to be greatest for gas tungsten arc welds and least for base metal specimens.

4. An important difference in bend test fracture mode was noted for aged T-111 and T-222 bend specimens compared with columbium-base alloys. Even though shifts in transition behavior were noted, fractures were ductile intergranular

separations which did not propagate from the weld metal into the base metal. Columbium-base alloys tended to display unarrested cracking and a classic, abrupt transition from ductile to brittle cleavage behavior. Hence, the bend transition temperature represents a design limit for columbium alloys but not for the tantalum alloys.

5. T-111, T-222, and FS-85 displayed similar responses to aging. These were detected only in measurements of the bend transition temperature, not being observed in tensile tests at room temperature or elevated temperatures. The fact that no evidence of a response was seen in high temperature tensile tests demonstrated that the thermal stability is excellent from a design standpoint. Of these, FS-85 alone would be limited but only in an unusual situation requiring periodic cycling from the aging temperatures to below the bend transition temperature.

## REFERENCES

1. Lessmann, G. G.: The Comparative Weldability of Refractory Metal Alloys. *Welding J. Res. Suppl.*, vol. 45, no. 12, Dec. 1966, pp. 540-s - 560-s.
2. Stoner, D. R.; and Lessmann, G. G.: Measurement and Control of Weld Chamber Atmospheres. *Welding J. Res. Suppl.*, vol. 44, no. 8, Aug. 1965, pp. 337-s - 346-s.
3. Stoner, D. R.; and Lessmann, G. G.: Operation of  $10^{-10}$  Torr Vacuum Heat Treating Furnaces in Routine Processing. *Transactions Vacuum Metallurgy Conference. American Vacuum Society*, 1965, pp. 17-40.
4. Ammon, R. L.; and Harrod, D. L.: Strengthening Effects in Ta-W-Hf Alloys. *Refractory Metals and Alloys IV, Research and Development. Vol. 1. R. I. Jaffee, G. M. Ault, J. Maltz, and M. Semchyshen, eds., Gordon and Breach Sci. Publ.*, 1968, pp. 423-442.
5. Ostermann, Friedrich; and Bollenrath, Franz: On the Precipitation Behavior of Niobium Alloy D-43 (Nb-10W-1Zr-0.1C). *6th Plansee Seminar. Vol. 1. Metallwerk Plansee AG, Reutte, Austria*, 1968.
6. Bewley, J. G.: Strengthening of Columbium Alloy Cb-752 by Duplex-Annealing Process. *Refractory Metals and Alloys IV, Research and Development. Vol. 1. R. I. Jaffee, G. M. Ault, J. Maltz, and M. Semchyshen, eds., Gordon and Breach Sci. Publ.*, 1968, pp. 369-386.

TABLE III-1. - ALLOYS EVALUATED FOR THERMAL STABILITY

| Alloy                            | Classification <sup>a</sup>   | Nominal composition, wt %   |
|----------------------------------|---|---|
| T-111<br>T-222<br>FS-85          | Highest creep strengths<br>Gettered alloys <sup>b</sup><br>Solid solution + dispersion strengthened | Ta-8W-2Hf<br>Ta-9.6W-2.4Hf-0.01C<br>Cb-27Ta-10W-1Zr                 |
| Ta-10W<br>SCb-291                | Solid solution strengthened<br>Ungettered alloys <sup>b</sup>                                       | Ta-10W<br>Cb-10W-10Ta   |
| B-66<br>D-43<br>C-129Y<br>Cb-752 | Solid solution + dispersion strengthened<br>Gettered alloys <sup>b</sup>                            | Cb-5Mo-5V-1Zr<br>Cb-10W-1Zr-0.1C<br>Cb-10W-10Hf + Y<br>Cb-10W-2.5Zr |

<sup>a</sup>For weldability ratings see ref. 1.<sup>b</sup>Reactive element addition, Zr or Hf, provides corrosion resistance in liquid alkali metals.

TABLE III-2. - OPTIMIZED WELD CONDITIONS FOR 0.035-INCH SHEET

| Alloy<br>(a) | Process | Parameters<br>(b) | 1-hr postweld<br>anneal<br>temperature,<br>°F<br>(c) | Weld width ratio,<br>top/bottom,<br>in. | BDBTT, <sup>d</sup> °F |                     |
|--------------|---------|-------------------|--|---|------------------------|---------------------|
|              |         |                   |  |   | Longitudinal<br>bends  | Transverse<br>bends |
| Ta-10W       | GTA     | 7.5-1/4-118       | No anneal  | 0.190/0.180                             | <-320                  | <-320               |
|              | EB      | 15-1/2-4.5        | No anneal  | .049/0.034                              | <-320                  | <-320               |
| T-111        | GTA     | 15-3/8-115        | 2400   | 0.195/0.189                             | <-320                  | <-320               |
|              | EB      | 15-1/2-3.8        | 2400   | .038/0.027                              | <-320                  | <-320               |
| T-222        | GTA     | 30-1/4-190        | 2400   | 0.180/0.159                             | <-320                  | <-320               |
|              | EB      | 15-1/2-3.8        | 2400   | .039/0.026                              | <-320                  | <-320               |
| B-66         | GTA     | 15-3/8-86         | No anneal  | 0.190/0.180                             | 0                      | +75                 |
|              | EB      | 25-3/16-3.2       | 1900   | .036/0.024                              | -225                   | -175                |
| C-129Y       | GTA     | 30-3/8-110        | 2400   | 0.180/0.130                             | -200                   | -225                |
|              | EB      | 50-1/2-4.1        | 2200   | .040/0.026                              | -250                   | -250                |
| Cb-752       | GTA     | 30-3/8-87         | 2200   | 0.129/0.090                             | -75                    | 0                   |
|              | EB      | 15-3/16-3.3       | 2400   | .036/0.017                              | -200                   | -200                |
| D-43         | GTA     | 30-3/8-114        | 2400   | 0.159/0.143                             | +100                   | 0                   |
|              | EB      | 50-1/2-4.4        | 2400   | .040/0.027                              | -225                   | <sup>e</sup> -225   |
| FS-85        | GTA     | 15-3/8-90         | 2400   | 0.204/0.195                             | -175                   | -175                |
|              | EB      | 50-3/16-4.4       | 2200   | .038/0.026                              | -200                   | -200                |
| SCb-291      | GTA     | 15-1/4-83         | 2200   | 0.160/0.150                             | -275                   | -275                |
|              | EB      | 50-1/2-4.4        | No anneal  | .038/0.027                              | <-320                  | -250                |

<sup>a</sup>As-received alloys were in the recrystallized condition.<sup>b</sup>For GTA welds: speed, in./min; clamp spacing, (in.)(A); for EB welds: speed, in./min; clamp spacing, (in.)(mA). (All EB welds with 60-cycle, 0.050-in. longitudinal deflection and 150-kV beam voltage.)<sup>c</sup>Postweld anneal was selected for optimum ductility but is also assumed to achieve an averaged structure with respect to internal reactive metal-oxygen reactions, which enhances its compatibility with alkali metals.<sup>d</sup>Bend ductile-brittle transition temperature at 1t bend radius for all except FS-85 welds; transition temperature at 2t bend radius for FS-85 welds.<sup>e</sup>Probable value (determined value <-125° F).

TABLE III-3. - IN-PROCESS INTERSTITIAL ANALYSES (wt. ppm)

| Alloy | Element | Base metal as-received | As-welded GTA welds | 500-hr age <sup>a</sup> |         | 10 000-hr age <sup>a</sup> |         |         |         |
|-------|---------|------------------------|---------------------|-------------------------|---------|----------------------------|---------|---------|---------|
|       |         |                        |                     | 1800° F                 | 2400° F | 1500° F                    | 1800° F | 2100° F | 2400° F |
| T-111 | C       | 48                     | 34                  | 36                      | 44      | 30                         | 80      | 53      | 45      |
|       | O       | 15                     | 24                  | 20                      | 13      | 12                         | 13      | 13      | 20      |
|       | N       | 18                     | 26                  | 24                      | 24      | 24                         | 27      | 23      | 21      |
| T-222 | C       | 100                    | 125                 | 79                      | 150     | 150                        | 150     | 140     | 140     |
|       | O       | 29                     | 22                  | 45                      | 32      | 25                         | 15      | 46      | 30      |
|       | N       | 10                     | 16                  | 66                      | 8       | 9                          | 8       | 8       | 7       |
| FS-85 | C       | 12                     | 14                  | 39                      | ---     | 48                         | 47      | 48      | 38      |
|       | O       | 98                     | 73                  | 75                      | ---     | 51                         | 96      | 70      | 75      |
|       | N       | 50                     | 41                  | 24                      | ---     | 45                         | 47      | 41      | 27      |

<sup>a</sup> Aged specimens in nearly all cases were base metal.

TABLE III-4. - RESULTS OF ELECTRON MICROPROBE STUDY OF  
MICROSEGREGATION IN T-111 GTA WELDS

| Specimen condition   | Weld region analyzed<br>(a) | Concentration, wt % |     |
|--|-----------------------------|---------------------|-----|
|  |                             | W                   | Hf  |
| As-welded plus 1-hr 2400° F postweld anneal                        | Near HAZ; IDB               | 7.9                 | 3.1 |
|  | Near HAZ; IDI               | 9.6                 | 1.7 |
| As-welded plus 1-hr 2400° F postweld anneal                        | Weld center; IDB            | 7.5                 | 3.5 |
|  | Weld center; IDI            | 9.8                 | 1.3 |
| As-welded plus 1-hr 2400° F and 10 000-hr 1800° F postweld anneals | Near HAZ; IDB               | 7.8                 | 4.5 |
|  | Near HAZ; IDI               | 10.1                | 1.9 |
| As-welded plus 1-hr 2400° F and 10 000-hr 1800° F postweld anneals | Weld center; IDB            | 8.6                 | 2.9 |
|  | Weld center; IDI            | 9.6                 | 1.9 |

<sup>a</sup> IDB, at the interdendritic boundaries; IDI, at the interdendritic interiors.

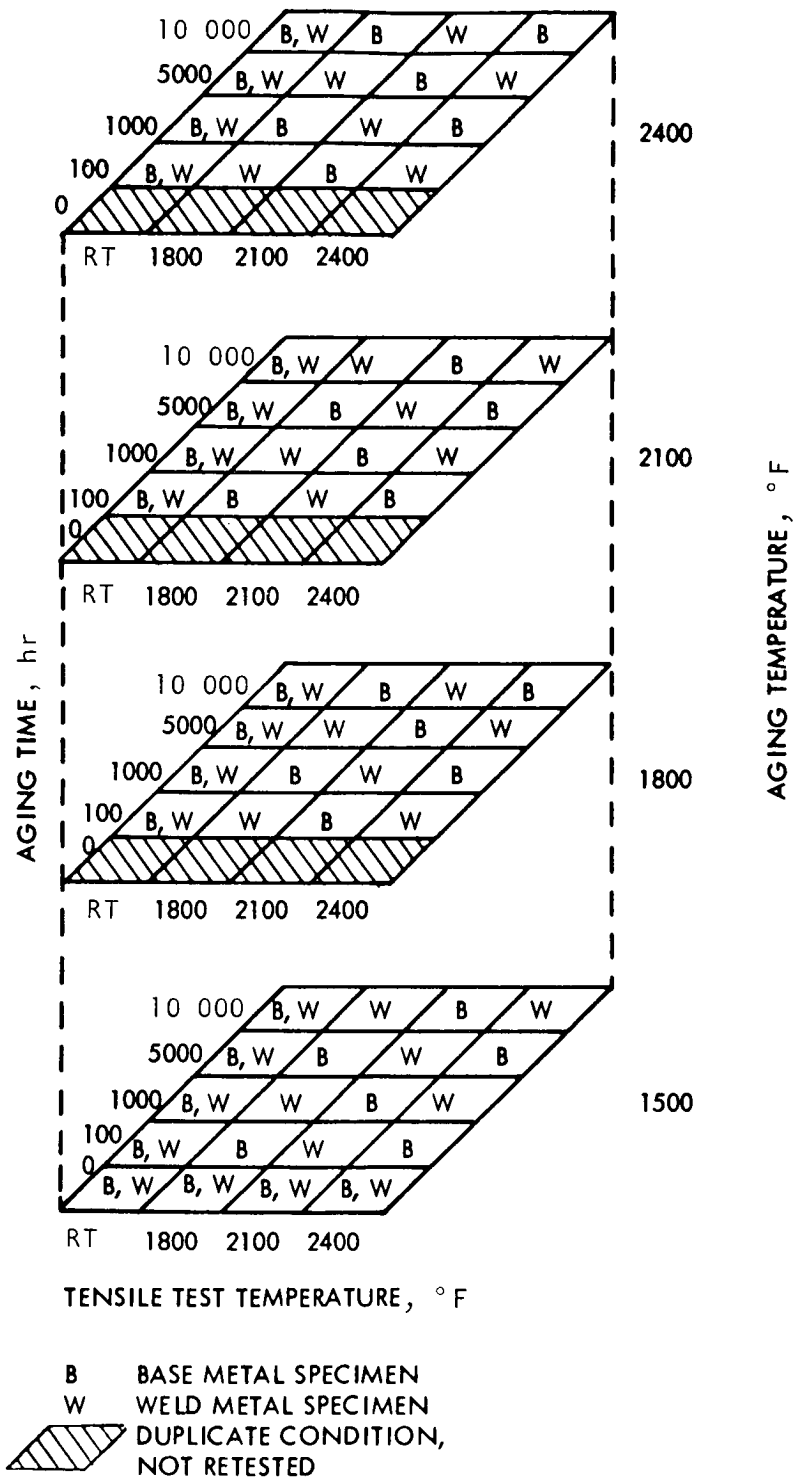


Figure III-1. - Typical tensile test schedule for aged specimens.

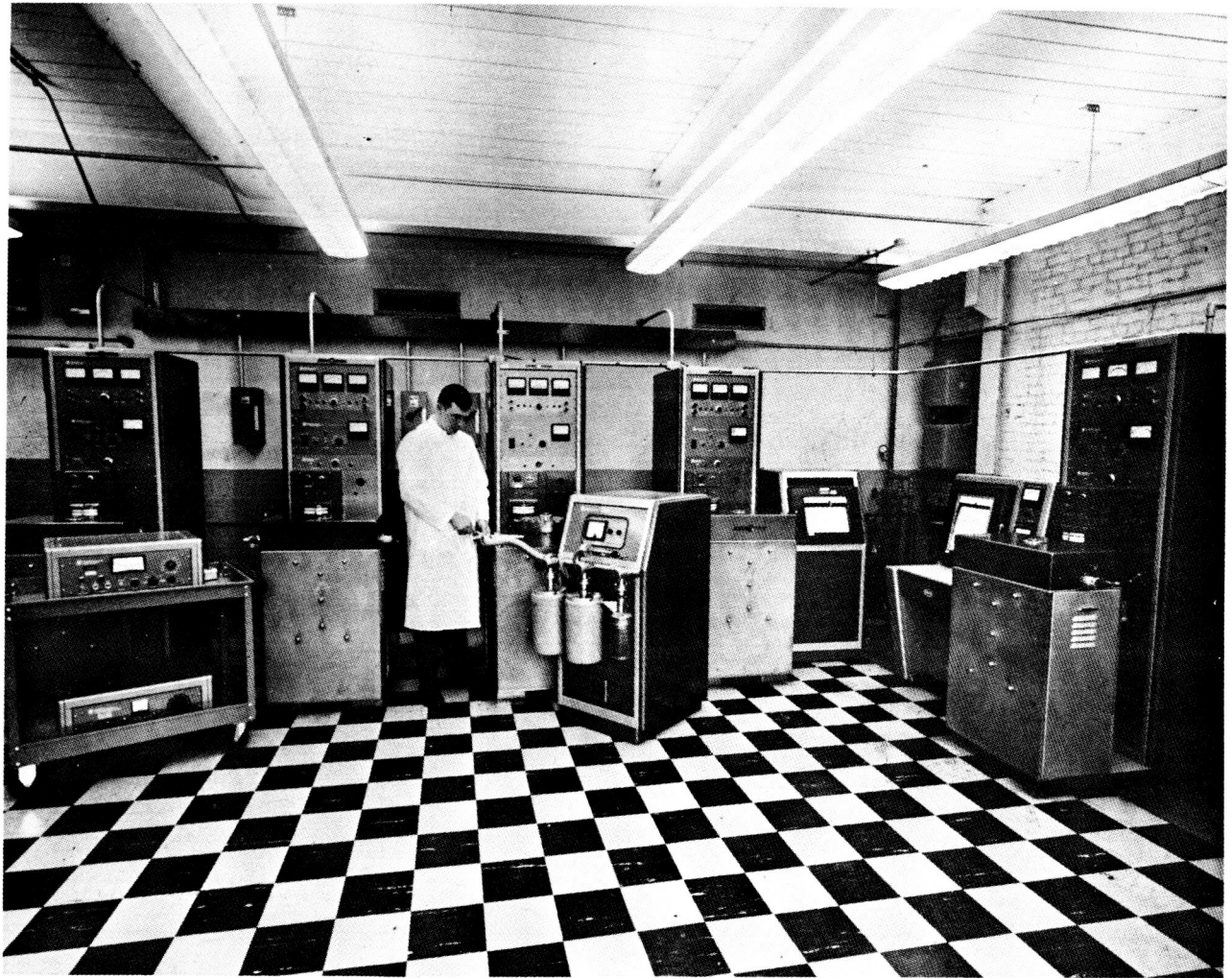


Figure III-2. - Ultrahigh vacuum annealing furnaces.

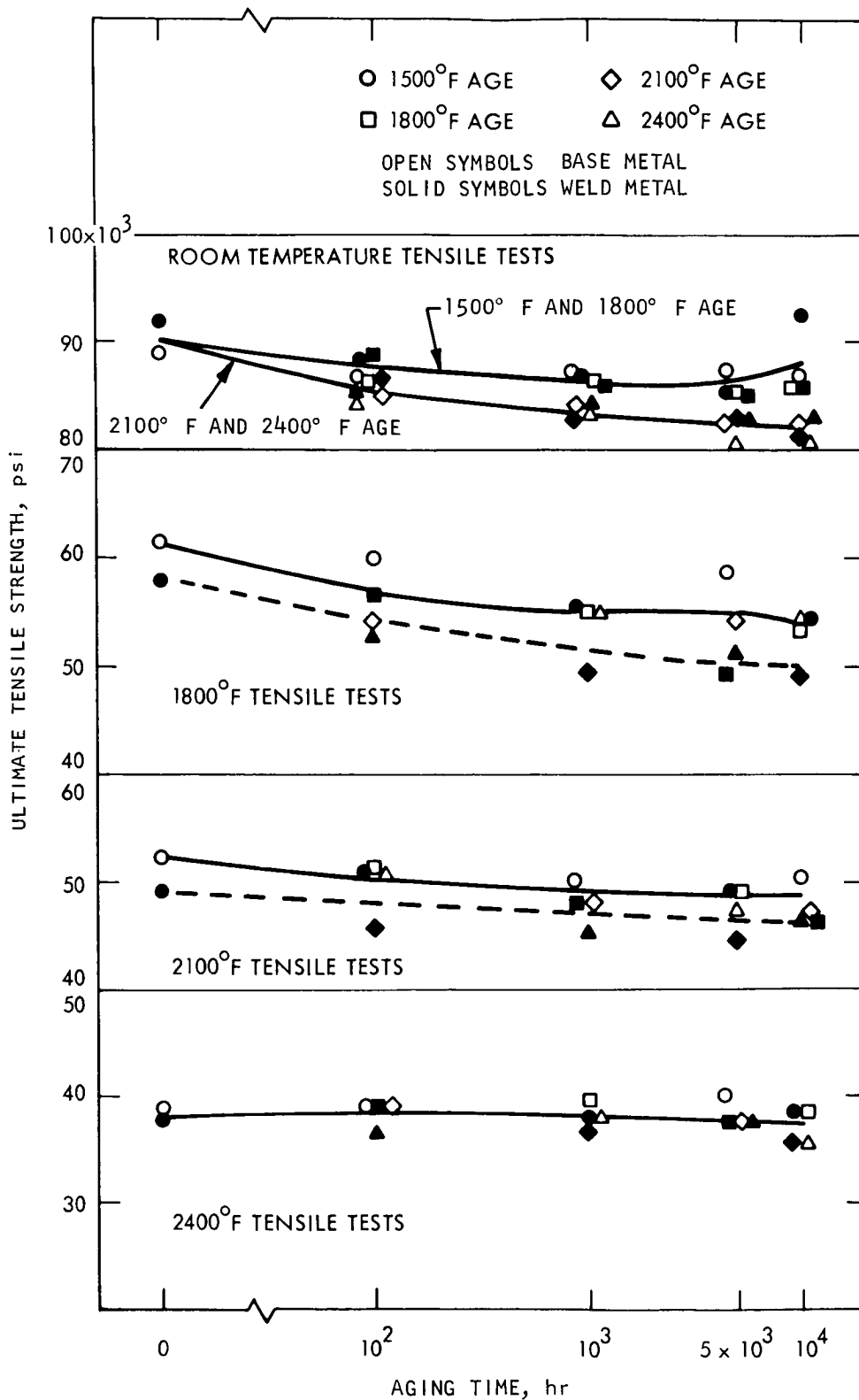


Figure III-3. - Ultimate tensile strength of T-111 as function of aging parameters. Optimum weld parameters; all samples annealed 1 hour at 2400° F prior to aging and testing.



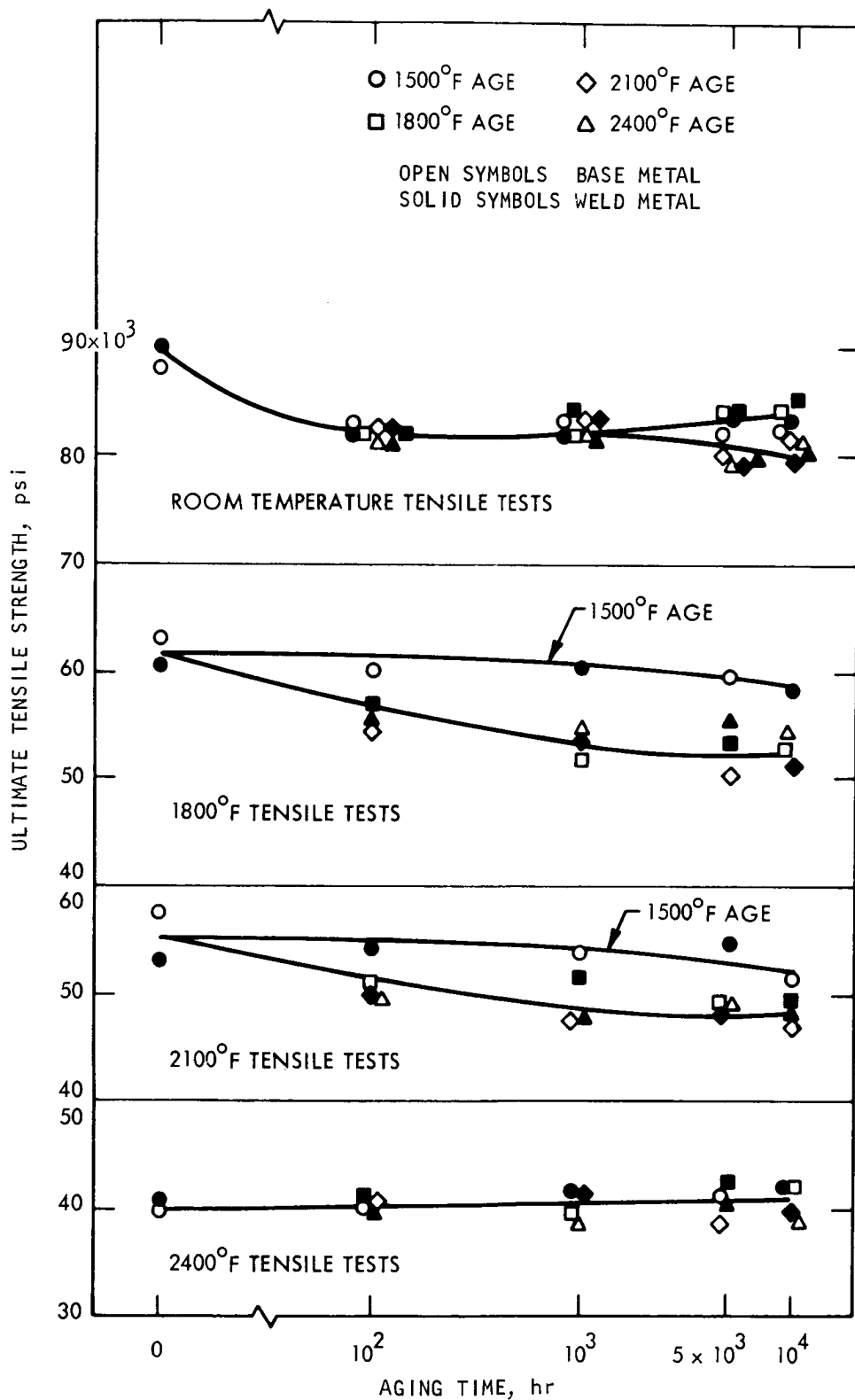


Figure III-4. - Ultimate tensile strength of T-222 as function of aging parameters. Optimum weld parameters; all samples annealed 1 hour at 2400° F prior to aging and testing.

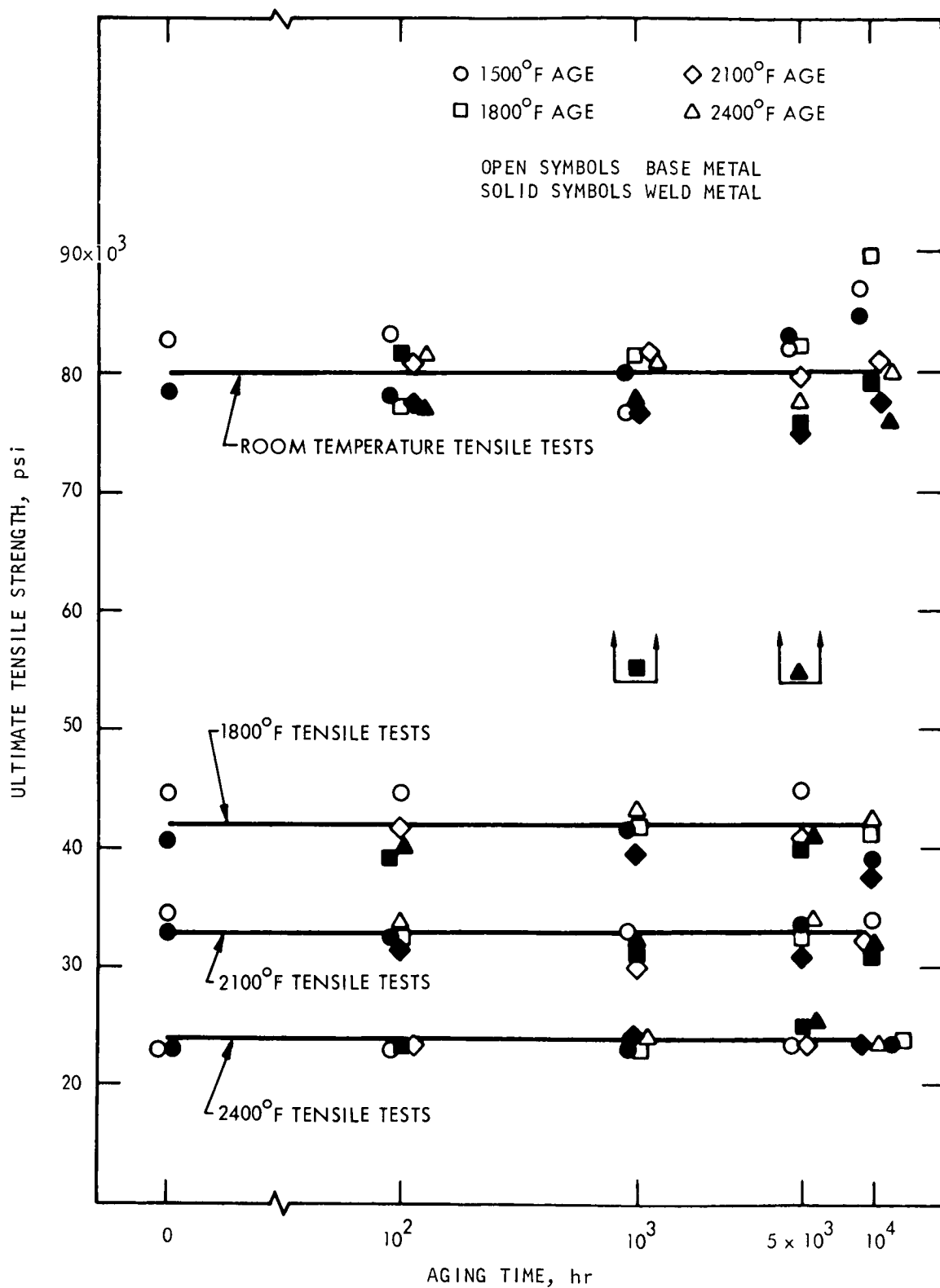


Figure III-5. - Ultimate tensile strength of FS-85 as function of aging parameters. Optimum weld parameters; all samples annealed 1 hour at 2400° F prior to aging and testing.

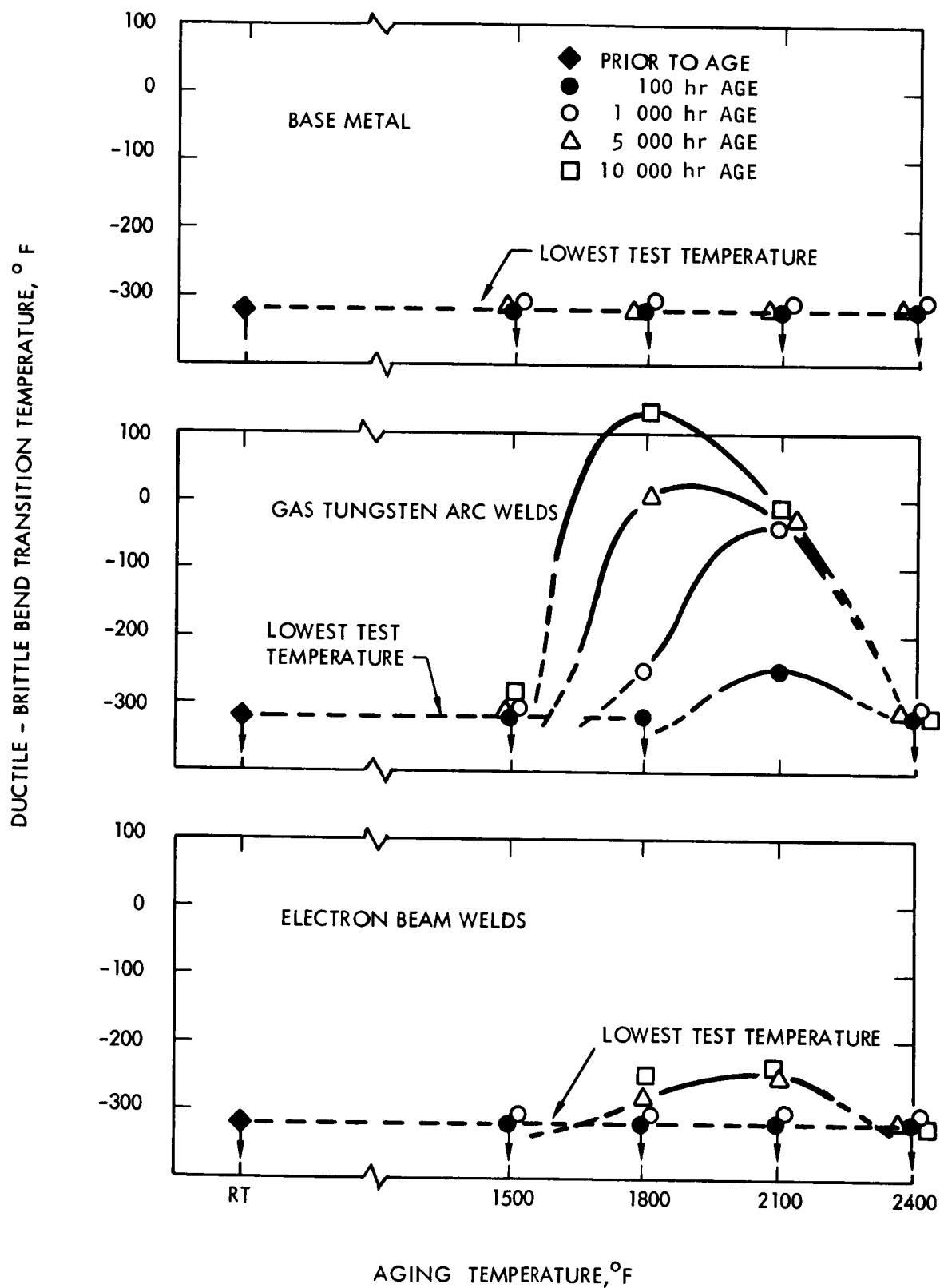


Figure III-6. - Bend ductile-brittle transition temperature of T-111 as function of aging parameters.

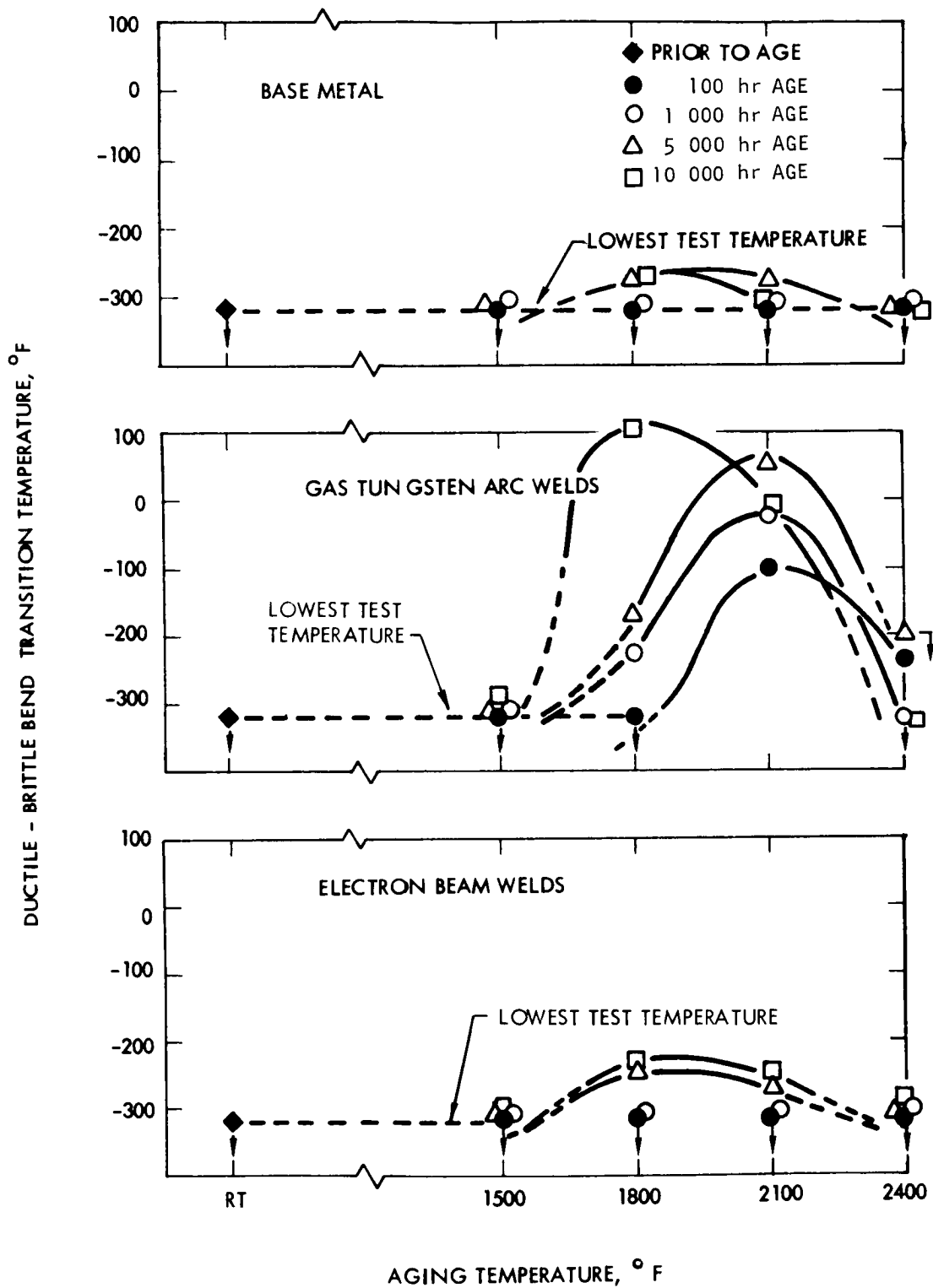


Figure III-7. - Bend ductile-brittle transition temperature of T-222 as function of aging parameters.

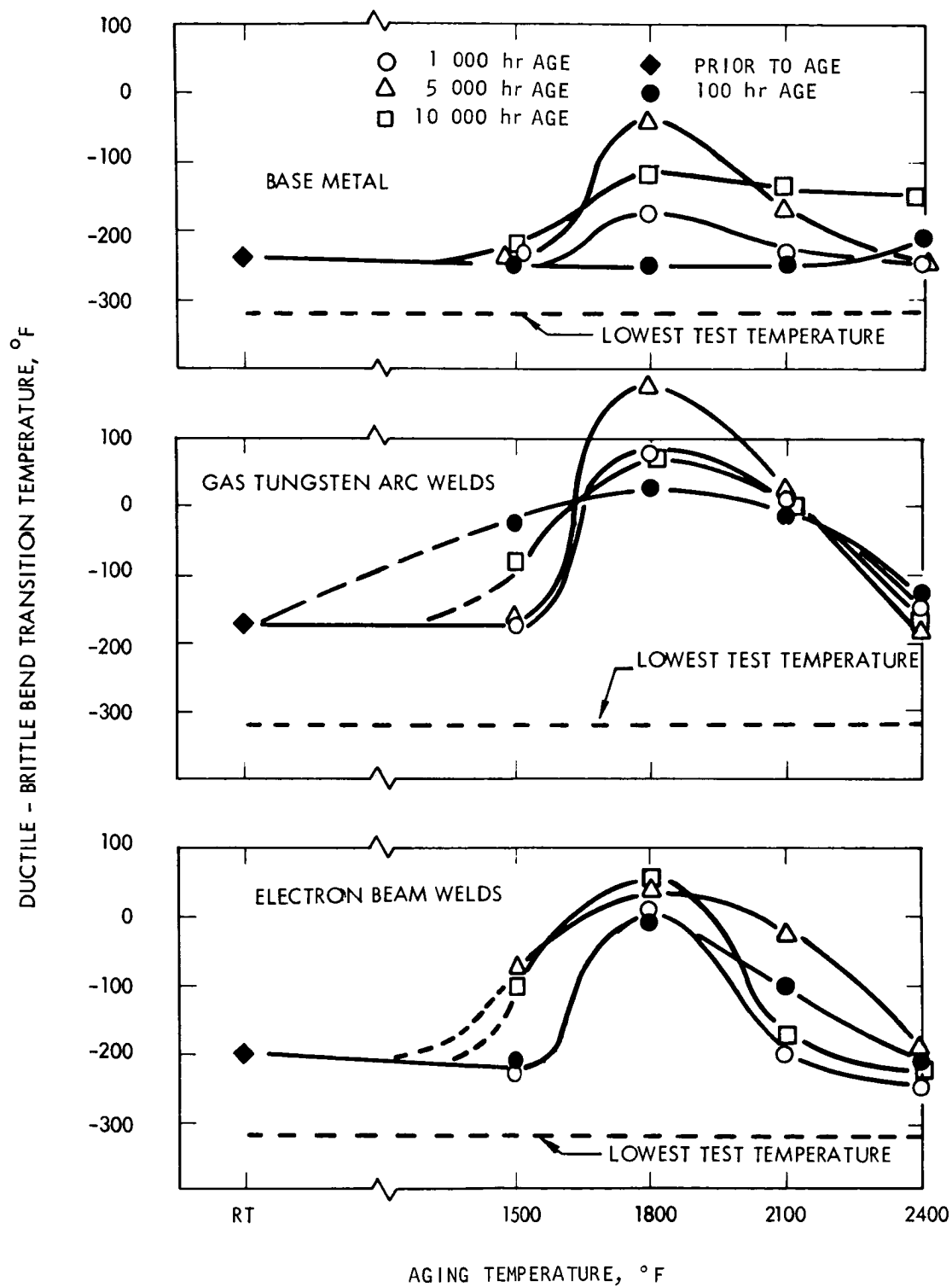


Figure III-8. - Bend ductile-brittle transition temperature of FS-85 as function of aging parameters.

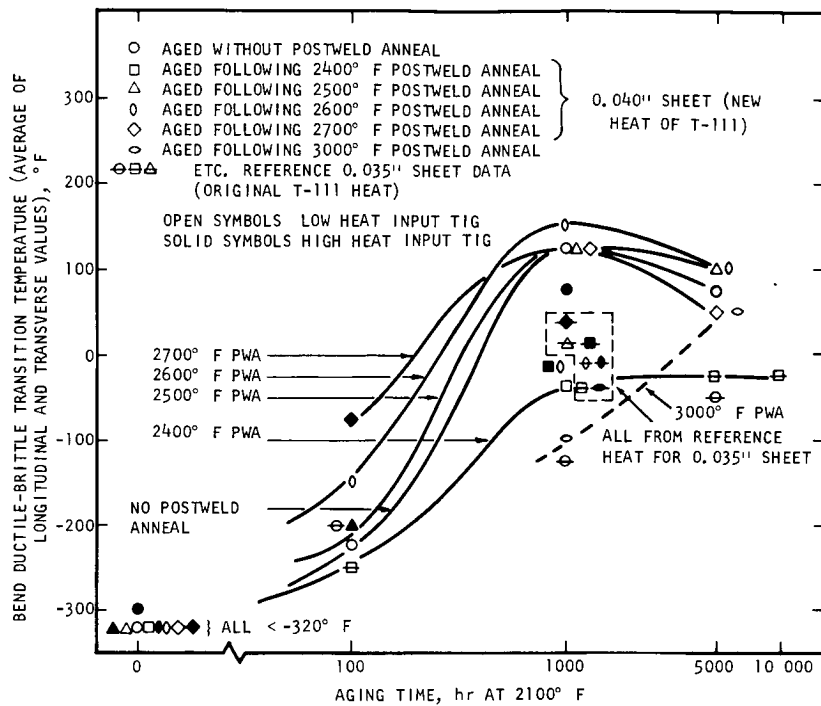


Figure III-9. - Effect of postweld annealing on aging in T-111 welds. Data points within dashed block for tests on T-111 heat used this program. Remaining points from additional heat of T-111. (Low heat input welds made at 15 in./min; high heat input welds made at 6 in./min.)

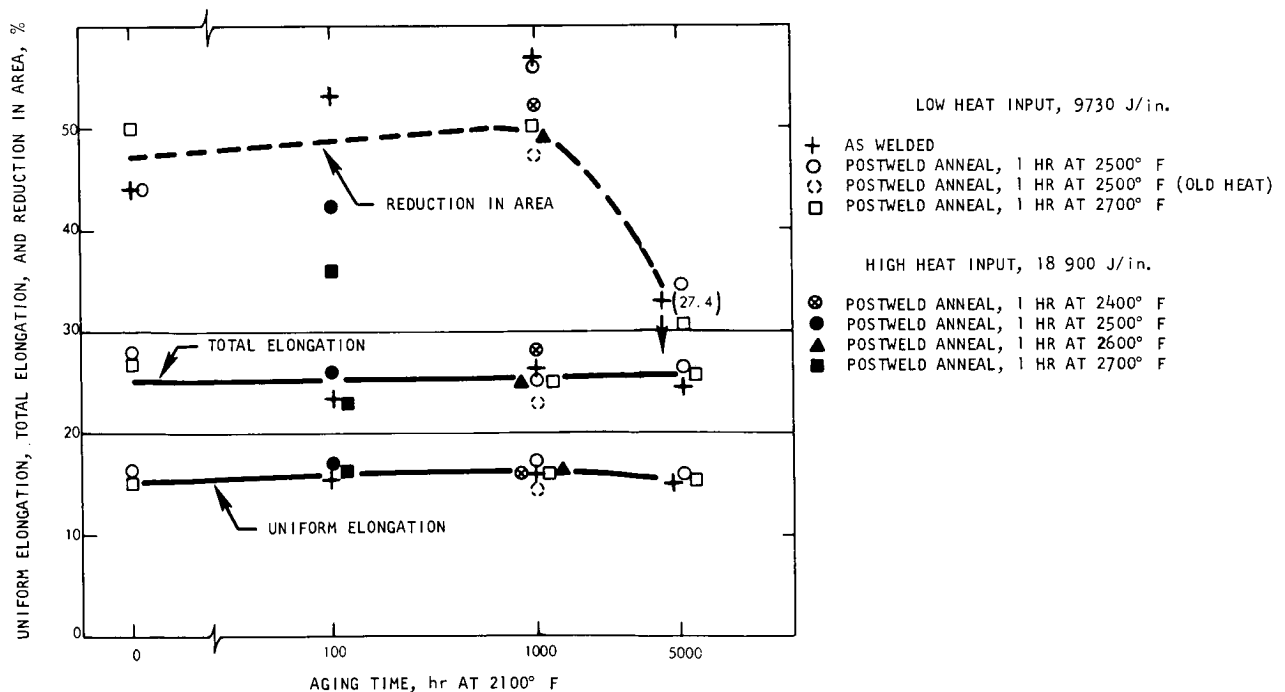


Figure III-10. - T-111 longitudinal weld tensile ductility at 32° F after aging as indicated. Data for T-111 heat used this study except as noted. (Low heat input welds made at 15 in./min; high heat input welds made at 6 in./min.)

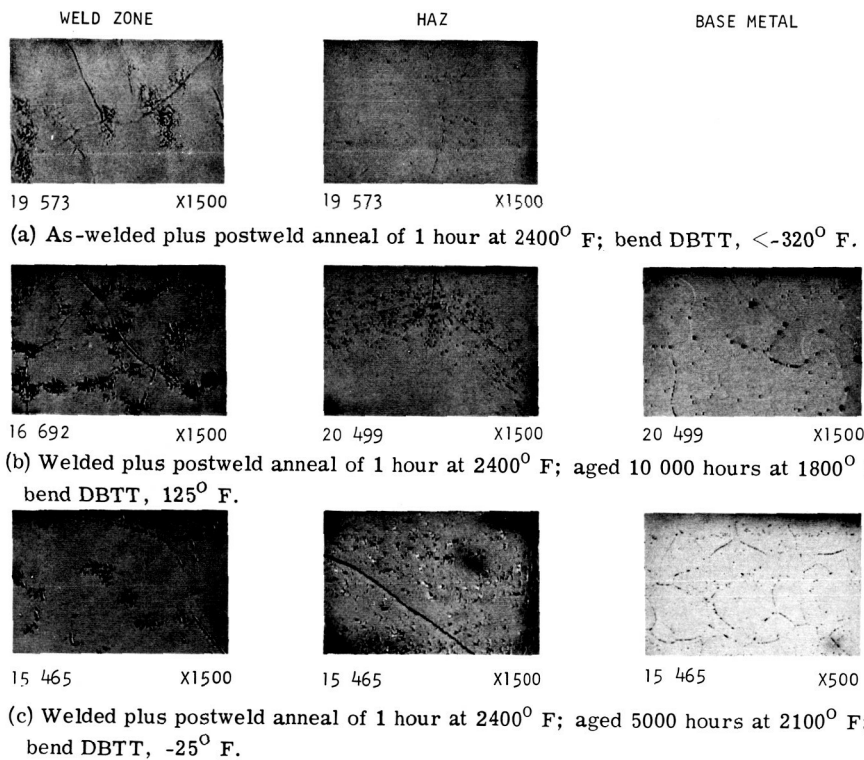


Figure III-11. - Typical microstructures of weld, HAZ, and base metal of T-111 GTA weld specimens as function of postweld thermal history.

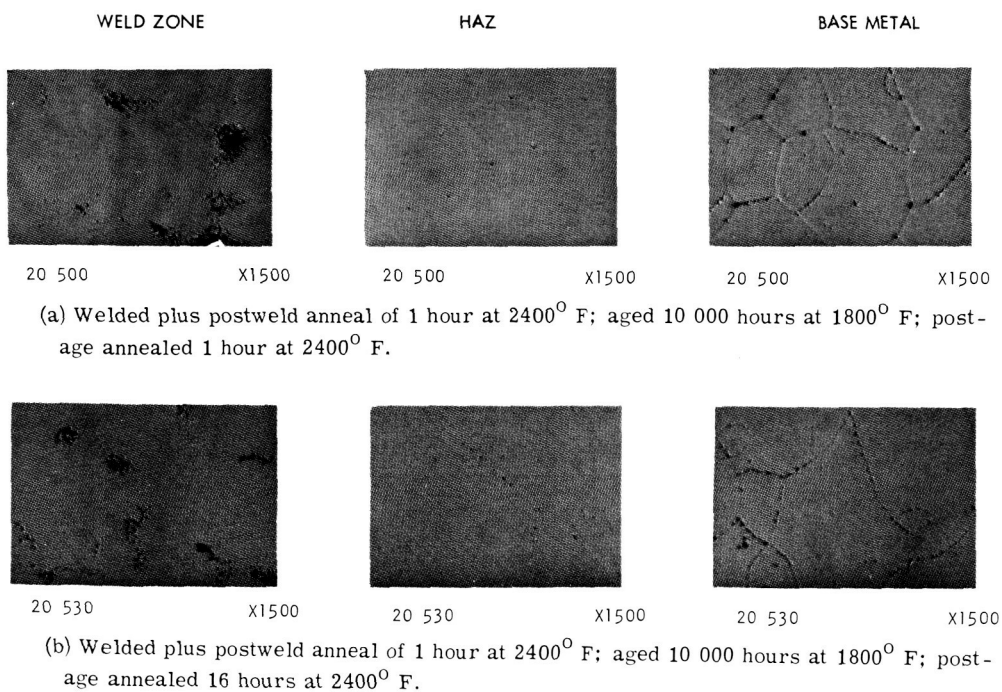
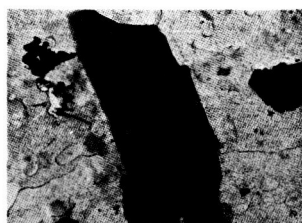


Figure III-12. - Microstructures of T-111 after indicated postage anneals.

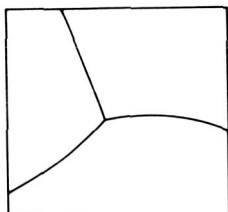


(a) Electron micrograph  
(X10 000).



(b) Electron diffraction  
single crystal point pat-  
tern.

Figure III-13. - Particle extracted from T-111 fracture surface.



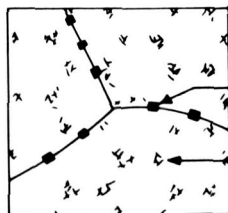
WELD STRUCTURE PRIOR TO AGING



AFTER AGING AT 1800° to 2100°F

GRAIN BOUNDARY PRECIPITATE - BELIEVED TO BE AN INTERSTITIAL COMPOUND; BEHAVIOR TYPIFIED BY THAT OF  $Ta_2C$ .

INTERDENDRITIC PRECIPITATE - BELIEVED TO BE AN INTERMETALLIC COMPOUND SUCH AS  $W_2Hf$ ; LARGE VOLUME FRACTION, SLUGGISH REACTION; ALMOST EXACT STOICHIOMETRIC COMPOSITION OBSERVED.



AFTER SHORT TIME POST AGE ANNEALS  
AT 2400°F

GRAIN BOUNDARY PRECIPITATE - SHOWN AFTER NEARLY COMPLETE DISSOLUTION; DISAPPEARS BEFORE THE INTERDENDRITIC PRECIPITATE.

INTERDENDRITIC PRECIPITATE - ALSO SHOWN PRIOR TO COMPLETE DISSOLUTION.

Figure III-14. - Schematic representation of response of T-111 weld structure to aging.



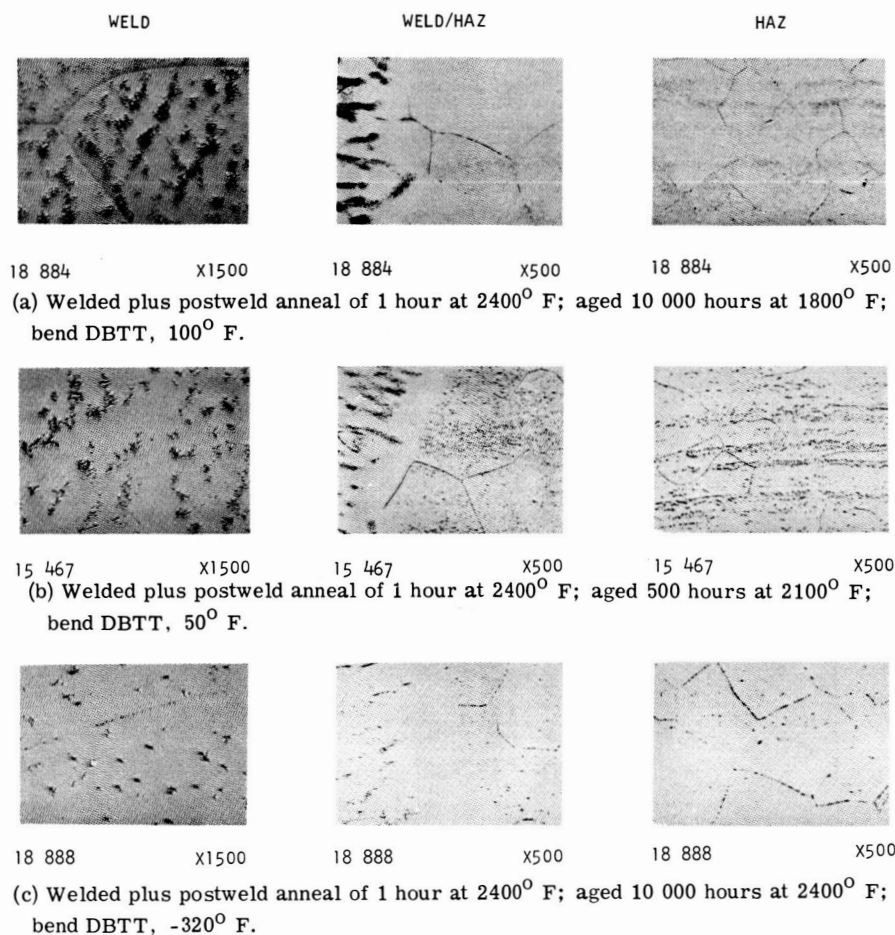


Figure III-15. - Typical microstructures of selected T-222 GTA weld specimens as function of postweld thermal history.

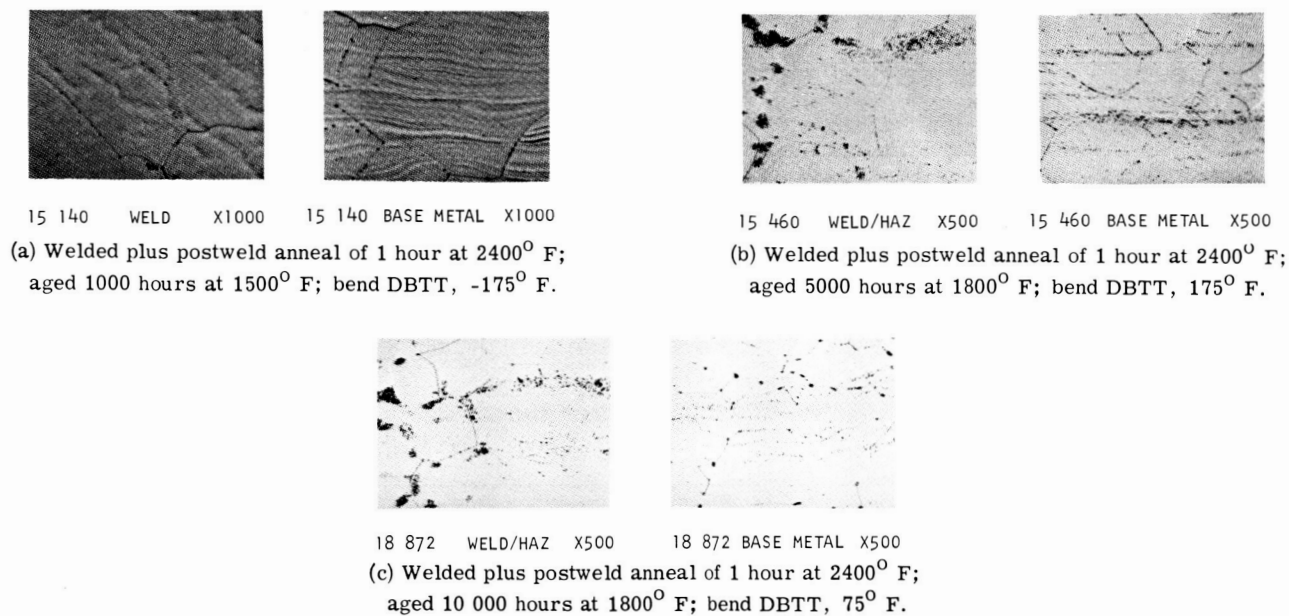


Figure III-16. - Typical microstructures of FS-85 GTA weld specimens as function of postweld thermal history.

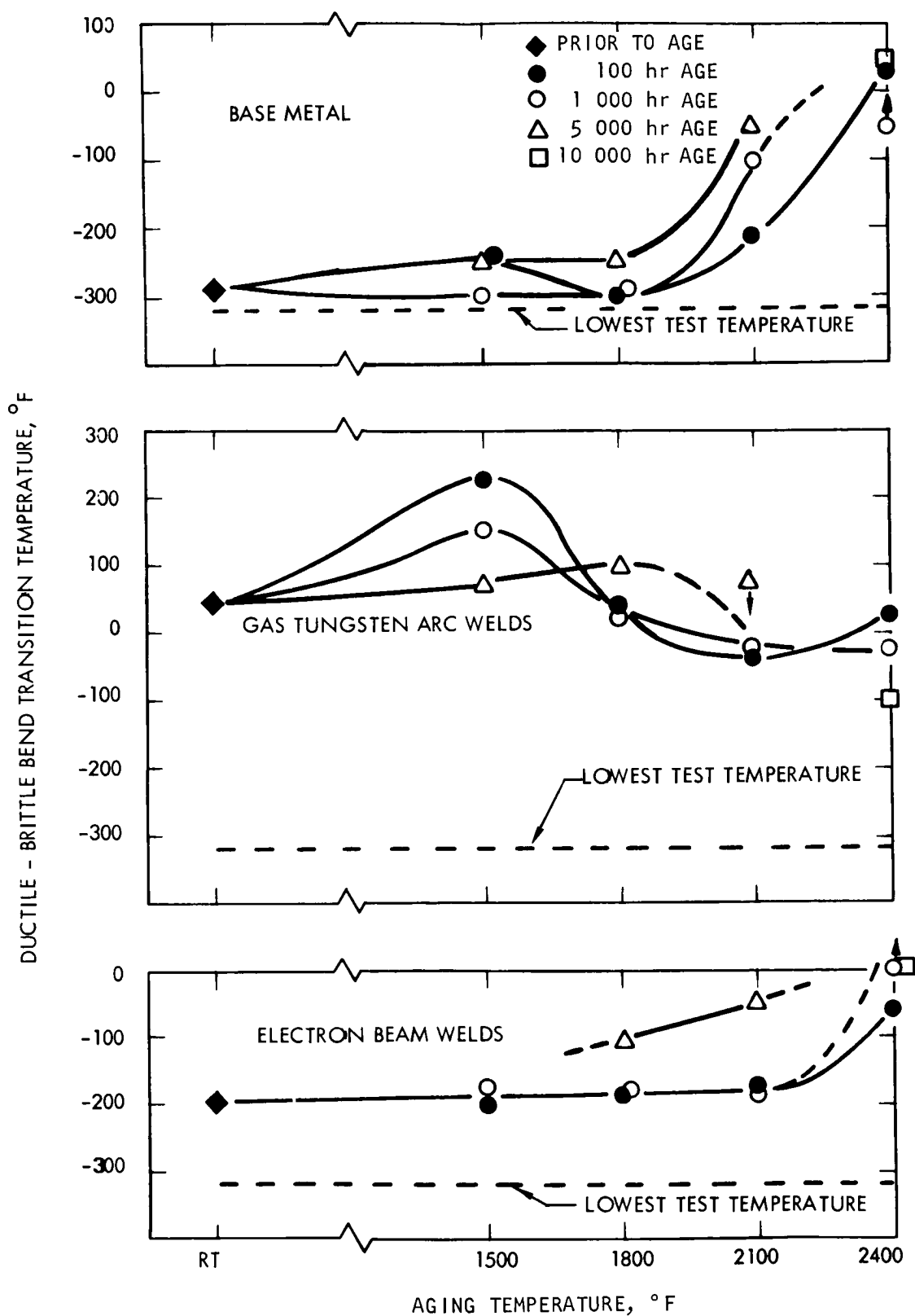


Figure III-17. - Bend ductile-brittle transition temperature of B-66 as function of aging parameters.

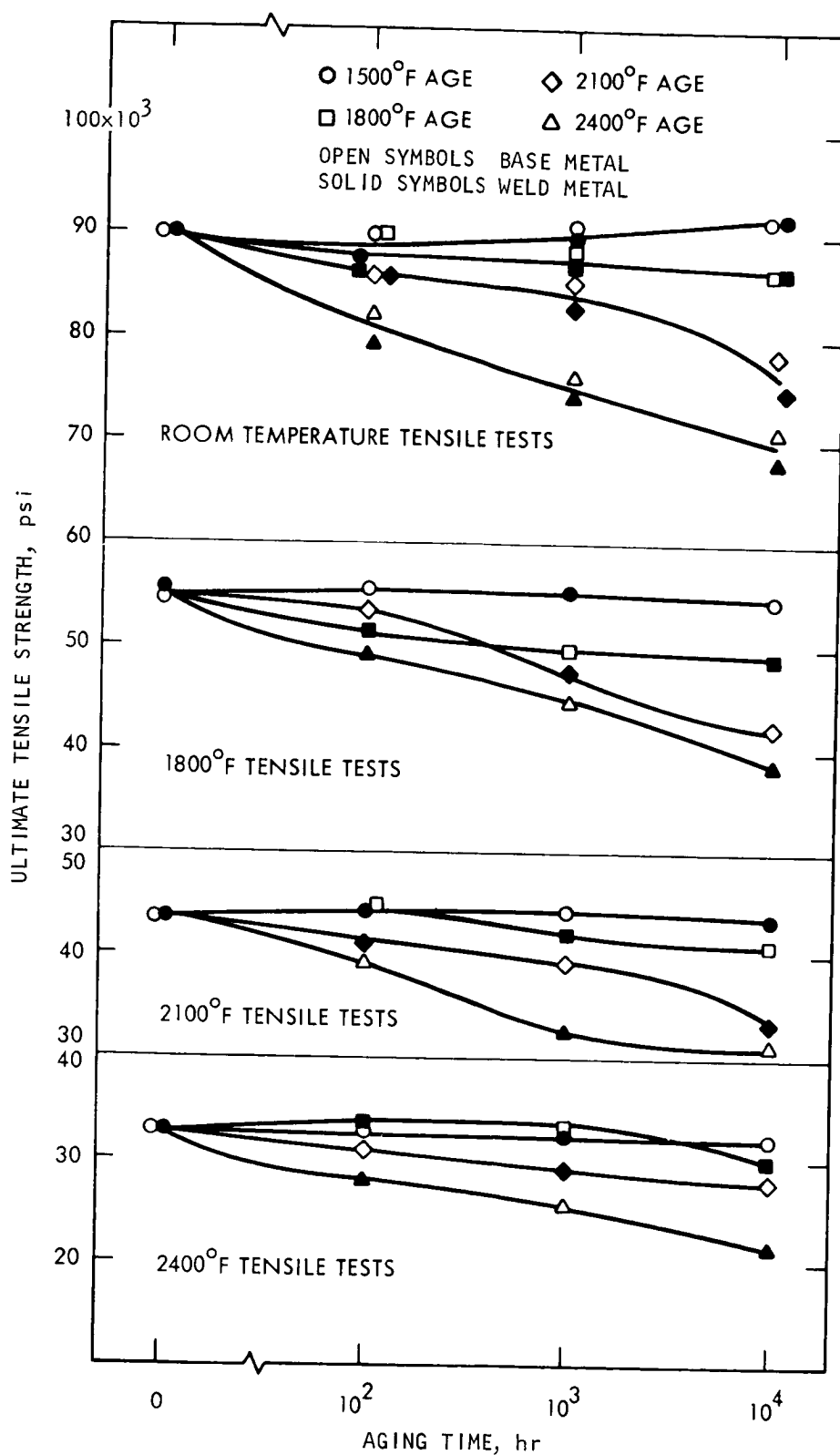
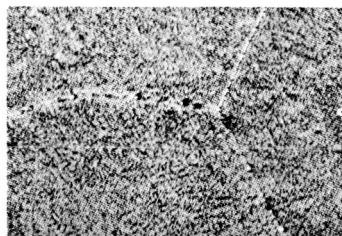
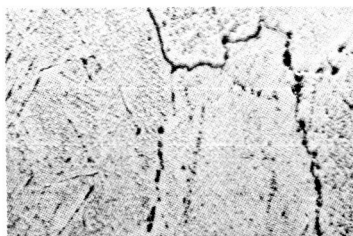


Figure III-18. - Ultimate tensile strength of D-43 as function of aging parameters. Optimum weld parameters; all samples annealed 1 hour at 2400° F prior to aging and testing.

BASE METAL

HAZ



18 865

X1500

18 866

X1500

(a) Welded plus postweld anneal of 1 hour at  $2400^{\circ}\text{F}$ ; aged 10 000 hours at  $1800^{\circ}\text{F}$ .



18 867

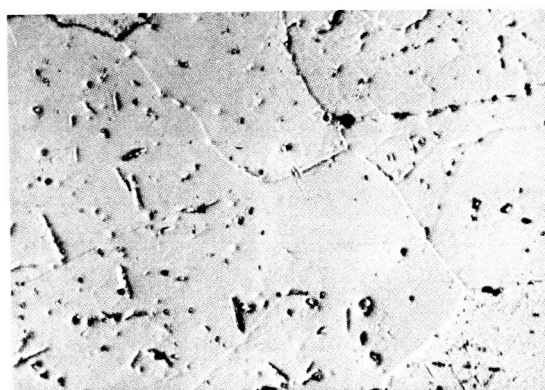
X1500

18 868

X1500

(b) Welded plus postweld anneal of 1 hour at  $2400^{\circ}\text{F}$ ; aged 10 000 hours at  $2100^{\circ}\text{F}$ .

Figure III-19. - Microstructures of D-43 GTA weld specimens as function of post-weld thermal history.



18 869

X1500

Figure III-20. - D-43 base metal aged 10 000 hours at  $2400^{\circ}\text{F}$ .

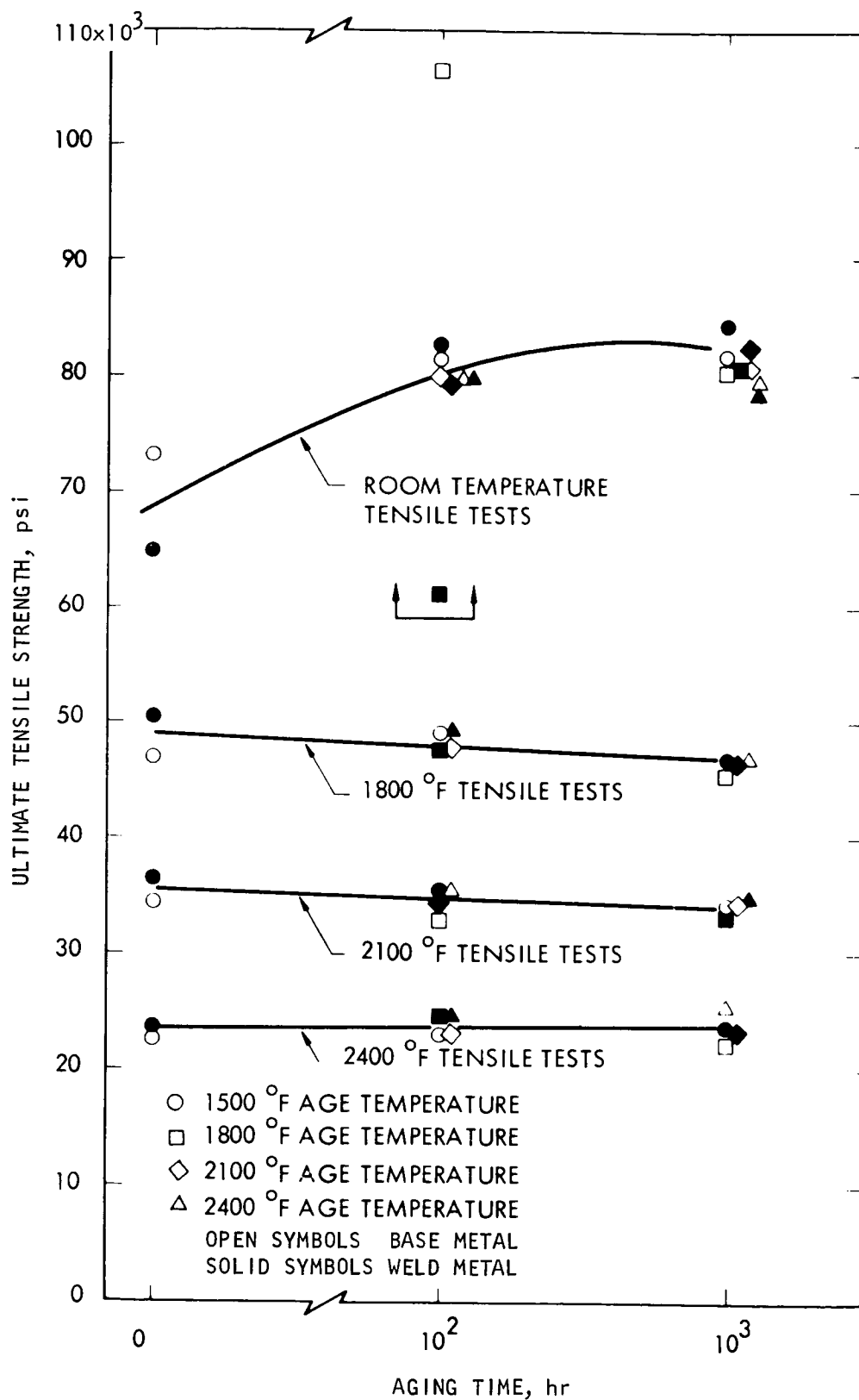


Figure III-21. - Ultimate tensile strength of Cb-752 as function of aging parameters. Optimum weld parameters; all samples annealed 1 hour at 2200° F prior to aging and testing.

**Page intentionally left blank**

## IV. CREEP BEHAVIOR OF REFRACTORY ALLOYS IN ULTRAHIGH VACUUM\*

K. D. Sheffler,<sup>†</sup> J. C. Sawyer,<sup>†</sup> and E. A. Steigerwald<sup>†</sup>

### SUMMARY

Several Cb, Ta, Mo, and W base alloys have been creep tested with both constant and continuously increasing loads in a vacuum environment of  $<1 \times 10^{-8}$  torr at temperatures and stresses chosen to provide between 1/2 and 1 percent creep in times up to 20 000 hours. Isostatic design data are presented in the form of a Larson-Miller plot for 1/2 or 1 percent creep life for each of these refractory alloys. Elevated temperature tension test data from the tantalum base alloy T-111 showed a strain aging reaction in the 1400° to 2200° F (760° to 1204° C) range which produced an unusual transient creep behavior. Analysis of the isostatic steady state creep data for this material showed that the minimum creep rate can be described by the expression

$$\dot{\epsilon} = 1.65 \times 10^9 \left[ \sinh(6.6 \times 10^{-5} \sigma) \right]^{3.17} e^{-90\,000/RT}$$

in the temperature and stress ranges of 1600° to 2600° F (870° to 1427° C) and 500 to 45 000 psi ( $0.34 \times 10^7$  to  $31.0 \times 10^7$  N/m<sup>2</sup>). These values of activation energy and stress exponent suggest that the isostatic steady state creep of T-111 is governed by a diffusion controlled microcreep mechanism rather than by nonconservative dislocation motion. The creep tests which were run on T-111 alloy with continuously increasing loads provided continuously increasing creep rates which were comparable to the isostatic steady state creep rates at equivalent stress levels. Methods have been developed for prediction of the 1 percent creep life under varying stress conditions from isostatic creep test data, and comparison of these predictions with the experimental results shows the dependence of analytical techniques on the character of the isostatic creep curves.

---

\*Based on work done under NASA contracts NAS 3-2545 and NAS 3-9439.

<sup>†</sup>TRW Equipment Laboratories, Cleveland, Ohio.

## INTRODUCTION

The exceptional elevated temperature strength of refractory alloys makes these materials ideally suited for use in space environments, where oxidation resistance is not a governing factor. The molybdenum base alloys TZC and TZM and the columbium alloys As-30 and CB-132 have therefore been considered for turbine components, while the tantalum and tungsten alloys are candidates for tubing or radioisotope capsule fabrication in space power systems. Long time creep strength of these materials is a critical design property under conditions where the partial pressure of reactive gases is extremely low. The creep strengths for these applications must be generated in ultrahigh vacuum to prevent contamination which would lead to erroneous results. The effects of testing in a good and poor vacuum are graphically illustrated by the comparison curves in figure IV-1. The work described in this paper was performed to develop creep data for molybdenum, tungsten, columbium, and tantalum alloys in an ultrahigh vacuum environment of less than  $10^{-8}$  torr at temperatures and stresses chosen to provide 1/2 to 1 percent creep in times up to 20 000 hours. Screening tests were conducted on the molybdenum, columbium, tungsten, and some of the tantalum alloys, while a full series of design tests was run on the tantalum alloy T-111. Extensive creep testing is also in progress on ASTAR-811C, a relatively new dispersion strengthened tantalum base alloy developed at the Westinghouse Astronuclear Laboratory.

The consideration of T-111 for radioisotope encapsulation has added yet another dimension to the problem of service characterization for this alloy. This problem centers on the fact that the proposed fuel is an  $\alpha$ -emitter, which means that after loading, the capsules are subjected to continuously increasing pressures because of the internal buildup of helium gas. In an effort to develop an understanding of the response of high temperature materials to continuously increasing stress, experiments were conducted under these conditions and compared to analytical predictions based on constant load data.

## EXPERIMENTAL DETAILS

### Creep Test Procedures

The creep program involved the testing of refractory alloys at temperatures ranging from  $1100^{\circ}$  to  $3200^{\circ}$  F ( $594^{\circ}$  to  $1760^{\circ}$  C) and at stresses between 500 and 65 000 psi (3.4 to 448 MN/m<sup>2</sup>). A combination of parameters was generally selected which would provide 1 percent total creep in 5000 to 20 000 hours. Two-inch



gage length, button-head bar-type specimens and double-shoulder, pin loaded, sheet-type specimens were used, respectively, for testing of plate and sheet-type materials. The orientation of the specimen with respect to the working direction is given in the following table:

| Material form | Specimen axis parallel to                  |
|---------------|--|
| Disk forging  | Radius                                     |
| Plate         | Extruding direction                        |
| Sheet         | Rolling direction (except where indicated) |
| Tubing        | Tube axis                                  |

The tubing was stressed parallel to the tube axis, with two flats being ground opposite one another to provide two webs in the gage section.

Both construction and operation of the ultrahigh vacuum creep test chambers and the service instruments in the laboratory have been described in detail elsewhere (refs. 1 and 2). The creep test procedure involved initial evacuation of the chamber to a pressure of less than  $5 \times 10^{-10}$  torr at room temperature, followed by heating of the test specimen at such a rate that the pressure never rose above  $1 \times 10^{-6}$  torr. Pretest heat treatments were performed in situ, and complete thermal equilibrium of the specimen was ensured by a 2 hour hold at the test temperature prior to load application. Pressure was always below  $1 \times 10^{-8}$  torr during the tests and generally fell into the  $10^{-10}$  torr range as testing proceeded. Specimen extension was determined over a 2-inch gage length with an optical extensometer which measured the distance between two scribed reference marks to an accuracy of  $\pm 50$  microinches. Creep strains were calculated using the loaded gage length as the original length. Specimen temperature was established at the beginning of each test using a thermocouple. An optical pyrometer having a precision of  $\pm 1^\circ$  F was calibrated against the thermocouple reading and was then used as the prime temperature reference throughout each test.

The response of T-111 alloy to variable stress conditions was studied by continuously increasing the load at various linear rates, starting at zero stress, while simultaneously measuring creep strain as a function of time. The steadily increasing load was achieved by using a motor driven screw to continuously feed lead shot at a uniform rate into a load pan attached to the bottom of the specimen. The weight of the shot added to the pan was monitored so that the exact load would be known at all times.

## Characterization of Test Materials

Sources of the test materials and details of the available processing histories have been previously presented (ref. 3). Chemical analyses of each of the heats tested are shown in table IV-1, and pertinent details of the processing histories are summarized in table IV-2.

Molybdenum alloys. - TZM was evaluated in three forms: a bar (heat 7463), a conventionally processed disk forged at 2200<sup>0</sup> F (heat 7502), and a section of another disk which had a higher than normal carbon level and was both hot and warm forged to produce improved creep resistance (heat KDTZM-1175). All of these heats were evaluated primarily in the stress relieved condition. Photomicrographs of each of the materials (fig. IV-2) show that the bar material and the conventional forging were relatively fine-grained, while the special forging had a somewhat coarser structure. Electron micrographs of the two disk forgings (fig. IV-3) show a similar carbide morphology, but with a somewhat higher density of carbides in the higher carbon material.

TZC was also evaluated in three different forms. Two rolled plates were obtained with widely different drafting practices. One plate was given very small reductions on each pass and a high finishing temperature (heat M-80), while the other was given relatively large reductions and finished at a lower temperature (heat M-91). The third TZC plate was side forged in the 2400<sup>0</sup> F range from extruded bar stock (heat 4345).

Both the stress-relieved and recrystallized structures were studied in TZC. The two rolled plates had a uniform and relatively fine-grained microstructure in the stress-relieved condition, while the extruded and forged plate had a more irregular and somewhat coarser structure (fig. IV-4). The responses of the rolled plates to a 1-hour annealing treatment at 3092<sup>0</sup> F differed markedly; the plate from heat M-91, which was given large reductions, was fully recrystallized, while the M-80 plate was only partially recrystallized (fig. IV-5). The difference presumably results from the higher degree of residual cold work in the plate finished at lower temperatures.

Columbium alloys. - The columbium alloy AS-30 was evaluated in the as-received condition (rolled at 2100<sup>0</sup> F), while Cb-132M was annealed 1 hour at 3092<sup>0</sup> F (1700<sup>0</sup> C) prior to testing. Microstructures of these two alloys are shown in figure IV-6.

Tungsten alloys. - Both arc-melted and vapor-deposited tungsten were evaluated. The arc-melted material was received as 0.030-inch sheet and recrystallized for hours at 3200<sup>0</sup> F prior to testing. The vapor-deposited material was tested as a bar specimen machined from a thick tube wall. The W - 25 percent Re

was also tested as 0.030-inch sheet obtained from an arc-melted ingot. Microstructures of the tungsten alloys are presented in figures IV-7, IV-8, and IV-9. In the case of the vapor-deposited material (fig. IV-8) the gage section represents a creep tested structure, while the head section is characteristic of untested material.

Tantalum alloys. - Pure tantalum was tested in the form of tubing, while all of the other tantalum alloys tested were in the form of nominal-0.030-inch-thick cold rolled sheet. All of the tantalum alloys were tested in the fully recrystallized condition. Photomicrographs of the pure tantalum, Ta-10W, and ASTAR-811C are shown in figures IV-10 to IV-12. Electron micrographs showing the influence of annealing time and temperature on carbide morphology in the ASTAR-811C alloy are shown in figure IV-13.

### Investigation of Strain Aging Behavior in T-111 Alloy

Because a complete characterization of mechanical properties was required for T-111 alloy, a more extensive test program was conducted to fully document the elevated temperature mechanical behavior of this material. Chemical analyses and room temperature mechanical properties of each heat tested are presented in table IV-3, while typical light and electron micrographs are shown in figures IV-14 and IV-15(a). Although the structure appears clean at optical magnifications, the electron micrographs show that the T-111 recrystallized 1 hour at 3000° F (1649° C) had an included second phase which was distributed preferentially at the grain boundaries. Electron probe micrographs emphasized this grain boundary network (fig. IV-16), but also showed a significant number of inclusions within the grains. Electron probe spectral distribution and emission scans indicated that these inclusions were hafnium oxides.

Elevated temperature tension tests were performed in a Brew furnace at pressures of the order of  $10^{-5}$  torr at an extension rate of 0.005 inch per inch per minute (except where noted). The influence of temperature on the tensile properties of recrystallized T-111 is shown in figures IV-17. These overlapping data from several different heats as well as from the literature (ref. 4) show a pronounced ultimate strength peak near 1400° F, together with a maximum in the strain hardening exponent. In addition, a Portevin-LeChatlier effect (serrated stress-strain curve) was observed in this temperature range, as illustrated in figure IV-18. Schmidt et al. (ref. 5) have noted similar strain aging effects at a much lower temperature (about 600° F (316° C)) in pure tantalum and in tantalum containing between 225 and 955 ppm C, O, and N additions. Comparison of the T-111 data with Schmidt's results suggests that strain aging in T-111 may be caused by a complex atmosphere-

dislocation interaction rather than by simple interstitial dislocation pinning. Baird and Jamieson (ref. 6) have found the complex atmosphere to be a much more potent strengthener than straightforward interstitial atom strain aging in the analogous Fe-Mn-C system, especially at higher temperatures.

In order to study the strain aging phenomenon in greater detail and perhaps identify the responsible atom species, a series of tension tests was conducted on T-111 at different strain rates and temperatures in the strain aging range. Results of these tests, shown in figure IV-19, further emphasize the presence of the strain aging by showing a very large negative strain rate sensitivity in the strain aging temperature range. Two other interesting effects are also apparent in figure IV-19. First, strain age strengthening is much more effective at the lower strain rates, indicating that this factor may be important in creep behavior. Second, the strength peak shifts to higher temperatures with increasing strain rate, presumably because of the more rapid diffusion required for strain aging in the faster tests. The latter behavior provides a possible method for identifying the interstitial atom species responsible for strain aging. Kinoshita (ref. 7) has pointed out that the activation energy for strain aging can be determined from the strain rate sensitivity of the strength peak by plotting strain rate against the reciprocal of the peak temperature. This Arrhenius type of representation, which is shown in figure IV-20, yields an activation energy of 22 000 calories per mole for the strain aging reaction in T-111. This value is very close to the activation energy reported by Schmidt et al. (refs. 5 and 8) for diffusion of oxygen in tantalum (22 900 cal/mole), but is much lower than the values reported for diffusion of C and N in tantalum (39 600 and 41 100 cal/mole, respectively). It thus seems likely that oxygen is the critical interstitial specie in the strain age strengthening of T-111.

## RESULTS AND DISCUSSION

Results from the refractory alloy creep program are divided into three basic categories. First, the data generated from the screening studies are presented and discussed briefly. Second, a detailed discussion of the creep behavior of T-111 alloy is presented, and finally the variable stress results are discussed.

### Screening Studies

Molybdenum alloys. - Typical creep curves for TZC (fig. IV-21) show an irregular extension behavior characteristic of the molybdenum base alloys. Such

behavior is only observed in specific alloys, indicating that the discontinuities in the curves are real and do not represent instrument error. The accuracy of the extension measurements is apparently great enough to show some of the intrinsically random nature of the thermally activated creep process.

The 1/2 percent creep results for TZC are summarized on a Larson-Miller plot in figure IV-22. In the annealed condition the rolled plate with the partially recrystallized structure (heat M-80) had better creep resistance than the fully recrystallized plate (heat M-91). The higher creep strength may be partially due to the more complex substructure associated with the higher yield strength of the cold worked material or may result from the somewhat higher carbon level in heat M-80. Analysis of the creep data in conjunction with short time mechanical behavior indicates that, among the three TZC forms tested, heat 4345 represents the best combination of both short and long term creep strength with room temperature ductility.

The TZM test results, summarized in figure IV-23 on a 1/2 percent creep Larson-Miller plot, show the superior creep strength of the specially processed disk forging. Although the electron microscopy of the TZM alloys (fig. IV-3) revealed a somewhat higher number of carbides in the specially forged material, neither forging possessed a carbide dispersion which was dense enough to provide significant dispersion hardening. This indicates that the improved creep strength of heat KDTZM-1175 may also be associated with the coarser metallurgical structure shown in figure IV-2, with the increased carbide density playing a secondary role by providing an improved thermal stability to the cold worked structure.

Comparison of the TZC and TZM results indicated that at higher stress levels and lower temperatures the specially processed TZM was superior to TZC in the stress relieved condition, while at the lower stress levels the behavior of the two materials was comparable. The elevated temperature yield strength of TZM heat 1175 is superior to TZC (table IV-4), and this factor is believed to contribute to the improved creep strength at the lower test temperatures.

None of the molybdenum base alloys tested showed a significant change of structure or composition as a result of the long time elevated temperature exposure to ultrahigh vacuum, although a modest increase in strength resulted from the relatively small creep strains achieved.

Columbium alloys. - Creep test results from AS-30 and Cb-132M are compared on a Larson-Miller plot in figure IV-24. Although Cb-132M has significantly greater creep strength than AS-30, the specially processed TZM disk forging had creep resistance greater than either columbium alloy. Post-test examination indicated that no change in hardness or structure occurred in the columbium alloys as a result of creep exposure.

Tungsten alloys. - A summary of the creep data for tungsten and tungsten-25

percent rhenium is given in table IV-5. The Larson-Miller values for 1 percent creep in the table are based on a constant of 15. The arc-melted and vapor-deposited tungsten had comparable creep strength, while the tungsten-25 percent rhenium alloy had a greater creep strength but only at the higher stress levels.

The results obtained on the arc-melted and vapor-deposited tungsten are compared in figure IV-25 to published creep data for pure tungsten (refs. 9 and 10) using a Larson-Miller parameter for 1 percent creep. The results of Schmidt and Ogden (ref. 9) were obtained with a powder metallurgy product, and tests were performed in an argon environment. A powder metallurgy product was also used by the Southern Research Institute (ref. 10), but the test environment was a  $10^{-4}$  torr vacuum. The creep strength of the arc-melted and vapor-deposited tungsten is definitely inferior to that of the powder metallurgy product of reference 9; however, the data from reference 10 appear to be an extension of those obtained with the arc-melted and vapor-deposited material.

Tantalum alloys. - A Larson-Miller plot of creep test results obtained on the tantalum base alloys T-111, Ta-10W, and ASTAR-811C and on pure tantalum is presented in figure IV-26 together with data from the literature on ASTAR-811C (ref. 11). The pure tantalum data show a significant variation of properties between heats. This effect is presumed to result from the fact that pure materials will be more sensitive to minor variations in trace impurity levels than the more heavily alloyed materials. However, the differences in creep strength may also be associated with the significant difference in grain size shown in figure IV-10. Further examination of the data in figure IV-26 indicates that the creep strengths of T-111 and Ta-10W alloys are comparable, while the ASTAR-811C alloy is significantly stronger. Heat treatment appears to have a considerable influence on the creep strength of ASTAR-811C, and the commercial heat is significantly stronger than either of the laboratory heats tested. Comparison of the various heat treatments studied with the carbide morphologies presented in figure IV-13 indicated that both grain size and carbide morphology significantly influenced ASTAR-811C creep behavior.

## Creep Analysis of T-111 Alloy

Rationalization of T-111 transient creep behavior. - Conventional first stage creep was not always observed in T-111 alloys, and certain tests showed a very unusual behavior, with the creep rate initially attaining a relatively low value and then increasing again to a steady state. The tendency toward this type of behavior was temperature dependent, with tests at the lower temperatures (near  $0.4 T_m$ )

curving upward more sharply than those at higher temperatures (near 0.5  $T_m$ ) (fig. IV-27).

Analysis of the unusual transient creep behavior in T-111 is facilitated by plotting true strain rate against true strain, as illustrated in figure IV-28 for the two tests shown in figure IV-27. This type of plot emphasizes the fact that the upward curvature is not classical third stage creep, since the right half of the low temperature curve in figure IV-28 shows a negative rather than a positive curvature. Both curves would presumably turn upward in true third stage creep if permitted to run long enough.

Comparison of the tensile and creep data on T-111 reveals that both the strain aging and the transient creep strengthening phenomenon are most pronounced at the lower test temperatures (in the 1600° F (870° C) range) and that both decrease gradually with increasing temperature and are essentially absent above about 2200° F (1204° C). This similarity of temperature dependence suggests that the two phenomena may be associated. Even so, it is difficult to explain why the effectiveness of a strain age strengthening mechanism should decrease with increasing test time. This phenomenon has been observed previously in an Fe-Cr-C alloy by DeBarbadillo (ref. 12), who attributed the decreasing strength to precipitation of chromium carbide. It was shown that both Cr and C were necessary by testing binary Fe-Cr and Fe-C alloys in which the unusual transient did not appear. Thus, as the chromium and carbon coprecipitated, the species necessary for strain aging was depleted from the matrix. DeBarbadillo further supported this supposition by showing that the kinetics of the precipitation reaction were such as to cause an abrupt creep rate transition of the observed form.

Examination of creep tested T-111 specimens showed that the precipitation mechanism was not directly applicable to the T-111 alloys. Figure IV-15(b) reveals an appreciable decrease rather than an increase in the number of inclusions after test. This decrease, which has been confirmed using the electron probe microanalyzer, is accompanied by a significant and consistent decrease in oxygen composition, as well as a drop in tensile strength and hardness in the tested material (table IV-6). Although sufficient creep tested material was not available to comprehensively evaluate the strength of the strain aging reaction in the post-tested specimens, a 56 percent decrease in the yield point drop was observed as a result of creep testing, indicating that less strain hardening occurred after creep test exposure.

On the basis of these results a mechanism similar to DeBarbadillo's involving softening of the creep tested material by depletion of the species responsible for strain age strengthening (oxygen) can be applied to the T-111 alloy to explain the transition in creep rate as a function of test time. Since oxygen removal proceeds

during creep testing, it causes a progressive weakening and a concomitant creep rate transition at the low test temperatures where strain aging is initially an important factor.

Analysis of T-111 steady state creep behavior. - Various standard analytical techniques were applied to the T-111 steady state creep data to gain better insight into the creep mechanisms involved. Neither the common engineering representation of log stress as a function of log minimum creep rate nor the Arrhenius plot would adequately correlate the results, so that it was necessary to utilize a temperature compensated creep rate parameter of the form

$$\dot{\epsilon} e^{\Delta H/RT}$$

in order to rationalize the steady state data. Although the usual approach to this treatment involves the use of the Arrhenius plot to obtain the activation energy, it is possible to obtain  $\Delta H$  directly through statistical evaluation of the degree of correlation between the chosen stress function and  $\dot{\epsilon} e^{\Delta H/RT}$ .

Three stress functions are commonly found in the literature:

(1) Power function:

$$\dot{\epsilon} \propto \sigma^n$$

(2) Exponential function:

$$\dot{\epsilon} \propto e^{B\sigma}$$

(3) Hyperbolic sine function:

$$\dot{\epsilon} \propto [\sinh(\alpha\sigma)]^n$$

Garofalo (ref. 13) has discussed the stress dependence of creep rate and has shown that, for a number of materials tested over wide ranges of stress, the power law provides a plot of  $\dot{\epsilon} e^{\Delta H/RT}$  against  $f(\sigma)$ , which is concave upward, while the exponential law provides a plot which is concave downward. Garofalo therefore proposed the hyperbolic sine relation to solve this problem, since it approximates the power law at low stresses and the exponential law at higher stresses. Figures IV-27, IV-30, and IV-31 show that these general observations apply to T-111, with the hyperbolic sine law being the only relation providing a linear correlation over the entire experimental stress range of 500 to 45 000 psi. It is interesting to note that the ultimate strength data at 1800° F (982° C), 2200° F (1204° C), and 2600° F (1427° C) all fall on the same line, with the creep data in figure IV-31 indicating



that at these temperatures and a strain rate of 0.005 inch per inch per minute tensile deformation is thermally activated in T-111 alloy. It should also be noted that, while the exponential and power laws do not fit the data over the entire stress range, there are limited stress ranges where each of these relations does provide a straight line fit of the data. For example, the exponential plot in figure IV-29 appears to provide a linear fit between 2.4 and 20 ksi despite the pronounced curvature over the wider stress range.

Evaluations of the straight line segments from each of the three stress representations all provided a  $\Delta H$  value of about 90 000 calories per mole, which is close to the value of 100 000 calories per mole reported in the literature (ref. 6) for self-diffusion in tantalum. Since lattice strains introduced by substitution of the somewhat smaller W atom in the Ta lattice should enhance diffusivity, the apparent activation energy for creep is probably very close to that for either Ta or W diffusion in T-111. This indication of diffusion controlled creep seems somewhat surprising in view of the low homologous temperature range examined (0.39 to 0.52); however, Sherby and Burke (ref. 14) have suggested that at very low strain rates diffusion controlled creep may occur at lower than normal temperatures as a result of the long times available for diffusion to occur, and this is probably the explanation in the present case.

Diffusion controlled creep is normally assumed to result either from nonconservative motion of jogged screw dislocations or from climb of edge dislocations. However, the stress exponent for these two processes should be near 5, as opposed to the value of about 3 observed in the present work. A value of  $n = 3$  conforms to that predicted by Weertman (ref. 15) for glide controlled creep, implying that steady state creep in T-111 may be controlled by substitutional solute atom drag. In this case, the  $\Delta H$  value reported should represent the activation energy for diffusion of W in T-111 rather than Ta in T-111. Unfortunately, no data on the diffusion of W in Ta are available in the literature to check this possibility. However, alloys which display microcreep often do not undergo primary creep and do not exhibit a well developed substructure, both of which are consistent with the observed behavior in T-111. It therefore seems likely that steady state creep of T-111 is controlled by a microcreep mechanism in the temperature and stress ranges studied.

### Analysis of Variable Stress Results on T-111 Alloy

The third major facet of the work presented in this paper deals with the behavior of T-111 alloy under continuously increasing loads. Typical creep curves obtained

from this type of test are presented in figure IV-32. The distribution of creep deformation through the test period depends on the relative loading rates and temperatures in these tests. At the higher temperatures and lower stress rate, creep strain is accumulated gradually throughout the test. On the other hand, at the lower temperatures and higher stress rates, very little creep occurs until the latter stages of the test, where most of the creep deformation is concentrated. For each temperature a stress rate existed above which the creep life was governed primarily by the rate of approach to the yield stress rather than by the creep rate, as indicated in table IV-7.

Using the time required to reach 1 percent extension as a creep life criterion, a parametric representation was developed for correlating the variable stress data. In this manner creep lives at different stress rates and temperatures could be combined and used for more reliable design predictions. McCoy (ref. 16) has pointed out that progressive stress results can be represented on the conventional log-log plot of stress against creep life, with stress rate substituted for stress. This type of plot provides a family of parallel, isothermal straight lines (fig. IV-33), each corresponding to the relation

$$\log \dot{\sigma} = M \log l + B \Big|_{\text{const. } T} \quad (1)$$

where  $\dot{\sigma}$  is stress rate,  $l$  is creep life, and  $M$  and  $B$  are the slope and intercept. The influence of temperature on the intercept  $B$  can be expressed as

$$B(T) = B' - \log T^n \quad (2)$$

and combining equations (1) and (2) leads to the expression

$$\log(\dot{\sigma}T^n) = M \log l + B' \quad (3)$$

The progressive stress creep results can be represented by a single straight line when  $\dot{\sigma}T^n$  is plotted as a function of creep life with  $n = 5.5$  (fig. IV-33), and the desired parametric representation is thereby obtained.

Analytical treatments. - From both a theoretical and a practical standpoint it is desirable to compare the creep results obtained from continuously increasing stress tests with conventional isostatic creep behavior. Manson (ref. 17) has discussed this problem in his "time hardening" and "strain hardening" theories, which provide conceptual guide lines for the manual assembly of variable stress creep curves from selected segments of conventional creep curves. McCoy (ref. 16) and Nichols and Winkler (ref. 18) have approached the specific problem of

using isostatic data to predict variable stress behavior in radioisotope capsules by using a "life fraction" concept in which the useful life of a specimen is considered to be exhausted when the sum of the instantaneous life fractions equals unity. Each individual life fraction is equal to the time spent at any specific set of test conditions divided by the total creep life at those conditions. McCoy uses equation (1) to define creep life  $l_i$  and then integrates the life fraction for the case where stress increases steadily at the rate  $\dot{\sigma}$ :

$$1 = \int_0^L \frac{dt}{l_i} = \int_0^L \frac{dt}{e^{-B/M}(\dot{\sigma}t)^{1/M}} \quad (4)$$

The variable stress creep life is the upper limit  $L$  in equation (4):

$$L = \left( \frac{M-1}{M} e^{-B/M} \dot{\sigma}^{1/M} \right)^{(1-M)/M} \quad (5)$$

Nichols and Winkler have generalized this technique by using the temperature compensated Larson-Miller parameter (LMP) to generate the creep life function and have developed a computer program for numerical integration of the resulting life fraction expression. This program was written specifically for application to the radioisotope capsule problem and will interchangeably generate capsule dimensions or capsule life for any analytically expressed stress or temperature variation, when provided with the appropriate conventional creep test data. Nichols and Winkler's program contains a subroutine which fits the isostatic creep data to an expression of the form

$$\sigma = \left\{ \frac{(e^{\alpha} \sigma_u)^{\gamma}}{(e^{\alpha})^{\gamma} + [\sigma_u e^{-m(\text{LMP})}]^{\gamma}} \right\}^{1/\gamma} \quad (6)$$

This expression provides a linear relation between  $\ln \sigma$  and the Larson-Miller parameter at high LMP values, while allowing  $\sigma$  to approach  $\sigma_u$  (ultimate strength) asymptotically at low LMP values. The constants  $M$  and  $\alpha$  are, respectively, the slope and intercept of the straight line, and  $\gamma$  is an imposed constant of the order of 2.

Another technique for prediction of increasing load creep life was developed in the present study from a previous analysis of T-111 creep data obtained under iso-

static load conditions (ref. 19). The earlier study had shown that the steady state creep rate of T-111 recrystallized 1 hour at 3000<sup>0</sup> F can be described analytically in the temperature and stress ranges of 1800<sup>0</sup> to 2400<sup>0</sup> F (982<sup>0</sup> to 1316<sup>0</sup> C) and 2400 to 20 000 psi ( $1.65 \times 10^7$  to  $13.8 \times 10^7$  N/m<sup>2</sup>) as

$$\dot{\epsilon} = A e^{B\sigma} e^{-\Delta H/RT} \quad (7)$$

with

$$\Delta H = 90\,000 \text{ cal/mole}$$

$$A = 4.68 \times 10^6 \text{ hr}^{-1}$$

$$B = 3.98 \times 10^{-4} \text{ psi}^{-1}$$

and R and T being, respectively, the universal gas constant and the absolute temperature in degrees Kelvin (ref. 19). This expression is convenient for comparison of conventional isostatic and increasing stress results since it allows steady state rates at different temperatures and stresses to be compared directly.

In the increasing stress tests the instantaneous strain rates were determined at various stress levels by numerical differentiation. These results are plotted in figure IV-34, where the increasing stress tests are compared with conventional test results. Although the scatter is somewhat greater, the creep strain rates observed in the increasing stress tests are with a few exceptions in the same range as the conventional test data. These results indicate that the creep rates obtained in the increasing stress tests are a unique function of stress and are relatively independent of creep strain for the conditions tested.

The above results also imply that integration of the conventional creep rates obtained under isostatic load conditions should predict the increasing stress creep lives. The strain at any point in an increasing stress test is simply the integral of the strain rate as a function of time:

$$\epsilon = \int_0^L \dot{\epsilon}(t) dt \quad (8)$$

If the functional relation of  $\dot{\epsilon}$  to stress and the time dependence of stress are known, this equation can be expressed in the form

$$\epsilon = \int_0^L \dot{\epsilon}[\sigma(t)] dt \quad (9)$$

The form of  $\dot{\epsilon}(\sigma)$  is known from equation (7), and  $\sigma(t)$  is simply

$$\sigma = \dot{\sigma} t \quad (10)$$

for the linearly increasing stress test. Inserting these two expressions in equation (9) yields

$$\epsilon = \int_0^L A e^{B \dot{\sigma} t} e^{-\Delta H/RT} dt \quad (11)$$

which can be integrated analytically to evaluate the upper limit (which is creep life) for any desired strain. Choosing  $\epsilon = 0.01$  results in an expression for 1 percent creep life of the form

$$0.01 = \frac{A e^{-\Delta H/RT}}{B \dot{\sigma}} (e^{B \dot{\sigma} L} - 1) \quad (12)$$

or, rearranging,

$$L = \frac{1}{B \dot{\sigma}} \ln \left( \frac{0.01 B \dot{\sigma}}{A e^{-\Delta H/RT}} + 1 \right) \quad (13)$$

where the constants  $A$ ,  $B$ , and  $\Delta H$  are as given for equation (7).

Comparison of creep life predictions with experimental data. - Predictions of each of the analytical techniques are compared with the experimental data in table IV-8. At the two lower test temperatures the strain rate integration technique predicts creep lives which are somewhat shorter than the experimental values, whereas the Nichols and Winkler predictions are somewhat larger than the observed lives. However, at 2200° F both techniques appear equally good, with statistical variation of the experimental results providing the major source of difference between predicted and observed values. The reason for this variability of predictions is illustrated schematically in figures IV-35 and IV-36. Figure IV-35 shows the basic relation between the life fraction and the strain rate integration techniques. The integrand in both cases is a creep rate, but whereas in the strain rate integration technique experimentally observed steady state creep rate  $\dot{\epsilon}_1$  is integrated, the creep rate integrated in the life fraction technique is a hypothetical rate established by the reciprocal of the 1 percent creep life  $\dot{\epsilon}_2$ . Thus, the relative success of each of these techniques will depend upon the degree to which the instantaneous strain rates in the increasing stress tests approximate either the hypothetical or the experimentally observed steady state creep rates.

The specific application of the above concept to T-111 alloy is illustrated in figure IV-36, which shows that T-111 undergoes a creep rate transition at low test temperatures (in the 1600° to 2000° F range), whereas it shows normal primary creep at high temperatures (near 2600° F). At temperatures between these two extremes, creep of T-111 exhibits neither a pronounced rate transition nor a pronounced first stage.

The importance of the low temperature creep rate transition is that the isostatic steady state creep rate is higher than the hypothetical life fraction creep rate in this temperature range, whereas it ordinarily would be lower when first stage creep appears as it does in the high temperature T-111 creep tests. Previous work referred to earlier showed that the creep rate transition in T-111 alloy is caused by a vacuum induced loss of oxygen, which provides significant strain age strengthening in the early stages of a low temperature T-111 creep test (ref. 19). Since this vacuum induced deoxidation can proceed independently of the creep deformation, the creep test specimens may be partially degassed when the load in the increasing stress test reaches a high enough level for significant creep to occur.

Thus, throughout much of the active life of a low temperature increasing stress test the creep rate should approximate the isostatic steady state creep rates, as shown by the experimental results in figure IV-34. The reason that the creep rates in the increasing stress tests tend to be slower than isostatic rates in the early stages of the increasing stress tests now becomes clear, since creep at this stage of the test may be occurring in only partially deoxidized material. The significance of the creep rate transition is that, when the experimental isostatic creep rates are integrated at low temperatures, the integrated strain will be slightly greater than, and the predicted 1 percent creep life slightly shorter than, the experimentally observed increasing stress creep life. Conversely, when the hypothetical creep rate established by the reciprocal of the creep life  $\dot{\epsilon}_2$  is integrated at low temperatures, the predicted creep life is slightly greater than the experimentally observed value. At high temperatures where primary creep occurs, the opposite would presumably be true; that is, the Nichols and Winkler life fraction integration should provide the conservative prediction while the steady state strain rate integration should predict creep lives which are longer than the experimentally observed values. While increasing stress data were not available at high temperatures to check this hypothesis, the data in table IV-8 show that at intermediate temperatures, where creep is essentially linear, the predictions of both methods are comparable and agree well with the experimental data.

## SUMMARY OF RESULTS

A Larson-Miller analysis of creep test results on molybdenum and columbium-base turbine alloys showed that at higher stress levels and low temperatures a specially processed lot of TZM having a somewhat higher than normal carbon content is superior to TZC in the stress relieved condition, whereas at higher temperatures and lower stresses, the behavior of the two materials is comparable. Both of the molybdenum alloys were superior to the columbium-base alloys AS-30 and CB-132M.

The creep tests indicated that arc-melted and vapor-deposited tungsten had comparable creep behavior. A comparison between these data and literature values for the powder metallurgy product tested in vacuum showed no difference on a Larson-Miller plot. However, the literature values indicated that powder metallurgy material tested in argon appeared substantially more creep resistant.

A detailed analysis of tension and creep test results on T-111 revealed that a complex atmosphere strain aging phenomenon involving oxygen and probably hafnium provides a transient strengthening in the early stages of T-111 creep tests in the 1600° to 2200° F (870° to 1204° C) range. At long test times, ultrahigh vacuum removal of oxygen depletes the strain aging strengthening species from the matrix and causes a creep rate transition to occur. After the creep rate transition, steady state creep proceeds according to the relation

$$\dot{\epsilon} = 1.65 \times 10^9 \left[ \sinh(6.6 \times 10^{-5} \sigma) \right]^{3.17} e^{-90\,000/RT}$$

where the values of activation energy and stress exponent suggest that steady state creep is governed by a diffusion controlled microcreep mechanism.

The creep tests conducted on T-111 alloy with continuously increasing loads provided continuously increasing creep rates which were comparable to the isostatic steady state creep rates at equivalent stress levels. Methods have been developed for prediction of the 1 percent creep life under varying stress conditions from isostatic creep test data, and comparison of these predictions with the experimental results shows the dependence of analytical techniques on the character of the isostatic creep curves.

## REFERENCES

1. Sawyer, J. C.: Design and Operation of Ultra-High Vacuum Creep Equipment. Transactions Vacuum Metallurgy Conference. L. M. Bianchi, ed., American Vacuum Society, 1965, pp. 41-55.

2. Sawyer, J. C.; and Steigerwald, E. A.: Creep Properties of Refractory Metal Alloys in Ultrahigh Vacuum. *J. Materials*, vol. 2, no. 3, June 1967, pp. 341-361.
3. Sheffler, K. D.; and Steigerwald, E. A.: Generation of Long Time Creep Data on Refractory Alloys at Elevated Temperatures. TRW Equipment Labs. (NASA CR-72391), Dec. 14, 1967.
4. Schmidt, F. F.; and Ogden, H. R.: The Engineering Properties of Tantalum and Tantalum Alloys. DMIC Rep. 189, Battelle Memorial Inst., Sept. 13, 1963. (Available from DDC as AD-426344.)
5. Schmidt, Frank F. et al.: Investigation of the Properties of Tantalum and Its Alloys. Battelle Memorial Inst. (WADD-TR-59-13, DDC No. AD-236957), Mar. 1960.
6. Baird, J. D.; and Jamieson, A.: Effects of Manganese and Nitrogen on the Tensile Properties of Iron in the Range 20-600<sup>o</sup> C. *J. Iron Steel Inst.*, vol. 204, pt. 8, Aug. 1966, pp. 793-803.
7. Kinoshita, S.; Wray, P. J.; and Horne, G. T.: Some Observations on the Portevin-Le Chatelier Effect in Iron. *Trans. AIME*, vol. 233, no. 10, Oct. 1965, pp. 1902-1904.
8. Schmidt, F. F.: Tantalum and Tantalum Alloys. DMIC Rep. 133, Battelle Memorial Inst., July 25, 1960.
9. Schmidt, F. F.; and Ogden, H. R.: The Engineering Properties of Tungsten and Tungsten Alloys. DMIC Rep. 191, Battelle Memorial Inst., Sept. 27, 1963. (Available from DDC as AD-425547.)
10. Anon.: The Mechanical and Thermal Properties of Tungsten and TZM Sheet Produced in the Refractory Metal Sheet Rolling Program. Pt. 1. Rep. 7563-1479-XII, Southern Research Inst., Aug. 31, 1966. (Available from DDC as AD-638631.)
11. Buckman, R. W., Jr.; and Goodspeed, R. C.: Development of Dispersion Strengthened Tantalum Base Alloy. Rep. WANL-PR-(Q)-013, Westinghouse Electric Corp. (NASA CR-72316), Nov. 20, 1966.
12. deBarbadillo, John J.: The Effect of Substitutional Alloying Elements on the Elevated Temperature Mechanical Properties of Alpha Iron. Ph.D. Thesis, Lehigh Univ., 1967.
13. Garofalo, F.: Fundamentals of Creep and Creep-Rupture in Metals. Macmillan Co., 1965.



14. Sherby, O. D.; and Burke, P. M.: Mechanical Behavior of Crystalline Solids at Elevated Temperature. Progress in Material Science, vol. 13, no. 7, 1967. Pergamon Press, 1968, p. 325.
15. Weertman, J.: Creep of Indium, Lead, and Some of Their Alloys with Various Metals. Trans. AIME, vol. 218, no. 2, Apr. 1960, pp. 207-218.
16. McCoy, H. E.: Creep-Rupture Properties under Conditions of Constant and Varying Stresses. Nucl. Appl., vol. 2, no. 6, Dec. 1966, pp. 481-485.
17. Manson, S. S.: Thermal Stress and Low-Cycle Fatigue. McGraw-Hill Book Co., Inc., 1966, p. 118.
18. Nichols, J. P.; and Winkler, D. R.: A Program for Calculating Optimum Dimensions of Alpha Radioisotope Capsules Exposed to Varying Stress and Temperature. Rep. ORNL-TM-1735, Oak Ridge National Lab. (NASA CR-72172), Apr. 1967.
19. Sheffler, K. D.; Sawyer, J. C.; and Steigerwald, E. A.: Mechanical Behavior of Tantalum-Base T-111 Alloy at Elevated Temperature. NASA CR-1436, 1969.

TABLE IV-1. - CHEMICAL COMPOSITION OF ALLOYS EVALUATED IN CREEP TEST PROGRAM

| Material                   | wt % |      |       |      |      |      |       |      |       | ppm            |                |                |
|----------------------------|------|------|-------|------|------|------|-------|------|-------|----------------|----------------|----------------|
|                            | Cb   | W    | Re    | Mo   | Ta   | Hf   | C     | Ti   | Zr    | N <sub>2</sub> | O <sub>2</sub> | H <sub>2</sub> |
| TZM                        |      |      |       |      |      |      |       |      |       |                |                |                |
| (Heat 7463)                | ---  | ---- | ----- | Bal. | ---- | ---- | 0.016 | 0.48 | 0.08  | 1              | 2              | 1              |
| (Heat 7502)                | ---  | ---- | ----- | Bal. | ---- | ---- | .010  | .51  | .091  | 100            | 20             | 7              |
| (Heat KDTZM-1175)          | ---  | ---- | ----- | Bal. | ---- | ---- | .035  | .61  | .120  | 43             | 34             | 9              |
| TZC                        |      |      |       |      |      |      |       |      |       |                |                |                |
| (Heat M-80)                | ---  | ---- | ----- | Bal. | ---- | ---- | .127  | 1.02 | .17   | 18             | 41             | 10             |
| (Heat M-91)                | ---  | ---- | ----- | Bal. | ---- | ---- | .113  | 1.17 | .270  | 34             | 37             | 10             |
| (Heat 4345)                | ---  | ---- | ----- | Bal. | ---- | ---- | .075  | 1.19 | .16   | 9              | 19             | 2              |
| AS-30                      | Bal. | 21.0 | ----- | ---- | ---- | ---- | .09   | ---- | 1.04  | 100            | 60             | 15             |
| Cb-132M                    | Bal. | 15.6 | ----- | 4.72 | 19.7 | ---- | .16   | ---- | 2.10  | 24             | 4              | 4              |
| W - Arc melted             |      |      |       |      |      |      |       |      |       |                |                |                |
| (Heat KC1357)              | ---  | Bal. | ----- | ---- | ---- | ---- | .0058 | ---- | ----- | 16             | 9              | 3              |
| Vapor deposited            | ---  | Bal. | ----- | ---- | ---- | ---- | .0012 | ---- | ----- | 15             | 13             | 2              |
| W-25 percent Re arc melted |      |      |       |      |      |      |       |      |       |                |                |                |
| (Heat 35-75002)            | ---  | ---- | 24.88 | ---- | ---- | ---- | .007  | ---- | ----- | 7              | 61             | 13             |
| ASTAR-811C                 |      |      |       |      |      |      |       |      |       |                |                |                |
| (Heat NASV-20-WS)          | ---  | 7.3  | 1.0   | ---- | Bal. | 0.86 | .024  | ---- | ----- | 20             | 14             | ----           |
| (Heat VAM-95)              | ---  | 7.6  | 1.1   | ---- | Bal. | .65  | .030  | ---- | ----- | 3              | 4              | .3             |
| (Heat 650056)              | ---  | 8.2  | 1.2   | ---- | Bal. | .9   | .020  | ---- | ----- | 14             | 30             | 3.5            |
| Ta-10W                     |      |      |       |      |      |      |       |      |       |                |                |                |
| (Heat 630002)              | ---  | 9.9  | ----- | ---- | Bal. | ---- | .0044 | ---- | ----- | 25             | 100            | 5              |
| Pure tantalum              |      |      |       |      |      |      |       |      |       |                |                |                |
| (Heat B-1962)              | ---  | ---- | ----- | ---- | Bal. | ---- | .0012 | ---- | ----- | 21             | 20             | 5              |
| (Heat 60249)               | ---  | ---- | ----- | ---- | Bal. | ---- | .0014 | ---- | ----- | 20             | 51             | 3              |
| T-111 - see table IV-3     | ---  | ---- | ----- | ---- | ---- | ---- | ----- | ---- | ----- | ---            | ---            | -----          |

TABLE IV-2. - SUMMARY OF TEST MATERIAL PROPERTIES AND PROCESSING DETAILS

| Material            | Heat       | Vendor                         | Pertinent processing details   | Heat treatment  | Tensile strength, ksi |                   | Percent elongation | DPH hardness |
|---------------------|------------|--------------------------------|--|-----------------|-----------------------|-------------------|--------------------|--------------|
|                     |            |                                |  |                 | Ultimate              | 0.2 Percent yield |                    |              |
| TZC                 | M-80       | General Electric               | Extruded 2.3:1 at 3092° F, cross-rolled at 2925° F with 4 percent reduction per pass   | 3092° F, 1 hr   | 68.6                  | 68.5              | 0.05               | 268          |
| TZC                 | M-91       | General Electric               | Extruded 2.3:1 at 3092° F, cross-rolled with large deformations per pass and finished at 2372° F   | 3092° F, 1 hr   | 85.0                  | 49.0              | 7.0                | 240          |
|                     |            |                                |  | 2500° F, 1 hr   | 106                   | 99                | 4                  | 303          |
| TZC                 | 4345       | Climax Molybdenum              | Extruded at 3000° F, heat treated at 3000° F, upset forged 40 percent at 2400° F, broad forged to 0.825 in. at 2400° F   | 2400° F, 1 hr   | 123                   | 117               | 12                 | 346          |
| TZM                 | 7502       | Climax Molybdenum              | Extruded from 10 $\frac{3}{4}$ to 6 $\frac{1}{4}$ in. diam, heat treated at 2700° F, upset forged at 2200° F   | 2200° F, 1 hr   | -----                 | -----             | -----              | 304          |
|                     |            |                                |  | 2850° F, 1 hr   | -----                 | -----             | -----              | 209          |
| TZM                 | KDTZM-1175 | Air Research-Universal Cyclops | Extruded from 10 $\frac{3}{4}$ to 6 $\frac{1}{4}$ in. diam, recrystallized at 2800° F for 4 hr, forged to 4 in. diam at 3400° to 2800° F, recrystallized at 2950° F for 2 hr, forged to 3/4 in. flat disk, 11 blows, at 2800° to 2160° F | 2300° F, 1 hr   | 122                   | 111               | 17.4               | 316          |
| TZM                 | 7463       | Climax Molybdenum              | Extruded from 11 $\frac{1}{2}$ to 6 $\frac{1}{2}$ in. diam, recrystallized, rolled to 2 in. diam, recrystallized, rolled to 1 in. diam, swaged to 5/8 in. diam   | 2250° F, 1/2 hr | 128                   | 117               | 30                 | 300          |
| AS-30               | C5         | General Electric               | Extruded from 4.8 to 4 by 1.625 in. sheet bar at 2825° F, cross rolled at 2100° F to 0.790 in.   | -----           | -----                 | -----             | -----              | 293          |
| Cb-132M             | KC1454     | Universal Cyclops              | Extruded from 3 $\frac{7}{8}$ to 1 $\frac{1}{2}$ in. at 3130° F, cross-rolled to 3/4 in. at 2400° F  | -----           | -----                 | -----             | -----              | 336          |
| W - Arc-melted      | KC1357     | Universal Cyclops              | Extruded 4:1 at 3100° F, forged at 2200° F, rolled at 2300°, 1800°, and 1400° F, stress relieved at 1700° F  | -----           | -----                 | -----             | -----              | 487          |
| W - Vapor deposited | -----      | -----                          | -----  | -----           | -----                 | -----             | -----              | ---          |
| W - 25 percent Re   | 3.5-75002  | Wah Chang                      | 0.055 in. sheet stress relieved at 2375° F, rolled to 0.035 in., stress relieved at 2550° F  | -----           | -----                 | -----             | -----              | 639          |
| T-111               | Typical    | Wah Chang                      | 6 $\frac{1}{2}$ in. diam ingot forged to 1 $\frac{1}{2}$ in. bar at 2200° F, annealed at 3000° F, rolled at 800° F to 1/4 in. thick, annealed at 3000° F, cold rolled to 0.030 in.   | 3000° F, 1 hr   | 94                    | Typical           | -----              | ---          |
| T-111               | Typical    | Fansteel                       | Extruded 3.25:1 at 2200° F, rod rolled and flat rolled to 0.030 in.  | 3000° F, 1 hr   | 94                    | 74                | 35                 | 250          |
| Pure Ta             | -----      | -----                          | Double e.b. melt extruded to 2 in. o.d. by 1/4 in. wall tube, reduced and drawn to 3/4 in. o.d. by 0.040 in. wall  | -----           | -----                 | -----             | -----              | ---          |
| ASTAR-811C          | Typical    | Westinghouse                   | Side forged from 3.9 in. diam by 5 in. long ingot to 7.2 by 7.5 by 1.133 in. thick bar at 2550° F, annealed at 2700° F for 2 hr, rolled to 1/4 in. at 500° F, annealed 1 hr at 3000° F, cold rolled to 0.040 in.                         | -----           | -----                 | -----             | -----              | 253          |

TABLE IV-3. - CHEMICAL COMPOSITION AND ROOM TEMPERATURE MECHANICAL

PROPERTIES OF T-111 ALLOYS ANNEALED 1 HOUR AT 3000<sup>0</sup> F (1649<sup>0</sup> C)

| Heat   | Composition    |     |        |                |                |                | Mechanical properties |                   |                    |
|--------|----------------|-----|--------|----------------|----------------|----------------|-----------------------|-------------------|--------------------|
|        | Weight percent |     |        | ppm            |                |                | Tensile strength, ksi |                   | Percent elongation |
|        | W              | Hf  | C      | N <sub>2</sub> | O <sub>2</sub> | H <sub>2</sub> | Ultimate              | 0.2 Percent yield |                    |
| 70616  | 8.5            | 2.3 | 0.0044 | 20             | 55             | 6              | (a)                   | (a)               | (a)                |
| 65079  | 8.7            | 2.3 | .0030  | 50             | 130            | 4              | 94.0                  | 72.0              | 35.2               |
| 65076  | 8.6            | 2.0 | .0040  | 20             | 100            | 3              | 93.2                  | 79.9              | 31.0               |
| D-1102 | 7.9            | 2.3 | .0030  | 34             | 20             | 3              | (a)                   | (a)               | (a)                |
| D-1670 | 7.9            | 2.4 | .0010  | 20             | 72             | <5             | (a)                   | (a)               | (a)                |
| D-1183 | 8.7            | 2.2 | .0036  | 10             | 25             | 6              | 94.3                  | 81.0              | 32.8               |
| 650028 | 8.3            | 2.1 | .0030  | 12             | 30             | 1.9            | 83.8                  | 77.8              | 30.1               |
| 848001 | 7.9            | 2.0 | .0010  | 13             | 21             | 1              | 79.3                  | 70.0              | 30.7               |
| 650038 | 8.6            | 2.0 | .0025  | 20             | 100            | 2.8            | 92.1                  | 76.8              | 29.8               |

<sup>a</sup>Not available.

TABLE IV-4. - TENSILE PROPERTIES OF STRESS RELIEVED

TZC AND TZM AT 2000<sup>0</sup> F

| Material               | Stress relief temperature, °F | Tensile strength, ksi |                   | Percent elongation | Percent reduction of area |
|------------------------|-------------------------------|-----------------------|-------------------|--------------------|---------------------------|
|                        |                               | Ultimate              | 0.2 Percent yield |                    |                           |
| TZM heat<br>KDTZM-1175 | 2300                          | 79                    | 74                | 19                 | 51                        |
| TZC heat 4345          | 2500                          | 70                    | 69                | 18                 | 61                        |

TABLE IV-5. - SUMMARY OF CREEP DATA FOR TUNGSTEN AND TUNGSTEN-BASE ALLOYS

| Material  | Specimen | Test temperature   |                    | Stress |                    | Hours to<br>1 percent<br>creep | Larson-Miller<br>parameter -<br>1 percent creep,<br>$T_{0R} (15 + \log t)$ | Creep rate,<br>in./in./hr |
|---|----------|--------------------|--------------------|--------|--------------------|--------------------------------|--|---------------------------|
|   |          | $^{\circ}\text{F}$ | $^{\circ}\text{C}$ | ksi    | $\text{N/m}^2$     |                                |  |                           |
| Tungsten, heat<br>KC-1357                           | S-5      | 3200               | 1760               | 3      | $2.07 \times 10^7$ | 6                              | $57.8 \times 10^3$   | $1.7 \times 10^{-3}$      |
|   | S-7      | 3200               | 1760               | .4     | $2.76 \times 10^6$ | (a)                            | (a)  | $1.7 \times 10^{-6}$      |
|   | S-9      | 3200               | 1760               | 1      | $6.89 \times 10^6$ | 675                            | 65.4   | $1.5 \times 10^{-5}$      |
|   | S-17     | 2800               | 1538               | 4      | $2.76 \times 10^7$ | 20                             | 53.1   | $5.0 \times 10^{-4}$      |
|   | S-18     | 2800               | 1538               | 3      | $2.07 \times 10^7$ | 125                            | 55.8   | $8.0 \times 10^{-5}$      |
| Vapor-deposited<br>tungsten                         | B-17     | 3200               | 1760               | 1      | $6.89 \times 10^6$ | 1140                           | $66.0 \times 10^3$   | $8.8 \times 10^{-6}$      |
|   | B-24     | 2800               | 1538               | 2      | $1.38 \times 10^7$ | 1500                           | 59.2   | 6.7                       |
| Tungsten - 25 percent<br>rhenium, heat<br>3.5-75002 | S-3      | 3200               | 1760               | 5      | $3.44 \times 10^7$ | 12                             | $58.9 \times 10^3$   | $8.3 \times 10^{-4}$      |
|   | S-4      | 3200               | 1760               | 3      | $2.07 \times 10^7$ | 25                             | 60.0   | $4.0 \times 10^{-4}$      |
|   | S-6      | 3200               | 1760               | .5     | $3.44 \times 10^6$ | (a)                            | (a)  | $3.6 \times 10^{-6}$      |
|   | S-8      | 3200               | 1760               | 1.5    | $1.03 \times 10^7$ | 315                            | 64.0   | $3.2 \times 10^{-5}$      |

<sup>a</sup>Too little creep to extrapolate.

TABLE IV-6. - EFFECT OF CREEP EXPOSURE ON ROOM TEMPERATURE MECHANICAL PROPERTIES  
AND COMPOSITION OF T-111 ANNEALED 1 HOUR AT 3000<sup>o</sup> F PRIOR TO CREEP TESTING

| Creep test conditions |        |                |                         |                         | Before<br>or<br>after<br>creep<br>testing | Ultimate<br>tensile<br>strength,<br>ksi | Percent<br>elongation    | Diamond<br>pyramid<br>hardness | Composition  |                |                |                |                |
|-----------------------|--------|----------------|-------------------------|-------------------------|---|---|--------------------------|--------------------------------|--------------|----------------|----------------|----------------|----------------|
| Test                  | Heat   | Stress,<br>ksi | Temper-<br>ature,<br>°F | Test<br>duration,<br>hr |   |   |                          |                                | Percent      |                | ppm            |                |                |
|                       |        |                |                         |                         |   |   |                          |                                | Hf           | C              | N <sub>2</sub> | O <sub>2</sub> | H <sub>2</sub> |
| S-26                  | D-1670 | 17             | 1800                    | 1624                    | Before<br>After                           | (a)                                     | (a)                      | (a)                            | 2.17<br>2.09 | 0.001<br>.0032 | 20<br>30       | 72<br>10       | 5<br>5         |
| <sup>b</sup> S-31     | 65079  | 5              | 2200                    | 6602                    | Before<br>After                           | 94.0<br>85.3                            | 35.0<br><sup>c</sup> 8.2 | (a)                            | (a)          | (a)            | (a)            | (a)            | (a)            |
| S-33                  | 65076  | 8              | 2200                    | 2976                    | Before<br>After                           | 93.1<br>85.7                            | 31.0<br>39.0             | 247<br>228                     | 1.95<br>2.07 | .004<br>.004   | 20<br>30       | 100<br>20      | 3<br>31        |
| S-32                  | D-1102 | 5              | 2200                    | 4322                    | Before<br>After                           | (a)                                     | (a)                      | (a)                            | 2.28<br>2.17 | .003<br>.003   | 34<br>30       | 20<br>10       | 3<br>24        |
| S-35                  | 65079  | 5              | 2200                    | 5522                    | Before<br>After                           | (a)                                     | (a)                      | 275<br>257                     | 2.30<br>2.14 | .003<br>.0046  | 50<br>30       | 130<br>10      | 4<br>5         |
| S-43                  | 65079  | 18             | 2000                    | 361                     | Before<br>After                           | (a)                                     | (a)                      | (a)                            | 2.30<br>1.33 | .003<br>.003   | 50<br>40       | 130<br>10      | 4<br>31        |

<sup>a</sup>Not available.

<sup>b</sup>Perpendicular to rolling direction.

<sup>c</sup>Reduced gage width.

TABLE IV-7. - LOADING RATES

ABOVE WHICH INCREASING

LOAD TESTS ARE YIELD

RATHER THAN

CREEP LIMITED

| Temperature    |                | Stress rate,<br>psi/hr |
|----------------|----------------|------------------------|
| <sup>o</sup> F | <sup>o</sup> C |                        |
| 1800           | 982            | 0.2                    |
| 2000           | 1093           | 8                      |
| 2200           | 1204           | 166                    |

TABLE IV-8. - PROGRESSIVE STRESS CREEP TEST RESULTS

FOR T-111 ALLOY

| Test temperature |                | Stress rate,<br>psi/hr | 1 Percent creep life |                        |                        |
|------------------|----------------|------------------------|----------------------|------------------------|------------------------|
| <sup>o</sup> F   | <sup>o</sup> C |                        | Observed             | Predicted <sup>a</sup> | Predicted <sup>b</sup> |
| 1800             | 982            | 20                     | 1660                 | 1430                   | 1809                   |
| 1800             | 982            | 5                      | 5500                 | 4990                   | 6466                   |
| 2000             | 1093           | 13                     | 1600                 | 1540                   | 1798                   |
| 2000             | 1093           | 5                      | 3850                 | 3500                   | 3957                   |
| 2000             | 1093           | 2                      | <sup>c</sup> 8000    | 7620                   | 8342                   |
| 2200             | 1204           | 16                     | 1080                 | 851                    | 895                    |
| 2200             | 1204           | 5                      | 2240                 | 2260                   | 2122                   |
| 2200             | 1204           | 1                      | 7750                 | 7340                   | 7450                   |

<sup>a</sup>Strain rate integration technique.<sup>b</sup>Life fraction technique (Nichols and Winkler program).<sup>c</sup>Extrapolated.

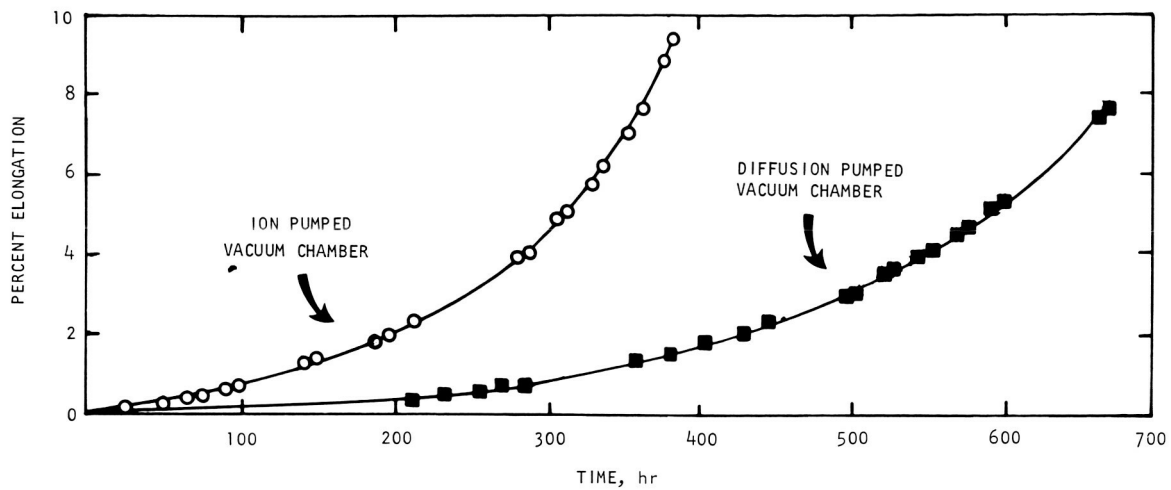


Figure IV-1. - Influence of environment on creep behavior of T-111 alloy at identical test conditions.



CONVENTIONALLY PROCESSED TZM DISK FORGING (HEAT 7502);  
EDGE PERPENDICULAR TO RADIAL DIRECTION

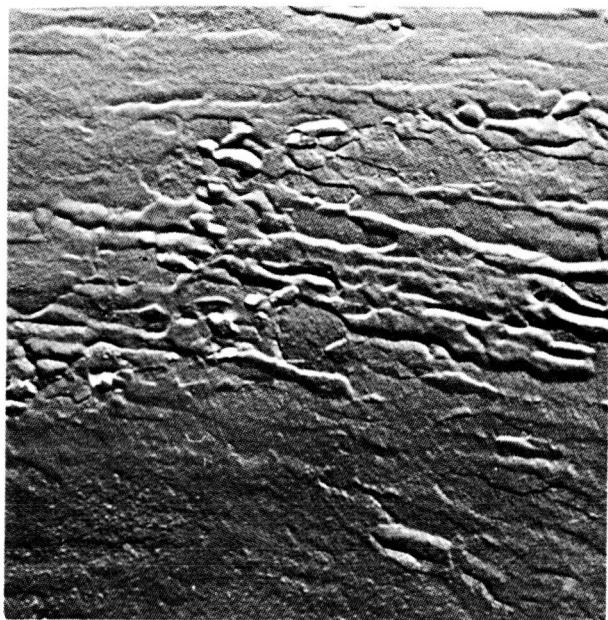


SPECIALLY PROCESSED TZM DISK FORGING (HEAT KDTZM-1175);  
EDGE PERPENDICULAR TO RADIAL DIRECTION



TZM BAR (HEAT 7463); LONGITUDINAL SECTION

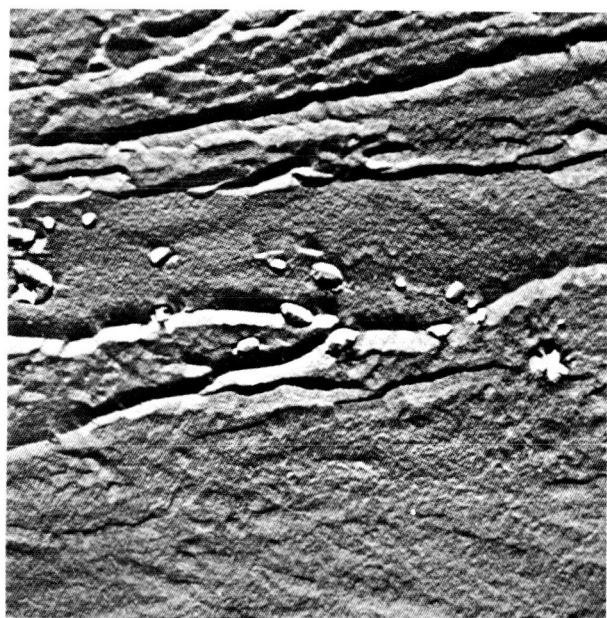
Figure IV-2. - Microstructures of stress relieved TZM.  $\times 100$ .



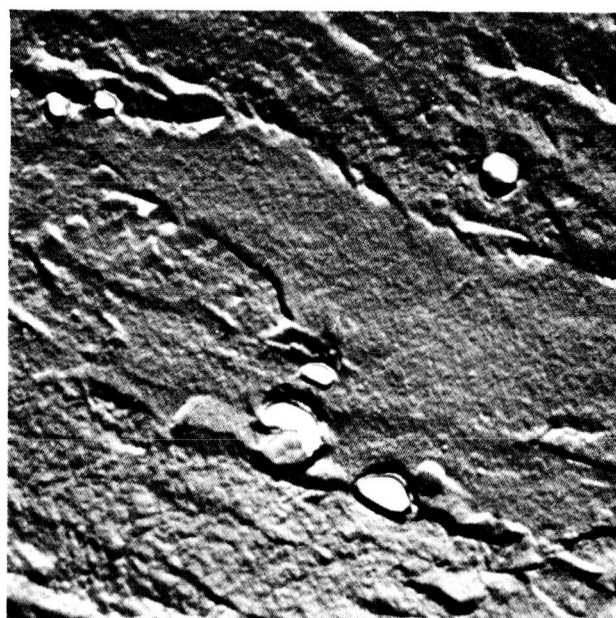
HEAT KDTZM-1175; X5000



HEAT KDTZM-1175; X10 000



HEAT 7502; X5000



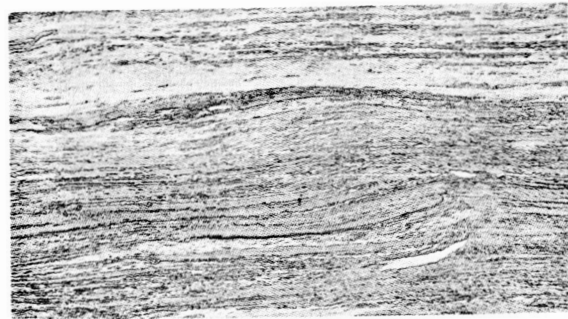
HEAT 7502; X10 000

Figure IV-3. - Electron micrographs of pancake forged and stress relieved TZM disks. Two stage replicas (cellulose nitrate and carbon) with chromium shadowing on primary replica. Reduced 10 percent for reproduction.





ROLLED PLATE; HEAVY DRAFTING PRACTICE, LOW TEMPERATURE FINISH (HEAT M-91); LONGITUDINAL VIEW

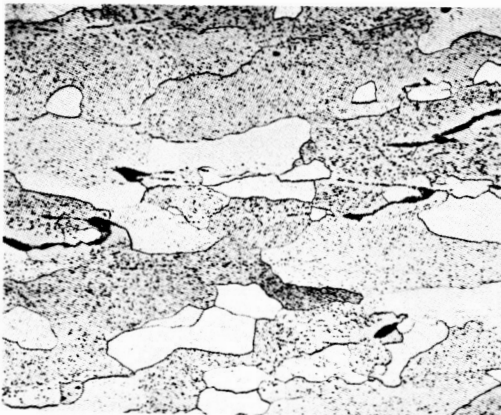


ROLLED PLATE; LIGHT DRAFTING PRACTICE, HIGH TEMPERATURE FINISH (HEAT M-80); LONGITUDINAL VIEW

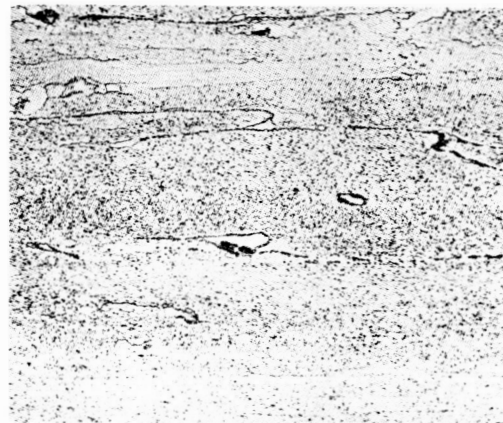


FORGED PLATE (HEAT 4345); EDGE OF PLATE PERPENDICULAR TO ORIGINAL EXTRUSION DIRECTION

Figure IV-4. - Microstructures of stress relieved TZC.  $\times 100$ .

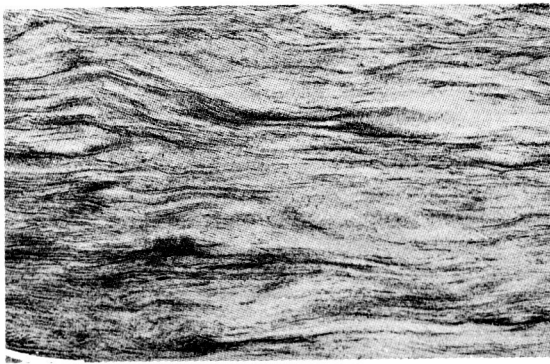


HEAVY DRAFTING PRACTICE; LOW TEMPERATURE FINISH (HEAT M-91)

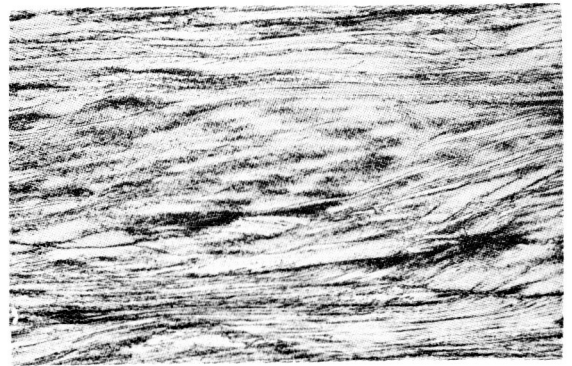


LIGHT DRAFTING PRACTICE; HIGH TEMPERATURE FINISH (HEAT M-80)

Figure IV-5. - Longitudinal microstructures of TZC rolled plates after annealing 1 hour at  $3092^{\circ}$  F.  $\times 500$ .



AS-30 AS ROLLED



Cb-132M AS ROLLED

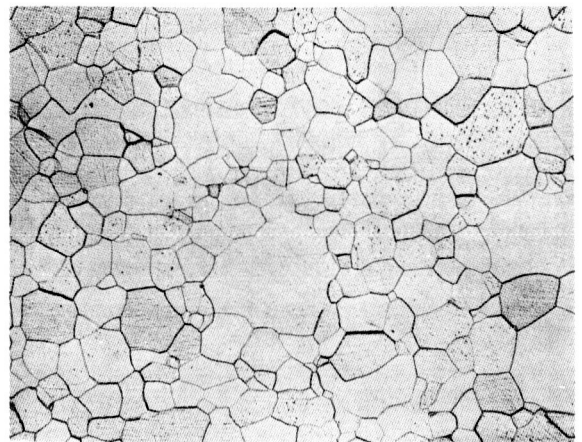


Cb-132M ANNEALED 1 HOUR AT 3092°F (1700°C)

Figure IV-6. - Microstructures of columbium base alloys tested in ultrahigh vacuum creep program.  $\times 100$ .



EDGE PERPENDICULAR TO ROLLING DIRECTION

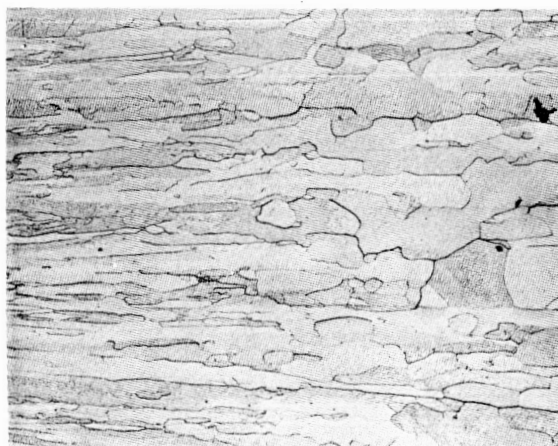


SURFACE OF SHEET

Figure IV-7. - Microstructure of tungsten sheet (heat KC 1357) annealed 1 hour at 3200° F (1760° C).  $\times 100$ .



⊕  
TENSILE  
AXIS



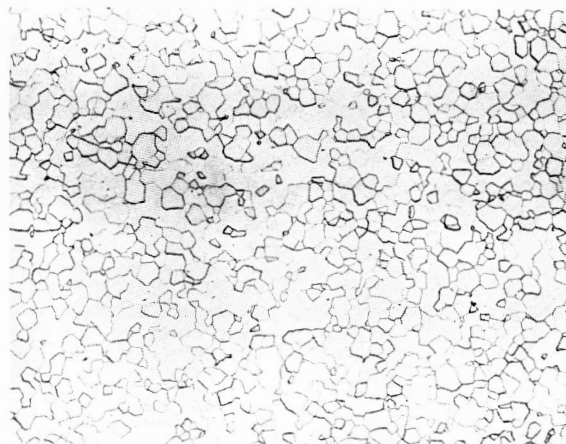
GAGE SECTION PERPENDICULAR TO SPECIMEN AXIS

HEAD SECTION PERPENDICULAR TO SPECIMEN AXIS

Figure IV-8. - Vapor deposited tungsten microstructure after test.  $\times 100$ .

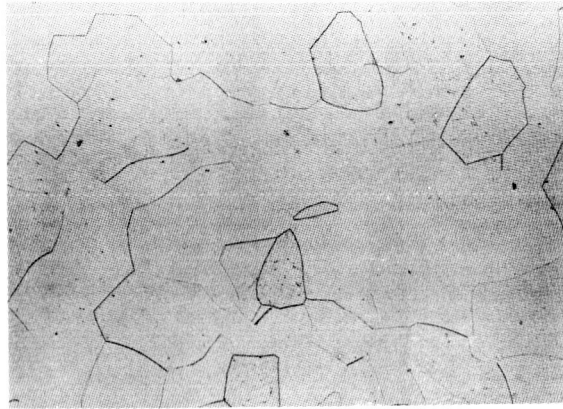


EDGE PERPENDICULAR TO ROLLING DIRECTION

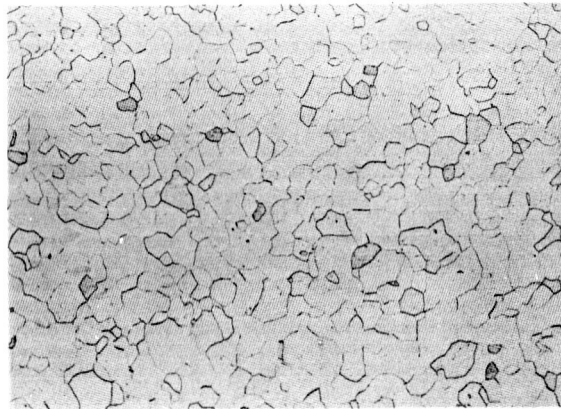


SURFACE OF SHEET

Figure IV-9. - Microstructure of tungsten-25 percent rhenium alloy sheet (heat 3.5-75002) annealed 1 hour at  $3200^{\circ}\text{F}$  ( $1760^{\circ}\text{C}$ ).  $\times 100$ .



HEAT B-1962 ANNEALED 1 HOUR AT 1832° F  
(1000° C); HARDNESS, 94 KHN; X100



HEAT 60249 ANNEALED 1 HOUR AT 2290° F  
(1254° C); HARDNESS, 90 KHN; X100

Figure IV-10. - Microstructures of pure tantalum tubing.

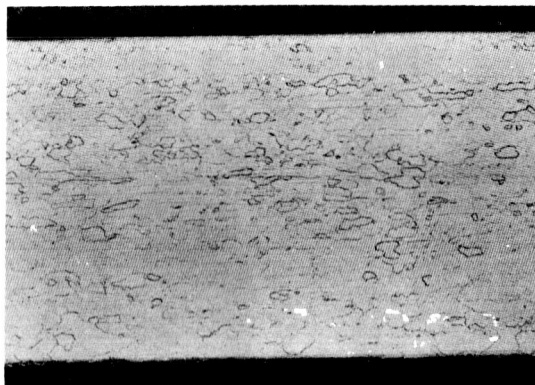
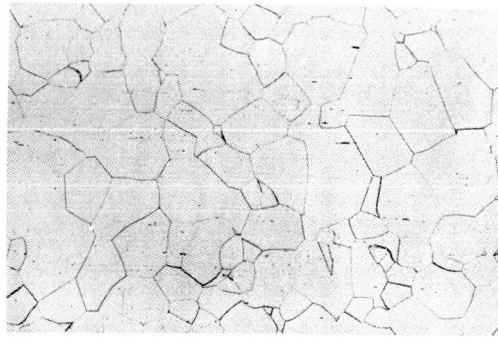
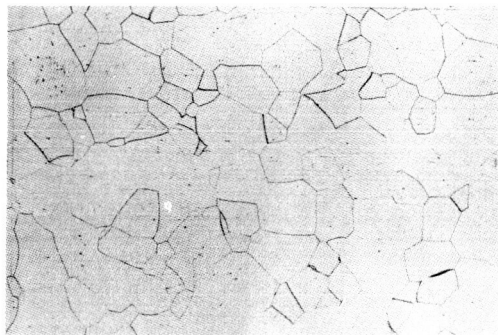


Figure IV-11. - Microstructure of Ta-10W alloy  
annealed 1 hour at 3000° F. X100.



15 MINUTES AT 3520°F (1940°C); X100



9 MINUTES AT 3600°F (1983°C); X100

Figure IV-12. - Microstructure of ASTAR 811C heat VAM-95 annealed to grain size of 0.066 millimeter at 3520° and 3600° F (1940° and 1983° C).

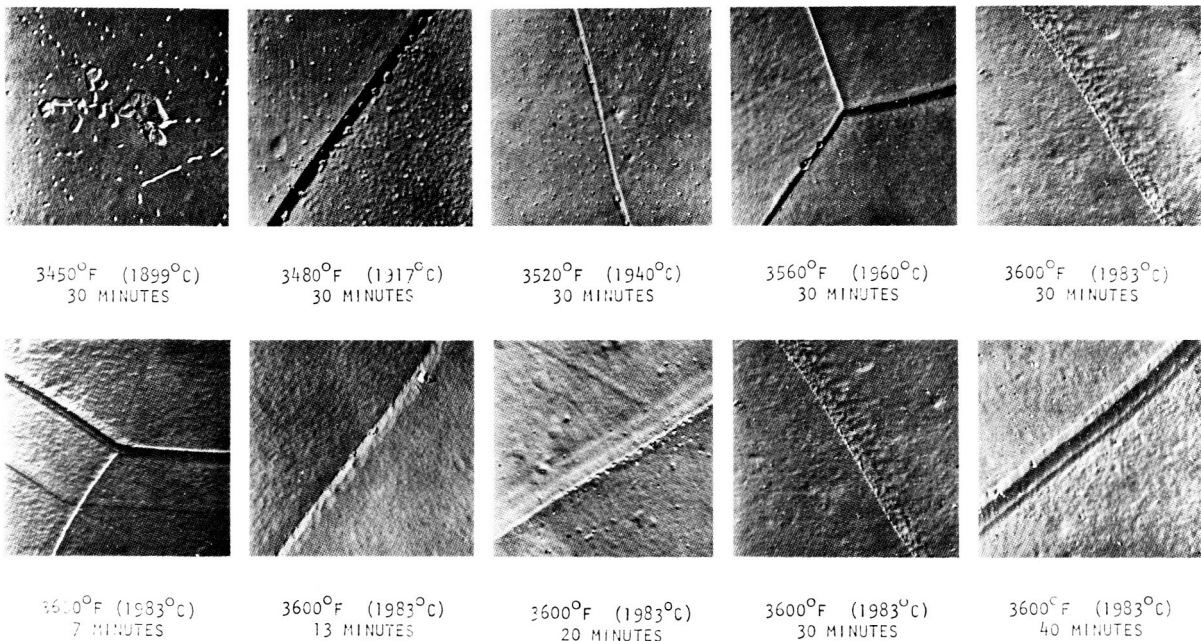
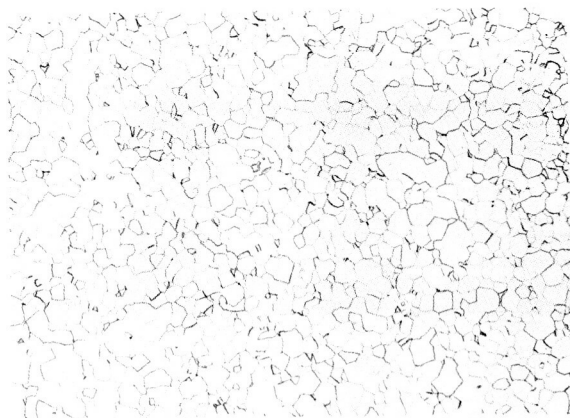
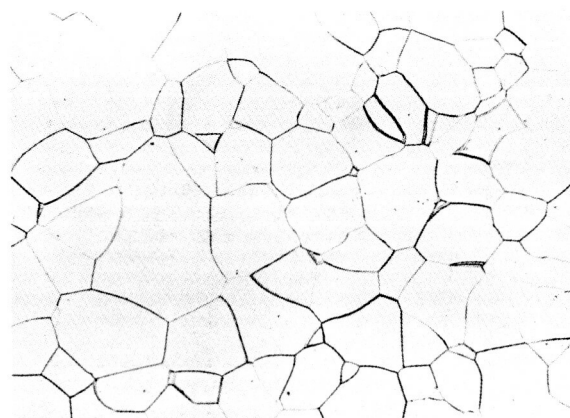


Figure IV-13. - Influence of annealing time and temperature on precipitate morphology in tantalum-base ASTAR 811C, heat NASV-20-WS.  $\times 7500$ , reduced 50 percent for reproduction.





X100



X500

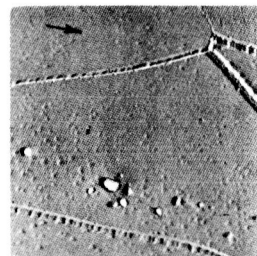
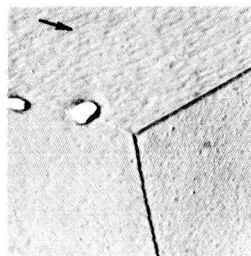
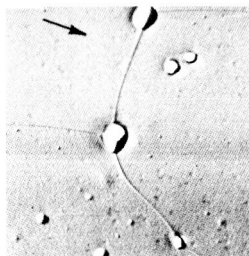
Figure IV-14. - Optical photomicrographs of T-111 heat 70616 recrystallized 1 hour at 3000° F (1649° C).

SPECIMEN S-40  
TESTED 8717 HOURS  
AT 1800° F (982° C)  
AND 17 ksi ( $11.7 \times 10^7$   
N/m<sup>2</sup>); TOTAL CREEP  
STRAIN, 1.028 PERCENT;  
HEAT D-1102

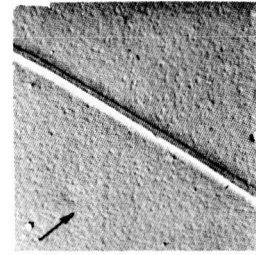
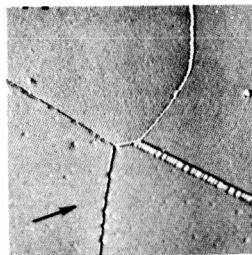
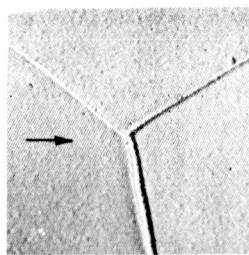
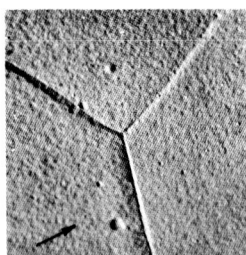
SPECIMEN S-26  
TESTED 9624 HOURS  
AT 1800° F (982° C)  
AND 17 ksi ( $11.7 \times 10^7$   
N/m<sup>2</sup>); TOTAL CREEP  
STRAIN, 1.030 PERCENT;  
HEAT D-1670

SPECIMEN S-33  
TESTED 2976 HOURS  
AT 2200° F (1204° C)  
AND 8 ksi ( $5.51 \times 10^7$   
N/m<sup>2</sup>); TOTAL CREEP  
STRAIN, 1.048 PERCENT  
HEAT 65076

SPECIMEN S-35  
TESTED 5522 HOURS  
AT 2200° F (1204° C)  
AND 5 ksi ( $3.44 \times 10^7$   
N/m<sup>2</sup>); TOTAL CREEP  
STRAIN, 1.092 PERCENT  
HEAT 65079

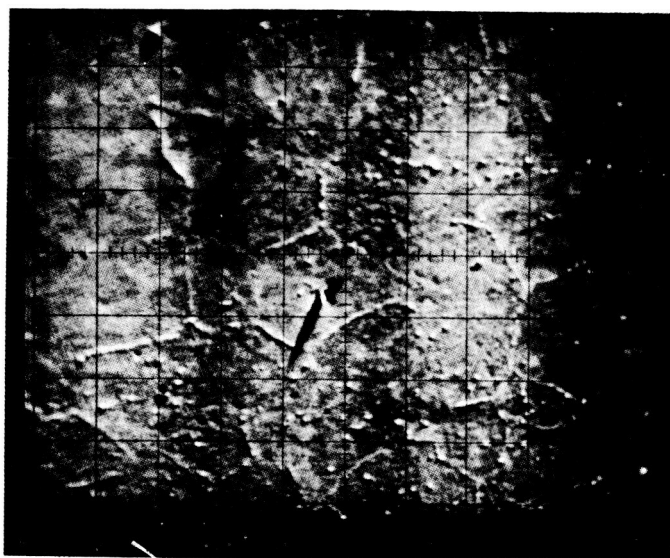


(a) Before creep testing.

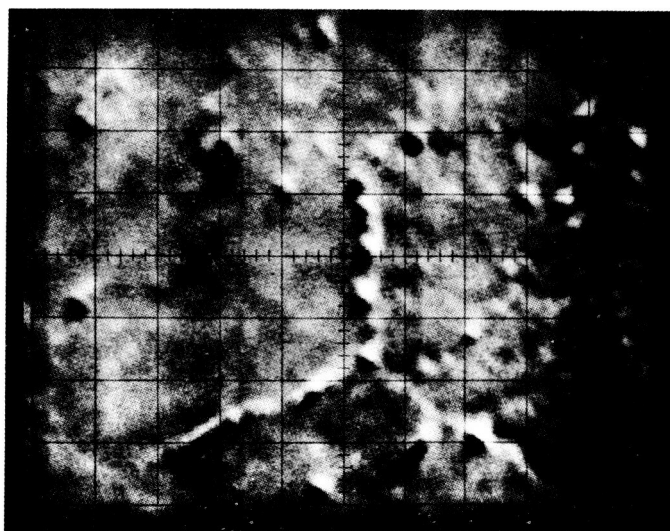


(b) After creep testing.

Figure IV-15. - Electron micrographs of tantalum T-111 alloy (Ta-8%-2%Hf) recrystallized 1 hour at 3000° F, before and after creep testing at indicated test conditions. Total chamber pressure, less than  $1 \times 10^{-8}$  torr; two stage replicas (cellulose nitrate and carbon); arrows indicate direction of chromium shadowing on primary replica.  $\times 7500$ , reduced 55 percent for reproduction.



X550



X1650

Figure IV-16. - Electron microprobe analyzer current images of T-111 heat D-1102 recrystallized 1 hour at  $3000^{\circ}\text{F}$  ( $1649^{\circ}\text{C}$ ). Bright spots represent included second phase particles.

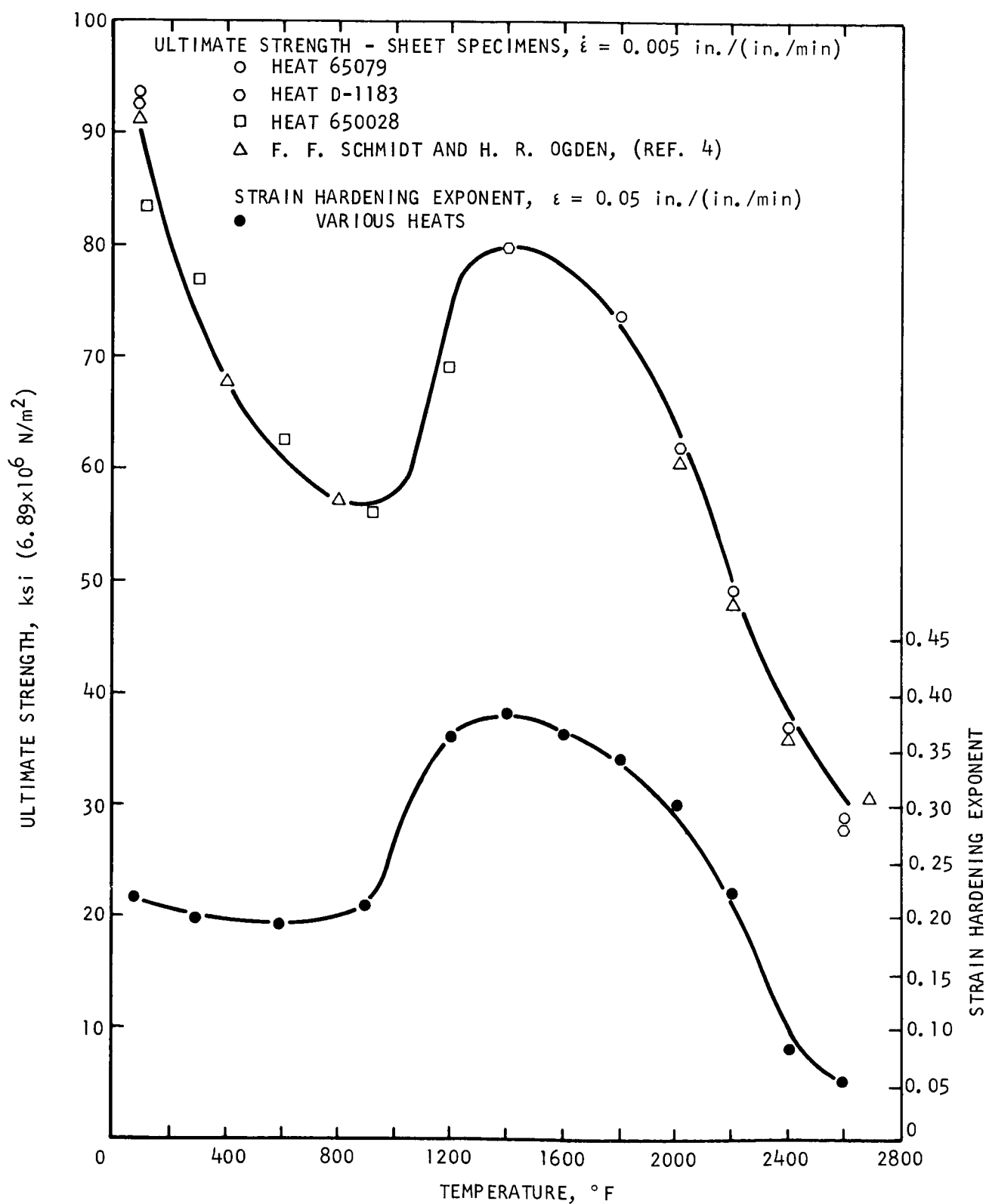


Figure IV-17. - Variation of ultimate strength, strain hardening exponent, 2 percent yield strength, and percent elongation with temperature in T-111 annealed 1 hour at 3000° F (1649° C).



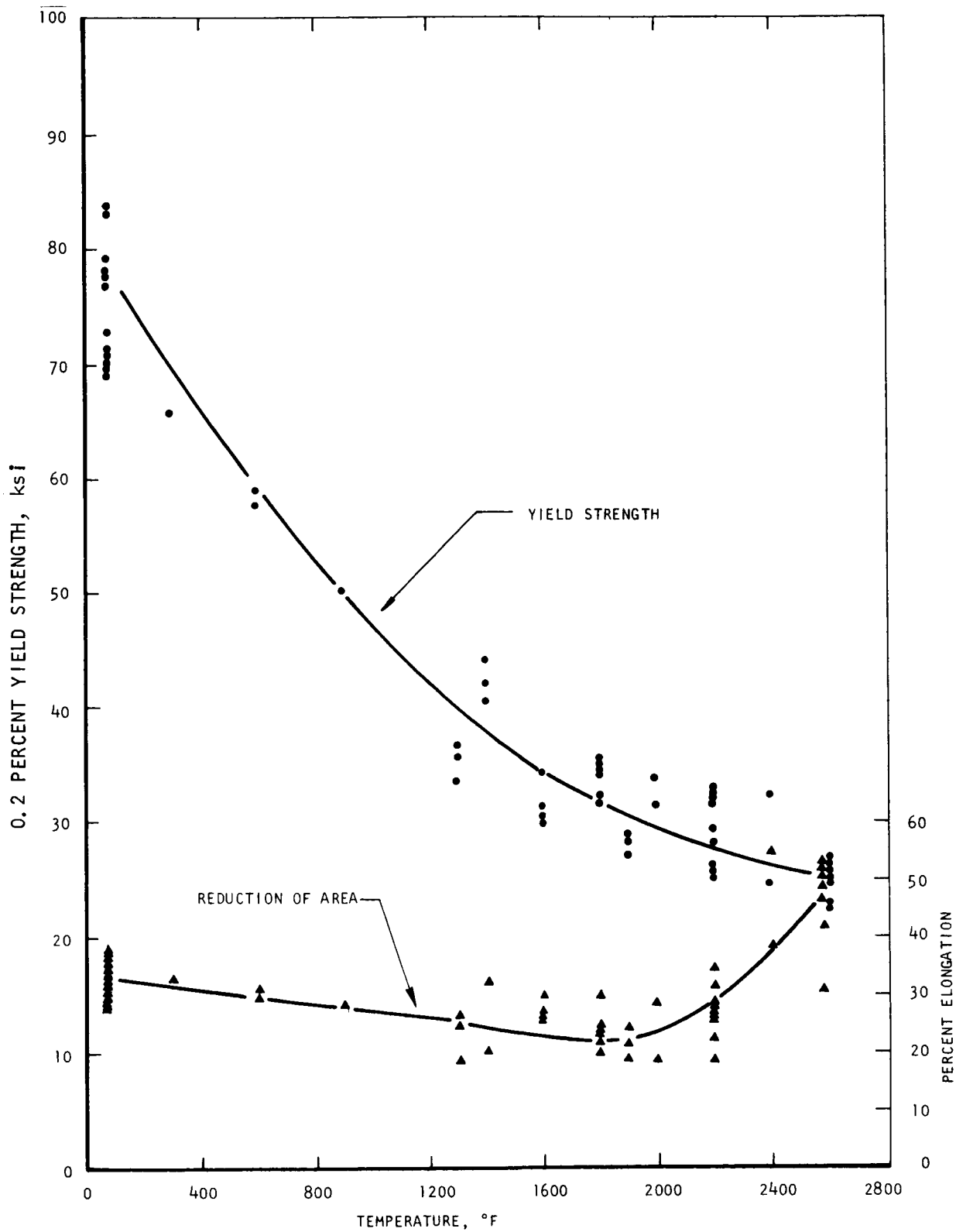


Figure IV-17. - Concluded.

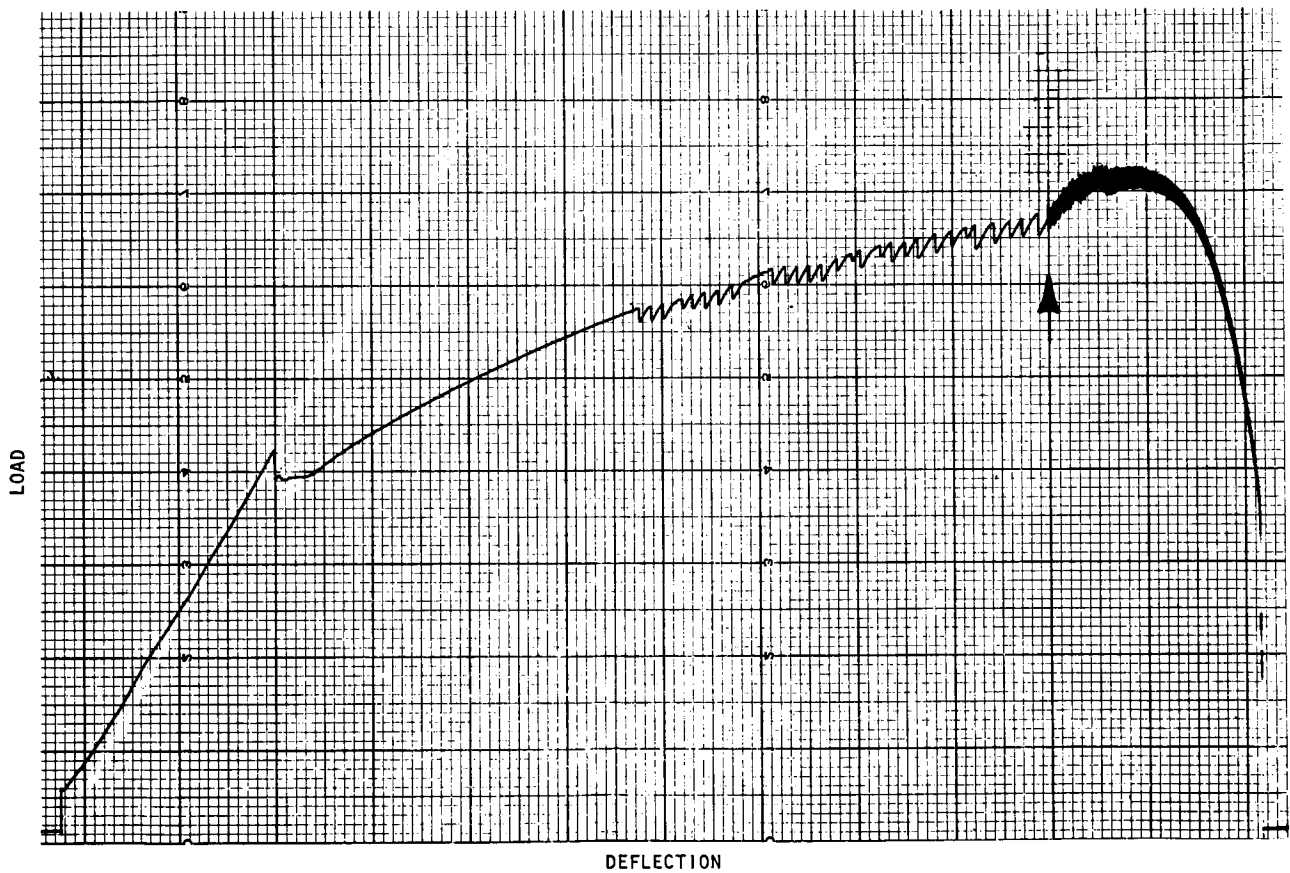


Figure IV-18. - Load-deflection curve of recrystallized T-111 at 1400° F. Arrow indicates decrease in chart speed.

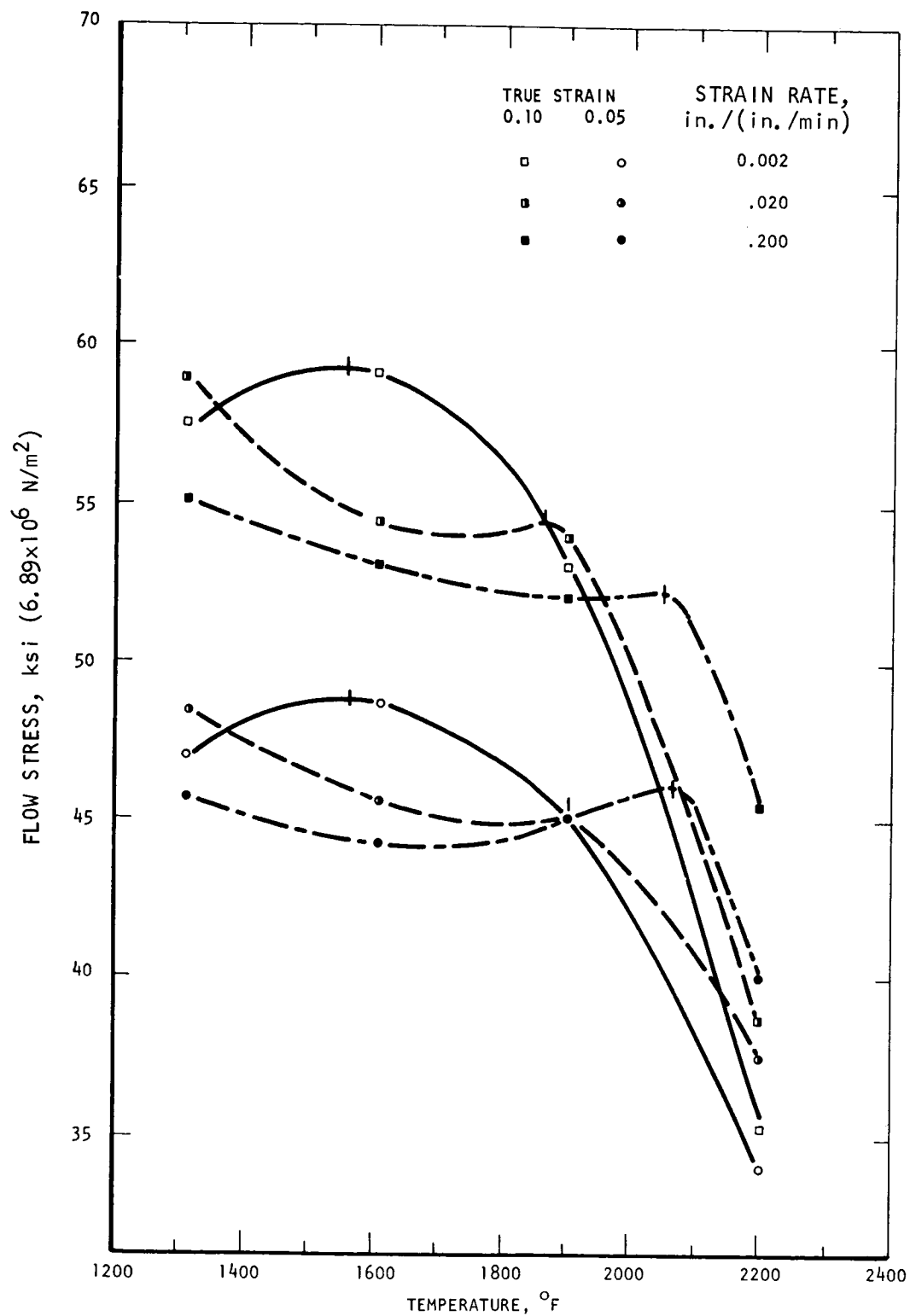


Figure IV-19. - Variation of flow stress with temperature and strain rate at two levels of true strain in T-111 annealed 1 hour at 3000° F (1649° C). Tick on each curve indicates strain aging peak.

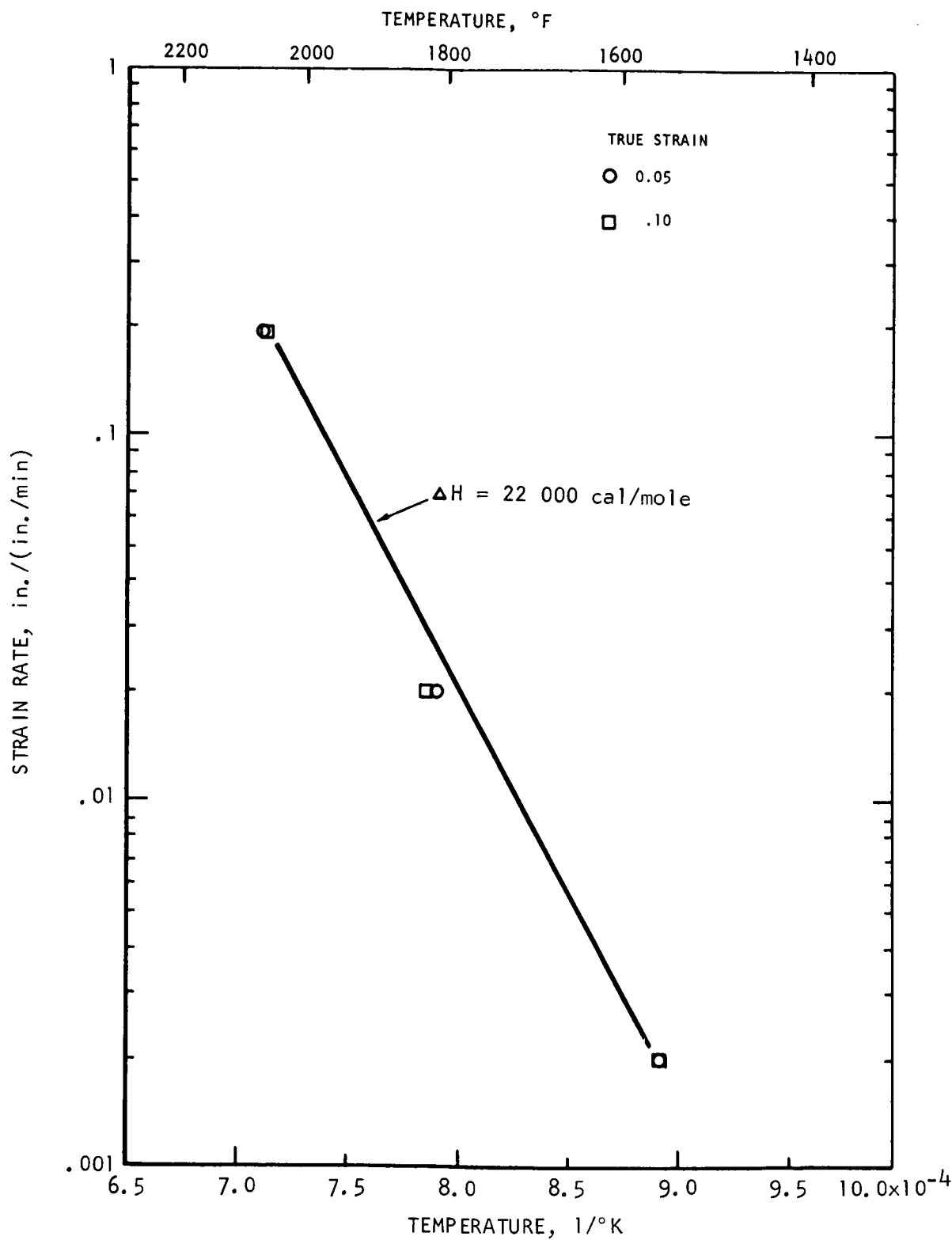


Figure IV-20. - Variation of strain aging peak temperature with strain rate at two levels of true strain in T-111 annealed 1 hour at 3000° F (1649° C). Slope of line represents activation energy for strain aging.

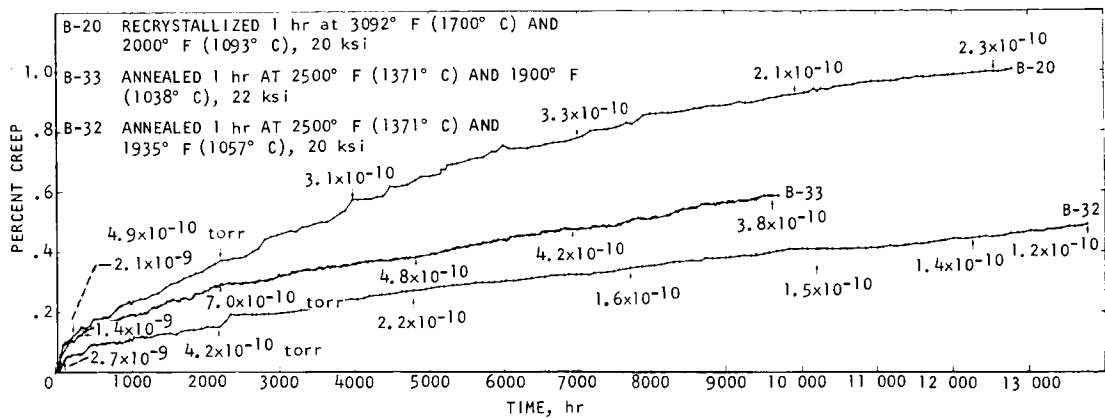


Figure IV-21. - Creep test data for TZC rolled plate (heat M-91) tested in vacuum environment of  $<1 \times 10^{-8}$  torr. Arrows on curves indicate chamber pressure at various intervals during test.

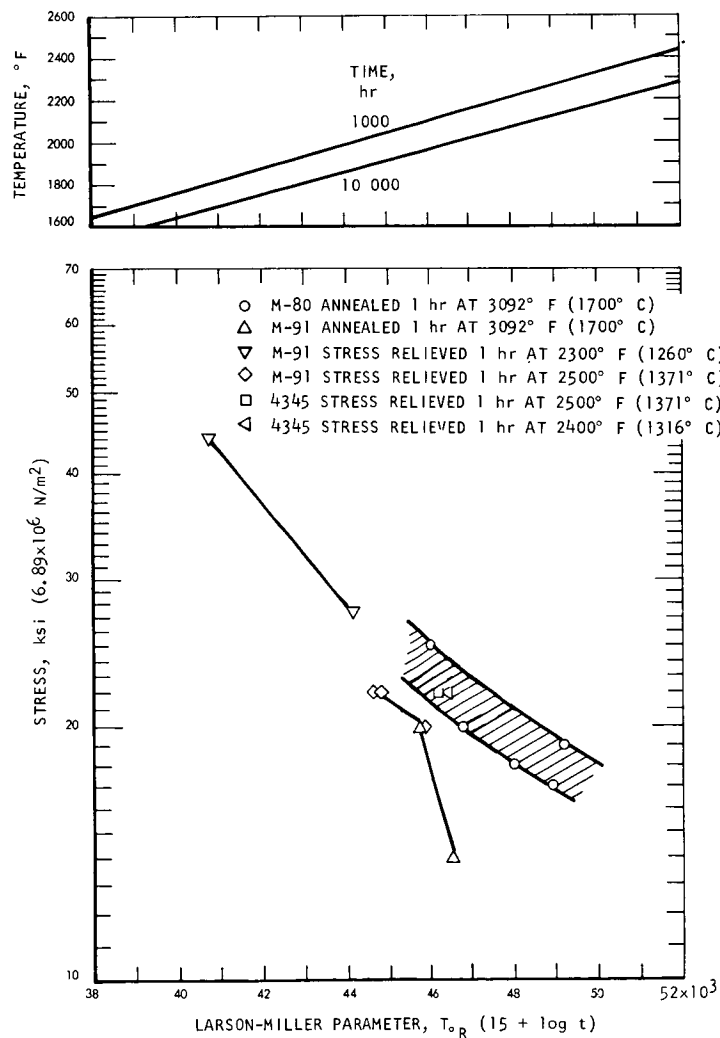


Figure IV-22. - 1/2 Percent creep test results for TZC tested in vacuum environment of  $<1 \times 10^{-8}$  torr.

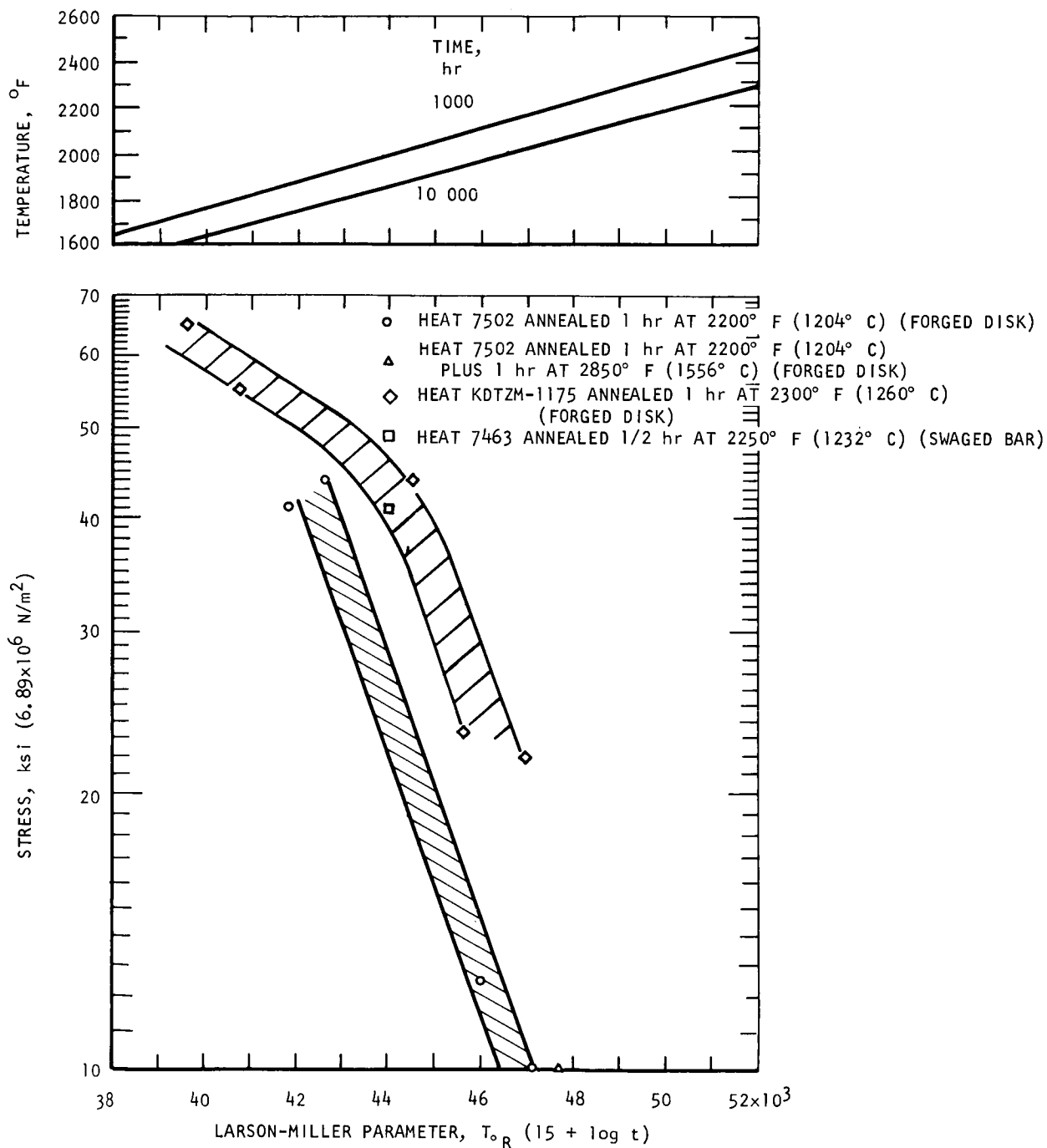


Figure IV-23. - 1/2 Percent creep test results for TZM tested in vacuum environment of  $<1 \times 10^{-8}$  torr.

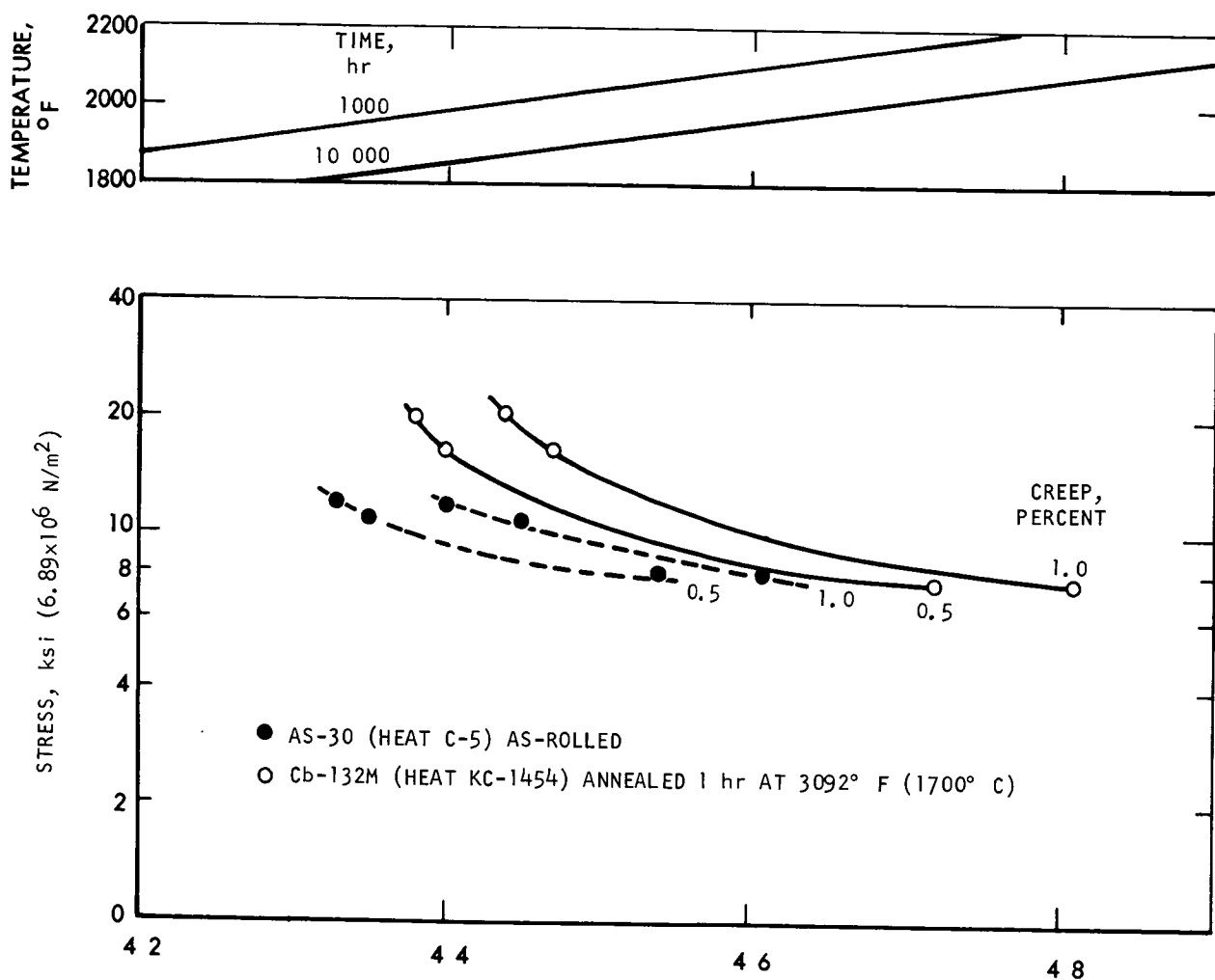


Figure IV-24. - Larson-Miller plot for 0.5 and 1.0 percent creep in AS-30 and Cb-132M plate tested in vacuum environment of  $<1 \times 10^{-8}$  torr.

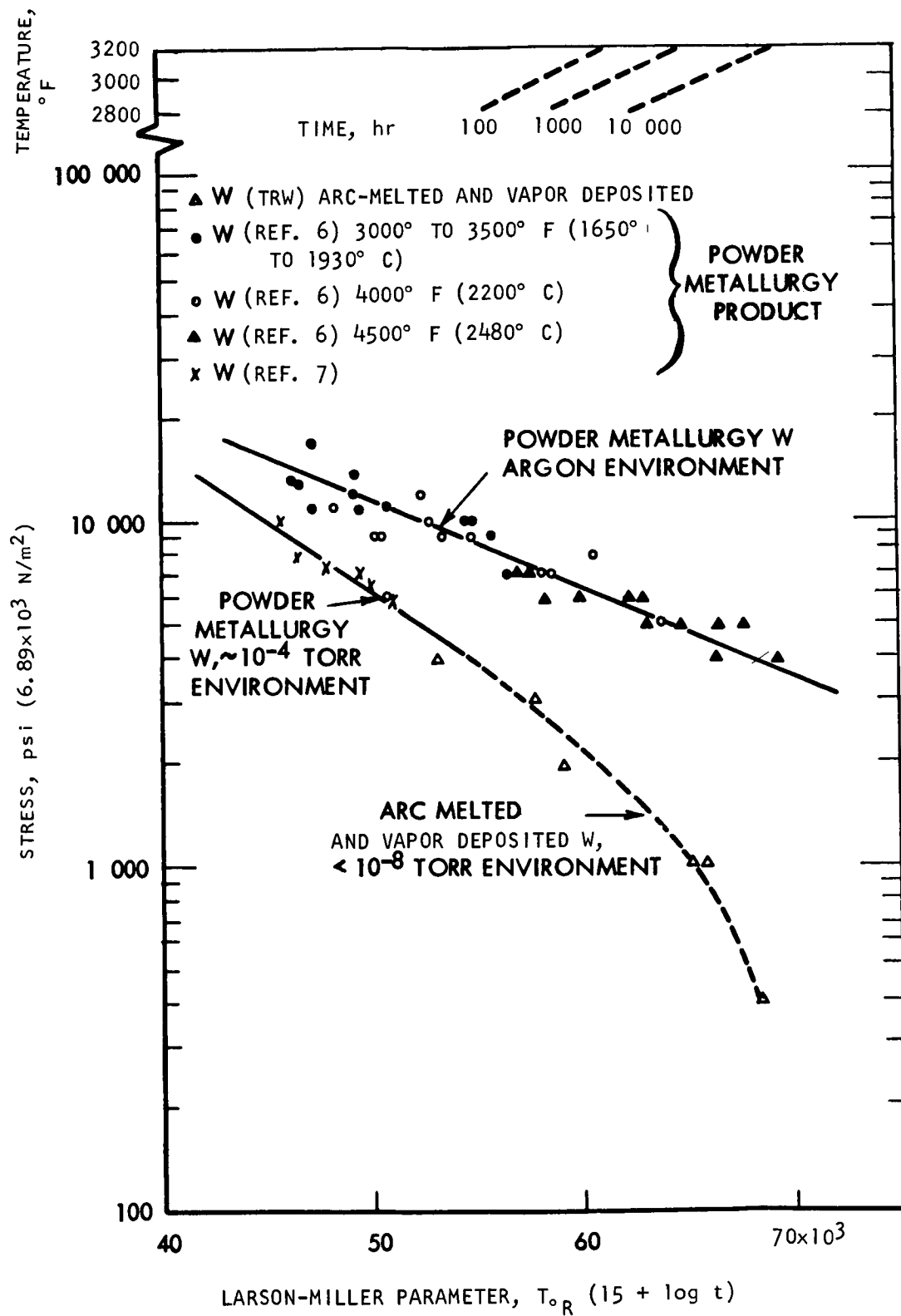


Figure IV-25. - Larson-Miller plot of tungsten 1 percent creep data.



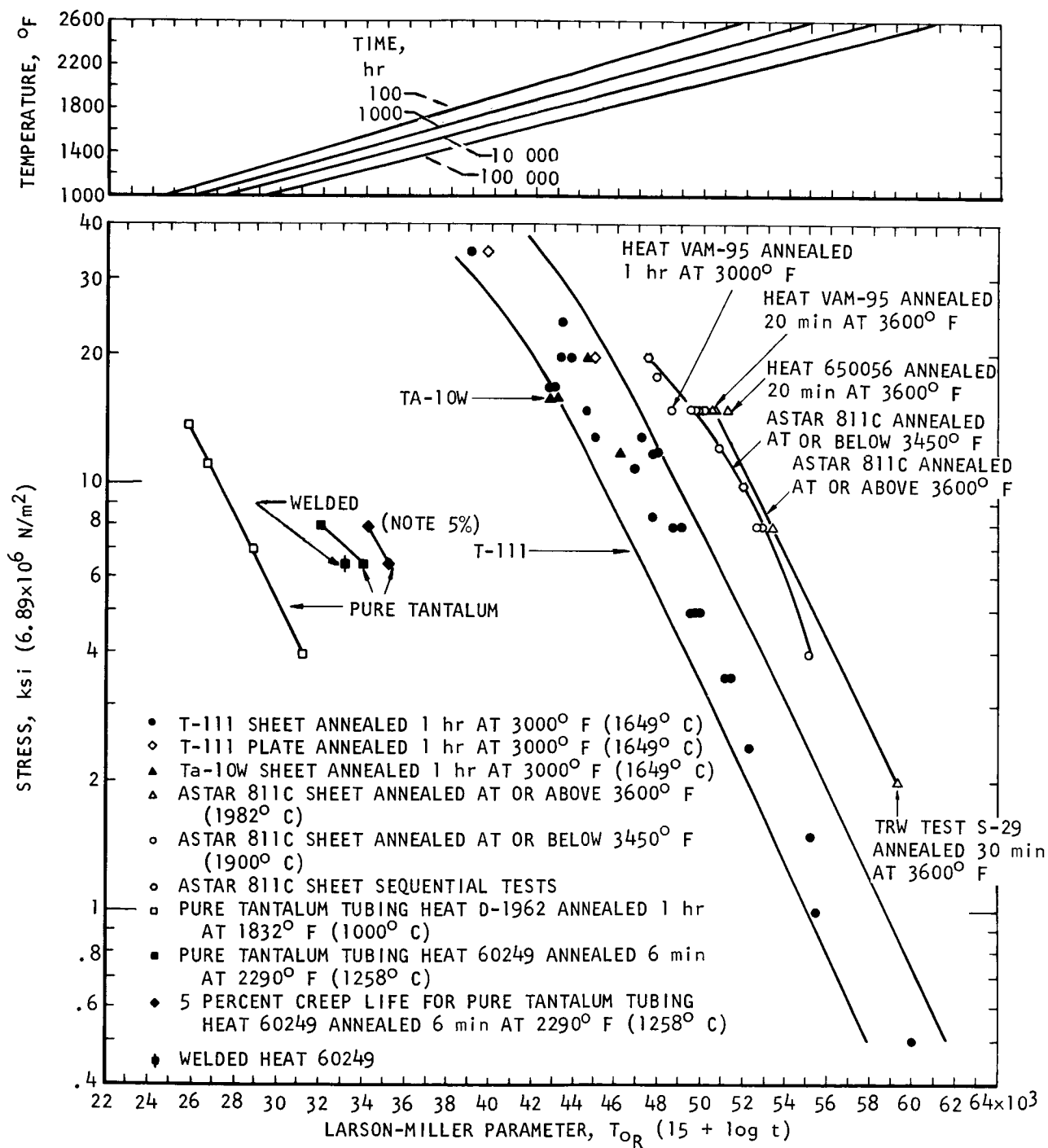


Figure IV-26. - Larson-Miller plot of 1 percent creep life data for tantalum-base alloys creep tested in vacuum of  $<1 \times 10^{-8}$  torr.

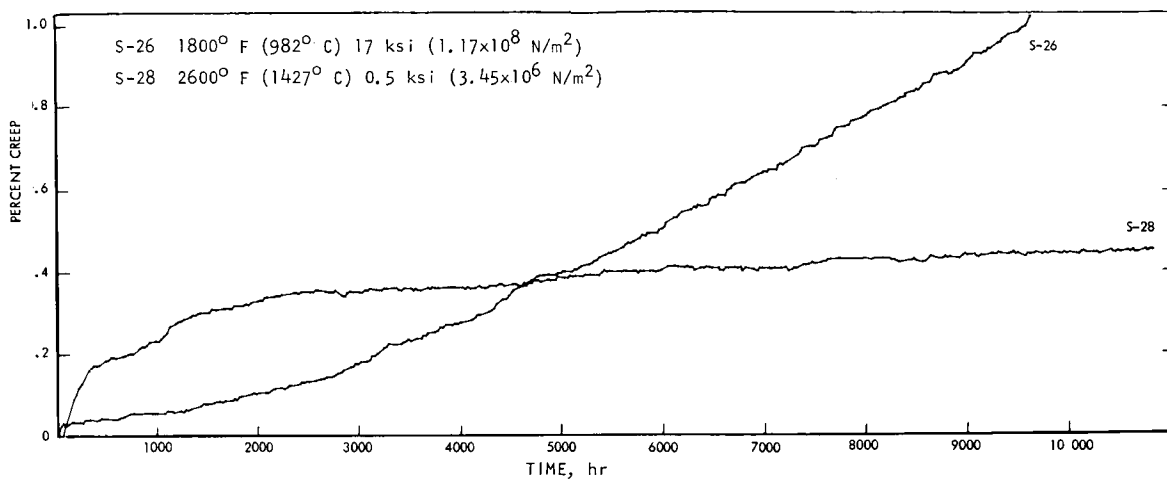


Figure IV-27. - Creep test data for T-111, heat D-1670, annealed 1 hour at 3000° F (1649° C) and tested in vacuum environment of  $<1 \times 10^{-8}$  torr.

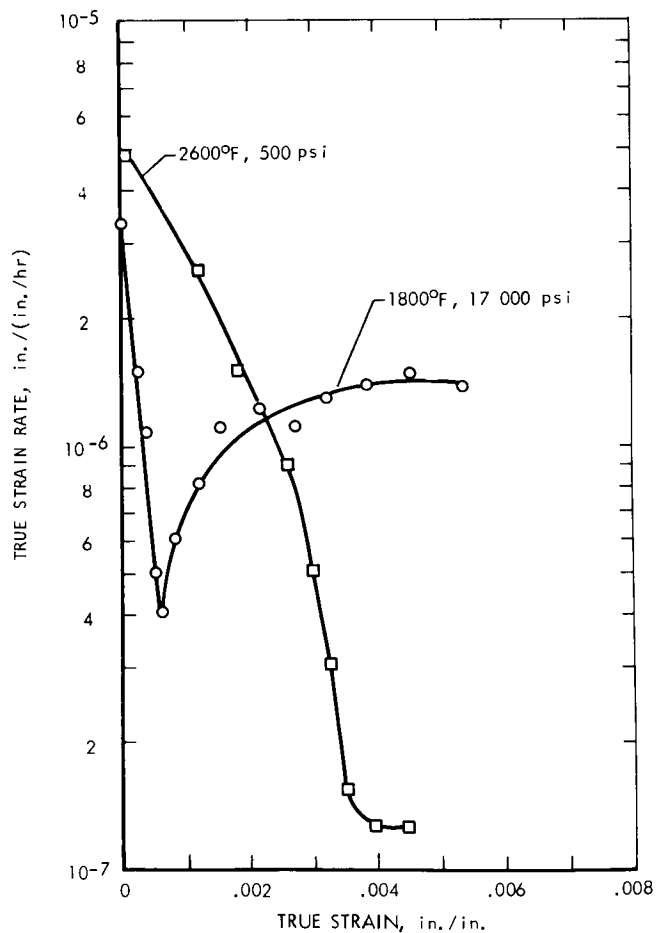


Figure IV-28. - True strain rate as function of true strain in T-111 annealed 1 hour at 3000° F (1649° C) and creep tested at indicated conditions.

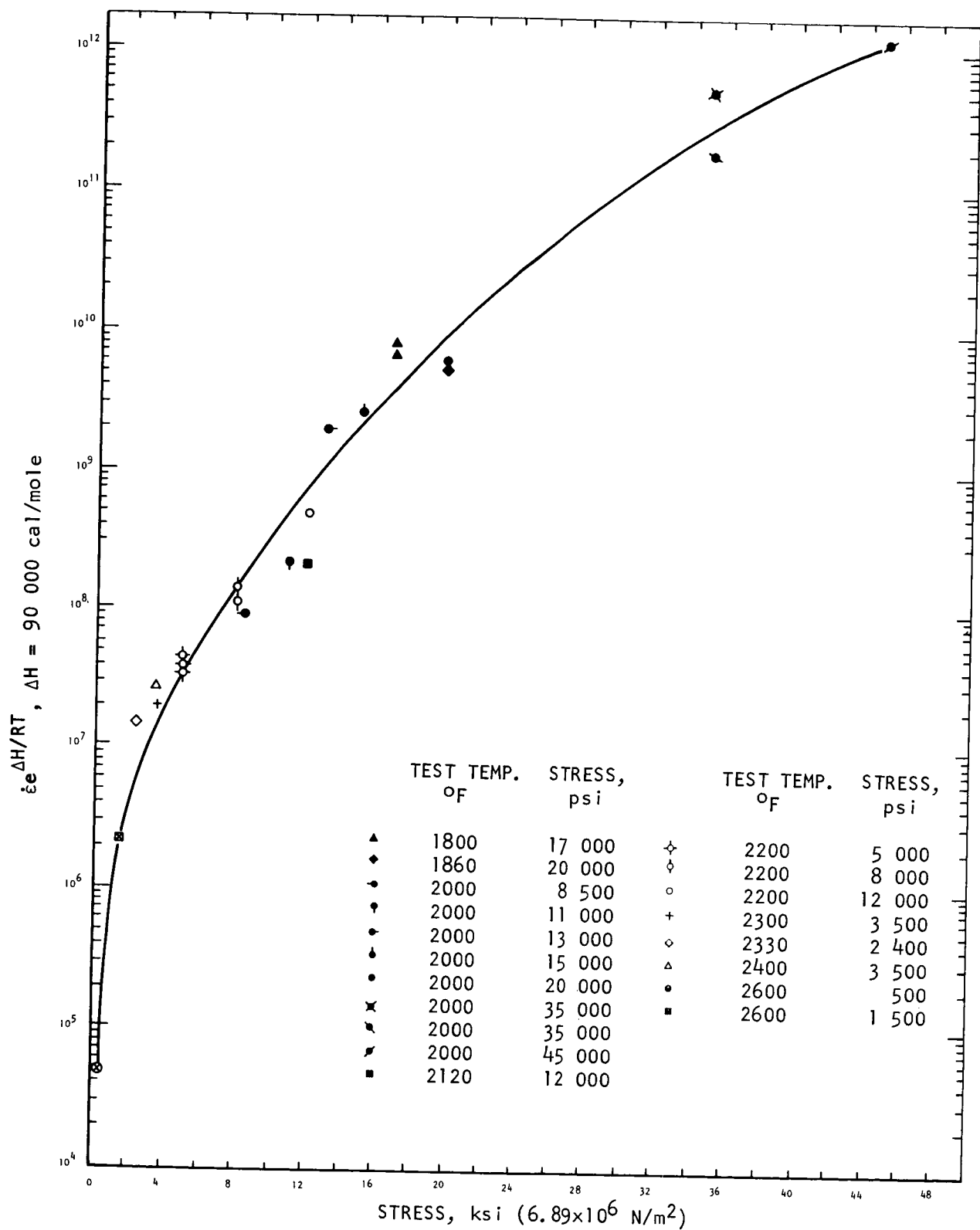


Figure IV-29. - Variation of temperature compensated true strain rate with stress in T-111 alloy annealed 1 hour at 3000° F (1649° C).

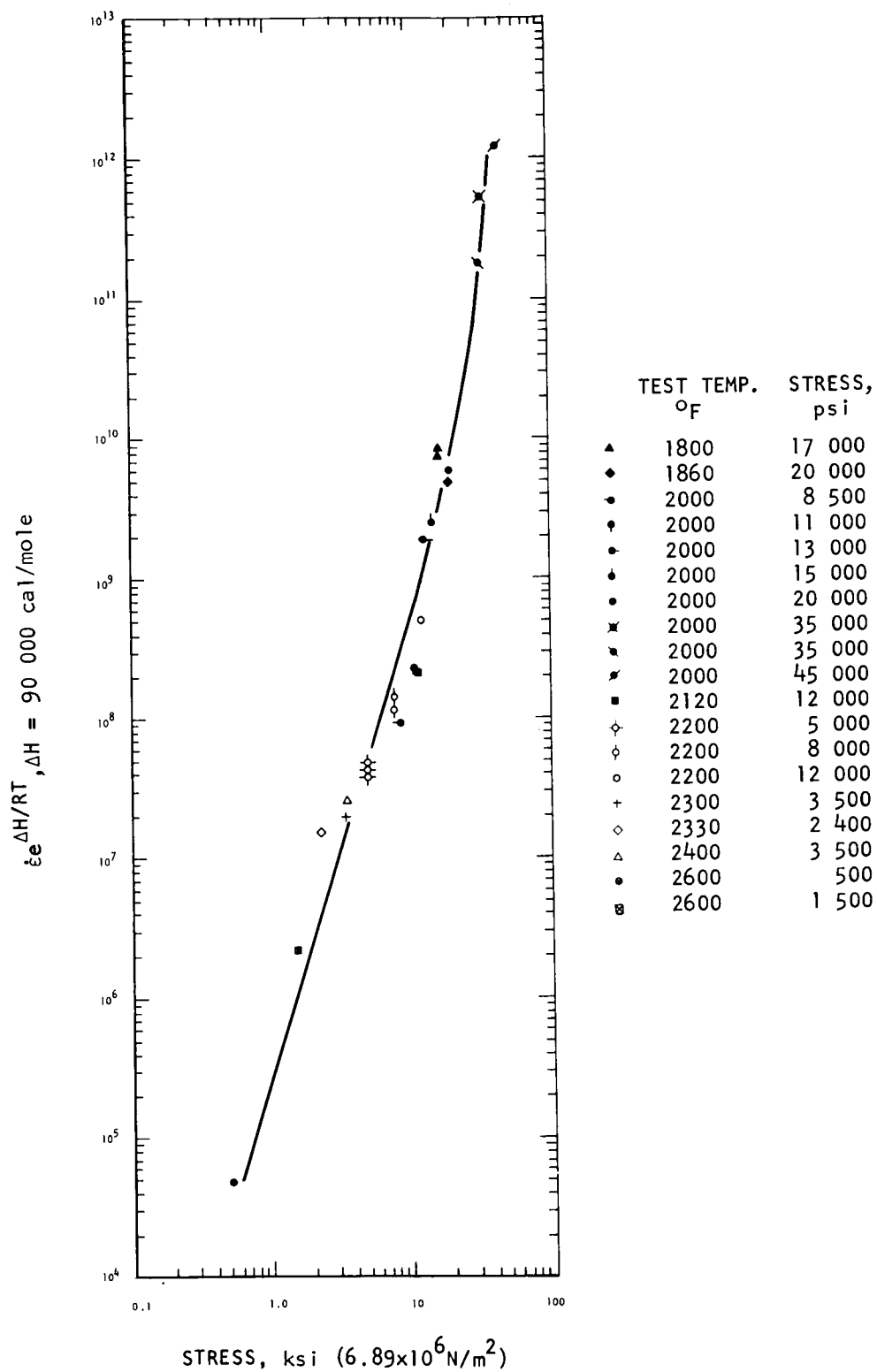


Figure IV-30. - Variation of temperature compensated true strain rate with log stress for T-111 alloy annealed 1 hour at 3000° F (1649° C).

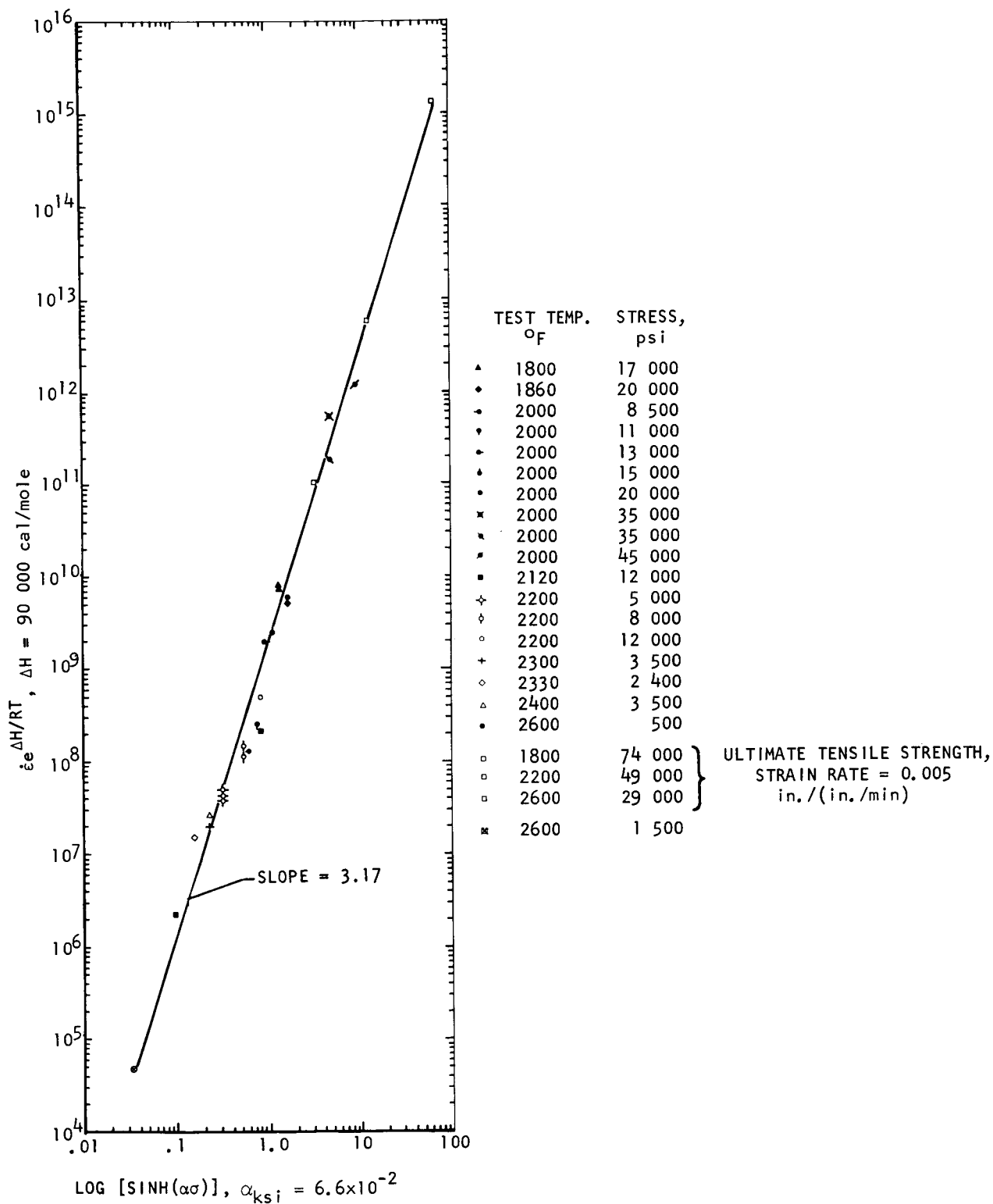


Figure IV-31. - Variation of temperature compensated true strain rate with  $\log [\sinh (\alpha \sigma)]^n$  in T-111 alloy annealed 1 hour at  $3000^{\circ} \text{F}$  ( $1649^{\circ} \text{C}$ ).

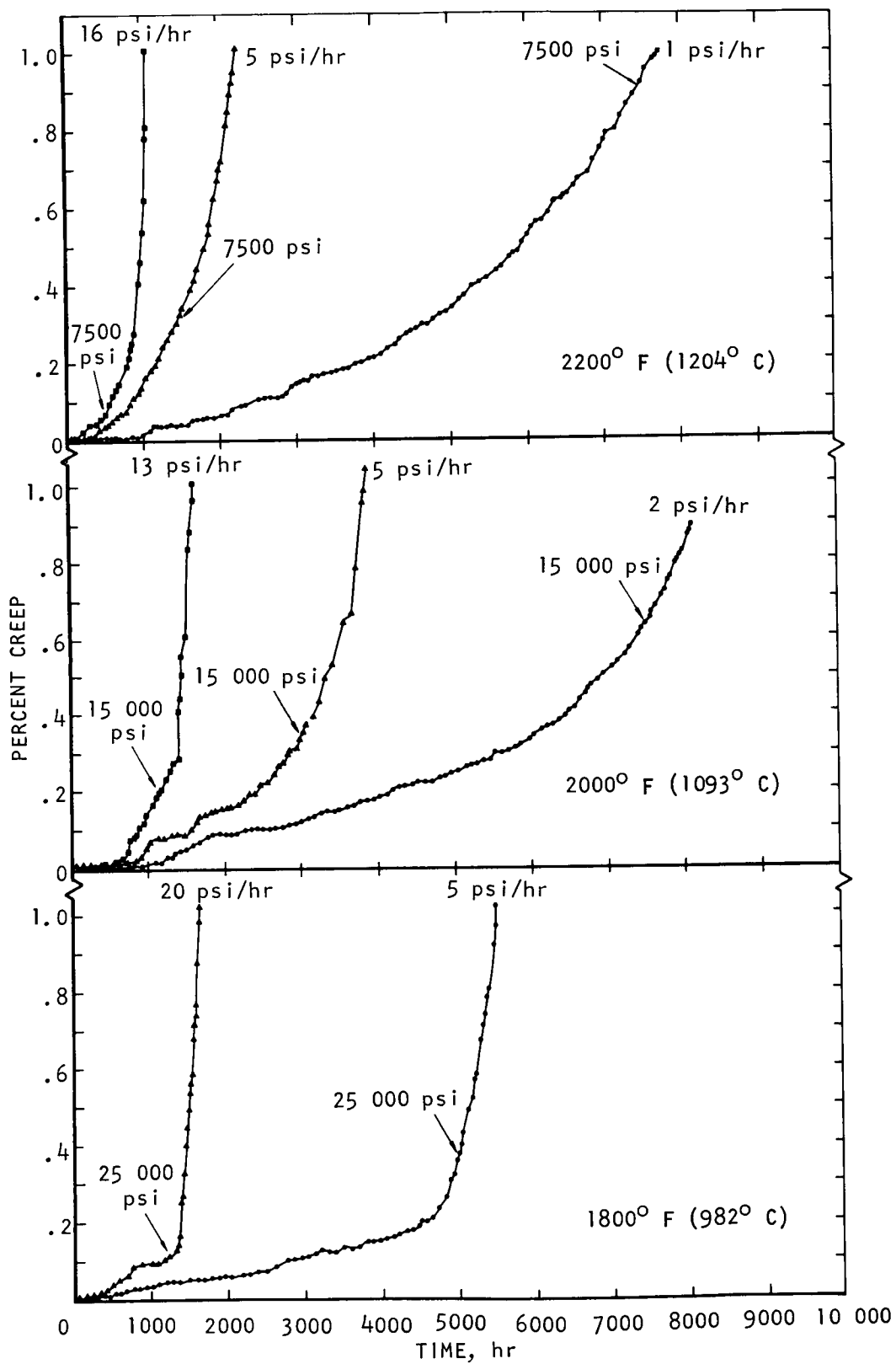


Figure IV-32. - Variable stress creep behavior of recrystallized T-111 alloy.

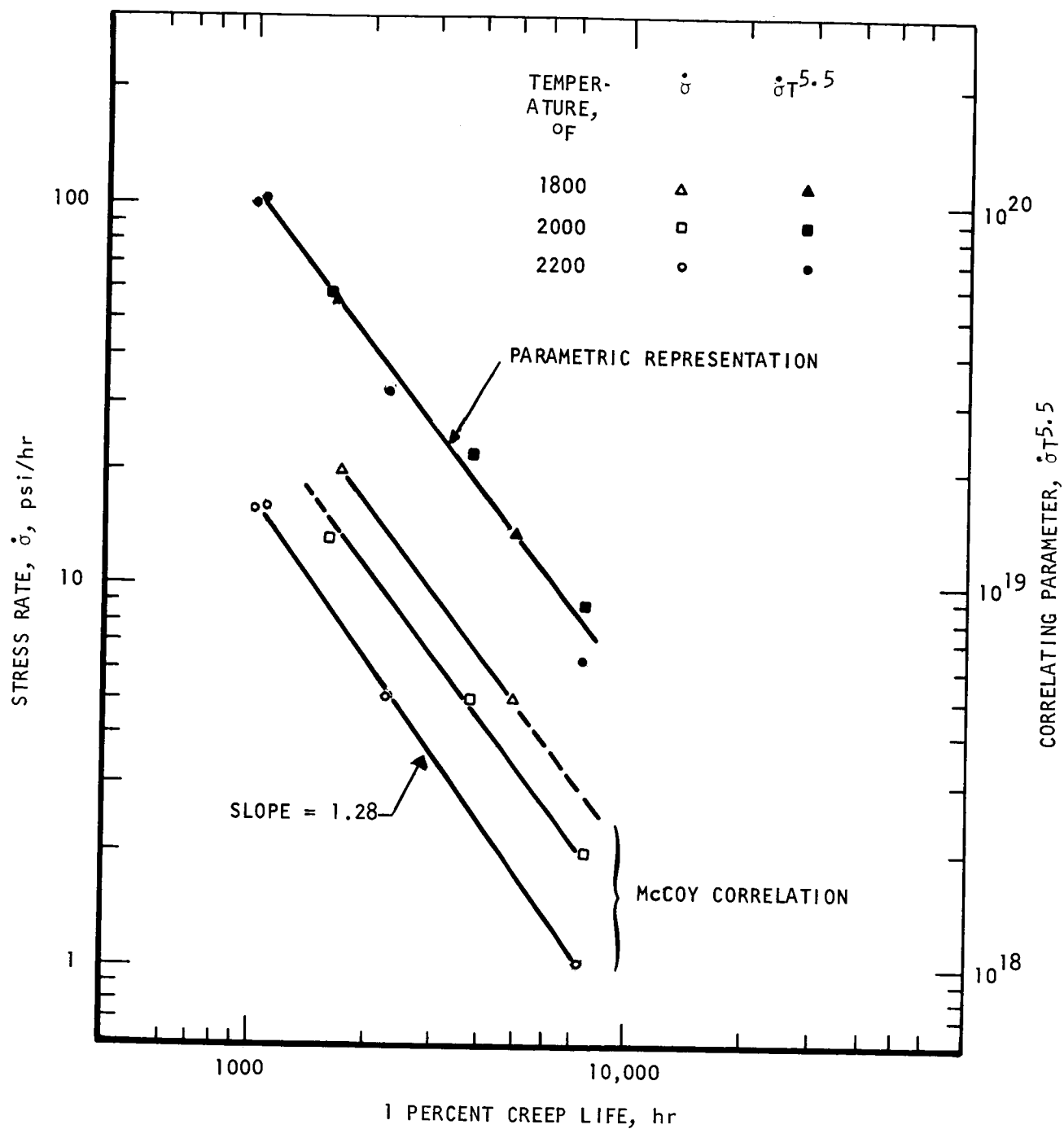


Figure IV-33. - Progressive stress 1 percent creep life data for T-111 alloy.

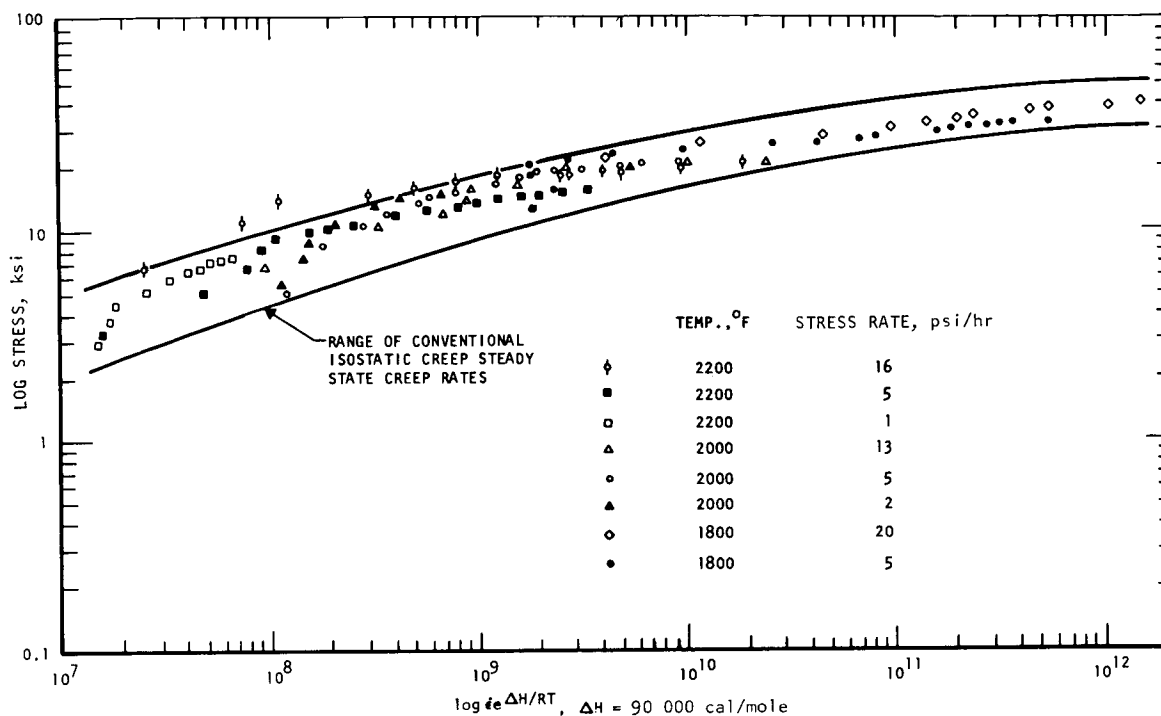


Figure IV-34. - Comparison of isostatic and variable stress creep rates in recrystallized T-111 alloy.

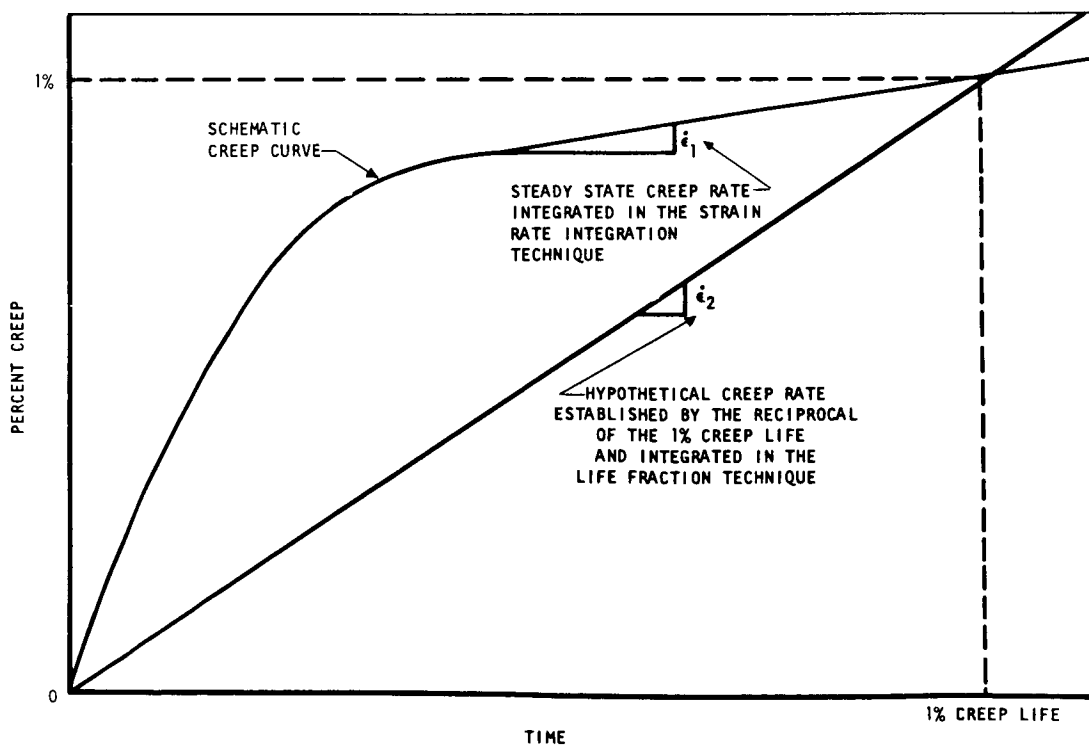


Figure IV-35. - Schematic creep curve showing hypothetical creep rate integrated in life fraction technique.



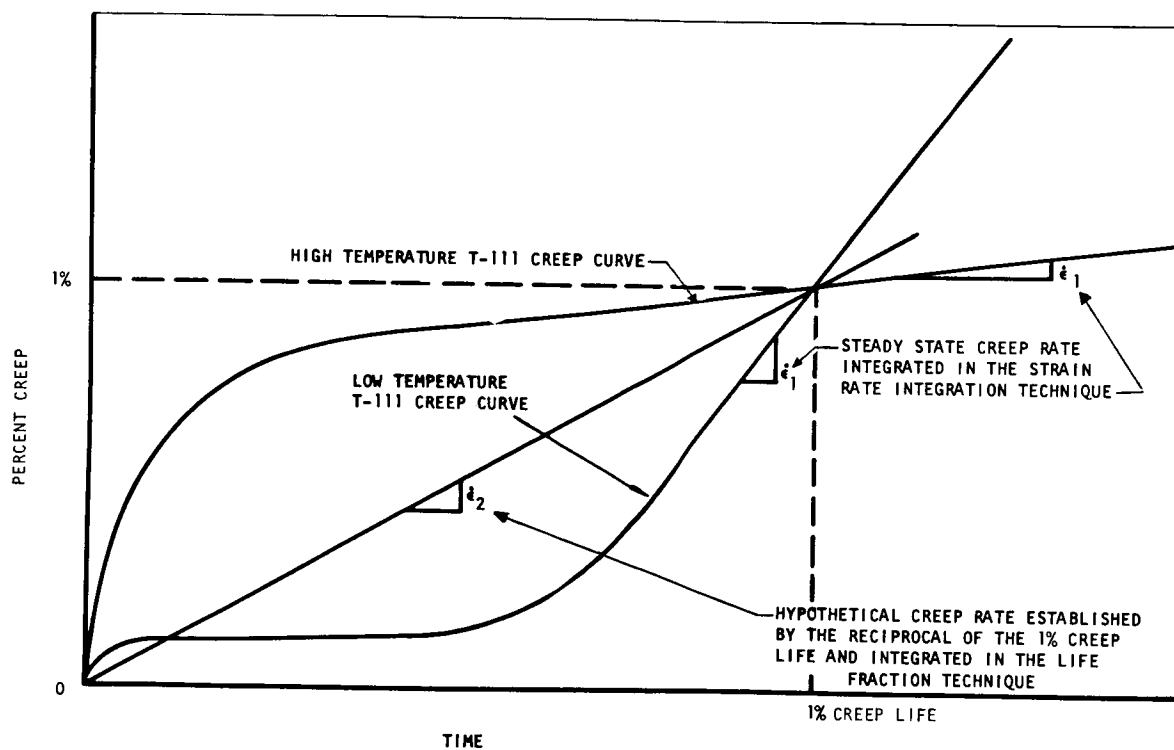


Figure IV-36. - Schematic creep curve for T-111 alloy showing relation between hypothetical strain rate integrated in life fraction technique and experimental isostatic creep rates integrated in strain rate integration technique.

**Page intentionally left blank**

# V. EFFECT OF HEAT TREATMENT ON CREEP PROPERTIES OF THE TANTALUM BASE ALLOY ASTAR-811C\*

D. L. Harrod<sup>†</sup> and R. W. Buckman, Jr.<sup>†</sup>

## INTRODUCTION

ASTAR-811C has the nominal composition Ta-8W-1Re-0.7Hf-0.025C and thus contains both solid solution and dispersed phase strengthening features. The present study was initiated to investigate the response of ASTAR-811C to heat treatment and the associated changes in mechanical properties. The first phase of this study has just been completed, and this paper presents the results. Specimens were heat treated for times of 5 to 60 minutes at temperatures between 3000° and 3800° F, and their creep properties and microstructures were evaluated.

## EXPERIMENTAL PROCEDURES

### Material Preparation

All test specimens came from a single heat of ASTAR-811C, designated Heat NASV-20. Sandwich-type electrodes were double consumable electrode vacuum arc melted to yield an 80-pound, 4-inch-diameter ingot. A 1-inch-high right-circular section of the ingot was upset forged at 2550° F by a single blow on a Dynapak to give a thickness reduction of 59 percent. After annealing 1 hour at 3000° F the forged disk was rolled first at 900° F and then at room temperature to give a combined 89 percent thickness reduction. Following another anneal for 1 hour at 3100° F, the material was cold rolled 33 percent at room temperature to give a finished sheet thickness of 0.035 inch from which test specimens were prepared.

---

\*Based on work done under NASA contract NAS 3-10939.

<sup>†</sup>Westinghouse Astronuclear Laboratory, Pittsburgh, Pennsylvania.

## Heat Treatment

Heat treatments were done in a cold wall vacuum furnace at  $<1 \times 10^{-5}$  torr. Unless otherwise specified, cooling was accomplished by injecting helium gas into the vacuum chamber as the power was turned off. This cooled the specimens to below  $2000^{\circ}$  F in less than 1 minute. Specimens heat treated at  $3600^{\circ}$  F and above were encapsulated in an evacuated tantalum envelope prior to heat treatment to prevent decarburization.

## Creep Tests

Creep specimens were of the pin-loaded type having a 1-inch gage length and 1/4-inch width in the gage section. The specimens were electropolished after heat treatment. Hydrogen bakeout following electropolishing was accomplished during heating for creep testing. Scribe lines were cut at the ends of the gage section to serve as reference marks for the optical strain measurements. The creep tests were run in ultrahigh vacuum ion-pumped systems with the pressure at test temperature being  $<1 \times 10^{-8}$  torr. Heating was by radiation from a split tantalum resistance heated element. Uniaxial stress was applied by dead weight loading.

## RESULTS

### Creep Behavior

Incremental type creep tests were employed in which the stress and temperature were progressively changed, beginning generally at  $2200^{\circ}$  F and 25 ksi and ending after about 300 hours at  $2600^{\circ}$  F and stresses as low as 5 ksi. An example of the type of creep curves obtained is shown in figure V-1.

The specimens all showed between 0.1 and 0.2 percent strain on loading to a stress level of 25 ksi at  $2200^{\circ}$  F. Most of the segments of the creep curves were linear. Where nonlinear segments were observed, the minimum creep rate is reported. The applied stresses were based upon the initial cross-sectional area. Thus, the true stress on the specimen during the later stages of test are higher than the values reported by up to about 5 percent. The reported creep rates have not been corrected for this effect, except for the test mentioned below.

To provide some measure of the effect of the prior creep strain on the creep rate at a given instant in the latter part of the test, a test like that shown in figure

V-1 was run and then the sequence was reversed. The creep rates for the up-cycle and down-cycle were compared after correcting for the true stress effect, and as shown in figure V-2 they are in good agreement.

The effect of annealing temperature on the creep behavior of ASTAR-811C is summarized in the Larson-Miller plot shown in figure V-3. The times to 1 percent strain values were calculated from the creep rate data obtained during the incremental temperature-stress tests. It is apparent that recrystallized ASTAR-811C has significantly better creep properties than the cold worked material. Increasing the final annealing temperature results in still further improvement in creep properties. The change is gradual though, with specimens annealed at 3400° F and below showing considerable data scatter, while there is little if any difference between the specimens annealed at 3600° and 3800° F. The spread in the band for the annealed specimens amounts to a vertical separation of about 5 ksi, or a horizontal separation of about 150° F in test temperature. (A change by one unit in the Larson-Miller parameter in fig. V-3 is equivalent to a change in test temperature of about 50° F.)

In figure V-4 the creep rate is plotted against stress for each test temperature. The circular symbols in this figure are for specimens annealed between 3000° and 3400° F, while the triangles represent specimens annealed at 3600° and 3800° F, the annealing time being 5, 30, and 60 minutes at each temperature. The trend of decreasing creep rate with increasing annealing temperature is again evident.

The solid-line and dashed-line curves in figure V-4 are plots of equations (1) and (2), respectively:

$$\dot{\epsilon} = A e^{B\sigma} e^{-Q/RT} \quad (1)$$

$$\dot{\epsilon} = A \sigma^n e^{-Q/RT} \quad (2)$$

These curves were drawn using values for the constants in equations (1) and (2) determined by treating all of the creep data as a group, that is, irrespective of heat treat condition. The values for these constants determined by a least-squares-computer program are as follows:

| Eq. (1)( $e^{B\sigma}$ ) |                           |                 | Eq. (2)( $\sigma^n$ )           |                     |                 |
|--------------------------|---------------------------|-----------------|---------------------------------|---------------------|-----------------|
| A,<br>%/hr               | B,<br>(ksi) <sup>-1</sup> | Q,<br>kcal/mole | A,<br>(%/hr)/(ksi) <sup>n</sup> | n,<br>dimensionless | Q,<br>kcal/mole |
| 1.6×10 <sup>14</sup>     | 3.73                      | 135.5           | 1.5×10 <sup>8</sup>             | 4.61                | 111.8           |

No particular physical significance is attached to the values obtained for these constants at the moment. However, equation (1), in particular, is useful for estimation purposes.

The effect of heat treatment on creep is shown in figure V-5 in terms of conventional (constant  $T, \sigma$ ) creep curves. The specimen annealed at  $3000^{\circ}\text{F}$  shows a monotonically increasing creep rate, while the sample annealed at  $3600^{\circ}\text{F}$  shows a linear creep rate out to at least 1000 hours. The difference in their creep behavior therefore increases with increasing time or strain. These two creep curves also depict the magnitude of the effect on creep due to the range of heat treatments being investigated. It is noted that the two curves start out about the same and even after 50 hours it is difficult to distinguish between them. This suggests the possibility that the incremental creep tests may minimize the differences in creep behavior due to heat treatment effects because of the short time increments employed at each combination of temperature and stress.

## Microstructure

After moderate to heavy cold working, ASTAR-811C recrystallizes in 1 hour at about  $2400^{\circ}$  to  $2600^{\circ}\text{F}$ . With increasing annealing temperature and time the grain size increases (fig. V-6) and the precipitates present in the cold worked material are gradually taken into solution (figs. V-7 to V-9). The precipitates in ASTAR-811C have been identified as the hexagonal close packed tantalum rich dimetal-carbide,  $(\text{Ta}, \text{W})_2\text{C}$ , regardless of the mechanical-thermal conditions.

The optical microstructure of samples annealed at  $3600^{\circ}\text{F}$  and above appears to be single phase (fig. V-9). There is no doubt that the carbides have been taken completely into solution. However, reprecipitation on a scale unresolvable by optical microscopy occurs during cooling, as shown by the electron transmission micrographs in figure V-10.

The precipitates shown in figure V-11 were extracted from creep specimens after being tested as shown in figure V-5. The initial precipitates (fig. V-10) in the specimen annealed at  $3630^{\circ}\text{F}$  grew into long, thin platelets (fig. V-11(b)) during creep testing. These precipitates are still much smaller than those in the specimen annealed at  $3000^{\circ}\text{F}$  (fig. V-11(a)). Figure V-12 shows a transmission micrograph of the creep specimen which had been annealed at  $3630^{\circ}\text{F}$  prior to testing. The dislocations appear to be pinned by the small precipitates and tangled around the larger ones.

## DISCUSSION AND FUTURE WORK

The two principal microstructural features which change for the range of heat treatments investigated are grain size and precipitate dispersion. Since both of these features can influence creep deformation, it is of interest to consider their relative contribution to the creep resistance of ASTAR-811C. Creep rate (from incremental tests) is plotted as a function of grain size in figure V-13 for several combinations of test temperature and stress. The circular points represent specimens annealed at 3400<sup>0</sup> F (below carbon solvus) and below while the triangular points are for specimens annealed at 3600<sup>0</sup> F (above carbon solvus) and above. There is little difference in the creep rates of specimens annealed at the higher temperatures (above the carbon solvus), even though the grain size varied by a factor of 4 or 5. In view of the observed changes in precipitate structure, it is believed that the trends shown in figure V-13 reflect for the most part the contribution of the precipitate dispersion.

Experimental work now in progress concerns the influence of cooling rate and various thermal-mechanical processing schedules, including welding, on the creep resistance of ASTAR-811C.

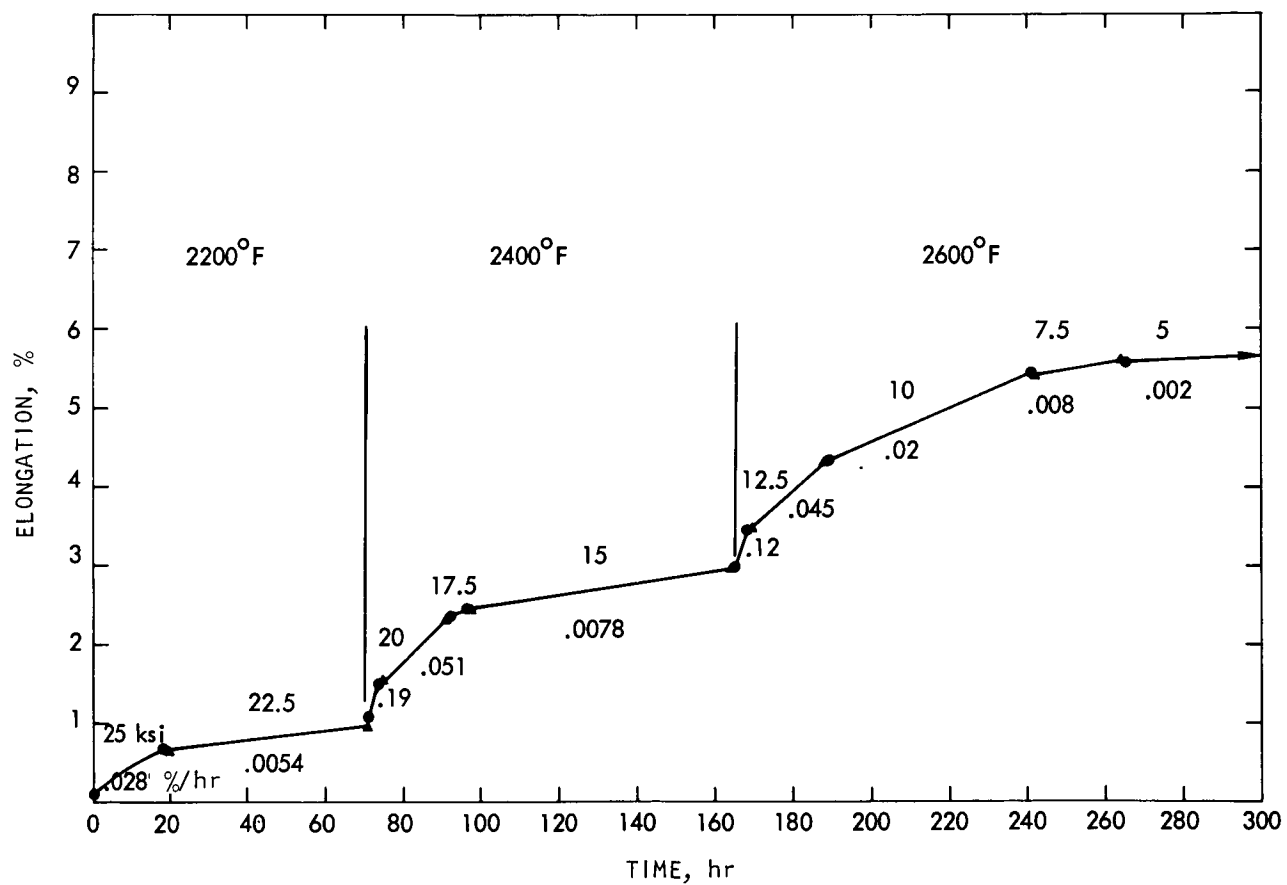


Figure V-1. - Creep behavior of ASTAR-811C during incremental stress and temperature testing. Specimen 1-34-30-H-C; prior treatment, 1/2 hour at 3400° F; grain size, 0.056 millimeter.



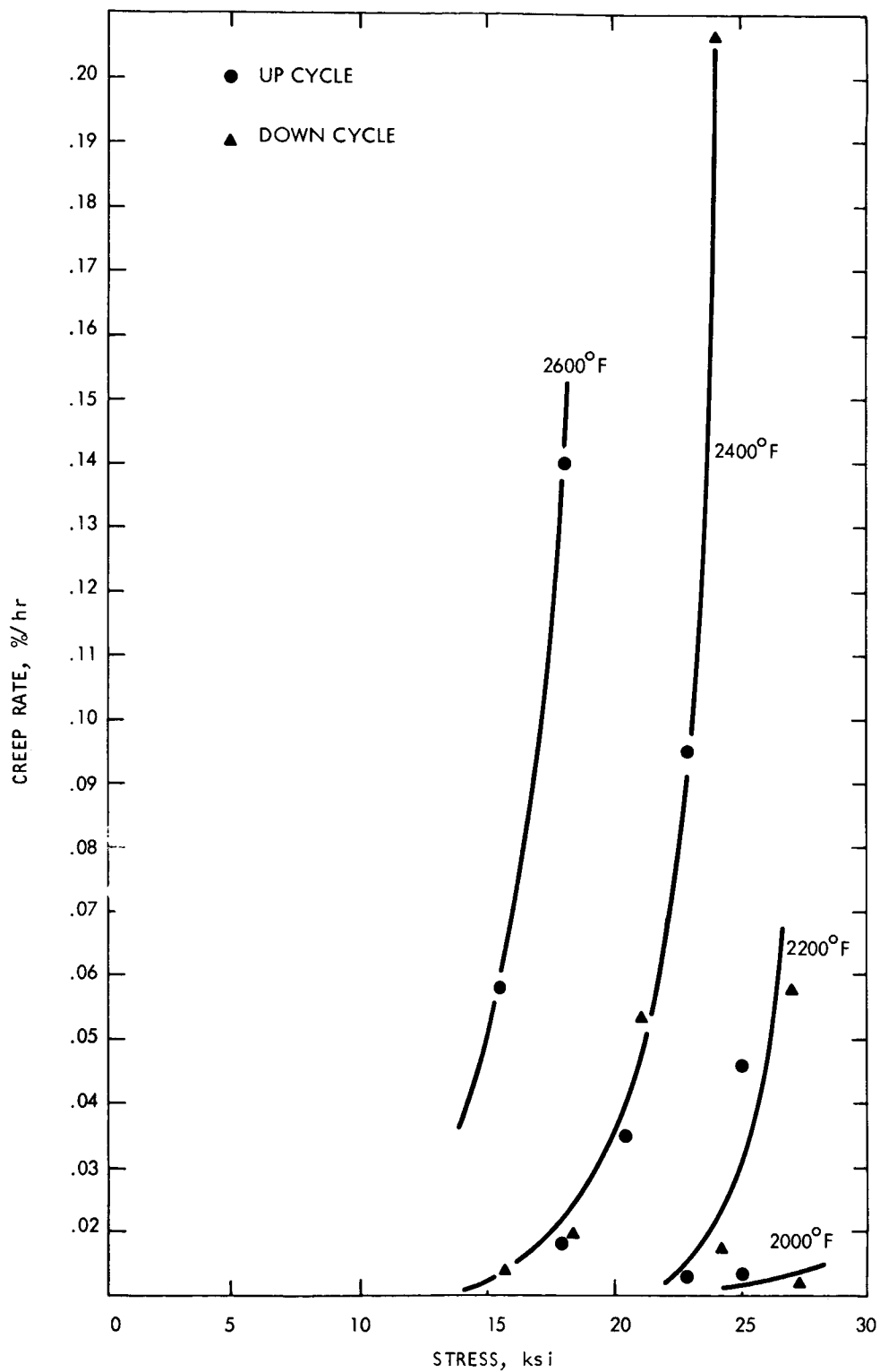


Figure V-2. - Effect of test sequence on creep behavior of ASTAR-811C during incremental stress and temperature testing. Prior treatment, 1/2 hour at 3600° F, cooled 50° F per minute.

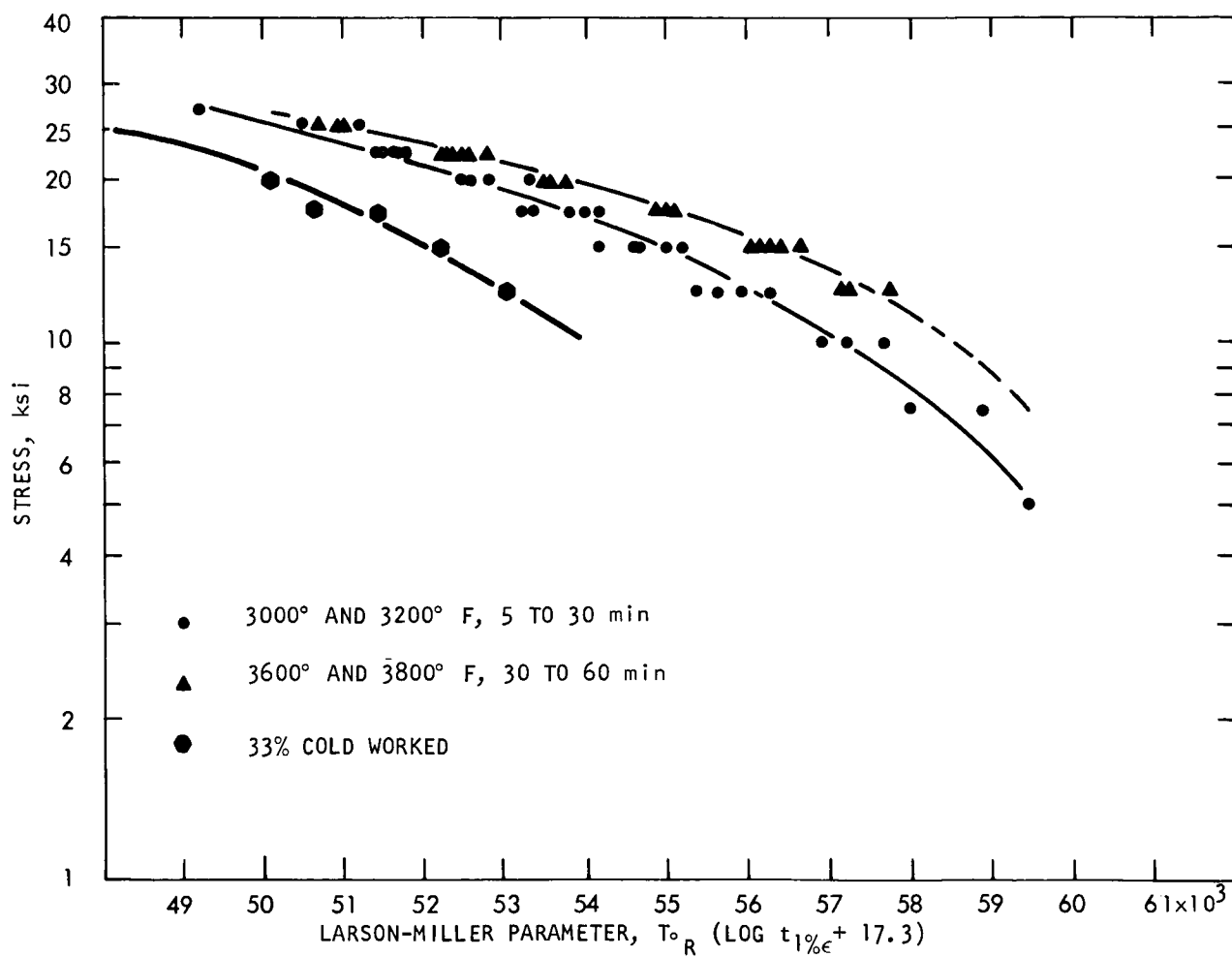


Figure V-3. - Larson-Miller plot of incremental creep test data on ASTAR-811C.

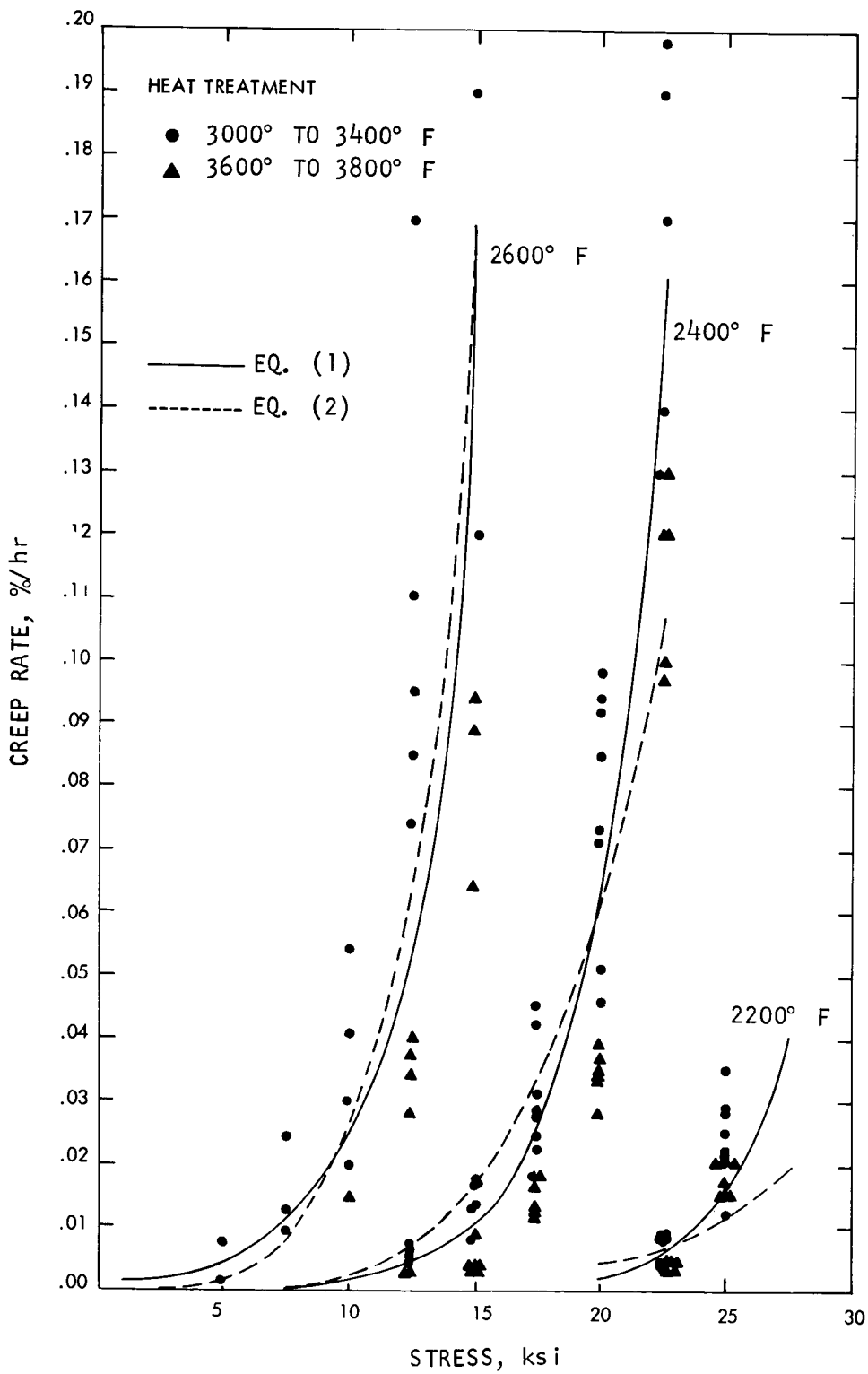


Figure V-4. - Temperature and stress dependence of creep of ASTAR-811C.

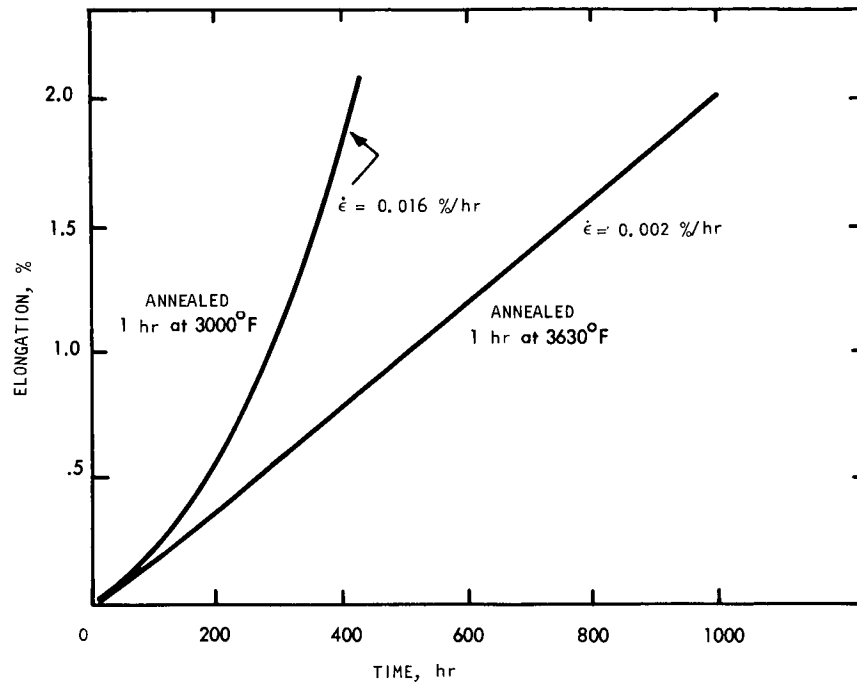


Figure V-5. - Effect of heat treatment on creep of ASTAR-811C in conventional test at constant stress (15 ksi) and constant temperature (2400° F).

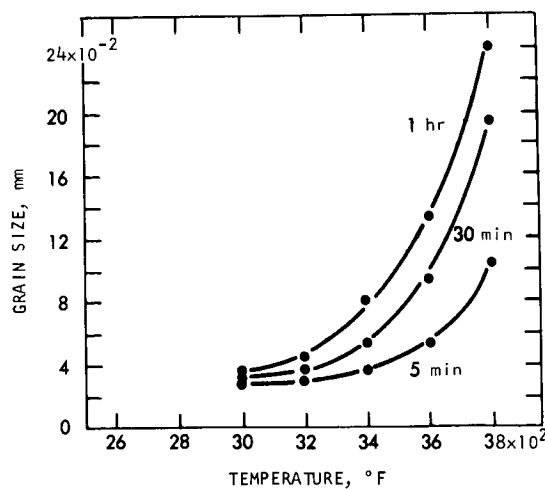


Figure V-6. - Grain size of ASTAR-811C as function of annealing temperature and time. Specimen thickness, 0.035 inch, reduced 33 percent by cold working.

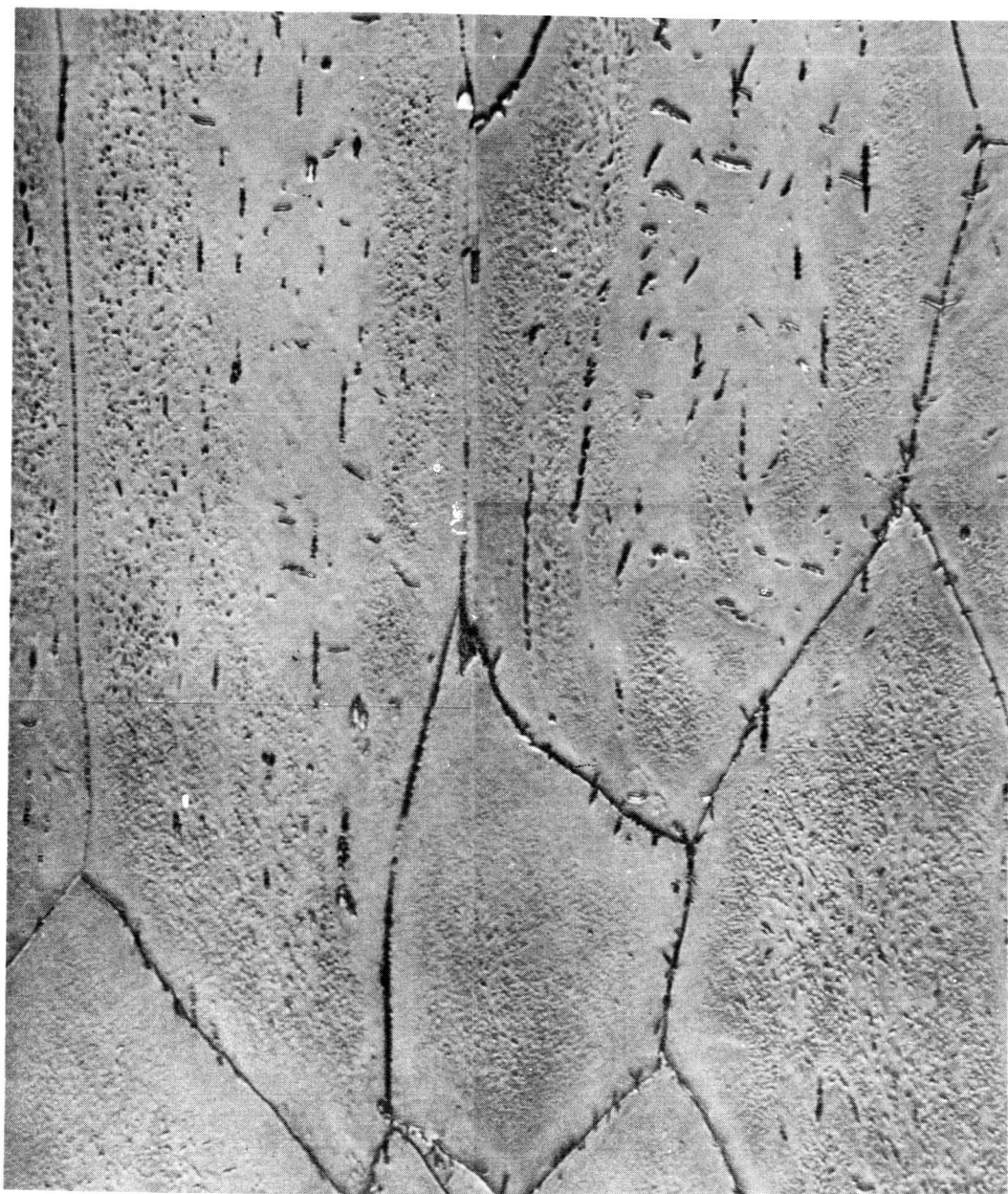


Figure V -7. - Microstructure of ASTAR-811C as-cold-worked 33 percent. Optical micro-graphic montage. X1500.

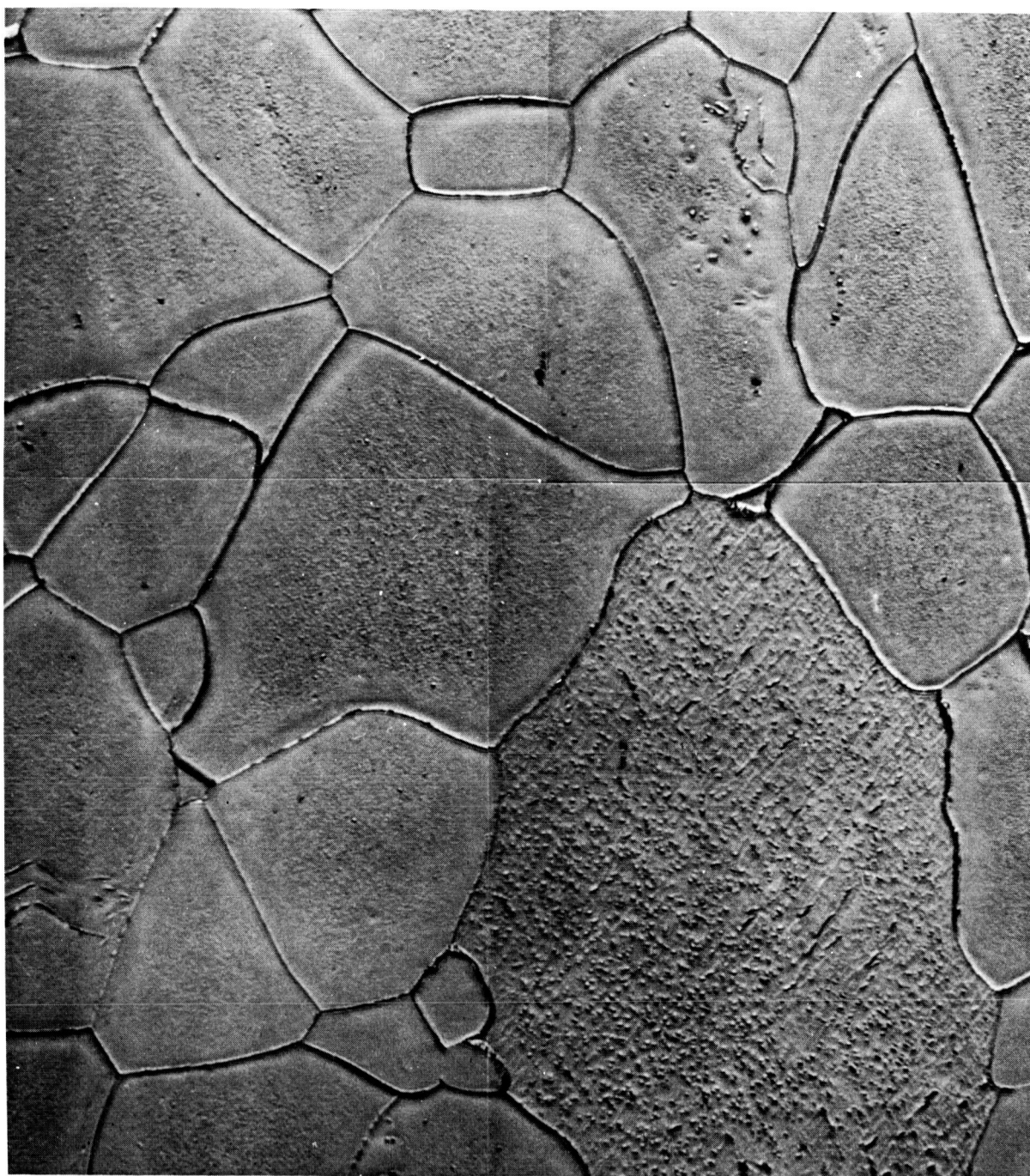


Figure V-8. - Microstructure of ASTAR-811C after annealing cold-worked material (fig. V-7) for 5 minutes at 3000<sup>0</sup> F. Optical micrographic montage, X1500.

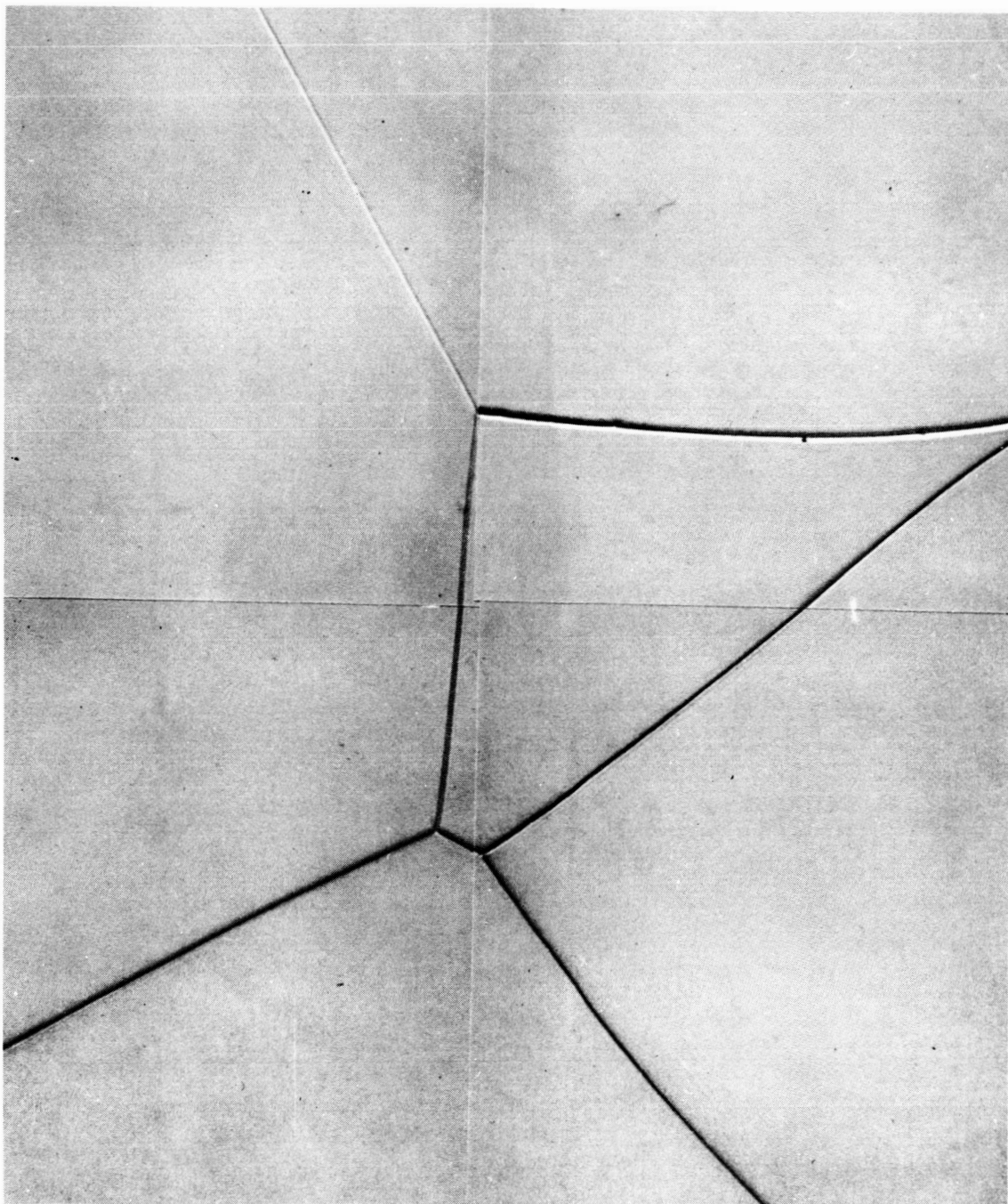
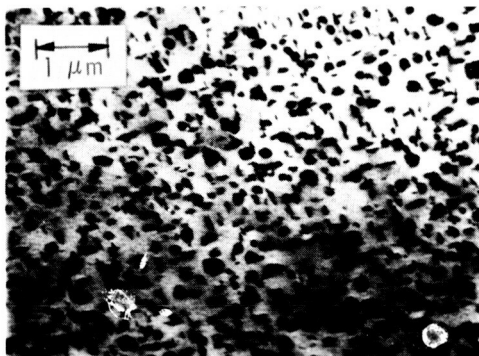


Figure V-9. - Microstructure of ASTAR-811C after annealing cold-worked material (fig. V-7) for 30 minutes at 3600<sup>0</sup> F. Optical micrographic montage, X1500.



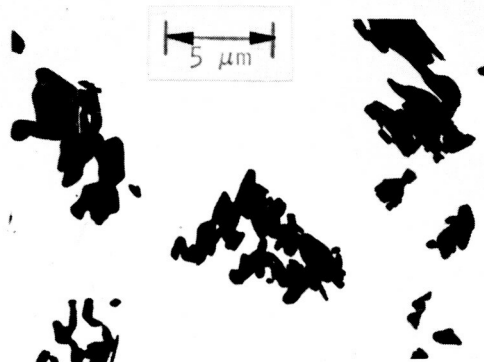


(a) Interior of grain.



(b) Grain boundary.

Figure V-10. - Electron transmission micrographs of ASTAR-811C after annealing for 1 hour at 3630° F.



(a) Annealed 1 hour at 3000° F and creep strained 2 percent in 500 hours.



(b) Annealed 1 hour at 3630° F and creep strained 2 percent in 1000 hours.



(c) Annealed 1 hour at 3630° F and creep strained 2 percent in 1000 hours. X40 000.

Figure V-11. - Electron micrographs of tantalum dimetal carbide ( $Ta_2C$ ) precipitate extracted from creep specimens (fig. V-5) tested at 2400° F and 15 ksi.



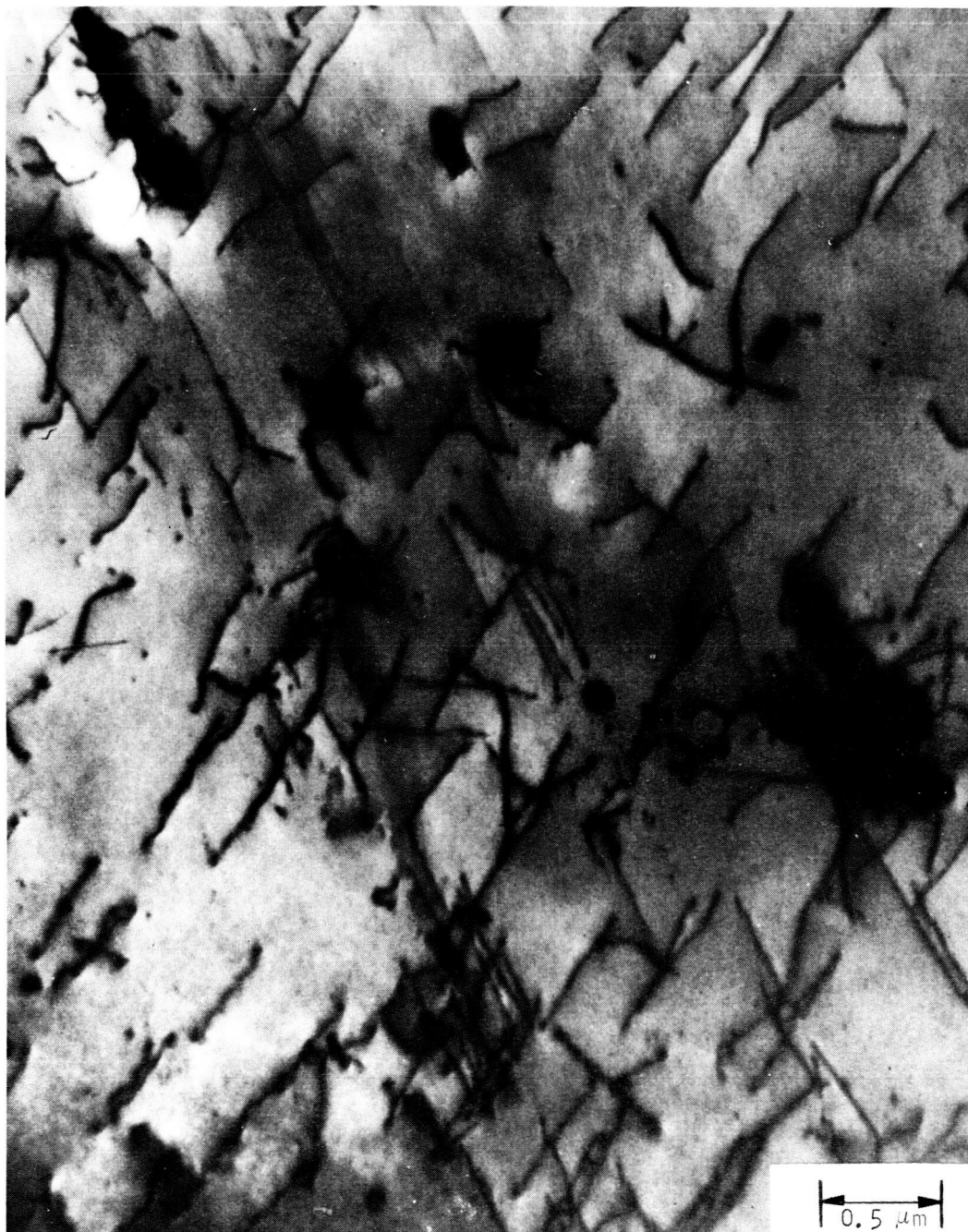


Figure V-12. - Electron transmission micrograph of ASTAR-811C creep specimen after testing at 2400<sup>o</sup> F and 15 ksi to 2 percent strain in 1000 hours. Pretest heat treatment, 1 hour at 3630<sup>o</sup> F. (See fig. V-5 for creep curve and fig. V-11 for pretest microstructure.)

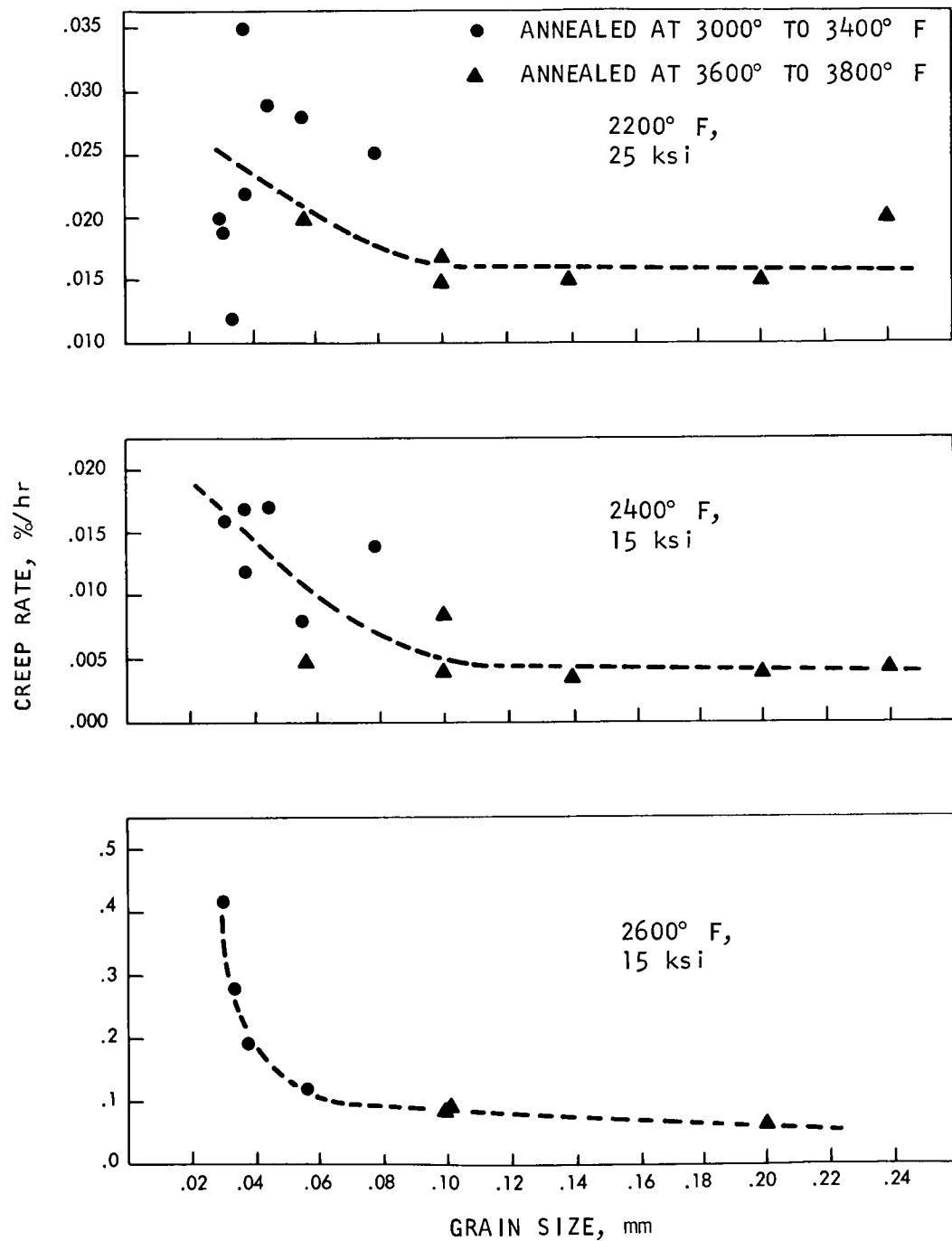


Figure V-13. - Creep rate (incremental tests) of ASTAR-811C as function of grain size for several combinations of test temperature and stress.

## VI. HIGH FREQUENCY FATIGUE PROPERTIES OF TZC AND T-111 ALLOYS\*

E. A. Steigerwald,<sup>†</sup> K. D. Sheffler,<sup>†</sup> and J. C. Sawyer<sup>†</sup>

### SUMMARY

High frequency fatigue tests were conducted in an ultrahigh vacuum environment on recrystallized molybdenum base alloy TZC and tantalum base alloy T-111 at temperatures between 1800° and 2200° F (982° and 1204° C). The results indicated that in this temperature range no well-defined endurance limit existed for either material. At A ratios of 0.45, fatigue strengths at 2000° F (1093° C) and 10<sup>9</sup> cycles were as low as 16 000 psi ( $11.0 \times 10^7$  N/m<sup>2</sup>) for the TZC and 34 000 psi ( $24.8 \times 10^7$  N/m<sup>2</sup>) for the T-111. The application of a cyclic load to a statically-loaded specimen produced a marked acceleration in the degree of specimen extension. In both the TZC and T-111 alloy the increase was characterized by a relatively rapid first stage creep extension (on the order of 1 to 10 percent) compared to the very small extensions (less than 0.01 percent) observed at the same temperatures and peak stresses in the isostatic creep tests. In the TZC alloy the dynamic loading increased the steady state creep rate by approximately two orders of magnitude; however, this acceleration was not observed for the T-111 alloy. Possible reasons for this behavior are discussed in terms of previous observations concerning the isostatic creep behavior of these materials.

### INTRODUCTION

In space power systems, refractory metal alloys are selected as materials for high temperature components because of their compatibility with the environment and their strength and creep resistance. However, in many instances the static creep load is accompanied by high frequency vibratory stresses which may actually represent a limiting design condition. For example, literature data indicate that

---

\*Based on work conducted under NASA contract NAS 3-6010.

<sup>†</sup>TRW Equipment Laboratories, Cleveland, Ohio.

below approximately 900° F (482° C) unalloyed molybdenum has a well-defined endurance limit with a ratio of fatigue strength to ultimate strength of approximately 0.7 (ref. 1). At higher temperatures the fatigue curve exhibits no characteristic endurance limit, and the fatigue strength continuously decreases with an increasing number of test cycles. In addition to representing a specific failure mode, the presence of vibratory stresses superimposed on a static load can also lead to a rapid acceleration of creep extension when metals are tested below a homologous temperature of approximately 0.5 (refs. 2 and 3). A consideration of this type of behavior indicates that a component could fail by extensive creep which is induced by the presence of the cyclic load. Constant load creep data obtained without regard to the influence of cyclic stresses would then provide a nonconservative design stress value.

The purpose of this investigation was to study the high frequency, high temperature fatigue behavior of the molybdenum-base alloy TZC and the tantalum-base alloy T-111. The data obtained from this study will provide an indication of the relative importance of fatigue as a possible failure mode and a measure of the influence which cyclic stressing can have on the creep behavior.

## MATERIALS AND PROCEDURE

The compositions and processing histories for the TZC and T-111 alloys used in the tests are given in tables VI-1 and VI-2. The TZC was recrystallized at 3092° F (1700° C) for 1 hour, and the T-111 at 3000° F (1649° C) for 1 hour in vacuum prior to testing. The conventional smooth tensile properties produced by these heat treatments are given in table VI-2. The microstructure for the recrystallized TZC material is presented in figure VI-1, while the structure of the T-111 is shown in figure VI-2.

The two test specimen geometries shown in figure VI-3 were used for the fatigue studies. In the tests on TZC where the mean stress was essentially zero, the notch geometry was required to allow sufficient stress to be generated to produce fatigue failure. (In all cases a very slight static load was present on the specimens as a result of the weight of the fixture used to hold the capacitive pickup for monitoring resonant conditions.) Both smooth and notched specimens were used on TZC for A ratios of approximately 0.45 to provide a measure of the validity of the method used to calculate peak stress in the notch specimens. (A ratio is defined as the dynamic stress single (mean to peak) amplitude divided by the mean stress.)

The tests were conducted in vacuum chambers equipped with ion pumps and tantalum resistance heated furnaces (see fig. VI-4, ref. 3). A resonant drive

train was used to produce the dynamic load with nodes at both the top port seal and the lower attachment point for the static load. The majority of tests were performed with a vibration train driven at approximately 20 kilohertz (kcps) by an externally mounted PZT piezoelectric transducer. Mechanical amplification was attained by suitable stepped-horn type velocity transformers (ref. 4), which provided a maximum displacement of approximately 0.001 inch at the 2000° F test temperature. Selected tests were also conducted at 10 and 15 kilohertz. In these cases appropriate changes were made in the specimen and load train geometry to produce resonance.

The test method involved mechanically mounting the specimen to the drive train, adjusting the capacitive vibration pickup, making preliminary checks to ensure that the system was in resonance, and pumping the unit to a vacuum better than  $1 \times 10^{-7}$  torr at room temperature. Testing was performed at this vacuum except during heating, when it was controlled so that the pressure never exceeded  $1 \times 10^{-6}$  torr.

A W-3%Re/W-25%Re thermocouple placed approximately 1/8 inch from the surface at the specimen midpoint was used for temperature measurement. Because of breakage produced by the vibration, the thermocouple could not be attached directly to the specimen. The temperature was stabilized for approximately 2 hours prior to the initiation of testing.

The application of the high frequency cyclic load produced heating of the fatigue specimen. As a result of a series of preliminary tests, the increment of temperature increase was determined as a function of drive level by optical pyrometer readings. It was then possible to adjust the initial furnace temperature setting to produce the desired temperature level in the specimen at the nodal point when the drive was applied.

The dynamic stress produced by the ultrasonic vibration was determined from displacement measurements made directly on the specimen with a cathetometer. In the smooth specimens two reference points were selected approximately equidistant from the specimen midpoint, and the displacements at these points were determined by averaging 10 readings which showed a variation of approximately 50 microinches. These reference points were slight perturbations in the 15 rms microinch finish on the specimens which were well defined by the specimen was assumed to follow the sinusoidal relation

$$\delta_x = \delta_o \sin \frac{2\pi x}{\lambda} \quad (1)$$

where  $2\delta_x$  is the total measured displacement at a distance  $x$  from the node at

the specimen midpoint,  $\delta_o$  is the maximum amplitude at an antinode, and  $\lambda$  is the resonant wavelength.

The maximum strain  $\epsilon_{\max}$  at the midpoint of the dumbbell type specimen was then determined from the equation

$$\epsilon_{\max} = \frac{2\pi\delta_o}{\lambda} \quad (2)$$

and the dynamic stress  $\sigma$  was obtained from the product of the strain and the elastic modulus at the particular test temperature

$$\sigma_{\max} = \epsilon_{\max} E \quad (3)$$

When the notch specimen was employed, the maximum stress  $\sigma$  was calculated on the basis of the following equation:

$$\sigma = K_T \left( \frac{D}{d} \right)^2 \left( \frac{2\pi}{\lambda} \right) \delta_o E \quad (4)$$

where  $K_T$  is the elastic stress concentration factor (equal to 1.87),  $D/d$  is the ratio of major to minor diameter in the notch specimen (equal to 1.20), and  $\delta_o$ ,  $E$ , and  $\lambda$  are defined in equation (1).

In the notch test  $\delta_o$  was determined from measurements of displacement ( $\delta_x$ ) taken on the major diameter and calculated from equations (1) and (4). The validity of using equation (4) to calculate the effective dynamic stress in notch specimens was determined by conducting both smooth and notch fatigue tests on TZC at an  $A$  ratio of 0.45. The results indicated that comparable fatigue curves were generated by both specimen configurations.

Although cracking of the test specimen was accompanied by a significant decrease in the resonant frequency, the tests were continued until the resonant frequency decreased 150 hertz (cps). This condition usually resulted in propagating the fatigue cracks through approximately one-half of the specimen cross section (see fig. VI-5). The time required for this crack propagation was generally short enough so that the fatigue lives reported can be considered as essentially the time required to initiate a fatigue crack.

In the tests on smooth specimens at the  $A$  ratios between 0.15 and 0.45, the influence of the cyclic stress on creep properties was evaluated by measuring the specimen extension over the distance between specimen shoulders. This procedure was necessary since gage marks could not be placed on the specimens without significantly altering the fatigue behavior.

## RESULTS AND DISCUSSION

### Molybdenum-Base Alloy TZC

The fatigue curves for tests conducted on TZC at 1800<sup>0</sup>, 2000<sup>0</sup>, and 2200<sup>0</sup> F (982<sup>0</sup>, 1093<sup>0</sup>, and 1204<sup>0</sup> C) with both the notch and smooth specimens are presented in figure VI-6. No variation in properties was observed as a function of heat of material, and the data for both heats are combined in the figures. A well-defined endurance limit was not present at any of the test temperatures. At 2200<sup>0</sup> F (1204<sup>0</sup> C) and an  $A$  ratio of approximately zero, a fatigue strength as low as 16 000 psi ( $11.0 \times 10^7$  N/m<sup>2</sup>) was observed at  $10^9$  cycles. The fatigue strength-tensile strength ratios are shown in table VI-3 for each of the test temperatures. The ratios are considerably lower than the 0.5 to 0.4 usually observed in materials which possess a well-defined endurance limit, such as steels, or the 0.7 value obtained for molybdenum when tested below 875<sup>0</sup> F (468<sup>0</sup> C), where dislocation locking can occur (ref. 1).

The fatigue results are plotted in the form of a modified Goodman diagram in figure VI-7. At the lower  $A$  ratios, the 2000<sup>0</sup> and 2200<sup>0</sup> F (1093<sup>0</sup> and 1204<sup>0</sup> C) test temperatures showed comparable fatigue behavior while the strength at 1800<sup>0</sup> F (982<sup>0</sup> C) was significantly greater.

In addition to actually causing total fatigue failure, the superposition of a dynamic load on a static load can produce a significant acceleration in creep. Typical creep curves obtained for TZC under cyclic load conditions at 1800<sup>0</sup>, 2000<sup>0</sup>, and 2200<sup>0</sup> F (982<sup>0</sup>, 1093<sup>0</sup>, and 1204<sup>0</sup> C) are shown in figures VI-8, VI-9, and VI-10. For comparative purposes, a creep curve obtained by testing under static load in a high vacuum environment is also presented in figure VI-9. The superposition of a dynamic stress on the static stress caused a very marked increase in total extension. Under the static-dynamic loading, the specimen exhibited a large initial extension within the first 30 minutes of testing, followed by a period where an approximately constant creep rate occurred. To further analyze the factors which control both the initial extension and the constant creep rate, the parameters  $\epsilon_1$  and  $\epsilon_2/t$  were defined as shown schematically in figure VI-11 and were plotted logarithmically as a function of peak stress in figures VI-12 and VI-13. The initial specimen extension ( $\epsilon_1$ ) which occurred early in the test sequence was essentially independent of the temperature in the 1800<sup>0</sup> to 2200<sup>0</sup> F (982<sup>0</sup> to 1204<sup>0</sup> C) range and  $A$  ratios in the 0.10 and 0.45 range. In cases where the dynamic drive on the specimen was removed for a period of time, and then reinitiated, the values of  $\epsilon_1$  were greatly reduced. The influence of peak stress on the steady state creep rate ( $\epsilon_2/t$ ) shown in figure VI-13 indicated that the creep rate under combined static-dynamic loading

conditions increased with increasing test temperature. By way of comparison, the creep rates obtained under static conditions at essentially the same peak stress values (i. e.,  $A = 0$ ) were almost two orders of magnitude less than those present in the tests where combined static-dynamic loading was used. Conversely, at the high  $A$  ratios ( $A \approx \infty$ ), no creep was observed so that the creep rate as a function of  $A$  ratio reached a maximum value at about  $A = 0.45$  (see fig. VI-14). The results indicate that relatively low values of vibratory stress superimposed on a static load can produce a significant increase in the steady state creep of TZC in the 2000° F (1093° C) temperature range.

The variation of fatigue strength as a function of frequency of load application is shown in figure VI-15. Decreasing the loading rate at 2000° F (1093° C) from 20 to 15 kilohertz resulted in a marked increase in fatigue life, while a further decrease to 10 kilohertz did not produce any additional variation. The decreasing test frequency also produced a retardation in the creep rate at an  $A$  ratio of 0.45. The variation in steady state creep rate at 2000° F (1093° C) could be expressed over the 10 to 20 kilohertz range as

$$\dot{\epsilon}_2 = Ae^{Bf}$$

where  $\dot{\epsilon}_2$  is the steady state creep rate  $\epsilon_2/t$  (in %/hr),  $f$  is the test frequency (in kHz), and  $A$  and  $B$  are constants equal to  $5.42 \times 10^{-3}$  and 0.281, respectively.

### Tantalum-Base Alloy T-111

The fatigue strength of T-111 as a function of cycles to failure is shown in figure VI-16 along with the comparative data for TZC. At 2000° F (1093° C) and 20 kilohertz the fatigue strength of T-111 was considerably greater than that obtained on the TZC alloy, despite the fact that the two materials had comparable tensile strengths.

The influence of ultrasonic vibration on the creep behavior of T-111 is illustrated in figure VI-17, which shows the very rapid first stage extension immediately upon application of the cyclic stress. The magnitude of this extension was comparable in both the T-111 and TZC alloys despite the higher fatigue strength of the T-111.

The T-111 was not susceptible to the dramatic acceleration of steady state creep when exposed to high frequency cyclic stresses as was the case for the TZC when comparisons were made with long time steady state creep rates. The iso-static and dynamic creep rates for T-111 are compared in figure VI-18 on the basis



of a temperature compensated creep parameter (paper IV of this volume). When the dynamic creep data were corrected for the nonlinear dependence of creep on stress which was present during the application of the cyclic loads, the agreement between the creep under steady state and steady state plus dynamic loads was excellent.

## General Discussion

In the case of the T-111 alloy no rapid steady state creep rate was observed when the creep behavior under dynamic conditions was compared to the constant load steady state creep which occurred in T-111 after the transition in creep rate. This isostatic creep rate transition which is shown schematically in figure VI-19 has been directly correlated with the removal of hafnia particles from the microstructure and a loss of oxygen to the high vacuum test environment, which eliminates a strain aging mechanism that retards creep (paper IV of this volume). In the case of the fatigue tests, electron micrographs indicated that the same structural refinement which occurred in several thousand hours of creep testing occurred in less than 100 hours when the dynamic load was applied. A significant oxygen loss was also measured in the fatigue tested samples; for example, post-test analyses were generally below 10 ppm as compared to 100 ppm before testing. On the basis of these results the cyclic stressing was believed to have accelerated the oxygen removal mechanism and produced a rapid steady state creep which was comparable to the steady state creep obtained in T-111 under constant load conditions after long periods of time.

In the case of TZC no microstructural variation was observed after fatigue testing and no creep transition was observed after long time isostatic creep exposure. The explanation for the observed behavior in T-111 cannot then be applied to TZC, and presently no satisfactory mechanism has been developed to quantitatively account for the accelerated creep behavior in this material. In addition, the very rapid first stage extension which was observed in both T-111 and TZC still requires further investigation to determine both its basic cause and its importance to component design situations.

## SUMMARY OF RESULTS

High frequency fatigue tests were conducted in an ultrahigh vacuum environment on molybdenum-base TZC and tantalum-base T-111 alloys in the temperature range of 1800° and 2200° F (982° and 1204° C). In this temperature range no well-

defined endurance limit existed for either material, and at  $10^9$  cycles fatigue strengths as low as 16 000 psi ( $11.0 \times 10^7$  N/m<sup>2</sup>) were observed for TZC and 34 000 psi ( $24.8 \times 10^7$  N/m<sup>2</sup>) for T-111.

In addition to classical fatigue failure, the superposition of a cyclic stress on a static stress produced a substantial increase in specimen extension. This increase occurred as an initially rapid creep rate during approximately the first 30 minutes of testing followed by a period where the creep rate was essentially constant. In both TZC and T-111, the rapid first stage creep was linearly related to the applied peak stress value, and this relation was independent of material, A ratio, and temperature over the range of variables studied. Decreasing the test frequency from 20 to 10 kilohertz increased the fatigue strength in TZC and minimized the acceleration in creep behavior produced by the application of cyclic stresses. In the steady state creep range the presence of the cyclic stresses produced a several order of magnitude increase in creep in the TZC alloy. However, in T-111 this acceleration was not observed when the comparisons were made on the basis of the long time isostatic creep where the structural refinement and loss of oxygen occurred in the alloy. In T-111 the application of the high frequency cyclic stresses increased the rate at which this loss of oxygen took place by several orders of magnitude. In the case of TZC the accelerated creep rate due to the superposition of cyclic stresses on a static load could not be explained in terms of a structural or compositional variation, and the specific mechanism was not defined.

## REFERENCES

1. Brock, G. W.; and Sinclair, G. M.: Elevated-Temperature Tensile and Fatigue Behavior of Unalloyed Arc-Cast Molybdenum. Proc. ASTM, vol. 60, 1960, p. 530.
2. Feltner, C. E.; and Sinclair, G. M.: Cyclic Stress Induced Creep of Close-Packed Metals. Joint International Conference on Creep. Inst. Mech. Eng., 1963, pp. 3-9 - 3-15.
3. Honeycutt, C. R.; Martin, T. F.; Sawyer, J. C.; and Steigerwald, E. A.: Elevated-Temperature Fatigue of TZC Molybdenum Alloy under High-Frequency and High-Vacuum Conditions. Trans. ASM, vol. 60, no. 3, Sept. 1967, pp. 450-458.
4. Neppiras, E. A.: Techniques and Equipment for Fatigue Testing at Very High Frequencies. Proc. ASTM, vol. 59, 1959, pp. 691-710.

TABLE VI-1. - CHEMICAL COMPOSITIONS OF TZC AND T-111 ALLOYS

## (a) TZC alloy

| Material | Heat | Form  | Vendor            | Composition, wt % |      |      |      |
|----------|------|-------|-------------------|-------------------|------|------|------|
|          |      |       |                   | Zr                | Ti   | C    | Mo   |
| TZC      | 4345 | Plate | Climax Molybdenum | 0.15              | 1.24 | 0.13 | Bal. |
| TZC      | 4350 | Plate | Climax Molybdenum | .17               | 1.30 | .125 | Bal. |

## (b) T-111 alloy

| Material | Heat   | Form  | Vendor    | Composition |    |      |     |     |    |     |  |
|----------|--------|-------|-----------|-------------|----|------|-----|-----|----|-----|--|
|          |        |       |           | wt %        |    |      | ppm |     |    |     |  |
|          |        |       |           | W           | Hf | Ta   | C   | O   | N  | H   |  |
| T-111    | 650038 | Plate | Wah Chang | 8.6         | 20 | Bal. | 25  | 100 | 20 | 2.8 |  |

TABLE VI-2. - SMOOTH TENSILE PROPERTIES OF TZC AND T-111 ALLOYS

## AFTER 1 HOUR RECRYSTALLIZATION

| Test temperature                          |      | Tensile strength |                      | 0.2 Percent yield strength |                      | Reduction<br>in area,<br>% | Elongation,<br>% |
|---|------|------------------|----------------------|----------------------------|----------------------|----------------------------|------------------|
| °F  | °C   | ksi              | N/m <sup>2</sup>     | ksi                        | N/m <sup>2</sup>     |                            |                  |
| TZC recrystallized at 3090° F (1700° C)   |      |                  |                      |                            |                      |                            |                  |
| 75  | 24   | 87.8             | 6.05×10 <sup>8</sup> | 50.3                       | 3.47×10 <sup>8</sup> | 16.8                       | 19.4             |
| 1800                                      | 982  | 63.0             | 4.34                 | 27.4                       | 1.89                 | 67.5                       | 29.3             |
| 2000                                      | 1093 | 60.8             | 4.19                 | 24.1                       | 1.66                 | 69.7                       | 28.2             |
| 2200                                      | 1204 | 54.2             | 3.71                 | 25.0                       | 1.72                 | 66.2                       | 29.1             |
| T-111 recrystallized at 3000° F (1649° C) |      |                  |                      |                            |                      |                            |                  |
| 75  | 24   | 92.1             | 6.35×10 <sup>8</sup> | 76.8                       | 5.29×10 <sup>8</sup> | 47.5                       | 29.8             |
| 1800                                      | 982  | 62.9             | 4.33                 | 32.1                       | 2.21                 | 76.7                       | 29.9             |
| 2000                                      | 1093 | 55.2             | 3.80                 | 31.5                       | 2.17                 | 50.0                       | 28.5             |
| 2200                                      | 1204 | 43.6             | 3.00                 | 28.1                       | 1.94                 | 48.7                       | 34.2             |

TABLE VI-3. - RATIO OF FATIGUE TO TENSILE STRENGTH FOR  
TZC MOLYBDENUM ALLOY, TESTED IN VACUUM  
( $1 \times 10^{-7}$  TORR) at 20 KILOHERTZ

| Test temperature   |                    | Tensile strength |                    | Fatigue strength at $10^9$ cycles |                    | Ratio of<br>fatigue to<br>tensile<br>strength |
|--------------------|--------------------|------------------|--------------------|-----------------------------------|--------------------|---|
| $^{\circ}\text{F}$ | $^{\circ}\text{C}$ | ksi              | $\text{N/m}^2$     | ksi                               | $\text{N/m}^2$     |   |
| 1800               | 982                | 63.0             | $4.34 \times 10^8$ | 18                                | $1.24 \times 10^8$ | 0.29  |
| 2000               | 1093               | 60.8             | 4.19               | 17                                | 1.17               | .28   |
| 2200               | 1204               | 54.2             | 3.71               | 16                                | 1.10               | .30   |



Figure VI-1. - Microstructure of molybdenum-base TZC alloy annealed at  $1700^{\circ}\text{C}$ . Etchant, 15 percent Hf, 15 percent  $\text{H}_2\text{SO}_4$ , 8 percent  $\text{HNO}_3$ , 62 percent  $\text{H}_2\text{O}$ .  $\times 100$ .

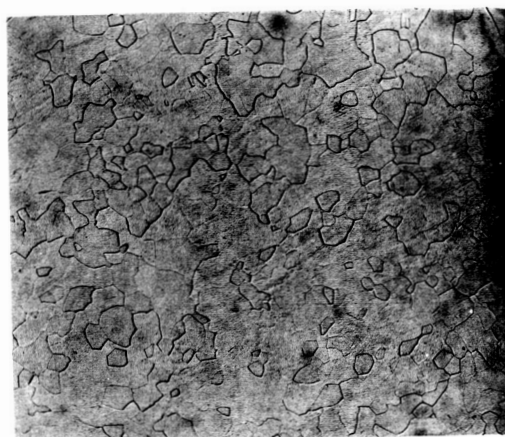


Figure VI-2. - Microstructure of T-111 heat 650038 recrystallized 1 hour at  $3000^{\circ}\text{F}$  ( $1649^{\circ}\text{C}$ ).  $\times 100$ .

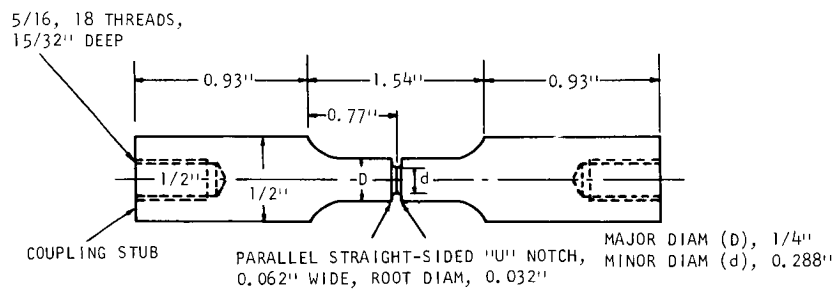
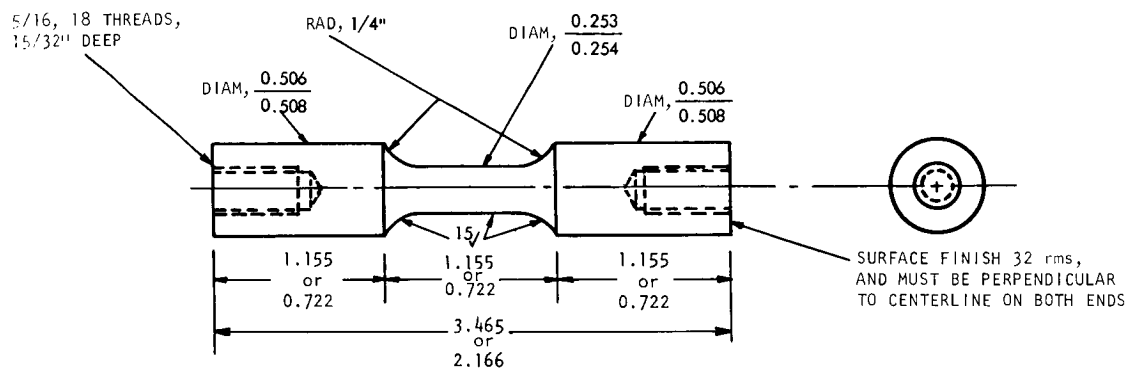


Figure VI-3. - Geometry of resonant test specimens. All diameter and thread ends must be concentric  $\pm 0.002$  total indicator reading, and minimum relief must be used on thread ends.

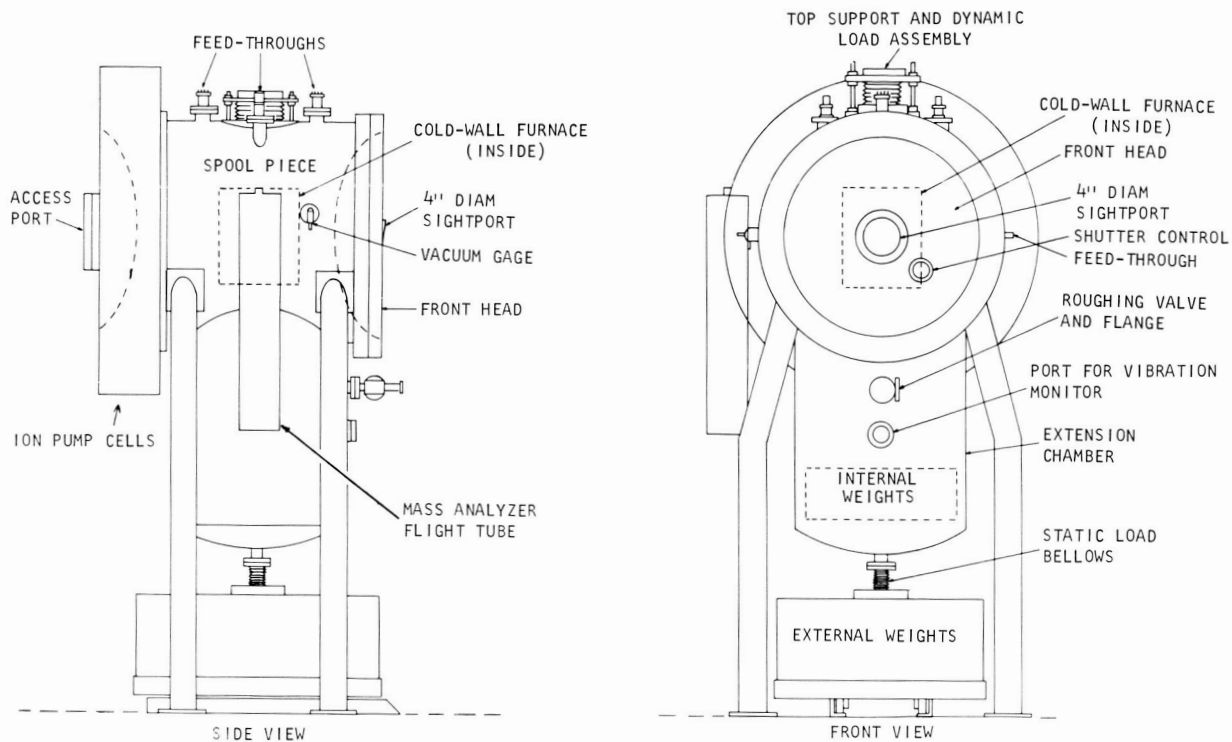


Figure VI-4. - Vacuum fatigue system.

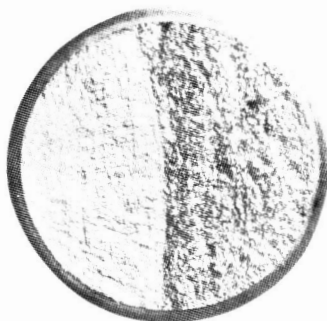


Figure VI-5. - Appearance of fracture surface of molybdenum-base TZC alloy fatigue tested at 2000° F (1093° C), 19 kilohertz, and  $<1 \times 10^{-7}$  torr vacuum,  $\times 10$ .

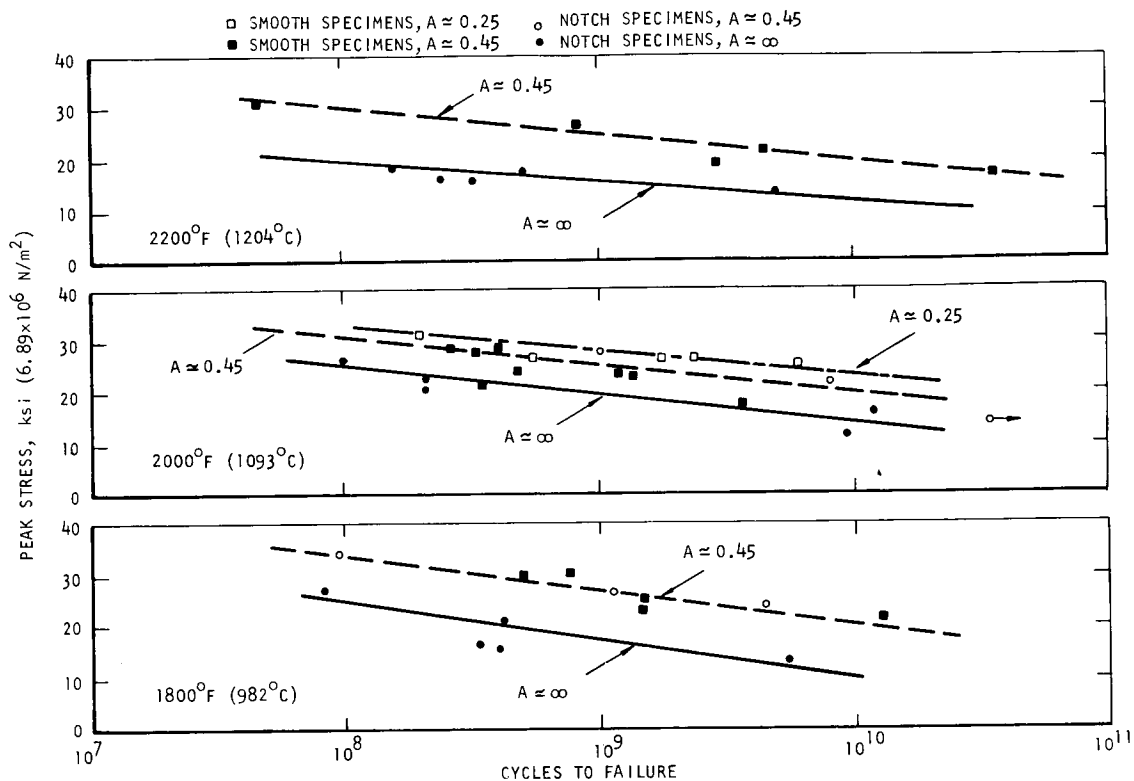


Figure VI-6. - Fatigue data for TZC recrystallized at 3092° F (1700° C) and tested at ~20 kilohertz in vacuum environment (<1×10<sup>-7</sup> torr).

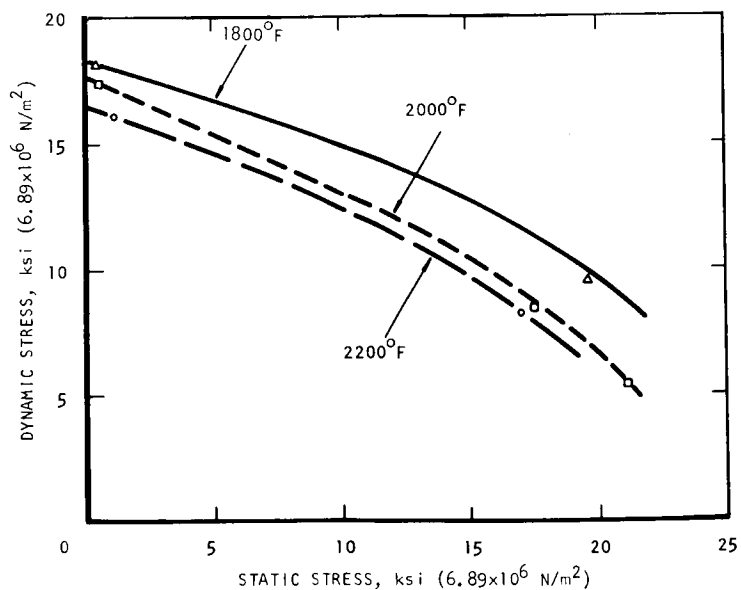


Figure VI-7. - Goodman diagram for 20 kilocycle fatigue strength of TZC alloy at 10<sup>9</sup> cycles. Tested in vacuum environment (<1×10<sup>-7</sup> torr).



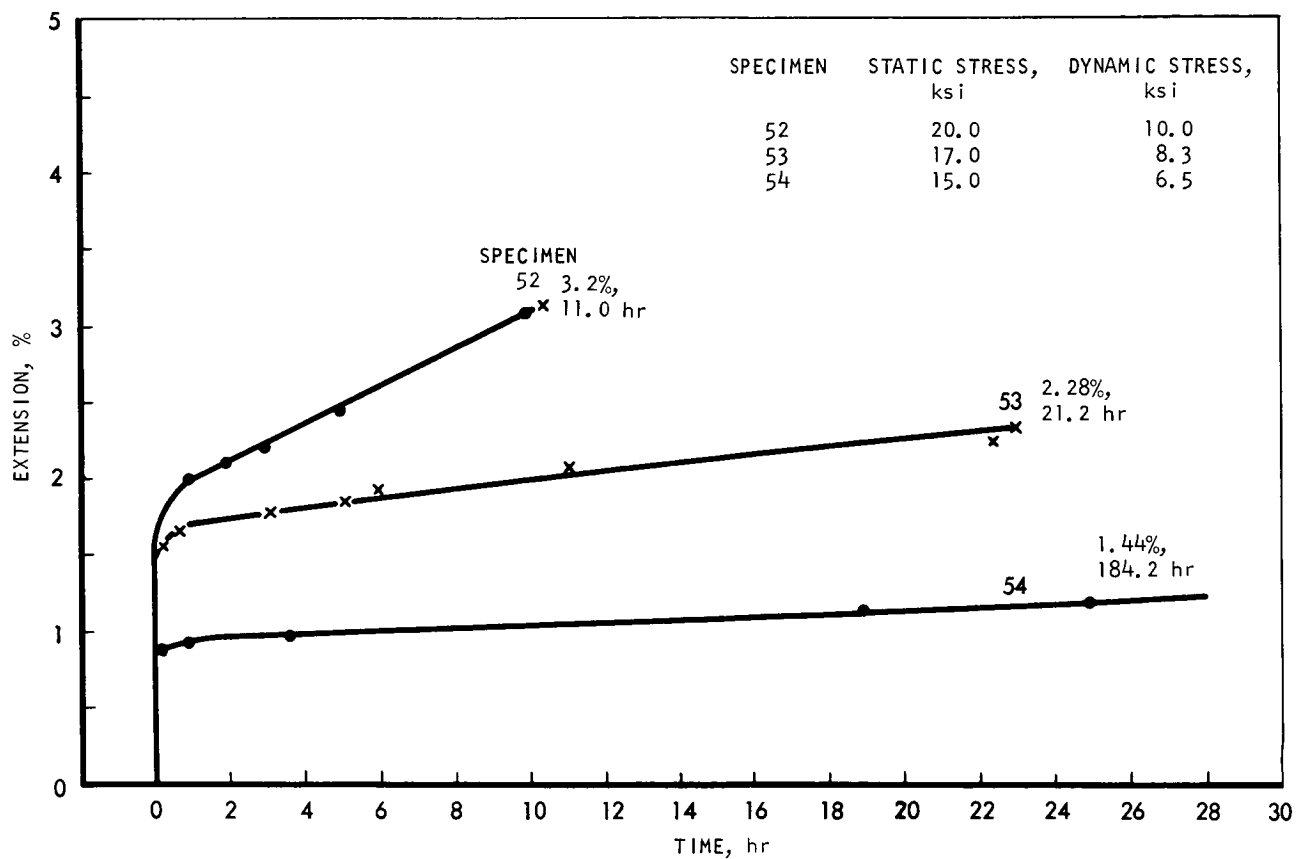


Figure VI-8. - Creep of TZC under dynamic load conditions. Test temperature, 1800° F; vacuum environment of  $<1 \times 10^{-7}$  torr;  $A \approx 0.45$ .

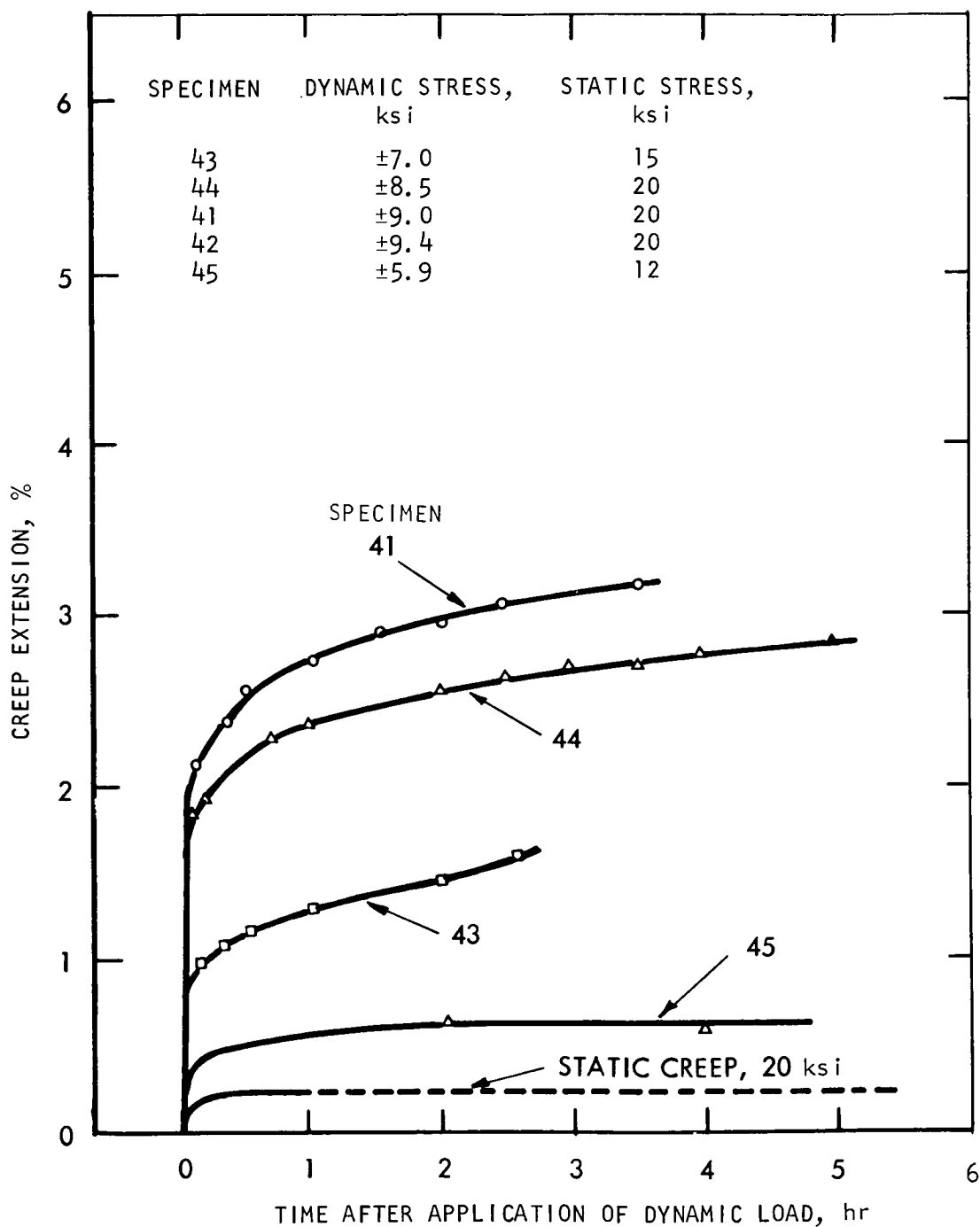


Figure VI-9. - Creep of TZC under static and dynamic load conditions. Test temperature, 2000<sup>o</sup> F; vacuum environment of  $<1 \times 10^{-7}$  torr.

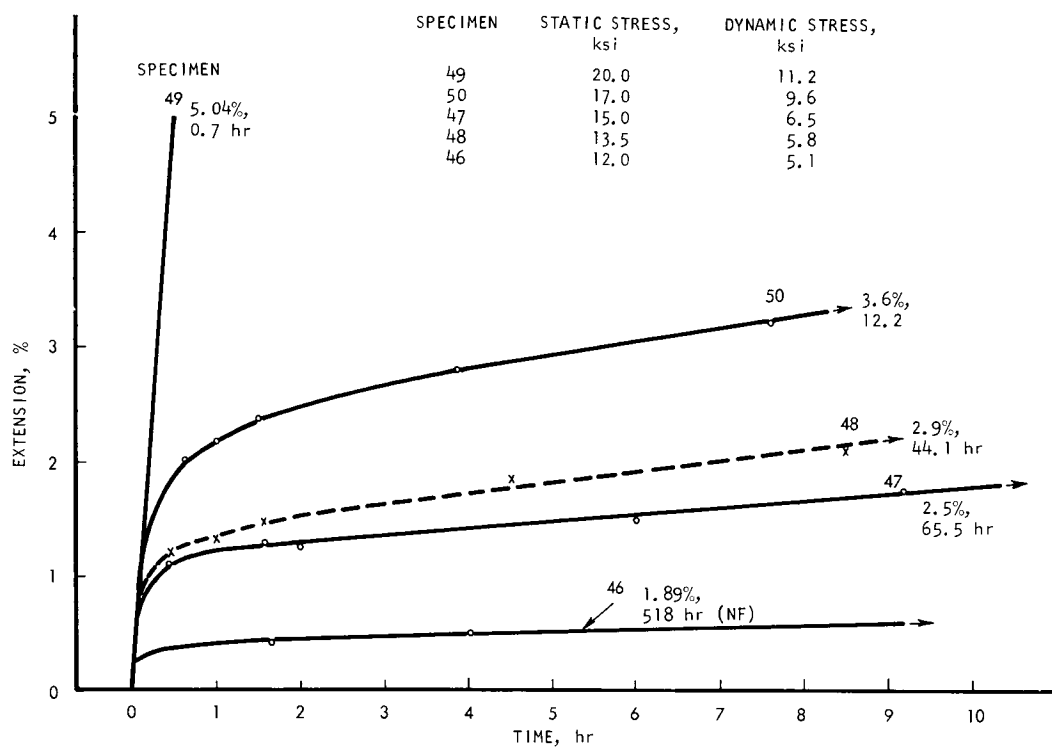


Figure VI-10. - Creep of TZC under dynamic load conditions. Test temperature, 2200° F; vacuum environment of  $<1 \times 10^{-7}$  torr.

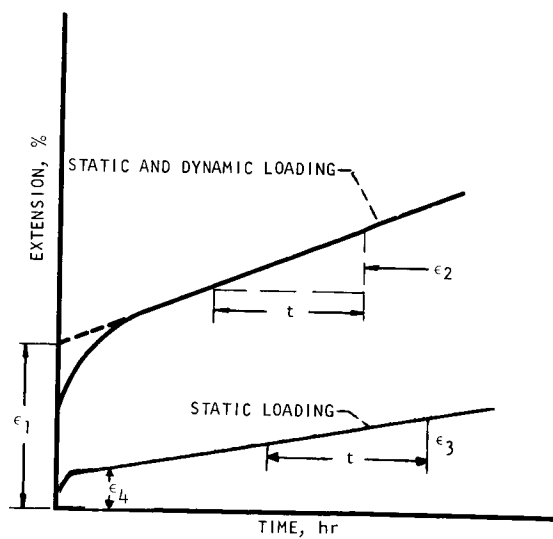


Figure VI-11. - Schematic illustration of typical creep behavior under combined static-dynamic loading conditions.  $\epsilon_1 > \epsilon_4$ ;  $\epsilon_2 > \epsilon_3$ .

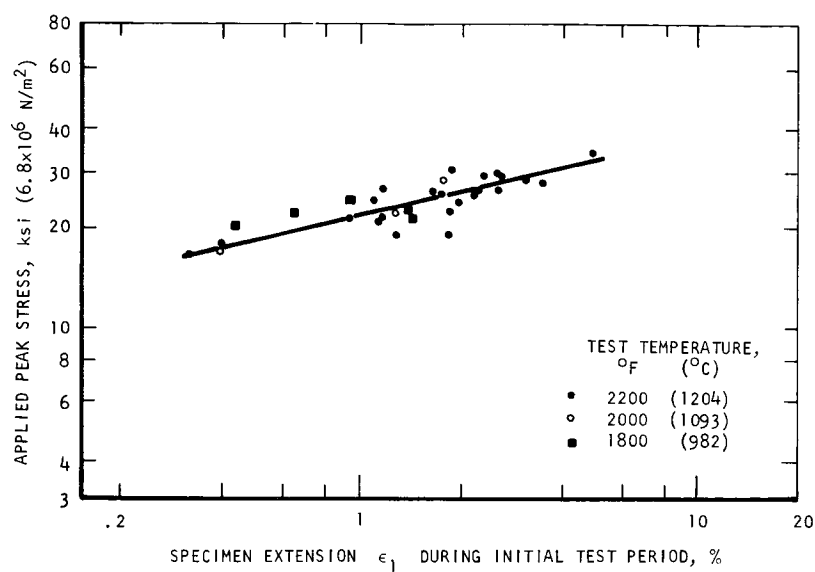


Figure VI-12. - Variation in initial creep extension with applied peak stress in cyclically loaded TZC alloy. Vacuum environment of  $<1 \times 10^{-7}$  torr;  $A \approx 0.45$  to  $0.10$ .

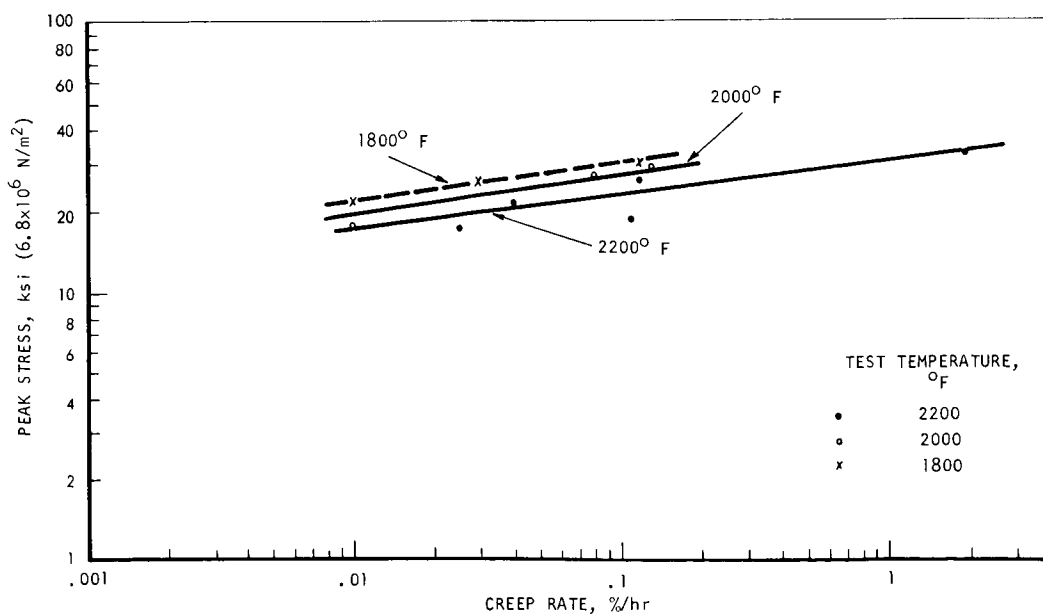


Figure VI-13. - Influence of peak stress in dynamic tests on creep rate of TZC. Vacuum environment of  $<1 \times 10^{-7}$  torr;  $A \approx 0.45$ .

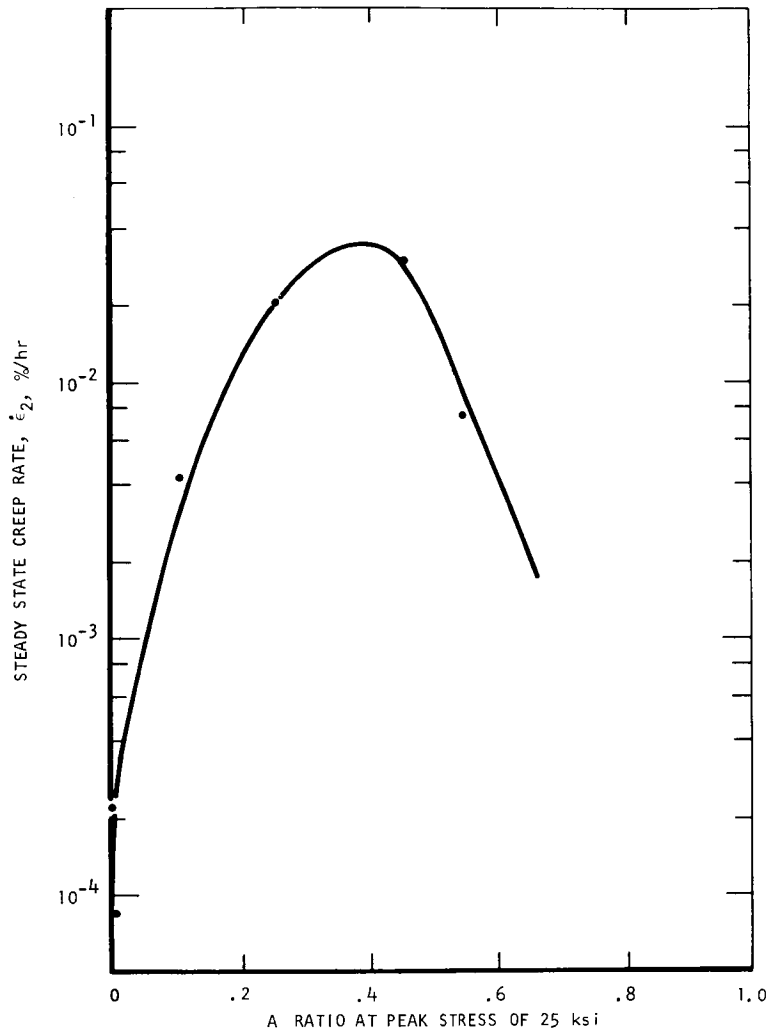


Figure VI-14. - Variation of  $\dot{\epsilon}_2$  with A ratio for fatigue tests at 20 kilocycles per second and  $2000^{\circ}\text{F}$ ; TZC annealed in ultrahigh vacuum environment.  $\dot{\epsilon} = 0$  at  $A = \infty$ .

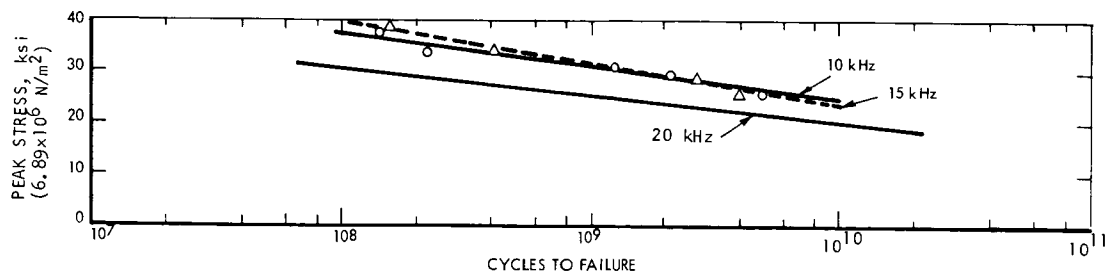


Figure VI-15. - Fatigue data for smooth specimens of TZC recrystallized at  $3092^{\circ}\text{F}$  ( $1700^{\circ}\text{C}$ ) and tested at 10 and 15 kilohertz in vacuum environment of  $<1 \times 10^{-7}$  torr. Test temperature,  $2000^{\circ}\text{F}$  ( $1093^{\circ}\text{C}$ ); A ratio = 0.45.

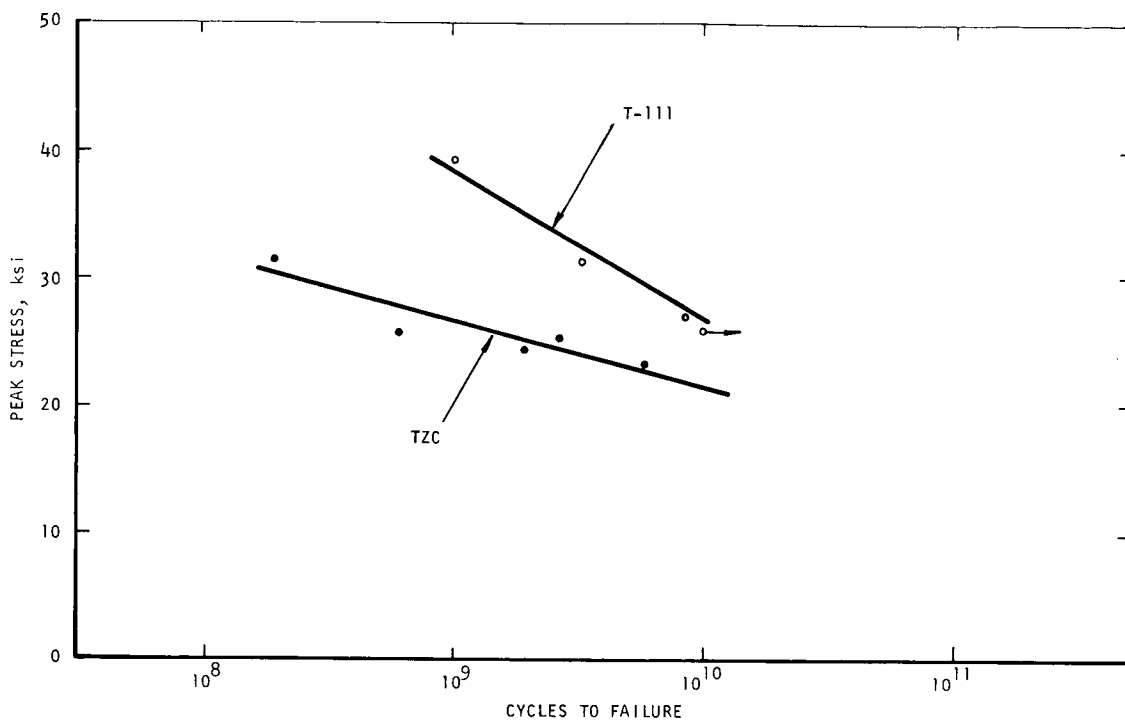


Figure VI-16. - Fatigue data for T-111 compared to TZC at 20 kilohertz and 2000° F (1093° C).  
A ratio = 0.25.

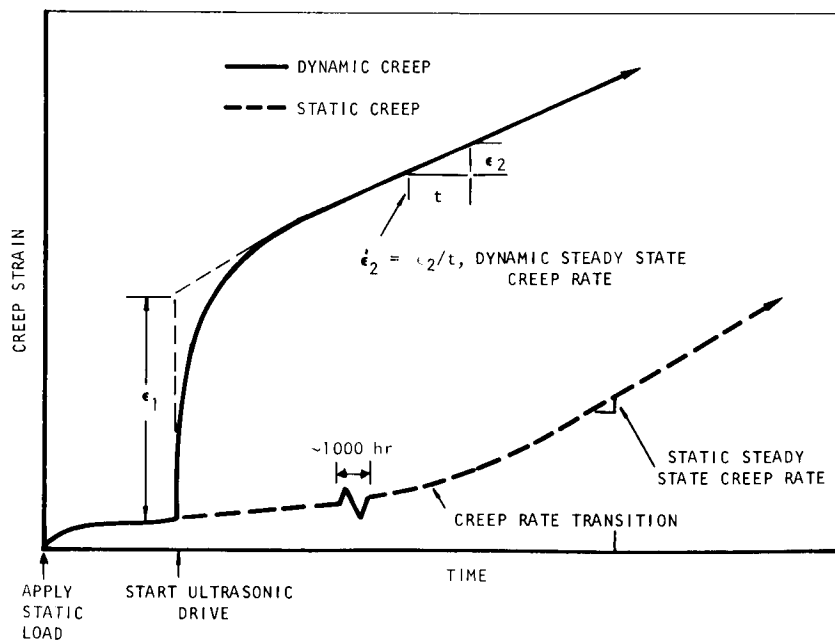


Figure VI-17. - Schematic representation of T-111 dynamic creep behavior at 2000° and 2200° F (1093° and 1204° C), shown superimposed on a static creep curve at same temperature and mean stress.

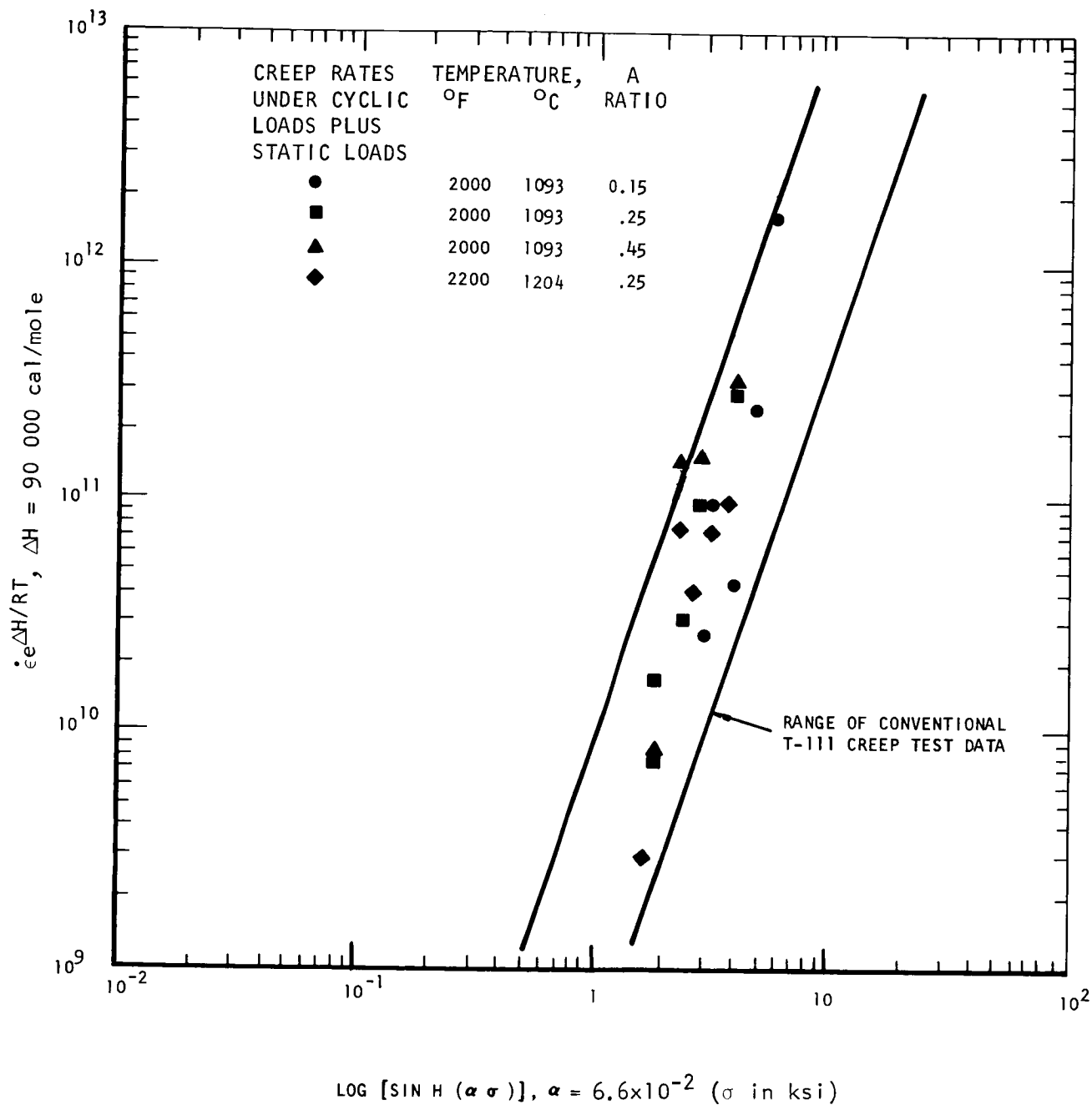


Figure VI-18. - Comparison of ultrasonic fatigue and conventional steady state creep rates in T-111 tested in ultrahigh vacuum.

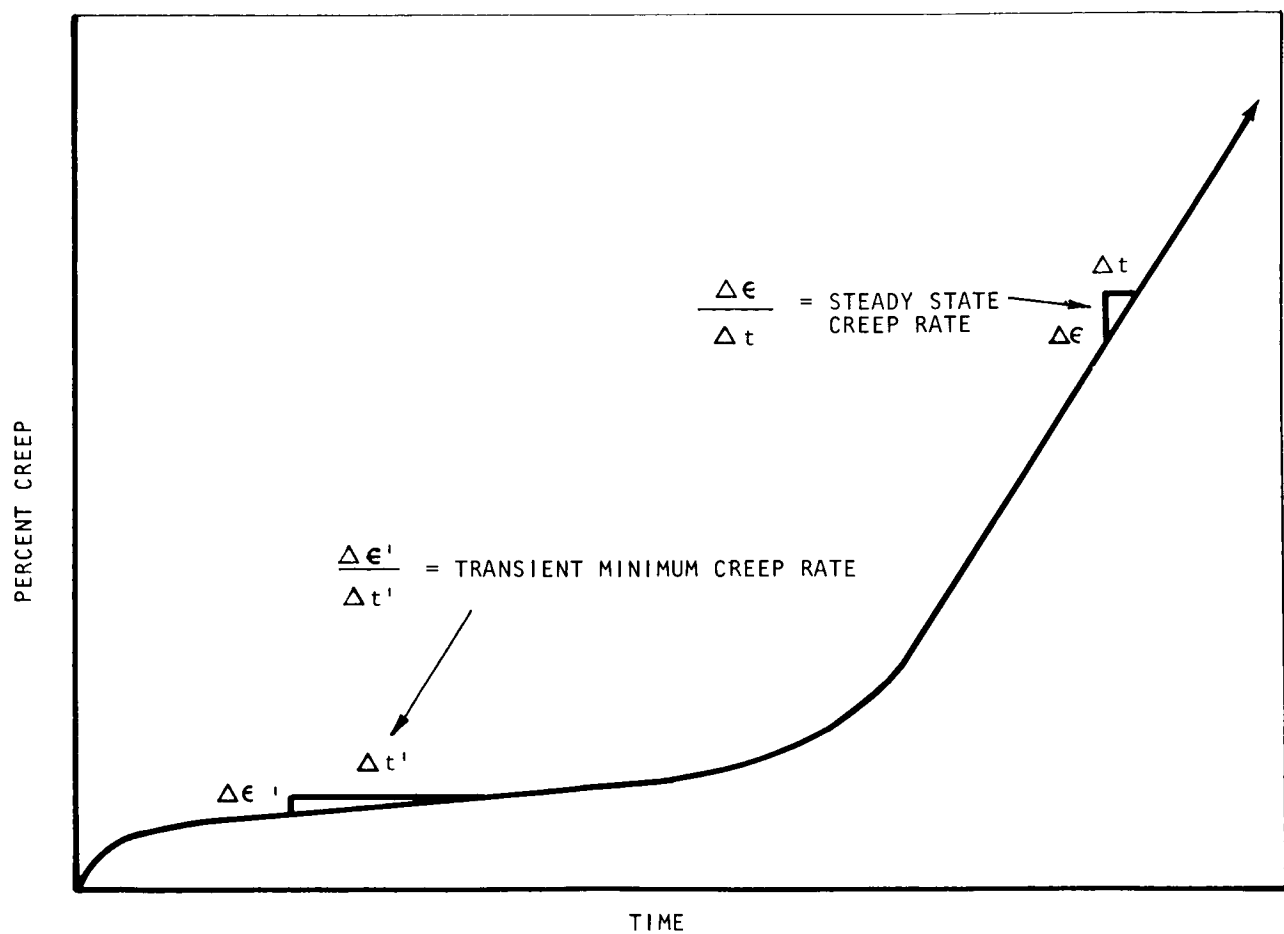


Figure VI-19. - Schematic representation of T-111 creep behavior in the 1600<sup>0</sup> to 2200<sup>0</sup> F (870<sup>0</sup> to 1204<sup>0</sup> C) range, showing unusual nature of transient first stage creep in this alloy.



## VII. FABRICATION OF T-111 TEST LOOP SYSTEMS\*

W. R. Young†

### INTRODUCTION

The construction of the first large T-111 alloy loop, corrosion loop I, was begun during early 1967. Previously, the performance and reliability of the individual components had been proven with Cb-1Zr alloy during the 5000-hour testing of the Cb-1Zr Rankine system corrosion test loop. Fabrication procedures proven with Cb-1Zr were, therefore, applied directly to the T-111 corrosion loop.

As the welding of T-111 proceeded, it became evident that more stringent requirements for joint alignments were required to prevent external loads during welding. Such loads resulted in a few instances of weld cracking. In general, however, components were fabricated with no more difficulty than normally expected in the first application of an alloy to large systems.

The most serious instance of weld cracking occurred in the boiler component and resulted in cross-leakage between the lithium and potassium circuits. The boiler repair procedures included removal of the boiler and reinstallation in the loop assembly. Since removal of this defect, the corrosion loop has accumulated over 3500 hours of operation at test conditions, thus reaffirming the basic system reliability.

The construction of the boiler development test loop is currently nearing completion. The discussion herein is limited to three components, the lithium heater, boiler, and condenser, which are unique to this system. In each case, the fabrication sequence and related welding techniques are given primary emphasis.

### T-111 CORROSION LOOP FABRICATION

The overall fabrication sequence for the T-111 Rankine system corrosion test loop is illustrated in figure VII-1. During loop fabrication, four major subassem-

---

\*Based on work conducted under NASA contract NAS 3-6474.

†General Electric Company, Cincinnati, Ohio.

blies, the boiler, condenser, lithium heater, and potassium surge tank, were constructed. The condenser and boiler subassemblies were postweld annealed at 2400<sup>0</sup> F for 1 hour in a vacuum furnace. In the other subassemblies, components were individually postweld annealed prior to assembly welding. These assembly welds were postweld annealed locally using a small refractory metal annealing furnace positioned over the weld joint.

The final loop assembly consisted of first joining the boiler and potassium surge tank major subassemblies. This unit together with the condenser and sodium heater was then positioned in the loop support structure. The welding fixture was then placed in position and attached to the various support positions on the loop. This fixture provided rotation of the loop within the welding chamber to facilitate welding of seven joints required during the final assembly. These welds were postweld annealed locally at 2400<sup>0</sup> F for 1 hour using a small refractory metal annealing furnace positioned over the weld joint.

The T-111 Rankine system corrosion test loop components as delineated in figure VII-1 were the boiler, condenser, lithium heater, turbine simulators, potassium preheater, two electromagnetic (EM) pump ducts, two surge tanks, a stressed diaphragm pressure transducer, five slack diaphragm pressure transducers, and two bellows sealed valves. The location of these components in the loop assembly is depicted in figure VII-2.

## GENERAL WELDING PROCEDURES

Prior to the welding of the T-111 Rankine system corrosion test loop, a preliminary qualification test of the welding equipment was conducted according to requirements defined in GE NSP specification 03-0025-00-A. This specification requires that the inert gas be purified to contain less than 1 ppm each of oxygen and water vapor by volume and that no contamination of the weld metal as determined by chemical analysis occurs during the welding cycle.

The mass spectrometer helium analysis system described in an earlier report (ref. 1) was used to monitor the welding chamber helium for oxygen and nitrogen. An electrolytic hygrometer was used to monitor the helium for moisture concentration. This analysis system was qualified according to specification 03-0025-00-A, which requires a measure of response time after introduction of oxygen (20 ppm), nitrogen (80 ppm), and water vapor (50 ppm) impurities. Response times recorded were 0.8, 2.3, and 4.0 minutes for oxygen, nitrogen, and water vapor, respectively. The full value of water vapor contamination required 14 minutes, because system response was limited by the rate of water evaporation into the helium envi-

ronment. The welding chamber shown in figures VII-3 and VII-4 was used for all tungsten inert gas welding performed on the loop. To accommodate long, straight tubing sections such as the boiler, an extension tube shown in figure VII-3 was attached to the basic chamber. During final loop assembly, the 8-foot-diameter extension tank illustrated in figure VII-4 was used.

The general welding procedure consisted of an overnight vacuum pumpdown with hot water bakeout (140<sup>0</sup> F) on the chamber. After the chamber was cooled, a pressure of less than  $1 \times 10^{-5}$  torr was attained. The pressure rise rate on the chamber was then taken prior to backfilling with purified helium gas. Welding operations were continued until completed or until gaseous contaminants reached the upper limits of GE NSP specification 03-0025-00-A, 5 ppm oxygen, 15 ppm nitrogen, and 20 ppm moisture (10 ppm moisture content in the case of components to contain lithium).

The welding machine used for both manual and automatic tungsten inert gas (TIG) welding is depicted in figure VII-5. This 400-ampere maximum constant current machine provides a complete weld sequence of upslope, weld, and downslope current control with time delay relays to provide for integration of motorized accessory equipment. During loop fabrication, a large percentage of the welding was done with the hand-held torch shown in figures VII-6 and VII-7. The molded silicon rubber and alumina insulator provide complete electrical insulation of the brass torch body and thus prevent inadvertent arcing to the workpiece. The single-piece chuck is easily accessible if the tungsten electrode requires replacement. Recently, as an added precaution, a T-111 chuck and a T-111 shield for the torch body have been incorporated into the torch design.

Full penetration butt joints were used wherever possible in loop design. Weld groove joint designs were in accordance with NSP specification 03-0015-00-A. This specification requires square grooves up to 0.06-inch thickness, a single 45<sup>0</sup> V between 0.06- and 0.19-inch thicknesses, and a single U for thicknesses greater than 0.19 inch. Special tantalum V blocks were used for tubular joint alinement. Full penetration tack welds on each side of the joint were then made to maintain alinement. After removal of the V blocks, the root and filler passes were made to complete the weld. Normally, approximately six weld starts and stops were required to complete each weld pass.

## CORROSION LOOP FABRICATION

### Loop Components

Lithium and potassium EM pump duct. - The typical EM pump fabrication is

illustrated in figure VII-8. Machining of the helical flow passage is the most critical fabrication step. The outer wrapper inside diameter is machined, honed, and inspected dimensionally. The helix is then ground to provide a 0.002-inch diametrical interference with the wrapper. The interference fit is produced by chilling the helix in liquid nitrogen and inserting it into the wrapper which is at room temperature. After completion of welding, the wrapper outside diameter is machined to the proper dimension for fitup with the bore of the EM pump stator. Postweld vacuum annealing at 2400° F for 1 hour is then performed to complete the fabrication cycle.

Slack diaphragm pressure transducers. - Six Taylor Instrument Companies pressure transducers were fabricated, five being required for the T-111 corrosion loop. Each transducer comprises upper and lower flanges, a slack convoluted diaphragm, a process tube, and a bimetallic joint between the Cb-1Zr and stainless steel. This joint, of the brazed tongue-in-groove design, provided for attachment of the stainless steel capillary tubing by Taylor Instrument Companies.

The weld between the diaphragm and upper flange was made by the electron beam process. Tungsten-inert-gas welding was used to join the process tube to the lower flange, the bimetallic joint assembly to the upper flange, and the final weld between the upper and lower flanges. The electron beam diaphragm weld is illustrated in figure VII-9. A trial electron beam weld is shown in figure VII-9(a) and the completed upper flange in figure VII-9(b). A metallographic cross section of this weld is shown in figure VII-9(c). The tungsten inert gas welding of the transducer housing is illustrated in figure VII-10. Radiographic inspection, heat treatment, and mass spectrometer leak tests were performed successfully. The six transducers were shipped to Taylor Instrument Companies for filling of the pressure transmitting capillary with NaK.

One of the six T-111 transducers was returned when a leak was detected across the diaphragm. This transducer was cut open and the defective diaphragm removed. Fluorescent penetrant inspection revealed two radial cracks in the diaphragm near the heat-affected zone of the weld. Subsequent metallographic examination revealed an intergranular crack in otherwise normal diaphragm material.

The transducer was repaired by welding a new diaphragm in place, and it was subsequently proof tested by applying 10 vacuum evacuation cycles on the NaK side of the diaphragm. Mass spectrometer leak testing indicated no failure, and welding and postweld annealing of the assembly was completed. A final mass spectrometer leak test indicated no diaphragm leakage.

The five acceptable transducers were each pulsated five times between vacuum and 0.5 psig by Taylor Instrument Companies. There was no evidence of leakage after testing.

The six transducers were then filled with NaK by Taylor Instrument Companies. A NaK sampler was also filled with NaK at the time of transducer filling. Chemical analysis indicated less than 3 ppm oxygen concentration in the NaK, an acceptable level.

Stressed diaphragm pressure transducer. - The components of the stressed diaphragm transducer are shown in figure VII-11. The 0.009-inch-thick T-111 alloy (Ta-8W-2Hf) diaphragm is welded to a T-111 alloy housing which is, in turn, welded to the T-111 body and process tube. A T-111 alloy probe mount is welded to the center of the diaphragm. The magnetic probe assembly is then brazed to the probe mount to complete the assembly.

The diaphragm assembly shown in figure VII-11(b) was produced by first electron beam welding the 0.020-inch-diameter W-25Re wire to the T-111 alloy probe mount. A second electron beam weld attached the probe mount to the T-222 alloy diaphragm. The diaphragm was then positioned between the T-111 housing and housing cap and electron beam welded. As an added precaution, an electron beam weld was made between the T-111 alloy housing and retainer body on the outside diameter, which, in combination with the internal tungsten inert gas weld, effected a double seal between these components.

The final fabrication step was the brazing of the magnetic probe to the 0.020-inch-diameter W-25Re wire. Brazing was accomplished using localized heating with a graphite-tipped heater probe under high-purity argon in the welding chamber shown in figure VII-4. The brazing alloy (72Ag-28Cu) was applied to the joint manually in wire form. The completed assembly, shown in figure VII-11(c), was mass spectrometer leak tested successfully and submitted to instrumentation for room temperature calibration prior to installation in the loop.

Boiler. - Fabrication of the T-111 boiler was initiated by butt welding straight lengths of the inner tube using the welding chamber tube extension (fig. VII-3) to provide sufficient lateral travel. Triform spacers, illustrated in figure VII-12, were tungsten inert gas welded at 10-inch intervals along the boiler tube. The boiler tube was inserted in the shell, and the assembly was formed by the Philadelphia Pipe Bending Company. Prior to forming, the inner tube and the annulus were packed with sugar to aid in maintaining concentricity. This technique had to be used previously during forming of a similar Cb-1Zr boiler.

Upon receipt of the formed boiler from the vendor, the sugar was removed by mechanical vibration. When no additional sugar could be removed, a deionized water flush was initiated. The water was heated to 150<sup>0</sup> F and was allowed to flush through the boiler for 15 hours. An additional cold water flush for 30 minutes was used for the final rinse. At this time water samples were equilibrated for 2 hours in the boiler and tested for sugar using the Molisch test (ref. 2). Duplicate test

determinations indicated less than 50 ppm sugar, which is the limit of detection of the method used.

Welding of the boiler shown in figure VII-13 was then initiated. The inner and outer tubes were cut to the proper length, and the tube plug was welded to the inner tube. After inspection of this weld, the end connectors for the outer tube were positioned and welded to the boiler shell and inlet plug. The inlet plug configuration shown in figure VII-13 was made by forming 0.060-inch-diameter T-111 wire into a 1.0-inch-pitch helix on the 0.125-inch-diameter T-111 center rod. One TIG weld tack per revolution of the plug wire was made to hold the wire in place. The plug was then positioned within the straight section of the boiler inlet pipe and welded to the inlet fitting. The welded assembly was radiographed and leak tested prior to its inclusion in the boiler subassembly.

Turbine simulator. - Each turbine simulator stage consisted of a nozzle, turbine blade, and two specimen support pads, as shown in figure VII-14 for the second stage. The fabrication and assembly procedures used to construct the turbine simulators were dictated by the requirement to obtain very precise weight change data on these components following the 10 000-hour test. The Mo-TZC and Cb-132M alloy blades were polished to a 16-rms surface finish by the vendor utilizing a 240-grit alumina cloth followed by a final polish with 5-micron alumina before final cleaning and assembly. The Mo-TZC and Cb-132M alloy nozzles were prepared by electropolishing, a refinement of electric spark discharge machining, to produce a 32-rms surface finish in the nozzle throat. The machining sequence is shown in figure VII-15. The surface was further polished with 400-grit alumina paper to remove approximately 0.001 inch from the surface. A polish with 5-micron alumina produced an 8-rms finish. Final hand polishing using 30- and 15-micron diamond paste was used to further improve the surface finish of the nozzles. Fluorescent penetrant inspection revealed three cracked Mo-TZC alloy blade support pads in the initial group. These pads were replaced with new Cb-132M alloy pads which passed inspection. After final weighing and cleaning operations, the nozzle assemblies were ready for positioning in the turbine simulator casing.

The first nozzle-blade assembly was positioned in a separate T-111 outer casing. The end caps, thermocouple wells, and 1-inch-diameter potassium flow tube were then welded to complete the single-stage turbine simulator. Postweld annealing of this subassembly was conducted after it was joined to the boiler to form a major subassembly.

The remaining nine nozzle-blade assemblies were positioned as shown in figure VII-16. These assemblies are rabbeted together and aligned in their T-111 casing with a 0.062-inch-diameter wire which extends through a keyway in the nozzles and casing. This wire insert prevents rotation of the individual nozzle in the

casing during test operation, but its primary purpose is to facilitate disassembly of the turbine simulator without damaging the individual nozzles and blades as this would make it impossible to obtain accurate weight change data on these components. The assembly of the nozzle-blade stack in the casing required careful handling since both unit straightness and axial alignment had to be maintained.

Condenser. - The 60-inch-long condenser was originally to be fabricated from a 1- by 2-inch cross section T-111 bar with a 0.406-inch-diameter hole gun-drilled the length of the bar. Twenty 0.25-inch-thick tantalum fins would then be welded along the length of the bar to provide radiant cooling.

Initial gun-drilling trials, however, resulted in failure due to a breakage of carbide drills or excessive wear of high-speed steel drills. A sample of T-111 alloy was then supplied to Standard Tool Company, a producer of gun drills for evaluation. Their report indicated the most success using a high-speed gun drill head to which they applied a positive rake chip break along with a  $10^{\circ}$  stack point. Additional material would be required to further define gun-drilling parameters.

Concurrent with the above investigation, one 32-inch-long condenser bar was committed for conventional drilling. A 0.406-inch-diameter hole was drilled successfully using a long fluted twist drill with an extension brazed to the shank. The drill was ground with an included angle of  $135^{\circ}$ . A hand feed of approximately 0.003 inch per revolution and a drill speed of 6 surface feet per minute produced the best cutting action. After the success of conventional drilling was demonstrated, the 63-inch-long condenser bar was cut in half and one additional section was drilled successfully to produce the two sections required for the 60-inch-long condenser. These two drilled bars were then finally machined and honed on the inside diameter.

The welding of the condenser was then completed with the joining of the two condenser bars and tantalum fins as shown in figure VII-17. During welding, alignment of the fins was maintained by the welding fixture shown in figure VII-18. Molybdenum blocks were incorporated in the fixture at each clamp location to provide refractory metal contact with the condenser.

## Major Subassemblies

During loop fabrication, four major subassemblies, the condenser, boiler, potassium surge tank, and lithium heater, were sequentially assembled as described in figure VII-1.

Condenser assembly. - The condenser assembly consists of the condenser, nine-stage turbine simulator, subcooler reservoir, and associated piping, as shown

in figure VII-19. A more detailed view of the turbine simulator and potassium vapor line is shown in figure VII-20. Radiographic inspection of this assembly revealed a 0.060-inch-diameter spherical defect in the weld between the subcooler reservoir and the condenser. Because of scheduling difficulties with the large vacuum furnace required to postweld anneal this assembly, this weld repair was postponed until the assembly anneal was completed as described below. Subsequently, the defect was removed and the weld repair completed. This weld was then locally annealed at 2400<sup>0</sup> F for 1 hour in accordance with GE NSP specification 03-0037-00-A.

The high-emittance coating of iron titanate ( $\text{Fe}_2\text{TiO}_5$ ) was then applied to the unalloyed tantalum condenser fins by Pratt and Whitney Aircraft using the procedures established previously (ref. 3).

Boiler assembly. - The boiler assembly consists of the boiler, single-stage turbine simulator, and potassium preheater, as shown in figure VII-21. Conventional tube joint welds join these components.

Potassium surge tank assembly. - The potassium surge tank subassembly (fig. VII-22) illustrates the intermediate fixturing required to maintain component orientation. During this fabrication the pressure transducer T welds and the weld between the surge tank and EM pump duct were made and postweld annealed locally. Each component had been postweld annealed previously.

Lithium heater subassembly. - The lithium heater subassembly, which consists of the lithium heater, EM pump duct, and surge tank, is shown in figure VII-23. Three welds were required to join these components, but extensive fixturing was again required to maintain component orientation.

## Postweld Annealing of Major Loop Subassemblies

The boiler and condenser major subassemblies and the lithium heater, all wrapped with one overlapping layer of Cb-1Zr foil, were postweld annealed at 2400<sup>0</sup> F for 1 hour in Stellite's Brew furnace Model 966 at Kokomo, Indiana. This anneal was conducted in accordance with GE NSP specification 03-0037-00-A. This furnace had previously been qualified at 3000<sup>0</sup> F using 0.040-inch-thick T-111 alloy test coupons both wrapped with Cb-1Zr alloy foil and unwrapped. The results of this qualification run are shown in table VII-1 and indicate no significant increase in interstitial element concentration occurred during annealing.

During the annealing, the various loop assemblies, which weighed approximately 250 pounds, were suspended from Ta-10W alloy hanger bars that were mounted on the top flanged dome of the chamber.



Four Pt/Pt-10Rh thermocouples were used to monitor the temperature of the loop components. These thermocouples were wrapped with two layers of Cb-1Zr foil wrap which surrounded the components. A W-5Re/W-26Re thermocouple was used to monitor the furnace temperature.

The furnace heating rate, which was programmed at 25° F per minute, was interrupted, and the temperature held constant at 1000°, 1500°, 2040°, and 2200° F for time periods of 10 to 15 minutes to allow time for thermal equilibration, outgassing, and pressure reduction. The chamber pressure was  $7 \times 10^{-6}$  torr at the start of the 1-hour anneal and decreased to  $3 \times 10^{-6}$  torr after 1 hour. The temperatures of the various components equilibrated with the furnace temperature in less than 10 minutes at 2400° F. The maximum temperature difference for the three components of 25° F indicated excellent temperature uniformity within the furnace.

### Final Loop Assembly

The completed lithium heater, condenser, boiler, and potassium surge tank subassemblies were positioned in the stainless steel support structure attached to the vacuum chamber spool section for reference alignment. The tubing which joins the boiler and potassium surge tank subassemblies was match marked for alignment, and the two subassemblies were removed from the spool section for welding in the 8-foot-diameter extension to the welding chamber. This assembly step was required because this particular weld could not be reached with the entire loop positioned in the welding chamber. After radiographic inspection of this weld, this unit was repositioned in the permanent support structure.

The lithium heater and condenser subassemblies were also positioned in the support structure. The final assembly weld fixture was attached to the loop (fig. VII-24) holding the subassemblies and three slack diaphragm pressure transducers (not shown) in alignment. The permanent support structure was disassembled and the loop, now supported by the welding fixture, was removed from the vacuum chamber spool section and placed in the welding chamber as shown in figure VII-25.

The seven welds required to join the subassemblies and attach the three pressure transducers were inspected radiographically and subsequently annealed in the welding chamber at 2400° F for 1 hour in accordance with NSP specification 03-0037-00-A.

The loop was removed from the welding chamber, and the electrode area of the lithium heater and the potassium preheater were grit blasted to increase emittance according to specification NSP 03-0011-00-A, "Grit Blasting of Columbium and Columbium Alloy Products." The loop was then positioned in the vacuum chamber

spool section, and the permanent support structure was affixed. After the loop was supported properly, the final welding fixture was removed. An overall view of the loop and spool piece is shown in figure VII-26. A closeup photograph of the components in the lower portion of the loop is given in figure VII-27.

The stainless steel tube attachments to the drain and gas pressurization lines were welded to the loop connections and vacuum chamber feed-throughs. A final mass spectrometer helium leak test was then performed on the entire loop with no leak indication. The vacuum connections for the NaK-filled tubes from the slack diaphragm pressure transducer and the EM pump duct stainless steel outer cans were welded to the appropriate vacuum spool section feed-throughs. The completed loop was then removed to the test site.

## Boiler Repair

After a short period of loop operation, a leak between the potassium and lithium circuits was discovered at a weld in the potassium boiler tube. The evaluation of this weld is discussed in paper VIII in this volume. Only the repair and reinstallation of the boiler are discussed in this paper. To effect the repair, a number of modifications to the boiler design were required, as shown schematically in figure VII-28. Since one coil was removed from the boiler, an additional length of T-111 1-inch-diameter tubing was added to the top of the boiler to achieve a total boiler height equal to the original boiler for correct fitting during installation into the loop. New fittings were required for attachment to the lithium inlet and outlet lines. During installation of the boiler the lithium lines originally on the loop were inserted into socket fittings to ensure correct alignment during welding. Butt welding is normally the technique utilized for joining tubing; however, because of the location of these welds and limited access during installation of the boiler into the loop, the socket weld approach was selected. The main concern with this type of weld joint was the possibility of an open gap between the socket fitting inside diameter and the outside diameter of the inserted tubing. A trial fitting was machined with a double socket, and weld experiments were performed to develop a technique to prevent this gap. The welded specimen is shown in figure VII-29. Subsequent radiographic and metallographic examination of this specimen indicated full penetration welds with no gaps were achieved when the tubing was inserted in the socket and pulled back slightly so the bottom of the tube did not contact the bottom of the socket. The joint between the 0.375-inch-outside diameter inner boiler tube and the 1-inch-outside diameter outer boiler tube at the top of the boiler was also modified with a new fitting similar to that used at the bottom of the boiler. This butt joint design was pre-

ferred over the previously employed tube-to-header joint. These design modifications are compared with the original design in figure VII-30.

In the initial welding step a new section of 0.375-inch-diameter tubing was butt welded to the inner boiler tube. Subsequent helium mass spectrometer leak checking and radiographic inspection indicated this weld to be sound. Two sections of 1-inch-diameter boiler tube were then welded in place as shown in figure VII-31. These pieces were obtained from the boiler coil which was removed during sectioning of the boiler. Following the joining of the new end fitting to the 0.375-inch-diameter tubing, the three welds were inspected by radiography and helium mass spectrometer leak checking and found to be sound. The boiler was completed with the addition of the lithium inlet fitting and boiler extension piece at the top of the boiler as shown in figure VII-32 and the addition of the lithium outlet fitting at the bottom of the boiler as shown in figure VII-33. The boiler plug was reattached at this time by tack welding to the bottom boiler fitting. The repaired boiler is compared with the original boiler in figure VII-34. The removal of one coil from the boiler reduced its total length by approximately 27 inches.

After appropriate postweld annealing and leak testing, the boiler was ready for reinstallation into the loop. The requirements of NSP specification 03-0025-00-A necessitated the purchase of a special welding chamber to be installed around the loop for the welding operations. The chamber, shown after installation on the T-111 corrosion loop test facility in figure VII-35, comprises two flanged spool sections 4 feet in diameter and 4 feet high such that each can be rotated independently for improved access to weld locations. Sight ports and glove ports were appropriately positioned in the areas where welding was performed at the top and bottom of the boiler location. An independently pumped tool port was also provided such that necessary tools could be brought into the chamber without contaminating the chamber environment.

Rough pumping was accomplished with the 260-liter-per-second turbomolecular pump, and the loop facility ion pumps were used to achieve the high vacuum ( $<1 \times 10^{-5}$  torr) called for in the welding specification. The chamber was backfilled with ultrahigh purity helium which was passed through a molecular sieve dryer before entering the chamber. The inert gas analysis equipment included C. E. C. (model 26-303) and Planametrics (model 1000) moisture monitors and the gas chromatograph shown in figure VII-36. Gas lines attached to the gas chromatograph made analysis of oxygen and nitrogen in the inlet gas as well as outlet gas from the chamber possible.

After weld chamber qualification, the boiler was welded into the loop as shown in figure VII-37. Four welds were required to reinstall the boiler; two at the top of the boiler and two at the bottom, as shown in figures VII-38 and VII-39, respec-

tively. Subsequent radiographs of the welds indicated a very small area in the upper lithium line weld of incomplete penetration, which was subsequently repaired. Mass spectrometer helium leak checking radiography of the welds showed no indications of leaks or weld defects. The four installation welds were postweld annealed in position using the annealing furnace shown in figure VII-40. The furnace comprises tantalum shields and shell, alumina insulations, and tungsten wire (0.050-in.-diam) elements. The power for heating the elements was supplied from a standard welding machine, one electrode being the welding torch and the other electrode grounded. The welds were annealed for 1 hour at 2400<sup>0</sup> F.

### POTASSIUM BOILER DEVELOPMENT LOOP FABRICATION

The overall fabrication sequence for this large T-111 alloy system followed the general guidelines established during corrosion loop fabrication. Preplanning of fabrication steps was incorporated into the design phase to assure trouble-free assembly within the limits of the welding chambers and to provide suitable locations for final assembly welds. The size of furnaces required for postweld annealing of components was also given careful consideration, and in certain instances this was the limiting factor in component design. General welding procedures were equivalent to those employed during T-111 corrosion loop fabrication. Many components, such as pressure transducers, valves, and EM pump ducts were also similar to those fabricated previously. However, the large lithium heater, boiler, and condenser presented unique fabrication problems which are discussed individually in this section. The location of these components is shown in the schematic of the potassium boiler development test rig, figure VII-41.

### LITHIUM HEATER

The lithium heater includes six heater coils. Each 11-inch-diameter coil is formed from 0.875-inch-outside diameter by 0.100-inch-wall T-111 tubing and has a developed length of 124 inches. Appropriate manifolds and electrodes were required to split the lithium flow uniformly and to provide attachment of high current electrical buses.

A fixture was designed to hold the lithium heater as shown in figure VII-42. A more detailed view of the three-tube manifold joints is shown in figure VII-43. The size and weight of this component made it difficult to handle manually within the welding chamber. To alleviate this problem, the multipurpose weld positioner

shown in figure VII-44 was utilized. This unit provides motor driven rotation and manual translation of the workpiece within the 8-foot-diameter welding chamber.

## CONDENSER

The three-tube potassium condenser is NaK-cooled on the shell side and is a basic hockey stick design. From the welding viewpoint, this component, being of multitube design, required the qualification and production of representative tube-to-header joints. In order to provide a fully inspectable butt joint, internal automatic welding was selected. In this process, a welding torch is positioned inside the joint as shown in figure VII-45 and is rotated by a motor drive which is controlled by the sequence control on the previously described automatic welder. The three tube-to-header joints shown in figure VII-46 were welded using this technique. After inspection of these welds, the tube bundle and support cage shown in figure VII-47 was slipped into the shell. The potassium outlet tubes were then bent and trimmed to proper length, and a reducer was welded to each tube, as shown in figure VII-48. These reducers were welded to the exit header, providing the same joint design as that of the inlet header. The completed condenser shown in figure VII-49 has connections of pressure transducers in addition to the NaK and potassium lines.

## BOILER

The potassium test boiler is C-shaped in design and has a 0.75-inch-outside-diameter by 0.040-inch-wall T-111 potassium boiler tube maintained concentric within a 1.325-inch-outside-diameter by 0.100-inch-wall shell. A helical fin insert shown in figure VII-50 extended approximately half the boiler length. At the end of the fin a helical wire coil was attached and continued throughout the remainder of the boiler tube. Because the boiler tube required forming after the inserts were in position and each insert had a different rigidity in bending, it was necessary to proceed cautiously during tube forming. It was therefore decided to bend the shell and boiler tube separately to provide the best assurance of proper tube concentricity in the formed boiler. Several trials with stainless steel mockup boilers preceded the T-111 boiler tube bending. Initial bending was performed manually using a 360° machined steel mandrel for the inside diameter contour and a steel roll on the outside diameter. Final sizing to the shell diameter was done on a conventional three-roll tube bender. Four tube spacers were then TIG tack welded to the formed boiler

tube as shown in figure VII-51. The boiler shell shown in figure VII-52 was then slipped over the boiler tube. Mechanical vibration was necessary during this operation to reduce the considerable drag between the sliding T-111 components.

The completed boiler assembly shown in figure VII-53 indicates the complexity of a fully instrumented test boiler. Provision for pressure transducers, insert thermocouples, and bulk fluid thermocouple wells necessitates many sequential welding and inspection steps to provide high reliability in the component.

## SUMMARY OF RESULTS

During the past 2 years, GE Nuclear Systems Programs Department has been committed to the fabrication of large T-111 components and alkali metal systems. As each project has progressed, understanding of the welding characteristics and metallurgy of T-111 alloy has been broadened. Particular instances of weld-associated cracking have been documented and are reported in paper VIII of this volume. However, the corrosion loop fabrication was accomplished without undue difficulties, as evidenced by the welding of rather complex components.

The boiler fracture, although a technical setback, necessitates the first repair of a T-111 component which had been previously exposed to alkali metals. The fact that many test hours have been accumulated since this repair is an important milestone in T-111 alloy utilization.

The boiler development test loop program provided the challenge of building components of a large T-111 alloy system. Concurrently, unique processes such as internal tube-to-header welding were applied to T-111 alloy. Each component provided a better understanding of the machining, forming, and welding processes required to fabricate large space power systems.

## REFERENCES

1. Lyon, T. F.: Potassium Corrosion Test Loop Development: Purification and Analysis of Helium for the Welding Chamber. General Electric Co. (NASA CR-54168), July 1, 1965, p. 35.
2. Cheronis, Nicholas D.: Micro and Semimicro Methods. Vol. 4 of Techniques of Organic Chemistry. Interscience Publ., 1954, pp. 466-467.
3. Hoffman, E. E., ed.: Potassium Corrosion Test Loop Development. General Electric Co. (NASA CR-54735), 1965, p. 37.

TABLE VII-1. - RESULTS OF QUALIFICATION TEST OF  
STELLITE'S BREW FURNACE MODEL 966

[Test time, 1 hr; temperature, 3000<sup>0</sup> F; maximum pressure at  
temperature,  $4.4 \times 10^{-5}$  torr.]

| Element <sup>a</sup> | Concentration, ppm <sup>b</sup> |   |                                    |
|----------------------|---------------------------------|---|------------------------------------|
|                      | Before anneal                   | Wrapped specimen <sup>c</sup><br>after anneal | Unwrapped specimen<br>after anneal |
| O                    | 26                              | 27  | 51                                 |
| N                    | 14                              | 12  | 14                                 |
| H                    | 1                               | 1   | 2                                  |
| C                    | <10                             | 11  | 27                                 |

<sup>a</sup>Test specimens: T-111 sheet, 0.040-inch-thick MCN 02A-078.

<sup>b</sup>Analytical methods: O, N, and H, vacuum fusion; C, combustion conductometric.

<sup>c</sup>Specimen was wrapped with layer of 0.002-inch-thick Cb-1Zr foil during heat treatment.

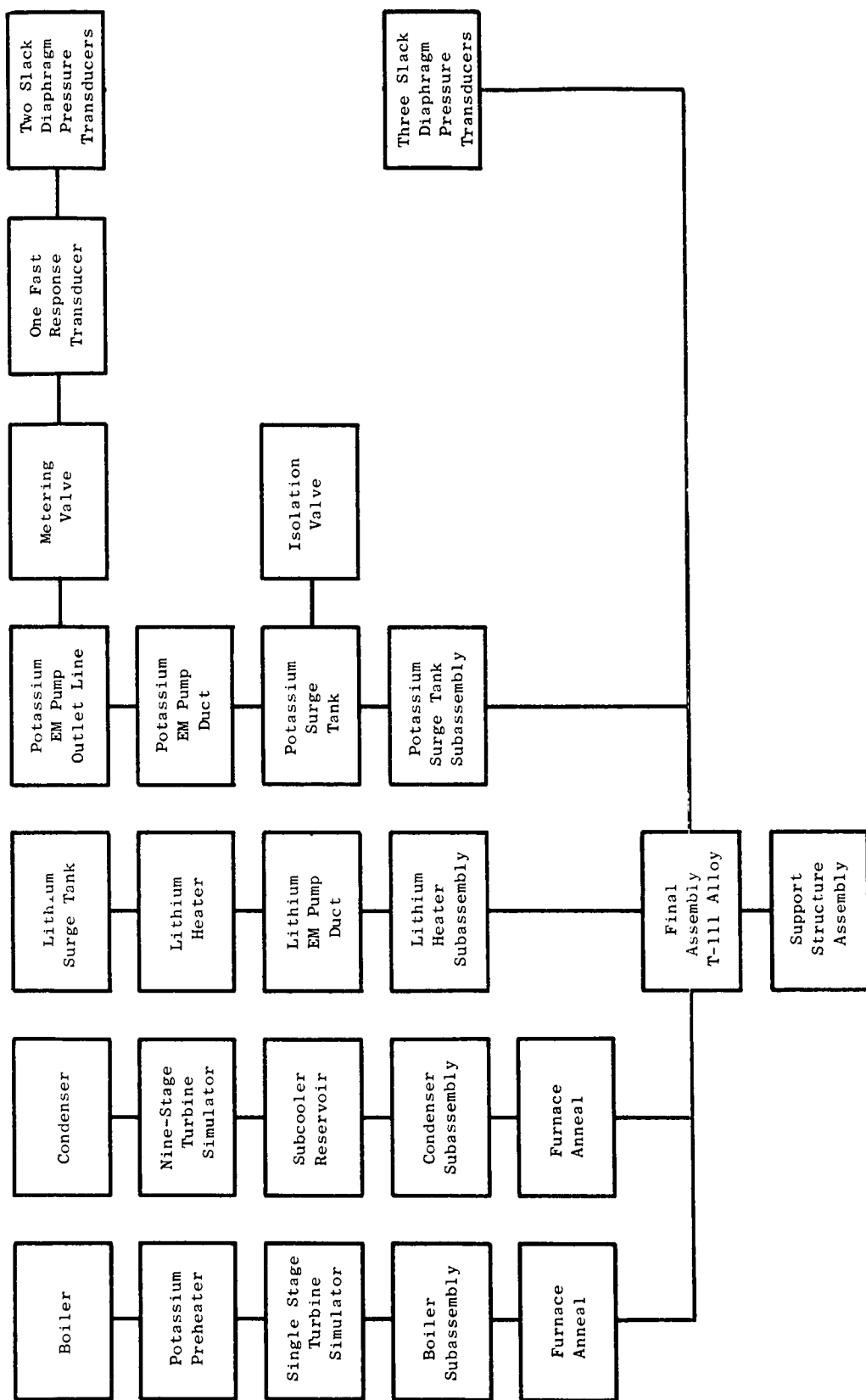


Figure VII-1. - Fabrication sequence for T-111 Rankine system corrosion test loop. All components other than boiler and condenser are furnace annealed prior to welding into major subassemblies. Assembly welds are annealed locally in welding chamber.



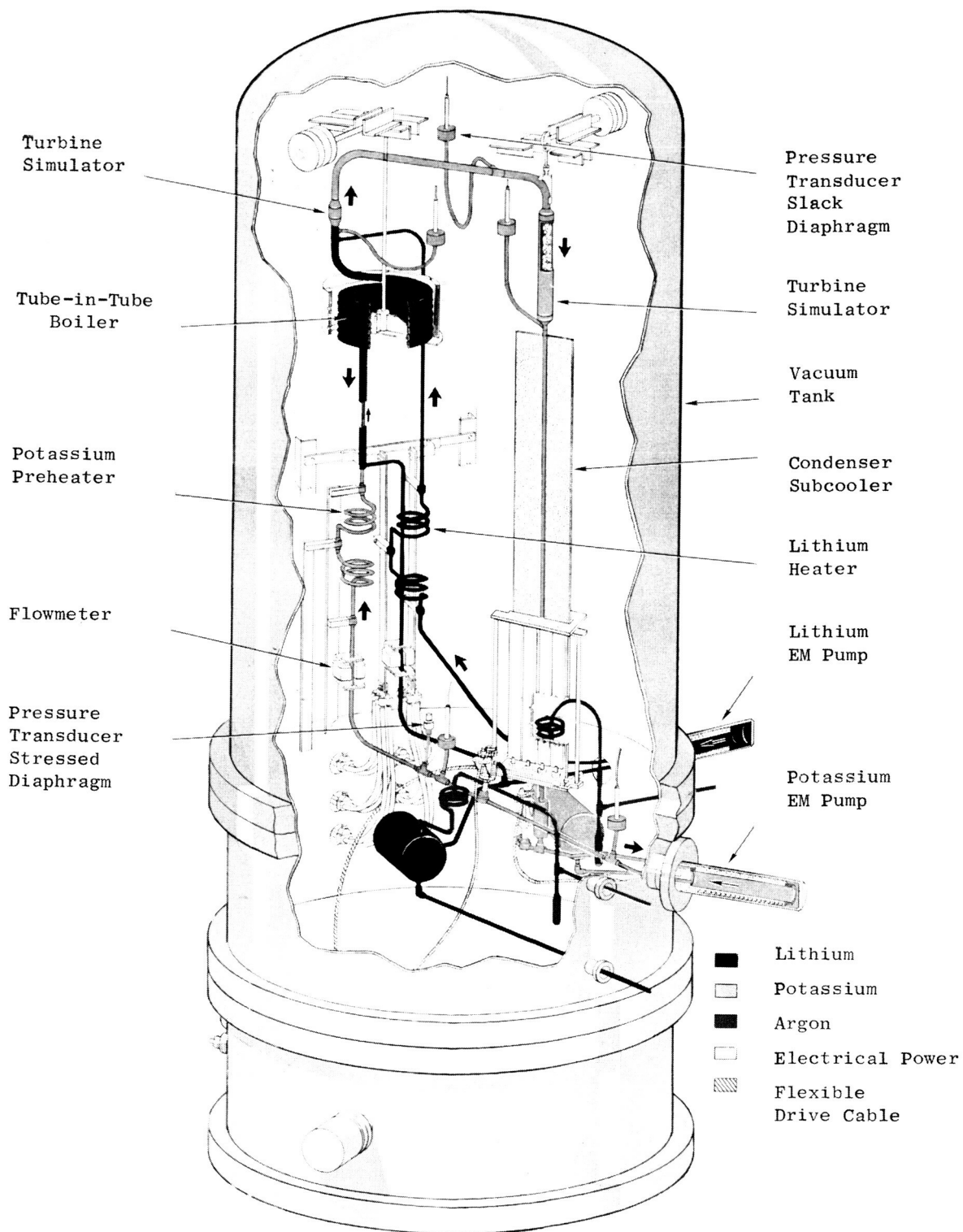


Figure VII-2. - Corrosion loop 1 (T-111).

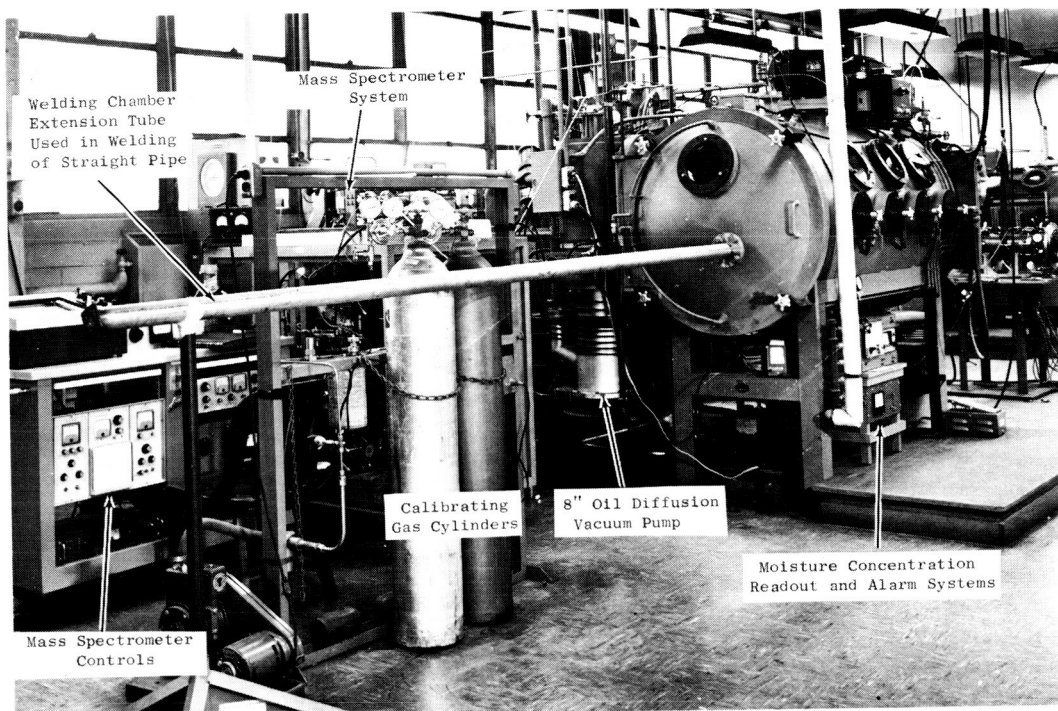


Figure VII-3. - Vacuum-purge inert gas welding chamber (3-ft diam by 6-ft long) with helium supply and purity control system showing pipe welding extension tube attached to chamber door.

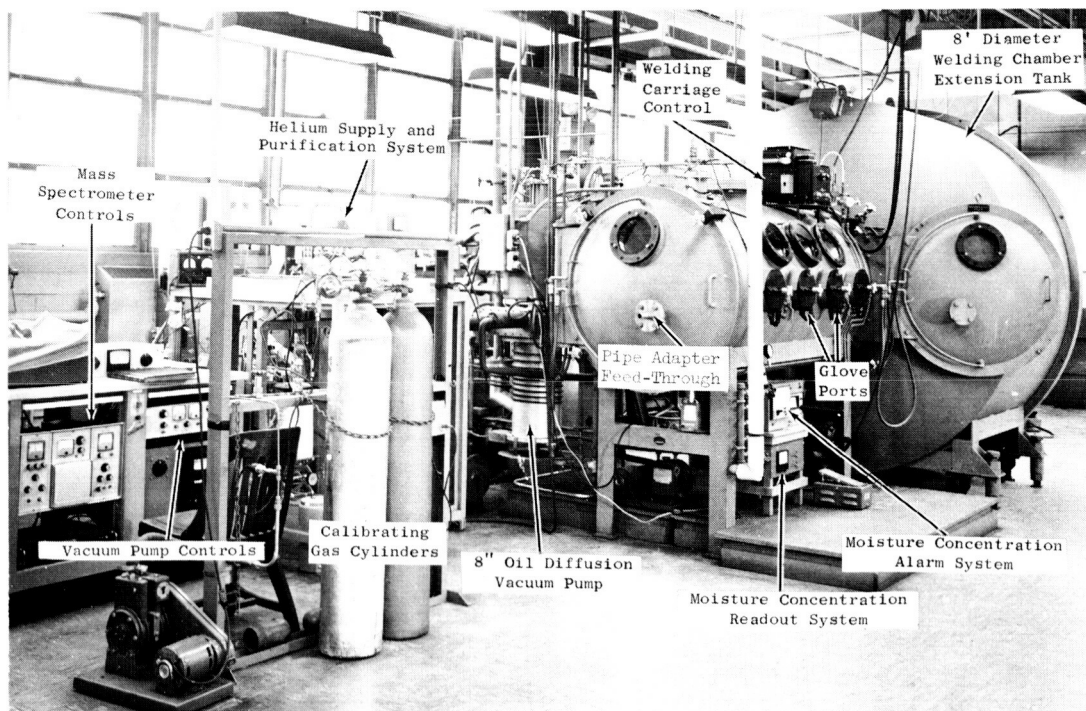


Figure VII-4. - Vacuum-purge inert gas welding chamber and helium purity control system with welding chamber extension tank attached to 3-foot-diameter by 6-foot-long welding chamber.

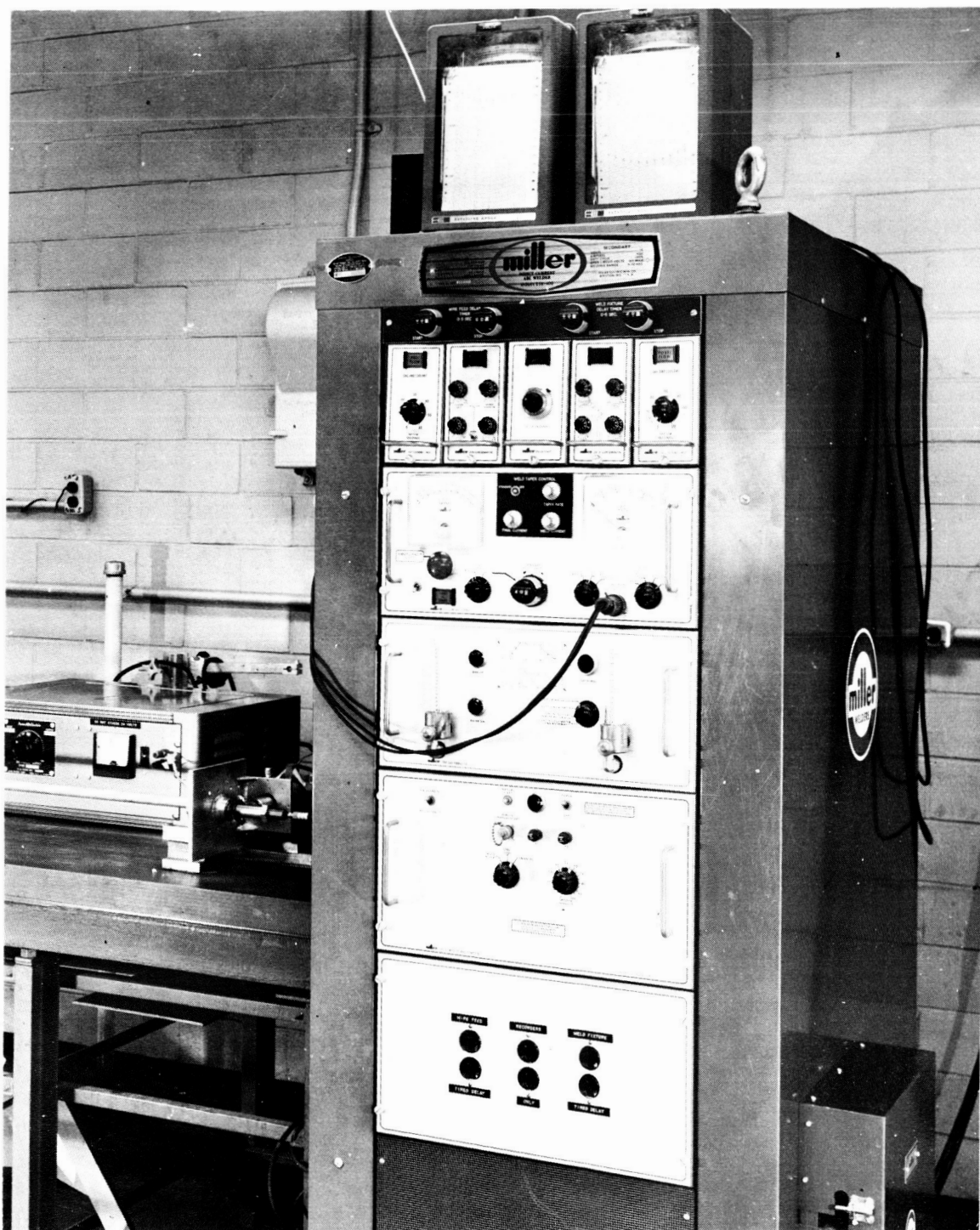


Figure VII-5. - Automatic tungsten inert gas welding machine controlled welding sequence.

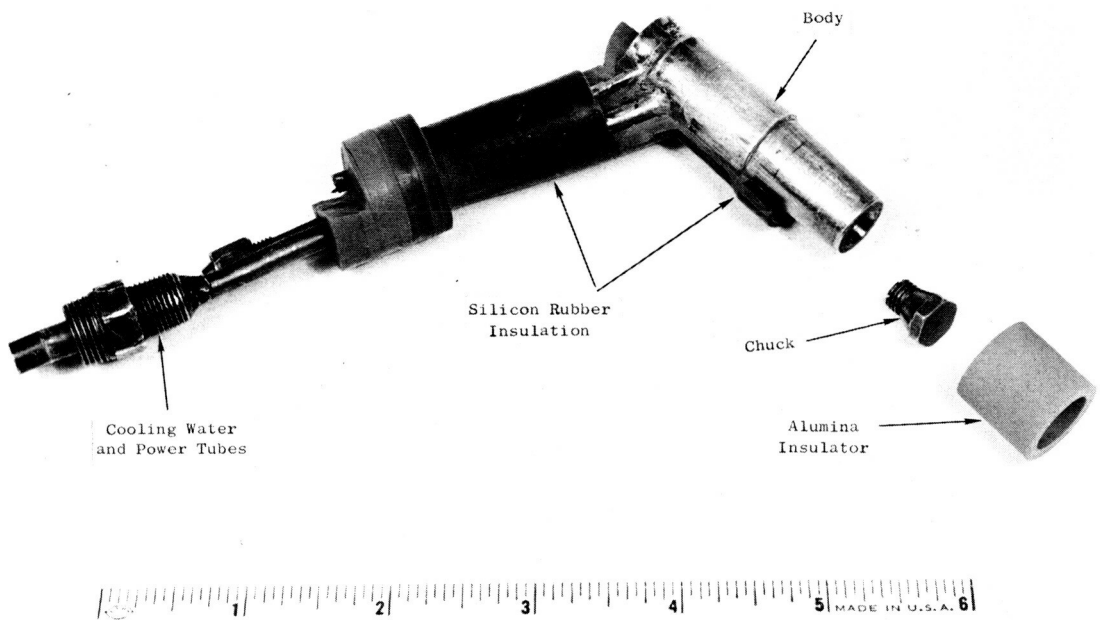


Figure VII-6. - Component parts of water-cooled TIG torch head.

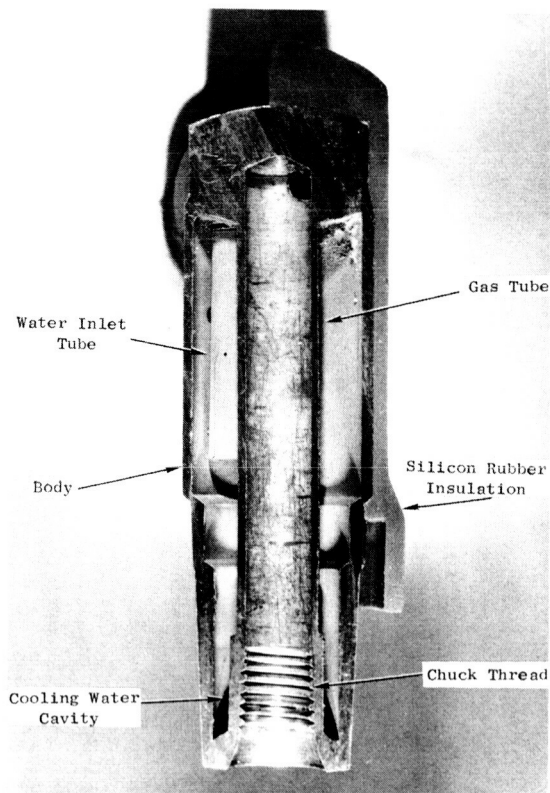


Figure VII-7. - Internal construction of water-cooled TIG welding torch.

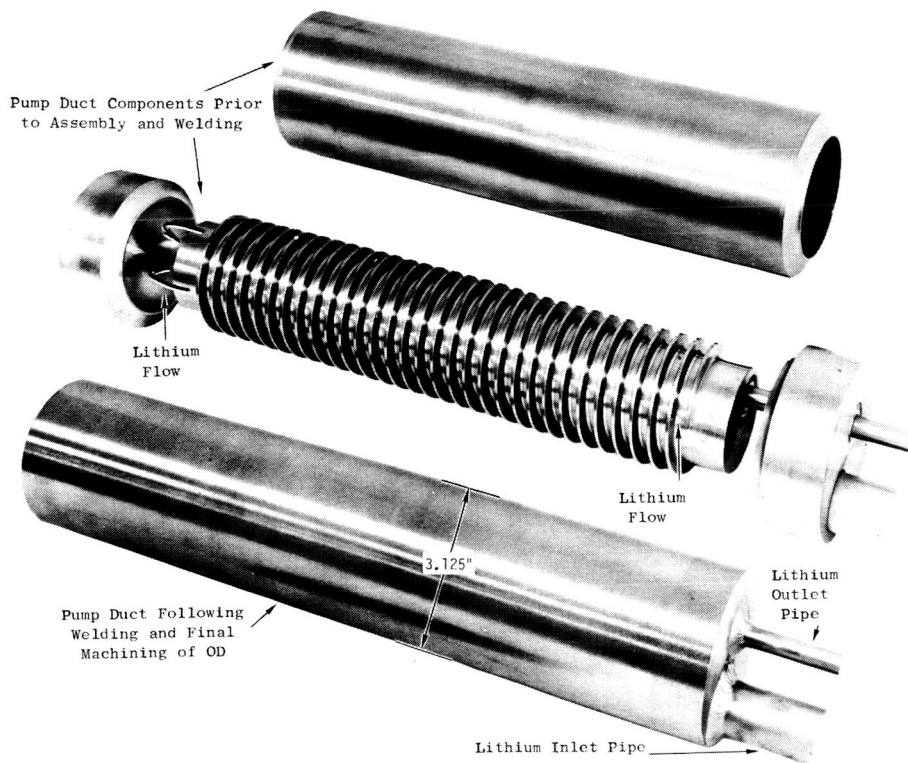
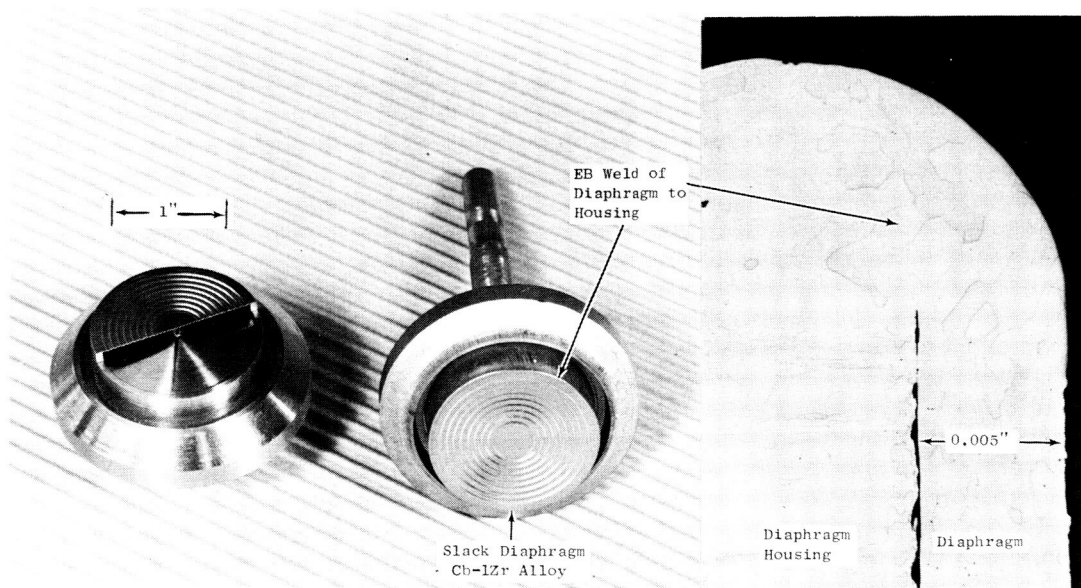


Figure VII-8. - Components of T-111 EM pump duct before and following final welding and machining.



(a) Cutaway showing diaphragm and housing construction.

(b) Completed upper flange.

(c) Cross section of weld.

Figure VII-9. - Slack diaphragm pressure transducer diaphragm and housing following EB welding.



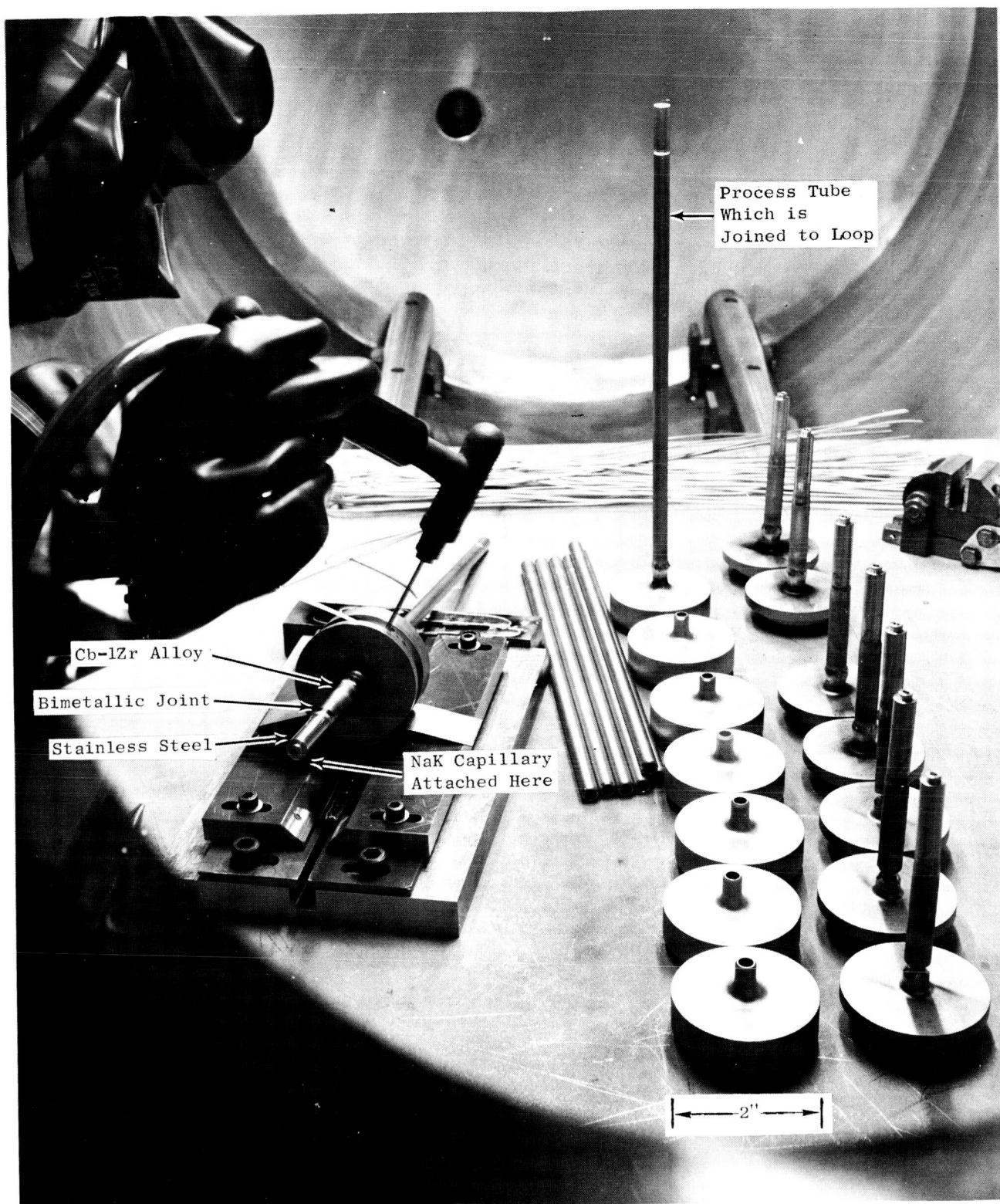


Figure VII-10. - Welding of Cb-1Zr alloy slack diaphragm pressure transducer housing.

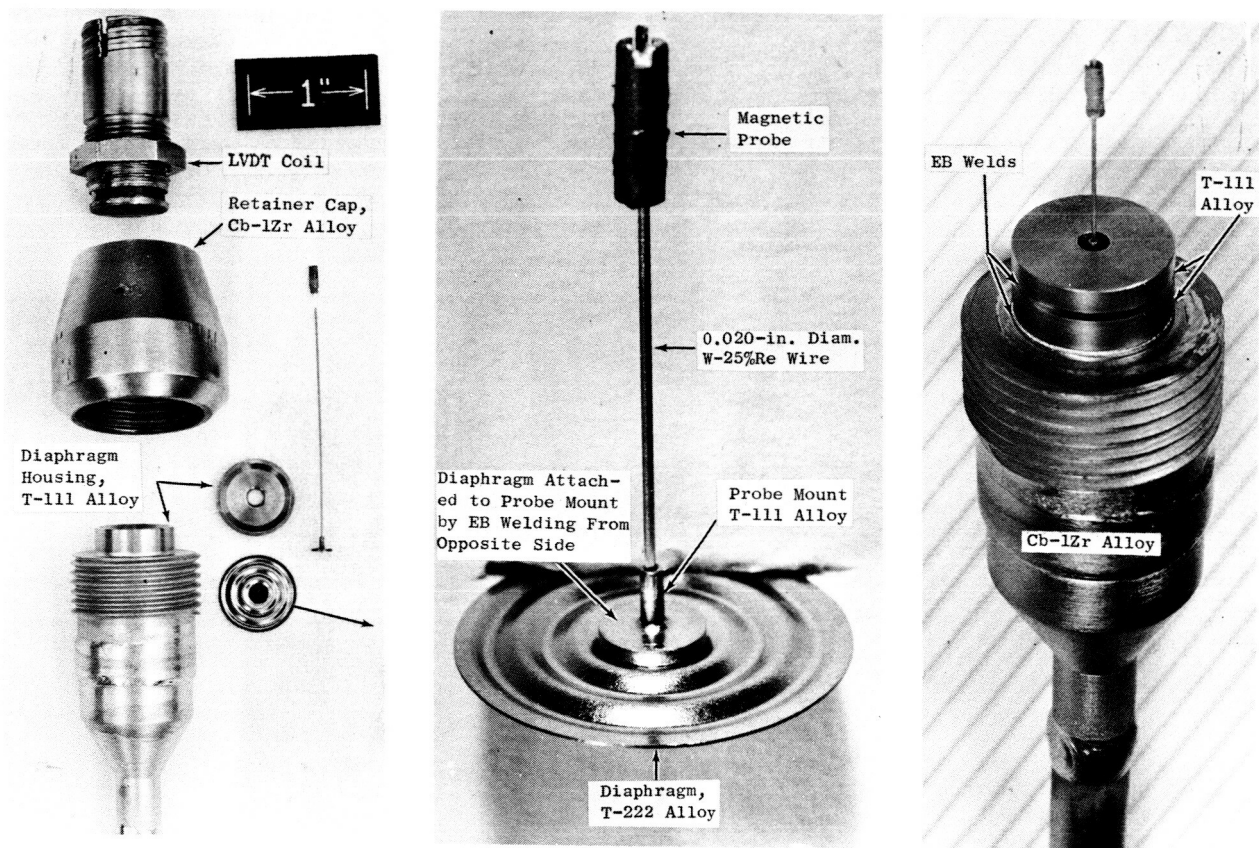


Figure VII-11. - Refractory alloy pressure transducer (stressed diaphragm).

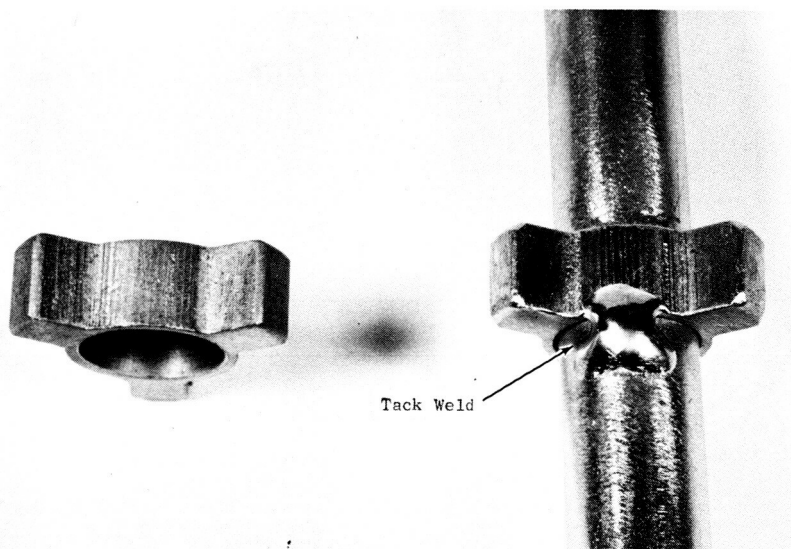


Figure VII-12. - Cb-1Zr boiler tube spacer before and following attachment to 0.375-inch Cb-1Zr potassium containment tube by welding.

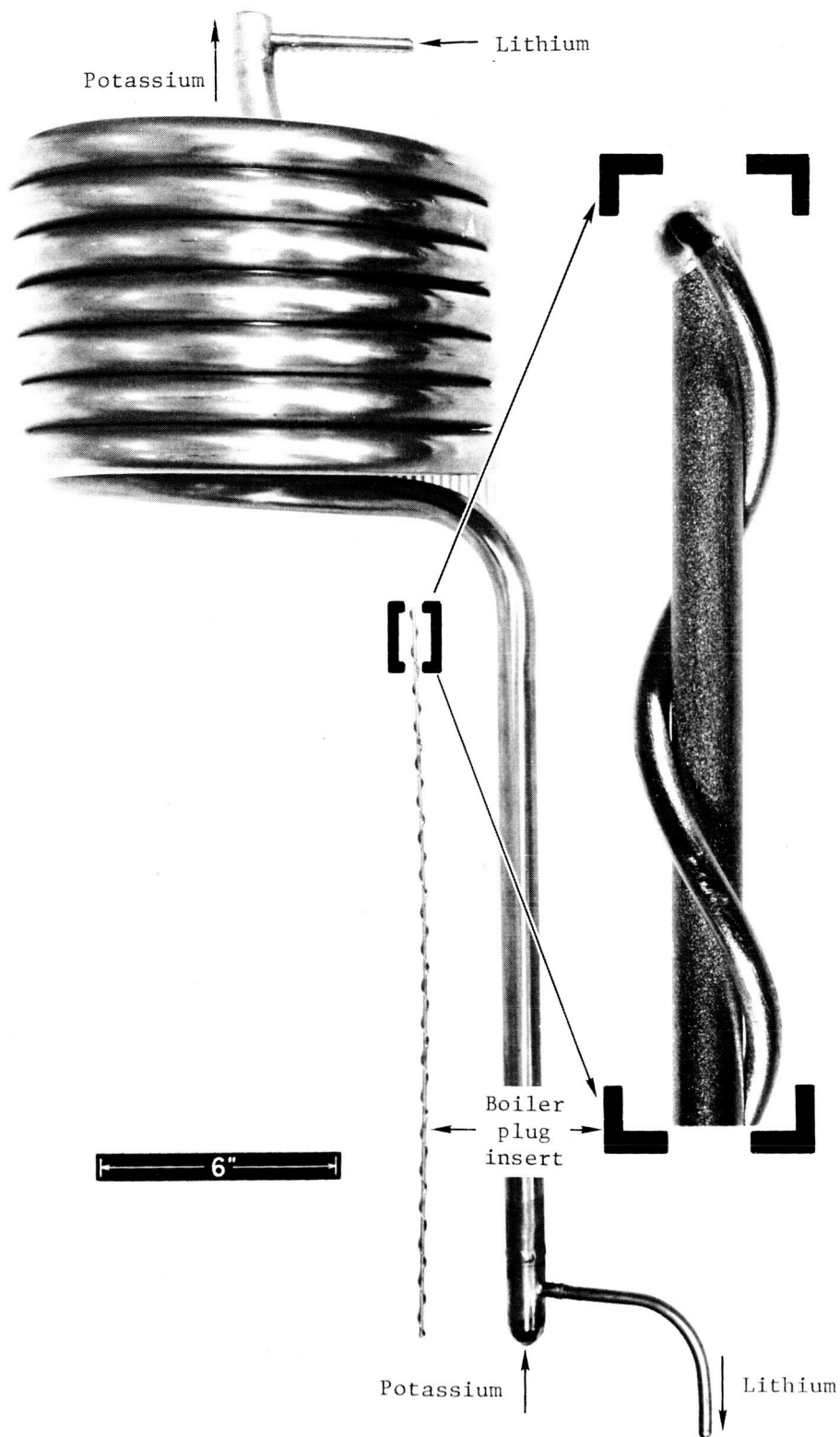


Figure VII-13. - Tube-in-tube boiler of corrosion loop 1 (T-111) prior to insertion of boiler plug.



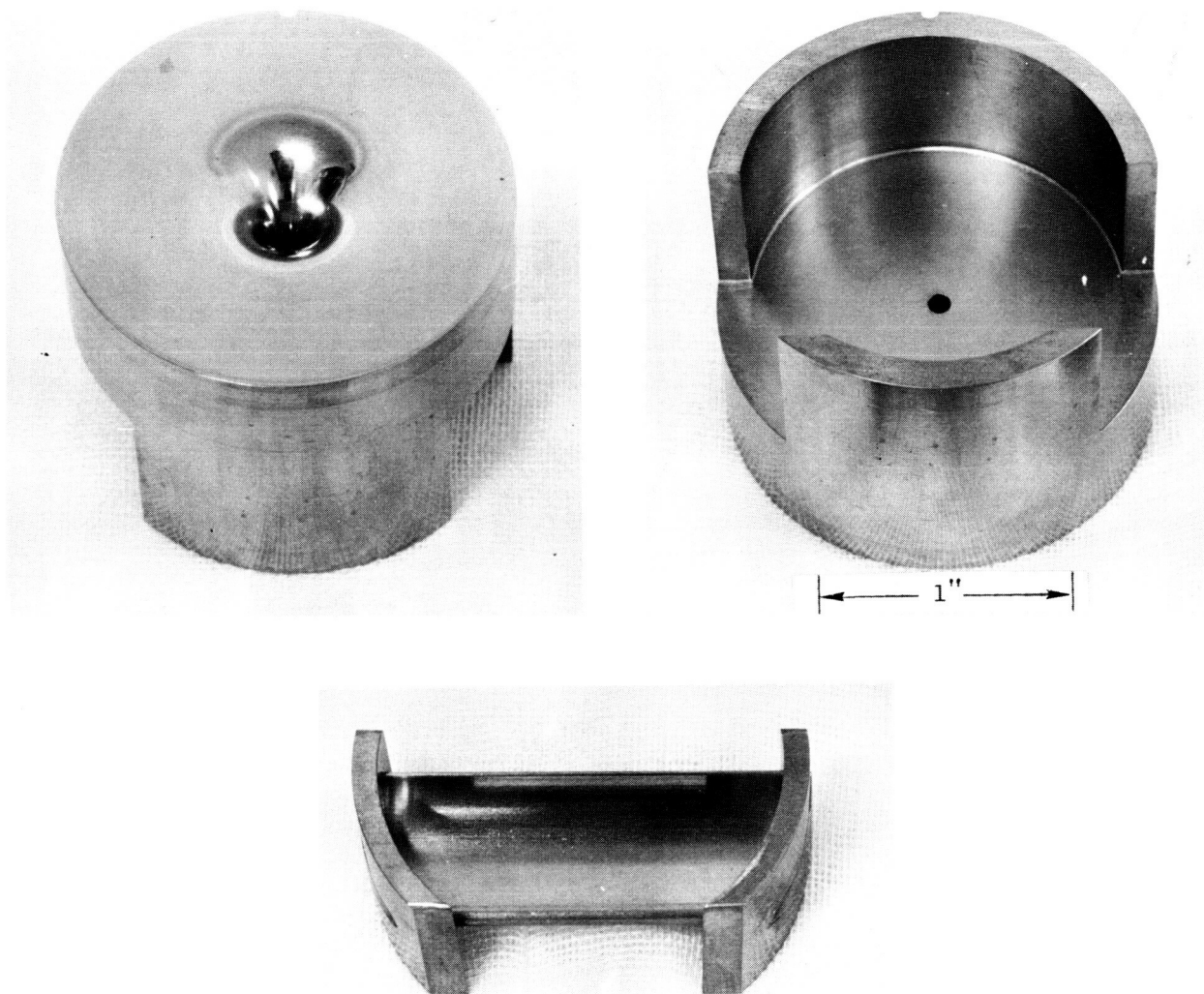


Figure VII-14. - Entrance and exit side of nozzle and blade assembly of second stage (Mo-TZC) of turbine simulator.

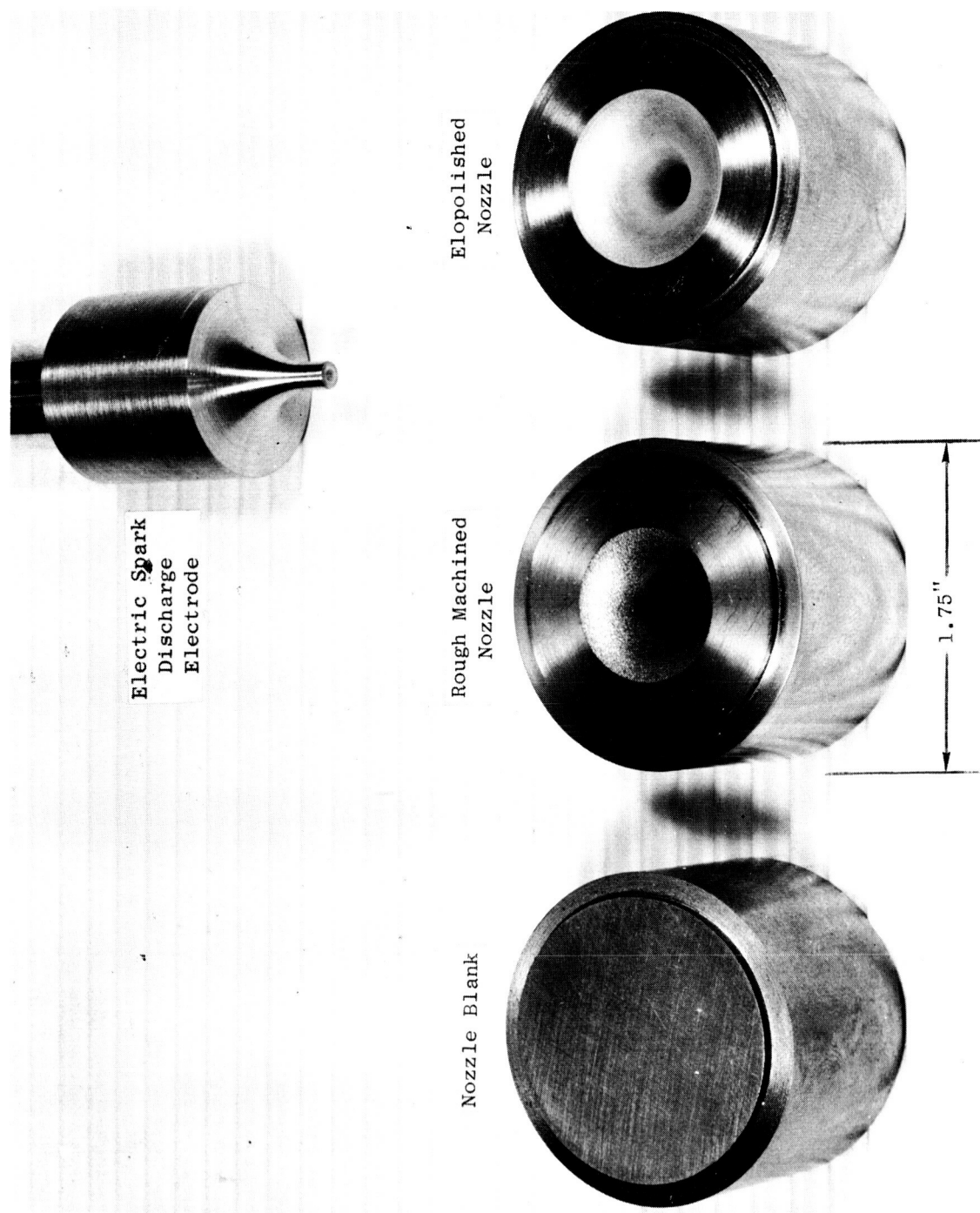


Figure VII-15. - Machining sequence required to produce Mo-TZM alloy nozzle for Cb-1Zr corrosion test loop turbine simulator. Two additional polishing operations are required to produce 8-rms surface finish.

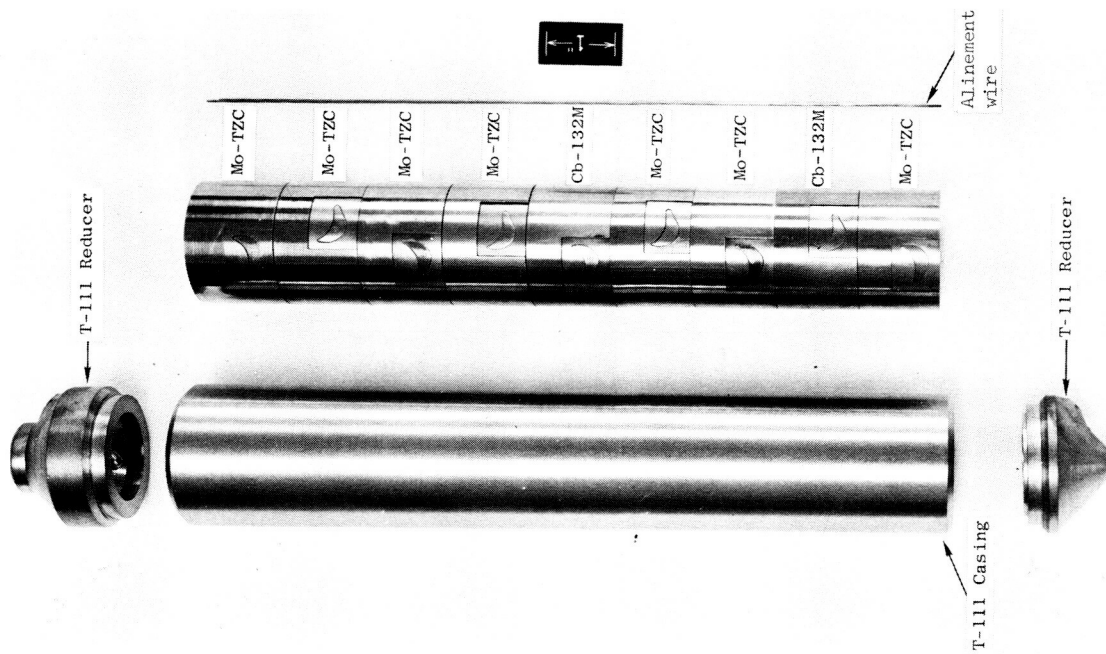


Figure VII-16. - Turbine simulator (stages 2 to 10) of T-111 corrosion loop 1 prior to assembly.

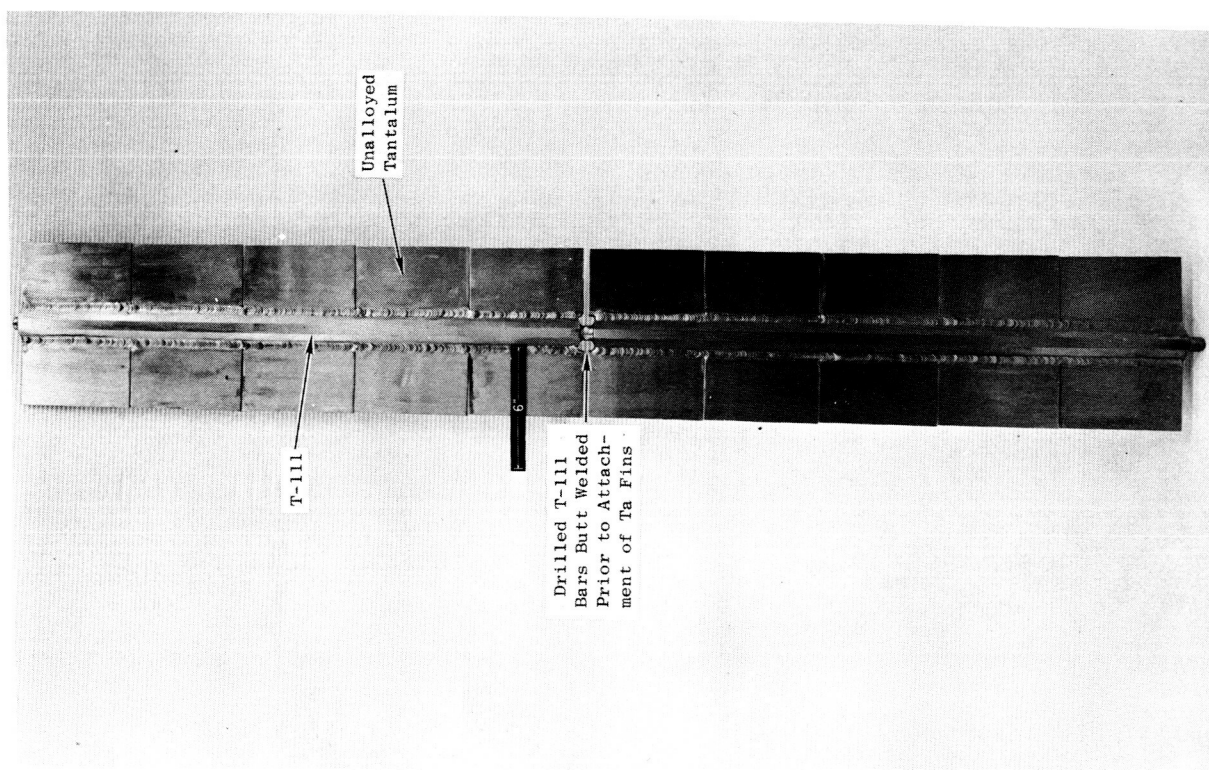


Figure VII-17. - Corrosion loop 1 (T-111) condenser prior to coating of tantalum fins with iron titanate.

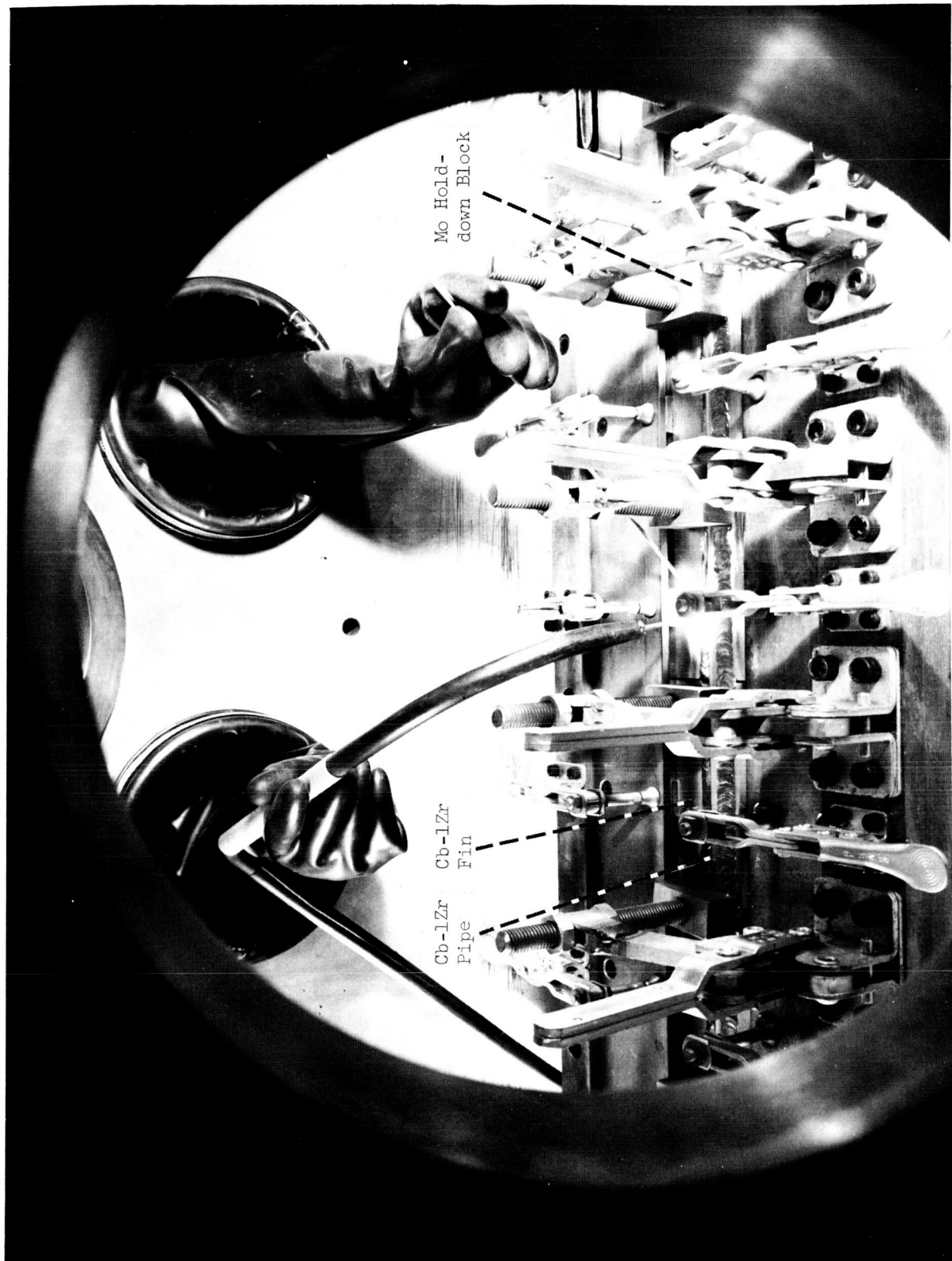


Figure VII-18. - Cb-1Zr corrosion test loop condenser and fixture during welding of fin to condenser pipe.

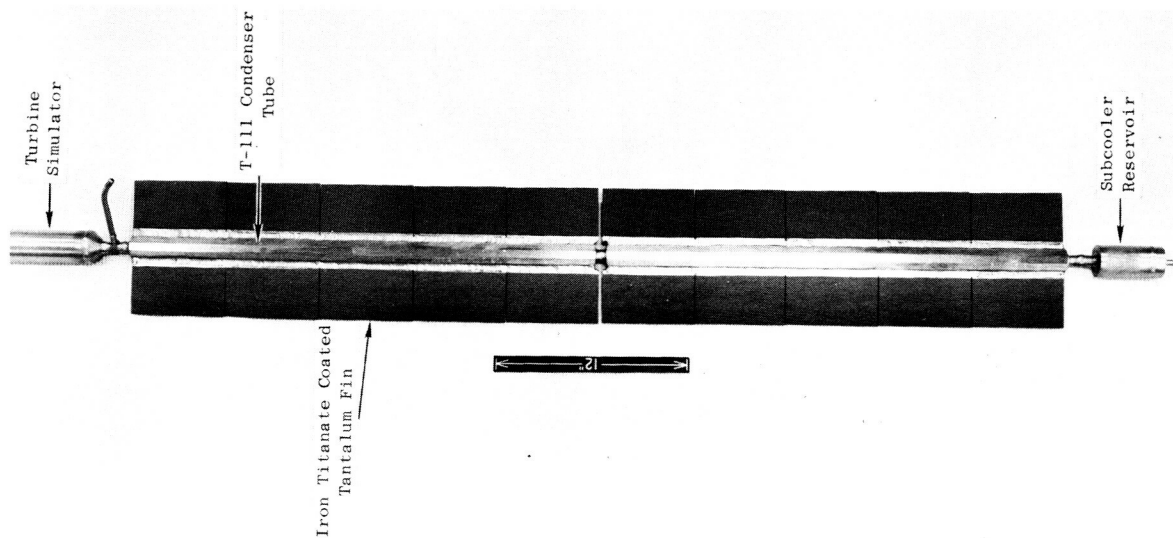


Figure VII-19. - Condenser-turbine-simulator assembly following application of iron titanate coating on tantalum fins.

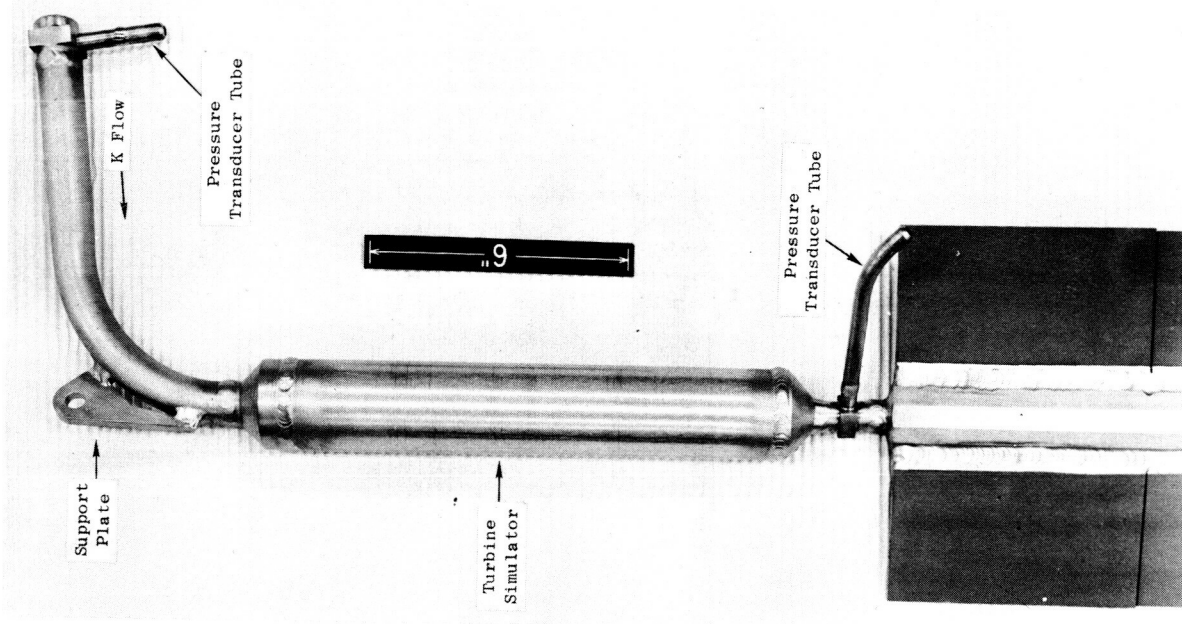


Figure VII-20. - Nine stage turbine simulator and top of condenser.



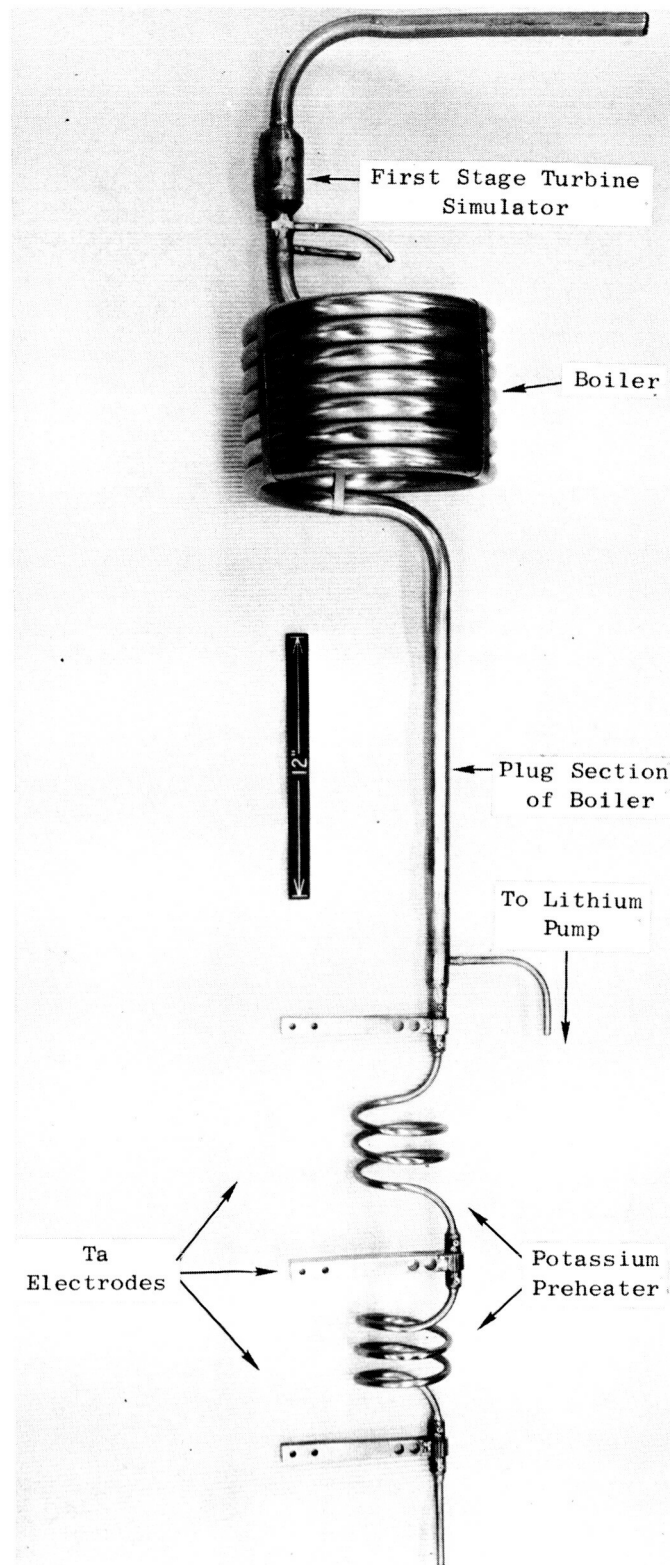


Figure VII-21. - Potassium preheater-boiler-first-stage-turbine-simulator assembly following postweld anneal.

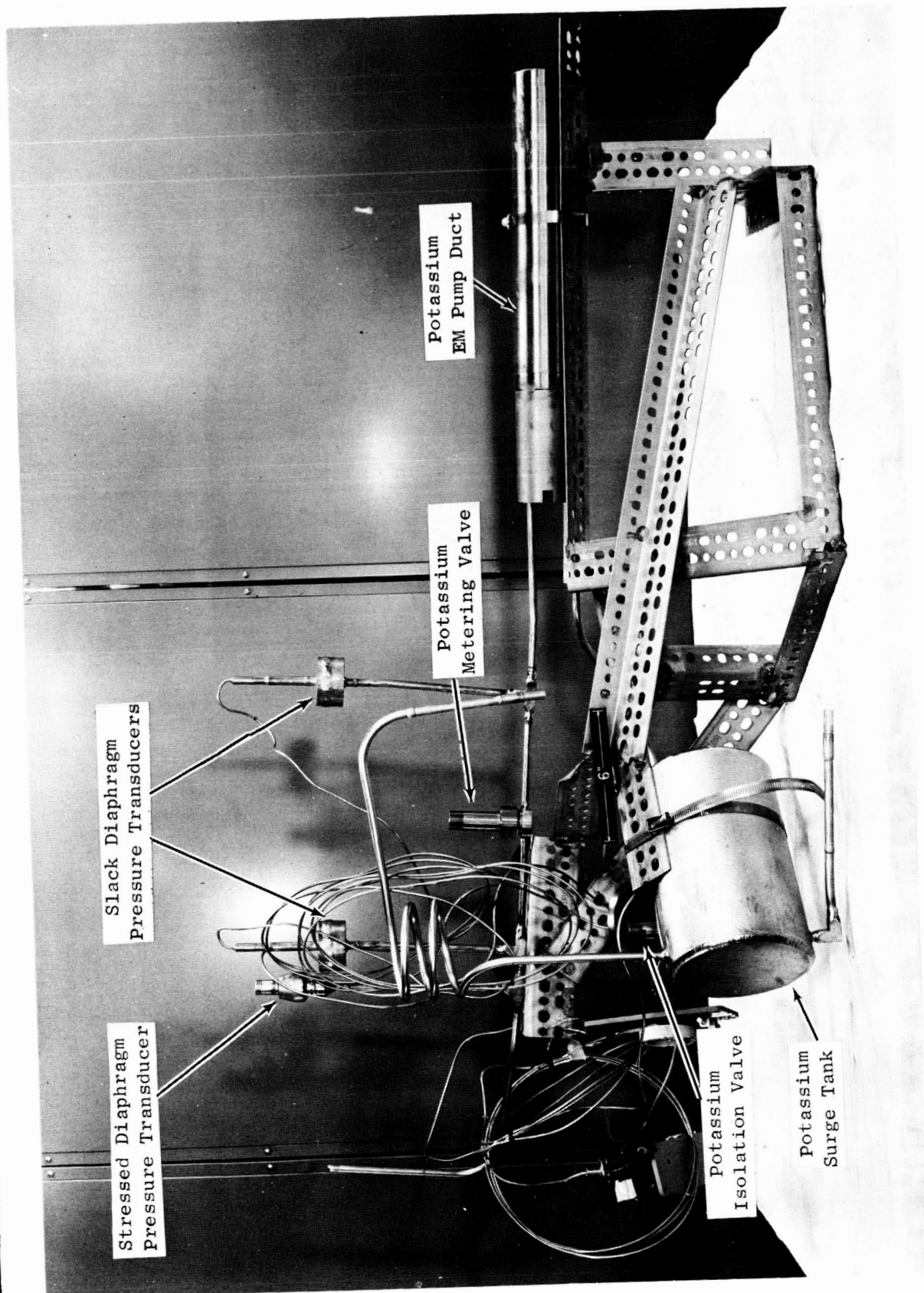


Figure VII-22. - Potassium surge tank and EM pump subassembly of T-111 corrosion test loop mounted on welding fixture.

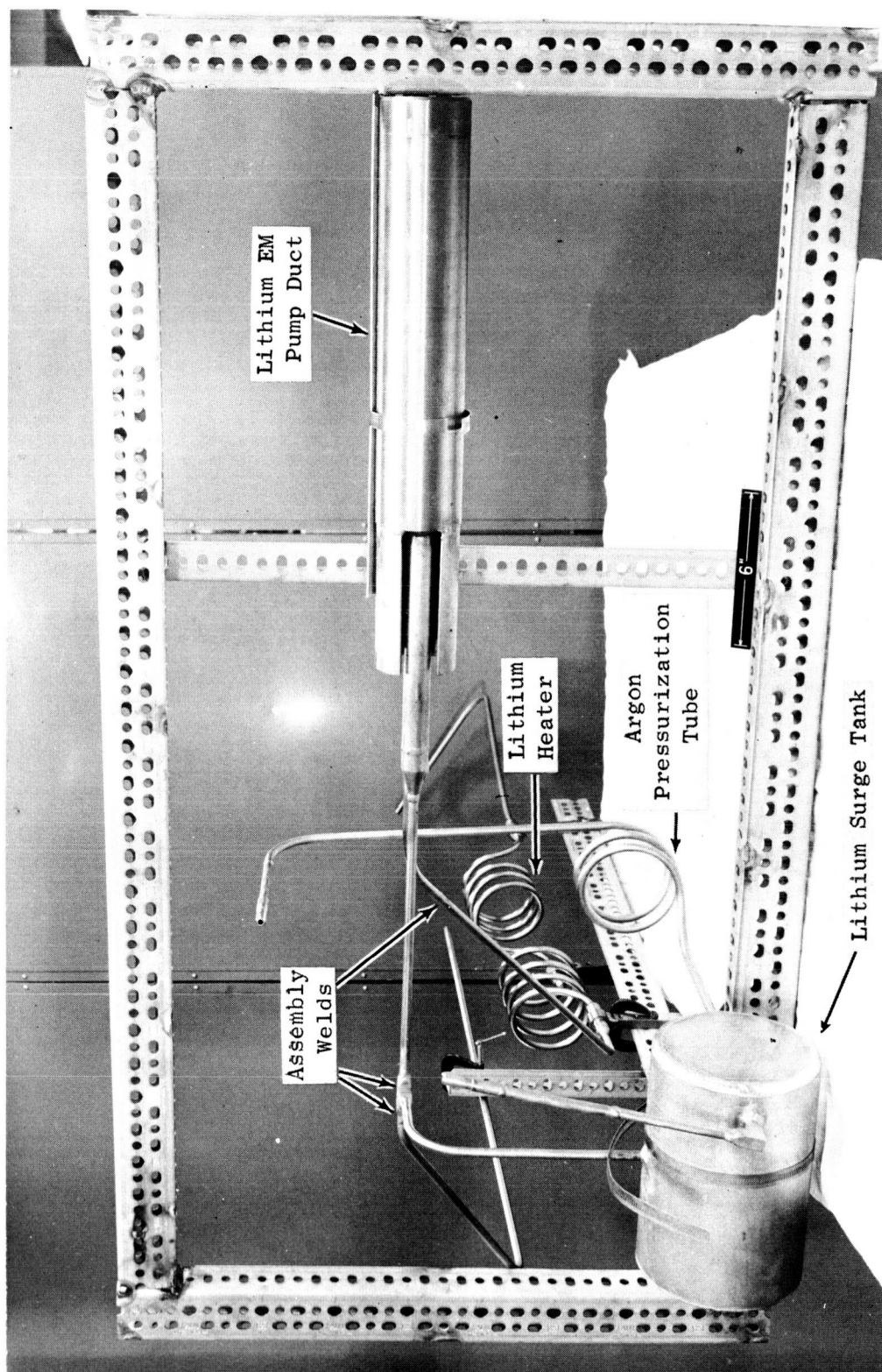


Figure VII-23. - Lithium heater pump subassembly of T-111 corrosion test loop mounted on welding fixture.



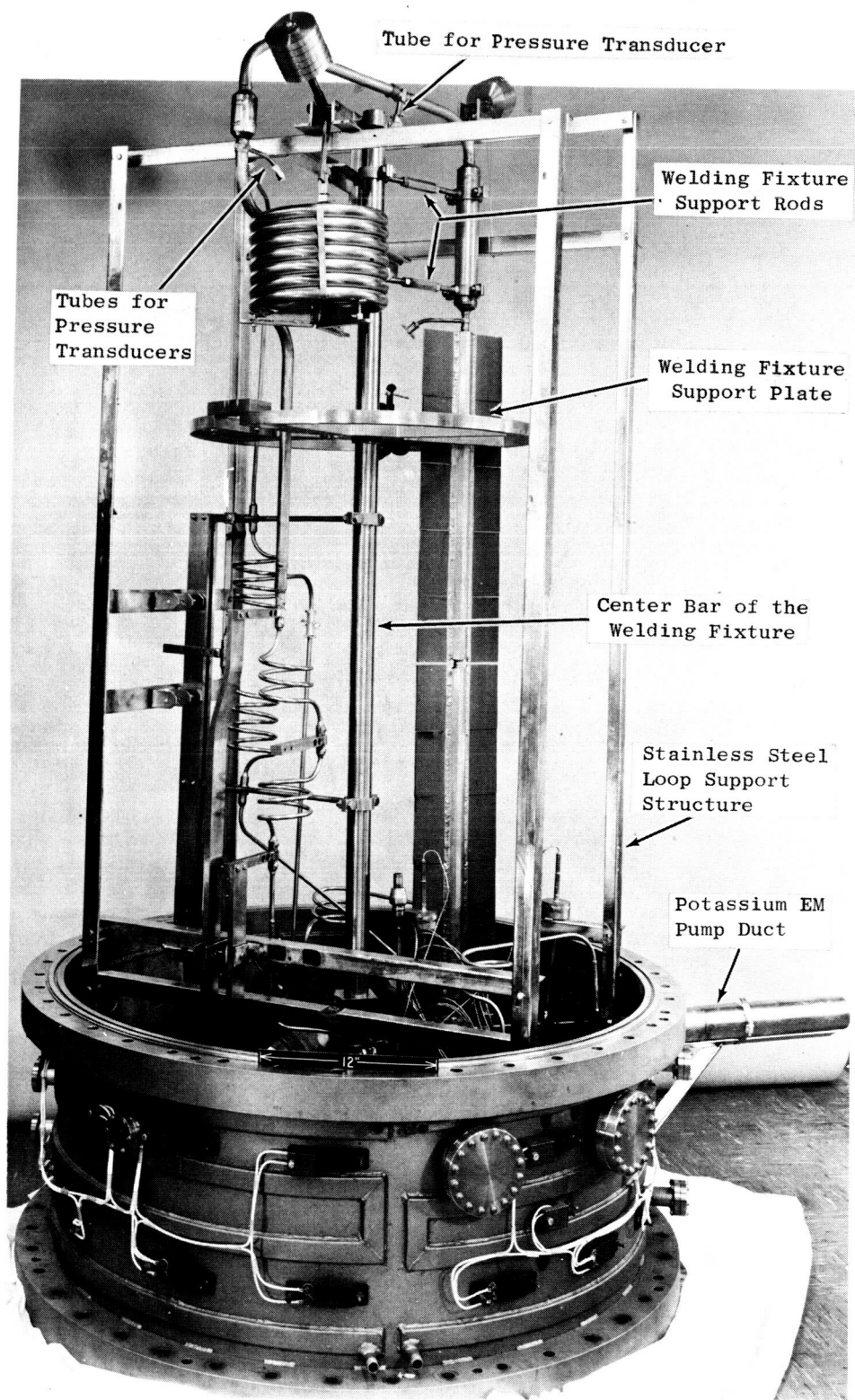


Figure VII-24. - T-111 corrosion test loop and chamber spool piece during transfer of loop from support structure to welding fixture.

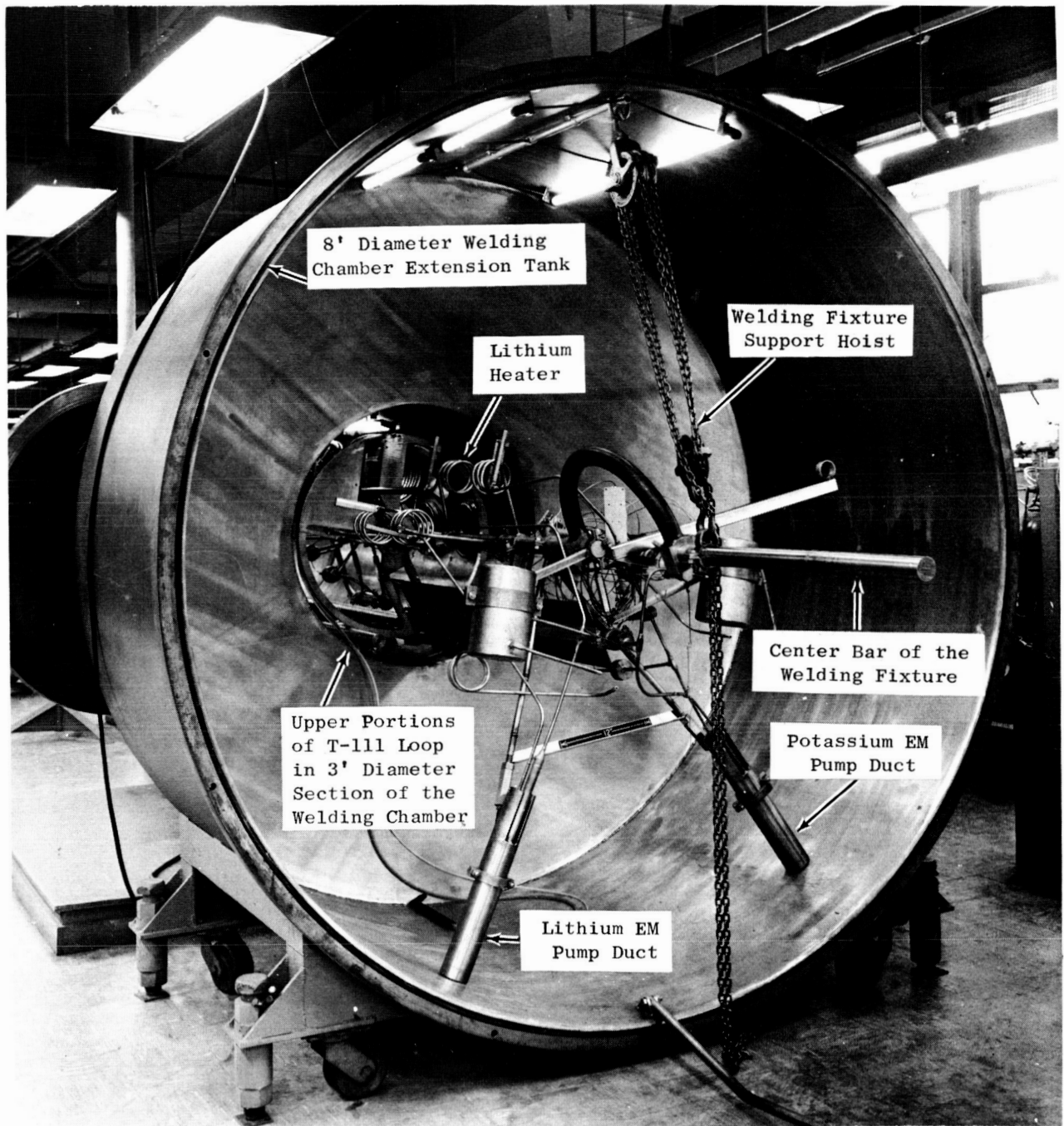


Figure VII-25. - T-111 corrosion test loop mounted on welding fixture prior to final welding and weld heat treatment operation.

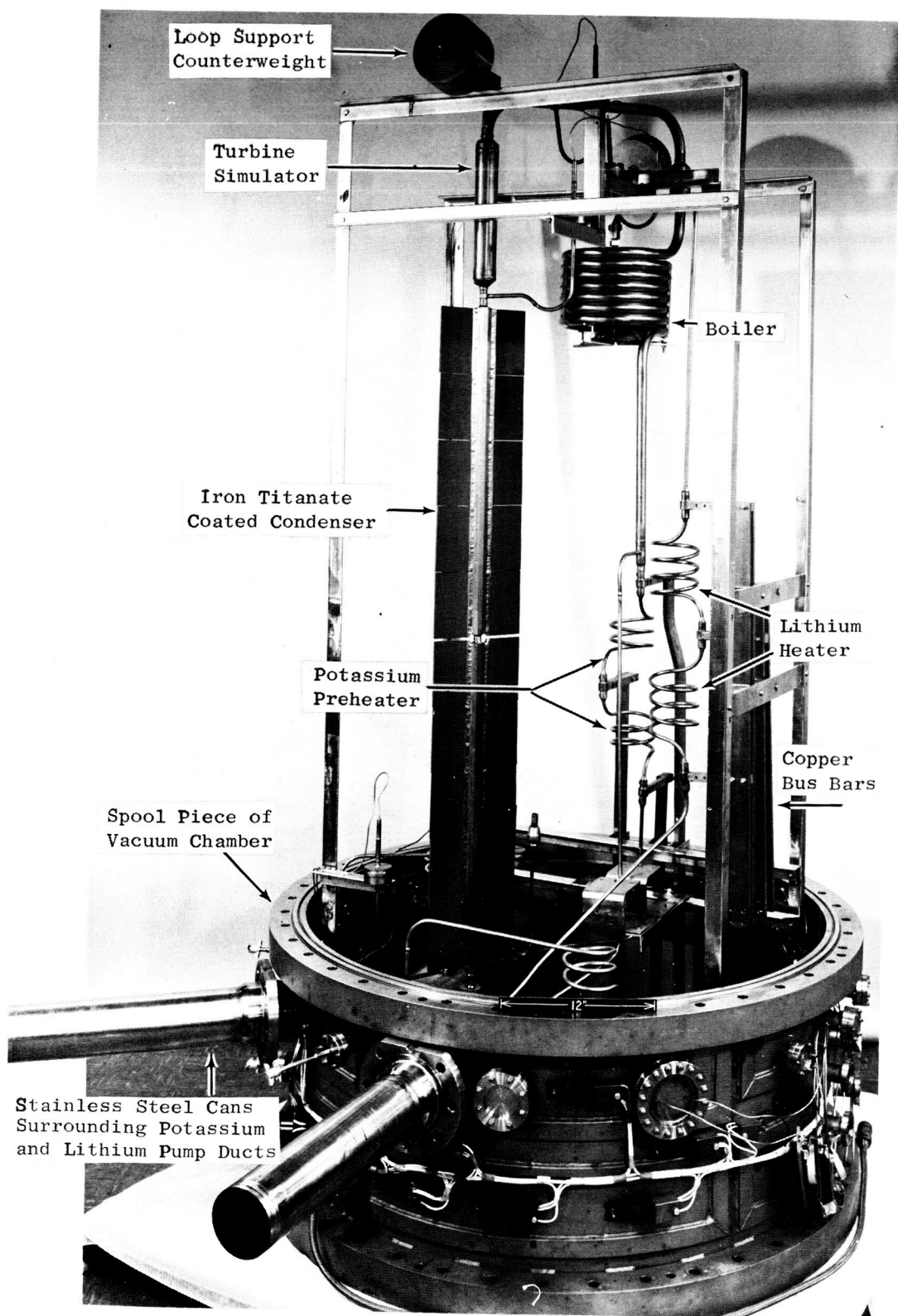


Figure VII-26. - T-111 corrosion test loop and vacuum chamber spool piece following completion of loop fabrication.

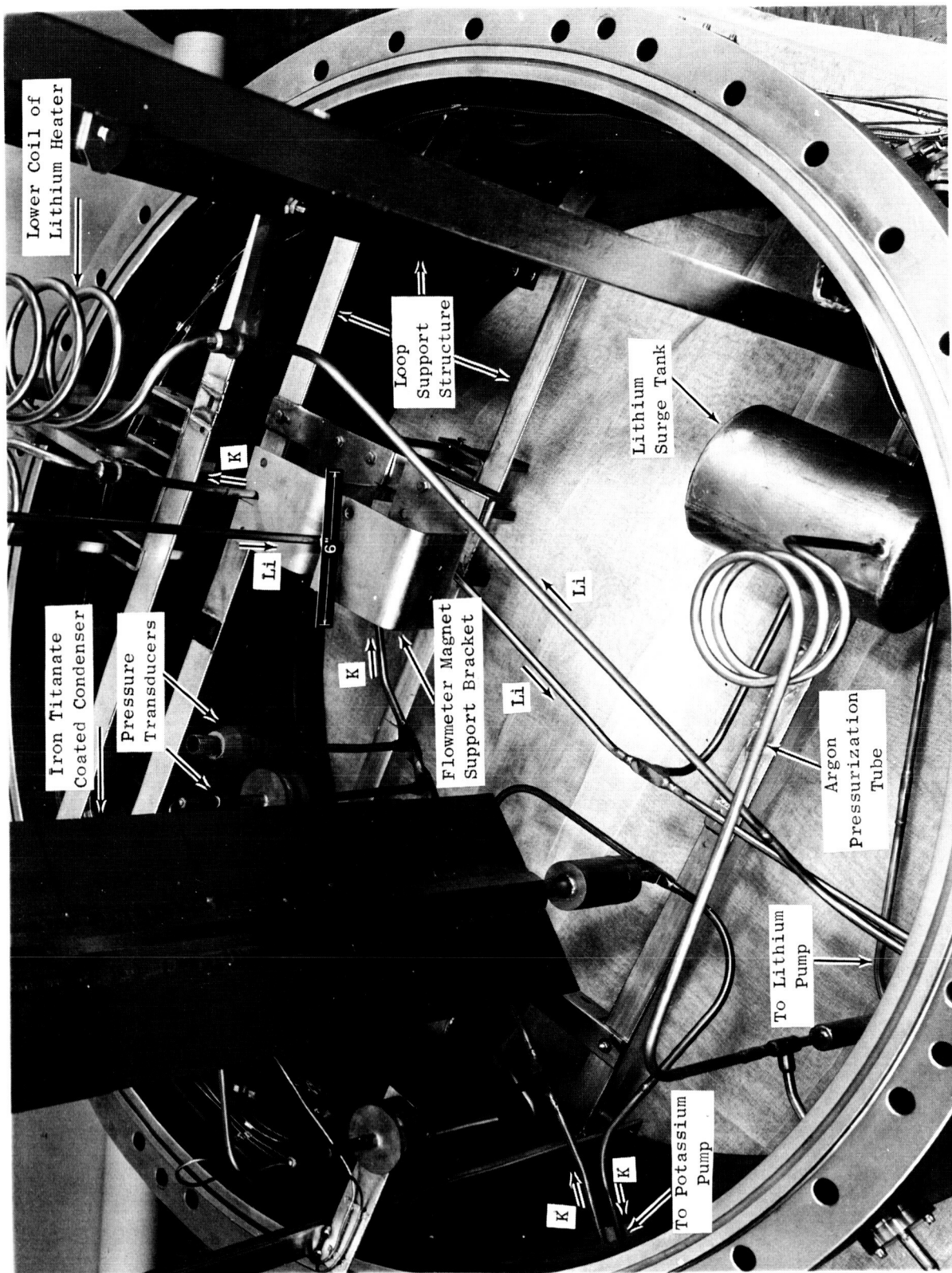


Figure VII-27. - Lower portion of T-111 corrosion test loop following completion of fabrication.



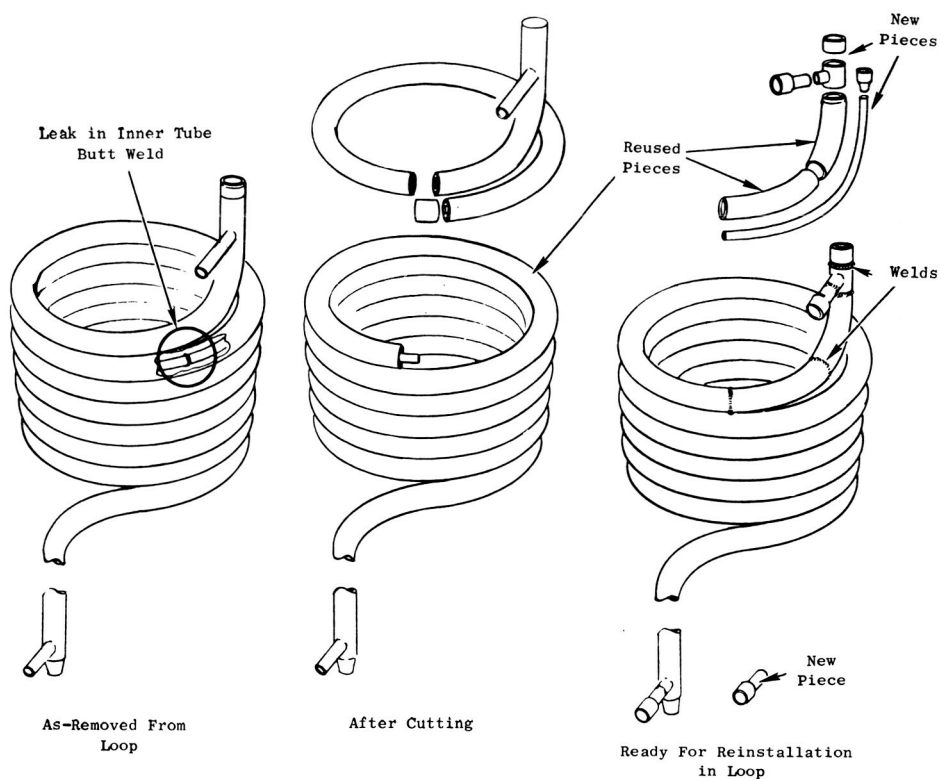
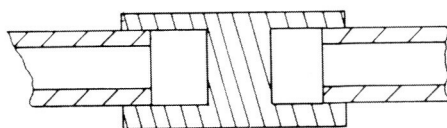


Figure VII-28. - Schematic of T-111 corrosion loop boiler repair.



Schematic Cross Section of Tube-to-Socket Weld Joint

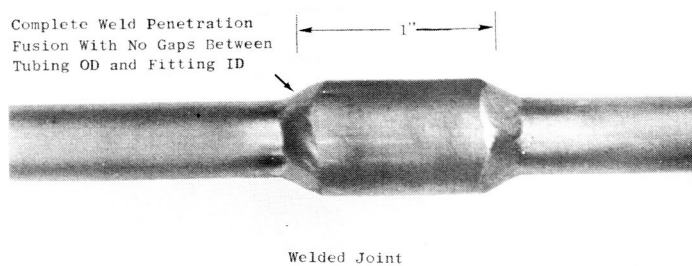
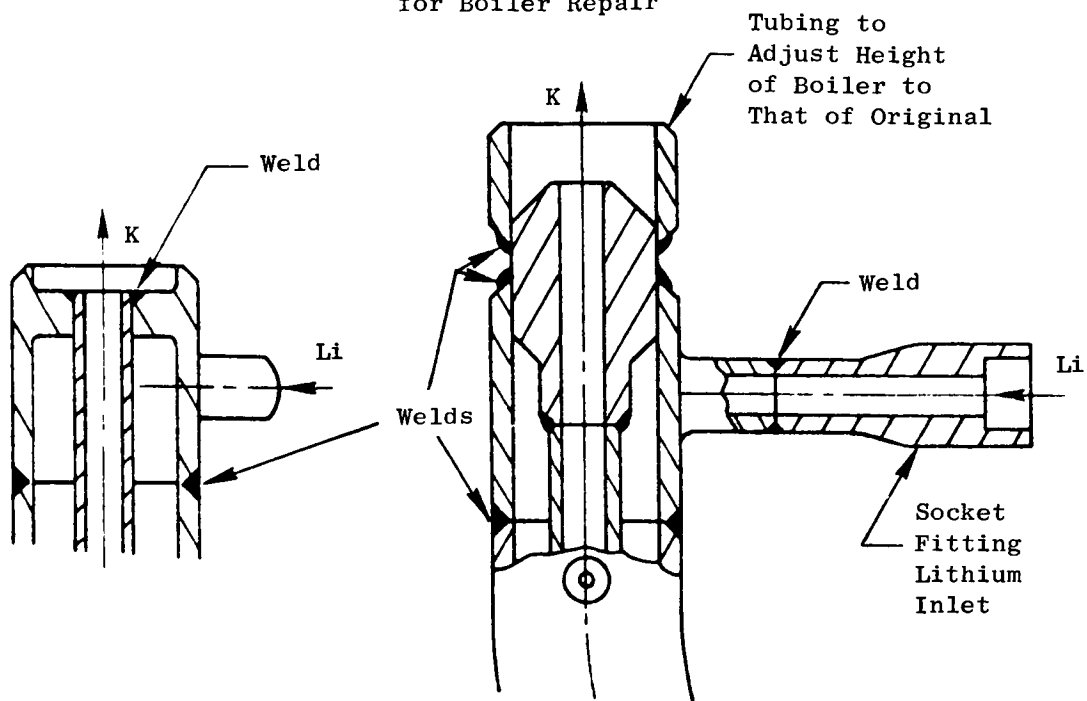


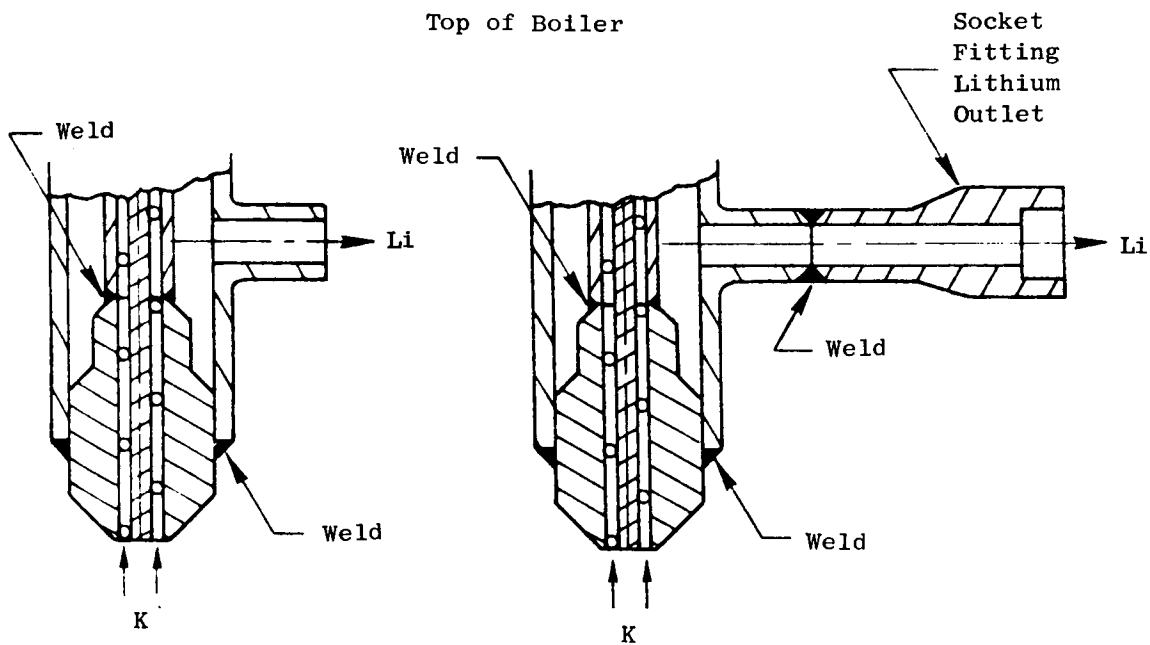
Figure VII-29. - Socket weld fitting specimen to qualify this joint design for T-111 corrosion loop boiler repair and reinstallation.

# Original Design

# Modified Design for Boiler Repair

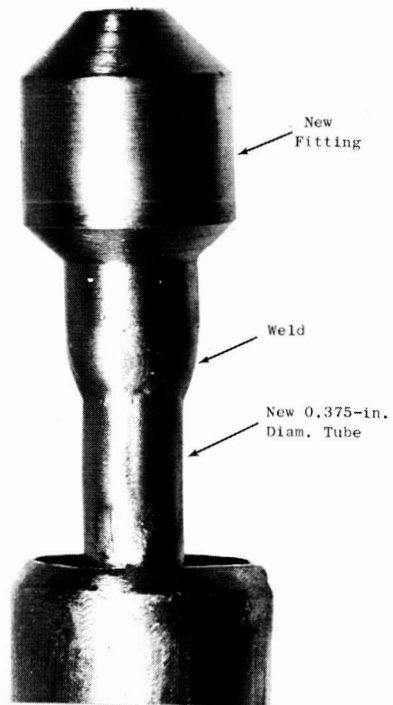
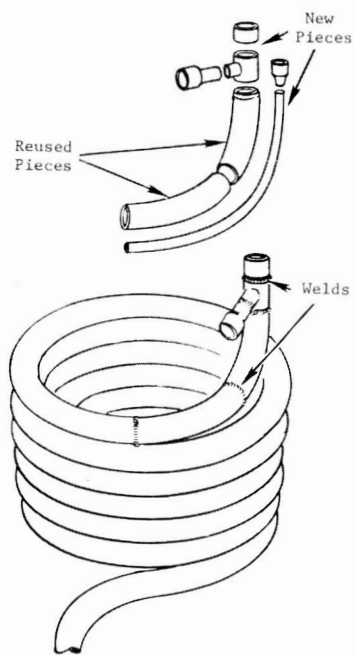


## Top of Boiler



## Bottom of Boiler

Figure VII-30. - Joint design at ends of T-111 corrosion loop boiler.



2"

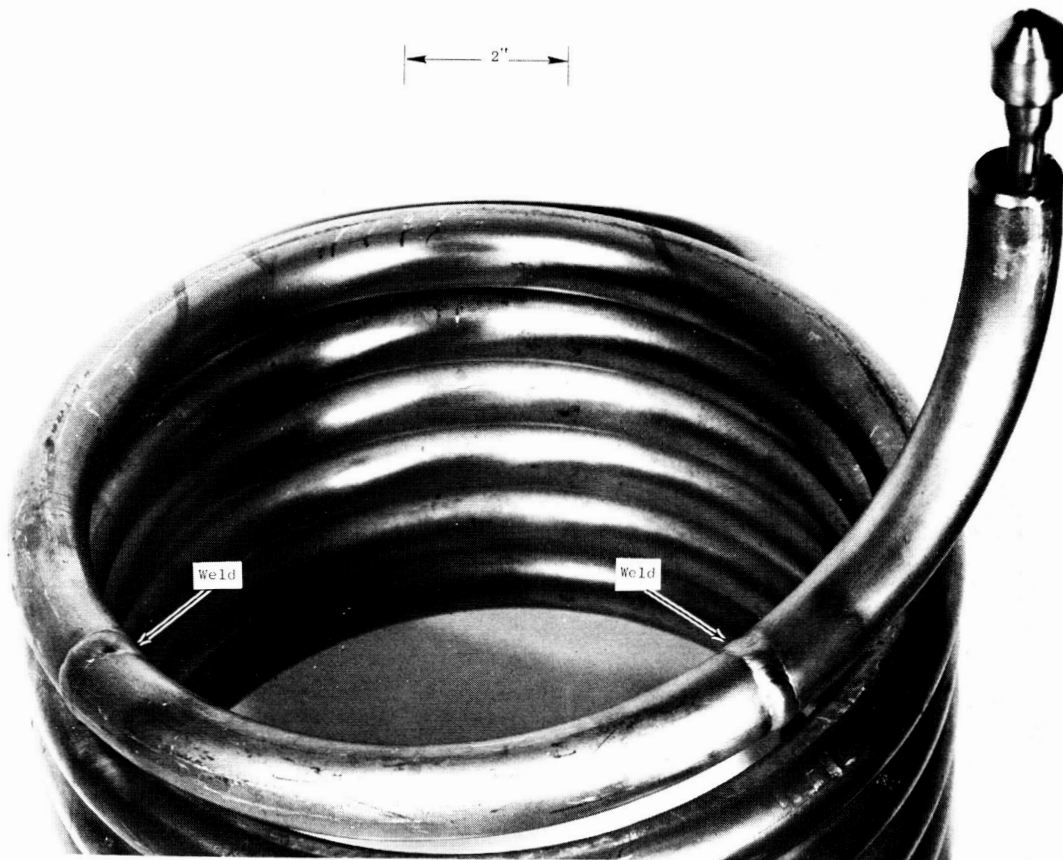


Figure VII-31. - Top of T-111 boiler following initial repair welds.

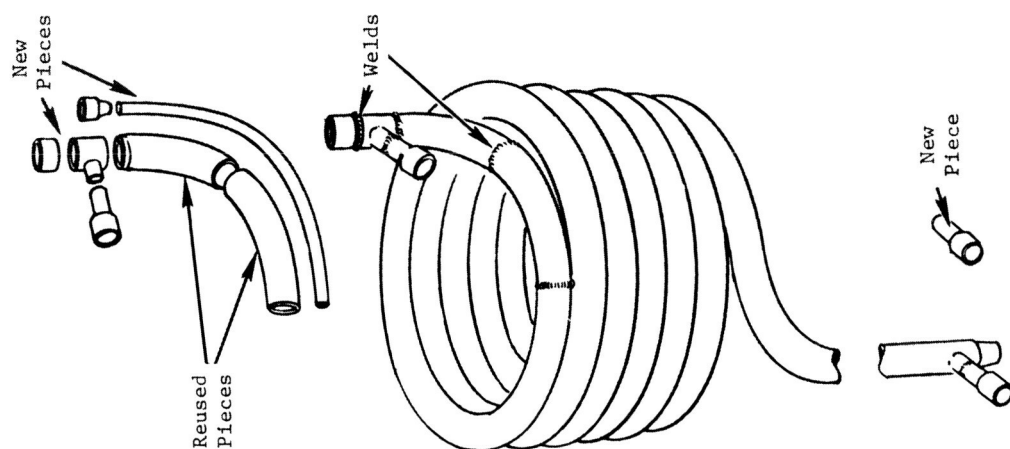


Figure VII-32. - Top of T-111 corrosion loop boiler following final repair welding.



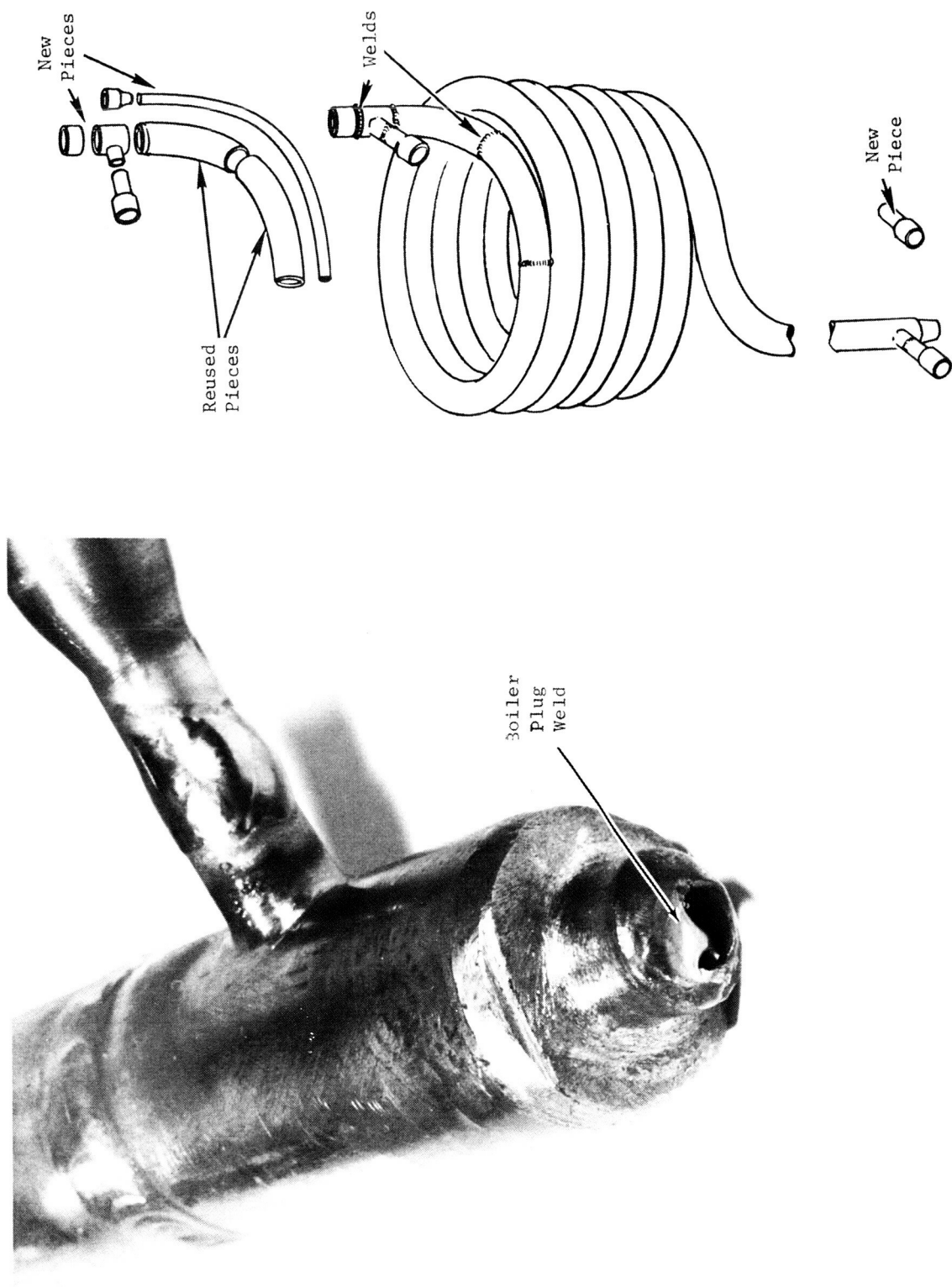
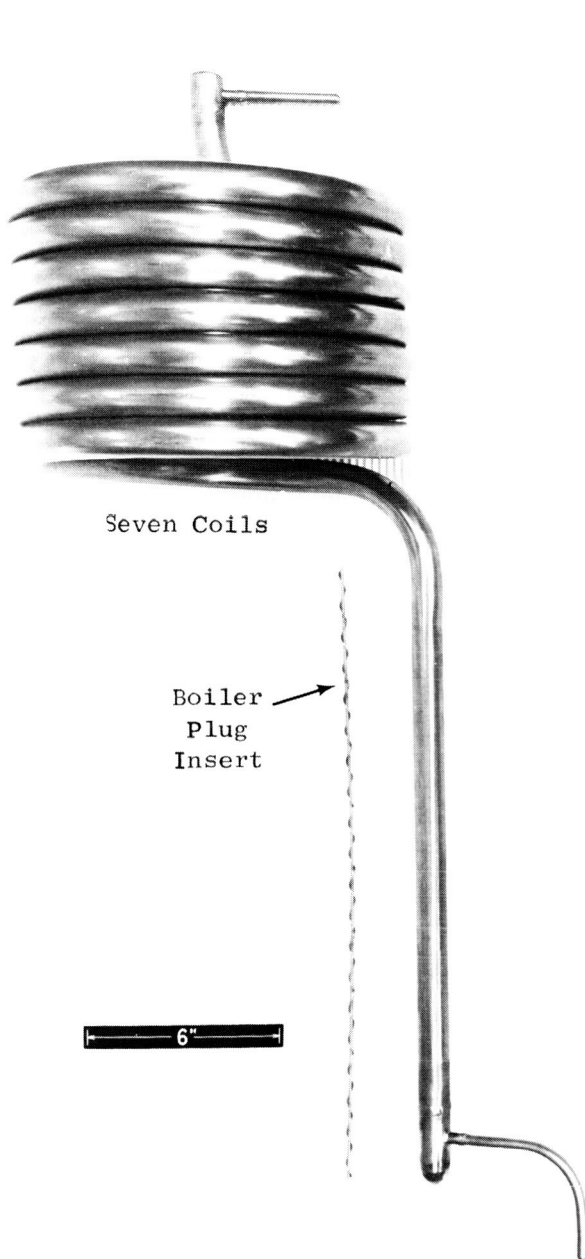


Figure VII-33. - Bottom of T-111 boiler following repair welding.



Following Initial  
Fabrication



Following Repair

Figure VII-34. - T-111 corrosion loop boiler.

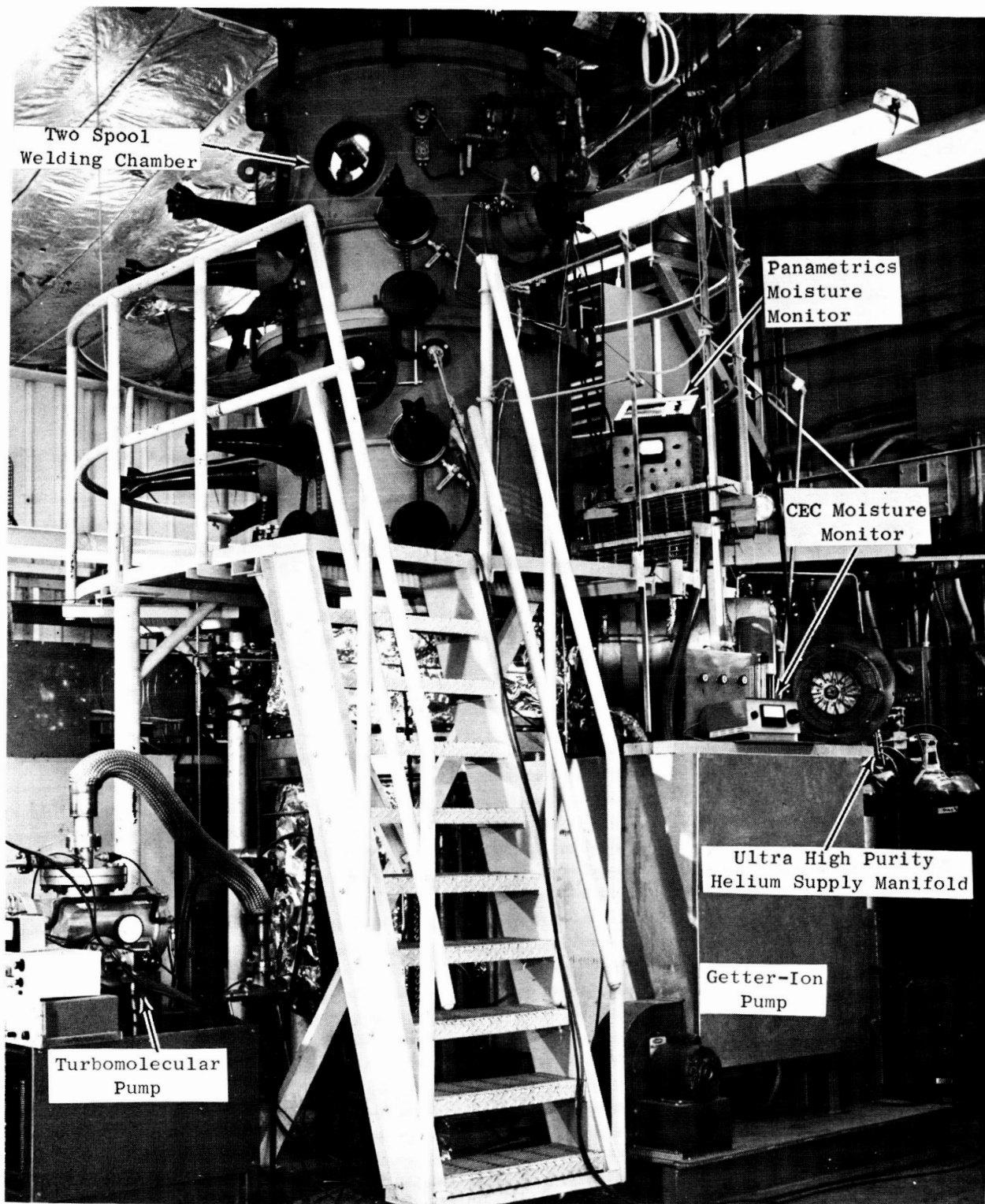


Figure VII-35. - Welding chamber and ancillary instrumentation installed on T-111 Rankine system corrosion test loop facility.

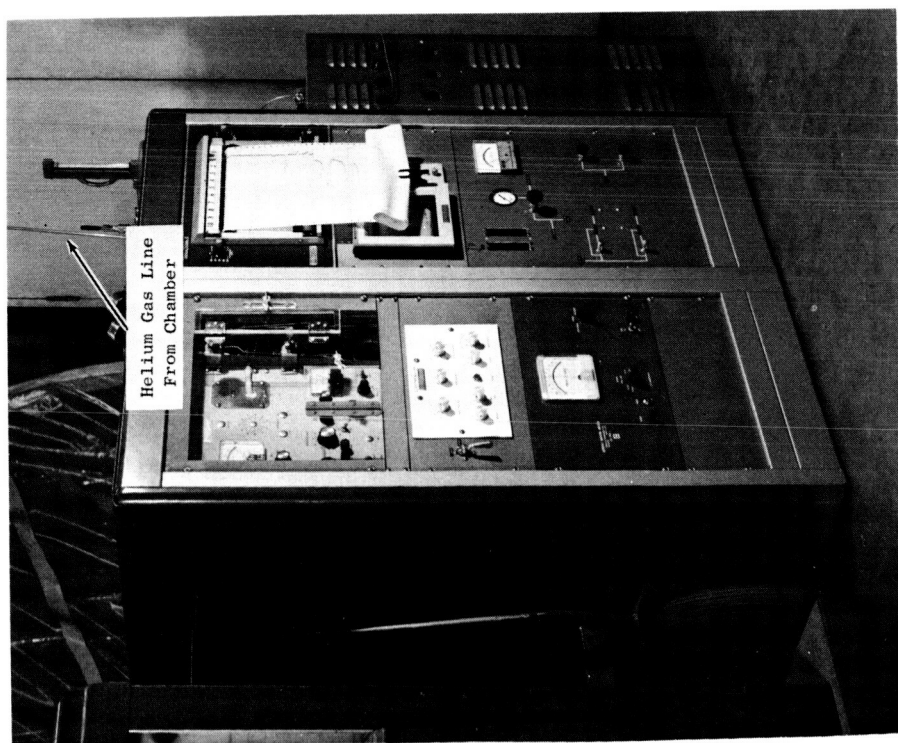


Figure VII-36. - Gas chromatograph used to analyze helium atmosphere in welding chamber for repair of T-111 corrosion loop.

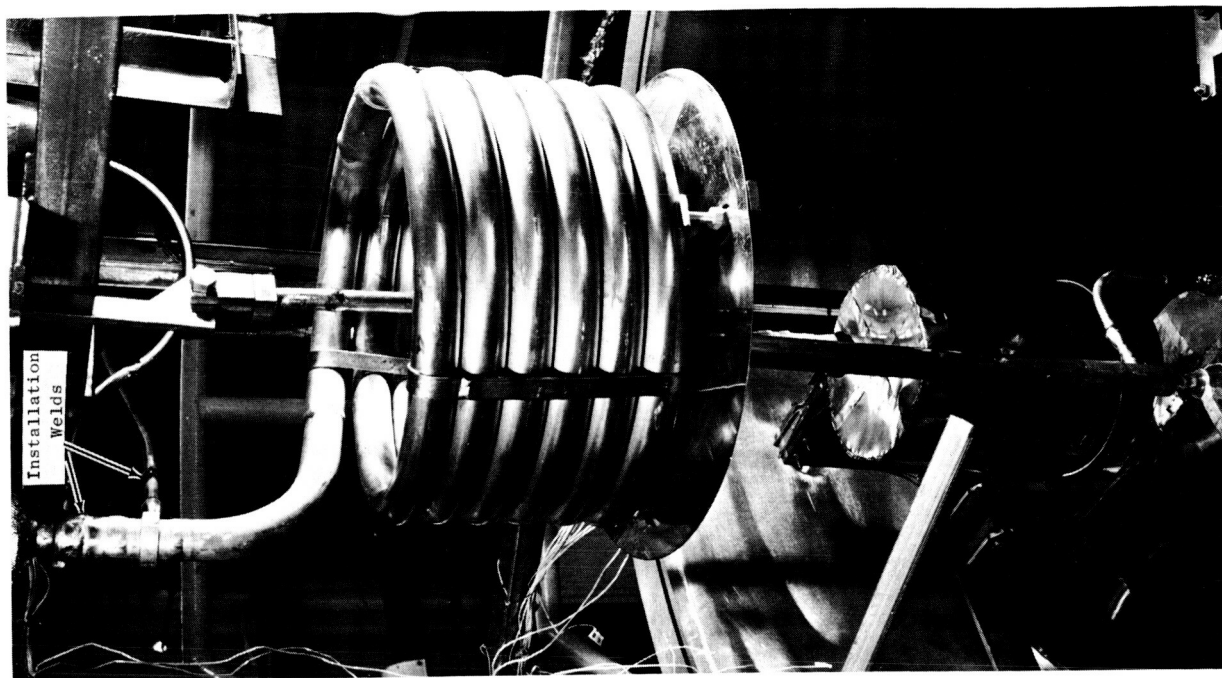


Figure VII-37. - Repaired boiler installed in T-111 corrosion loop.

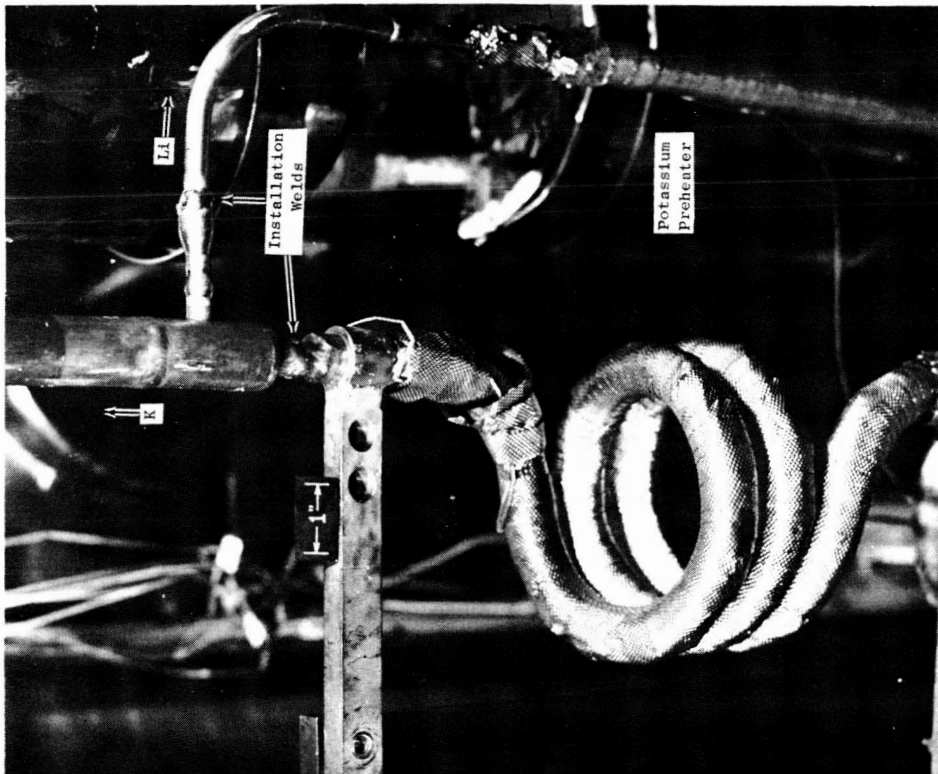


Figure VII-39. - Bottom of repaired boiler after installation in T-111 corrosion loop.

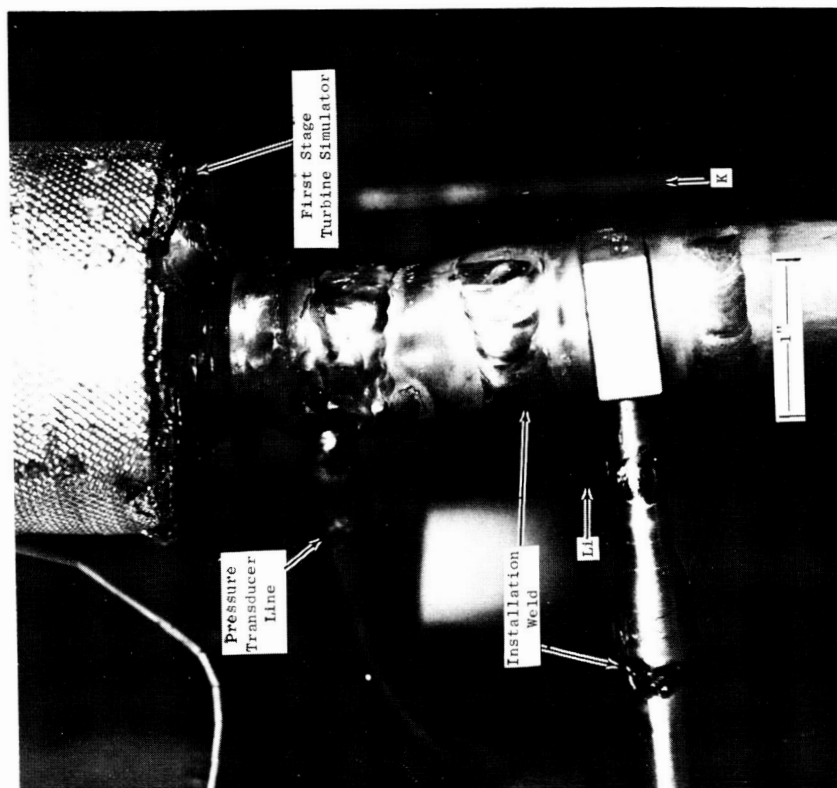


Figure VII-38. - Top of repaired boiler after installation in T-111 corrosion loop.



Figure VII-40. - Refractory metal furnace for annealing of corrosion loop weldments.

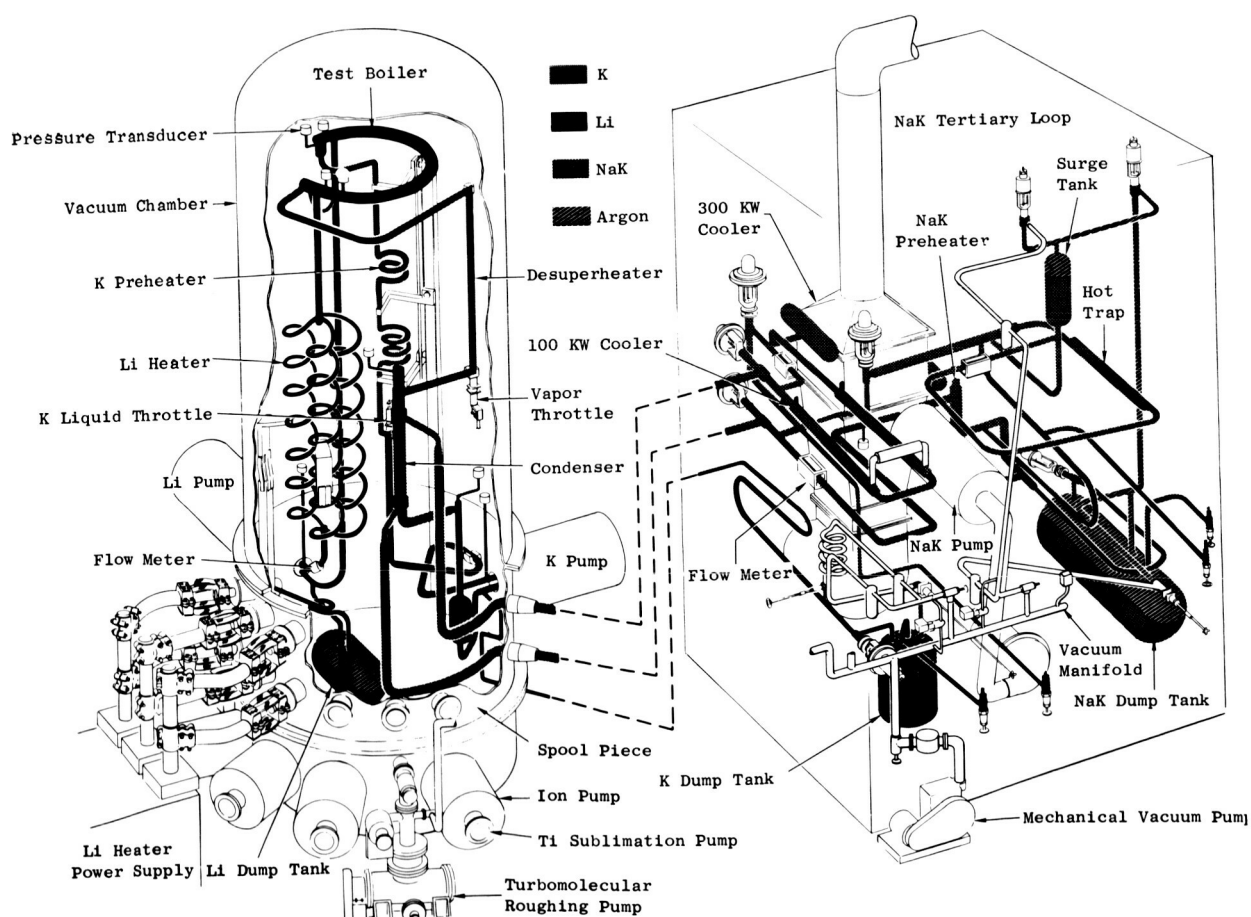


Figure VII-41. - Potassium boiler development test rig.



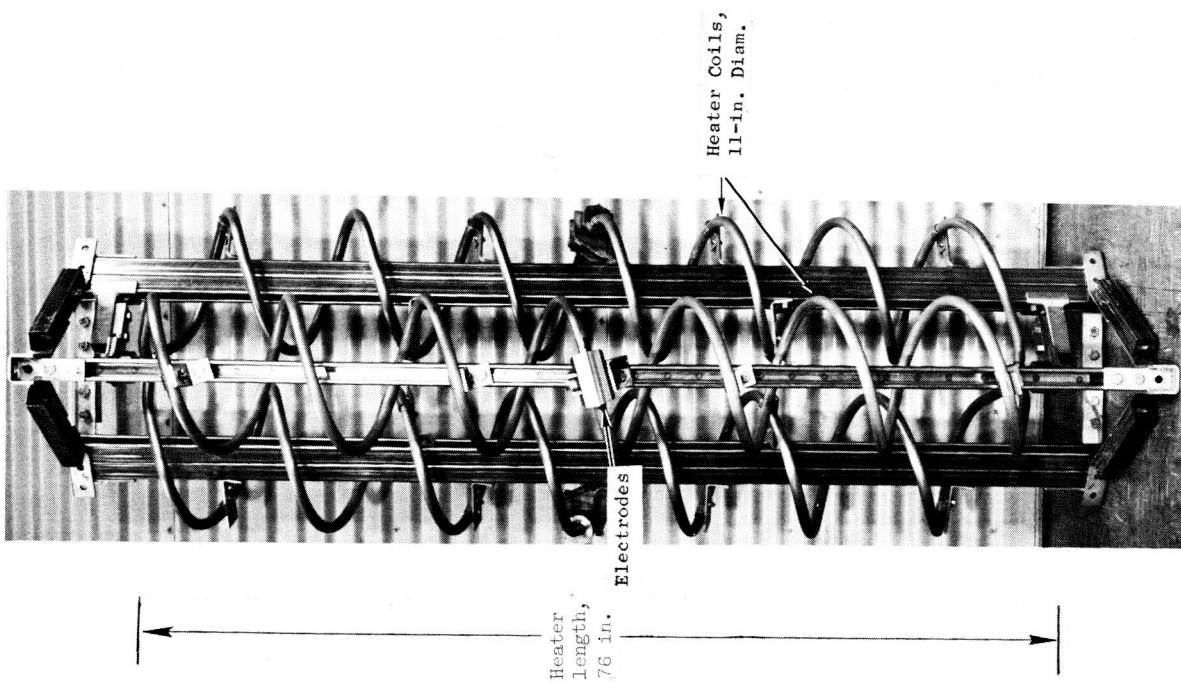


Figure VII-42. - T-111 lithium heater positioned in support structure.



Figure VII-43. - T-111 lithium heater manifold joints.



Figure VII-44. - T-111 lithium heater in multipurpose weld positioner.



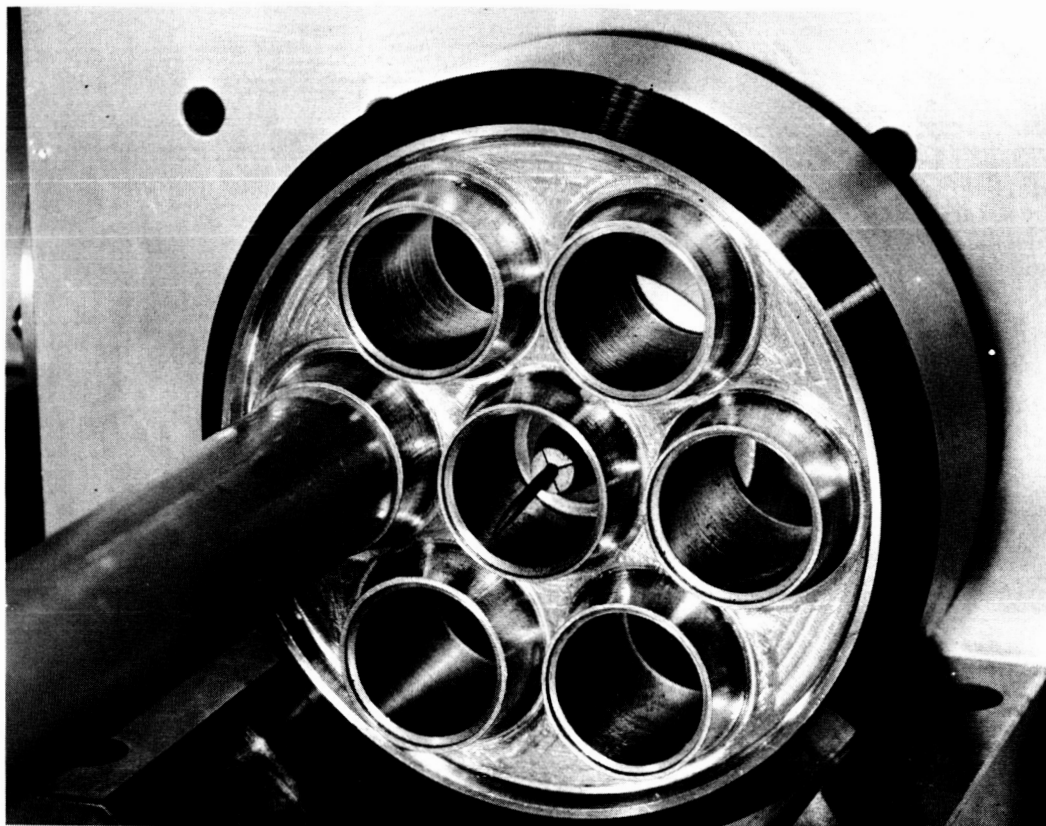


Figure VII-45. - View of seven tube header with internal rotating tungsten electrode shown in center tube boss.

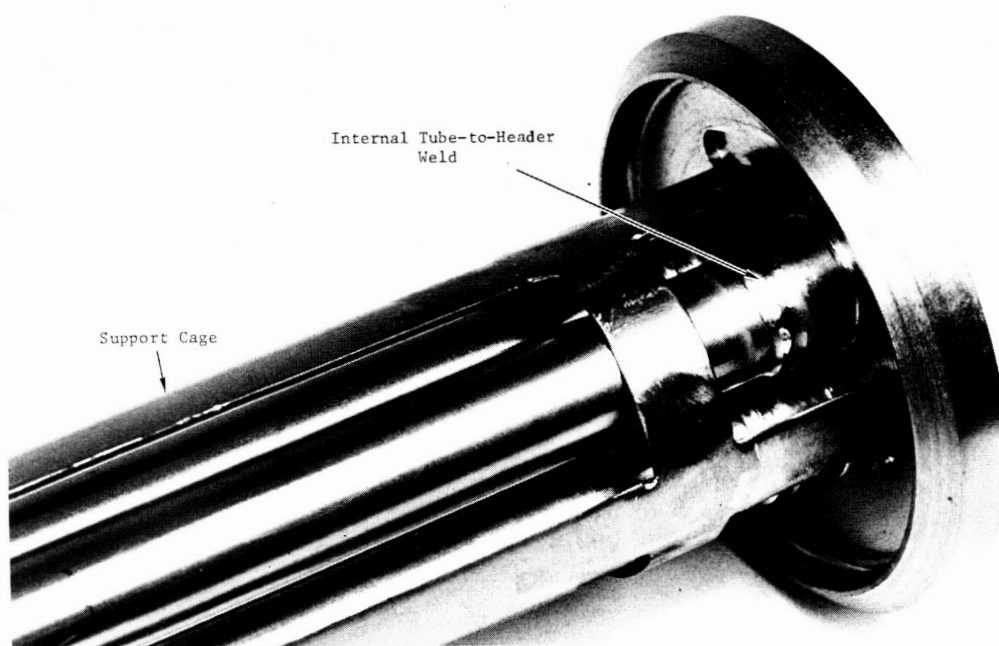


Figure VII-46. - T-111 three-tube condenser potassium inlet header.

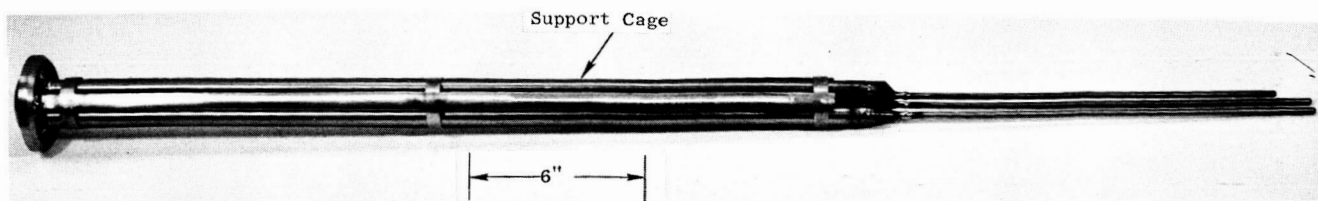


Figure VII-47. - T-111 three-tube condenser tube bundle and support cage.

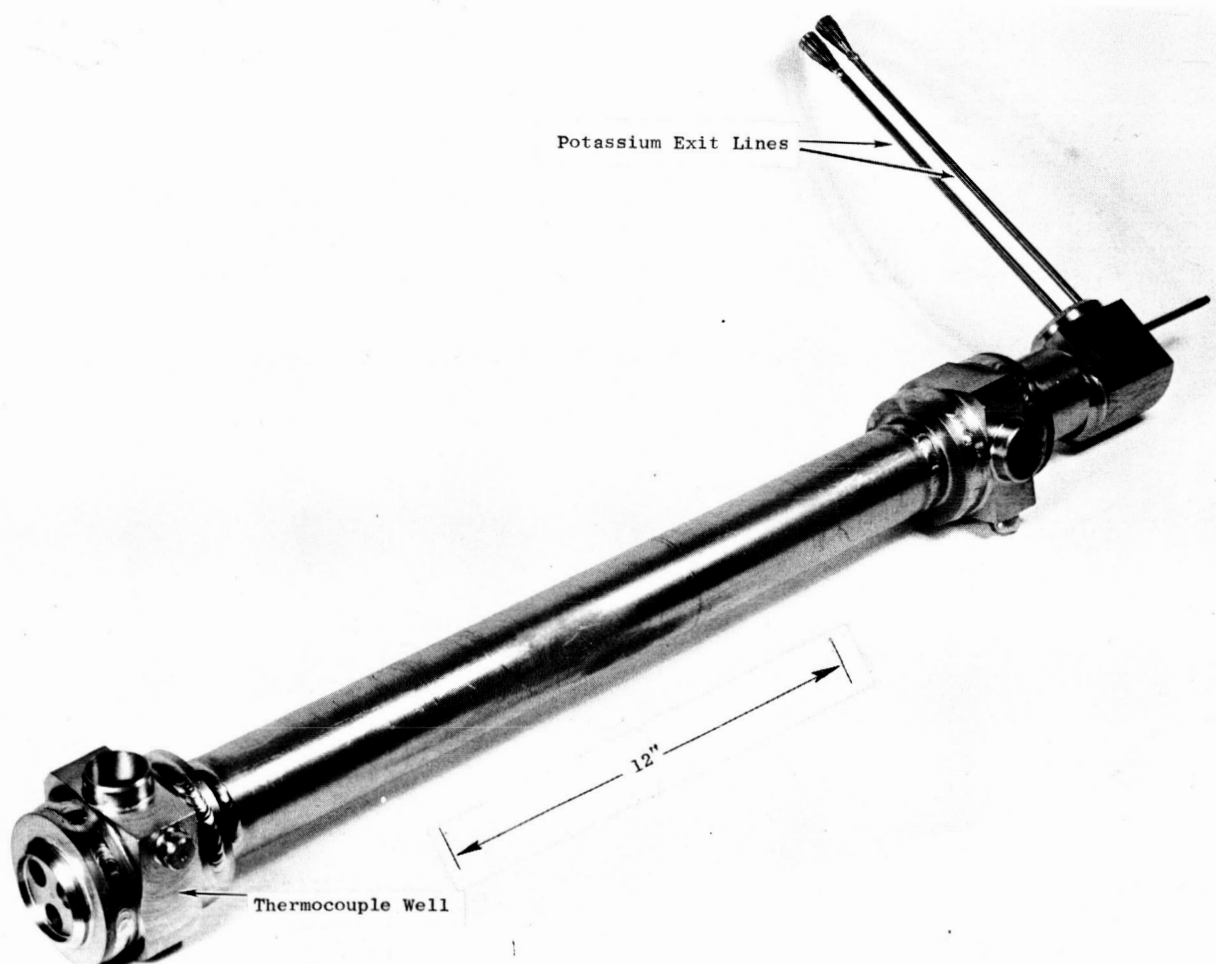


Figure VII-48. - T-111 three-tube condenser during fabrication.

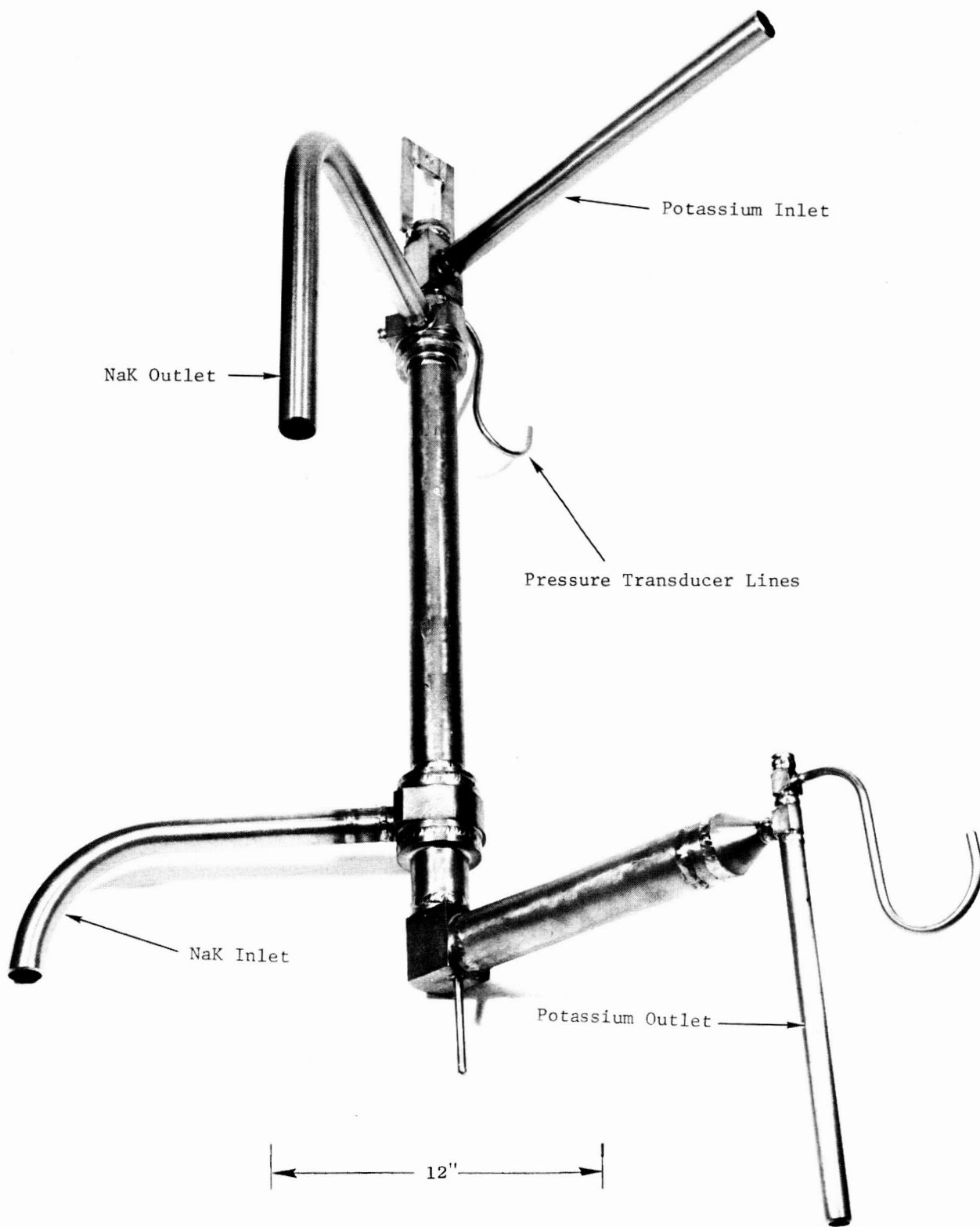


Figure VII-49. - Three-tube condenser for boiler development program.

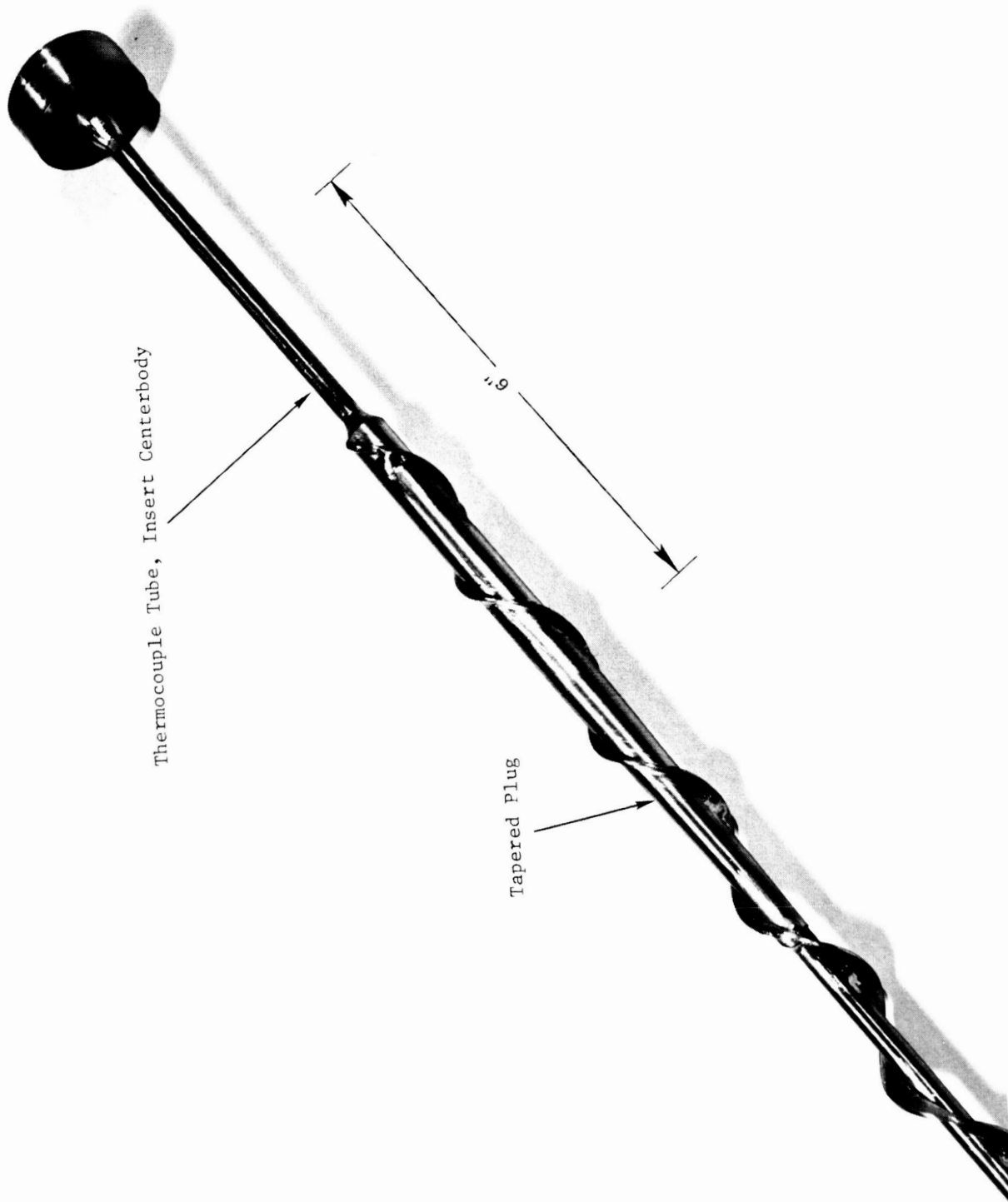


Figure VII-50. - Helical fin boiler tube insert for boiler 1.

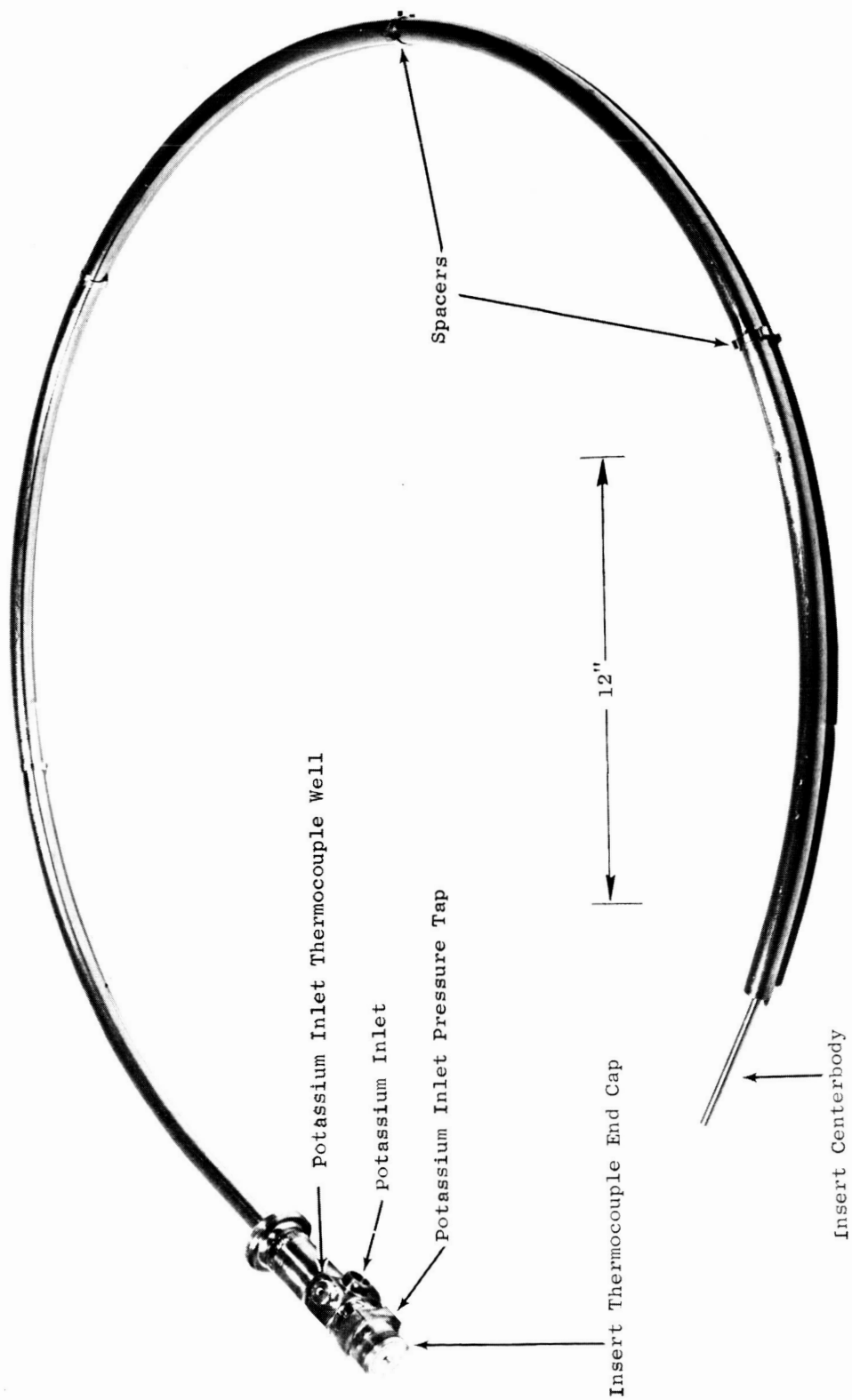


Figure VII-51. - Potassium boiler tube.

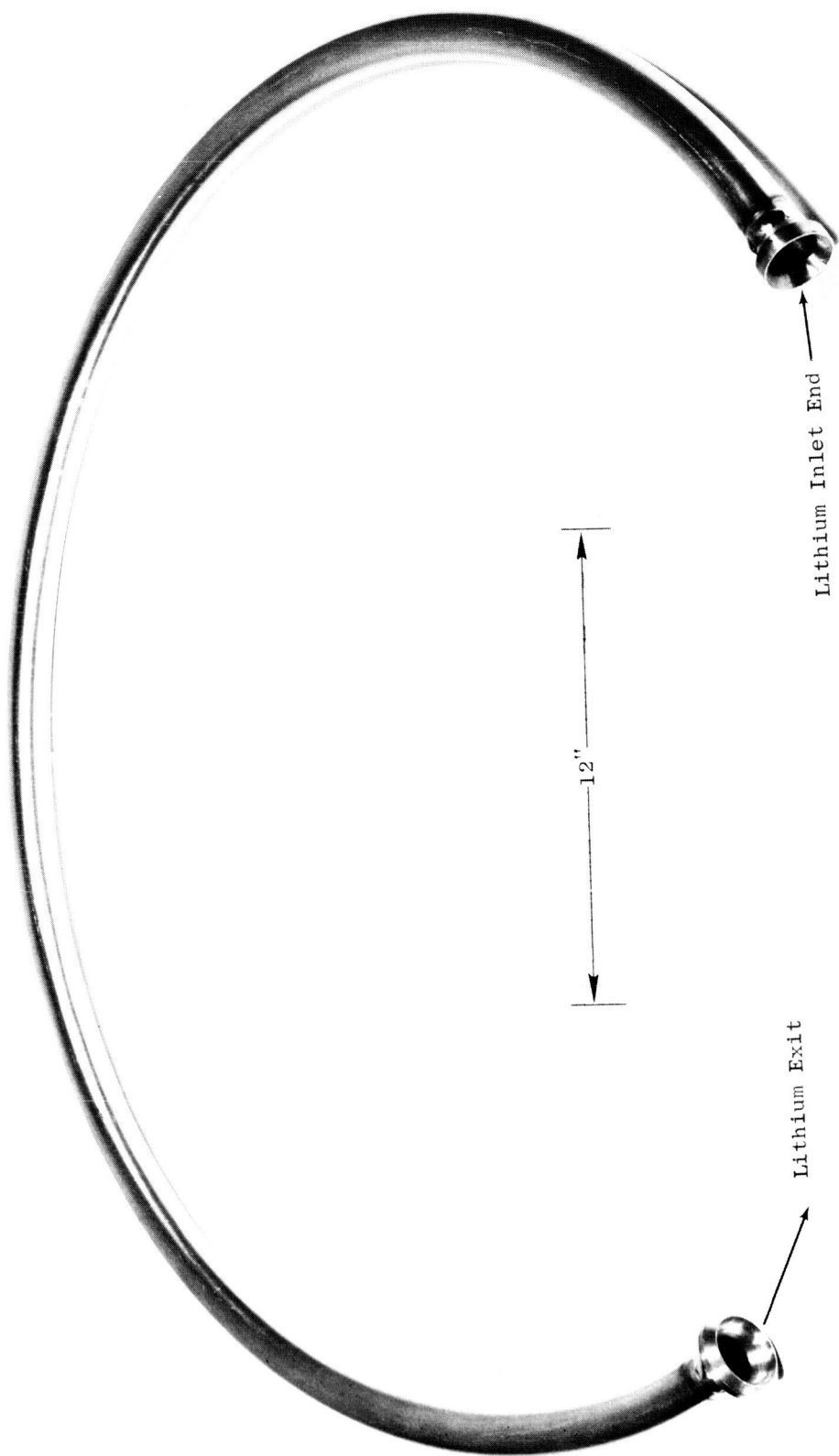


Figure VII-52. - Potassium boiler shell.

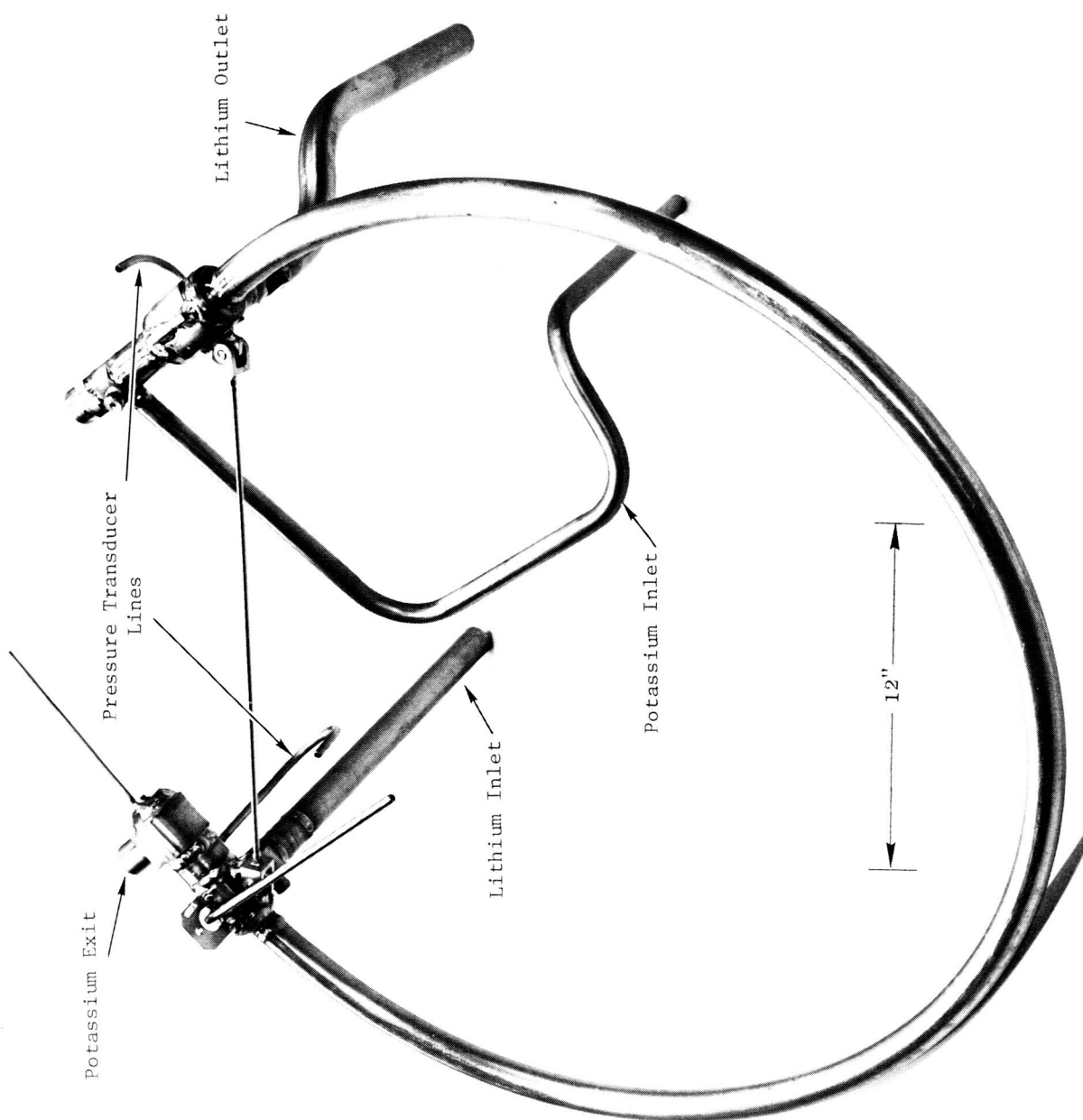


Figure VII-53. - T-111 single tube test boiler 1.

**Page intentionally left blank**



## VIII. T-111 ALLOY CRACKING PROBLEMS DURING PROCESSING AND FABRICATION\*

R. A. Ekvall,<sup>†</sup> R. G. Frank,<sup>†</sup> and W. R. Young<sup>†</sup>

### SUMMARY

A review is made of T-111 cracking encountered at General Electric Nuclear Systems Programs Department during fabrication of advanced space power Rankine cycle system components since 1965. Cracking has been observed after machining, forming, and welding. A majority of crack incidents have been associated with welding. Although tungsten inert gas welding is the primary joining technique used, cracks have also been found after electron beam and spot tack welding.

Cracking phenomena associated with each fabrication method are described with emphasis on weld related cracking. Preventative measures adopted for each type of cracking are reviewed. Possible causes for cracking, including attempts at correlating cracking incidents with material properties and processing history, are discussed. The frequency of crack occurrences and the requirements for highly reliable system components indicate the need for an investigation of the basic mechanism(s) underlying T-111 alloy cracking.

### INTRODUCTION

The transition of a material from the laboratory to production mill products and then into machined, formed, and welded components, assemblies, and system configurations is normally accompanied by some technical difficulties. T-111 alloy is a material that is still in this stage of development. Laboratory testing of T-111 alloy has shown it to be a very ductile alloy, but numerous examples of brittle cracking of the alloy have been seen during mill processing and during secondary fabrication into system components. The observed cracking is intergranular in nature and appears to fall into two broad phenomenological categories: (1) cracking

---

\*Based on work conducted under NASA contracts NAS 3-6474 and NAS 3-9426.

<sup>†</sup>General Electric Company, Cincinnati, Ohio.

associated with elevated temperature grain boundary sliding and (2) brittle propagation of cracks at room temperature under applied stress.

Over the last 4 years, General Electric Nuclear Systems Programs (GE-NSP) has procured between 4000 and 4500 pounds of T-111 alloy in all mill forms for five NASA sponsored space electric power programs; however, the bulk of the alloy was procured for two current NASA sponsored programs, the advanced refractory alloy corrosion loop program (contract NAS 3-6474) and the potassium boiler development program (contract NAS 3-9426). Tables VIII-1 and VIII-2 summarize the sizes and quantities of the T-111 alloy procured for each program. Solids of round cross sections ranged from 0.062-inch-diameter wire to rods 4.625 inches in diameter. Solids of rectangular cross sections ranged from 0.005-inch-thick foil to 0.500-inch-thick plate. Tubing items have been as small as 0.25-inch outside diameter by 0.050-inch wall to 1.5-inch outside diameter by 0.100-inch wall. Tubular shapes larger than 1.5-inch outside diameter were made by machining solid rod. In processing T-111 alloy for these requirements, refractory metal producers encountered cracking during forging, extrusion, rolling, and tube reduction. However, the purpose of this paper is not to review the incidents of cracking associated with primary processing, many of which are of a proprietary nature. The primary emphasis of this paper is to review the cracking incidents that have been encountered at GE-NSP since its first major commitment (1965) to build a T-111 alloy system for NASA on the advanced refractory alloy corrosion loop program (ref. 1). Cracking has been observed during the cutting, machining, forming, and welding of T-111 alloy components.

NASA sponsored advanced Rankine cycle power system work at GE-NSP has been mainly concerned with the design, building, and testing of components and the determination of the alkali metal corrosion resistance of candidate advanced refractory alloys. Investigations of the mechanisms underlying the observed cracking in T-111 alloy were not included in the scope of this work. GE-NSP policy has been to (1) appraise NASA of the cracking problems encountered, (2) document the cracking encountered with informal letter reports and photographs, and (3) promptly determine means for solving the immediate cracking problem to minimize program delays. In a number of cases, the cracked parts were rather easily repaired, non-destructively evaluated to ensure their suitability for service, and used. In such cases, no destructive evaluation was performed. However, other cracking incidents required destructive evaluation before a plan for repair or replacement could be devised. In a few instances, even when a remedy was found for a particularly puzzling cracking problem or one likely to be encountered often, further but limited destructive evaluation was performed on similar parts in an attempt to identify the cause(s). For these reasons, each cracking event described in this paper has not

received equivalent evaluation effort, and the discussion may raise as many or more questions than are answered.

Prior to proceeding with the discussion of individual cracking events, some general remarks are in order regarding the quality and processing history of the material which exhibited cracking. It is a policy and contractual requirement at GE-NSP to maintain traceability back to the ingot for all T-111 alloy components. This capability enabled GE-NSP to review the quality and processing history of the as-received material used for each item that cracked to determine if a common material properties and/or processing history might be responsible for the observed cracking. The properties and processing histories of the cracked material were also compared with T-111 alloy mill products that did not crack. No property variation was found that was clearly associated with T-111 alloy that eventually cracked. Evaluating the contribution of processing history to cracking proved to be difficult. Some of the processing information was incomplete because the vendor supplying the T-111 alloy considered the information proprietary. Within the limits of available information, fair comparison of processing procedures was further complicated by the following processing differences among the vendors: number of heats melted, melting practice, size of ingots, primary conversion techniques, and secondary fabrication techniques. It can be said that some type of cracking was observed, during fabrication at GE-NSP, of material supplied by each vendor. No conclusive evidence could be found that showed that one processing approach was clearly superior to another. However, based on overall experience with T-111 alloy vendors, some general suggestions for improving the compositional control and the chances of successful ingot conversion are (1) Hf additions should be made by the vacuum arc melting process (two melts are preferred with the ingot being inverted between melts to improve Hf homogenization); (2) Hf content should be on the low side ( $<2.0$  percent) of the specification; (3) initial conversion temperatures around  $2000^{\circ}$  F should be avoided because of possible low ductility (ref. 2); (4) reduction limits should be observed in extrusion ( $>3:1$ ) and primary forging to avoid cracking; (5) proper cutting and grinding procedures should be used to avoid crack initiation and subsequent propagation; and (6) contact between T-111 alloy and copper or copper alloys should be avoided whenever possible.

The discussion of individual T-111 alloy cracking incidents at GE-NSP, which follows, is arbitrarily divided into three major categories: (1) cracks related to cutting and forming; (2) cracks related to machining and forming; and (3) cracks related to welding, including tungsten-inert-gas (TIG), electron beam (EB), and spot tack welding. In all cases, the material referred to is T-111 alloy unless otherwise specified.

## CRACKS RELATED TO CUTTING AND FORMING

Cutting of T-111 alloy mill products with an alumina abrasive (Allison VA 1202 MRA) cutoff wheel frequently produced cracks in the cut surfaces. The cracks induced by abrasive cutting always propagated in a brittle manner upon subsequent bending (fig. VIII-1). Although water cooling of the T-111 alloy and wheel was used in all cases, the cooling did not prevent cracking. Generally, slow feeding of the T-111 alloy mill products into the wheel resulted in more severe cracking than occurred with fast feeding. The effect of cutting T-111 alloy with an alumina abrasive wheel at varying speeds is illustrated in figure VIII-2, which shows transverse sections of a 0.375-inch-outside-diameter tube that were partially flattened after cutting. Removing 0.060 to 0.080 inch from the cut tube surfaces by grinding was sufficient to remove the cracks generated during cutting, and the tubing could then be bent without cracking (fig. VIII-3). Further evidence of the damage that can be caused by the use of an improper cutoff wheel is exhibited in figure VIII-4. Cracks were observed in T-111 alloy tube hollows during initial attempts to tube reduce the hollows. The deep cracks shown apparently propagated from shallow cracks resulting from cutting with an abrasive cutoff wheel. The sound portions of the tube hollows were used to successfully fabricate tubular bellows blanks (0.625-in. o.d. by 0.0085-in. wall). Alumina abrasive cutoff wheel induced cracking was not limited to tubing mill forms. Cracking also was observed in solid rods, as shown in figure VIII-5.

The cracking that occurs in both solid rod and tubing is intergranular in nature. However, the mechanism of the crack formation in T-111 alloy and, of even greater interest, the mechanism which causes the cracks to propagate in a brittle manner are not understood. However, embrittlement with nascent hydrogen from breakdown of coolant or abrasive binder is a possibility.

In limited testing to find a way to avoid crack initiation during cutting operations, it was found that cracking could be eliminated by the use of SiC cutoff wheels (Allison C120-K-RA), tube cutters, or band saws. Because of the limited testing and possible inadvertent use of the wrong wheels, GE-NSP has adopted the policy of using tube cutters and band saws for cutting operations.

## CRACKS RELATED TO MACHINING AND FORMING

Cracks related to machining have been observed in parts subsequently formed or welded; no cracking has been seen in as-machined parts at GE-NSP. Cracks in machined and welded parts are described later in this paper. Probably the most

striking example of failure of machined parts during forming is the brittle fracture of machined parts during forming is the brittle fracture of machined thermocouple wells during bending (fig. VIII-6(a)). Five wells were machined from 1.0-inch-diameter rod. The wells were jig bore drilled with a 0.156-inch-diameter hole to a depth of ~2.75 inches using Tap Magic as the cutting fluid. Then the part was turned on a lathe to final dimensions of 2.45- to 0.255-inch diameter to a 63 rms finish. After machining, the straight thermocouple well was placed between matched concave and convex aluminum blocks machined to a 1.01- to 0.99-inch radius with a 0.125-inch-radius groove in each block, and an attempt was made to form the machined T-111 alloy thermocouple well to an angle of  $86^{\circ}$  to  $84^{\circ}$ . Cracking began almost immediately and resulted in brittle fracture. The same type of failure occurred during initial attempts to bend a second machined thermocouple well. It was suspected that residual surface stresses present at the completion of the machining operations were responsible for the cracking during bending. In an attempt to alleviate this problem, subsequent thermocouple wells were given a stress relief heat treatment of  $2400^{\circ}$  F for 1 hour in a vacuum of  $\sim 10^{-5}$  torr after machining and prior to bending. The remaining three thermocouple wells were bent successfully without cracking, as determined by fluorescent penetrant inspection (fig. VIII-6(b)).

Metallographic and X-ray diffraction evaluations of the cracked thermocouple wells were performed. The metallographic results showed the major fracture to be intergranular and also revealed several areas of incipient intergranular cracking near the outside diameter of the tube on the tension side of the bend (fig. VIII-7). No cracking was observed in the inside diameter of the thermocouple wells. A comparison of the microstructure of an as-machined and a machined and stress relieved thermocouple well indicated the overall structures to be similar with the exception that recrystallization had occurred in a thin worked surface layer of the stress relieved thermocouple well. X-ray diffraction analyses qualitatively indicated that a reduction in residual stresses from machining and bending had occurred as a result of the  $2400^{\circ}$  F, 1-hour heat treatment.

Subsequent attempts to reproduce a brittle fracture in sheet samples (0.055-in. thick) after removal of 0.010 inch from each side using a shaping machine were unsuccessful. Neither samples machined to a surface finish similar to that of the thermocouple wells nor samples machined more severely to produce a very rough surface fractured when bent  $180^{\circ}$  over a  $1/2$  T bend radius at temperatures as low as  $-320^{\circ}$  F.

Although stress relief treatments solved the immediate problem of fabricating thermocouple wells, the cause of the brittle intergranular fracture remains a matter for speculation. To reduce the possibility of cracking in other machined parts, a

specification (GE-NSP 03-0071-00-A) requiring that all machined parts of T-111 alloy be given a postmachining stress relief treatment at 2400<sup>0</sup> F for 1 hour was prepared and issued.

## CRACKS RELATED TO WELDING

The preponderance of cracking observed at GE-NSP has been related to welding. Selected incidents of cracking associated with each method of welding are discussed in this section.

### EB Welding

Welded and reworked tube. - To compare the biaxial creep properties of EB welded and seamless tubing, two 2.0-inch-outside-diameter by 0.25-inch-wall tube hollows (one welded and one seamless) made from the same heat of material were tube reduced and drawn to 1.5-inch-outside-diameter by 0.100-inch-wall tubing. The weld in the "welded" hollow was a simulated full penetration EB weld running the length of the hollow parallel to its longitudinal axis. The weld was formed by making two consecutive EB welding passes on a seamless hollow. The second pass was made to smooth the rough weld surface produced by the first pass. No defects were found in the "welded" tube hollow during ultrasonic and fluorescent penetrant inspections to NSP specifications 03-0001-00-C and 03-0027-00-A, respectively. After a 37-percent tube reduction, intermittent transverse cracks were observed in the heat-affected zones on either side of the weld for the entire length of the tube. Grinding the tube within allowable tolerances did not completely remove the cracks. Without further conditioning, the tube was annealed, processed to final size, and final annealed at 3000<sup>0</sup> F for 1 hour. The appearance of the finished tube is shown in figures VIII-8 and VIII-9. Because the quantity of the "welded" material required for the program was critical, no metallography was performed on the tubing after cracking was first observed. It is difficult to determine with certainty from the recrystallized structure of the finished tube whether or not the cracking was intergranular.

It is believed that residual stresses in the tube surface, promoted primarily by the second weld pass, were a major contributing factor to the observed cracking. Although a postweld stress relief treatment might have avoided the problem, it would seem wise to avoid multipass welds whenever possible. Details of the tube history, processing, and ultimate utilization have been reported (ref. 3).

Pressure transducer diaphragm. - Helium mass spectrometer leak checking and visual examination of the 0.005-inch-thick T-111 alloy diaphragm of a pressure transducer shown in figure VIII-10 revealed two diametrically opposed cracks. The cracks were approximately 0.040 inch from the fusion zone joining the diaphragm to the transducer housing. The transducer had been postweld annealed (2400° F for 1 hr) prior to the discovery of the leaks. Metallography indicated the cracks were intergranular. The microstructure appeared normal, and no significant variations in microhardness were found in the cracked sample. Bend tests of foil similar to that used to fabricate the diaphragms and heat treated similarly (2400° F for 1 hr) showed the material to be ductile. The cause of the cracking is not known, as numerous pressure transducers have been fabricated using the same procedure without cracking of the weld.

## TIG Welding

Since TIG welding is the most common welding technique used for joining T-111 alloy at GE-NSP, it is not surprising that most weld related cracks have been observed in TIG welds. Intergranular cracking was found in each cracking incident that was metallographically evaluated. Evidence indicates that the cracking occurring at elevated temperatures in T-111 alloy appears to be related to grain boundary sliding (ref. 4).

Butt weld joint. - During welding of a tube (0.375-in. o.d. by 0.065-in. wall) butt weld joint, one of the tubes was unsupported and sagged. In order to straighten the tube sections, the welded assembly was clamped between Mo plates and heated on one side of the weld nugget with a TIG torch. Intergranular cracking appeared on the side (tension side) of the weld nugget opposite the TIG torch. The cracks and grain boundary sliding observed in the weld nugget are exhibited in figure VIII-11. Similar grain boundary separation has been noted in welds inadvertently deformed at Oak Ridge National Laboratory (data obtained from B. Fleisher of ORNL).

Prevention, by providing adequate support for parts being welded, was the obvious solution to this problem.

Electromagnetic pump duct. - In repairing an electromagnetic (EM) pump duct, it was necessary to run a circumferential TIG weld approximately 0.8 inch (weld centerline distance) from a preexisting circumferential weld as illustrated in figure VIII-12. Cracking and grain boundary relief were noted in the machined duct surface between the welds after completion of the second weld. The location of the

cracking implies a critical temperature at which grain boundary sliding and separation occurs.

The cracks and grain boundary relief were removed by machining, benching, and hand polishing. Final visual, helium leak check, and X-ray inspection indicated the part was sound.

Absolute pressure transducers. - Cracks were discovered in three of six Taylor absolute pressure transducers after welding. Immediate leak testing with a helium mass spectrometer leak detector, according to NSP specification 03-0013-00-B, revealed that none of the transducers leaked. (A full section view drawing of a typical Taylor absolute transducer showing its functional relation to a test loop is given in fig. VIII-13.) The cracks were found near the circumferential TIG welds joining the top and bottom flanges. Photographs of the most severely cracked transducer (no. 14) are presented in figure VIII-14. The crack on the outer surfaces of the bottom flange of the transducer was approximately 0.5 inch deep, as can be seen in figure VIII-15, which shows the flange after removal of the weld nugget. Photomicrographs of end A of the crack are exhibited in figure VIII-16. The crack was quite wide where it intersected the outer circumferential surface of the flange, and it was not possible to definitely determine the mode of fracture. In figure VIII-16, however, cracking appears to be intergranular at end A.

It is interesting to note the amount of distortion in the grain shown by the arrow in figure VIII-16(b). It is possible that this distortion was not sufficient to relieve local stresses which resulted in grain boundary separation and subsequent propagation toward the surface. The fact that the crack width is larger at the surface than the center would tend to discount this theory by indicating the crack started at the surface. However, if residual stresses were induced at the surface during welding, there would be a considerable amount of spring back as the crack broke through the surface from the inside. This would cause a larger crack width at the surface, which would decrease as the spring back effects decreased from the edge to the center.

Cracks in all transducers (except the bottom flange of no. 14, which was metallographically sectioned) were removed by benching the material to a depth of approximately 0.030 inch. The shallowness of the cracks (except on transducer no. 14) indicates that the cracks may have been related to the surface condition of the machined transducers. The flanges were stress relieved at 2400<sup>0</sup> F for 1 hour following machining; however, X-ray diffraction studies have shown that this treatment does not completely relieve residual stresses. A longer time at 2400<sup>0</sup> F or a higher stress relief treatment might be necessary if residual stress from machining is the cause or contributes to the cause of the cracking.



Multipass tube welds. - One of the most reproducible incidents of cracking found in T-111 alloy is that which occurs in multipass welds (T-111 alloy filler material) of the type needed to join heavy sections (ref. 5). Grain boundary separation is first visible in the root pass after the second weld pass has been made. The grain boundary separation becomes more pronounced after the third pass and was found to extend into the second pass material after the fourth pass was complete. (Similar observations with multipass TIG welding of T-111 alloy have been made by R. Begley and W. Buckman of Westinghouse Electric Co.) Cracking and grain boundary separation were found predominantly in the periphery of the fusion zone (circled areas of fig. VIII-17(b)). Photomicrographs of a portion of one of these areas are presented in figure VIII-18. Although grain boundary separation was found primarily near the periphery of the fusion zone, some grain boundary separation was noted in the center of the fusion zone also. Occasionally grain boundary separation was found in the heat-affected zone near the edge of the fusion zone.

To determine the effect of filler wire composition on the cracking behavior of multipass welds, two 2.5-inch-outside-diameter by 0.375-inch-wall T-111 alloy tubes with solid ends were machined from 2.5-inch-diameter rod and subsequently butt welded using the TIG process with T-111, Ta-10W, and Cb-1Zr alloy filler wires. A J-shaped weld preparation was machined in each part prior to welding. The first weld pass, or root pass, was a T-111 alloy fusion pass except for a short region of the joint which was not welded to allow for the venting of the tube interior. Three additional passes were made using T-111 alloy filler for one 120° segment around the tube, Ta-10W alloy filler for another 120° segment, and finally Cb-1Zr alloy filler for the last 120° segment. A photograph of a section through the welded parts is shown in figure VIII-17(a). The welded tube was metallographically sectioned through each of the three segments representing the three filler materials. Photomicrographs of transverse sections through these welds are shown in figures VIII-19, VIII-20, and VIII-21. The major observations of this study are (1) grain boundary separation occurs in the T-111 alloy root pass for all three filler alloys, and (2) grain boundary separation is not observed in the Cb-1Zr or Ta-10W alloy portions of the corresponding weld segments. These observations indicate that hafnium, present only in T-111 alloy, is a significant factor contributing to the grain boundary separations in the T-111 alloy weldments.

Of the possible solutions to the multipass weld cracking in T-111 alloy, the most obvious solution is to design to avoid the use of heavy sections requiring multipass welds wherever possible; no weld cracking has been observed on TIG welds of parts having thin sections (~0.100 in.). Other suggested solutions include designing for single-pass EB instead of TIG welding, intermediate stress relieving, alloy modification, and alloy overlay.

Boiler weld failure. - During the initial startup of a T-111 alloy corrosion test loop, a leak developed between the lithium primary circuit and the potassium secondary circuit (refs. 6 and 7). The leak in the coaxial T-111 alloy tube boiler was traced to a crack in the weld nugget of the 0.375-inch-outside-diameter by 0.062-inch-wall inner tube, as shown in figure VIII-22. During operation of the boiler ( $\sim 2100^{\circ}$  F), lithium flowed in one direction in the annulus between the two tubes, and potassium flowed in the opposite direction within the inner tube. After the cracked segment of tube was cut from the boiler, stepwise removal of material from the surface of a longitudinal section through the crack, to a depth of 0.006 inch, clearly showed the crack to be intergranular (fig. VIII-23) with entire grains delineated as the result of grain boundary separation (fig. VIII-24). The appearance of grain boundary separation suggests some action of lithium which has penetrated into the crack. Although the intermittent voids in the grain boundaries are similar in appearance to those observed as a result of attack by lithium, the crack is not believed to have been initiated by a corrosion mechanism, since corrosion by lithium would not be expected in T-111 having an oxygen concentration as low as that (40 ppm) of the as-received boiler tube.

To determine the possibility of reusing the boiler tube (except for that section containing the leak), specimens from the boiler tube in the vicinity of the crack were removed and submitted for metallographic examination, microprobe evaluation, and chemical analyses for major metallic and interstitial elements. The ductility of the T-111 alloy was determined qualitatively by tube flattening tests.

Results of the various analyses (ref. 5) indicated no contamination of the T-111 alloy material had occurred, and no cracking was observed during flattening of the tubes. Further, interstitial analyses of the T-111 alloy weld quality assurance specimens welded before and after the welding of the boiler tube, as part of NSP specification 03-0025-00-A, indicated no contamination occurred during welding of the boiler tube.

Although the cause of the crack is not evident, it is believed that the most likely explanation would be that straining of the weld nugget while it was hot might have caused grain boundary separation similar to that which occurred during butt welding of tubes (described in the section Butt weld joint). Propagation of such a crack could have occurred during subsequent bending to form the helically shaped boiler.

## Spot Tack Welding

Prior to the postweld vacuum annealing of T-111 alloy at  $2400^{\circ}$  F for 1 hour, Cb-1Zr alloy foil was wrapped around two tubular T-111 alloy assemblies and

fastened in place by spot tack welding. After heat treatment, cracking was observed in the T-111 alloy in the vicinity of the tack welds. No cracking had been observed previously in spot tack welding of Cb-1Zr foil to T-111 alloy using a molybdenum (Mo) tipped welding electrode. The subassemblies exhibiting cracks, however, had been spot welded using a copper (Cu) electrode. The utilization of the Cu electrode was believed to be responsible for the observed failures. The highlights of an investigation to identify and eliminate the cause of cracking are summarized in the next paragraph (ref. 8).

A study was initiated to determine the effects of electrode materials (Cu, Mo, and Cb-1Zr), spot welding parameters, surface conditions and stresses in the tubing, and subsequent 2400° F, 1-hour vacuum exposures on the cracking tendencies of various sizes of T-111 alloy tubing. Preliminary results showed that only spot welds made with a Cu electrode produced areas in the T-111 alloy tubing that were subject to failure upon subsequent heat treatment. Metallographic examination of as-spot-welded samples revealed no microcracking or interdiffusion regardless of the electrode material, as shown in the sample in figure VIII-25(a), in which T-111 alloy was spot welded with a Cu electrode. Copper deposited on the T-111 alloy surface, from welding with that electrode, is shown in the photomicrograph. When the spot tack welded samples were heated to 2400° F for 1 hour, microcracking was seen only in those specimens which were spot tack welded using a copper electrode (figs. VIII-25(b) and VIII-26). (The light colored grain boundary phase was identified later in similar samples as a Cu/Hf phase.) The difference in the magnitude of the cracks between the 1.5- and 0.375-inch-diameter tubes may be due to differences in residual stresses resulting from straightening operations. Further tests in which Cu was simply placed on T-111 alloy and heated indicated that spot welding with a copper electrode only served to provide a source of copper for subsequent reaction with T-111 alloy in heating to 2400° F. The results of one such test are given in figure VIII-27. A Cb-1Zr foil boat (consisting of two layers of 0.002-in.-thick foil) containing copper was lightly spot tack welded (using a Mo electrode) to a 1.5-inch-diameter by 0.100-inch-wall T-111 alloy tube section. When the assembled ring section was heated to 2400° F, the Cu penetrated through the Cb-1Zr foil layers and completely through the tube wall producing the crack shown in figure VIII-27. Additional metallographic studies and microprobe analyses of the test specimens indicated that a Cu/Hf reaction at grain boundaries during heat treatment, in combination with some residual stress, caused intergranular failures in T-111 alloy. The one test sample in which microprobe analyses positively identified a Cu/Hf phase in the T-111 alloy grain boundaries is shown in figure VIII-28(a). A T-111 alloy sheet (0.063-in.-thick) sample was notched and bent (with the notched side in tension) and Cu placed in the notch. Then the sample was heated at 2400° F

for 1 hour. Microcracking was found at symmetrical locations on each side of the notch, as illustrated in figure VIII-28(b). An identical notched, bent, and heat treated sheet specimen without Cu did not exhibit microcracking. The notched sheet sample, heated to 2400<sup>0</sup> F, with Cu in the notch was examined with a microprobe at the failure location and at random positions throughout the specimen. The phase present at sample grain boundaries next to the failure contained Hf concentrations significantly higher than the matrix; Cu was also found in these grain boundaries. Cu was not present within the grains of the sample nor in grain boundaries remote from the failure. These results indicated that a Cu/Hf reaction, at grain boundaries originally high in Hf content, was the probable major factor causing Cu penetrations and the resultant failures.

## SUMMARY OF RESULTS

A summary of the cracking incidents observed during the fabrication of T-111 alloy loop components, their possible causes, and preventative measures is given in the following table:

| Cracking problem during - | Probable cause or contributing cause(s)  | Preventative measures  |
|---------------------------|--|--|
| Cutting and forming       | Possible nacent hydrogen embrittlement from coolant or binder in cutting wheel | Use bandsaw or tube cutters as appropriate.<br>Use acceptable cutoff wheel and grind away cut surface to assure no cracks are present.   |
| Machining and forming     | Residual stresses and possible hydrogen embrittlement                          | Use appropriate vacuum stress relief anneal.   |
| EB and TIG welding        | Low strength of grain boundaries relative to matrix<br>Residual stresses       | Design to avoid multipass welds.<br>Use alloy overlay technique or intermediate stress relief for multipass welds when necessary.<br>Use EB welding as much as possible.<br>Stay on low Hf side of specification and use double arc melted alloy.<br>Stress relieve machined parts before welding.<br>Provide adequate mechanical support for welding. |
| Spot tack welding         | Cu<br>High Hf concentration in grain boundaries                                | Avoid use of Cu electrode; use Mo electrode  |

An examination of this table clearly shows that the problems of T-111 alloy cracking are remediable. Although nondestructive evaluation of machined parts or welded joints is not mentioned in the table, X-ray, fluorescent penetrant, helium mass spectrometer leak checking, and visual inspection are recommended and were performed, as appropriate, to prevent installation of cracked components into test systems. GE-NSP performs visual inspections (at magnifications up to 30) of all welded joints. Also, thermal cyclic testing has been used as a proof test of critical components or assemblies containing welds.

It is obvious from the table that there is still much to be learned about the basic mechanisms underlying cracking in T-111 alloy. Some general observations that are particularly noteworthy when considering cracking mechanisms are (1) whenever metallography has been performed, cracking has been found to be intergranular in nature; (2) only multipass weld cracking has been found to be readily reproducible; (3) cracking related to cutting and machining has been particularly difficult to reproduce; and (4) the intermittent appearance of cracking may indicate local contamination (e.g., with copper). It should also be noted that the mechanism of crack initiation and brittle crack propagation at room temperature has not been explained. Until the underlying crack-provoking mechanisms can be found and corrective action taken, those working with T-111 alloy should avoid the obvious pitfalls described in this paper and be alert to potential problems not yet uncovered.

In conclusion, there are three major points to be kept in mind, particularly by those who hasten to draw pessimistic conclusions concerning the use of T-111 alloy in space systems: (1) T-111 alloy is still in the development stage with respect to manufacturing complex hardware, and some difficulties and a learning period should be expected; (2) cracking observed to date is remediable; and (3) the T-111 alloy Rankine system corrosion test loop has now completed over 3500 hours of continuous, stable, trouble-free operation at a maximum lithium temperature of 2250<sup>0</sup> F.

## REFERENCES

1. Harrison, R. W.: Advanced Refractory Alloy Corrosion Loop Program. Rep. GESP-258, General Electric Co. (NASA CR-72560), May 16, 1969.
2. Turner, F. S.: Tantalum Alloy Tubing Development Program. Rep. RTD-8-109(1), Allegheny Ludlum Steel Corp., Oct. 1963.
3. Engel, L. B., Jr.: Determination of Biaxial Creep Strength of T-111 Tantalum Alloy. Rep. GESP-237, General Electric Co. (NASA CR-72541), June 17, 1969.

4. Begley, R. T.; and Godshall, J. L.: Some Observations on the Role of Grain Boundaries in High Temperature Deformation and Fracture of Refractory Alloys. Presented at the AIME Symposium on the Physical Metallurgy of Refractory Metals, French Lick, Ind., Oct. 3-5, 1965.
5. Brandenburg, G. P.: Evaluation of T-111, Ta-10W, and Cb-1Zr Alloy Filler Materials in T-111 Alloy Multipass Tube Welds. Rep. GESP-385, General Electric Co., 1970.
6. Harrison, R. W.: Advanced Refractory Alloy Corrosion Loop Program. Rep. GESP-182, General Electric Co. (NASA CR-72483), 1968.
7. Harrison, R. W.: Advanced Refractory Alloy Corrosion Loop Program. Rep. GESP-189, General Electric Co. (NASA CR-72505), Mar. 20, 1969.
8. Thompson, S. R.: Investigation of the Cracking in T-111 Alloy Tubing Associated with Spot Tack Welding. Rep. GESP-384, General Electric Co., 1970.

TABLE VIII-1. - T-111 ALLOY PROCURED BY

GE-NSP FOR NASA CONTRACT NAS 3-6474,

## ADVANCED REFRACTORY ALLOY

## CORROSION LOOP

| Item and size,<br>in.    | Weight,<br>lb |
|--------------------------|---------------|
| Rod                      |               |
| 0.250 diam               | 1             |
| 0.500 diam               | 11            |
| 0.625 diam               | 5             |
| 1.000 diam               | 40            |
| 1.125 diam               | 10            |
| 1.500 diam               | 13            |
| 2.000 diam               | 85            |
| 2.500 diam               | 93            |
| 3.125 diam               | 74            |
|                          | 332           |
| Bar                      |               |
| 1.0 by 1.0               | 30            |
| 1.0 by 2.0               | 115           |
|                          | 145           |
| Wire                     |               |
| 0.062 diam               | 13            |
| 0.094 diam               | 8             |
| 0.125 diam               | 31            |
|                          | 52            |
| Foil, sheet, or plate    |               |
| 0.005 by 3.5             | 2             |
| 0.009 by 3.5             | 1             |
| 0.035 by 1.0             | 1             |
| 0.040 by 12.0            | 29            |
| 0.125 by 6.0             | 5             |
| 0.500 by 6.125           | 41            |
|                          | 79            |
| Tube                     |               |
| 0.375 o.d. by 0.065 wall | 66            |
| 1.00 o.d. by 0.065 wall  | 104           |
| 2.25 o.d. by 0.375 wall  | 40            |
| 2.50 o.d. by 0.450 wall  | 46            |
| 3.00 o.d. by 0.375 wall  | 50            |
| 3.25 o.d. by 0.250 wall  | 40            |
| 3.25 o.d. by 0.500 wall  | 73            |
|                          | 419           |
| Total                    | 1027          |

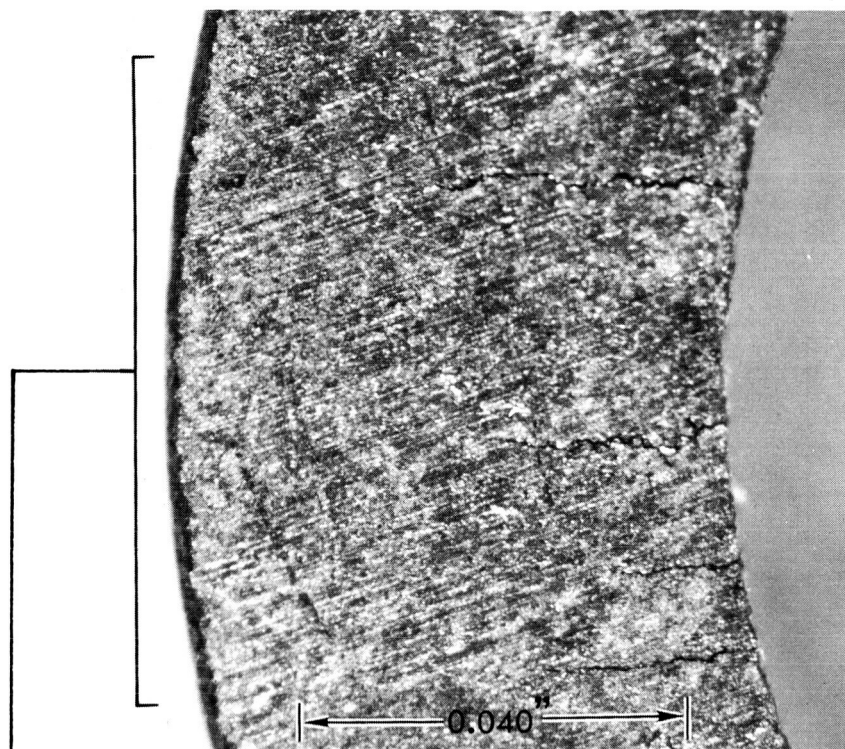
TABLE VIII-2. - T-111 ALLOY PROCURED BY

GE-NSP FOR NASA CONTRACT NAS 3-9426,

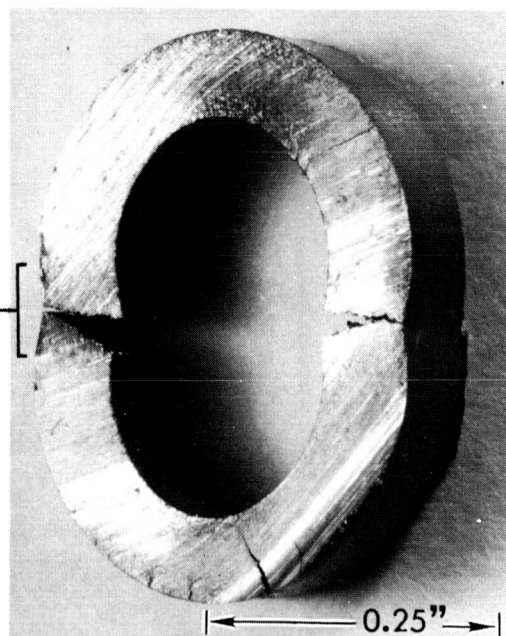
## DEVELOPMENT OF A SINGLE TUBE

## POTASSIUM BOILER

| Item and size,<br>in.    | Weight,<br>lb |
|--------------------------|---------------|
| Rod                      |               |
| 0.125 diam               | 4             |
| 0.250 diam               | 4             |
| 0.690 diam               | 10            |
| 0.750 diam               | 9             |
| 1.000 diam               | 38            |
| 1.375 diam               | 128           |
| 1.500 diam               | 34            |
| 2.000 diam               | 38            |
| 2.250 diam               | 77            |
| 2.500 diam               | 303           |
| 3.063 diam               | 389           |
| 3.688 diam               | 121           |
| 4.438 diam               | 163           |
| 4.625 diam               | 176           |
|                          | 1494          |
| Wire                     |               |
| 0.062 diam               | 10            |
| 0.094 diam               | 15            |
| 0.125 diam               | 26            |
|                          | 51            |
| Foil, sheet, or plate    |               |
| 0.005 by 3.5             | 1             |
| 0.005 by 5.5             | 1             |
| 0.040 by 20.5            | 55            |
| 0.063 by 6.0             | 3             |
| 0.100 by 9.0             | 23            |
| 0.125 by 22.0            | 51            |
| 0.250 by 8.0             | 105           |
| 0.400 by 6.0             | 44            |
|                          | 283           |
| Tube                     |               |
| 0.250 o.d. by 0.050 wall | 16            |
| 0.375 o.d. by 0.065 wall | 14            |
| 0.500 o.d. by 0.075 wall | 18            |
| 0.625 o.d. by 0.008 wall | 8             |
| 0.690 o.d. by 0.045 wall | 13            |
| 0.750 o.d. by 0.04 wall  | 17            |
| 0.875 o.d. by 0.100 wall | 363           |
| 1.325 o.d. by 0.100 wall | 70            |
| 1.500 o.d. by 0.100 wall | 190           |
| 2.375 o.d. by 0.220 wall | 79            |
| 4.386 o.d. by 1.343 wall | 180           |
| 4.420 o.d. by 0.537 wall | 92            |
| 4.424 o.d. by 1.362 wall | 184           |
| 4.625 o.d. by 0.225 wall | 45            |
| 4.625 o.d. by 0.275 wall | 55            |
| 4.625 o.d. by 0.409 wall | 79            |
|                          | 1423          |
| Total                    | 3251          |



(a) Before bending.



(b) After bending.

Figure VIII-1. - T-111 alloy tubing (0.375-in. by 0.062-in. wall) after cutting with water-cooled alumina abrasive cutoff wheel.



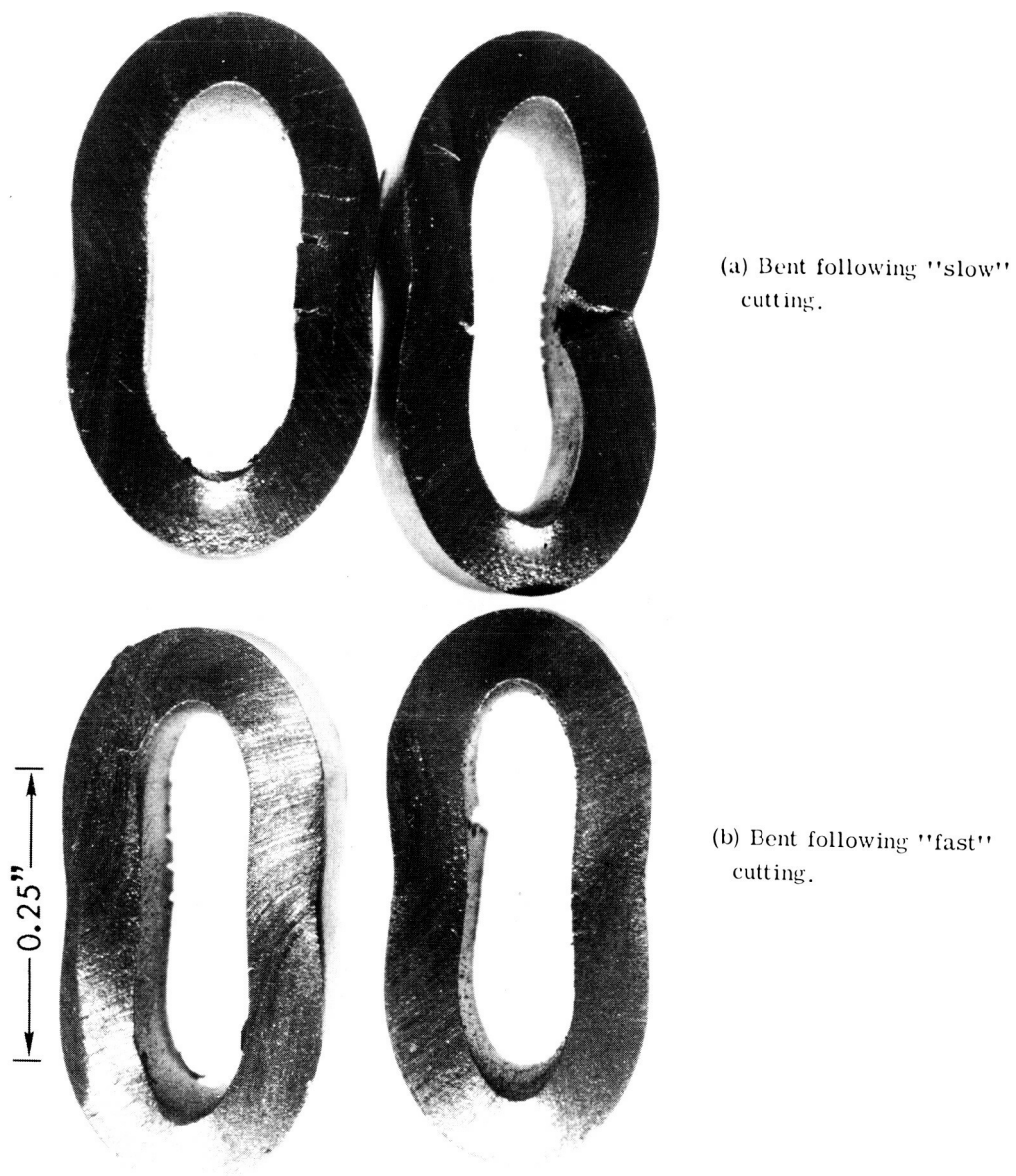
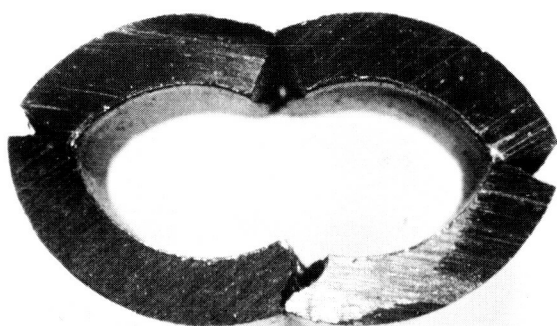
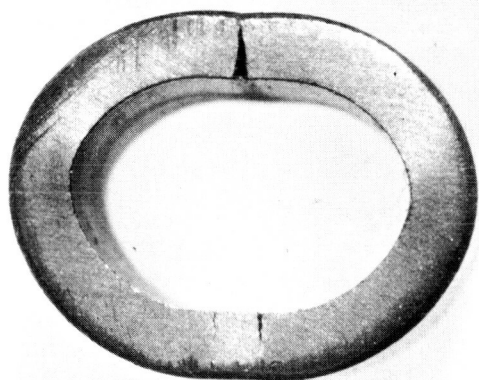


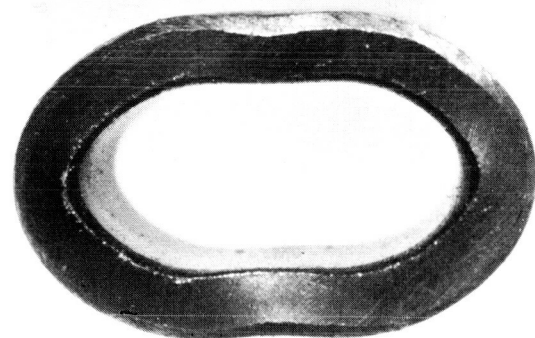
Figure VIII-2. - T-111 alloy tubing (0.375-in. by 0.062-in. wall) showing effect of cutting speed on cracking. Tubing was cut using alumina abrasive cutoff wheel.



(a) Bent as cut.



(b) 0.040 Inch ground off cut surfaces prior to bending.



(c) 0.10 Inch ground off cut surfaces prior to bending.

|← 0.25" →|

Figure VIII-3. - Effect of removing cracked surface prior to bending of T-111 alloy tubing (0.375-in.) cut with alumina cutoff wheel. Tubing was supplied by ORNL from tubing described in Westinghouse Report WANL-PR(N)-004.

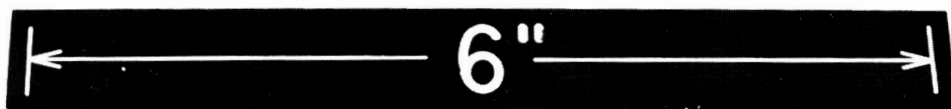
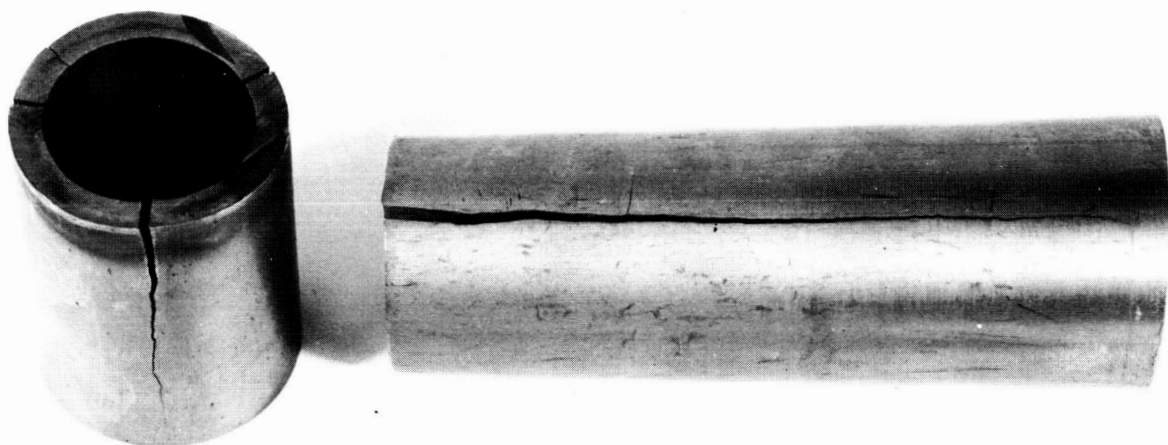
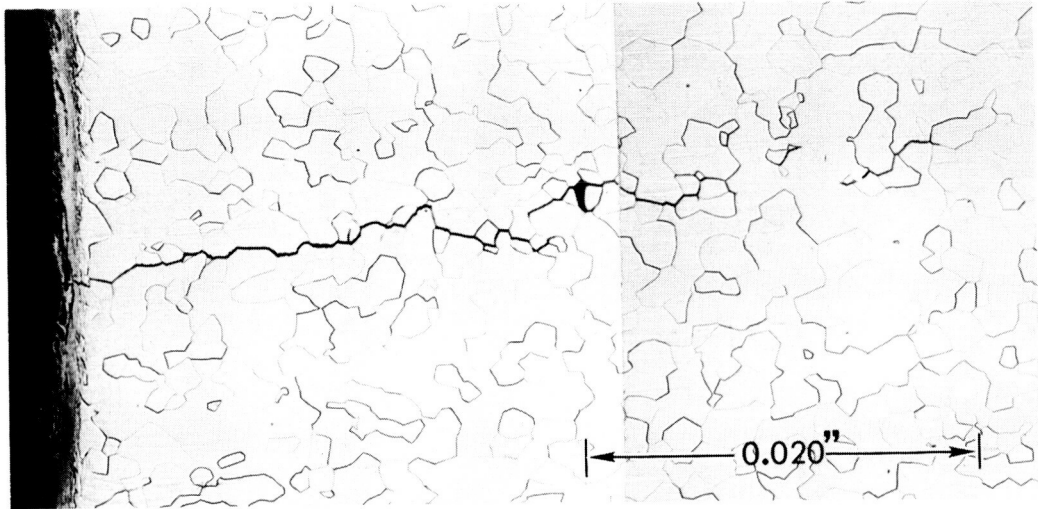
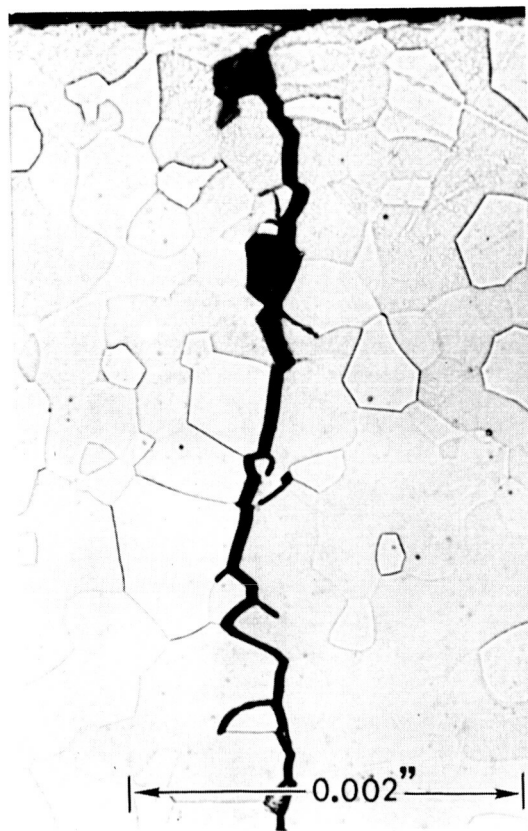


Figure VIII-4. - Cracks in T-111 alloy tube hollows (2-in. by 0.25-in. wall) observed during initial tube reducing. The cracks apparently propagated from shallow cracks introduced when hollows were cut with abrasive cutoff wheel.

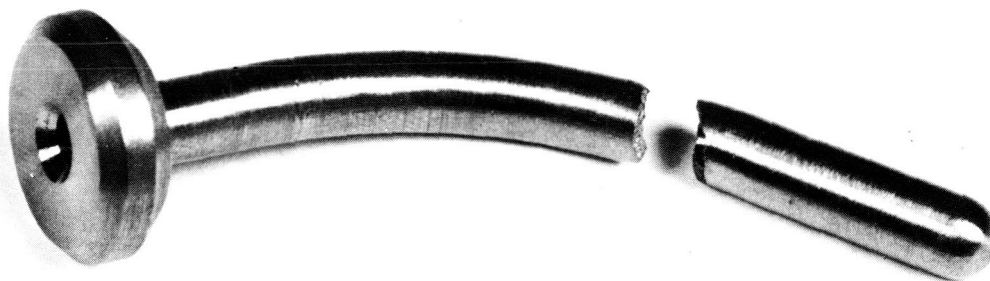


(a) 1.5-Inch-diameter rod.



(b) 0.5-Inch-diameter rod.

Figure VIII-5. - Intergranular cracks in T-111 alloy rod cut with water-cooled alumina abrasive cutoff wheel. Etchant: 30 grams  $\text{NH}_4\text{F}$ , 50 milliliters  $\text{HNO}_3$ , 20 milliliters  $\text{H}_2\text{O}$ .



(a) No stress relief before bending.



(b) 2400<sup>0</sup> F, 1-hour stress relief before bending.

Figure VIII-6. - Machined T-111 alloy thermocouple wells after bending.

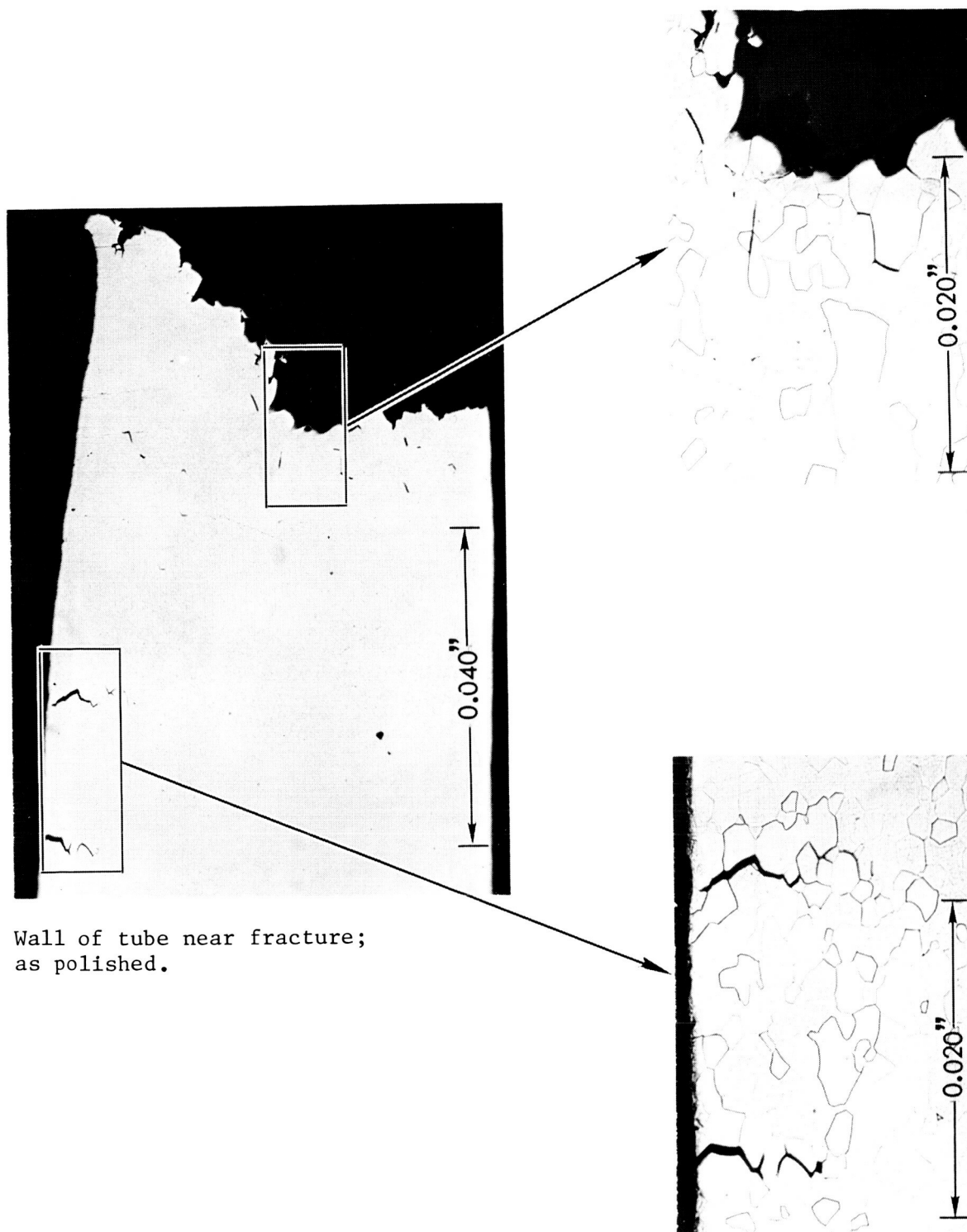


Figure VIII-7. - Longitudinal sections of fractured T-111 alloy thermocouple well after bending showing intergranular cracking in the wall on tension side of bend. Etchant: 30 grams  $\text{NH}_4\text{F}$ , 50 milliliters  $\text{HNO}_3$ , 20 milliliters  $\text{H}_2\text{O}$ .

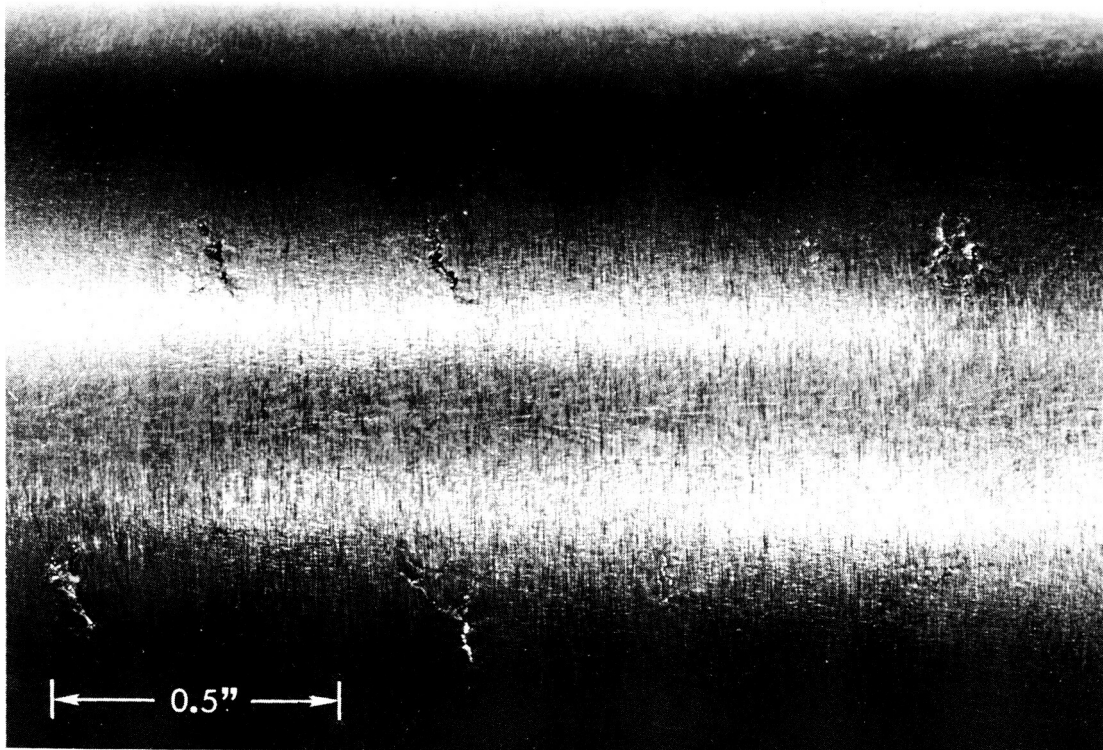
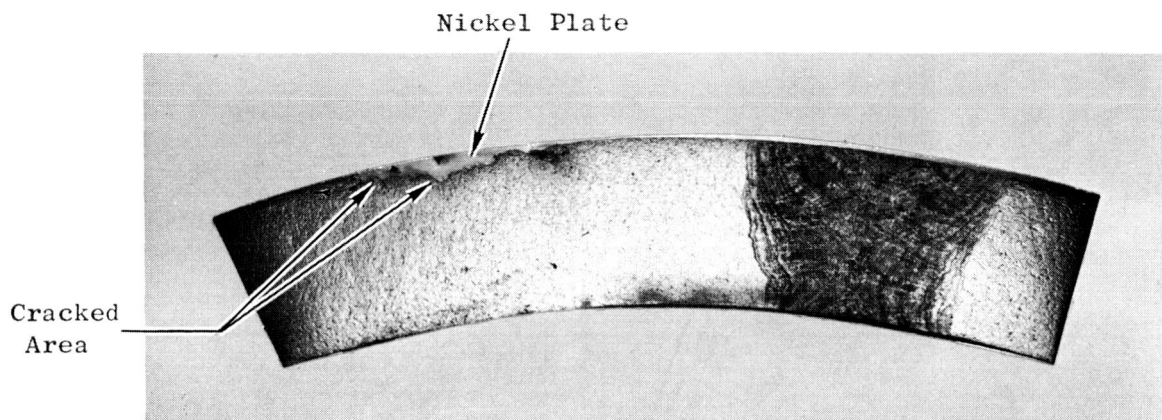
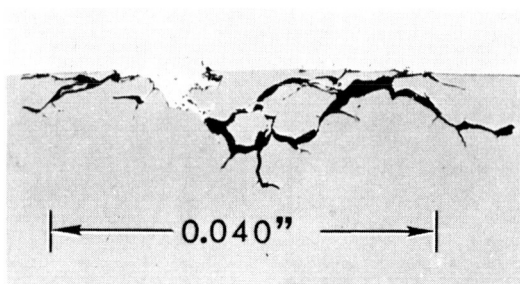


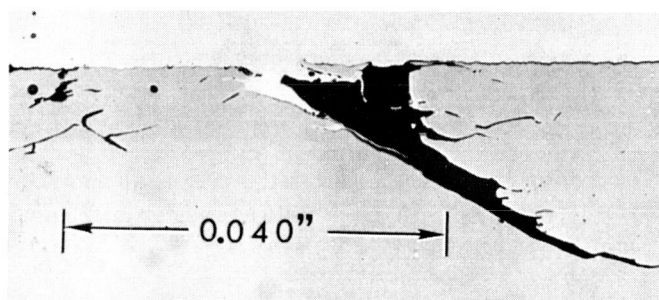
Figure VIII-8. - Transverse cracks in the heat-affected zone adjacent to weld on outside diameter of 1.5-inch-outside-diameter by 0.100-inch-wall EB welded and reworked T-111 alloy tube.



(a) Transverse section; etched.



(b) Transverse section; as polished.



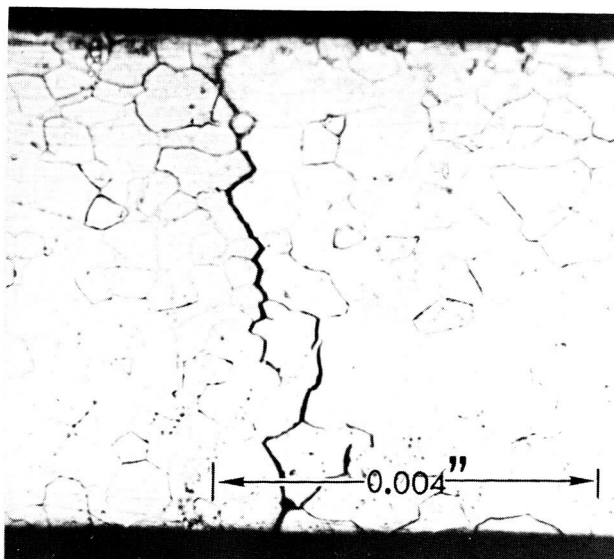
(c) Longitudinal section; as polished.

Figure VIII-9. - Sections through cracks in 1.5-inch-outside-diameter by 0.100-inch-wall EB welded and reworked T-111 alloy tube after final anneal at 3000<sup>0</sup> F for 1 hour. Etchant: 30 grams NH<sub>4</sub>F, 50 milliliters HNO<sub>3</sub>, 20 milliliters H<sub>2</sub>O.



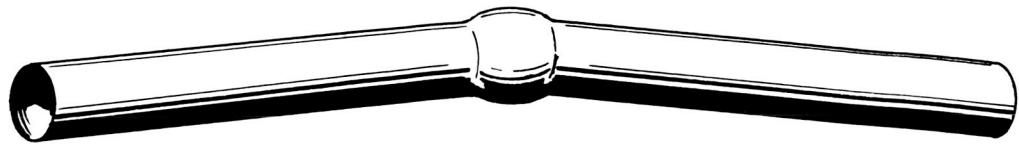


(a) Cracks (arrows).



(b) Transverse section through one cracked area of T-111 alloy diaphragm; etched.

Figure VIII-10. - Intergranular cracks in T-111 alloy pressure transducer diaphragm. Etchant: 30 grams  $\text{NH}_4\text{F}$ , 50 milliliters  $\text{HNO}_3$ , 20 milliliters  $\text{H}_2\text{O}$ .



(a) Sagged butt weld joint.



(b) Joint after straightening.



(c) Intergranular cracking.



(d) Grain boundary sliding.

Figure VIII-11. - Cracking in T-111 alloy tube-to-tube (0.375-in. by 0.065-in. wall) butt weld joint. Cracking occurred during attempts to straighten tube after it had sagged during welding.

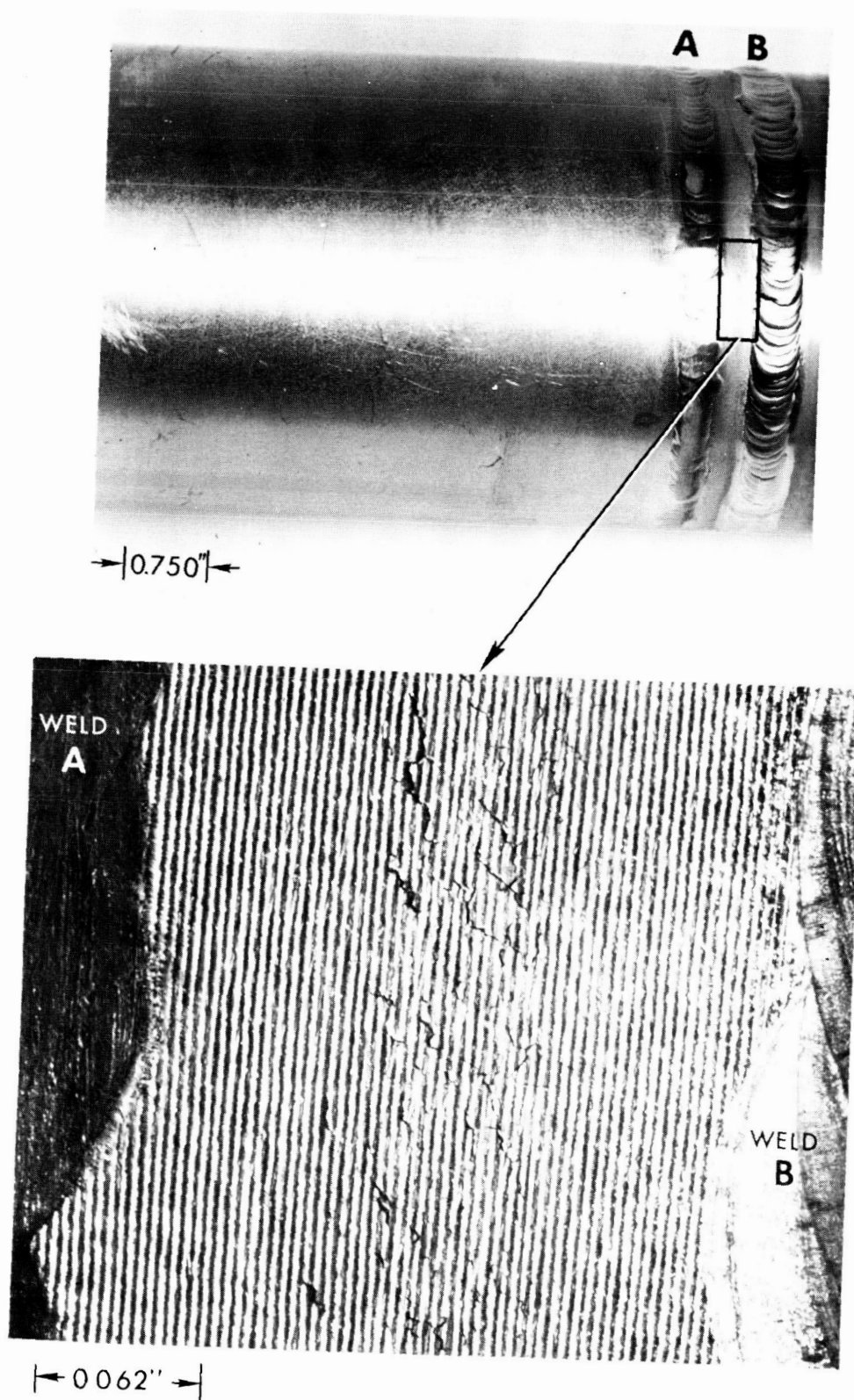


Figure VIII-12. - Typical area of cracking between GTA welds of T-111 alloy EM pump duct.

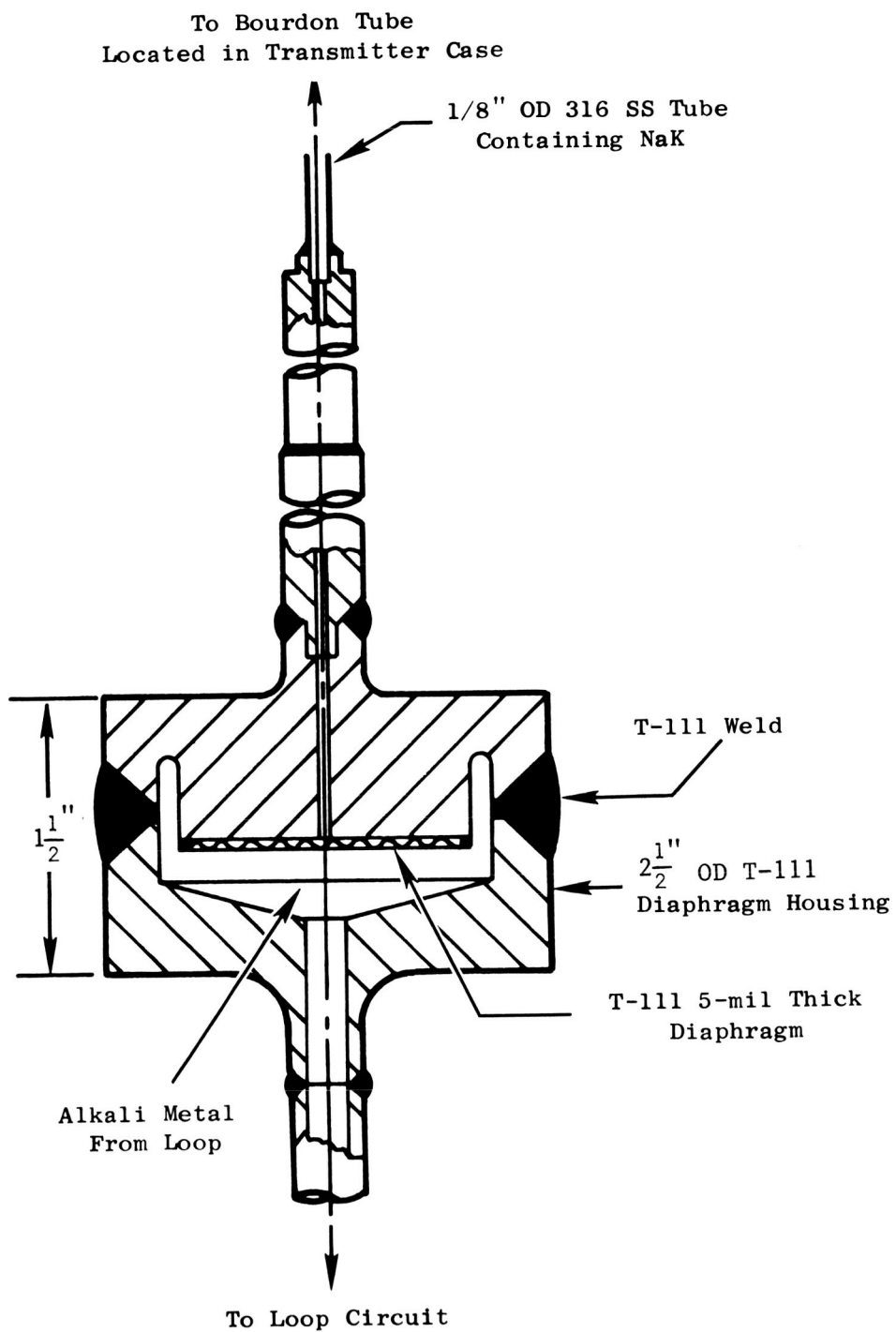


Figure VIII-13. - Full section view of Taylor pressure transducer showing its functional relation to loops of boiler test rig.

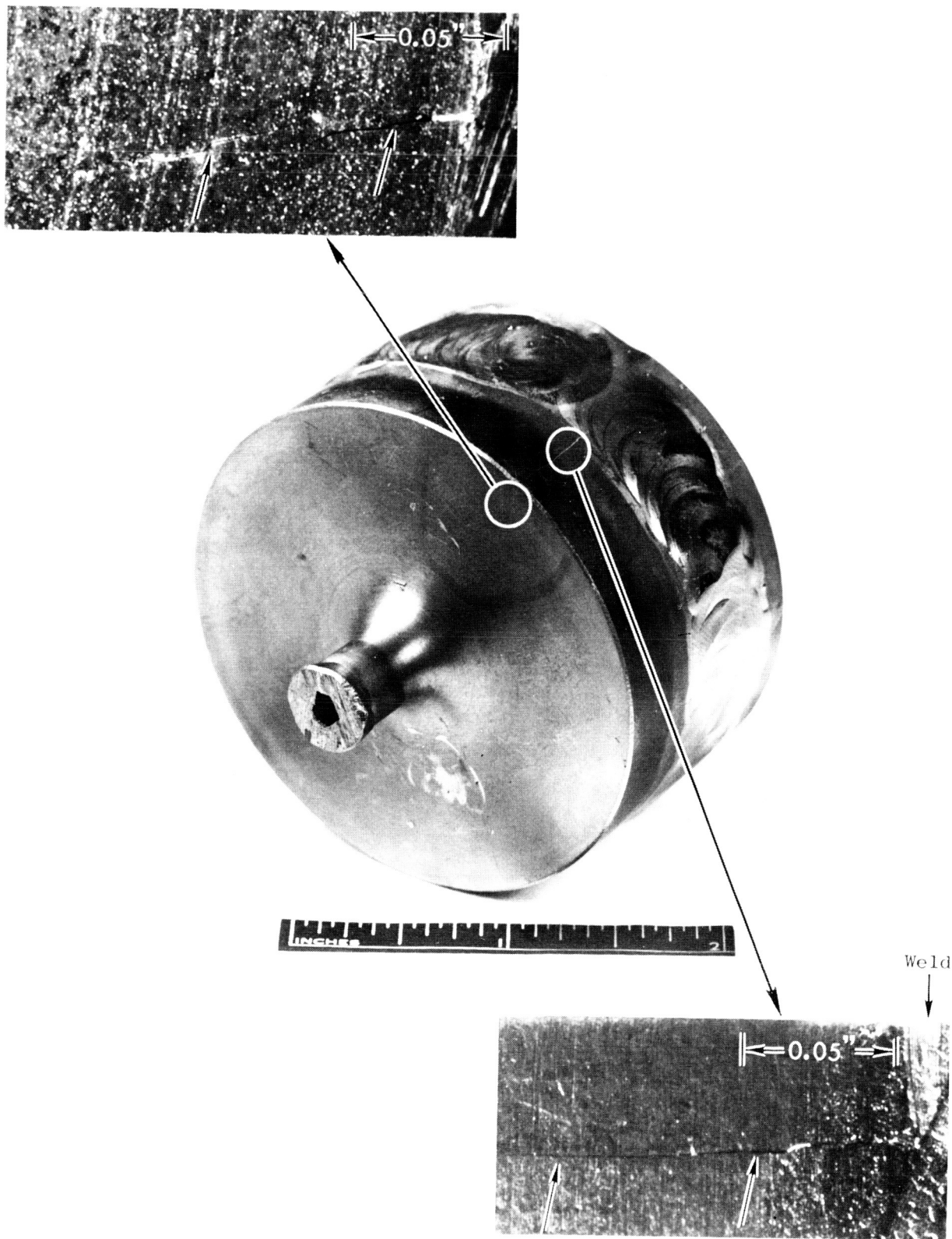


Figure VIII-14. - Taylor absolute pressure transducer 14 showing large crack (see arrows in enlargements of cracked areas) extending from edge of weld nugget to flat surface of bottom flange.

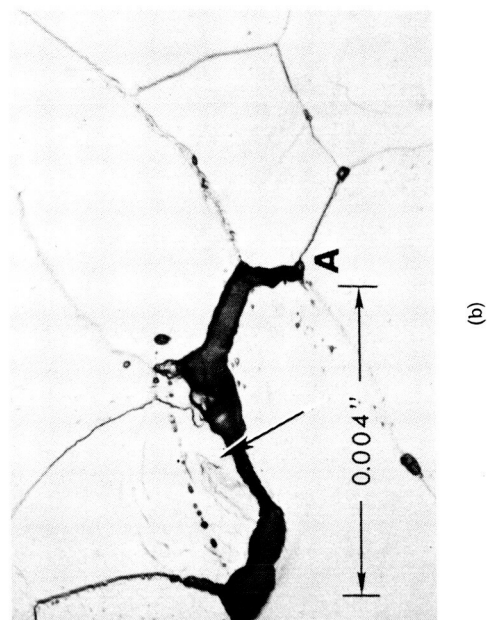


Figure VIII-16. - Photomicrographs of end A of crack shown in Figure VIII-15 at two magnifications. The arrow in photomicrograph (b) shows presence of highly distorted grain near end of crack. Etchant: 30 grams  $\text{NH}_4\text{F}$ , 50 milliliters  $\text{HNO}_3$ , 20 milliliters  $\text{H}_2\text{O}$ .

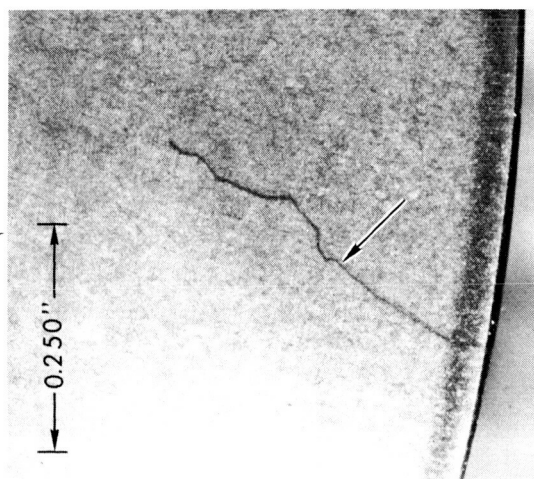
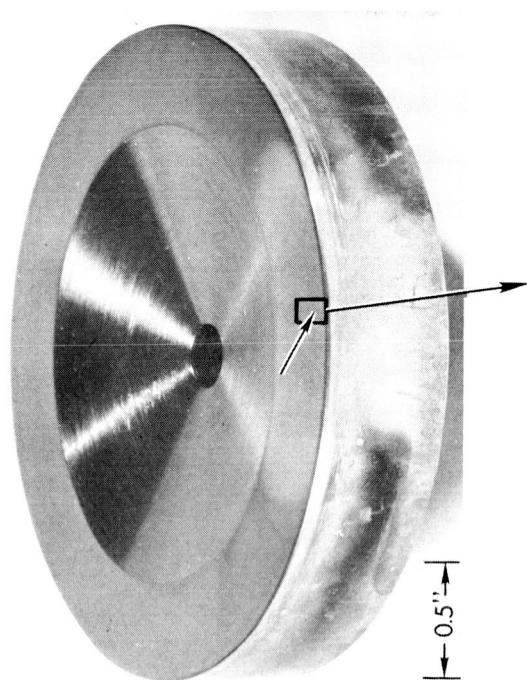


Figure VIII-15. - Bottom flange of pressure transducer 14 after removal of weld nugget. Enlargement of inside facing flange shows depth of crack propagation.



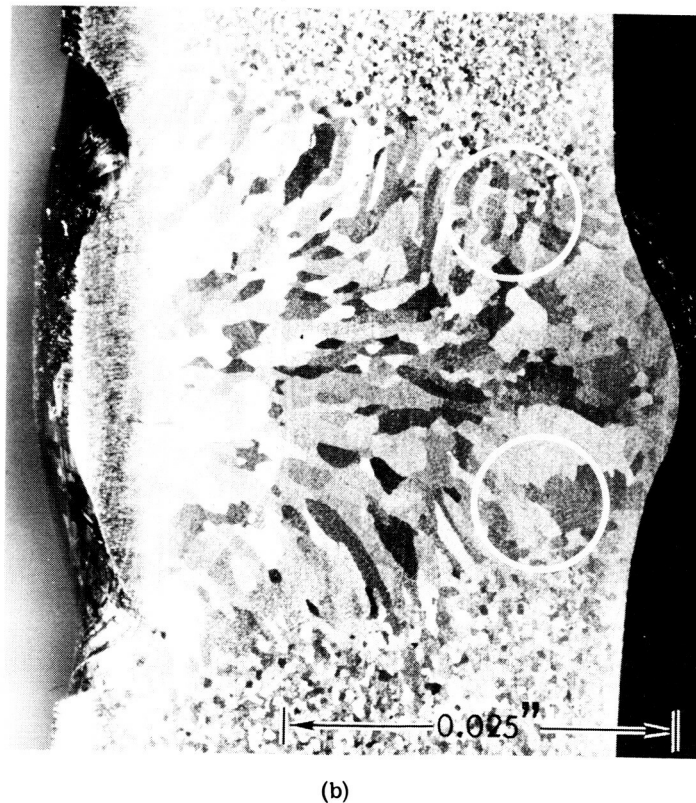
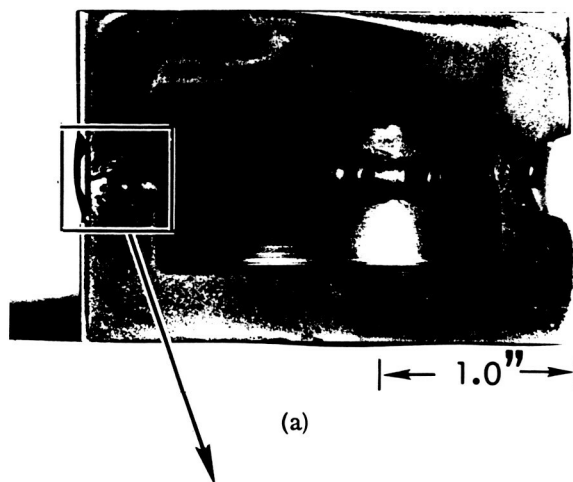
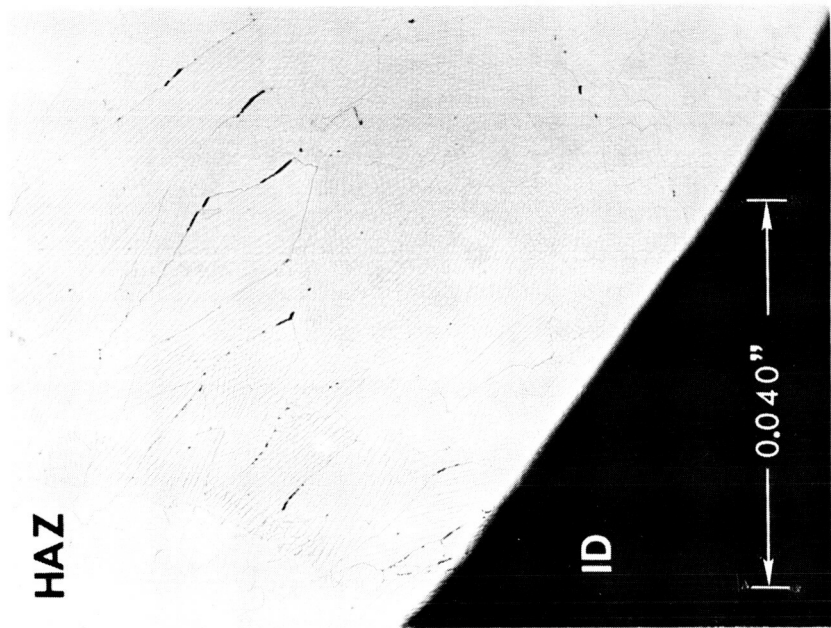


Figure VIII-17. - Multipass GTA weld sample formed by joining two 2.5-inch-outside-diameter by 0.375-inch-wall T-111 alloy closed end tubes with three different filler wires, T-111 alloy, Cb-1Zr, and Ta-10W. The circled areas in (b) indicate approximate locations of most cracking observed.



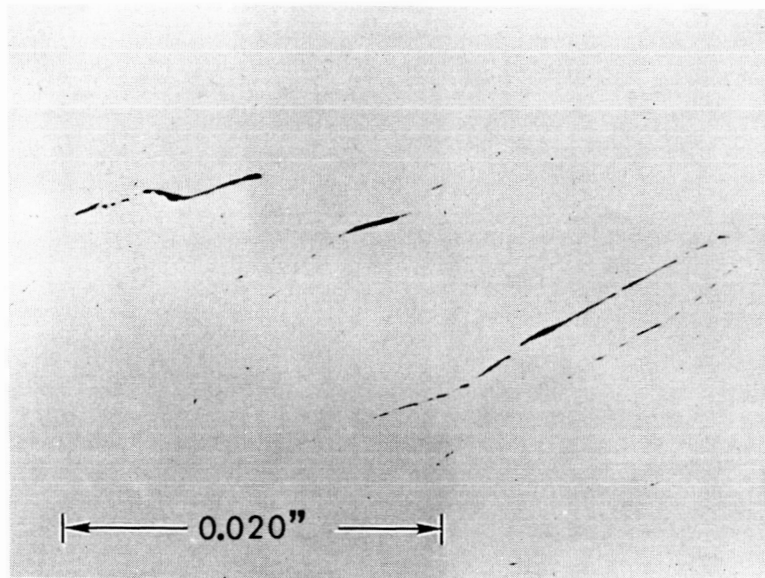
Lightly Etched



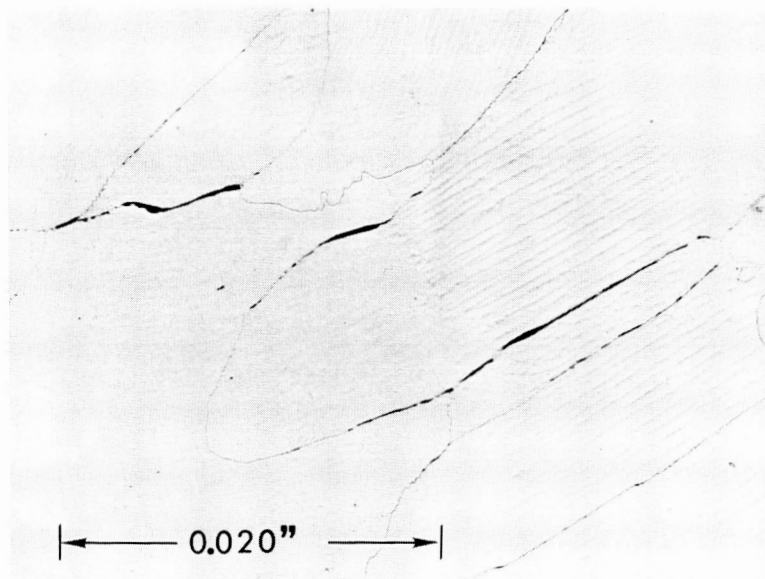
As Polished

Figure VIII-18. - Transverse microstructure near edge of weld nugget in three-pass T-111 alloy weld showing cracking typical of this area. Etchant: 30 grams  $\text{NH}_4\text{F}$ , 50 milliliters  $\text{HNO}_3$ , 20 milliliters  $\text{H}_2\text{O}$ .





**As Polished**



**Lightly Etched**

Figure VIII-19. - Transverse microstructure of T-111 alloy fusion pass of multipass T-111 alloy tube weld using T-111 alloy filler showing grain boundary separation. Etchant: 30 grams  $\text{NH}_4\text{F}$ , 50 milliliters  $\text{HNO}_3$ , 20 milliliters  $\text{H}_2\text{O}$ .

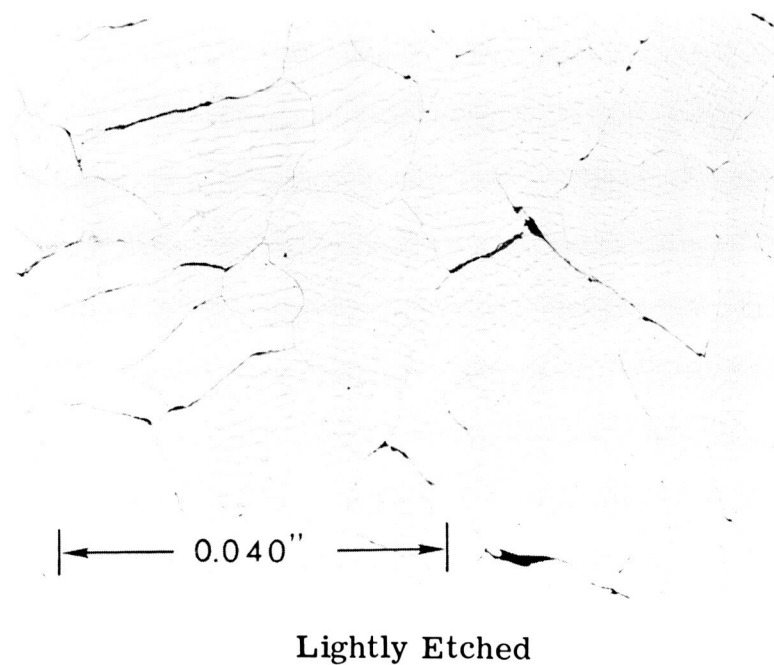
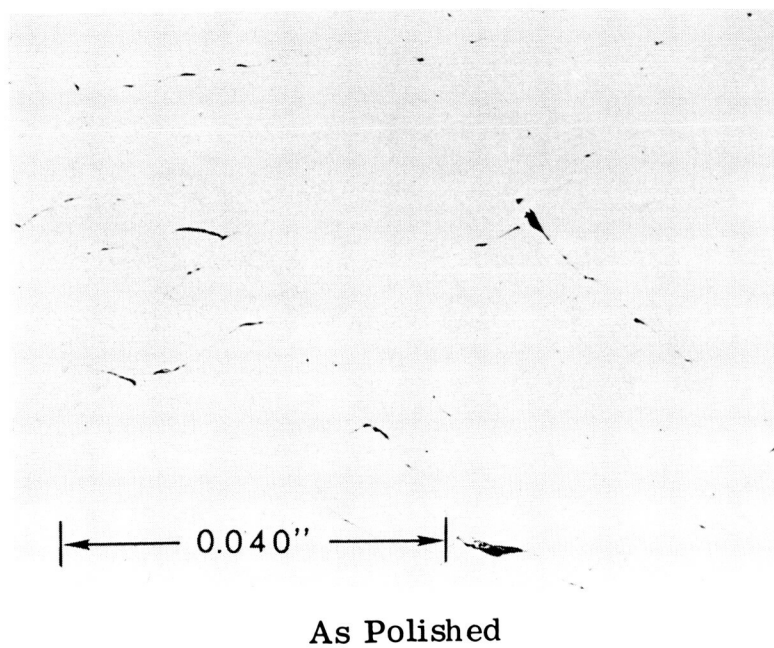
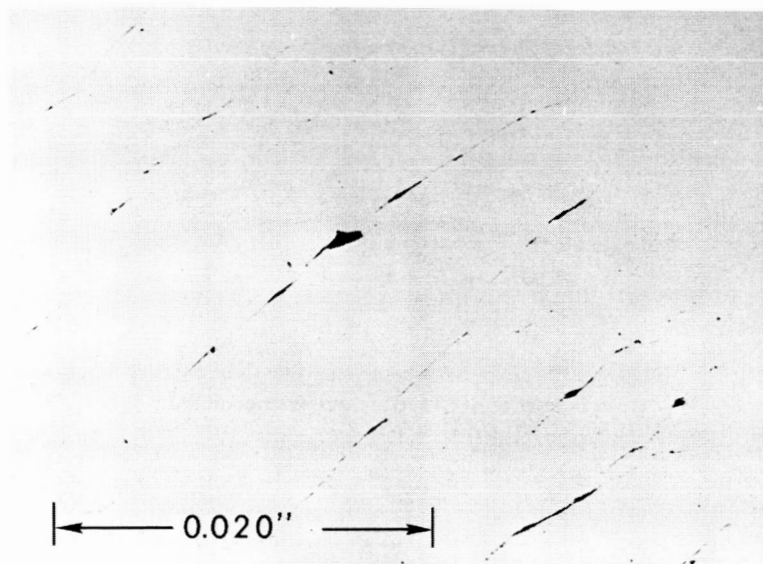
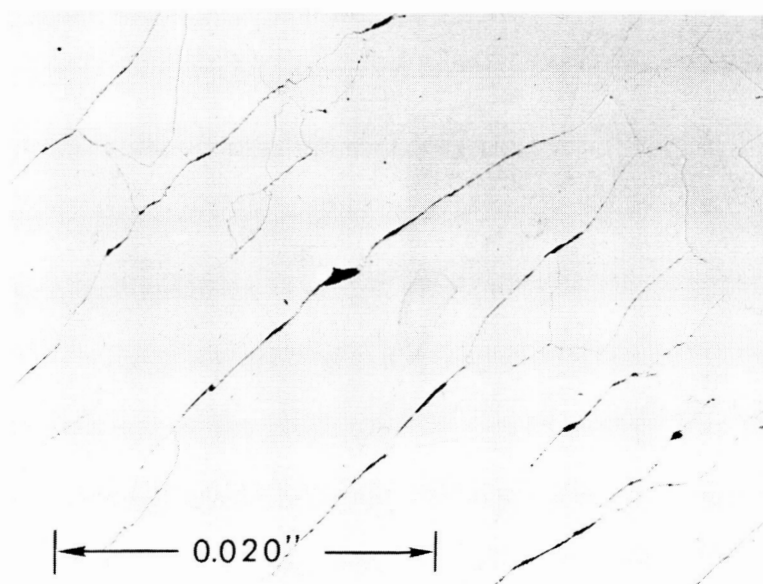


Figure VIII-20. - Transverse microstructure of T-111 alloy fusion pass of multipass T-111 alloy tube weld using Cb-1Zr alloy filler showing grain boundary separation. Etchant: 30 grams  $\text{HN}_4\text{F}$ , 50 milliliters  $\text{HNO}_3$ , 20 milliliters  $\text{H}_2\text{O}$ . X100.



**As Polished**



**Lightly Etched**

Figure VIII-21. - Transverse microstructure of T-111 alloy fusion pass of multipass T-111 alloy tube weld using Ta-10W alloy filler showing grain boundary separation. Etchant: 30 grams  $\text{HN}_4\text{F}$ , 50 milliliters  $\text{HNO}_3$ , 20 milliliters  $\text{H}_2\text{O}$ .

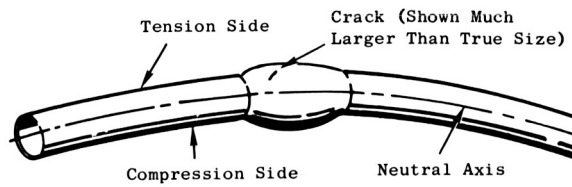


Figure VIII-22. - Sketch showing location of crack in weld nugget of T-111 alloy tube removed from corrosion test loop boiler.

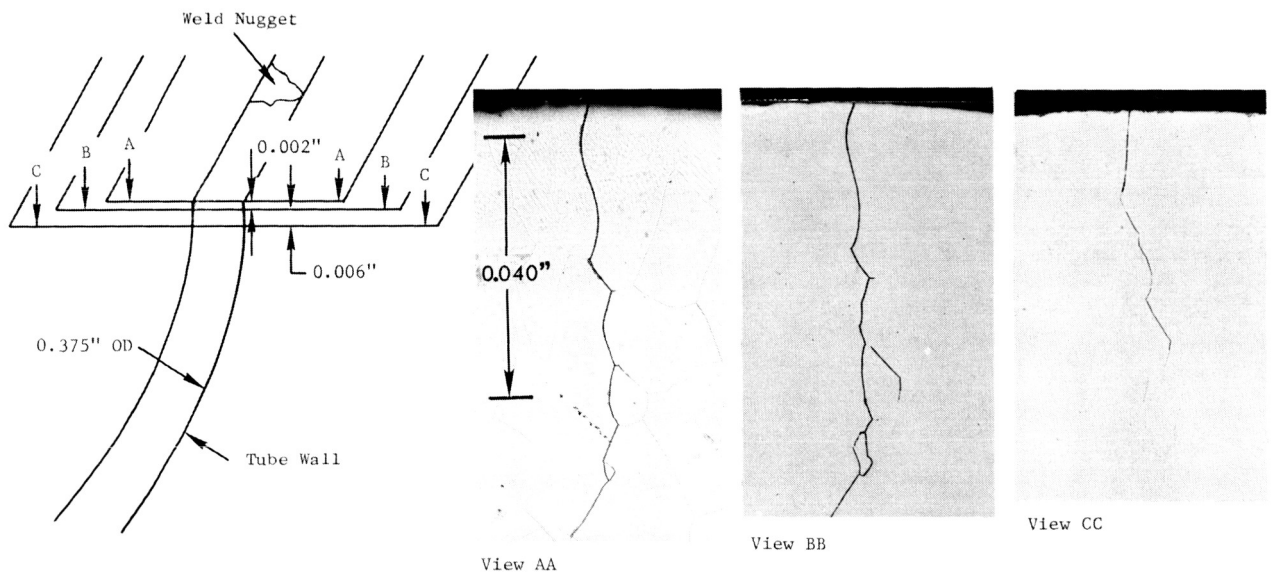


Figure VIII-23. - Intergranular crack in weld nugget of 0.375-inch-diameter T-111 boiler tube removed from T-111 Rankine system corrosion test loop.

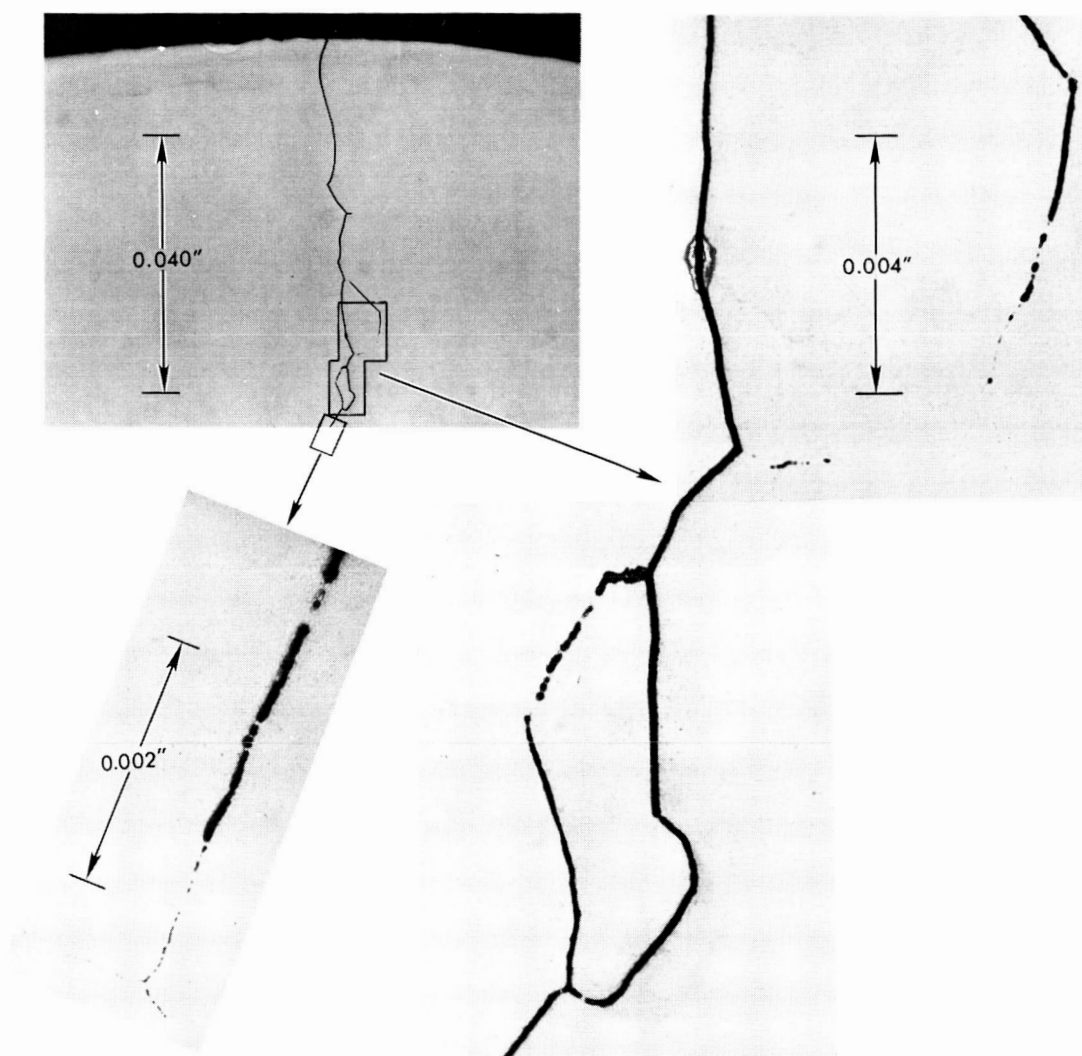
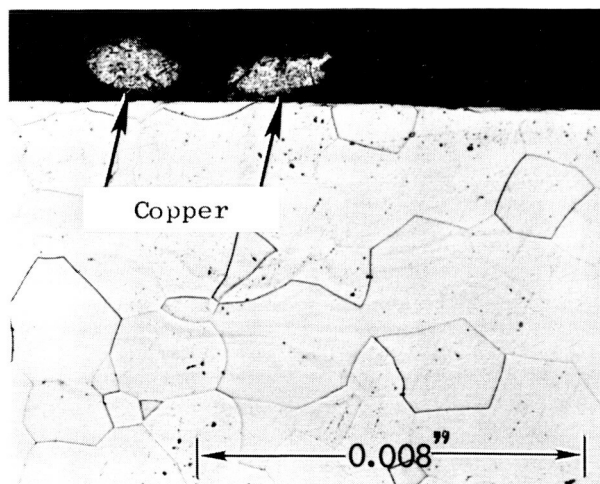
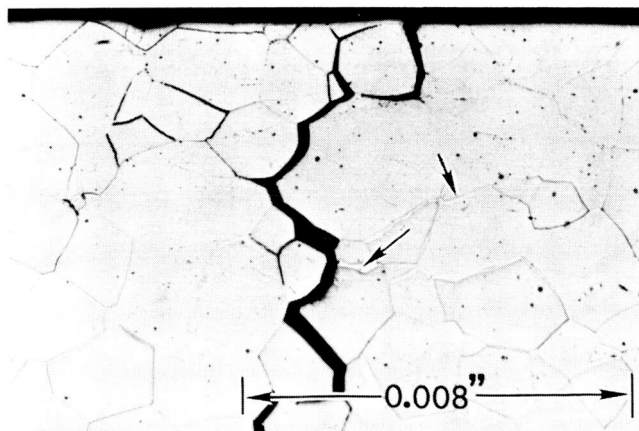


Figure VIII-24. - Intergranular crack in weld nugget of 0.375-inch-diameter T-111 boiler tube removed from T-111 Rankine system corrosion test loop.



(a) As tack welded.



(b) Tack welded followed by 2400° F, 1-hour heat treatment.

Figure VIII-25. - T-111 alloy tubing (1.5-in. by 0.100-in. wall) tack welded with copper electrode. Residual copper shown by arrows in (a). Etchant: equal volumes of  $\text{H}_2\text{O}$ ,  $\text{H}_2\text{O}_2$ ,  $\text{H}_2\text{SO}_4$ , HF.

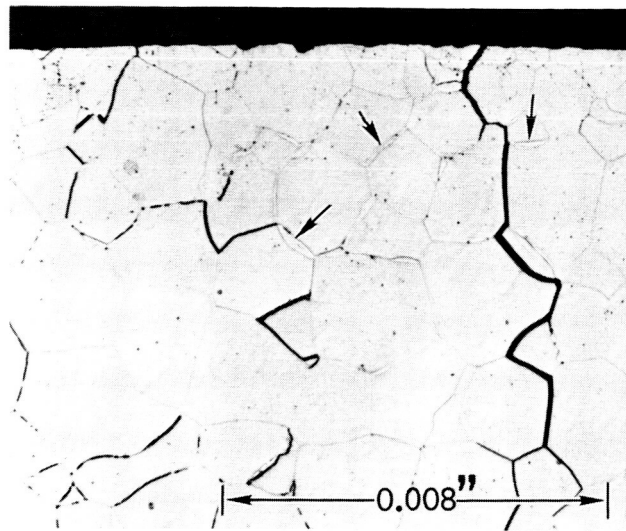


Figure VIII-26. - Intergranular cracking of T-111 alloy tubing (0.375-in. by 0.065-in. wall) tack welded using copper electrode and heated to 2400<sup>0</sup> F for 1 hour.  
Etchant: equal volumes of H<sub>2</sub>O, H<sub>2</sub>O<sub>2</sub>, H<sub>2</sub>SO<sub>4</sub>, HF.

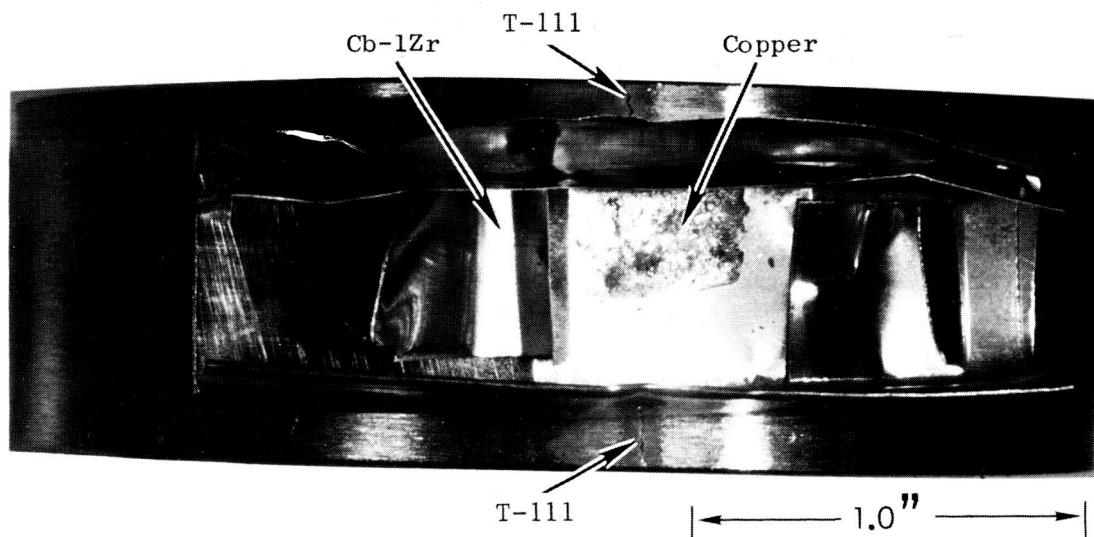


Figure VIII-27. - Crack (see arrows) in T-111 alloy tube (1.5-in. by 0.100-in. wall) produced by copper diffusion into tube through multilayers of 0.002-inch-thick Cb-1Zr foil during heat treatment at 2400<sup>0</sup> F for 1 hour.

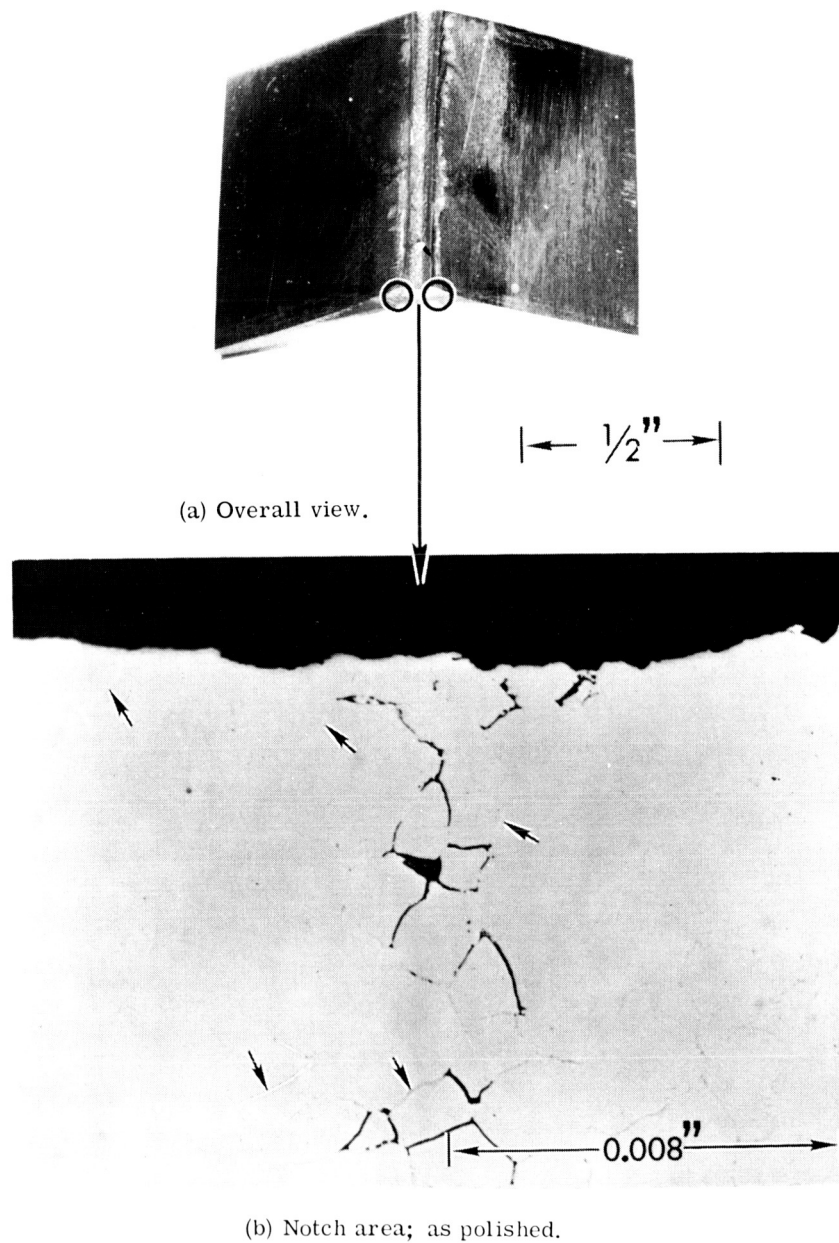


Figure VIII-28. - Copper filled notch in T-111 alloy bend sample (0.063 in. thick) after heat treatment at 2400<sup>o</sup> F for 1 hour. Light colored grain boundary phase in (b) is rich in Cu and Hf.



## IX. WELDABILITY OF TUNGSTEN BASE ALLOYS\*

G. G. Lessmann<sup>†</sup> and R. E. Gold<sup>†</sup>

### SUMMARY

The weldability of unalloyed tungsten and two tungsten alloys was evaluated. The alloys were W-25Re (wt %) and W-25Re-30Mo (at. %). These were evaluated as arc cast material and for the ternary alloy also as a powder metallurgy product. The most important aspect of welding unalloyed tungsten was that it is very sensitive to thermal shock. High preheat temperatures (to 1400<sup>0</sup> F) alleviated this problem. W-25Re had improved thermal shock resistance but was shown to be basically hot tear sensitive in gas tungsten arc welding. Preheat temperatures of 1400<sup>0</sup> F were again beneficial. The powder metallurgy W-25Re-30Mo alloy displayed excellent weldability, whereas the arc cast material displayed extensive hot tearing and, hence, poor weldability. The anomalous hot tearing behavior of the arc cast W-25Re-30Mo alloy was ascribed to a very high sensitivity to oxygen contamination. The effects of postweld annealing, joint preparation, and aging for 1000 hours at temperatures to 3000<sup>0</sup> F were evaluated. The high temperature tensile strength of base metal, gas tungsten arc welds, and electron beam welds in W-25Re-30Mo was determined.

### INTRODUCTION

The studies described in this paper complement a series of programs designed to upgrade refractory metal alloy technology in terms of space power requirements. Contemplated systems would provide either direct conversion of thermal to electric energy as with thermoelectric or thermionic devices or mechanical conversion using Rankine or Brayton cycles. The major design objective of high thermal efficiency with minimum system weight is approached by designing for maximum operating temperatures. Application of tungsten or tungsten alloys seems to offer the ultimate potential in this respect because tungsten has the highest melting point of

---

\*Based on work conducted under NASA contract NAS 3-2540.

<sup>†</sup>Westinghouse Astronuclear Laboratory, Pittsburgh, Pennsylvania.

all metals, 6170<sup>o</sup> F. On the negative side, tungsten has a ductile-to-brittle transition temperature which is well above room temperature for recrystallized or cast (weld) structures. Hence, considerable reserve must be exercised in the application of this metal in fabricated structures typical of those required for space power systems.

This weldability study was designed to lend further definition to the general problems which would be encountered in fabrication of tungsten, or tungsten alloy structures, by welding. Stimulus for this evaluation was provided by the introduction of alloys of improved ductility such as the binary W-Re or ternary W-Re-Mo alloys. Further, techniques to convert these alloys from arc cast ingots have been recently developed. Arc cast material has historically demonstrated greater fabricability than the powder metallurgy product. Hence, the availability of arc cast material provided an additional incentive for initiating this welding study.

The basic objective of this program was to define the weldability of tungsten and its alloys in terms comparable to those employed in evaluating other refractory metal alloys (Cb or Ta based) which are prime candidates for space power system applications (ref. 1). The alloys of current interest in this respect are W-25Re (wt %) and W-25Re-30Mo (at. %). These were evaluated for the first time in this program as material converted from arc cast ingots along with arc cast unalloyed tungsten. The ternary alloy was also evaluated as a powder metallurgy product. The primary factors evaluated were

- (1) Basic weldability of sheet material using the gas tungsten arc and electron beam processes
- (2) Effect of weld atmosphere control on basic weldability
- (3) Effect of weld preheat to 1400<sup>o</sup> F
- (4) Importance of joint preparation
- (5) Effect of postweld annealing
- (6) Effect of long-time, high-temperature thermal exposure

## TECHNICAL PROGRAM

### Alloys Evaluated

The unalloyed tungsten and the tungsten alloys evaluated in this program are listed in the following table along with their respective melting points and densities.

|                                  | Melting point,<br>°F | Density,<br>lb/in. <sup>3</sup> |
|----------------------------------|----------------------|---------------------------------|
| Unalloyed tungsten               | 6170                 | 0.697                           |
| W-25Re (wt %)                    | 5650                 | .714                            |
| W-25Re-30Mo (at. %) <sup>a</sup> | 5270                 | .651                            |

<sup>a</sup>Conventional designation of this alloy is in at. % and is used in this paper; composition in wt % is W-29.5Re-18.2Mo.

The unalloyed tungsten and the binary tungsten-rhenium alloy were evaluated solely as arc-cast (AC) sheet, while the ternary tungsten-rhenium-molybdenum alloy was evaluated both as arc-cast (AC) and powder-metallurgy (PM) sheet. Evaluation of arc cast material was emphasized because initial welding results on unalloyed tungsten showed that porosity free welds could only be made in arc cast material. Further, the general trend in refractory metal technology has historically been towards arc cast material for higher purity and greater fabricability.

The phase diagrams pertinent to these alloys are shown in figures IX-1, IX-2, and IX-3. In figure IX-3 the 1830° F (1000° C) isotherm for the W-Re-Mo ternary is shown. The location of the alloy composition used in this study is indicated. From these diagrams it is seen that both the binary and ternary alloys are nominally single phase but lie quite near the limiting solvus lines.

The binary W-Re and Mo-Re diagrams are quite similar. From the standpoint of weldability, however, a very important difference exists. W-Re alloys with compositions in the  $\alpha$ -phase region would be expected to be subject to considerably more constitutional segregation than would similar Mo-Re alloys. This follows from a direct comparison of the temperature range through which the metal must cool as it solidifies. Freezing point depression of the binary W-Re alloy would be expected to be pronounced in rapidly solidified cored weld structures. These phase relations imply that the W-Re-Mo system should experience considerably less segregation than the binary W-25Re alloy. This is based on the very narrow liquidus-solidus separation in the binary Mo-Re alloy for the ternary solute ratio (~60%Re). Data presented later in this paper tend to substantiate this expectation.

The interest in the binary W-Re alloy results from the well-known but poorly understood "rhenium ductilizing effect." This effect is not limited to W but has also been seen for Re additions to the other Group VIA metals, molybdenum and chromium. A recent review of this effect by Klopp (ref. 2) indicates the general lack of understanding of the mechanism(s) involved. Based on experimental evi-

dence two conclusions seem indicated:

(1) Re additions to Group VIA metals such as tungsten promote twinning as a major means of deformation. This implies a significant reduction in the normally high stacking fault energy of these metals.

(2) Some change in the morphology and/or distribution of interstitial compounds, particularly oxides, occurs. This would appear to be important since Stephens (ref. 3) has shown that the DBTT for pure W rises rapidly with oxygen content, the fractures being invariably intergranular.

The ternary W-Re-Mo alloy is a more recently developed material (ref. 4). Molybdenum additions to the W-Re binary alloys are attractive for several reasons. The ternary, with molybdenum replacing tungsten, is less expensive to produce and has a lower density than either W or W-Re binary alloys. However, the melting point is considerably lower and as a result the long-time high temperature strength is somewhat less than that of the higher melting binary alloys.

The short time strength properties determined for the ternary alloy are compared with typical values for arc cast tungsten and W-25Re in figures IX-4 and IX-5. Data relating the corresponding tensile elongations are listed in table IX-1. Up to 3000° F, the highest test temperature used, the differences are not very significant; but for higher temperatures, it is expected the ternary alloy would not continue to be competitive with the higher melting W-25Re and unalloyed tungsten.

Bend ductility (4t bend radius) of the as-received alloys is shown in table IX-2 along with notes regarding the as-received structures. Interstitial chemical analyses are provided in table IX-3. It is important to note that all of these metals have quite low solid solubilities for the interstitial elements. Hence, segregation of interstitials often occurs at grain boundaries and other regions of high disregistry in the lattice. This resultant segregation is thought to be responsible, in part, for the characteristic grain-boundary nucleated fractures so prevalent in these materials.

An unambiguous definition of the factors which control brittleness in tungsten and its alloys has not been achieved. However, it is well known that wrought, stress-relieved structures possess significantly greater ductility than that of recrystallized structures. This advantage has led to the widespread use of tungsten-base materials in the wrought, stress-relieved condition. This is the reason the materials used in this study were stress relieved rather than recrystallized. The influence of structure on ductility adds importance to the aging studies, which were conducted to assess the effects of long time, high temperature thermal exposures on structural stability.

An interesting feature of the interstitial analyses of table IX-3 is that, for the ternary alloy, the oxygen and nitrogen contents of the PM product are lower than those of the AC product. This is contrary to the normal relation and reflects the

fact that this alloy was originally developed as a PM product and evolved from a program which had as one of its major goals the development of techniques for obtaining extremely low interstitial impurity levels in tungsten and molybdenum alloy powders. The data in table IX-3 attest to the efficiency of these procedures. A similar comparison was not made for metallic impurities, but it is expected these would be somewhat lower in the AC sheet by virtue of the purification which occurs during vacuum arc melting.

## Alloy Weldability

Basic considerations. - Weldability of tungsten and tungsten alloy sheet was investigated by evaluating responses to electron beam and gas tungsten arc welding over a wide parameter range. This approach provides a delineation of alloy sensitivity to process variations and a definition of weldability limitations.

The primary welding variable in this respect is welding speed. Weld speed is the controlling factor in unit weld length heat input for achieving a given target weld size, as shown graphically in figure IX-6. The significant effect of weld speed is obvious in this figure. Heat input is nearly a function of  $1/v$ , or the dwell time of the arc. At slower speeds a small decrease in speed causes a large increase in heat input, and consequently increases the magnitude of the thermal disturbance. This effect would seem to be most important from a metallurgical standpoint. On the other hand, higher weld speeds can be considered to represent a greater thermal shock. In some materials the magnitude of the thermal disturbance plays the most significant role in establishing weldability limitations, while in others thermal shock is the overriding consideration. Because of the brittle nature of the materials evaluated in this program, thermal shock played a more important role in defining weldability.

Electron beam welding provides a minimum sized weld and hence minimum heat input throughout the welding speed range. This is also shown in figure IX-6. Frequently, minimizing weld size is beneficial in improving weld properties, but like higher speed GTA welding, minimizing heat input characteristically increases thermal shock. Again, this proved to be important in welding tungsten alloys, as described later in this paper. Hence, by employing both the GTA and EB welding processes in this study, extremes of both the thermal disturbance and thermal shock effects of welding were evaluated.

A further interesting feature of the heat input requirements developed in this program is the decrease in heat input for the higher solute content alloys (also lower melting point alloys). Hence, while the advanced tungsten alloys were devel-

oped for improved ductility alone, from a welding standpoint both improved ductility and lower thermal shock can potentially combine in these alloys for improved weldability. Decreased thermal shock in the alloys results from the lower heat input requirement (at a given weld size and welding speed) coupled with the lowered melting point. This combination decreases the instantaneous thermal gradient during welding.

Welding procedures. - All gas tungsten arc welding was conducted in a very pure, precisely controlled, helium environment employing the vacuum purged weld chamber shown in figure IX-7. The welding atmosphere was monitored during welding so that oxygen and moisture levels were always maintained at less than 5 ppm. The method of achieving and maintaining these purity levels is described in detail in references 1 and 5. During this investigation the importance of providing a high quality welding atmosphere for welding tungsten alloys was demonstrated. This aspect is discussed under the heading Hot Tearing in the RESULTS section of this paper. All gas tungsten arc welding was accomplished using straight polarity DC current.

Electron beam welding was accomplished using a Hamilton Zeiss 2-kilowatt, 150 000-volt welder. A vacuum of  $10^{-5}$  torr or less was employed for welding. Basic process variables evaluated included selected beam deflection patterns and clamp spacing as well as welding speed.

Either butt welds or bead-on-plate welds were used in this study. Geometric effects in welding narrow specimens dictated that most of the welds produced in this evaluation be bead-on-plate welds to conserve material. Hence, results in the weld evaluation are largely independent of joint preparation. However, the effect of joint preparation on the soundness of welds was separately evaluated.

Weld preheat. - As described previously, the general philosophy pursued in welding these alloys was that of treating the welding process as a thermal disturbance, the time-temperature relations of which are controlled by the weld parameter selection. Thermal shock proved to play a significant role in defining weldability of tungsten and its alloys. Consequently, weld preheat up to  $1400^{\circ}$  F was introduced as a variable into the welding study. Since  $1400^{\circ}$  F appeared to be above the ductile-to-brittle transition temperatures of both base and weld metal, preheat was selected as a means of providing increased flexibility in weld parameter selection. The preheat fixture designed for this purpose is shown in figure IX-8. This fixture was designed for sheet welding. The weld specimen is held in place with clamp down bars containing molybdenum inserts. The backup bar is also of molybdenum. The fixture heater is located in a cavity behind the molybdenum backup bar. Clamp bars, backup bar, and heater support are insulated from the bulk of the heater so that a maximum specimen temperature of  $1500^{\circ}$  F can be achieved.

Postweld annealing. - Postweld annealing was evaluated as a means of improving ductility of welds for all the material evaluated. Annealing was accomplished in diffusion pumped vacuum furnaces at a vacuum of  $<5 \times 10^{-5}$  torr and temperatures between  $2500^{\circ}$  and  $3200^{\circ}$  F. Holding times of 1 hour were employed for all anneals.

Thermal stability. - The thermal stability of welds in both powder metallurgy and arc cast W-25Re-30Mo was determined by aging for 1000 hours in ultrahigh vacuum furnaces at temperatures of  $2600^{\circ}$ ,  $2800^{\circ}$ , and  $3000^{\circ}$  F. The sputter-ion pumped furnaces used for this purpose are shown in figure IX-9. These units are capable of maintaining  $<10^{-8}$  torr pressure at temperature. Pressures tend to continually decrease during aging runs such that final pressures are  $\sim 10^{-9}$  torr.

Weld evaluations. - All welds made in this program were checked for basic quality using visual, dye penetrant, and radiographic techniques.

The primary mechanical method of evaluation was bend testing using a 4t bend radius (11% outer fiber strain). Bend testing was used to define the bend-ductile-to-brittle transition temperature for weld specimens taken in both the transverse and longitudinal directions. The bend test parameters and specimen orientations are defined in figure IX-10. Transverse specimens were oriented for bending with the weld axis at a slight angle to the punch axis to ensure that the entire weld transverse cross section would be subjected to bending rather than merely the weakest areas. Load-deflection curves were generated during each bend test, and bending was terminated when crack initiation was indicated by an abrupt load decrease. This permits measuring, or calculating, the bend angle achieved at the moment of crack initiation as well as identifying the location of crack initiation. Normally four specimens are required to define a transition temperature. Bend test data are recorded graphically as shown in figure IX-11. This method of presentation identifies all the pertinent data, including crack location and extent of crack propagation for each specimen as well as the transition curve defined by the bend angle achieved as a function of temperature. Longitudinal and transverse curves are coded for presentation on the same graph. Bend testing was conducted at temperatures up to  $1000^{\circ}$  F, the test fixture operating limit. Some anomalous results were noted when the rhenium containing alloys were tested in air above  $600^{\circ}$  F. This was attributed to the tendency of rhenium to form low melting oxides, which demonstrated that an inert shield gas should be employed in bend testing these alloys. The expanded discussion of this general problem is included in the discussion of results under the heading Hot Tearing.

A restricted amount of tensile testing was conducted using longitudinal GTA and EB weld specimens and base metal of the W-Re-Mo alloy. These data are presented in figures IX-4 and IX-5. Tensile tests at elevated temperatures were conducted at strain rates of 0.05 inch per inch per minute while room temperature

tests were run at 0.005 inch per inch per minute to the 0.6 percent offset yield point and then at 0.05 inch per inch per minute to failure. Weld specimens were ground flat and parallel. A 1.000 inch long by 0.250 inch wide gage length was employed.

Specimen preparation. - The tungsten alloys did not lend themselves to convenient specimen blanking because of generally poor ductility. As a result, weldment specimen blanking throughout this program was accomplished by electrodischarge machining. Following welding, bend and tensile specimens were blanked using a wet cutoff wheel. Tensile specimens and butt joint edges were finish machined by grinding. All specimens were pickled before welding, annealing, aging, or testing above 1000° F. All other specimens (bend) were degreased prior to testing. Selection of the pickling procedures is discussed in the RESULTS section of this paper since proper pickling techniques are necessary to avoid excessive weld porosity.

## RESULTS

### Basic Weldability

Weld parameters, weld inspection results, and bend transition temperatures for all welds produced in screening the four materials for basic weldability are summarized in tables IX-4 and IX-5. All the variables investigated are indicated. Extreme care was taken to hold all other possible variables constant. This included electrode configuration, arc gap, shielding gas, edge preparation, and clamp spacing in GTA welding, and beam focus and voltage in EB welding.

Weld size was treated as a general variable in GTA welding, and target weld sizes were selected. Since any particular application would require a particular weld size, and since heat input is a function of weld size, size was considered an important metallurgical variable. In electron beam welding, however, weld size (width) is a much more independent variable which is usually held as small as possible. Hence, EB weld size was not treated as a practical variable. Clamp spacing was treated as a variable in EB welding but was held constant in GTA welding.

EB welding speeds were higher than those used for GTA welding, as is normal. Although higher weld speeds were attempted in GTA welding, the lower speeds were necessarily favored in an effort to increase the probability of obtaining sound welds. Hence, the indicated parameters reflect a chronological adjustment of the original plan which was sensibly altered as the evaluation proceeded.

The types of defects which occurred varied considerably for the four alloys:

(1) Arc cast unalloyed tungsten welds failed apparently as a result of brittleness and hence inability to accommodate weld stresses. EB welding produced the most



dramatic failures, which included delamination of adjacent base metal as well as transverse cracks and fractures (figs. IX-12 and IX-13). The EB delaminations are apparently the result of the high thermal shock developed in this welding process. High preheat (1400° F) improved GTA weldability, particularly as indicated by the ability to produce larger welds at higher speed. Weld fractures of the type indicated were the only types of defects detected in welding unalloyed tungsten.

(2) Arc cast W-25Re, like unalloyed tungsten, was GTA welded with difficulty. However, it was readily EB welded. GTA welding became increasingly difficult with higher welding speeds. Transverse arrested cracks (weld and heat affected zone only) occurred in one 15-inch-per-minute weld and in three 30-inch-per-minute welds. One 7.5-inch-per-minute weld contained a centerline crack which may have been a hot tear. Such cracks were also observed in welding a circular bead-on-plate patch test specimen in this alloy. The 1400° F preheat proved advantageous in this respect with only one short starting tear developing in a 15-inch-per-minute weld. There was no need to evaluate preheating for EB welding of this alloy because of the excellent weldability displayed.

(3) The powder metallurgy W-Re-Mo alloy displayed excellent weldability using both the GTA (fig. IX-14) and EB welding processes with only one minor starting crack occurring in one GTA weld.

(4) The arc cast W-Re-Mo behaved in a very anomalous manner by hot tearing (fig. IX-15) and developing transverse cracks during GTA welding. Although EB welding was satisfactory, this material was essentially unweldable by the GTA process. This was unexpected, and this problem was given special attention, as discussed later.

## Supplemental Weldability Results

The other important features of basic weldability evaluated in this program are discussed in this section. These included the effect of weld parameters on as-welded ductility, the effect of weld preheat, the effect of postweld annealing, a comparison of edge preparation methods (pickling solutions), and a comparison of porosity in arc cast and powder metallurgy W-Re-Mo alloys.

The effect of weld parameters on the ductility of welds as measured by the bend transition temperature is summarized as part of the basic weldability data in tables IX-4 and IX-5. Bend test results were carefully reviewed, but no correlation was established based on a thermal response analysis as previously accomplished using a similar approach for evaluating columbium base alloys (ref. 1). In this study failure to achieve a satisfactory correlation is ascribed to the nominal variability of

properties associated with the brittleness and/or hot tear sensitivity of these materials. From a statistical standpoint these materials can be expected to behave inconsistently. Hence, a much greater sample is required to achieve a meaningful correlation than required with readily weldable materials.

The variation of weld preheat, like the other weld parameters, was ineffective in demonstrating a definite trend in controlling as-welded ductility. However, as previously described, preheating was very instrumental in improving weldability (i. e., preheating enhanced flexibility in terms of insensitivity of weld quality to variation of the conventional welding parameters). This advantage was realized most effectively with the 1400° F preheat.

Preheating is not required for GTA welding W-25Re-30Mo if the welding characteristics of the powder metallurgy alloy can be consistently realized. On the other hand, not even preheat was beneficial in GTA welding arc cast W-25Re-30Mo.

Preheating is not beneficial for EB welding the tungsten alloys but is probably necessary for EB welding unalloyed tungsten and is preferred for GTA welding tungsten. Preheating for GTA welds in W-25Re is necessary only with high welding speeds.

The effect of postweld annealing as a method of improving as-welded ductility is summarized in table IX-6. Unalloyed tungsten was evaluated with a 1 hour, 2560° F GTA weld stress relief only without realizing any benefit. The same anneal on W-25Re was quite effective for EB welds but ineffectual for GTA welds. This was interpreted as indicating that a stress relief of EB welds is desirable. This also indicated that residual stresses are not the controlling factor in GTA weld ductility impairment. However, W-25Re GTA weld ductility was improved with a 3270° F anneal. This temperature was selected for solution of nonequilibrium sigma phase which could be responsible for ductility impairment. Even though sigma phase was not detected metallographically, its presence as a continuous or semicontinuous grain boundary or intercellular film in welds can be inferred from the intergranular nature of the fracture observed and from the improved ductility realized with the high temperature anneal.

Powder metallurgy W-Re-Mo welds were improved by annealing in the stress relief and potentially sigma forming range, 2400° and 2800° F, but not in the recrystallization-sigma solution range, near 3200° F. Hence, development of sigma phase did not appear to be a problem with this alloy. Arc cast W-Re-Mo, which had better as-welded ductility (EB welds only) than the powder metallurgy sheet, decreased in ductility on annealing to about the same final level as annealed powder metallurgy welds. Hence, these two materials merely seemed to normalize through the thermal stability study, as discussed later. Annealing naturally has a detrimental effect on wrought base metal, as indicated for the W-Re-Mo alloy an-

nealed at 2800° F.

Pickling solution selection proved to have a significant influence on the occurrence of porosity in the W-25Re-30Mo alloy. The developer of this alloy recommended using a volume ratio solution of 30 lactic acid - 3 HNO<sub>3</sub> - 1 HF. This was compared with the 9HF-1HNO<sub>3</sub> solution which was used satisfactorily for preparing the other two alloys. Specimens pickled with both solutions were degassed in vacuum (10<sup>-5</sup> torr) at 2000° F prior to welding, as was the practice throughout this program for all weld blanks. The results of this investigation are shown in figure IX-16. The recommended solution is clearly preferred for the W-25Re-30Mo alloy to avoid weld porosity even though the 9HF-1HNO<sub>3</sub> solution was satisfactory for the other materials.

Another factor resolved in this evaluation is the greater tendency of powder metallurgy alloy welds than arc cast alloy welds to contain porosity. Typical results in this respect are shown in figure IX-17. Powder metallurgy W-25Re-30Mo consistently displayed a greater tendency towards weld porosity than did the arc cast material.

The reason for this could not be determined, but the trend agrees with that observed in the preliminary survey for this program leading to the selection of arc cast rather than powder metallurgy tungsten for evaluation. No correlation between weld ductility and porosity was demonstrated. Several welds in W-25Re-30Mo were produced with high porosity and bend tested without any apparent increase in transition temperature.

## Hot Tearing

Hot tearing, quite often catastrophic in extent, occurred in gas-tungsten-arc welds in the AC W-25Re and the AC W-Re-Mo alloy with sufficient regularity to warrant closer examination in an effort to identify the causes. The problem was serious enough in the AC ternary alloy that full-scale evaluation of GTA welds was not possible because of a lack of sound weld metal.

Hot tearing is not peculiar to welds; rather it is a problem common to many aspects of metallurgical processing. Although a precise definition of the obtaining mechanisms has proven elusive, a definite relation has been established between the occurrence of hot tearing and the existence of a liquid phase at temperatures well below the solidus temperature of the alloy. This situation is often predictable from the equilibrium diagram (ref. 6). The inability of the liquid phase to accommodate strains induced by solidification and subsequent shrinkage results in parting at the liquid film region. At first appearance it might be expected EB welds would

be more subject to this problem than GTA welds because of their high cooling rates. However, the instantaneous volume of liquid present and magnitude of thermal straining is quite small for EB welds, and this apparently mitigates the tendency for hot tearing.

It was previously noted that a high degree of constitutional segregation and subsequent depression of the freezing point in weldments is expected in the W-Re system (fig. IX-1). This could play two possible roles in the hot tearing noted in W-Re binary alloy welds. Should the cooling rate be sufficiently great, the Re-rich phase, that is, the last constituent to solidify, could serve to fulfill the liquid film requirements outlined above and induce hot tearing. A more subtle role, also related to the existence of a Re-rich phase, stems from the high affinity which Re exhibits for oxygen. Although easily formed,  $\text{Re}_2\text{O}_7$  is unstable, melting at  $565^\circ\text{F}$  and boiling at  $685^\circ\text{F}$ , and is believed to be responsible for the hot shortness which prevents elevated temperature working of Re in air (ref. 7).

The low level of oxygen in the binary W-Re (table IX-3) and the ultraclean welding procedures followed seem to obviate consideration of the latter mechanism as being responsible for the observed hot tearing. However, this mechanism seems quite feasible as an explanation for the anomalous bend test results noted for tests in air at temperatures above  $\sim 600^\circ\text{F}$ . The use of an inert (argon) shield gas eliminated this erratic behavior.

As opposed to the binary alloy the hot tearing of GTA welds in the AC W-Re-Mo alloy was totally unexpected. First, the amount of constitutional segregation expected in this alloy is not nearly so great as that expected for the binary W-Re alloy. Hence, the possibility of a depressed-melting-point liquid film at a critical stage in the solidification is not as likely. Second, GTA welds of the PM W-Re-Mo alloy were accomplished without a single incident of hot tearing.

In an effort to identify the cause(s) for this dual behavior, a complete review was made of the processing histories and the chemical analyses of the AC and PM sheets. This review indicated differences in oxygen content (table IX-3) for the two products might be responsible for the erratic weldability of the AC sheet. The mechanism would be similar to that which has been observed in welding molybdenum. It has been reported (ref. 8) and verified (ref. 9) that oxygen contents of only 100 ppm (by wt.) in molybdenum have been sufficient to consistently lead to hot tearing during welding. This is related to the presence of a continuous film of Mo-MoO<sub>2</sub> eutectic (melting point  $\sim 3800^\circ\text{F}$ ) at the grain boundaries for oxygen concentrations of 100 ppm or more. Fractographic studies (ref. 10) indicate the transition from discrete oxide particles to a continuous grain boundary film may occur for oxygen levels as low as only 10 to 50 ppm. Accumulation of critical oxygen concentrations could conceivably result from partitioning effects between the solid and

liquid phases during solidification.

Evidence which tends to confirm that this mechanism is responsible for hot tearing of GTA welds in the AC W-Re-Mo sheet was obtained by inducing similar behavior in GTA welds in the PM sheet. Hot tearing had not been noted in the PM product, yet severe hot tearing was induced in a series of test welds made in oxygen-contaminated welding atmospheres. Photographs of two of these welds are shown in figure IX-18. Immediately below each weld is a positive print of an X-ray negative of the same weld. The threshold for the hot tearing occurred at approximately 500 ppm oxygen in the welding atmosphere. Attempts to more accurately define this behavior by chemical analyses for oxygen pickup in the weld metal met with limited success.

Although the oxygen effect hypothesis for this experiment was based on the effect of oxygen on hot tear sensitivity in molybdenum, the extension to alloys containing tungsten and rhenium seems reasonable because of their similarity in chemical behavior to molybdenum, particularly with respect to interstitial elements.

## Thermal Stability

The objective of the 1000 hour aging runs was to determine the effects of long-time high-temperature exposures on the ductility of the ternary W-Re-Mo alloy. Base metal and EB and GTA welds of the PM sheet were aged, while for the AC sheet only base metal and EB welds were used. All welds used in the aging study were made using the parameters found previously to give welds having optimum ductility. In addition, wherever material availability permitted, additional specimens were first aged and subsequently welded, again using optimized weld parameters.

For single phase alloys, such as the ternary W-Re-Mo alloys evaluated, the effects of long time exposures at elevated temperatures are mainly those associated with primary grain growth. In tungsten-base alloys this results in loss of ductility. The proximity of the alloy to the alpha-sigma phase boundary (fig. IX-3) suggests the possibility of an embrittling reaction due to localized precipitation of sigma phase during aging. To allow for this possibility, three sets of specimens were aged at 2800<sup>o</sup> F. One set was tested as aged, while the other sets were given 1 hour postage anneals at 3200<sup>o</sup> and 3400<sup>o</sup> F to dissolve any sigma phase that may have formed.

Bend test results pertinent to these efforts are summarized in table IX-7. Data for as-received PM and AC sheet and PM sheet annealed 1 hour at 2800<sup>o</sup> F are included to provide information regarding changes in ductility not related to welding.

The transition temperature for longitudinal (L) and transverse (T) test specimens are indicated as well as the average of these two values.

Ductility of the base metal specimens decreased with increasing thermal exposure. This was true for both the AC and the PM sheet over the full range of conditions evaluated. Metallographic examination was performed in an effort to determine the cause for this behavior. The results, shown in figure IX-19 (dashed lines) as recrystallized grain size as a function of temperature, indicate grain growth as the mechanism most likely responsible for the loss of ductility. Special attention should be directed toward the results found for the PM product. This alloy exhibited both normal and secondary grain growth for all aging temperatures, and hence two curves are shown for these specimens. The volume of the specimen affected by secondary recrystallization (i. e., abnormal grain growth) increased with aging temperature such that after 1000 hours at 3000<sup>0</sup> F only quite small areas remained unaffected. To provide additional information regarding this phenomenon, a series of 1 hour anneals at 200<sup>0</sup> F intervals from 2200<sup>0</sup> to 3600<sup>0</sup> F were given base metal specimens of the PM W-Re-Mo alloy. Specimens of the AC W-Re-Mo alloy and the AC W-25Re alloy were similarly annealed to provide direct comparisons of thermal response. These results are also included in figure IX-19 (solid lines), where the AC binary and ternary alloys are seen to observe normal grain growth behavior; that is, although the average grain size increases, the distribution of grain sizes remains nearly constant throughout the process. Again, secondary recrystallization was noted for the PM W-Re-Mo specimen annealed 1 hour at 3600<sup>0</sup> F (fig. IX-20).

Thermal exposure had no discernible effect on the bend ductility of EB and GTA welds in the PM sheet or on the ductility of EB welds in the AC sheet. This was found to be true for welds made by either sequence, weld and age or age and weld. In view of the complexity of responses possible for the variety of conditions employed, it is evident that the data lend themselves best to a rationale developed strictly on the basis of grain size.

The bend transition temperatures leveled off with increased thermal exposure. This suggests a lower limit of ductility is being approached for the W-Re-Mo alloy. Fractures in aged PM and AC specimens were invariably intergranular. Probably the greatest constitutional segregation coupled with minimum transverse grain boundary length occurs at the weld centerline. These factors probably combine and result in high transverse transition temperatures, since transverse specimens almost always failed along the weld centerline grain boundaries.

## CONCLUSIONS

1. The weldability of unalloyed tungsten is marginal because of its high ductile-to-brittle transition temperature in the welded or recrystallized condition. The high melting point and low ductility in combination make tungsten susceptible to failure by thermal shock during welding. Hence, weldability is enhanced by high weld preheating. It is not apparent that use of arc cast tungsten is advantageous over powder metallurgy tungsten except for the absence of porosity in welds. Post-weld annealing was not particularly beneficial in improving ductility.

2. The weldability of W-25Re is improved over that of unalloyed tungsten because of slightly better as-welded and recrystallized ductility. Improved ductility coupled with a lower melting point makes this alloy less susceptible to thermal shock failures. However, the W-Re phase relations are such that this alloy exhibits a tendency toward hot tearing.

Preheat in welding was not beneficial in improving as-welded ductility but permitted welding at higher welding speeds and, hence, essentially improved weldability.

A stress relief postweld anneal ( $2560^{\circ}$  F) was beneficial for EB welds. This implied high residual stress in EB welded W-25Re tends to correlate with the thermal shock behavior observed for tungsten EB welds. GTA welds were not improved by stress relief, but instead required a solution anneal ( $3270^{\circ}$  F), which implies that sigma phase develops at grain boundaries during GTA welding. In this respect EB welding was advantageous since embrittlement by the sigma phase and hot tearing were observed only in GTA welds. Both the development of sigma phase and hot tearing result from constitutional segregation on freezing which is apparently more pronounced in GTA welds.

3. The W-25Re-30Mo alloy displayed generally excellent weldability except for an extreme sensitivity to oxygen contamination which causes hot tearing. Undesirable levels of oxygen contamination occur at a very low level in the base metal and make detection difficult. Welding atmospheres, however, can be easily controlled if properly monitored to eliminate welding as a potential source of contamination.

A postweld stress relief was beneficial in improving the ductility of welds in this alloy. Otherwise, all thermal treatments to which this material was exposed tended to normalize ductility to that of a large grain size recrystallized structure. This trend persisted even through 1000 hour anneals at temperatures to  $3000^{\circ}$  F.

On aging this alloy tends to behave quite simply as a solid solution system. However, the powder metallurgy material exhibited secondary recrystallization which could well be a metallurgical instability brought on by the dissolution of finely dispersed impurity precipitates.

4. In several checks made in this program welds in powder metallurgy product always contained porosity, whereas arc cast material produced porosity-free welds.

## REFERENCES

1. Lessman, G. G.: The Comparative Weldability of Refractory Metal Alloys. *Welding J. Res. Suppl.*, vol. 45, no. 12, Dec. 1966, pp. 540-s - 560-s.
2. Klopp, William D.: Review of Ductilizing of Group VIA Elements by Rhenium and Other Solutes. NASA TN D-4955, 1968.
3. Stephens, Joseph R.: Effects of Interstitial Impurities on the Low-Temperature Tensile Properties of Tungsten. NASA TN D-2287, 1964.
4. Collins, C. G.; and Bohlander, K. M.: Physical Metallurgy of Refractory Metal Alloys. AEC Fuels and Materials Development Program Progress Report No. 71, Rep. GEMP-1002, General Electric Co., Dec. 29, 1967, pp. 77-82.
5. Stoner, D. R.; and Lessmann, G. G.: Measurement and Control of Weld Chamber Atmospheres. *Welding J. Res. Suppl.*, vol. 44, no. 8, Aug. 1965, pp. 337-s - 346-s.
6. Pellini, W. S.: Strain Theory of Hot Tearing. *Foundry*, vol. 80, no. 11, Nov. 1952, pp. 125-133, 192, 194, 196, 199.
7. Sims, C. T.: Properties of Rhenium. *Rhenium*. B. W. Gonser, ed., Elsevier Publ. Co., 1962, pp. 23-35.
8. Perry, Timothy; Spacil, H. S.; and Wulff, John: The Effect of Oxygen on Welding and Brazing Molybdenum. *Welding J. Res. Suppl.*, vol. 33, no. 9, Sept. 1954, pp. 442-s - 448-s.
9. Platte, W. N.: Welding of Molybdenum. *The Metal Molybdenum*. Julius J. Harwood, ed., Am. Soc. Metals, 1958, pp. 151-191.
10. Mallett, M. W.; and Hansen, W. R.: Determination of Gases in Molybdenum. *The Metal Molybdenum*. Julius J. Harwood, ed., Am. Soc. Metals, 1958, pp. 365-393.
11. Raffo, Peter L.: Yielding and Fracture in Tungsten and Tungsten-Rhenium Alloys. NASA TN D-4567, 1968.
12. English, J. J.: Binary and Ternary Phase Diagrams of Columbium, Molybdenum, Tantalum, and Tungsten. DMIC Rep. 152, Battelle Memorial Inst., Apr. 28, 1961.



TABLE IX-1. - TENSILE ELONGATION DATA FOR  
TUNGSTEN-BASE ALLOYS

| Alloy                  | Temperature, °F                    |      |      |
|------------------------|------------------------------------|------|------|
|                        | 2000                               | 2600 | 3000 |
|                        | Elongation in 1-in. gage length, % |      |      |
| AC Tungsten            | 12                                 | 23   | 30   |
| AC W-25Re (wt %)       | 5                                  | 16   | 30   |
| PM W-25Re-30Mo (at. %) |                                    |      |      |
| Base <sup>a</sup>      | 54                                 | 36   | 33   |
| EB                     | 33                                 | 26.5 | 25   |
| GTA                    | 37                                 | 23.5 | 18   |
| AC W-25Re-30Mo (at. %) |                                    |      |      |
| Base <sup>a</sup>      | 9                                  | 32   | 79   |
| EB                     | 15                                 | 17   | 61   |

<sup>a</sup>Wrought, stress-relieved sheet.

TABLE IX-2. - BASE METAL BEND DUCTILITY

| Alloy                  | Longitudinal                                   | Transverse | As-received condition                |
|------------------------|--|------------|--------------------------------------|
|                        | Bend transition temperature<br>for 4t rad., °F |            | (a)                                  |
| Tungsten               | 425  | 275        | Stress relieved 1 hr<br>at 1700° F   |
| W-25Re (wt %)          | -200   | -75        | Stress relieved 1 hr<br>at 2550° F   |
| PM W-25Re-30Mo (at. %) | -150   | -50        | Stress relieved 1/2 hr<br>at 2100° F |
| AC W-25Re-30Mo (at. %) | <-320  | -250       | Stress relieved 1/2 hr<br>at 1920° F |

<sup>a</sup>All as-received structures were in wrought condition.

TABLE IX-3. - BASE METAL INTERSTITIAL CHEMICAL ANALYSES

| Alloy                  | Carbon                     |                              | Oxygen                     |                             | Nitrogen  |           |
|------------------------|----------------------------|------------------------------|----------------------------|-----------------------------|-----------|-----------|
|                        | ppm (wt.)                  | ppm (at.)                    | ppm (wt.)                  | ppm (at.)                   | ppm (wt.) | ppm (at.) |
| AC Tungsten            | <sup>a</sup> <sub>8</sub>  | <sup>a</sup> <sub>122</sub>  | <sup>a</sup> <sub>12</sub> | <sup>a</sup> <sub>138</sub> | 10        | 131       |
| AC W-25Re (wt %)       | 8                          | 123                          | 8                          | 92                          | 10        | 132       |
| AC W-25Re-30Mo (at. %) | 48                         | 632                          | 24                         | 237                         | 10        | 113       |
| PM W-25Re-30Mo (at. %) |                            |                              |                            |                             |           |           |
| Lot A                  | <sup>a</sup> <sub>19</sub> | <sup>a</sup> <sub>250</sub>  | <sup>a</sup> <sub>5</sub>  | <sup>a</sup> <sub>49</sub>  | <3        | <34       |
| Lot B                  | <sup>a</sup> <sub>81</sub> | <sup>a</sup> <sub>1070</sub> | <sup>a</sup> <sub>4</sub>  | <sup>a</sup> <sub>39</sub>  | <3        | <34       |

<sup>a</sup>Average of two analyses.

TABLE IX-4. - GTA WELD PARAMETER EVALUATION

| Target weld size                                    | Weld speed, in./min | Arc cast unalloyed tungsten |                        |                   | Arc cast W-25Re (wt %) |                        |                   | W-25Re-30Mo (at. %) |                |                 |                    |
|---|---------------------|-----------------------------|------------------------|-------------------|------------------------|------------------------|-------------------|---------------------|----------------|-----------------|--------------------|
|   |                     | No pre-heat                 | 450° to 600° F preheat | 1400° F preheat   | No pre-heat            | 450° to 600° F preheat | 1400° F preheat   | No pre-heat         | 800° F preheat | 1400° F preheat | Arc cast           |
|   |                     |                             |                        |                   |                        |                        |                   |                     |                |                 |                    |
| 4t bend transition temperature, °F<br>(a), (b)      |                     |                             |                        |                   |                        |                        |                   |                     |                |                 |                    |
| Small welds, 0.120" wide, nominal (0.080 to 0.140") | 3.0                 | -----                       | -----                  | -----             | 1000, L, S             | 800, L, S              | -----             | -----               | -----          | -----           | -----              |
|   | 7.5                 | D                           | >1000, L, S            | >1000, L, T, S    | 800, L, S              | 590, L, S              | -----             | -----               | -----          | -----           | -----              |
|   | 15                  | S                           | 1000, L, S             | 850, L, 800, T, S | 600, L, S              | -----                  | 1000, T, D        | 400, L, S           | 500, L, S      | -----           | 250, L, D, D       |
|   | 25                  | -----                       | -----                  | -----             | -----                  | -----                  | -----             | -----               | 550, L, S      | -----           | -----              |
|   | 30                  | 700, L, D                   | -----                  | -----             | -----                  | >1000, L, D            | >1000, L, T, S, S | 500, L, S, S        | -----          | D               | 450, L, T, S, D, D |
|   | 35                  | -----                       | -----                  | -----             | -----                  | -----                  | -----             | -----               | 400, L, S      | 550, L, S       | -----              |
|   | 45                  | -----                       | -----                  | -----             | -----                  | -----                  | 800, L, T, S      | -----               | -----          | -----           | -----              |
| Large welds, 0.180" wide, nominal (0.150 to 0.210") | 3.0                 | -----                       | -----                  | -----             | -----                  | -----                  | -----             | -----               | -----          | -----           | -----              |
|   | 7.5                 | 700, L, S                   | 700, L, S              | -----             | 1000, L, S             | D                      | -----             | -----               | -----          | -----           | -----              |
|   | 15                  | D                           | S                      | -----             | 1000, L, D             | >1000, L, S            | -----             | -----               | 450, L, D      | -----           | -----              |
|   | 25                  | -----                       | -----                  | -----             | -----                  | -----                  | -----             | -----               | -----          | -----           | -----              |
|   | 30                  | -----                       | D                      | 800, L, T, S, S   | D                      | >1000, L, D            | -----             | -----               | -----          | -----           | -----              |
|   | 35                  | -----                       | -----                  | -----             | -----                  | -----                  | -----             | -----               | -----          | -----           | -----              |
|   | 45                  | -----                       | -----                  | -----             | -----                  | -----                  | -----             | -----               | -----          | -----           | -----              |

<sup>a</sup>Longitudinal bend, L; transverse bend, T.<sup>b</sup>Sound weld, S; defective weld, D.

TABLE IX-5. - EB WELD PARAMETER EVALUATION

| Weld speed, in./min                | Direction of 60-cycle, 0.050 in. beam deflection | Clamp spacing, in.                    |                                    |                     |                     |                         |                   |     |
|------------------------------------|--|---------------------------------------|------------------------------------|---------------------|---------------------|-------------------------|-------------------|-----|
|                                    |  | 3/16                                  | 1/2                                | 3/32                | 1/4                 | 3/8                     | 3/16              | 3/8 |
|                                    |  | Arc cast alloyed tungsten; no preheat | Arc cast W-25Re (wt %); no preheat | W-25Re-30Mo (at. %) |                     |                         | Arc cast          |     |
|                                    |  |                                       |                                    | Powder metallurgy   |                     |                         |                   |     |
|                                    |  | No preheat                            | 800° F preheat                     | 1400° F preheat     | No preheat          | 1400° F preheat         |                   |     |
| 4t bend transition temperature, °F |  |                                       |                                    |                     |                     |                         |                   |     |
| (a), (b)                           |  |                                       |                                    |                     |                     |                         |                   |     |
| 15                                 | Transverse                                       | D                                     | <1000, L, D                        | -----               | 400, L, >1000, T, S | -----                   | -----             |     |
|                                    | Zero   | -----                                 | -----                              | -----               | 400, L, >1000, T, S | -----                   | -----             |     |
|                                    | Longitudinal                                     | <800, L, >1000, T, D                  | >1000, L, T, D                     | 600, L, >1000, T, S | 500, L, >1000, T, S | 200, L, 600, T, S       | -----             |     |
| 25                                 | Longitudinal                                     | <800, L, >1000, T, D                  | >1000, L, T, D                     | 450, L, >1000, T, S | -----               | 200, L, 500, T, S, S, S | 150, L, 250, T, S |     |
| 50                                 | Zero   | -----                                 | -----                              | >1000, L, T, S      | 400, L, >1000, T, S | -----                   | -----             |     |
|                                    | Longitudinal                                     | D                                     | D                                  | 600, L, >1000, T, S | 600, L, >1000, T, S | 225, L, 500, T, S       | 200, L, 600, T, S |     |
| 100                                | Zero   | D                                     | D                                  | -----               | -----               | -----                   | -----             |     |
|                                    | Longitudinal                                     | D                                     | D                                  | 900, L, >1000, T, S | >1000, L, T, S      | -----                   | -----             |     |

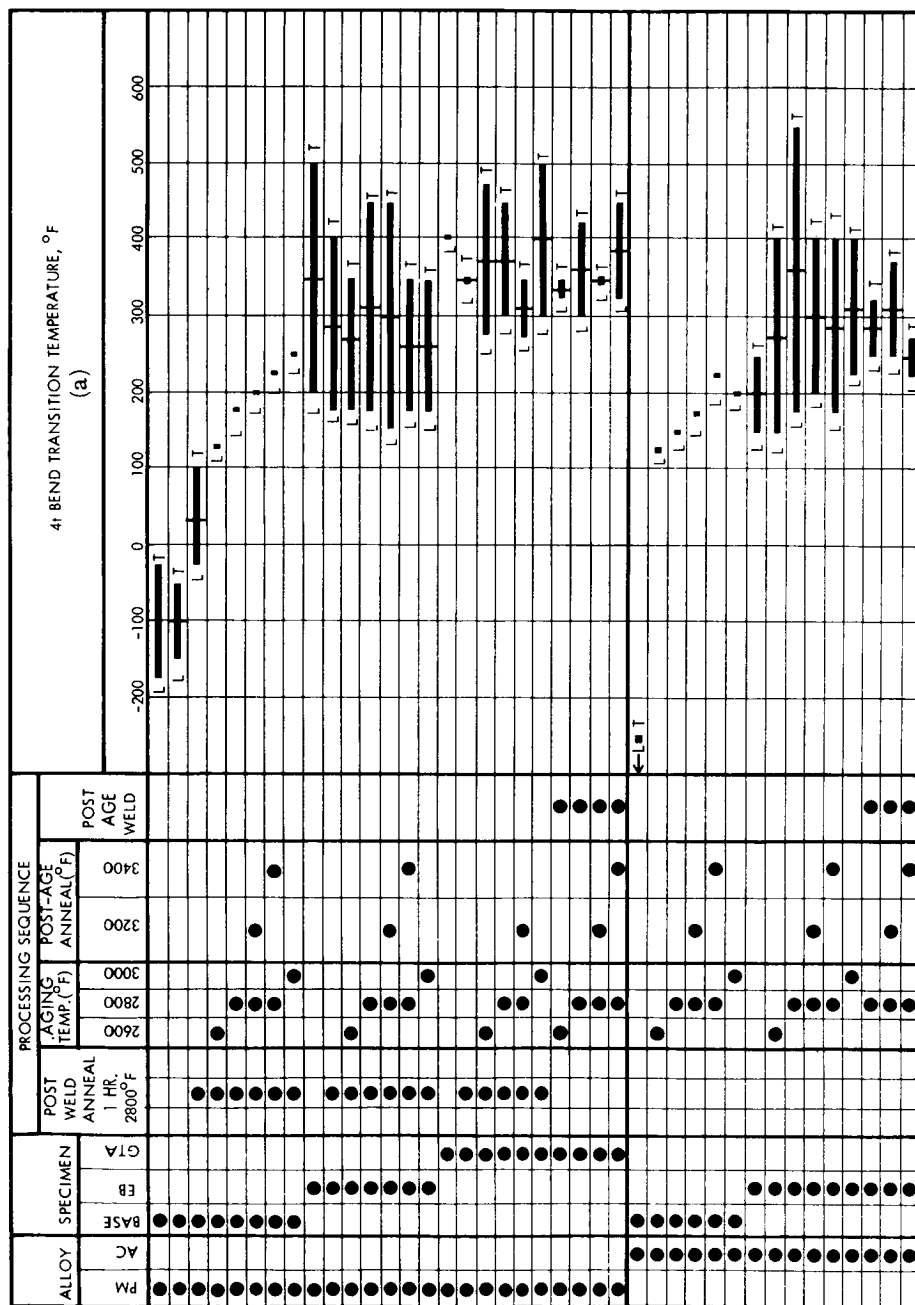
<sup>a</sup> Longitudinal bend, L; transverse bend, T.<sup>b</sup> Sound weld, S; defective weld, D.

TABLE IX-6. - POSTWELD ANNEALING RESULTS

| Alloy        | Structure   | Weld preheat       | 1 hr<br>anneal<br>temper-<br>ature,<br>°F | Change in<br>4t bend<br>transition<br>temperature,<br>°F<br>(a) | Bend type<br>(b)           | Lowest<br>DBTT,<br>°F<br>(b)      |
|--------------|-------------|--------------------|---|---|----------------------------|-----------------------------------|
| W            | GTA weld    | None               | 2560                                      | 100   | L                          | 700                               |
| W            | GTA weld    | 550° F             | 2560                                      | -100  | L                          | 900                               |
| W            | GTA weld    | None               | 2560                                      | Increased   | L                          | 700                               |
| W-25Re       | GTA weld    | 550° F             | 2560                                      | 200   | L                          | 800                               |
| W-25Re       | 4 GTA welds | 3-550° F           | 2560                                      | Increased<br>ductility<br>implied                               | -----                      | 800                               |
| W-25Re       | 4 GTA welds | 1-None<br>3-550° F | 2560                                      | Decreased<br>ductility<br>implied                               | -----                      | 800                               |
| W-25Re       | 3 GTA welds | 1400° F            | 3270                                      | -400 Max.   | L and T                    | 600                               |
| W-25Re       | GTA weld    | 1400° F            | 3270                                      | Questionable  | -----                      | 1000                              |
| W-25Re       | 11 EB welds | None               | 2560                                      | -500 Max.   | T                          | 500                               |
| W-Re-Mo (PM) | GTA weld    | None               | 2400<br>2800                              | -50 to -100   | L                          | 350                               |
| W-Re-Mo (PM) | GTA weld    | None               | 3200                                      | 25  | L                          | 425                               |
| W-Re-Mo (PM) | EB welds    | None               | 2400<br>2800<br>3200                      | -25<br>>-25<br>25   | } L and T                  | 175 (L)                           |
| W-Re-Mo (PM) | Base metal  | -----              | 2800                                      | 125   |                            | 400 (T)                           |
| W-Re-Mo (AC) | EB welds    | 1400° F            | 2400<br>2800<br>3200                      | 175<br>50<br>200<br>50<br>250<br>100<br>250                     | L<br>T<br>L<br>T<br>L<br>T | -150<br>-75<br>150 (L)<br>200 (T) |

<sup>a</sup>DBTT for annealed or unannealed, whichever is lower.<sup>b</sup>Longitudinal bend, L; transverse bend, T.

TABLE IX-7. - SUMMARY OF BEND TEST RESULTS PERTINENT TO THERMAL STABILITY



<sup>a</sup>Bend type, longitudinal, L; transverse, T.

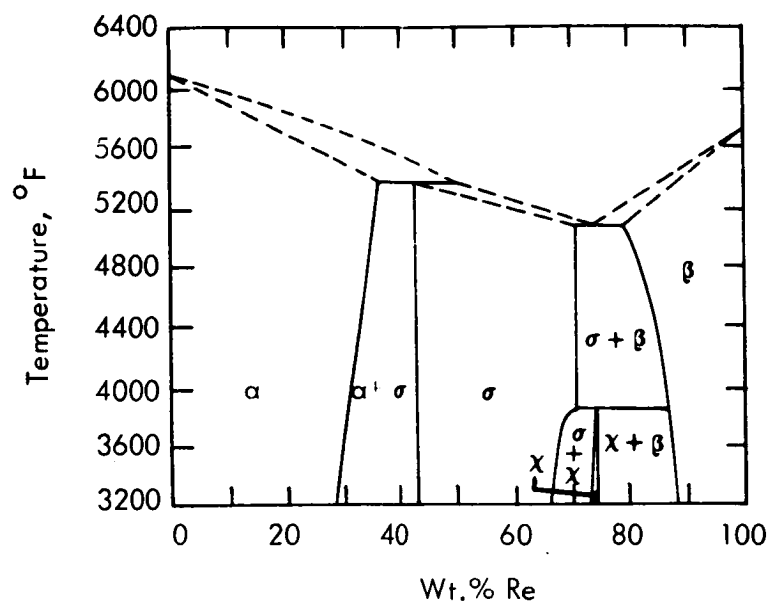


Figure IX-1. - Tungsten-rhenium phase diagram (ref. 11).

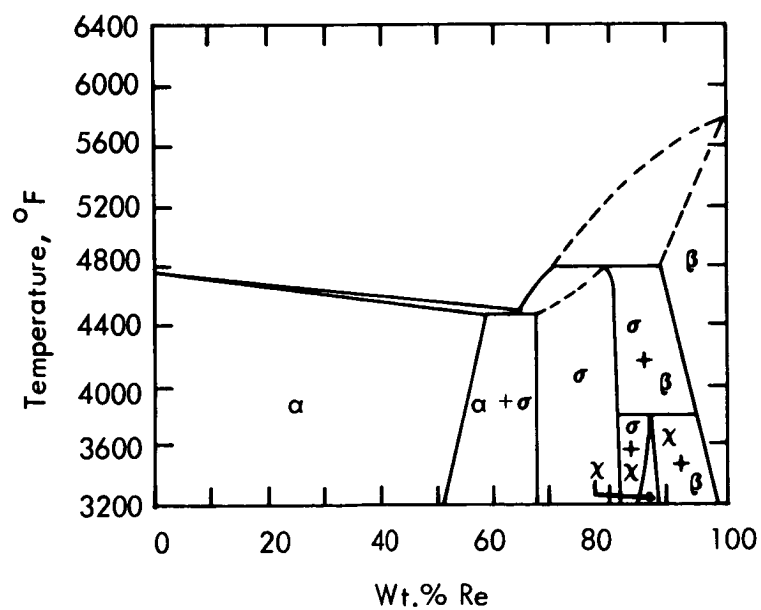


Figure IX-2. - Molybdenum-rhenium phase diagram (ref. 12)

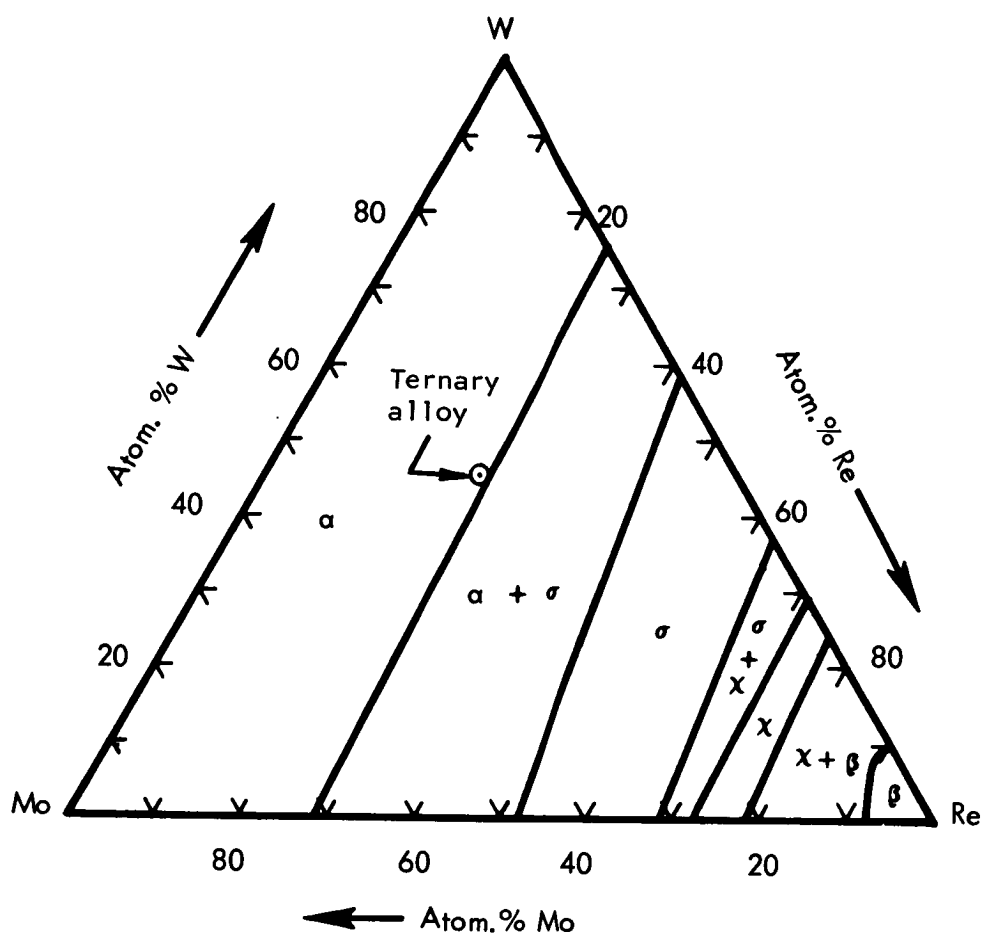


Figure IX-3. - Tungsten-rhenium-molybdenum ternary phase diagram: 1830° F isotherm (ref. 4).

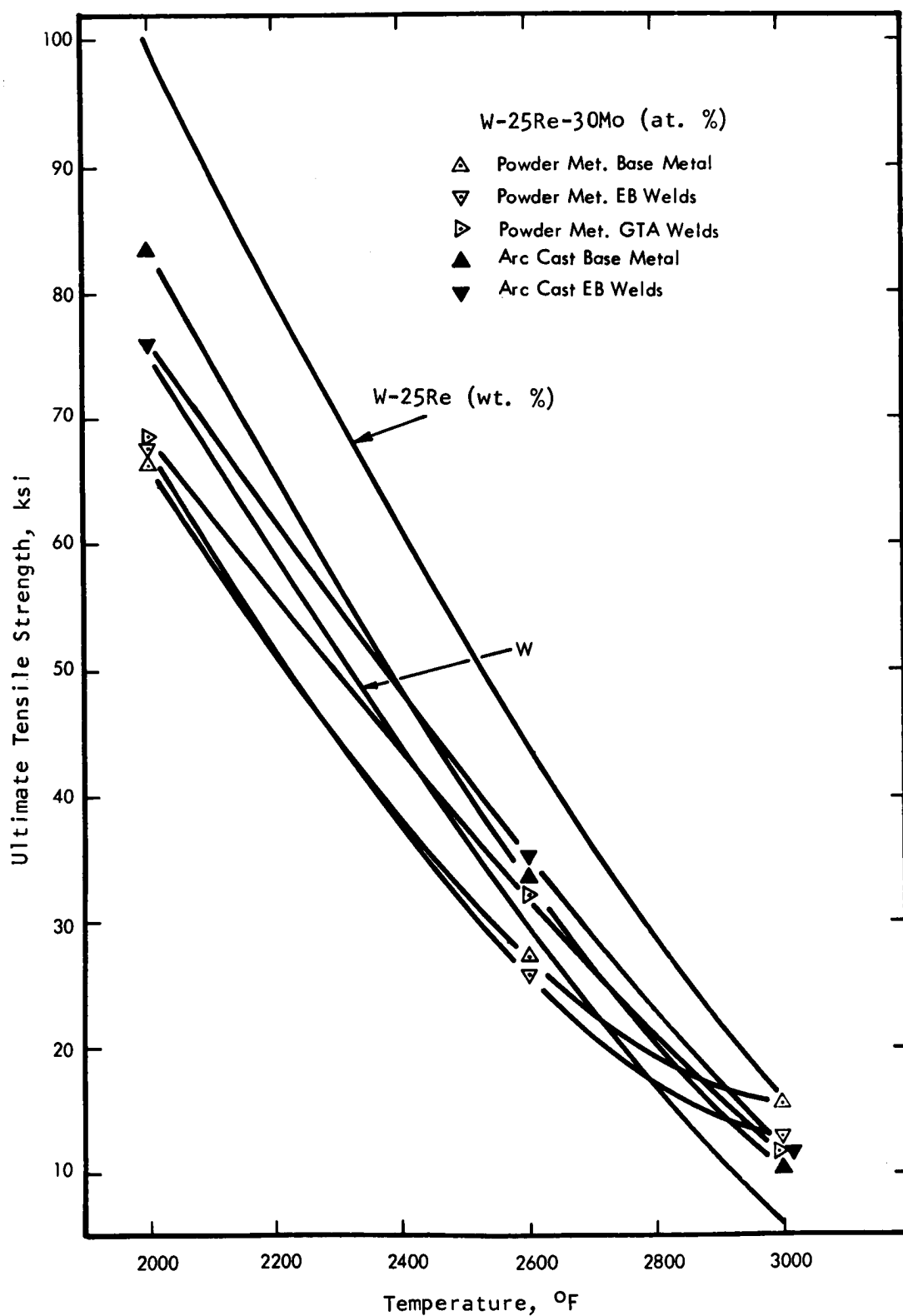


Figure IX-4. - Elevated temperature ultimate tensile strength of tungsten-base alloys.



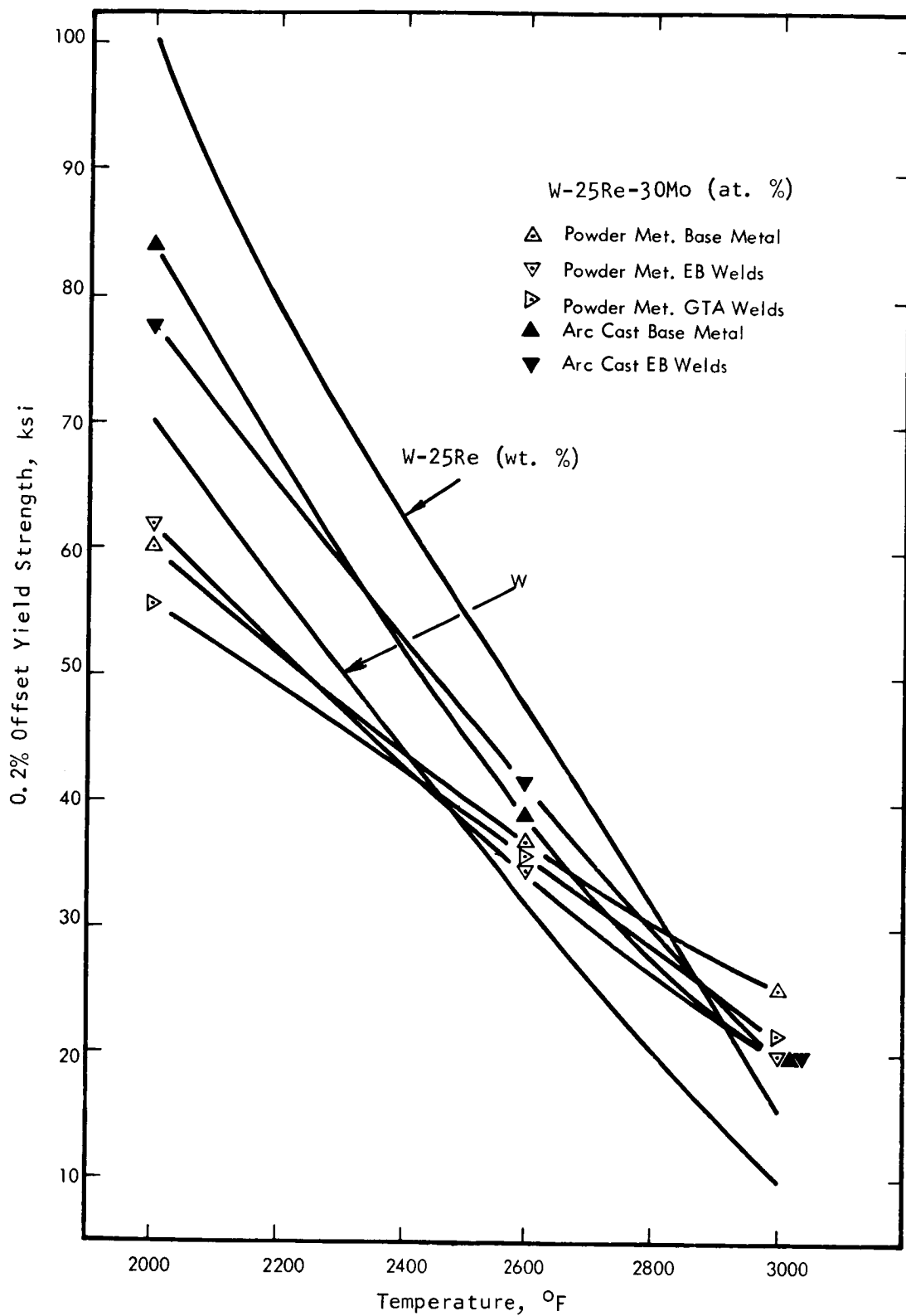


Figure IX-5. - Elevated temperature 0.2 percent offset yield strength of tungsten-base alloys.

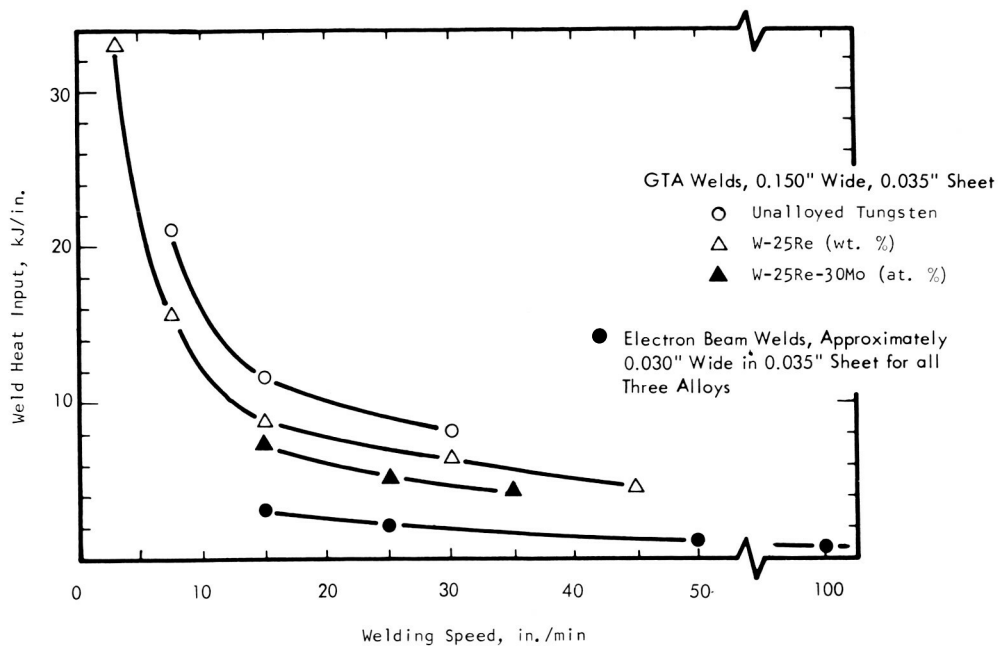


Figure IX-6. - Unit weld length heat input requirements as function of welding speed for tungsten-base alloys.



Figure IX-7. - Vacuum purged weld chamber.

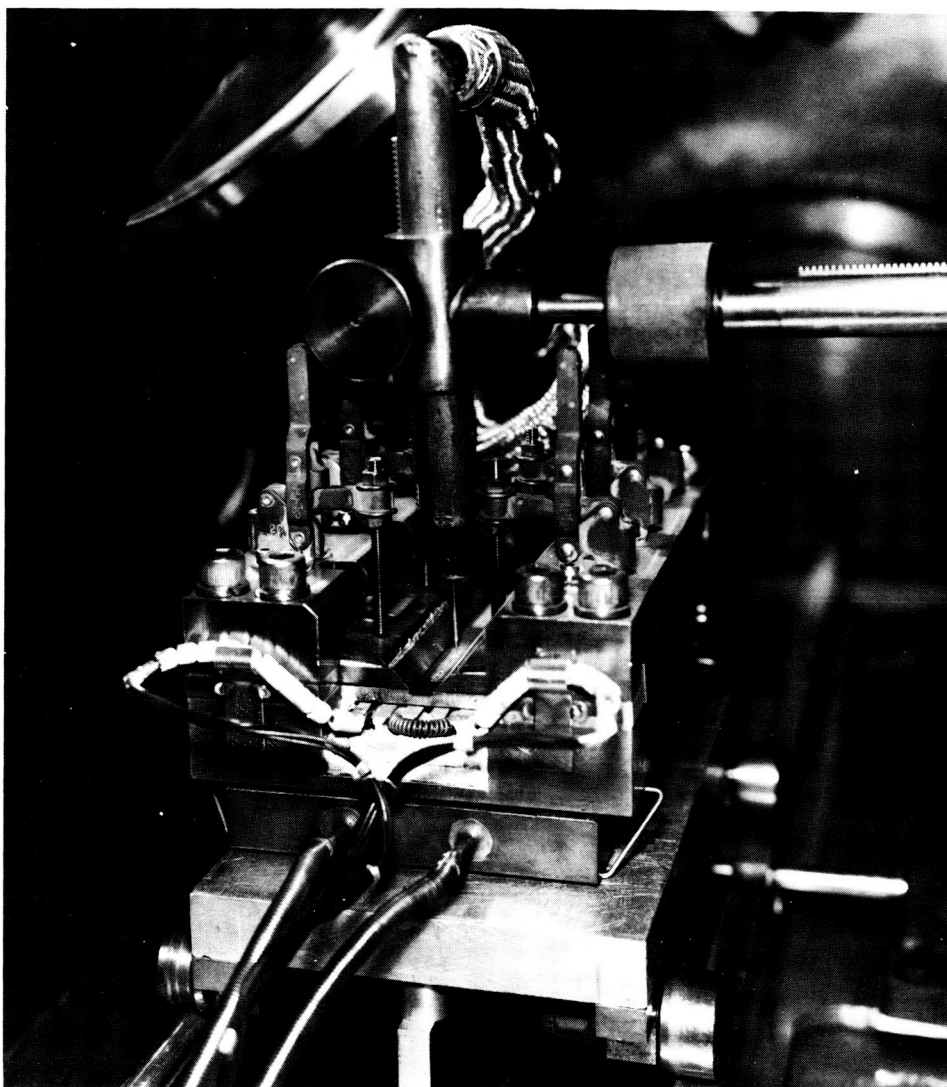


Figure IX-8. - Sheet welding fixture used for welding tungsten-base alloys with preheat to 1400<sup>0</sup> F.



Figure IX-9. - Sputter ion pumped ultrahigh vacuum furnaces used for thermal stability study.

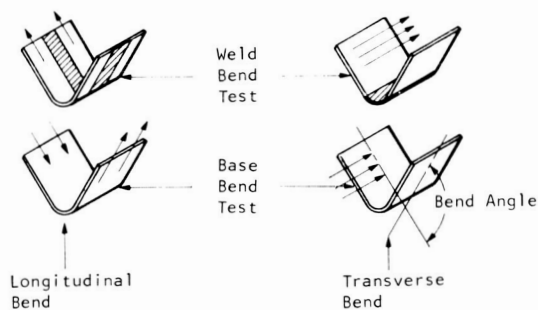


Figure IX-10. - Bend test specimens. Thickness,  $t$ , 0.035 inch; width,  $12t$ ; length,  $24t$ ; test span,  $15t$ ; punch speed, 1 inch per minute; variable temperature; variable punch radius, generally  $1t$ ,  $2t$ ,  $4t$ , or  $6t$ ; bend ductile to brittle transition temperature, lowest temperature for  $90^\circ$  bend without cracking. Arrows show rolling direction.

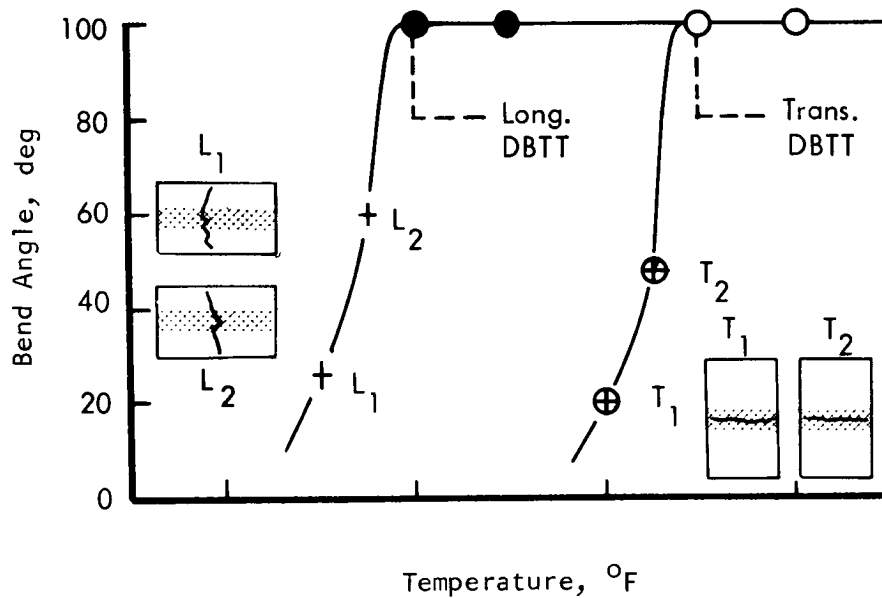
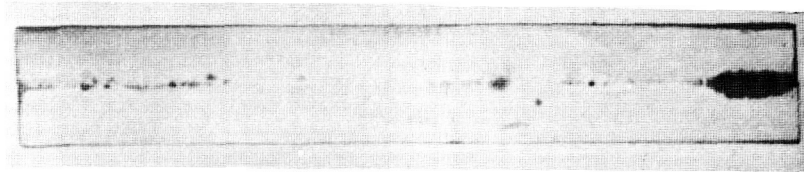
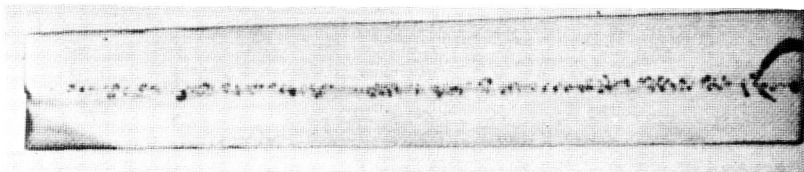


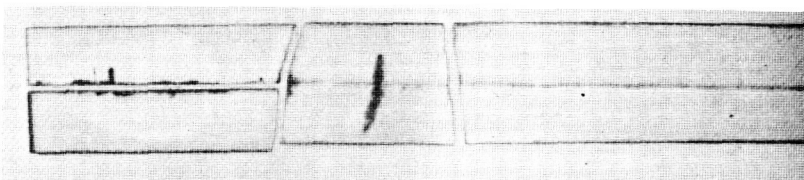
Figure IX-11. - Method of recording bend test data for analysis (GTA welds shown).



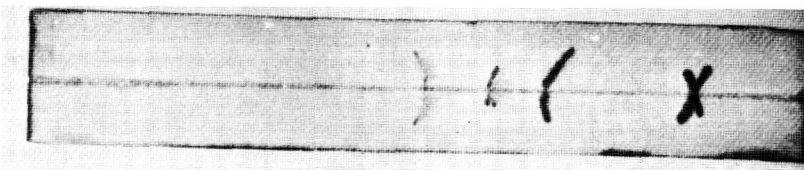
Weld 1; speed, 15 in. /min; 2.98 kJ/in.



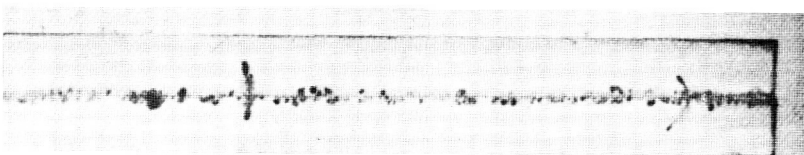
Weld 4; speed, 15 in. /min; 3.24 kJ/in.



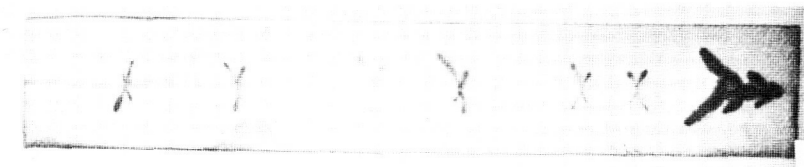
Weld 7; speed, 50 in. /min; 1.19 kJ/in.



Weld 10; speed, 15 in. /min; 3.12 kJ/in.



Weld 11; speed, 50 in. /min; 1.30 kJ/in.



Weld 12; speed, 100 in. /min; 0.76 kJ/in.

Figure IX-12. - Typical dye-penetrant results of electron beam welds in arc cast unalloyed tungsten sheet.

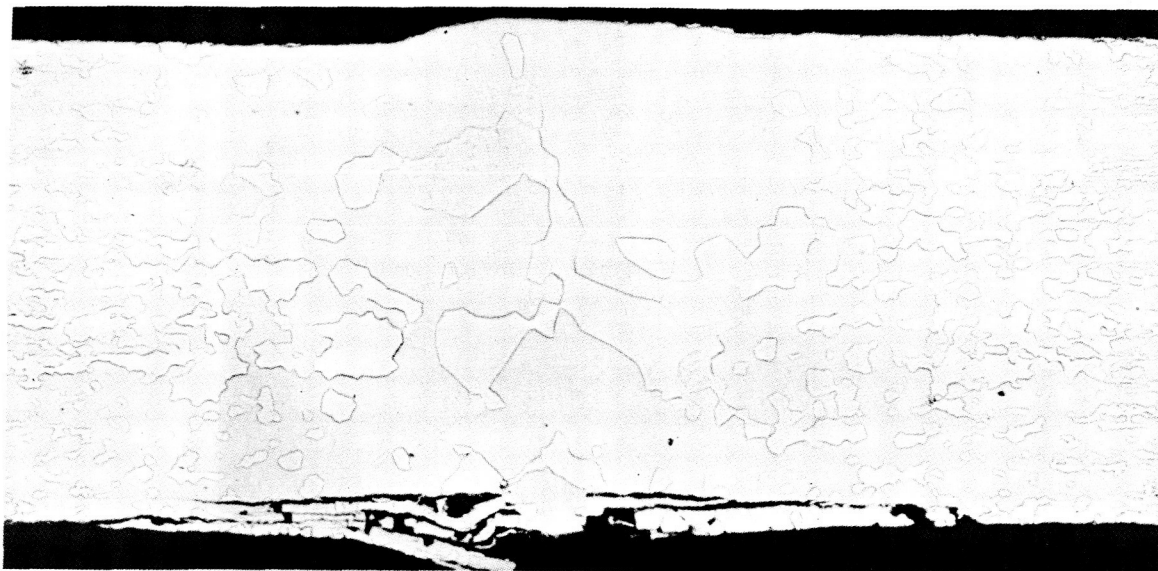


Figure IX-13. - Typical section of electron beam weld in unalloyed tungsten.  $\times 80$ .

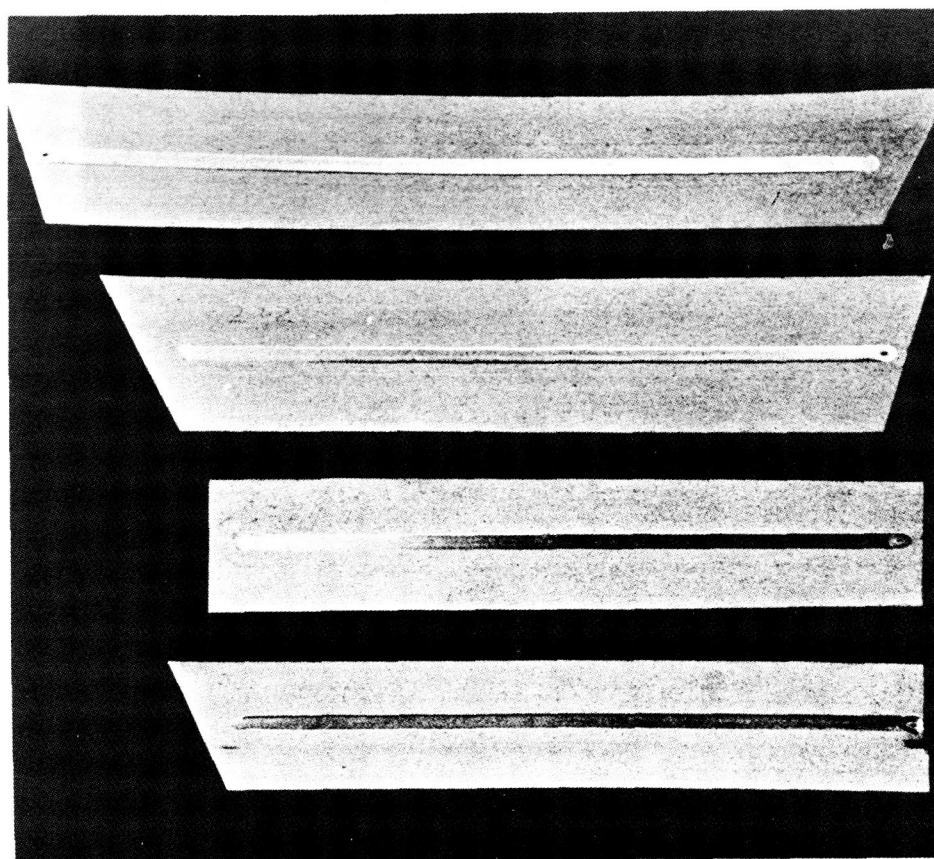


Figure IX-14. - Bead-on-plate GTA welds on 0.030-inch powder metallurgy W-25Re-30Mo alloy sheet.

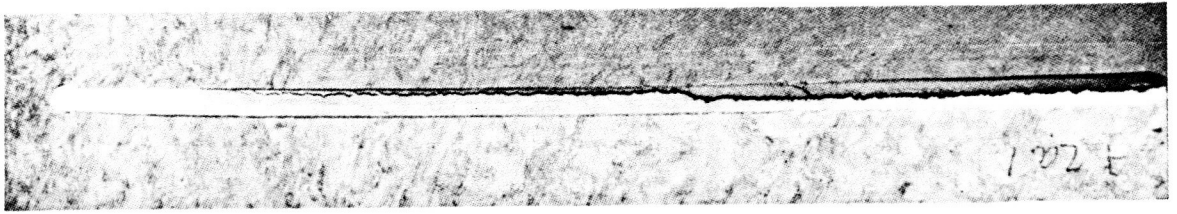
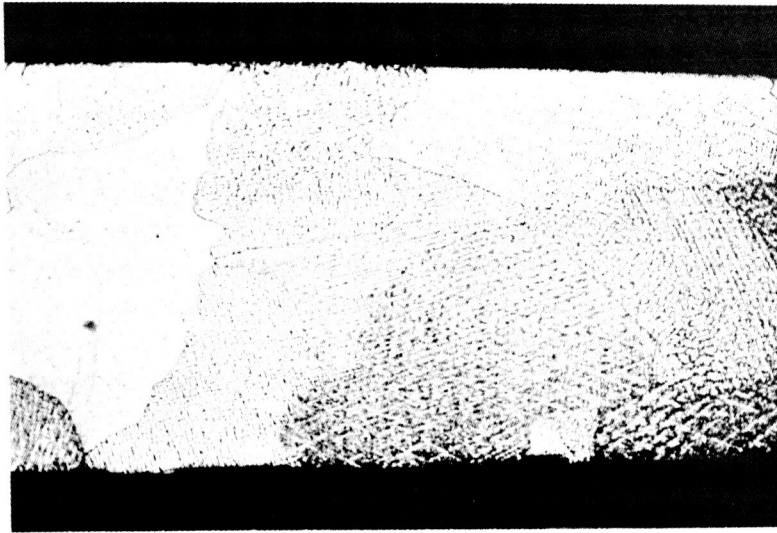


Figure IX-15. - Typical hot tear on bead-on-plate GTA weld on 0.030-inch arc cast W-25Re-30Mo alloy sheet.



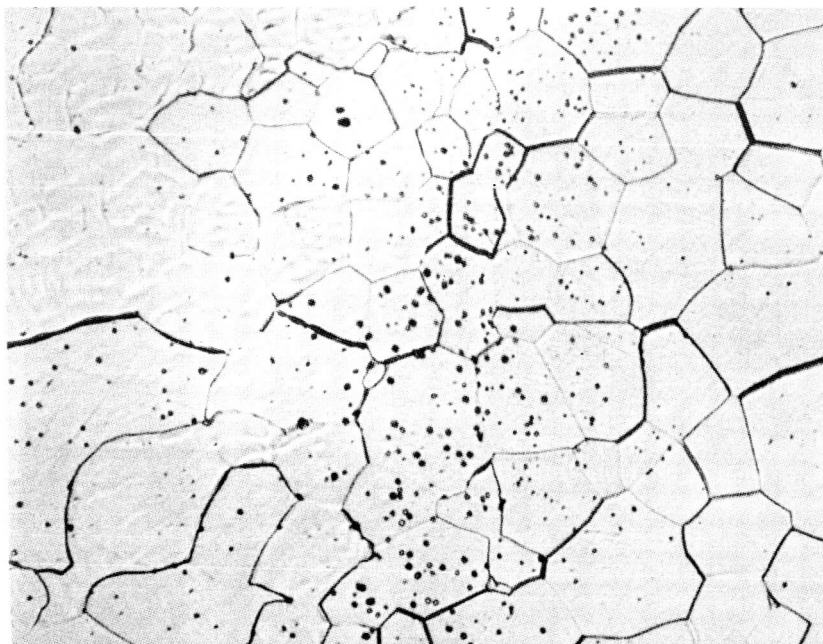
Prepared using 30 lactic- $3\text{HNO}_3$ -1HF (vol. ratio)



Prepared using 9HF-1 $\text{HNO}_3$  (vol. ratio)

Figure IX-16. - Center areas of GTA welds in W-25Re-30Mo sheet showing effect of pickling solution used for joint preparation.  $\times 75$ .



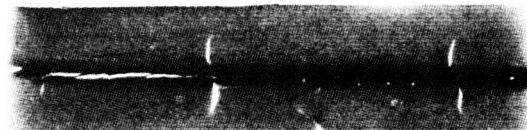
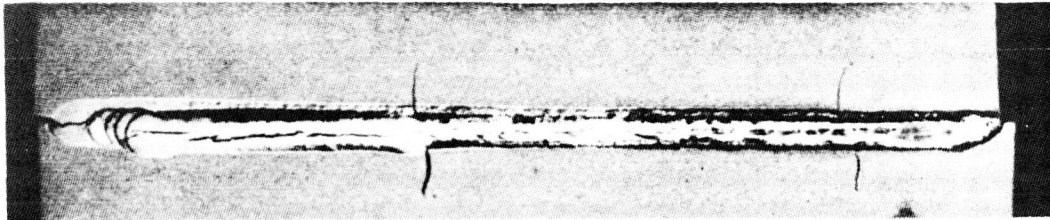


Powder metallurgy

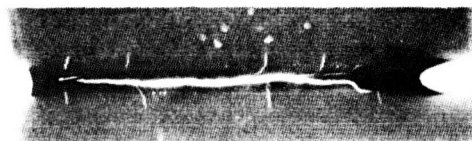
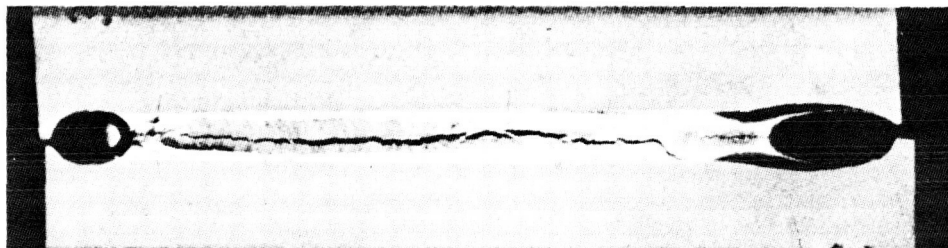


Arc cast

Figure IX-17. - Comparison of typical porosity levels in GTA HAZ welds in powder metallurgy and arc cast W-25Re-30Mo alloy sheet.  $\times 400$ .



500 ppm Oxygen in Weld Atmosphere



1800 ppm Oxygen in Weld Atmosphere

Figure IX-18. - GTA Welds in PM W-25Re-30Mo sheet. Weld atmospheres contaminated with oxygen as indicated.

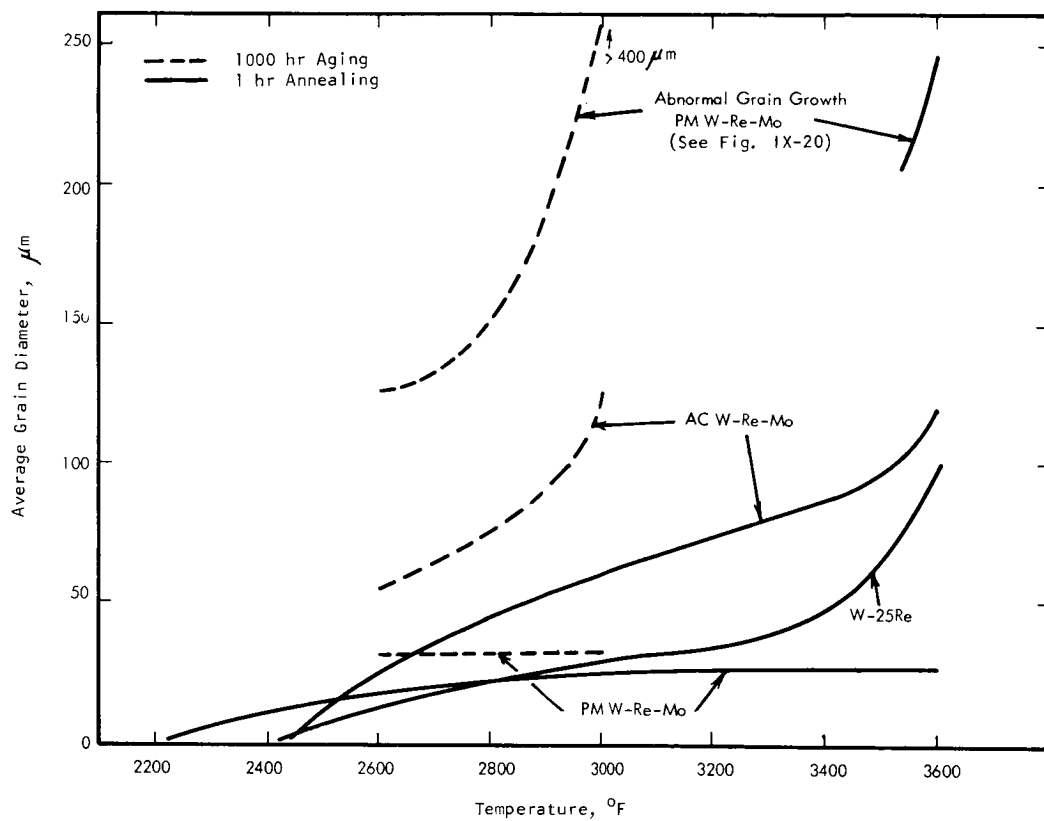
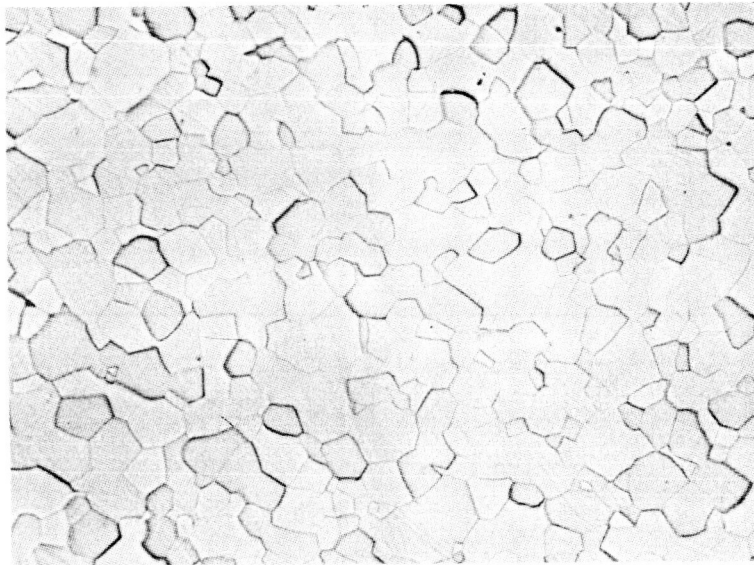
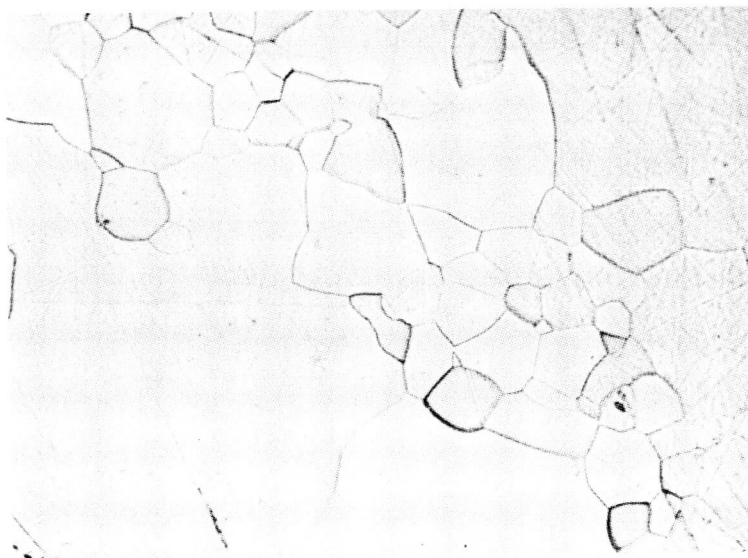


Figure IX-19. - Average grain size as function of 1000 hour aging and 1 hour annealing temperature for tungsten-base alloys.



3400° F



3600° F

Figure IX-20. - Microstructure of powder metallurgy W-25Re-30Mo sheet following 1 hour anneals at temperatures indicated. Abnormal grain growth occurred at 3600° F.  $\times 200$ .